CANADIAN THESES ON MICROFICHE

THÈSES CANADIENNES SUR MICROFICHE

National Library of Canada
Collections Development Branch

Canadian Theses on
Microfiche Service

Ottawa, Canada
K1A 0N4

Bibliothèque nationale du Canada
Direction du développement des collections

Service des thèses canadiennes
sur microfiche

NOTICE

The quality of this microfiche is heavily dependent upon the quality of the original thesis submitted for microfilming. Every effort has been made to ensure the highest quality of reproduction possible.

If pages are missing, contact the university which granted the degree.

Some pages may have indistinct print especially if the original pages were typed with a poor typewriter ribbon or if the university sent us an inferior photocopy.

Previously copyrighted materials (journal articles, published tests, etc.) are not filmed.

Reproduction in full or in part of this film is governed by the Canadian Copyright Act, R.S.C. 1970, c. C-30. Please read the authorization forms which accompany this thesis.

AVIS

La qualité de cette microfiche dépend grandement de la qualité de la thèse soumise au microfilmage. Nous avons tout fait pour assurer une qualité supérieure de reproduction.

S'il manque des pages, veuillez communiquer avec l'université qui a conféré le grade.

La qualité d'impression de certaines pages peut laisser à désirer, surtout si les pages originales ont été dactylographiées à l'aide d'un ruban usé ou si l'université nous a fait parvenir une photocopie de qualité inférieure.

Les documents qui font déjà l'objet d'un droit d'auteur (articles de revue, examens publiés, etc.) ne sont pas microfilmés.

La reproduction, même partielle, de ce microfilm est soumise à la Loi canadienne sur le droit d'auteur, SRC 1970, c. C-30. Veuillez prendre connaissance des formules d'autorisation qui accompagnent cette thèse.

THIS DISSERTATION HAS BEEN MICROFILMED EXACTLY AS RECEIVED

LA THÈSE A ÉTÉ MICROFILMÉE TELLE QUE NOUS L'AVONS REÇUE

Canada

NL 339 (r. 85/09)

0-315-19426-4

National Library of Canada
Bibliothèque nationale du Canada

Canadian Theses Division
Division des thèses canadiennes

(101)

Ottawa, Canada
K1A 0N4

67354

PERMISSION TO MICROFILM — AUTORISATION DE MICROFILMER

• Please print or type — Écrire en lettres moulées ou dactylographier

Full Name of Author — Nom complet de l'auteur

Thomas Rockwell Mackie

Date of Birth — Date de naissance	Country of Birth — Lieu de naissance
October 27, 1954	Canada

Permanent Address — Résidence fixe

6117 - 5th Avenue
Regina, Saskatchewan
S4T 6R8

Title of Thesis — Titre de la thèse

A Study of Charged Particles and Scattered Photons in Megavoltage X-ray Beams

University — Université

University of Alberta

Degree for which thesis was presented — Grade pour lequel cette thèse fut présentée

Ph.D. (Physics)

Year this degree conferred — Année d'obtention de ce grade	Name of Supervisor — Nom du directeur de thèse
1984	J.W. Scrimger

Permission is hereby granted to the NATIONAL LIBRARY OF CANADA to microfilm this thesis and to lend or sell copies of the film.

The author reserves other publication rights, and neither the thesis nor extensive extracts from it may be printed or otherwise reproduced without the author's written permission.

L'autorisation est, par la présente, accordée à la BIBLIOTHÈQUE NATIONALE DU CANADA de microfilmer cette thèse et de prêter ou de vendre des exemplaires du film.

L'auteur se réserve les autres droits de publication; ni la thèse ni de longs extraits de celle-ci ne doivent être imprimés ou autrement reproduits sans l'autorisation écrite de l'auteur.

Date	Signature
Oct 17, 1984	T R Mackie

THE UNIVERSITY OF ALBERTA

"A STUDY OF CHARGED PARTICLES AND SCATTERED PHOTONS IN MEGAVOLTAGE X-RAY BEAMS"

by

THOMAS ROCKWELL MACKIE

(C)

A THESIS

SUBMITTED TO THE FACULTY OF GRADUATE STUDIES AND RESEARCH

IN PARTIAL FULFILMENT OF THE REQUIREMENTS FOR THE DEGREE

OF DOCTOR OF PHILOSOPHY

DEPARTMENT OF PHYSICS

EDMONTON, ALBERTA

FALL 1984

THE UNIVERSITY OF ALBERTA

"A STUDY OF CHARGED PARTICLES AND SCATTERED PHOTONS IN MEGAVOLTAGE X-RAY BEAMS"

by

THOMAS ROCKWELL MACKIE

A THESIS

SUBMITTED TO THE FACULTY OF GRADUATE STUDIES AND RESEARCH

IN PARTIAL FULFILMENT OF THE REQUIREMENTS FOR THE DEGREE

OF DOCTOR OF PHILOSOPHY

DEPARTMENT OF PHYSICS

EDMONTON, ALBERTA

FALL 1984

ALBERTA CANCER BOARD

CROSS CANCER INSTITUTE
NORTHERN ALBERTA CANCER PROGRAM

November 13, 1984

Dr. T.R. Mackie
Dept. of Medical Physics
Allan Blair Memorial Clinic
4101 Dewdney Avenue
Regina, Saskatchewan
S4T 7T1

Dear Rock,

Please regard this letter as an assignment of copyright to you of all publications which we have co-authored.

Sincerely,

J.W. Scrimger, Ph.D.
Senior Medical Physicist
Dept. of Medical Physics
Cross Cancer Institute

THE UNIVERSITY OF ALBERTA

RELEASE FORM

NAME OF AUTHOR: THOMAS ROCKWELL MACKIE

TITLE OF THESIS: "A STUDY OF CHARGED PARTICLES AND SCATTERED PHOTONS IN MEGAVOLTAGE X-RAY BEAMS"

DEGREE FOR WHICH THESIS WAS PRESENTED: DOCTOR OF PHILOSOPHY

YEAR THIS DEGREE GRANTED: 1984

Permission is hereby granted to THE UNIVERSITY OF ALBERTA LIBRARY to reproduce single copies of this thesis and to lend or sell such copies for private, scholarly or scientific research purposes only.

The author reserves other publication rights, and neither the thesis nor extensive extracts from it may be printed or otherwise reproduced without the author's written permission.

T R Mackie

PERMANENT ADDRESS:

10918 129 STREET

EDMONTON, ALBERTA

CANADA T5M 0X9

DATED: JULY 23, 1984.

THE UNIVERSITY OF ALBERTA

FACULTY OF GRADUATE STUDIES AND RESEARCH

The undersigned certify that they have read, and recommend to the Faculty of Graduate Studies and Research, for acceptance, a thesis entitled, "A STUDY OF CHARGED PARTICLES AND SCATTERED PHOTONS IN MEGAVOLTAGE X-RAY BEAMS", submitted by Thomas Rockwell Mackie in partial fulfilment of the requirements for the degree of Doctor of Philosophy in Physics.

.....
Supervisor

.....

.....

.....

.....

.....
External Examiner

Date: JULY 23, 1984

This work is dedicated to:

My parents who brought me here,
and Pamela who kept me here.

ABSTRACT

The 6 MV and 15 MV photon beams produced by linear accelerators were studied for electron and scattered photon contamination. Tissue maximum ratios with and without accessories in the field indicate the presence of contamination. The surface dose was found to be attributable to contamination electrons and backscatter photons. The surface dose produced by accessories was reduced when electron filters made of materials with high atomic numbers were placed underneath the accessory. The surface dose for rectangular fields was measured and the equivalent squares for the surface dose were derived from these measurements. The 15 MV accelerator had a Gaussian lateral distribution, a linear dependence on field width for square fields and an inverse square dependence on distance from the bottom of the fixed head assembly. This geometrical dependence is consistent with the proposal that the field flattening filter is the main source of electron contamination at large field sizes when accessories are present. The electron contamination at 6 MV could not be localized to the same location. A permanent magnet was used to sweep electrons from the field. In general, electron contamination measured by a probe was produced by material close to the probe. A penetration curve for electron and scattered photon contamination was produced utilizing the linearity of dose with respect to field width. The derived contamination curve was similar to the measured build-up curve outside the field. The phantom generated tissue maximum ratio, obtained by subtracting the contamination contributions showed no dependence on

field size, source-to-probe distance or presence of accessories. The phantom generated tissue maximum ratio was verified independently by Monte Carlo simulation. The clinical aspects of the study and the requirements for an electromagnet to sweep a large field completely free of contaminant electrons were discussed.

Volume 2 is introduced with a review of dose computation methods for radiotherapy. Several deficiencies were revealed, of which the most important was a failure to account for the dose in situations of electronic disequilibrium. It was shown that the reduced central axis dose in a low-density heterogeneous region was due to electronic disequilibrium. It was also shown that electronic equilibrium never exists near the beam boundary and this gives rise to the beam penumbra for high energy linear accelerator beams.

A dose calculation method based on convolution was introduced which accounts for both the transport of charged particles and scattered photons. Arrays were generated using the Monte Carlo method representing the energy absorbed throughout water-like phantoms from charged particles and scattered radiation set in motion by primary x-ray interactions at one location. The resulting "dose spread arrays" were normalized to the collision fraction of the kinetic energy released by the primary x-rays. These arrays are convolved with the relative primary fluence interacting in a phantom to obtain 3-dimensional dose distributions. The method gives good agreement for the dose in electronic disequilibrium situations such as the build-up region, near beam boundaries and near low-density heterogeneities irradiated by beams with small field sizes.

Preface

Volume 1 entitled, "Contamination of Megavoltage X-Ray Beams By Electrons And Scattered Photons", was originally written as a thesis for the partial fulfilment of a Master of Science degree. At the defense of the thesis in September of 1982, it was felt by the examining committee that Volume 1 should be used towards a Doctor of Philosophy degree.

Section 3, in Volume 1, addressed the problem of the transport of charged particles in the build-up region of a unit-density phantom. The committee felt that this Section provided a good foundation for a more complete study of the transport of charged particles generated by photon beams in an inhomogeneous medium. A decision was made to undertake this investigation to complete the thesis. Volume 2 contains the results of this study as well as a method to calculate the primary and scattered dose in heterogeneous media.

It was decided to break the thesis into two Volumes because Volume 1 is a self-contained study of photon beam contamination. The contents of Volume 2 are not referenced in Volume 1. For this reason, the Discussion, Conclusions and Appendices concerning contamination are left in Volume 1. However, in a number of instances, the reader of Volume 2 is referred to Volume 1, therefore, the pagination in Volume 2 is a continuation of Volume 1.

ACKNOWLEDGEMENTS

Many parts of this study were suggested by my supervisor, Dr. John Scrimger. He has given me encouragement, sound advice and has freely shared his experiences in medical physics with me. I have also benefitted from the wisdom and knowledge of the physicists, Dr. Sid Usiskin, Dr. Jerry Battista and Rob Barnett. A special thanks must go to Rick Crilly, Adriano Zenari and David Perry who were always willing to talk through an idea.

Lee Santon and Colin Field eased me into the world of VAX. Linda Fleury patiently typed many early drafts of parts of the thesis. Lorentz Stenger, Frank Dolynchuk, John Issit and Finn Mortensen produced the specialized phantoms and devices used in the study. Sig Labahn instructed me in many aspects of the operation of the accelerators.

The Audio-Visual Department contributed a great deal to this thesis. Gene Brooks patiently drew all the graphs and many of the figures and Karl Liesner produced the excellent photographs.

I would also like to thank the Department of Radiotherapy for the use of their equipment.

This work was sponsored by the Alberta Heritage Foundation for Medical Research, the Provincial Cancer Hospitals Board (Alberta), the Alberta Division of the Canadian Cancer Society and the Physics Department of the University of Alberta.

This work has been dedicated to my wife, Pamela Kosti, because without her it would not have been possible. Not only did she read, correct and immaculately type the manuscript but she also gave me emotional support and guidance. She did not complain about my late laboratory evenings or my abstract absences when physically present.

TABLE OF CONTENTS

Chapter		Page
1.	INTRODUCTION	1
	1.1 Rationale and Introduction to the Study	2
	1.2 Production and Interaction of X-Rays with Matter	4
	1.3 Interaction of Electrons with Matter	15
	1.4 Medical Electron Linear Accelerators	18
	1.5 Ionization Dosimetry	31
	1.6 Review of Previous Work on Contamination of Photon Beams	40
2.	EXPERIMENTAL TECHNIQUES AND RESULTS	49
	2.1 Open Field Build-Up Curves	50
	2.2 Accessory Build-Up Curves	55
	2.3 Filtering the Electron Contamination	64
	2.4 Distance Distribution of the Surface Dose	68
	2.4.1 SPD Dependence of the Surface Dose	68
	2.4.2 Determination of the Apparent Source of Contamination Electrons	68
	2.5 Lateral Distribution of the Surface Dose	74
	2.6 Surface Dose Measurements for Rectangular Fields	78
	2.7 Penetration Curves Outside the Field	81
	2.7.1 Transmission Through the Collimators	81
	2.7.2 Determination of the Penetration Curves Outside the Field	81
	2.8 Increase of Dose with Increasing Field Width	87
	2.8.1 Measurement of the Stem Effect	87
	2.8.2 Increase of Dose with Increasing Field Width	87
	2.9 Determination of the Amount of Photon Backscatter from the Phantom	97
	2.10 Sweeping Electrons from the Field Using a Permanent Magnet	101
	2.10.1 Determination of the Field Distribution of the Magnet	101
	2.10.2 Verifying Electrons are Swept by the Magnet	101
	2.10.3 The Surface Dose with and without the Magnet in Place	108
	2.10.4 Determination of the Penetration Curves of Electron Contamination Produced Between the Target and Magnet	127

TABLE OF CONTENTS (CONT'D)

Chapter — Page

2.11 A Method for Separating Contamination from Phantom Generated Penetration Curves 133

2.11.1 Determination of the Contamination Penetration Curves 133

2.11.2 Determination of the Phantom Generated Build-Up Curves. 135

2.12 Blocking the Primary Beam. 156

2.13 Penetration Curve Outside a Magnetically Swept Field. 160

3. DISCUSSION 162

3.1 Independent Modelling of the Phantom Generated Build-Up Curves. 163

3.1.1 Introduction 163
3.1.2 Data Preparation Programs. 163
3.1.3 Generation of Charged Particles Set in Motion. 164
3.1.4 The Monte Carlo Program. 178
3.1.5 Scattering Angle Transformation. 186
3.1.6 Assigning Dose 190
3.1.7 Results. 192

3.2 The Source and Nature of Contamination 200

3.3 Clinical Use of the Results. 217

4. CONCLUSIONS. 221

4.1 Conclusions. 222

REFERENCES 227

APPENDICES 231

1. Numerical Values of Constants. 232
2. Total and Compton Attenuation Coefficients 233
3. Total Stopping Power of Electrons in Water 234
4. Mean Square Mass Angular Scattering Power of Electrons in Water and Lead 235
5. Listing and Documentation for 'Seprimary.For'. 236
6. Listing and Documentation for 'Buildup3.For' 237
7. Listing and Documentation for 'Normdist.For' 248
8. Listing and Documentation for 'Addose.For' 249
9. Reprint of "Contamination of a 15-MV Photon Beam by Electrons and Scattered Photons" 250

TABLE OF CONTENTS FOR VOLUME 2

Chapter — Page

5. INTRODUCTION TO RADIOTHERAPY DOSE COMPUTATION ... 257

5.1 Statement of Purpose 258
5.2 Electronic Equilibrium 262
5.3 Contour Corrections 273
5.4 Corrections For Tissue Heterogeneity 281

6. MODELLING DOSE USING THE EGS MONTE CARLO CODE ... 295

7. A CONVOLUTION METHOD OF CALCULATING DOSE 308

7.1 Introduction 309
7.2 Primary Dose Spread Arrays 311

7.2.1 Definition of a Primary Dose Spread Array 311
7.2.2 The Generation of Dose Spread Arrays Using the MOCA Monte Carlo Code 311
7.2.3 Results 321

7.3 Scatter Dose Spread Arrays 332
7.4 Convolution Dose Calculation in a Homogeneous Phantom 337
7.5 Extension to Heterogeneous Media 360
7.6 The Spatial Invariance of the Dose Spread Arrays 380
7.7 Comparison with Other Methods and Potential Improvements 384
7.8 Dose in a Non-Water-Like Heterogeneous Phantom 394

8. DISCUSSION AND CONCLUSIONS CONCERNING THE CONVOLUTION METHOD 397

8.1 Discussion 398
8.2 Conclusions 403

REFERENCES 406

APPENDICES 411

10. Listing of the MOCA Monte Carlo Code ... 412
11. Listing of the program Volve.for 429
12. Comparison of Heterogeneous Dose Spread Arrays Calculated by the Convolution Method and by the Monte Carlo Method 441

VITA 460

LIST OF TABLES

Table		Page
1.	Conclusions of a Number of Authors on the Nature and Source of Contamination	48
2.	Surface Normalized Dose and Equivalent Squares for Rectangular Fields at 15 MV	79
3.	Contamination Dose Normalized to the Maximum Contamination Dose at 15 MV	136
4.	Normalized Dose, Tissue Maximum Ratio and Associated Errors for a 15 MV Beam at an SPD of 100 cm for Field Sizes of 3 cm x 3 cm and 4 cm x 4 cm in an Open Field.	141
5.	Normalized Dose, Tissue Maximum Ratio and Associated Errors for a 15 MV Beam at an SPD of 100 cm for Field Sizes of 5 cm x 5 cm and 8 cm x 8 cm in an Open Field	142
6.	Normalized Dose, Tissue Maximum Ratio and Associated Errors for a 15 MV Beam at an SPD of 100 cm for Field Sizes of 10 cm x 10 cm and 12 cm x 12 cm in an Open Field	143
7.	Normalized Dose, Tissue Maximum Ratio and Associated Errors for a 15 MV Beam at an SPD of 100 cm for Field Sizes of 15 cm x 15 cm and 20 cm x 20 cm in an Open Field	144
8.	Normalized Dose, Tissue Maximum Ratio and Associated Errors for a 15 MV Beam at an SPD of 100 cm for a Field Size of 25 cm x 25 cm in an Open Field	145
9.	Normalized Dose, Tissue Maximum Ratio and Associated Errors for a 15 MV Beam at an SPD of 75 cm for a Field Size of 10 cm x 10 cm in an Open Field and with a 0.64 cm Lucite Accessory	146
10.	Normalized Dose, Tissue Maximum Ratio and Associated Errors for a 15 MV Beam at an SPD of 75 cm for a Field Size of 30 cm x 30 cm in an Open Field and with a 0.64 cm Lucite Accessory	147
11.	Normalized Dose, Tissue Maximum Ratio and Associated Errors for a 15 MV Beam at an SPD of 100 cm with a 3.18 cm Lucite Accessory and at an SPD of 140 cm with an Open Field Both at a Field Size of 30 cm x 30 cm	148

Table Page

12. Normalized Dose, Tissue Maximum Ratio and Associated Errors for a 6 MV Beam at an SPD of 100 cm for Field Sizes of 5 cm x 5 cm and 10 cm x 10 cm in an Open Field 149

13. Normalized Dose, Tissue Maximum Ratio and Associated Errors for a 6 MV Beam at an SPD of 100 cm for Field Sizes of 20 cm x 20 cm and 30 cm x 30 cm. 150

14. Normalized Dose, Tissue Maximum Ratio and Associated Errors for a 6 MV Beam at an SPD of 75 cm for a Field Size of 30 cm x 30 cm in an Open Field and with a 0.64 cm Lucite Accessory. 151

15. Normalized Dose, Tissue Maximum Ratio and Associated Errors for a 6 MV Beam with a 3.18 Lucite Accessory in a 30 cm x 30 cm Field at 75 cm SPD and a 10 cm x 10 cm Field at 100 cm SPD 152

16. Surface Normalized Dose with and without a Cerrobond Primary Beam Block Present on the Accessory Tray and the Surface Normalized Dose with the Accessory Tray in Place for a 4 cm x 4 cm Field. 157

17. Difference Between the Primary Beam Blocked and Not Blocked with the Contamination Dose Removed 159

18. Determination of the 6 MV Differential Spectrum from Measured Spectra 167

19. Tissue Maximum Ratios in the Build-Up Region as Predicted by Equation 1.5.16. 208

LIST OF TABLES FOR VOLUME 2

Table Page

20. Parameters for determining the effective attenuation coefficient for 15 MV x-rays 339

LIST OF FIGURES

Figure | Page

1. Diagram of the Compton Effect. 7
2. Narrow and Broad Beam Geometries 12
3. One Oscillation of an Electromagnetic Cavity 19
4. An Electron Buncher. 20
5. Travelling Wave Accelerating Section 22
6. Side-Coupled Standing Wave Accelerating Section. 24
7. A 270^{o} Achromatic Beam-Bending Magnet. 25
8. Treatment Head of a Mevatron -20 Medical Linear Accelerator. 27
9. The Field Defining System. 28
10. A Parallel-Plate Ionization Chamber. 32
11. The Arrangements for Measuring Percent Depth-Dose and Tissue Maximum Ratios. 37
12. Central Axis Open Field Build-Up Curve at 100 cm SPD for a 15 MV Beam 51
13. Central Axis Open Field Build-Up Curves at 100 cm SPD for a 6 MV Beam. 52
14. Comparison Between 6 MV and 15 MV Central Axis Open Field Build-Up Curves. 54
15. Accessory Build-Up Curves at 140 cm SPD for a 15 MV Beam 56
16. Accessory Build-Up Curves at 100 cm SPD for a 15 MV Beam 57
17. Accessory Build-Up Curves at 75 cm SPD for a 15 MV Beam 58
18. Accessory Build-Up Curves at 75 cm SPD for a 6 MV Beam 59
19. Accessory Build-Up Curves at 100 cm SPD for a 6 MV Beam 60

LIST OF FIGURES (CONT'D)

Figure | Page

20. Comparison Between 6 MV and 15 MV Accessory Build-Up Curves at 75 cm SPD. 62

21. Comparison Between 6 MV and 15 MV Accessory Build-Up Curves at 100 cm SPD 63

22. Surface Dose with Electron Filters at 15 MV. 65

23. Surface Dose with Electron Filters at 6 MV 67

24. Distribution of the Surface Dose as a Function of SPD at 15 MV 69

25. Graph Illustrating the Inverse Square Dependence of the Surface Dose on the Distance to the Source of Contamination at 15 MV 72

26. Graph Illustrating the Failure at 6 MV of the Inverse Square Dependence to a Localized Source of Contamination . . . 73

27. Gaussian Distribution of the Surface Dose at 15 MV 75

28. Comparison Between 6 MV and 15 MV of the Lateral Distribution of the Surface Dose at 100 cm SPD 76

29. Transmission Measurements Through the Collimators at 15 MV 82

30. The Experimental Arrangement to Determine the Penetration Curve Outside the Field. 84

31. Penetration Curve at 15 MV Obtained 3 cm Outside of a 30 cm x 30 cm Field 85

32. Penetration Curve at 6 MV Obtained 3 cm Outside of a 30 cm x 30 cm Field 86

33. Linearity of the Surface Dose with Respect to Field Width Under a Variety of Conditions at 15 MV 90

34. Experimental Arrangement to Measure the Increase in Contamination with Increasing Field Width. 91

35. The Increase in ND Versus Field Width for Various Depths in an Open Field at 100 cm SPD for the 15 MV Beam 93

36. The Increase in ND Versus Field Width for Various Depths in an Open Field at 75 cm SPD for the 15 MV Beam 94

LIST OF FIGURES (CONT'D)

Figure — Page

37. The Increase in ND Versus Field Width for Various Depths with a 3.18 cm Lucite Accessory at 100 cm SPD for the 15 MV Beam 95

38. The Increase in ND Versus Field Width for Various Depths in an Open Field at 100 cm SPD for the 6 MV Beam 96

39. The Normalized Dose Due to Backscatter Photons at 6 MV 98

40. The Normalized Dose Due to Backscatter Photons at 15 MV 99

41. The Magnetic Field Distribution of the Permanent Magnet 102

42. The Angle of Deflection of an Electron in a Uniform Magnetic Field and the Measured Deflection of 18 MeV Electrons 103

43. The Set-Up to Verify that Contamination Electrons were Being Swept from the Field of the 15 MV Beam 106

44. Image of the Swept Electron Contamination 107

45. The Magnet Attached to its Holder 109

46. The Magnet Mounted from the Accessory Holder Position 110

47. The Surface Normalized Dose with the Magnet in for Various Conditions at 100 cm SPD for the 15 MV Beam 111

48. Normalized Dose Due to Contamination Produced in Air as a Function of Field Width for an Open Field at 15 MV 113

49. Normalized Dose Due to Contamination Produced in Air as a Function of Field Width for an Open Field at 6 MV 114

50. Normalized Dose Due to Contamination Produced Between the Target and Magnet as a Function of Field Width for an Open Field at 15 MV 116

51. Normalized Dose Due to Contamination Produced Between the Target and Magnet as a Function of Field Width for an Open Field at 6 MV 117

Figure Page

52. Normalized Dose Due to Contamination Produced in Air as a Function of SPD for an Open Field at 15 MV 119

53. Normalized Dose Due to Contamination Produced Between the Target and Magnet as a Function of SPD for an Open Field at 15 MV. 120

54. Normalized Dose Due to Contamination Produced in Air as a Function of SPD for an Open Field at 6 MV. 121

55. Normalized Dose Due to Contamination Produced Between the Target and Magnet as a Function of SPD for an Open Field at 6 MV 122

56. Dependence of the Dose Produced Between the Target and Magnet on the Inverse Square of the Distance from the Apparent Source with the Cross-Hair Tray in Place at 15 MV 123

57. Dependence of the Dose Produced Between the Target and Magnet on the Inverse Square of the Distance from the Apparenet Source with the Cross-Hair Tray in Place at 6 MV. 124

58. Dependence of the Dose Produced Between the Target and Magnet on the Inverse Square of the Distance from the Apparent Source with the Cross-Hair Tray Not in Place at 15 MV 125

59. Central Axis Penetration Curve for Electron Contamination Produced Between the Target and Magnet by the 15 MV Beam. 128

60. Penetration Curve for Electron Contamination Produced Between the Target and Magnet Measured Outside the Field of a 15 MV Beam 129

61. Central Axis Penetration Curve for Electron Contamination Produced Between the Target and Magnet by the 6 MV Beam 130

62. Comparison Between the 15 MV and 6 MV Contamination Produced Between the Target and Magnet. 131

63. Contamination Penetration Curve Determined by the Increase in Dose in a Limited Phantom as a Function of Field Width for a 15 MV Beam 137

Figure Page

64. Contamination Penetration Curve Determined by the Increase in Dose in a Limited Phantom as a Function of Field Width for a 6 MV Beam 138

65. The Phantom Generated Output Factor Compared to the Total Output Factor at 6 MV. 154

66. The Phantom Generated Output Factor Compared to the Total Output Factor at 15 MV 155

67. The Scattered Photon Contamination Build-Up Curve Obtained Outside a Magnetically Swept 15 MV Field. 161

68. The Determination of the Zenith Scattering Angle 165

69. The Smoothed and Unsmoothed Unnormalized Primary Photon Number Spectrum at 6 MV 169

70. The Smoothed and Unsmoothed Unnormalized Primary Photon Number Spectrum at 15 MV. 170

71. The Flow Chart for Subroutine Impulse. 172

72. The Angular Distribution of Charged Particles Set in Motion by a 15 MV Photon Beam. 179

73. The Flow Chart for the Monte Carlo Section of the Main Program Buildup3.For. 182

74. Comparison Between the Monte Carlo Program and Spencer's Analytic Technique 187

75. Relationship between Scattering Angles in the Particle and Phantom Coordinate Systems 189

76. Distribution of Dose in a Semi-Infinite Water Phantom due to Electrons Set in Motion in the Top 0.1 cm Slab by a 6 MV Photon Beam. 193

77. Distribution of Dose in a Semi-Infinite Water Phantom due to Electrons Set in Motion in the Top 0.1 cm Slab by a 15 MV Photon Beam. 194

78. Comparison between Experiment and Computer Modelling of the Phantom Generated TMR Curve at 6 MV 198

79. Comparison between Experiment and Computer Modelling of the Phantom Generated TMR Curve at 15 MV. 199

80. Comparison between Various Penetration Curves at 15 MV 210

81. Comparison between Various Penetration Curves at 6 MV. 212

LIST OF FIGURES FOR VOLUME 2

Figure		Page
82.	The state of longitudinal equilibrium in a heterogeneous phantom	263
83.	Lateral electronic equilibrium in a homogeneous phantom	266
84.	Lateral electronic equilibrium in a heterogeneous phantom	268
85.	The experimental set-up to measure the inhomogeneity correction factor	270
86.	The correction factor, for the experimental set-up illustrated in Figure 85	271
87.	Geometry to take into account contour corrections	274
88.	The definition of the zero-area TAR and the scatter-air-ratio	278
89.	The geometrical parameters required for the Batho or power-law method	283
90.	An illustration of O'Connor's theorem	284
91.	In the equivalent TAR method, the 3-dimensional electron density information is "coalesced" into one cross-sectional slice	288
92.	The measurement of the perturbation of dose by a polystyrene annulus placed in a water tank	292
93.	The dose at point P gets a dose contribution from an annulus by "revolving" a pencil dose distribution about point P	298
94.	The measured TMR is compared to the EGS calculation of the TMR	299
95.	A comparison between pencil beam isodose curves in homogeneous and heterogeneous phantoms	302
96.	A comparison of measured inhomogeneity correction factors and ones calculated using the EGS Monte Carlo code	304
97.	A comparison between the calculated profiles of KERMA and dose for a heterogeneous and a homogeneous phantom	305

LIST OF FIGURES FOR VOLUME 2 (CONT'D)

Figure		Page
98.	A comparison between dose and KERMA correction factors for the 15 MV spectrum and its spectral components	307
99.	Primary photons interact in the interaction voxel and the charged particles set in motion are followed through the phantom	312
100.	Flow chart for photon transport part of MOCA	314
101.	Flow chart for the part of MOCA dealing with the type of photon interaction	315
102.	Flow chart for the charged particle transport part of MOCA	316
103.	The Compton differential cross-section as function of kinetic energy	318
104.	The choice of the kinetic energy for a Compton recoil electron	319
105.	The choice of the kinetic energy for a pair production charged particle set in motion	320
106.	A comparison of components of the percent dose predicted by MOCA and EGS for Cobalt-60 photons	322
107.	A comparison of components of the percent dose predicted by MOCA and EGS for 5 MeV photons	323
108.	Primary dose spread arrays for 15 MV photons for gravimetric densities of 1.0, 0.8, and 0.6 when the voxel dimension is 1cm	324
109.	Primary dose spread arrays for 15 MV photons for gravimetric densities of 0.4 and 0.2 when the voxel dimension is 1cm	325
110.	Primary dose spread arrays for 6 MV and Co-60 photons	328
111.	Primary dose spread array for 15 MV photons for a gravimetric density of 0.2 when the voxel dimension is 5cm	330
112.	Truncated first scatter (TFS) dose spread array for 15 MV photons	334

Figure Page

113. Residual first and multiple scatter (RFMS) dose spread array for 15 MV photons 335

114. Illustration of the dose contribution from the interaction point of view 338

115. The variation of the effective attenuation coefficient as a function of depth 341

116. The variation of the measured effective attenuation coefficients as a function of nominal beam energy .. 342

117. Illustration of the dose contribution from the the dose deposition point of view 346

118. Measured and calculated TMR's for a 15 MV beam as a function of depth along the central axis 349

119. Measured and calculated percent depth-dose data for a 6 MV beam as a function of depth along the central axis 350

120. Measured and calculated dose profiles at dmax for a 15 MV beam 351

121. Dose profiles at dmax in homogeneous phantoms with various densities 352

122. The relative primary fluence profile for 15 MV beam wedges and the fluence profile used to obtain the calculated isodose curve in Figure 123 .. 354

123. The calculated isodose curve for the fluence profile shown in Figure 122 and the measured isodose curve for a 60 degree wedge for a 15 MV beam 355

124. The measured dose profile at a depth of 5 cm when a shield is placed in the 15 MV beam 357

125. The bar shield represented by three fields 359

126. Components of the percent depth dose in a homogeneous water phantom predicted by MOCA for a 6 MV beam 361

127. Components of the percent depth dose in a heterogeneous phantom predicted by MOCA for a 6 MV beam 362

Figure Page

128. Determination of the average density between the interaction and dose deposition voxels 364

129. Ray tracing is performed by sampling the density between the interaction and dose deposition voxels 366

130. Schematic representation of the slab phantoms tested to verify the approximations used in determining the dose in heterogeneous phantoms 370

131. The experimental and measured TMR correction factor for a 15 MV 5cm x 5cm beam 373

132. The experimental and measured TMR correction factor for a 15 MV 10cm x 10cm beam 374

133. The calculated homogeneous and heterogeneous TMR profile for a 15 MV 376

134. A comparison of separating the task of determining the wedge dose distribution and calculating an inhomogeneity correction factor and performing the calculation in one step 378

135. The dose spread array should be tilted to simulate the dose deposition from a divergent primary pencil beam interacting at i,j,k 382

136. A comparison of the convolution method with existing dose calculating methods 386

137. A flow chart of the host computer calculations required if an array processor is used to perform part of the convolution calculations 390

138. A flow chart of the array processor calculations ... 391

139. The part of an average density array calculated for one beam, that intersects with the average density array of another beam, may be reused by the second beam 392

140. The flow chart of the determination of the dose spread array and primary attenuation coefficient based on the transmission spectrum of a linear accelerator 401

VOLUME 1

CONTAMINATION OF MEGAVOLTAGE X-RAY BEAMS BY ELECTRONS AND SCATTERED PHOTONS

1. INTRODUCTION

> The errors of definitions
> multiply themselves accordingly
> as the reckoning proceeds;
> and lead men into absurdities,
> which at last they cannot avoid;
> without reckoning anew
> from the beginning.
>
> Thomas Hobbs

1.1 Rationale and Introduction to the Study

Megavoltage photon beams are the radiation modality most often used in the treatment of cancer by radiotherapy. Photons produced by medical linear accelerators have become the most important method of delivery of these beams.*

Megavoltage photon beams become contaminated with relativistic electrons and scattered photons. An understanding of the role of electron and scattered photon contamination is required to characterize dosimetry in the build-up region. Clinically, high energy x-ray build-up produces a skin-sparing effect and contamination tends to reduce this effect.

The Cross Cancer Institute in Edmonton, Alberta employs three Siemens linear accelerators, two of which operate at 6 MV photons and one which delivers a 15 MV photon beam. These accelerators have a very similar design so an opportunity existed to compare and contrast the contamination at two different nominal energies.

The dependence of position inside and outside the photon beam, distance from the source of primary photons and cross-sectional dimensions (field size) of the beam on the nature and amount of contamination was investigated. Accessories were placed in the path of the beam to determine their effect on contamination.

The photon beam was passed through the poles of a permanent magnet to sweep the contamination electrons out of the beam. The depth of penetration of the contamination electrons was determined by comparing dose measurements at depth in a phantom with and without the magnet in place.

* Cobalt-60 isotope sources and betatrons can deliver megavoltage photon beams as well.

The depth of penetration for the electron and scattered photon components was determined utilizing the increase in dose with respect to the field size of the beam. The tissue maximum ratio (TMR) in the build-up region of the phantom generated component was obtained by subtraction of the contaminant contribution.

A knowledge of the nature of the primary photon component of the beam is important to the clinical use of such a photon beam because most treatment planning systems isolate the primary from the scattered photon component of dose. The validity of the phantom generated build-up curve, as obtained by subtraction of the contamination fraction, was verified by computer modelling the primary photon contribution.

The nature and sources of electron and scattered photon contamination, based on the experimental and calculated results, is discussed in detail.

The role in clinical radiotherapy of electromagnets to sweep electron contamination from the field, and electron "filters" to scatter electron contamination, is discussed briefly.

1.2 Production and Interaction of X-Rays with Matter

Megavoltage photons are packets of energy exceeding 1 million electron volts (MeV) each.* Although photons have dual wave and particle properties, photons (as their name implies) in radiation physics, are treated as if they were particles.

X-rays are photons produced by the interaction of charged particles with matter. In commercial x-ray equipment each photon is produced by the interaction of a relativistic electron with an atomic electron or nucleus of a target material. This process is called bremsstrahlung. The differential cross-section with respect to the photon energy, $h\nu$, for bremsstrahlung production, $\frac{d\sigma_{brem}}{d(h\nu)}$, from a charged particle interacting with an atomic nucleus is given by:

$$\frac{d\sigma_{brem}}{d(h\nu)} = \frac{e^2}{\hbar c}\left\{\frac{e^2}{m_o c^2}\right\}^2 Z^2 \frac{T+m_o c^2}{Th\nu} B \qquad (1.2.1)$$

where e is the electric quantum of charge

$\hbar$ is Plank's constant $\hbar = (h/2\pi)$

m_o is the charged particle mass

c is the speed of light

Z is the atomic number of the target nucleus

T is the charged particle kinetic energy

$h\nu$ is photon energy

$B = B(Z, h\nu/T)$ is a dimensionless quantity from quantum electrodynanic theory and is of the order of unity (1)

(Appendix 1 lists numerical values of physical constants).

* 1 MeV = 1.602×10^{-13} J

The effect of interactions with atomic electrons can approximately by taken into account by replacing the factor Z^2 in Eqn. 1.2.1 by $Z(Z+1)$. The second order dependence of the cross-section on Z means that high atomic number materials are the most efficient targets for the production of bremsstrahlung. The inverse square dependence on charged particle mass explains why electron beams are always the accelerated charged particles used in commercial x-ray devices.

The number of photons produced by bremsstrahlung per photon energy intervals at a given electron energy is proportional to Eqn. 1.2.1 and so is proportional to $1/h\nu$. Therefore, the value of the photon number spectrum for bremsstrahlung produced by monoenergetic electrons is greater for lower energies. In the practical situation the electron beam interacting with the target is not monoenergetic. The initial energy of electrons has a small spread. More importantly, as the electrons interact with a target of finite thickness they lose energy as they traverse it. This results in fewer high energy photons and more lower energy photons than predicted using a "thin-target" bremsstrahlung approximation so the spectrum is strongly peaked at low photon energy. Consequently, the nominal megavoltage designation of photon sources produced by bremsstrahlung refers to the maximum photon energy of the beam.

With minor exceptions the interaction of photons with matter occurs via the photoelectric effect, Compton effect and pair production.

In the photoelectric process a photon is completely absorbed by an atom which becomes ionized by ejecting an electron. The photon energy is almost completely shared between the kinitic energy of the electron and the binding energy of the electron. Very little kinetic

energy is given to the ionized atom but most of the photon momentum is transferred to the atom. The probability of interaction is highest when the photon energy is near to but greater than an electron binding energy. For this reason, the photoelectric absorption probability for an element is discontinuous at the atomic shell binding energies. The interaction of the K-shell electrons contribute about 80% to the atomic cross-section. To a first approximation, the dependence of the atomic cross-section, $_{a}T$, on Z and incident photon energy has the form (1):

$$_{a}T \propto \frac{Z^{n}}{(h\nu)^{3}} \qquad (1.2.2)$$

where n is found empirically to vary between 4.0 and 4.6 depending on the photon energy. The photoelectric effect is the dominant mode of interation at low x-ray energies in high atomic number materials.

At intermediate photon energies the Compton effect dominates*. In the Compton effect an incoming photon interacts with an electron. The photon is absorbed and another photon with a lower energy is created. The electron recoils with an energy representing almost all of the difference between the incoming and outgoing photon. The outgoing photon, usually termed the scattered photon, and recoil electron directions are in the same plane as the incoming photon direction. The directions of the scattered photon, ϕ, and recoil electron, θ, shown in Figure 1, are given by (2):

* The Compton effect is the most important process from 30 KeV to 20 MeV in water and from 600 KeV to 4 MeV in lead (9).

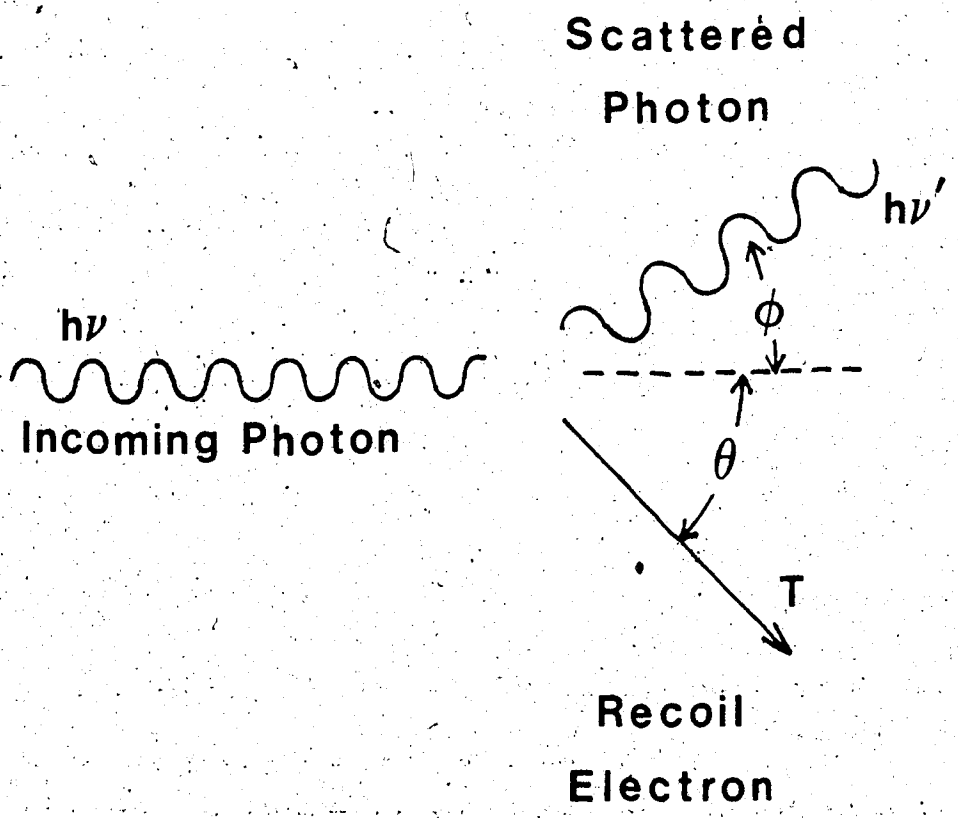

Figure 1. The Compton effect is an interaction of a photon with energy, hν, with an electron at rest. A scattered photon with energy, hν', and a recoil electron with kinetic energy, T, result from the interaction.

$$\cos\phi = 1 - \frac{T}{\alpha_o(h\nu - T)} \qquad (1.2.3)$$

$$\tan\theta = \frac{1}{(1+\alpha_o)\tan(\phi/2)} \qquad (1.2.4)$$

where $\alpha_o = \frac{h\nu}{m_o c^2}$

Equations 1.2.3 and 1.2.4 were derived from considerations of conservation of energy and momentum. Equations 1.2.3 and 1.2.4 suggest that the scattered photon and recoil electron directions are forward peaked at high incident photon energy. Scattered photons, each possessing a direction different from the incident primary photon direction, degrade the collimation of the primary photon beam.

The differential cross-section with respect to recoil electron energy for the Compton interaction, $d\sigma/dT$, is given by (3):

$$\frac{d\sigma}{dT} = \pi r_o^2 m_o c^2 C(h\nu, T) \qquad (1.2.5)$$

$$C(h\nu,T) = \frac{1}{(h\nu-T)^2}\left\{\left[\frac{m_o c^2 T}{(h\nu)^2}\right]^2 + 2\left[\frac{h\nu-T}{h\nu}\right]^2 + \frac{h\nu-T}{(h\nu)^3}\left[(T-m_o c^2)^2 - (m_o c^2)^2\right]\right\} \qquad (1.2.6)$$

where $r_o = \frac{e^2}{m_o c^2}$

Klein and Nishina in deriving the above equations assumed that the electron is originally at rest and the binding energy of the electron to the atom is negligible compared to the energies of the primary and scattered photon and recoil electron. Both of these assumptions are equivalent to assuming a free electron at rest in the laboratory frame. These assumptions result in the total Compton atomic cross-

section, $_a\sigma_t$, being proportional to the number of electrons in the atom, i.e., proportional to Z.

The interaction of a photon with the Coulomb field of a charged particle sometimes causes the photon to disappear with the creation of an electron and positron. Consequently, the energy threshold for this interaction is equal to the rest mass of the pair of 1.022 MeV. The remaining photon energy released is transformed into kinetic energy of the charged particles. When the Coulomb field is due to a nucleus, the process is called pair production. Triplet production is when an atomic electron, rather than a nucleus, is involved in the interaction. In this case, the atomic electron recoils with a considerable fraction of the available kinetic energy; consequently, the threshold for triplet production is higher than that of pair production.

The differential cross-section for the pair production interaction with respect to charged particle (electron or positron) energy, $d\pi/dT$, is given by (4):

$$\frac{d\pi}{dT} = 4\alpha_o r_o^2 \frac{Z}{h\nu} P(h\nu,T) \qquad (1.2.7)$$

$P(h\nu,T)$ is the kinetic energy dependent part of the differential cross-section which can be expressed in a compact form if an energy parameter, v, is defined (4):

$$v = \frac{T+m_o c^2}{h\nu} \qquad (1.2.8)$$

Therefore, v is the ratio of total charged particle energy compared to the photon energy.

$$P(h\nu,v) = \left[v^2 + (1-v)^2 + \frac{2v}{3}(1-v)\right]\left[\ln\left(\frac{2E}{m_o c^2}v(1-v)\right) - \frac{1}{2} - c(\gamma)\right] \qquad (1.2.9)$$

where $c(\gamma)$ is a dimensionless quantity usually much less than 1 which decreases rapidly with increasing γ. γ is the dimensionless screening parameter in the Fermi-Thomas model of the atom and is given by (4):

$$\gamma = 100 \frac{m_o c^2}{h\nu} \frac{v}{1-v} Z^{-1/3} \qquad (1.2.10)$$

In low Z materials and for megavoltage energies less than 20 MeV, the parameter, $c(\gamma)$, may be assumed to be zero. Triplet production may be included by replacing Z in Equation 1.2.7 with Z+1.

The root mean angle between the direction of a secondary charged particle and the primary photon is given by (4):

$$\left(\overline{\theta^2}\right)^{1/2} = q(T,h\nu,Z) \frac{\ell n\ \alpha_o}{\alpha_o} \qquad (1.2.11)$$

where $q(T,h\nu,Z)$ is of the order unity and is given in Appendix 1.

The total atomic pair production cross-section, $_a\pi$, is proportional to Z^2 so high atomic number materials have a large cross-section.

When a positron and electron get close enough they annihilate liberating their energy. This usually occurs when the positron and electron have little kinetic energy. The rest energy is converted to two 511 KeV photons which are emitted in opposite directions.

Other less important interactions of photons with matter occur such as photodisintegration, Cerenkov radiation, Auger electron production and fluorescence. Of these, fluorescence is the most important, especially in crystal structures. Atoms can be excited due to the passage of x-rays. When the atom returns to its ground state fluorescence radiation is emitted. When the process is delayed long after the initial excitation, the radiation emitted is called phosphorescence.

The total cross-section for a beam of photons interacting in matter depends on the beam geometry. In narrow beam geometry both absorption

and scattering of photons are effective in reducing the intensity at the detector. Figure 2 illustrates a narrow beam of photons interacting in a thin layer of matter, dx, between the incident beam and a small detector. The number of photons that arrive at the detector is given by:

$$N(x) = N(x=0)e^{-\mu_t x} \qquad (1.2.12)$$

μ_t is the total linear attenuation coefficient and is given by:

$$\mu_t = \frac{N_o}{A} \rho ({}_aT + {}_a\sigma + {}_a\pi) \qquad (1.2.13)$$

where N_o = Avagadaro's number

A = molar weight

ρ = physical density

[redacted] ${}_a\sigma$ and ${}_a\pi$ are the photoelectric, Compton and pair production [redacted]ross-sections, respectively.

[redacted]oad-beam geometry assumes that the cross-section of the primary [redacted] beam is wide. Only complete absorption of photons contributes [redacted]he attenuation. Scattering of photons away from the detector are [redacted]ensated by scattering of photons toward the detector. The number [redacted] photons arriving at the detector from a broad beam is given by:

$$\mu_a = \frac{N_o \rho}{A} ({}_aT + {}_a\sigma_a + {}_a\pi) \qquad (1.2.15)$$

where ${}_a\sigma_a$ is the Compton atomic absorption coefficient.

${}_a\sigma_a$ represents the average fraction of the primary energy absorbed by the electron multiplied by the total Compton attenuation coefficient.

$${}_a\sigma_a = \frac{\overline{(h\nu - h\nu')}}{h\nu} {}_a\sigma_t \qquad (1.2.16)$$

where [redacted]' is the energy of the scattered photon. The Compton atom[redacted]cattering coefficient, ${}_a\sigma_s$, is a complementary quantity to ${}_a\sigma_a$:

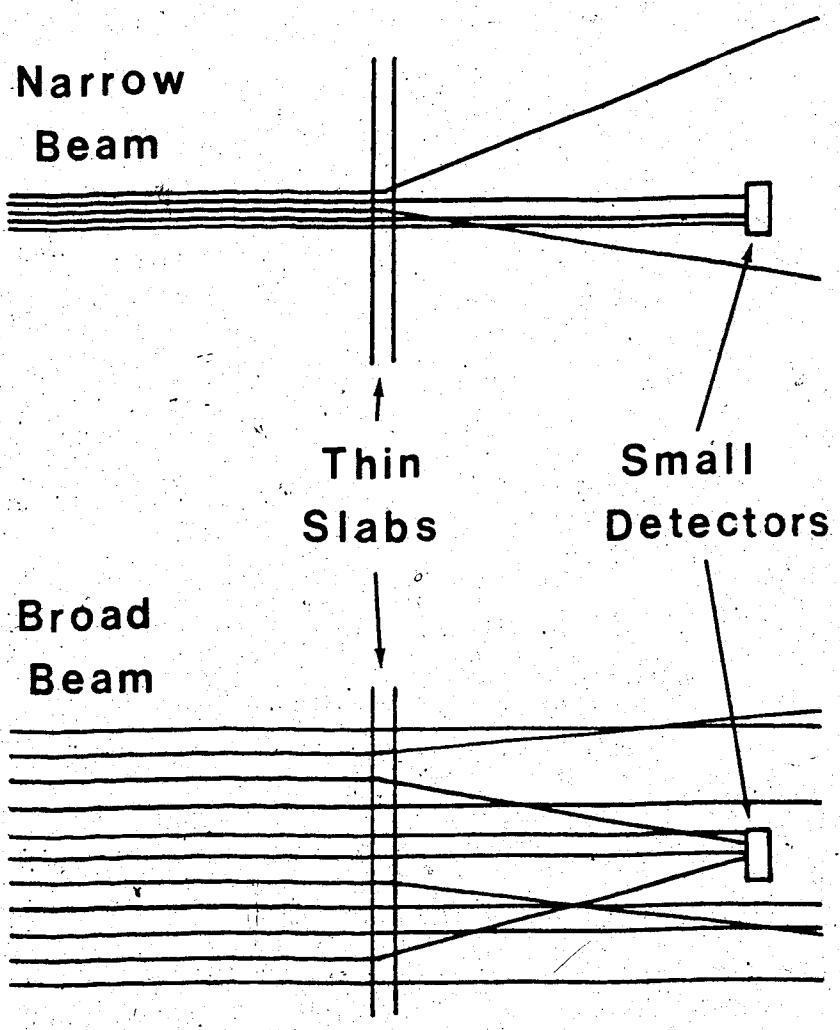

Figure 2. Narrow beam geometry assumes that all scattered photons are not detected. Broad beam geometry assumes that as many photons are scattered toward as away from the detector.

$$a\sigma_s = \frac{h\nu'}{h\nu}\, a\sigma_t = a\sigma_t - a\sigma_s \qquad (1.2.17)$$

At low energies $a\sigma_s$ approaches $a\sigma_t$ and at high energies $a\sigma_a$ contributes most of the attenuation. A listing of total attenuation coefficients, μ_t, and total Compton attenuation coefficients, $a\sigma\frac{N_o\rho}{A}$, for water at selected energies appears in Appendix 2.

The linear coefficients, μ_a and μ_t are often normalized to the physical density, ρ, and then the term "mass" replaces "linear". The mass attenuation coefficient, μ_t/ρ, for ice and water, are the same even though their linear attenuation coefficients are different.

Other linear absorption coefficients are often used. The mass energy transfer coefficient, μ_k/ρ, and the mass energy absorption coefficient, μ_{en}/ρ, are defined analogously to the mass absorption coefficient, μ_a/ρ. μ_a/ρ takes into account the escape of Compton scattered photons. μ_k/ρ takes into account the escape of Compton scattered photons, fluorescence and annihilation photons. μ_{en}/ρ takes into consideration all the escape photons that μ_k/ρ does and includes bremsstrahlung photons. The general formulae for all these coefficients are (9):

$$\mu_x/\rho = \frac{N_o}{A}(a\tau f_x^{\tau} + a\sigma f_x^{\sigma} + a\pi f_x^{\pi}) \qquad (1.2.18)$$

where x can be "k", "a" or "en"

f_x's are conversion factors which weight the average fraction of photon energy that is converted to charged particle kinetic energy taking into account the amount and form of energy that escapes the region of primary interaction.

For example, we have seen earlier that $f_a^{\tau} = f_a^{\pi} = 1$ $\quad f_a^{\sigma} = \frac{h\nu - h\nu'}{h\nu}$

(see Equation 1.2.16)

Sometimes it is convenient to compare the linear attenuation or absorption properties of two types of matter. The equivalent thickness of one substance compared to another is defined to be:

$$(t_{eq})'_t = \frac{\mu_t t}{\mu'_t} \qquad (1.2.19)$$

The primed and unprimed coefficients refer to two different materials.

Since the linear attenuation coefficient depends on energy, the photon spectrum is going to be modified as it passes through matter. This especially affects low energy (below megavoltage energies) spectra because the photoelectric effect is strongly energy dependent. Low energy photons will be depleted faster than high energy photons so the mean energy of the beam will increase. This is known as hardening of the beam.

Hardening is not as important in megavoltage beams because few of the interactions (in low Z materials) occur via the photoelectric effect. Most of the interactions occur via the Compton effect.* Forward scattered photons tend to replenish the low energy part of the spectrum. In addition, the linear attenuation coefficient, over the energy range of megavoltage spectra, does not decrease rapidly with energy (in low Z materials). The photon spectrum of a beam of x-rays is often called the "quality" of the beam.

* If very high energies are employed, pair production could become important. The pair production cross-section increases with increasing energy so the spectrum would be depleted in high energy photons. "Softening" could be said to occur.

1.3 Interaction of Electrons with Matter

For the purpose of medical physics, a free electron can be thought of as a point particle with a rest energy of 511 KeV (rest mass = 9.11×10^{-31} kg) and an electric charge of 1.602×10^{-19} Coulombs.* Free electrons are produced through ionization of atoms. The source of electrons in a linear accelerator is from thermionic emission from a heated filament or indirectly heated cathode. The photoelectric, Compton and pair production interactions also produce free electrons with a considerable kinetic energy.

When an electron traverses through matter the Coulomb interaction between it and atomic electrons produce ionization of the atomic electrons and excitation of the ionized atom. This results in the kinetic energy of the electron, t, being deposited along its path which results in the electron slowing down. The energy lost in any given collision may be as low as a few electron volts or as high as one half of the electron energy. The energy lost per unit mass of matter is defined to be the radiation dose absorbed by the matter. The collision or ionization stopping power is defined to be the average amount of energy lost per unit path length traversed, $\left[dT/dx\right]_{ion}$, and is given by:

$$\left[\frac{dT}{dx}\right]_{ion} = \frac{2\pi e^4}{m_o c^2}\frac{N_o Z_\rho}{A}\left\{\frac{(T+m_o c)^2}{T(T+2m_o c)^2}\ln\left[\left(\frac{T+2m_o c^2}{m_o c^2}\right)\frac{T^2}{I^2}\right] - 1\right\} \qquad (1.3.1)$$

* Since electron beams encountered in medical physics are not polarized, spin effects of free electron can be neglected.

where I is the average ionization potential of the atoms through which the electron is traversing.

The factor $(N_o Z\rho/A)$ has the dimensions of cm^{-3} and represents the number of electrons per cm^3 of a material and is called the electron density.

When T is large ($T>>m_o c^2$) the collisional stopping power increases slowly because the factor in front of the logarithm approaches unity and taking the logarithm modifies the approximate T^3 dependence of its argument. At low energies ($T<<m_o c^2$) the stopping power increases approximately inversely with decreasing electron kinetic energy.

As was discussed in Section 1.2, bremsstrahlung is produced by fast electrons interacting in matter. The stopping power due to bremsstrahlung, often called the radiative stopping power, can be found from the differential bremsstrahlung cross-section (Equation 1.2.1):

$$\left[\frac{dT}{dx}\right]_{brems} = \frac{N_o \rho}{A} \int_o^T h\nu \, d\sigma_{brems} \qquad (1.3.2)$$

The collisional stopping power is much greater than the radiative stopping power except at high electron energy or high atomic number materials. The total stopping power is just the sum of the collisional and radiative stopping powers. Appendix 3 lists the total stopping powers of electrons in water as a function of electron energy.

The average path length, P.L., traversed by the electron is given by:

$$P.L. = \int_{T_{min}}^{T_o} \left[\frac{1}{dT/dx}\right]_{tot} dT + P.L._{residual} \qquad (1.3.3)$$

where T_o is the initial energy

T_{min} is the kinetic energy when the electron can be considered to be almost stopped

$P.L._{residual}$ is the residual path length after the electron has reached an energy, T_{min}.

All electrons do not have the same path length because of the considerable fluctuation of collisional energy loss.

The range of an electron in matter can be defined to be the distance between the point of entry of the electron in matter and the position where it stops. The mean range is always less than the mean path length. The electron having a small mass is easily scattered by the Coulomb field of the atomic nucleus. These interactions are usually elastic so only the electron direction is changed. The multiple scattering of electrons after passing through a path, ℓ, is often assumed to have a Gaussian angular distribution. The mean square mass angular scattering power $\overline{\theta^2}/\rho\cdot\ell$ of a material is a measure of the angular spread of an electron beam. $\overline{\theta^2}/\rho\cdot\ell$ is directly proportional to Z^2/T^2 so the scattering increases rapidly with high atomic number materials and decreasing electron kinetic energy. Appendix 4 lists $\overline{\theta^2}/\rho\cdot\ell$ as a function of kinetic energy for electrons in water and lead.

If an electron source is located at a point and directed in a direction, $\vec{z}$, then the electron fluence, Φ, at a distance, r, from the point compared to the initial electron fluence, Φ_o, after it has traversed a distance, z, into a material is (5):

$$\Phi = \frac{\Phi_o e^{-\theta^2/2\overline{\theta}^2}}{1+\tan^2\theta} \qquad (1.3.4)$$

where θ is the angle between the $\vec{z}$ and $\vec{r}$ directions

$$1+\tan^2\theta = r^2/z^2$$

1.4 Medical Electron Linear Accelerators

The x-ray tube common to all diagnostic x-ray units is the simplest type of electron accelerating device. Potentials larger than 1 MVp across a space of a few centimeters cannot be maintained because dielectric breakdown occurs. In order to produce high kinetic energies, a linear accelerator requires an accelerating electric field travelling in the same direction and velocity as the electrons. In a linear accelerator, an electron can gain several MeV/m, yet the potential difference between any two points at any time can be less than several hundred kVp.

The basic accelerating unit is the microwave resonance cavity. A cavity is merely a microwave waveguide that has been enclosed at the electric field minima points. Figure 3 illustrates the relation between the magnetic and electric fields in a microwave cavity for one complete oscillation. The cavity oscillation can be set up by connecting the cavity to a source of microwave radiation such as a klystron or magnetron.

A klystron comprises two coupled microwave cavities (6) - one called the buncher and the other called the catcher (see Figure 4). The oscillating electric field from a low amplitude, high stability microwave source alternately retards and accelerates a continuous stream of low energy electrons produced by a hot filament. This modulates the velocities of the electrons leaving the buncher. The buncher and collector tubes are joined by a drift tube which allows higher velocity electrons to catch up to lower velocity electrons. When the electrons enter the catcher cavity they generate strong retarding electric fields by inducing charges on the ends of the cavity.

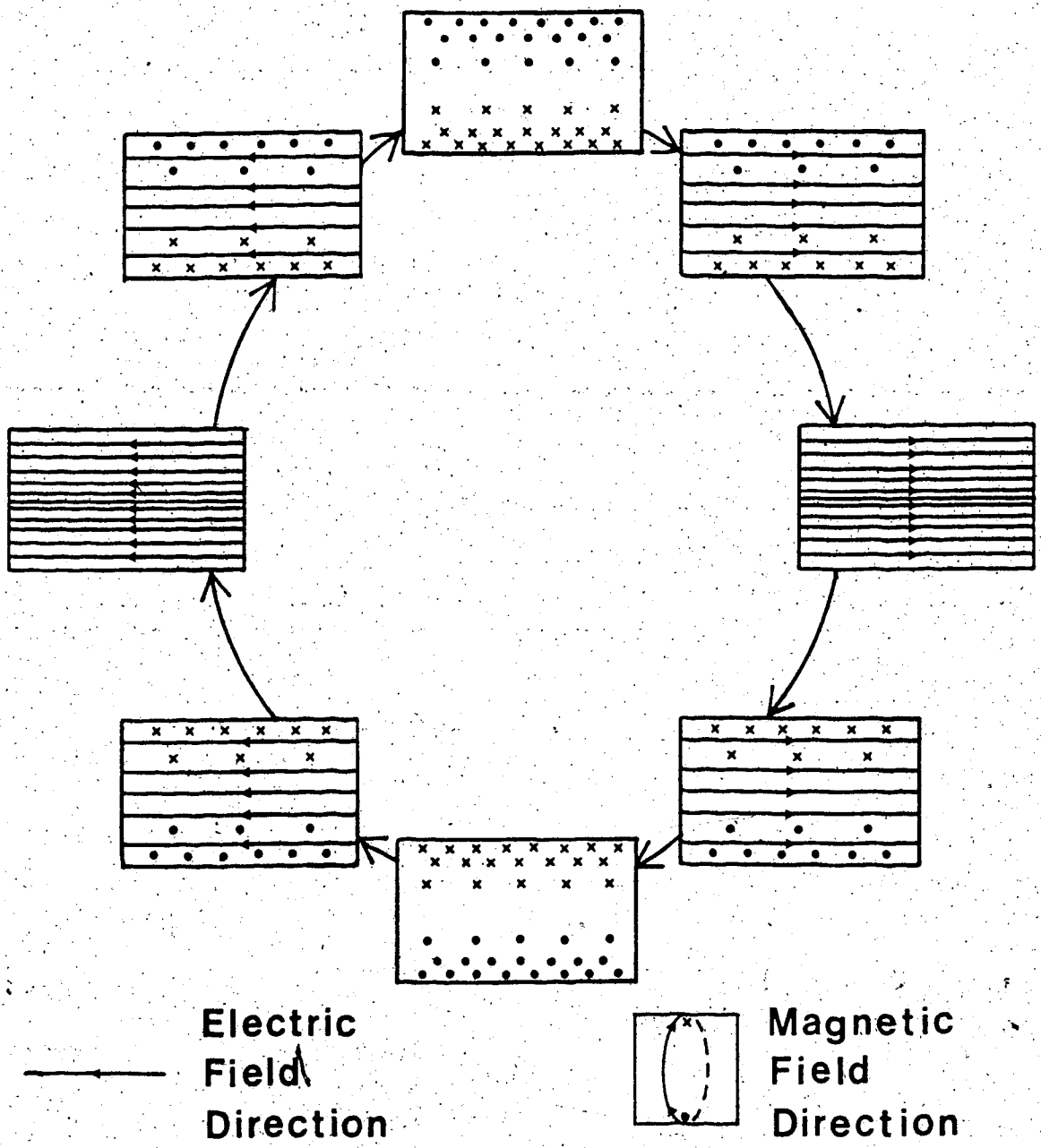

Figure 3. One oscillation of an electromagnetic cavity. The electric field is a result of charges at either end of the cavity. The magnetic field is due to charges moving along the cavity in response to the electric field. Microwaves can induce or be produced by such oscillations.

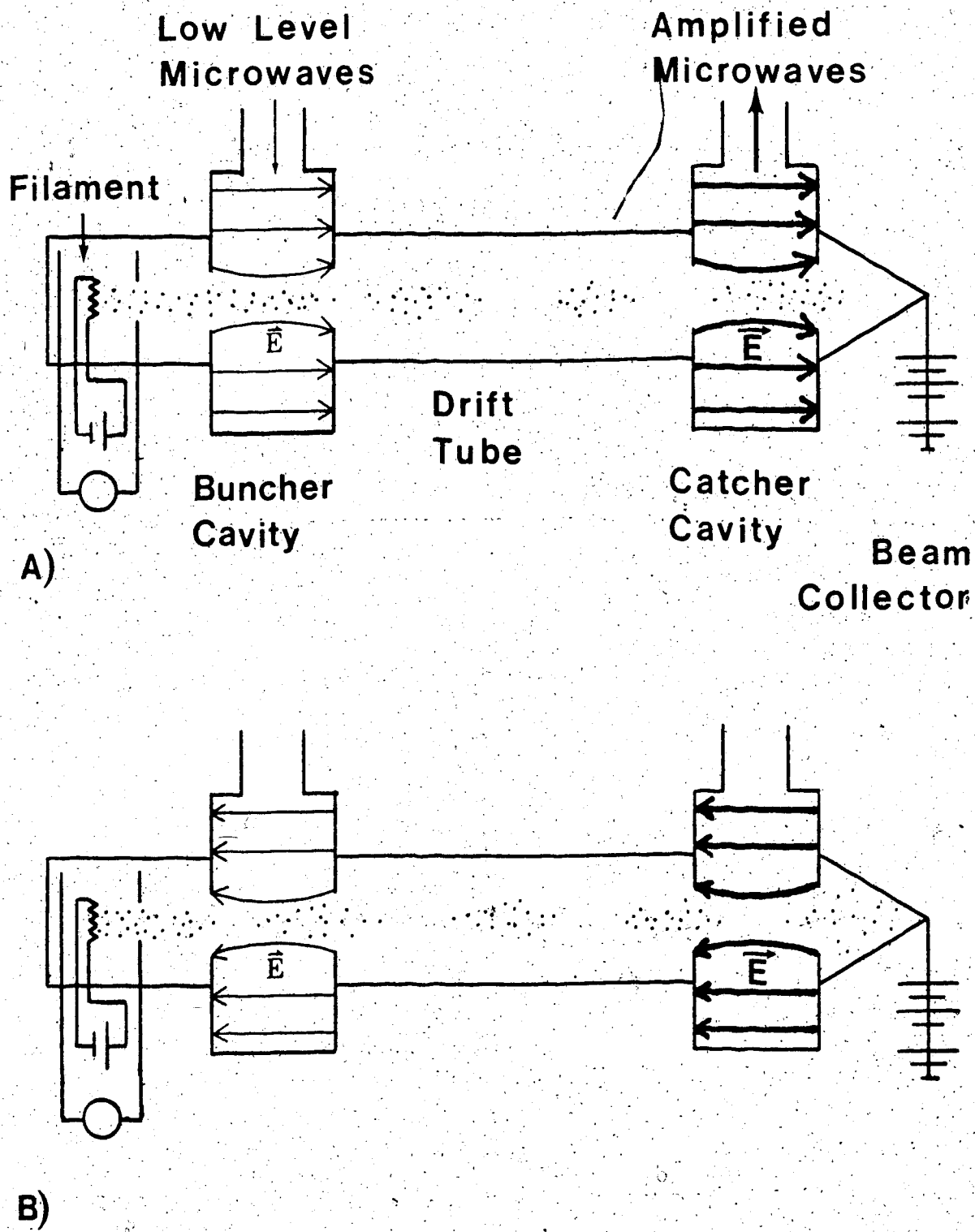

Figure 4. A) Retarding and B) accelerating phases of the operation of a buncher. A weak microwave cavity modulates an electron beam. The kinetic energy of the beam is transformed into an amplified microwave signal.

This reduces the electron velocity. The modulated beam current arriving at the catcher induces high amplitude microwaves utilizing most of the kinetic energy of the electrons. The electron beam collector is a dump for removing the electrons. The kinetic energy not converted to microwaves heats the collector which must be water cooled. Some low energy bremsstrahlung is produced in the collector which must, therefore, be shielded. The microwave power is produced by a klystron in the Mevatron -20 accelerator.

In the Mevatron -6 accelerator the microwave power is produced by a magnetron. A magnetron has a flat cylindrical geometry. A central cylindrical cathode is surrounded by an outer anode which is separated by a drift space. A D.C. magnet field is applied perpendicularly to the plane of the cylinder. A pulsed electric field is applied radially inward. Electrons spiralling from the cathode to anode induce an alternating charge distribution on the anode which produces, and has the same frequency as, the microwaves. Most of the electron kinetic energy is converted to microwave energy.

The two types of accelerator structures in use are the travelling wave and standing wave side-coupled designs. Both accelerators used in the study were standing wave side-coupled designs so the travelling wave design will be mentioned only briefly. Both types of accelerators accelerate electrons that have been produced and grouped in much the same fashion as a buncher cavity of a klystron.

In a travelling wave accelerator, radiofrequency power enters the first cavity (see Figure 5). The electric field travels down the waveguide which is a series of resonant cavities at the same group velocity as the accelerating electrons. Since the electron

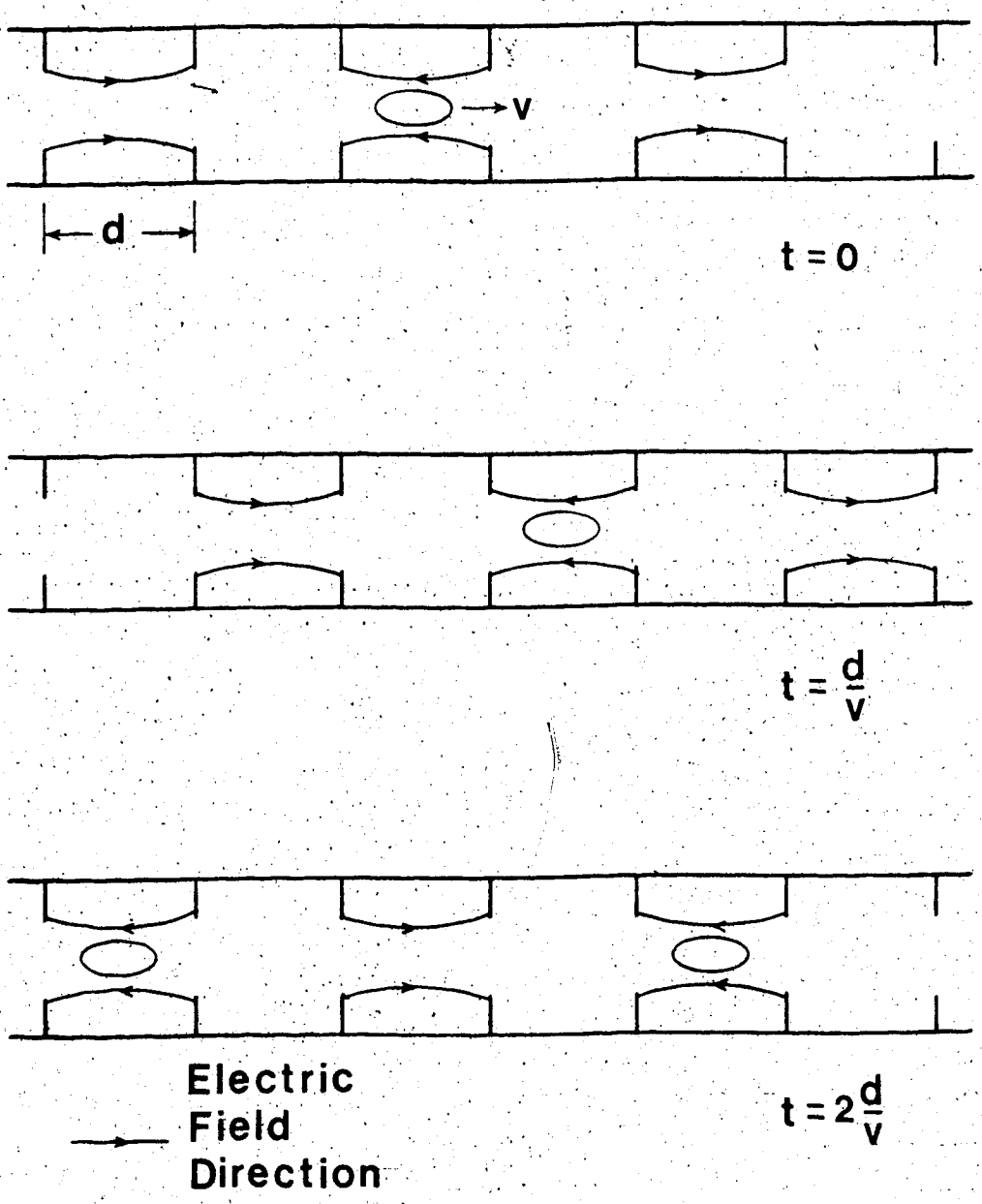

Figure 5. Schematic diagram of a travelling wave accelerator accelerating section.

velocity increases, the spacing between the cavities are increased in length toward the distal end of the waveguide. Upon reaching the distal end of the waveguide, the radiofrequency power is dissipated in a resistive load.

In a standing wave accelerator the microwaves are not dissipated with a concomitant saving of energy, but are allowed to reflect such that a standing wave is set up throughout the waveguide (see Figure 6). Since half of the cavities have a zero or small electric field at all times and so play a small role in acceleration, these cavities may be moved off axis. A waveguide with such a configuration is said to be side-coupled. The separation of the roles of the coupling and accelerating cavities allows optimization of the size and shape of each cavity type. This increases the amount of energy that can be gained per unit length which reduces the waveguide length. Figure 6 illustrates hypothetical longitudinal and cross-sections of a standing wave side-coupled accelerator waveguide. The phase velocity of the standing waves are matched to the electron velocity such that a group of electrons experiences the same direction and magnitude of electric field throughout its passage along the accelerator structure.

To be effective in treating patients from all directions, the accelerator must be able to be rotated about an axis. Since the accelerator structure is more than a meter long it has proven convenient to place the accelerating waveguide parallel or nearly parallel to the axis of rotation. In order to direct the beam perpendicular to the axis, a magnet must be employed to bend the beam. To accomplish this the beam could be bent through a right angle, but a 270^{o} achromatic bending magnet is usually employed (see Figure 7).

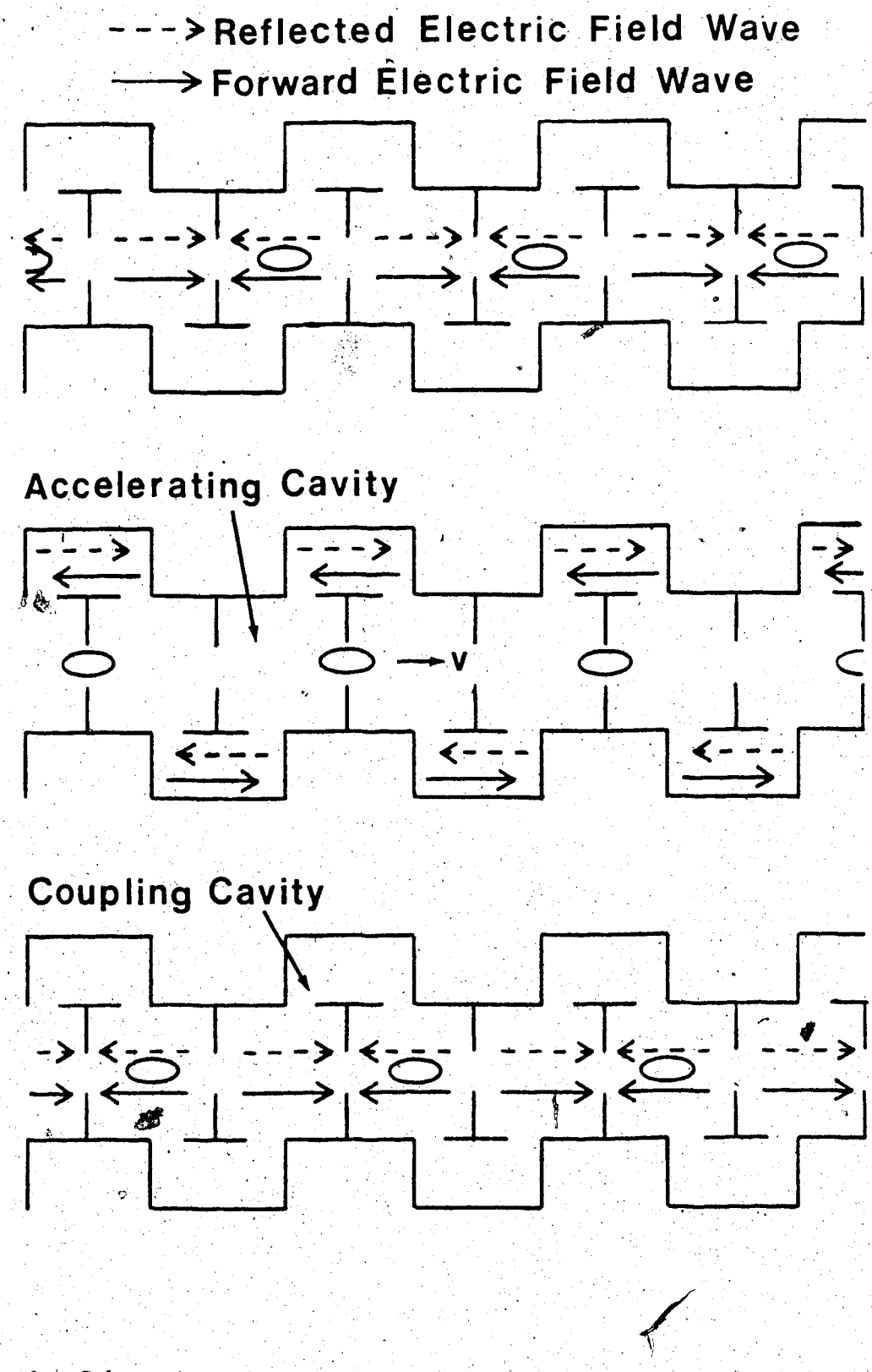

Figure 6. Schematic diagram of a side-coupled standing wave accelerator accelerating section. The forward wave travels from left to right and the reflected from right to left. The waves travel between accelerating cavities via coupling cavities.

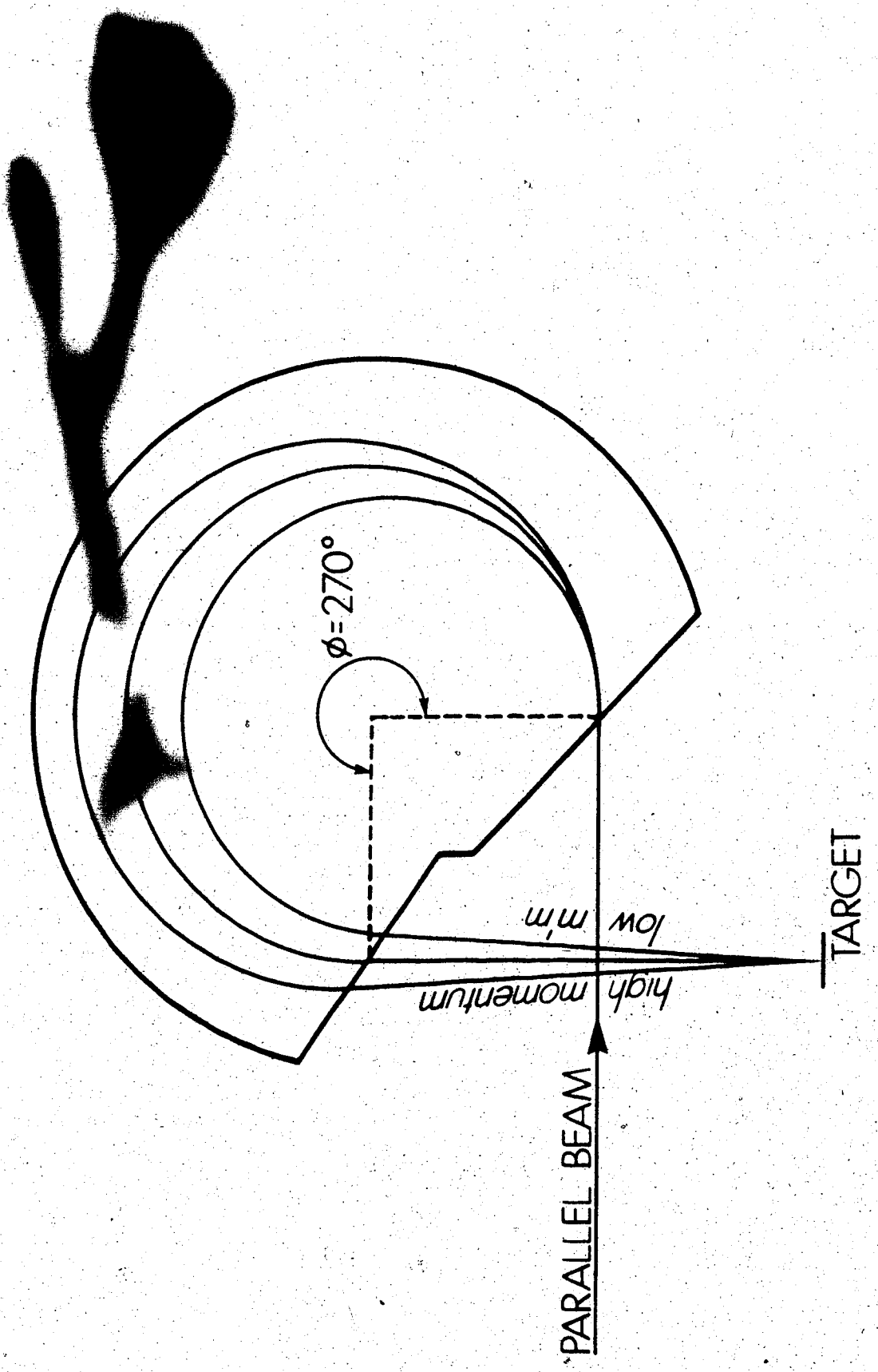

Figure 7. A 270° achromatic beam-bending magnet.

The relationship between the kinetic energy, magnetic field strength and the radius of curvature of a particle in a magnetic field is given by:

$$r = \frac{m_o c}{eB}\left[\left(\frac{T+m_o c^2}{m_o c^2}\right)^2 - 1\right]^{1/2} \qquad (1.4.1)$$

where B is the magnitude of the magnetic field.

An achromatic bending magnet has a greater magnetic field near the outside of the magnet. Electrons with higher than average kinetic energy will travel to outer radial parts of the field where they will be bent more. Slower electrons experience an opposite effect. The net result is that all electrons, regardless of small deviations in their kinetic energy, arrive at the same point. This is desirable because if a target (see Figure 8) is placed at this point the bremsstrahlung produced will emerge from a limited area. Photons from a small source when collimated will produce sharply defined edges, i.e. a small penumbra (see Figure 9). Additionally, an achromatic magnet results in a more stable delivery of electrons to the target.

The treatment head can be divided into the fixed head assembly and the movable collimator. The fixed head assembly consists of the target, electron absorbers, primary collimator, field flattening filter, monitor ion chamber and field light mirror (see Figures 8 and 9).

The electron absorber is a low Z material placed in the beam after the target to stop low energy electrons. The primary collimator limits the beams angular width to 22^o.

The bremsstrahlung produced by the target is forward peaked in intensity so there are more photons directed along the central axis than at points off axis. The field flattening filter is machined in a conical

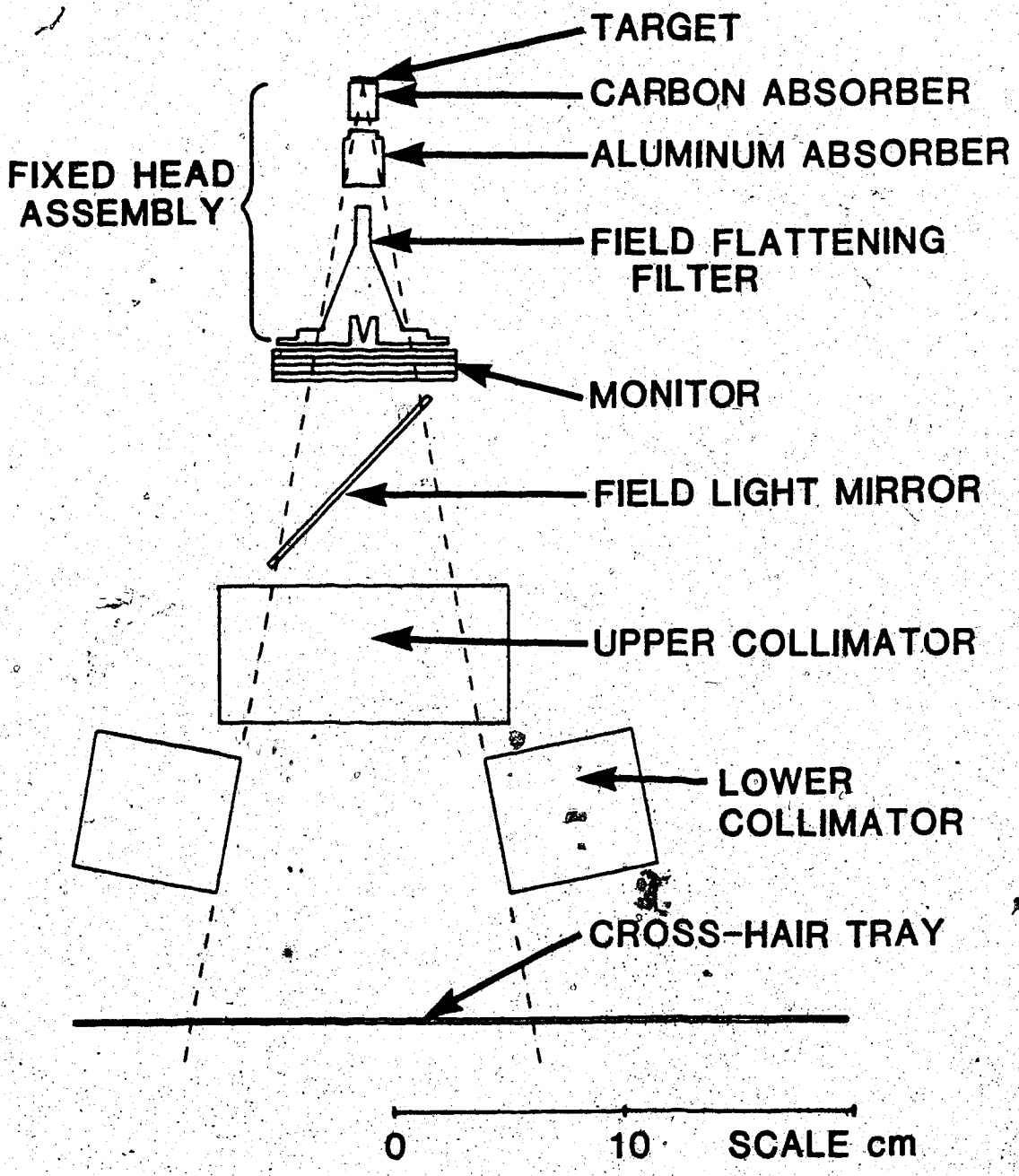

Figure 8. Scale drawing of the treatment head of a Mevatron -20 medical linear accelerator.

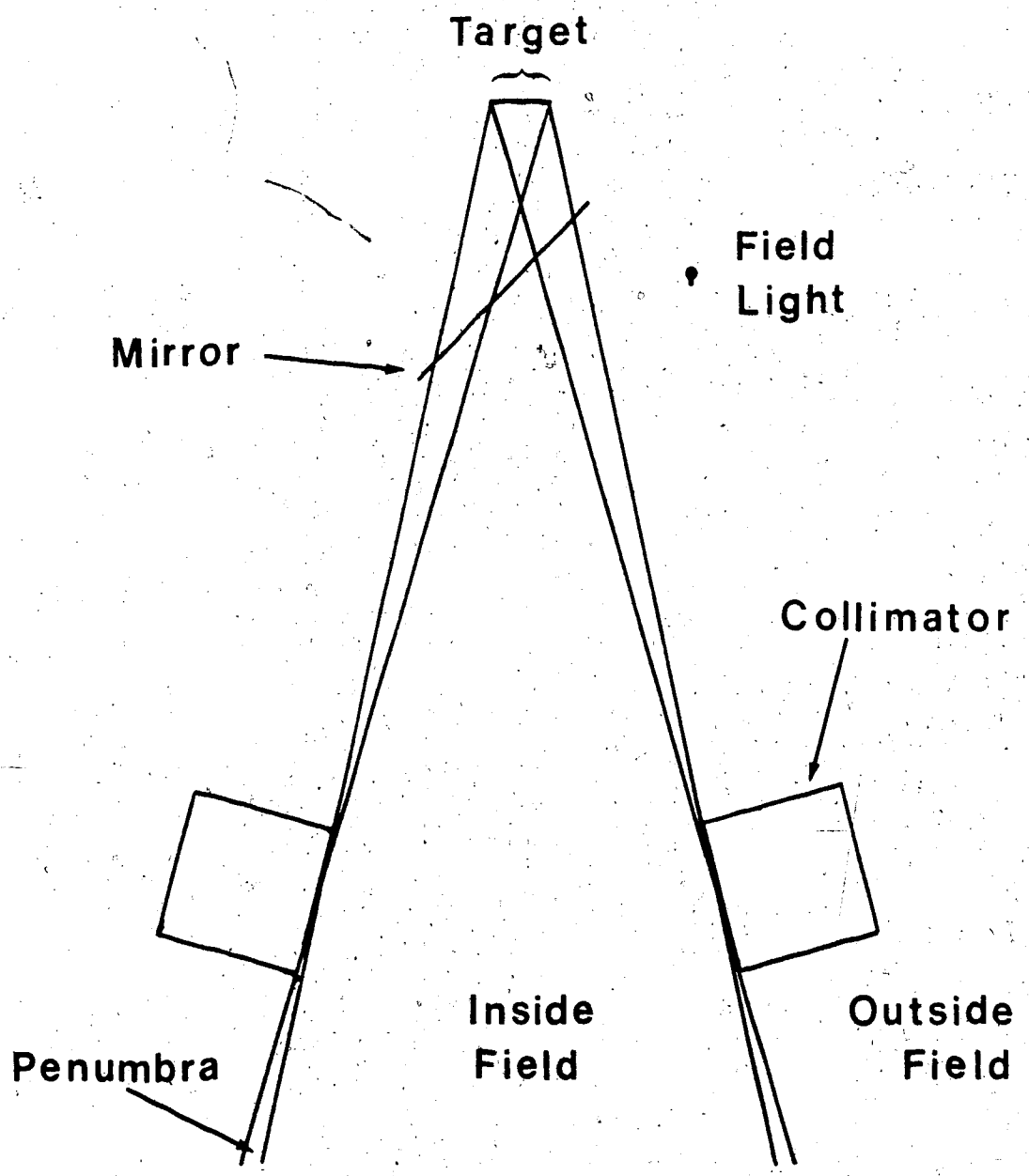

Figure 9. Diagram of the field defining system.

shape to attenuate the photon beam preferentially along rays near the central axis. The result is a photon fluence distribution which is relatively uniform over the entire cross-sectional area of the beam. Since introducing attenuation into a photon beam tends to harden the beam, the lateral distribution of the photon spectrum is not uniform. This can produce a nonuniform distribution of dose.

A multiplate ion chamber is usually placed in the fixed head assembly to measure dose rate, integral dose and field symmetry. This allows monitoring of the dose received by patients (timer systems are always used as back-ups) and is used as part of the verification of the safe operational status of the accelerator.

A field light, the source of which appears to be at the same position as the x-ray source, illuminates the field. This illusion is obtained by placing a thin mirror in the field and placing the light source off axis (see Figure 9).

The collimator system can consist of steel, lead, tungsten alloy or depleted uranium blocks thick enough to reduce the primary photon fluence to a fraction of a percent of the fluence in the field without producing photoactivation neutrons. A penumbra at the field edge occurs because of the finite width of the electron beam and target thickness (see Figure 9). The field boundary is defined to be where the dose falls to 50% of the dose at the central axis. The amount of the collimator jaws covering the field are continuously adjustable to produce square or rectangular fields with dimensions up to 30 cm x 30 cm.

A removable thin lucite tray with cross-hairs inscribed on it can be placed directly beneath the collimator jaws (see Figure 8). The shadow of the cross-hairs in the illuminated field define the position

of the central axis.

The beam axis of rotation for most accelerators is 100 cm from the photon source. Accessories such as beam wedges or blocking filters are often placed between the collimators and the patient at a distance of 60 cm from the source in the Mevatron accelerators on a Lucite accessory or "shadow" tray. When there are no accessories or beam modifying devices in place the field is said to be open.

A phantom consists of tissue equivalent material such as polystyrene or water, in the case of soft tissue, in which a radiation measuring device has been placed. The distance from the source to the phantom is specified by the source to (phantom) surface distance, SSD, and the source to probe distance, SPD. The phantom material used for all the experiments to be reported is polystyrene (electron density = 3.50×10^{23} e^-/cm^3, physical density = 1.08 g/cm^3) and the probe was usually a thin-window parallel-plate ion chamber.

1.5 Ionization Dosimetry

The absorbed dose, or simply, dose, is the amount of kinetic energy deposited in a small mass of material or:

$$\text{Dose} = \frac{\Delta T}{\Delta m} \qquad (1.5.1)$$

Dose is not a differential quantity. The dimension of the energy absorbing mass, Δm, must be much larger than the average distance between ionization-excitation events given by:

$$\text{Average Distance Between Ionization Events} = \frac{\overline{W}}{dT/dx} \qquad (1.5.2)$$

where $\overline{W}$ is the average energy lost in an ionization-excitation event. Typically, the average distance between events produced by fast electrons is less than a micron so the dose can be defined for very small masses. Dose is defined in terms of an amount of kinetic energy absorbed. The amount of rest energy deposited is not included so dose cannot be defined in terms of ΔE where $E = T + m_o c^2$.

The Gray (1 Gray = 1J/kg) is the SI unit of dose. However, for historical reasons the rad = 1 centiGray is often unofficially used.

An ion chamber measures the amount of charge accumulated due to ionization of air. One of the simplest ion chambers in design and the type used in most of the experiments conducted is the parallel-plate ionization chamber (see Figure 10). In essence, it is a single element parallel-plate capacitor separated by air. A potential is maintained between the plates. The potential is sufficient such that all ion pairs produced in the air are accelerated to the plates but not large enough for the accelerated ions to produce more ionization of the air. There is some recombination of ion pairs as they traverse the chamber,

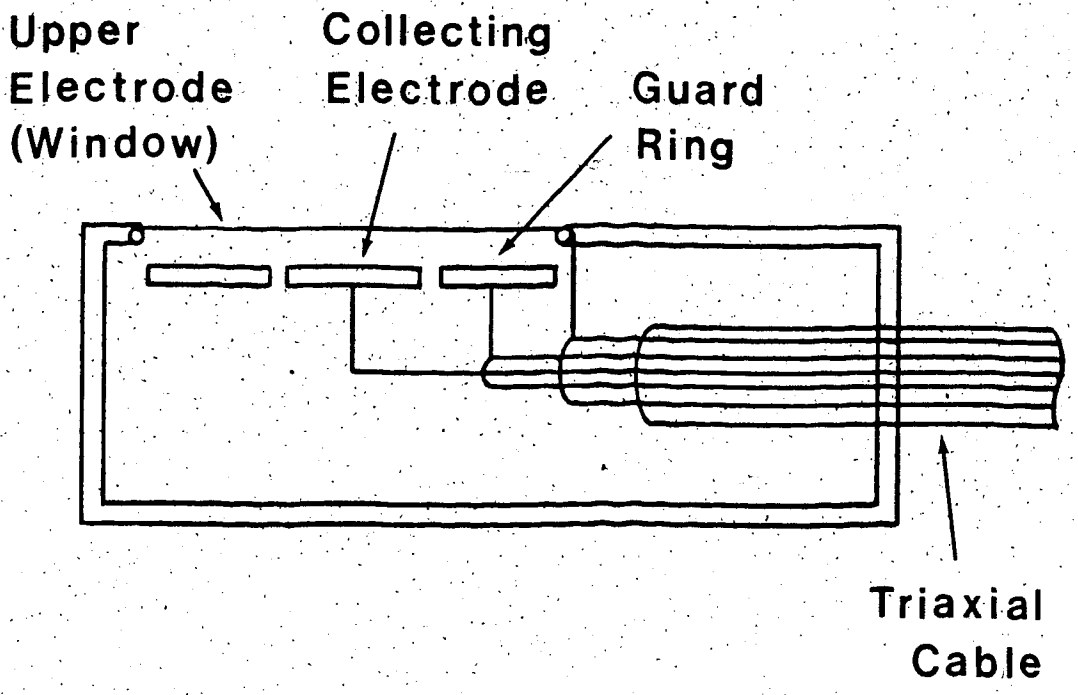

Figure 10. Schematic drawing of a parallel-plate ionization chamber.

but if the ionization current density is low the amount of recombination will be negligible. The amount of charge required is determined using an electrometer by measuring the amount of charge placed on the parallel-plates required to maintain a constant potential.

Although an ion chamber reading does not yield an absolute measure of dose, it is possible to theoretically relate the ionization in the ion chamber probe with the dose received in matter in the absence of the probe (7). In practice, the conversion relating the amount of ionization in a given probe to dose is established by a standards laboratory. The amount of dose is given by (8):

$$\text{Dose} = C\ C\lambda\ K_1\ K_2\ P\ R \qquad (1.5.3)$$

where R is reading of charge accumulated per unit mass of air

C is the calibration factor

$C\lambda$ is the energy dependent conversion factor between charge/mass and dose

K_1 is a temperature and pressure correction factor

K_2 is a factor that corrects for difference such as the quality of the radiation beam

P is a factor that takes into account the perturbance the probe makes in the fluence of the medium

Dose deposition due to photons is a two-stage process. First, charge particles are set in motion, then the charged particles slow down depositing their kinetic energy as dose. The concept of KERMA, kinetic energy released in the medium, describes the first step. KERMA is given by:

$$\text{KERMA} = h\nu \frac{\mu_k}{\rho} \Phi_\gamma \qquad (1.5.4)$$

where μ_k/ρ is the mass energy transfer coefficient

Φ_γ is the photon fluence in particles per unit area

Since the photon fluence is decreasing as a function of depth in the phantom, the KERMA decreases as well. The charge particles set in motion are mostly forward directed so their fluence as a function of depth initially builds up. Once set in motion these charged particles slow down and are stopped so their fluence reaches a maximum intensity at some depth. At this position, maximum fluence will produce maximum ionization in a probe placed there. This point is called d_{max}. After d_{max} the charged particle fluence decrease follows the KERMA decrease. The following differential equation has been used to describe the region where the dose builds up:*

$$\frac{d\Psi_{e^{\pm}}(x)}{dx} = \frac{\bar{\mu}_{\gamma}}{\rho}\,\Psi_{\gamma}(x) - \frac{\mu_{e^{\pm}}}{\rho}\,\Psi_{e^{\pm}}(x) \qquad (1.5.6)$$

and the solution is

$$\Psi_{\gamma}(x) = (\Psi_{\gamma})_{o}\, e^{-(\mu_{\gamma}/\rho)x} \qquad (1.5.7)$$

$$\Psi_{e^{\pm}}(x) = \frac{\mu_{\gamma}(\Psi_{\gamma})_{o}}{\mu_{e^{\pm}} - \mu_{\gamma}}\left(e^{-(\mu_{\gamma}/\rho)x} - e^{-(\mu_{e^{\pm}}/\rho)x}\right) \qquad (1.5.8)$$

where $\Psi_{\gamma}(x)$ is the total amount of energy fluence due to a full spectrum of photons and is given by:

$$\Psi_{\gamma}(x) = \int_{\text{spectrum}} \Phi_{\gamma}(h\nu, x)\, dh\nu \qquad (1.5.9)$$

where $(\Psi_{\gamma})_{o}$ is the initial photon energy fluence

$\Psi_{e^{\pm}}(x)$ is the energy fluence of charged particles and is defined analogously to Equation 1.5.7

* Equations 1.5.6, 1.5.7 and 1.5.8 have been modified from similar ones by Cassen, Corrigan and Hayden (10).

x is the thickness of phantom (in units of mass/area)

μ_γ is the energy weighted mean linear energy absorption coefficient and is given by:

$$\mu_\gamma(x) = \frac{\int_{\text{spectrum}} \mu_k(h\nu)\Phi_\gamma(h\nu,x)d(h\nu)}{\int_{\text{spectrum}} \Phi_\gamma(h\nu,x)d(h\nu)} \qquad (1.5.10)$$

$\mu_{e^\pm}$ is the mean "energy absorption coefficient" of charged particles set in motion at a point (in units of mass/area)

The above expression is analogous to the decay of a parent-daughter isotope if the daughter isotope initially has zero concentration. The effective energy transfer coefficient and the mean energy absorption of charged particles is depth dependent due to hardening of the beam, and the production of scattered photons. However, to a good approximation they can be considered to be a constant in the build-up region. The energy absorption coefficient can be used instead of the energy transfer coefficient at low energies in low Z materials. It has been assumed that once produced the energy fluence of electrons set in motion at a given point in the phantom decays exponentially with depth. The first term on the right hand side of Equation 1.5.6 represents the total KERMA of the beam.

The depth of the maximum dose, d_{max}, occurs at the point of the maximum charged particle energy fluence and is given by:

$$d_{max} = \frac{1}{\mu_{e^\pm} - \mu_\gamma} \ln \frac{\mu_{e^\pm}}{\mu_\gamma} \qquad (1.5.11)$$

The output factor is defined to be the reading at d_{max} for a given field size and SPD divided by the reading at a field size of

10 cm x 10 cm at the same field size. The output factor has a small dependence on SPD.

The dose at a given depth is often normalized to the dose which occurs at a reference depth. There are two common procedures for doing this. They are the percentage depth dose, $P(x,x_o,W_s,SSD,(h\nu)_{max})$ and the tissue maximum ratio, $TMR\ (x,W,(h\nu)_{max})$.

The percentage depth dose depends on the depth (measured from the surface) in the phantom, x, the depth to the reference point, x_o, the field dimension measured at the surface, W_s, the source-to-surface distance, SSD, and the nominal photon beam energy $(h\nu)_{max}$. The percentage depth dose is defined to be (8):

$$P(x,x_o,W_s,SSD,(h\nu)_{max}) = \left(\frac{\text{Dose at } x}{\text{Dose at } x_o}\right) 100\% \qquad (1.5.12)$$

The position of the dose measured at points x and x_o are shown in Figure 11. The percentage dose is obtained by keeping the SSD constant and determining the dose at each depth by moving the measuring probe.

The tissue maximum ratio is a ratio between the dose as measured at a depth, x, in a phantom compared to the dose as measured at d_{max}. The measurements are made by keeping the source-to-probe distance, SPD, constant and the depth from the surface is varied by changing the thickness of overlying material. The field dimension is measured at the source-to-probe distance. The tissue maximum ratio is defined to be (8):

$$TMR(x,W,(h\nu)_{max}) = \frac{\text{Dose at } x}{\text{Dose at } d_{max}} \qquad (1.5.13)$$

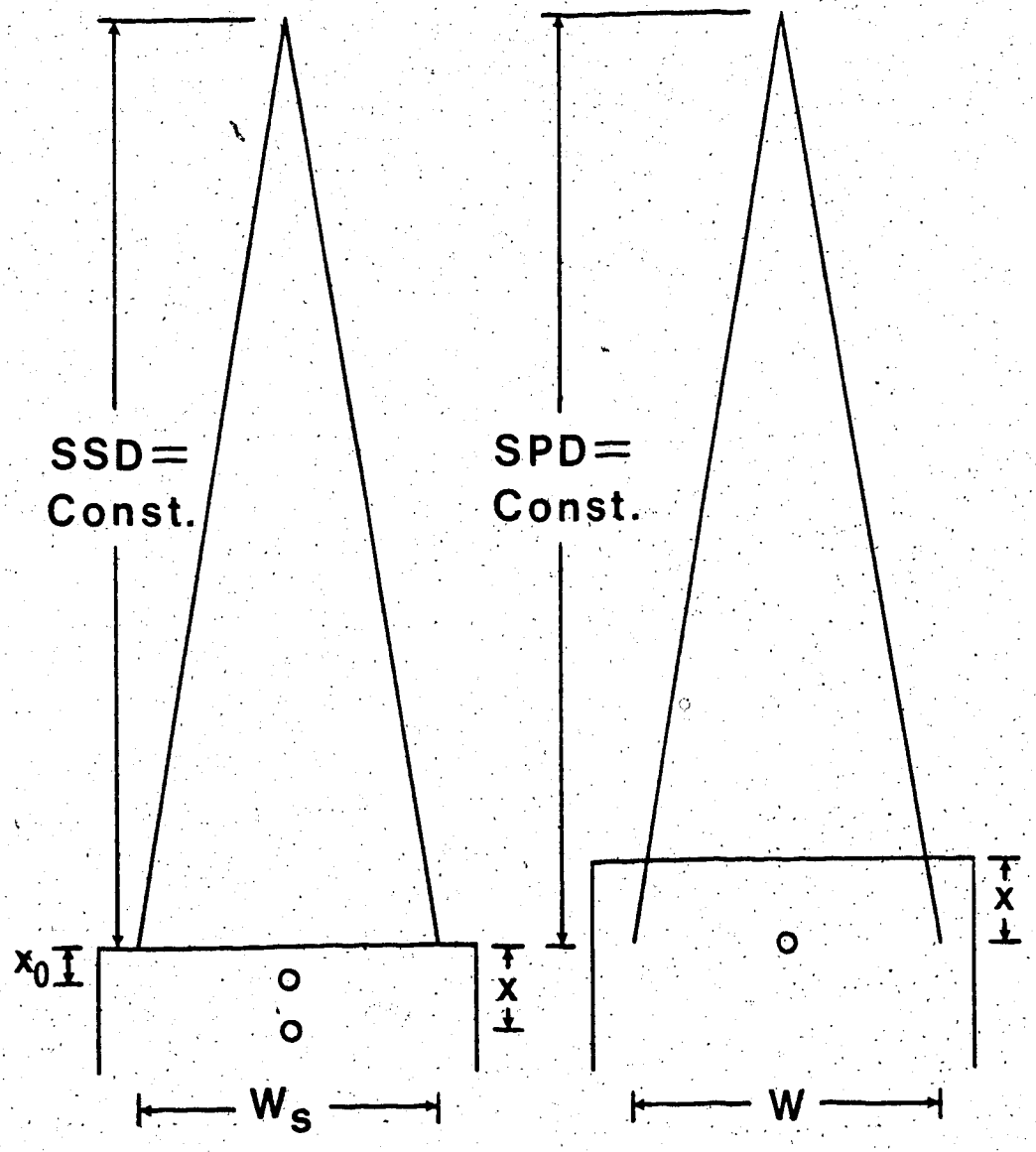

Figure 4. The arrangements for measuring percent depth dose is shown on the left and tissue maximum ratios on the right. The position of maximum dose in the TMR measurement, d_{max}, is not shown.

The dose at point x is shown in Figure 11. The percentage depth dose can be obtained from tissue maximum ratios by the expression (8):

$$P(x,x_o,W,SSD,(h\nu)_{max}) = \frac{TMR(x,W,(h\nu)_{max})}{TMR(x_o,W,(h\nu)_{max})}\left(\frac{SSD+x_o}{SSD+x}\right)^2 \times 100\% \qquad (1.5.14)$$

where $\left(\frac{SSD+x_o}{SSD+x}\right)^2$ takes into account a $1/r^2$ fall-off in the primary fluence between points x_o and x.

Using Equation 1.5.3, the tissue maximum ratio can be found:

$$TMR = \frac{C_\lambda(x)k_2(x)R(x)}{C_\lambda(d_{max})k_2(d_{max})R(d_{max})} \qquad (1.5.15)$$

In the build-up region the quality of radiation does not change appreciably so the ratio $k_2(x)/k_2(d_{max})$ can be taken as unity. The ratio $C_\lambda(x)/C_\lambda(d_{max})$ is approximately unity as well.* Therefore, the tissue maximum ratio is just the ratio of readings taken at a depth, x, and at d_{max}.

Using Equation 1.5.8, the tissue maximum ratio is predicted to be:

$$TMR = \frac{e^{-(\mu_\gamma/\rho)x} - e^{-(\mu_{e^\pm}/\rho)x}}{e^{-(\mu_\gamma/\rho)d_{max}} - e^{-(\mu_\gamma/\rho)d_{max}}} \qquad (1.5.16)$$

Equations 1.5.8 and 1.5.16 predict that the dose at the proximal surface of the phantom (i.e. x=0) is zero. The reason is that no charged particles have been set in motion. The low surface dose can have important clinical effects. For example, the skin is a fairly radiosensitive tissue and often is not affected by deeper seated cancerous tissue. When this

* $C_\lambda(x)/C_\lambda(d_{max})$ is approximately equal to $\bar{S}^{water}_{air}(x)/\bar{S}^{water}_{air}(d_{max})$ (7) where $\bar{S}^{water}_{air}(x)$ is the stopping power ratio of water to air averaged over the electron fluence at a depth, x, in the phantom. Nahum (53) has shown that $\bar{S}^{water}_{air}(x=0)$ is within 2% of $\bar{S}^{water}_{air}(d_{max})$ in the energy range between 6 MV and 15 MV.

is the case, the dose to the skin should be as low as possible.

In practice, the surface dose is non-zero. In part this is due to backscattered radiation. The backscatter dose can be divided into two components. Some dose is due to forward directed primary photons which produce charged particles set in motion near the surface of the phantom which scatter backwards. The rest is due to photons scattering backwards and producing charged particles set in motion which are then mainly back directed.

The rest of the surface dose is due to contamination. The contamination component of the beam is defined as charged particles and scattered photons produced by interactions of the primary beam with material outside the phantom. Since the dose is directly due to the slowing down of charged particles, the surface contamination dose is due to charged particles produced outside the phantom.

The primary photon beam is defined to be photons emerging through the collimators which appear to have been produced by bremsstrahlung in the target.*

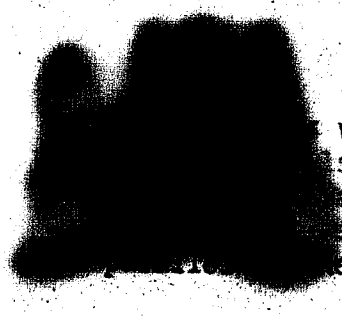

which are indistinguishable from bremsstrahlung produced so considered primary. These include bremsstrahlung ave been forward scattered by beam modifying components ld flattening filter or annihilation photons directed e primary photon beam.

1.6 Review of Previous Work on Contamination of Megavoltage Photon Beams

The University of Illinois (Urbana, Illinois) betatron was the first device used in radiotherapy to produce a megavoltage photon beam. This betatron could produce bremsstrahlung photons from electrons with kinetic energies of 5 MeV to 20 MeV. The presence of electron contamination was evident in the beam. Quoting from a 1942 paper by Koch, Kerst and Morrison (11):

> "Experience in taking these [depth-dose] data has shown that the surface dose can be greatly affected by stray electrons striking the phantom. These electrons arise from two sources; some are original beam electrons which escape in large numbers from the acceleration chamber and others are Compton electrons scattered from objects near the x-ray beam. To obtain consistent results the primary beam was stopped by absorbers placed close to the target and the secondaries [contamination electrons] were avoided by keeping scattering objects from the vicinity of the beam. The magnetic field of the betatron undoubtedly removes a great number of secondary electrons."

The surface dose, when compared to the maximum dose produced by the Illinois betatron, decreased as a function of increasing nominal beam energy.

A 1941 paper by Johns, Darby, Haslam, Katz and Harrington (13) described the depth-dose and isodose distributions from a 22 MeV betatron. There is no mention of the production of contamination. They claim depth-dose curves are independent of field size or source to surface distance (retrospectively, there was some small dependence on these factors). The measuring equipment employed did not allow measurements to be made less than 0.5 cm from the surface and the largest field was a 10 cm diameter circle measured at 70 cm SPD. These conditions are not conducive to observing contamination.

The absence of a build-up dose dependence on field size found on the Saskatchewan betatron was contradicted by Laughlin, Beattie, Lindsay and Harvey who found a dependence on field size when the Illinois betatron was operating at 25 MV (12).

The introduction of the Co^{60} isotope therapy devices clearly indicated that megavoltage primary photon beams were contaminated. Johns, Epp, Cormack and Fedoruk (14) determined that the beam was being contaminated mainly by electrons. They found that the surface dose, as measured with a thin window parallel-plate chamber, increased as a function of field width and decreased with greater source to surface distance. The contamination resulted in a shift in d_{max} towards the surface and produced an elevated value of the maximum dose. They recommended a distance of 20 cm between the diaphragm (secondary collimator) and the patient's surface. An aluminum absorber placed in the beam following the primary collimator reduced the amount of contamination.

The results of the measurements of Johns et al have been confirmed for Co^{60} beams by many other investigators. The dose in the build-up region increases as a function of increasing field size (15-21). The dose at depths below d_{max} increases with decreasing distance to the source (15, 17, 20, 22). Contamination of Co^{60} beams produces a dramatic shift in the position of the maximum dose (15, 20, 21).

Following the theoretical calculations of Wilson and Perry (23) in 1951 which showed that medium Z materials could be used to reduce electron contamination, many authors experimentally confirmed their findings. The best electron filter materials were claimed to be cadmium, Z=48, (15); tin, Z=50, (22); and copper, Z=29 (26, 27). Other

authors used low or high Z materials as electron filters, for example, lead, Z=82, (17); leaded glass (25) and perspex (21).

In contrast to the findings that materials placed in the beam reduced the amount of contamination, it was found by authors that accessories placed in a Co^{60} field increased the amount of contamination (26).

In linear accelerators a great deal of contamination is produced by the introduction of accessories into the beam. Rao, Pillai and Gregg (28) measured contamination at many beam energies produced by accessories. They found that the amount of contamination increased with accessory tray thickness up to a certain thickness (about 8 mm for a lucite accessory 29 cm above the phantom when the field size was 25 cm x 25 cm in a 6 MV beam) and was constant with increasing thickness for greater thicknesses. The amount of accessory tray contamination increases with larger fields and smaller source to surface distances. Other authors have confirmed these results for linear accelerators (19, 25).

Rao, Pillai and Gregg (28) found that a lead sheet placed under the accessory tray reduced the dose at all depths below d_{max}. Gray (25), based on the success of Co^{60} contaminant filtering, suggested using a leaded glass accessory tray in linear accelerators and Wu (29) recommended placing a tin sheet beneath the accessory tray in 10 MV photon beams.

Scrimger and Kolitsi (30) studied the effect outside the beam when scattering layers were placed inside the field. An 8 MV linear accelerator was used. The relative dose outside the field fell off rapidly with depth suggesting that the scattered radiation is mostly electrons. The amount of scattered radiation outside the field increased

with field area and decreased with increasing distance to the scatterer.

A field flattening filter is designed so that the lateral distribution at d_{max} for megavoltage photon beams is as flat as possible. However, it has been found that the surface dose is generally higher near the central axis compared to the dose near and beyond the beam edges (19, 21, 25, 30, 36).

As was observed for Co^{60} beams, megavoltage photon beams from linear accelerators have an increased dose due to contamination when the field size is large or the source to probe distance is small (25, 28, 29, 31, 32, 33, 34, 35).

Contaminated accelerator beams produce a shift in d_{max} through the entire range of energies currently employed in radiotherapy; for example, at 2 MV (24), 4 MV (18, 25), 10 MV (38), 25 MV (18, 37, 39), 34 MV (34) and 45 MV (40).

Penetration characteristics of the contamination component have been measured in an number of different ways. Dawson (34) produced what he called "difference curves". The difference in dose between neighboring field sizes at a fixed depth and source to surface represents the effect of an increase in field size. At shallow depths the difference curves decrease rapidly. Attenuation of the dose due to contamination electrons is cited as the cause. These measurements were done in a phantom greater in extent than the field so some of the difference between the dose at neighboring field sizes is due to photons scattered in the phantom arriving at the measuring point. This is evident in Dawson's data because the difference curves increase with depth when measurements are made at a depth beyond d_{max}.

Marbach and Almond (37) placed a lead pyramid-shaped block on the

accessory tray to shield a detector from the primary beam. Contamination was then claimed to be the only component of the beam arriving at the phantom. They measured depth-dose curves for the contamination component. Unfortunately, the shallowest depth-dose measurement obtained was 2 cm from the surface. A key to the validity of such an approach is to confirm that the lead block does not shield or produce a significant amount of contamination. Surface dose measurements taken before and after the placement of the lead blocks would have determined if there was any change in contamination.

Marbach and Almond subtracted the contamination curves from the total curves to yield the primary depth-dose curves. The primary depth-dose curves did not have a shift in d_{max} and when normalized to their own maxima were independent of field size.

Marbach and Almond went on to hypothesize that electrons were not the cause of the d_{max} shift. They placed a 1/4 inch aluminum plate in the field below the collimators in the anticipation that this would remove all of the electron contamination. Since there was little change in the depth dose curve, they concluded there were no contamination electrons in the beam. Their interpretation was not necessarily valid. As many electrons may have been produced as were stopped and scattered. Indeed, even though their contamination depth-dose did not include shallow depths, a rapid increase in dose with decreasing depth is evidence for an electron contamination component.

Biggs and Ling (41) repeated the method of primary beam blocking developed by Marbach and Almond (37). They produced contamination attenuation curves that included the dose at the surface and at other depths below d_{max}. These curves exhibit a rapid fall off at shallow

depths and tend to be an asymptotic constant at deeper depths. They did not subtract the contaminant component to obtain the primary build-up curves.

Clifton Ling and colleagues (41, 43, 44, 45) have employed electromagnets with maximum central magnetic fields between 1.8 kG and 3.9 kG to sweep electrons from the field. Padikal and Deye (42) used a permanent magnet with variable gap pole pieces. The smallest central field strength still capable of sweeping all of the 10 MV contamination electrons produced between the target and the magnet was 0.5 kG.

Biggs and Ling (41) showed that the build-up curve for a 25 MV photon beam was field size independent when the magnet was sweeping contamination electrons from the field.

Padikal and Deye (42) defined a parameter, α, to be the difference between the reading of the ionization chamber without the magnet and the ionization reading with the magnet normalized to the reading at d_{max}. Since the only difference between the readings was an absence of electrons produced between the target and magnet, α represents the component of the TMR curve attributable to those contaminant electrons. The electron contaminant TMR curve had a peak between 1 and 2 mm and rapidly decreased to zero at about 2.5 cm. Despite evidence to the contrary, they claimed that the shift in d_{max} with field size is due to a relative enhancement in the soft x-ray component as the collimator jaws are opened.

Ling (43) has shown that a magnet in a 4 MV photon beam produced no shift in d_{max}. There is a slight field size dependence of the surface dose and the build-up curves at shallow depths. This is interpreted as due to electrons originating from the air volume between

the magnet and the phantom. Ling, Schell and Rustgi (45) repeated the measurements at 10 MV and found similar results. They measured the build-up curves with the magnet in place at two different source to surface distances to see if the contamination that was previously attributed to air was SSD dependent as theory would predict (37). Their results were inconclusive so they have stated that they will repeat the measurements with a helium-filled bag to replace the air volume.

Ling, Rustgi and Gromadzki (44) have measured the production of secondary radiation by 10 MV photons from scatterers placed in the beam. The measurements were done outside the primary beam field when a magnet was off and on. The depth of ionization curves for scattered photons and electrons were obtained separately. They investigated the amount of electron production as a function of the atomic number of the scatterer. For a target thickness of 1.7 gm/cm^2 and a scattering angle of 10^o high Z materials such as lead produced less ionization.

Recently, Nilsson and Brahme (46) have done calculations predicting the nature and amount of contamination due to scattered photons using the Monte Carlo method. The scattered photon spectrum for both 6 MV and 21 MV does not change appreciably between the central axis and the field edge for a 20 cm circular field. The maximum energy of the scattered photons is about 85% of the maximum energy of the primary spectrum. The peak in the scattered and primary spectrum occur at the same energy although the relative number of photons in the peak are greater in the scattered photon spectrum. The absorbed dose at d_{max} due to scattered photon contamination for both 6 MV and 21 MV photons was found to be about 2.5 - 3.0% at the central axis for a 20 cm circular

field. The main source of scattered photons was the collimator for a 6 MV photon beam and the field flattening filter for a 21 MV photon beam.

The main disagreement in the literature concerns the type and origin of contamination. Some authors say electrons and others say scattered photons are the main cause. Every component between the source of primary radiation and the phantom has been suggested as the main source of contamination. Table 1 summarizes the conclusions of a number of authors on the nature and source of the contamination.

Table 1 Conclusions Of A Number Of Authors On The Nature And Source Of Contamination

Author	Date	Type	Source		
			Field Flattenning Filter	Collimator	Air
Johns, Epp, Cormack, Fedoruk	1952	Electron		X	X
Richardson, Kerman, Brucer	1954	Electron		X	X
Ibbott, Hendee	1970	Electron		X	
Jackson	1971	Electron			X
Gray	1973	Electron	X	X	
Bagne	1974	Photon		X	
Velkley, Manson Purdy, Oliver	1975	Electron		X	
Dawson	1976	Electron		X	
Smith, Sutherland	1976	Electron		X	
Marbach, Almond	1977	Photon	X		
Padikal, Deye	1978	Electron, Photon		X	
Nilsson, Brahme	1979	Electron			X
Bagne	1980	Electron	X	X	X
Wu	1980	Electron		X	

— The documentation
of experimentation
often has too much elaboration
and not enough elocution.

2.1 Open Field Build-Up Curves

Tissue maximum ratio curves were measured for 15 MV and 6 MV photon beams from Siemens Mevatron -20 and Mevatron -6 linear accelerators. A schematic diagram of the beam defining head of the Mevatron -20 is shown in Figure 8. The Mevatron -6 has a similar design. All determinations were made at constant source-to-probe distances (SPD) using 0.16 cm (1/16") thick and 0.64 cm (1/4") thick square polystyrene slabs. The phantom slabs used in the determination of the open field build-up curves each had cross-sectional dimensions of 25 cm x 25 cm.

The detector used in this section and others was a Capintec 192A electrometer with a PS-033 thin window parallel-plate ionization chamber which has an effective volume of 0.5 mℓ. The entrance window was aluminized polyester film 0.5 mg/cm^2 thick.

The field size is referred to as the lateral field dimensions defined at 100 cm. Only square fields were used.

The central axis build-up curves at SPD = 100 cm for a 15 MV beam for various field sizes are illustrated in Figure 12. These build-up curves demonstrate a field size dependence. There is little backscatter expected at 15 MV so the dose at the surface should be very small and only weakly dependent on field size. Therefore, most of the field size dependence and the elevated surface dose can be attributed to contamination.

The open field build-up curve at SPD = 100 cm for a 6 MV beam are shown in Figure 13. The build-up curves were measured at the central axis for various field sizes. Greater field sizes result in larger tissue maximum ratios (TMR) for the same depth. Since a very similar effect was observed at 15 MV, the open field build-up curves at the two

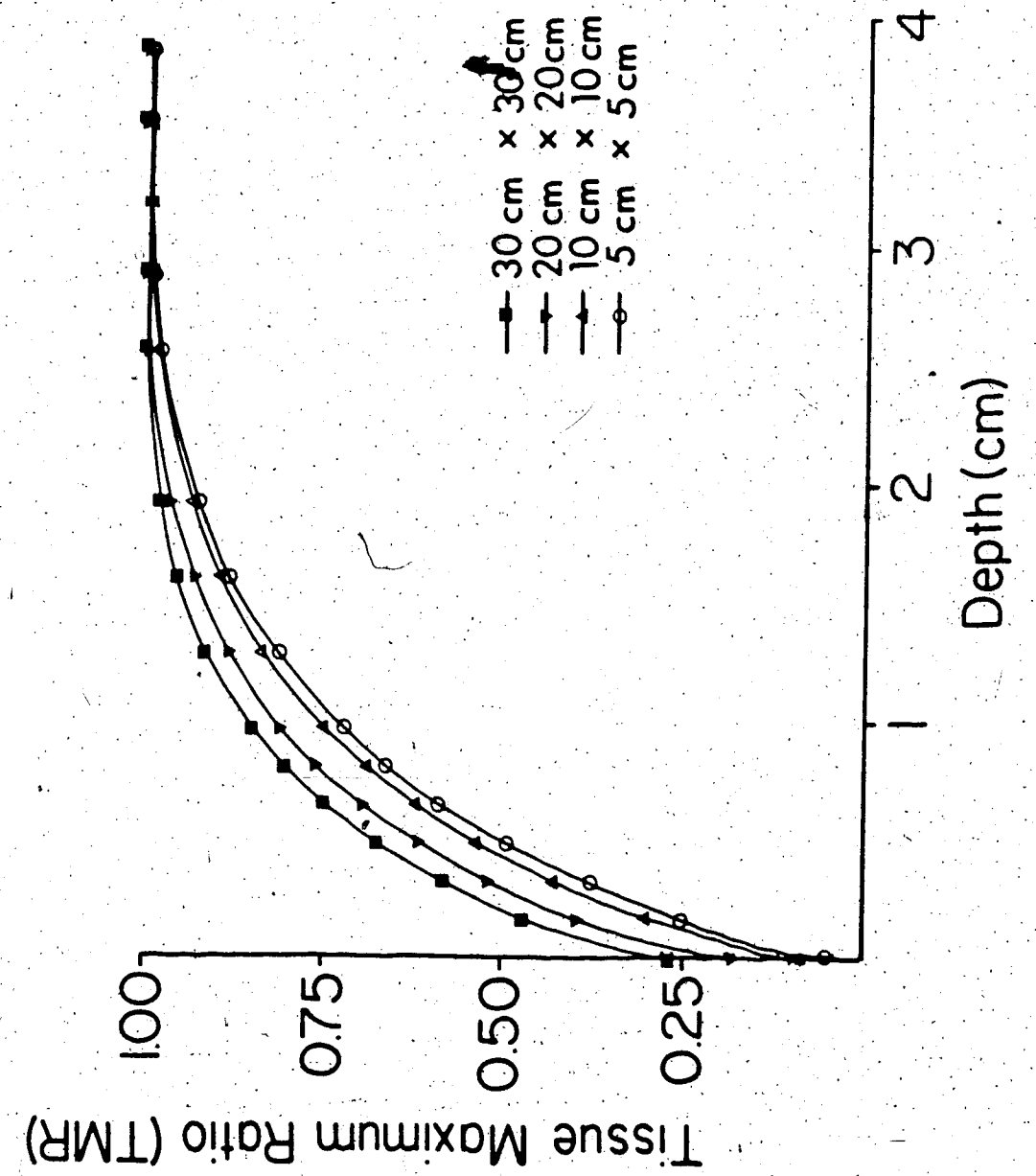

Figure 12. Central axis open field build-up curve at 100 cm SPD for a 15 MV be

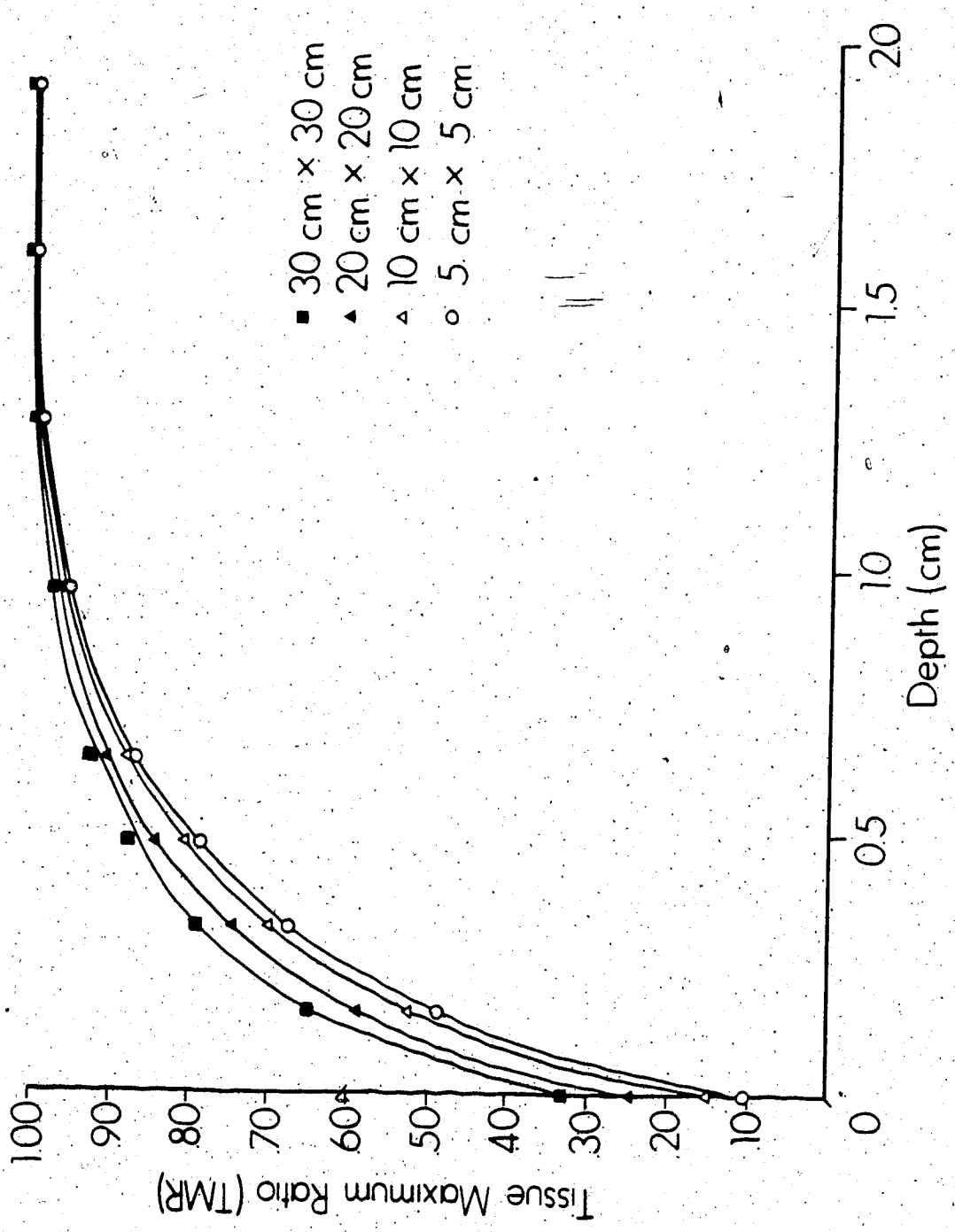

Figure 13. Central axis open field build-up curve at 100 cm SPD for a 6 MV beam.

energies have been compared by normalizing the depth with respect to d_{max} of each curve. The result is illustrated in Figure 14. At field sizes of 10 cm x 10 cm and 30 cm x 30 cm, the TMR curves for the 6 MV photon beam have a similar form to those for the 15 MV beam at depths less than d_{max}. However, at any normalized depth the TMR values for 6 MV slightly exceed those for 15 MV. The 6 MV surface dose exceeds that of the 15 MV beam for the same field size.

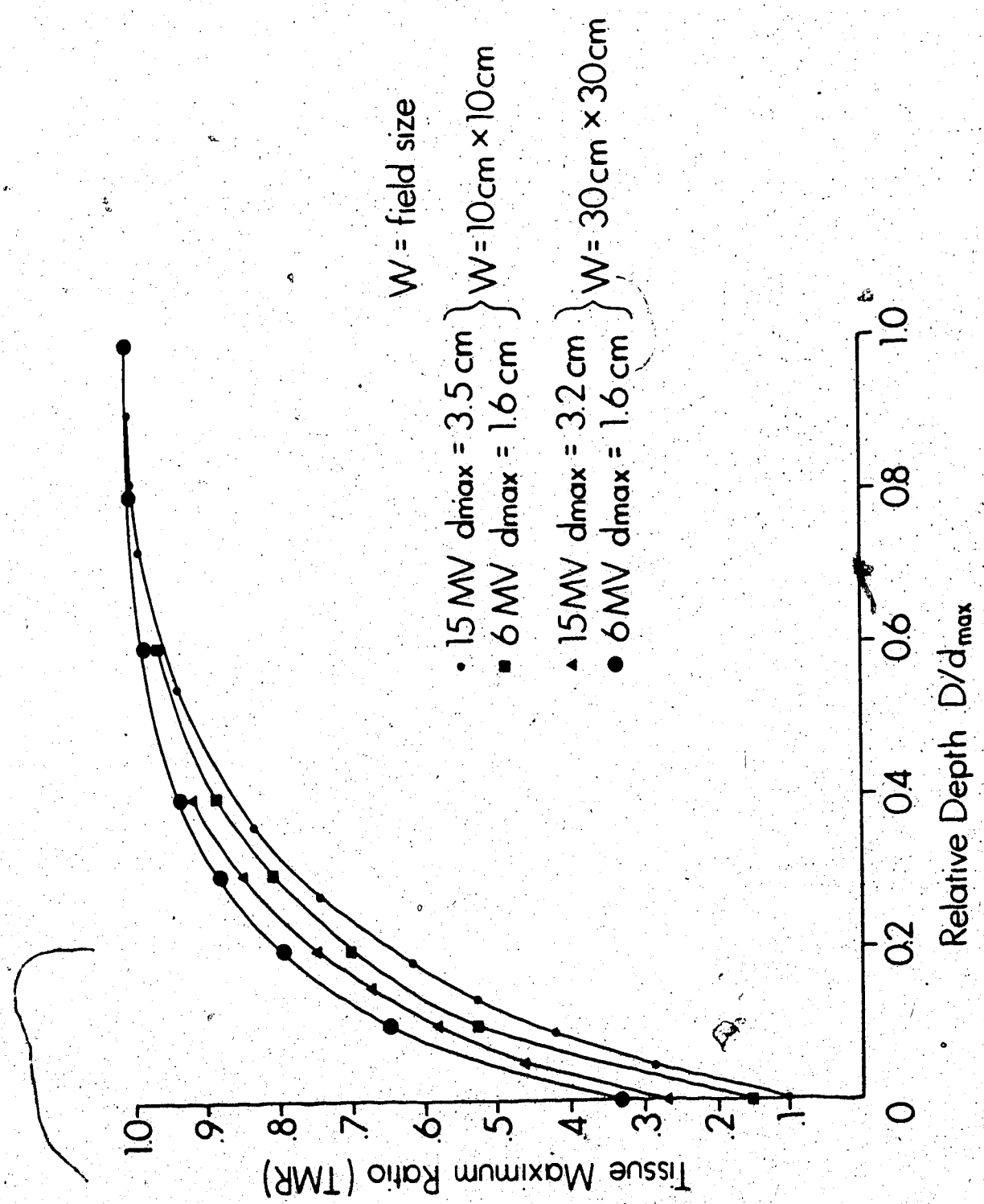

Figure 14. Comparison between 6 MV and 15 MV central axis open field build-up curves.

2.2 Accessory Build-Up Curves

Various thicknesses of Lucite (density = 1.18 g/cm^3) alone or Lucite and lead (density = 11.4 g/cm^3) slabs were placed in the beam to determine their effect on the build-up curves. The distal surface of the slabs was placed at the accessory tray holder position 56 cm from the source. In all cases, a Lucite surface was facing the probe.

Figures 15, 16 and 17 show the build-up at an SPD of 140, 100 and 75 cm, respectively. The field size in all cases is 30 cm x 30 cm. When accessories are placed in the field at the tray holder position, a larger TMR for all depths less than d_{max} is observed. There is also a shift in the point of d_{max} to shallower depths. This is more pronounced at SPD = 75 cm (Figure 17). There is virtually no difference in the build-up curves between a 3.2 cm (1-1/4") Lucite accessory and a 0.30 cm lead slab on top of a 0.64 cm (1/4") Lucite tray.

At smaller source-to-probe distances there is a greater difference between the tissue maximum ratio with and without accessories present. Therefore, as the distance to the source of contamination decreases, the dose increases. The tissue maximum ratio for SPD = 75 cm (Figure 17) is greater than the tissue maximum ratios for SPD = 100 cm and SPD = 120 cm (Figures 15 and 16) at all depths. The difference between the tissue maximum ratios as a function of source-to-probe distance is most pronounced at the surface.

The accessory build-up curves were measured on the Mevatron -6 for SPD = 75 cm and SPD = 100 cm. They show very similar features when compared to the 15 MV curves (see Figures 18 and 19). Accessories placed in the field increase the TMR at all depths below d_{max}. There

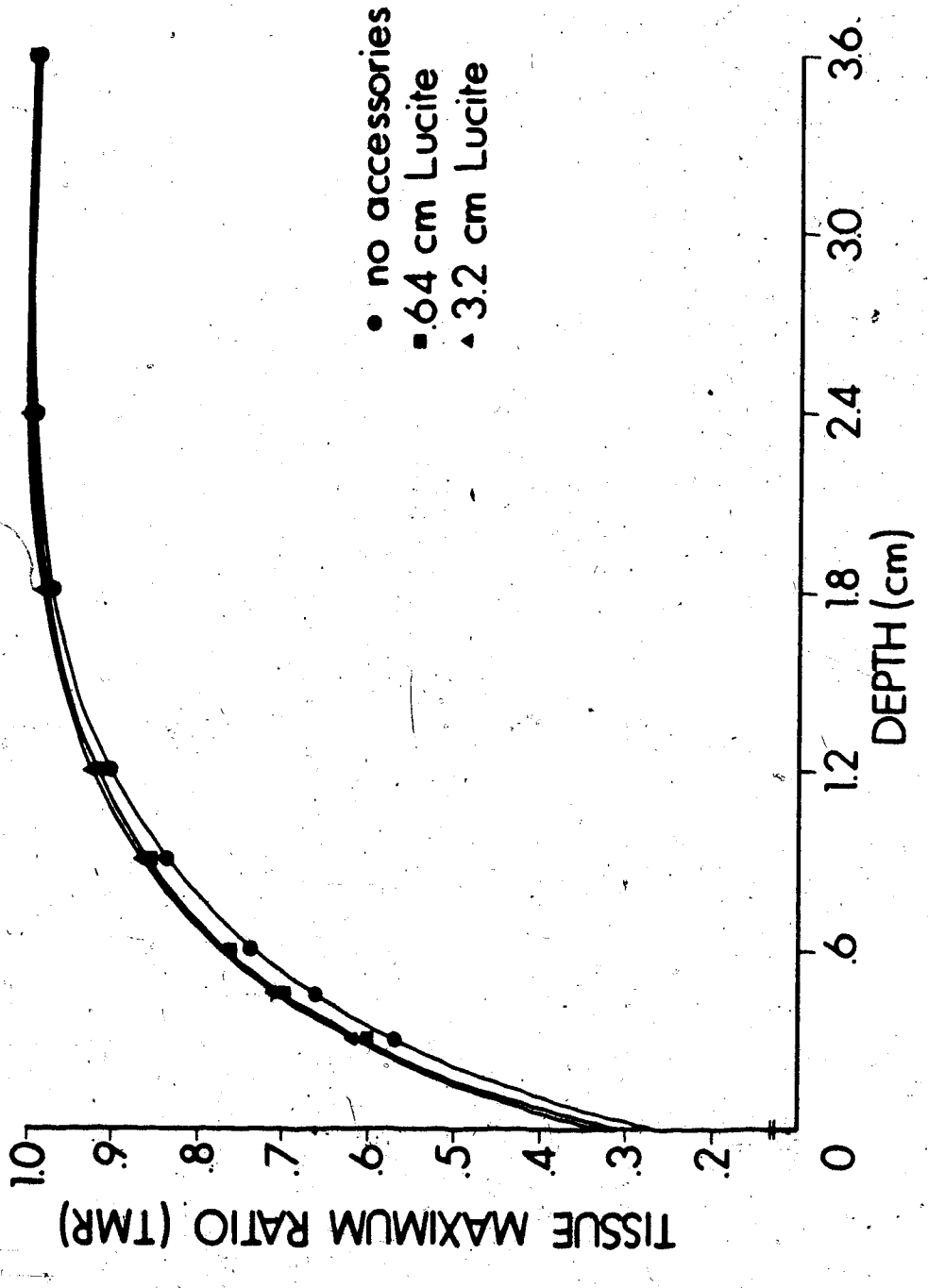

Figure 15. Accessory build-up curves at 140 cm SPD for a 15 MV beam.

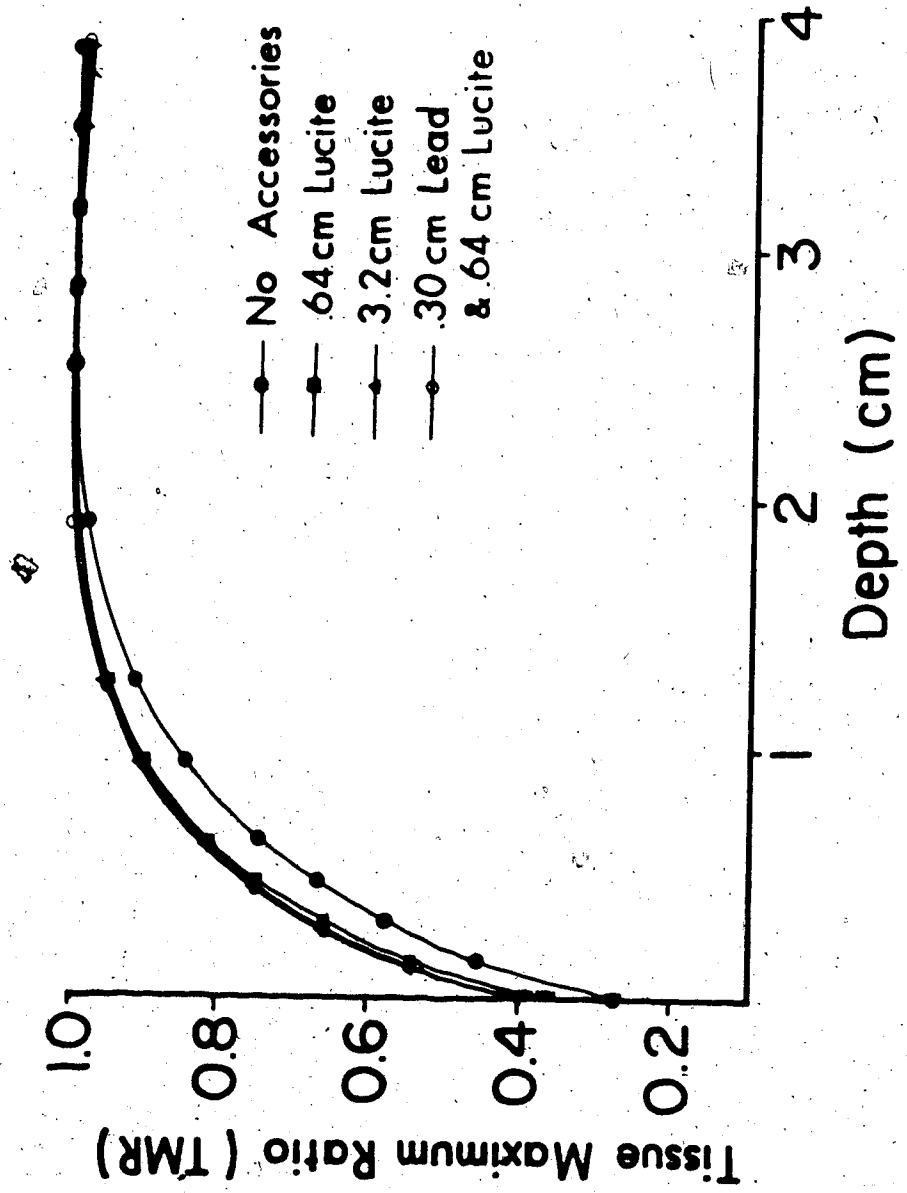

Figure 16. Accessory build-up curves at 100 cm SPD for a 15 MV beam.

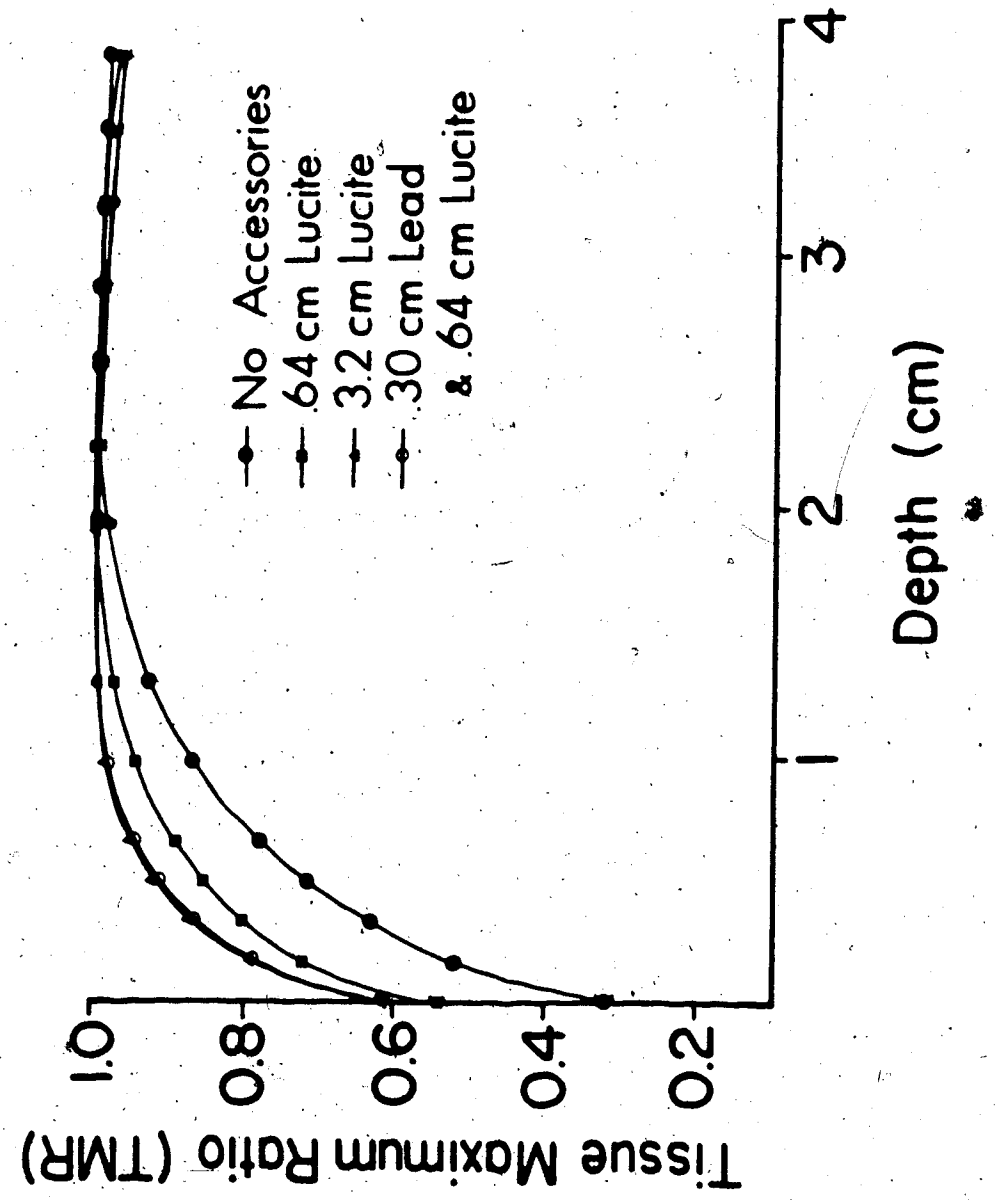

Figure 17. Accessory build-up curves at 75 cm SPD for a 15 MV beam.

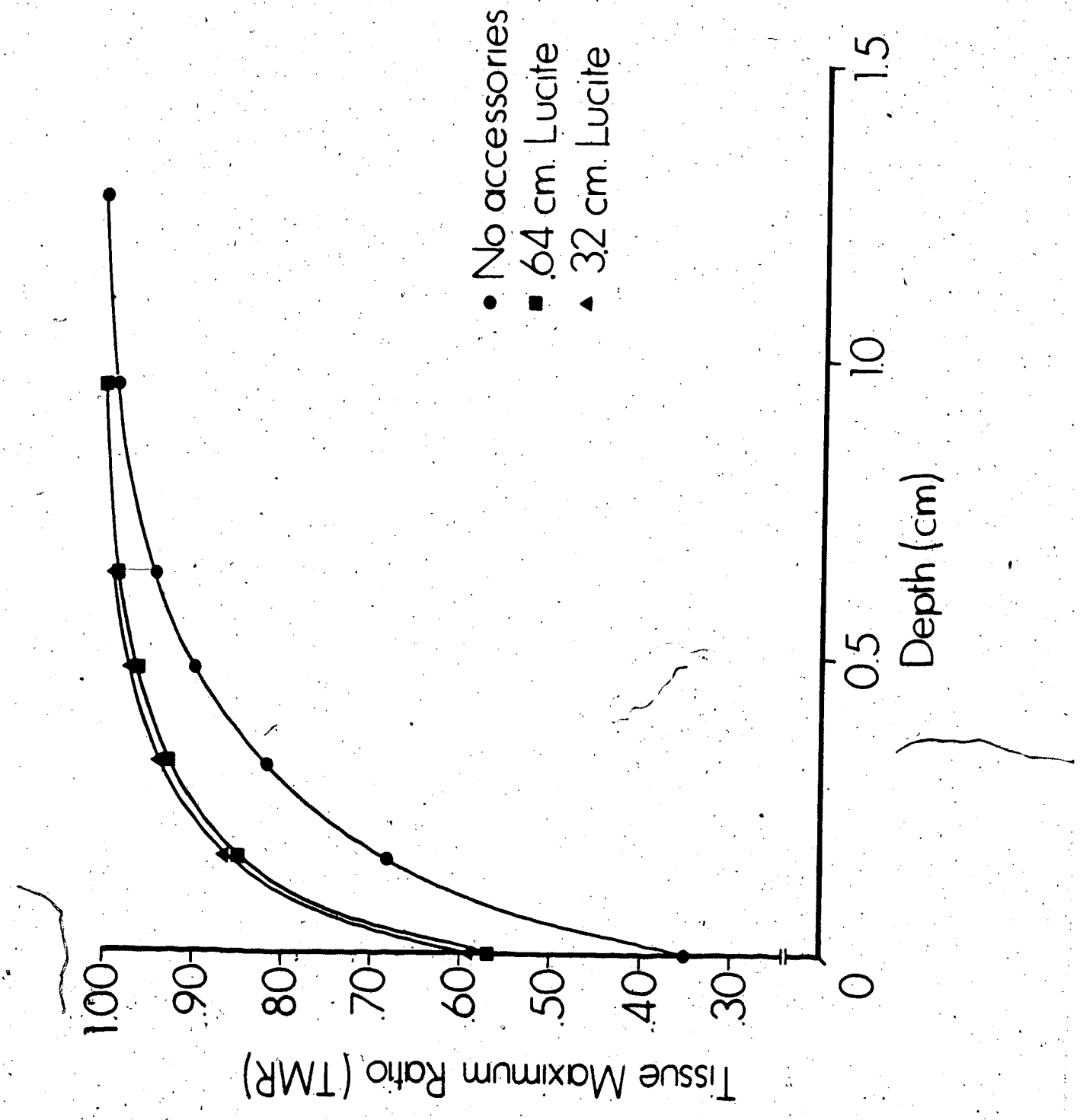

Figure 18. Accessory build-up curves at 75 cm SPD for a 6 MV beam.

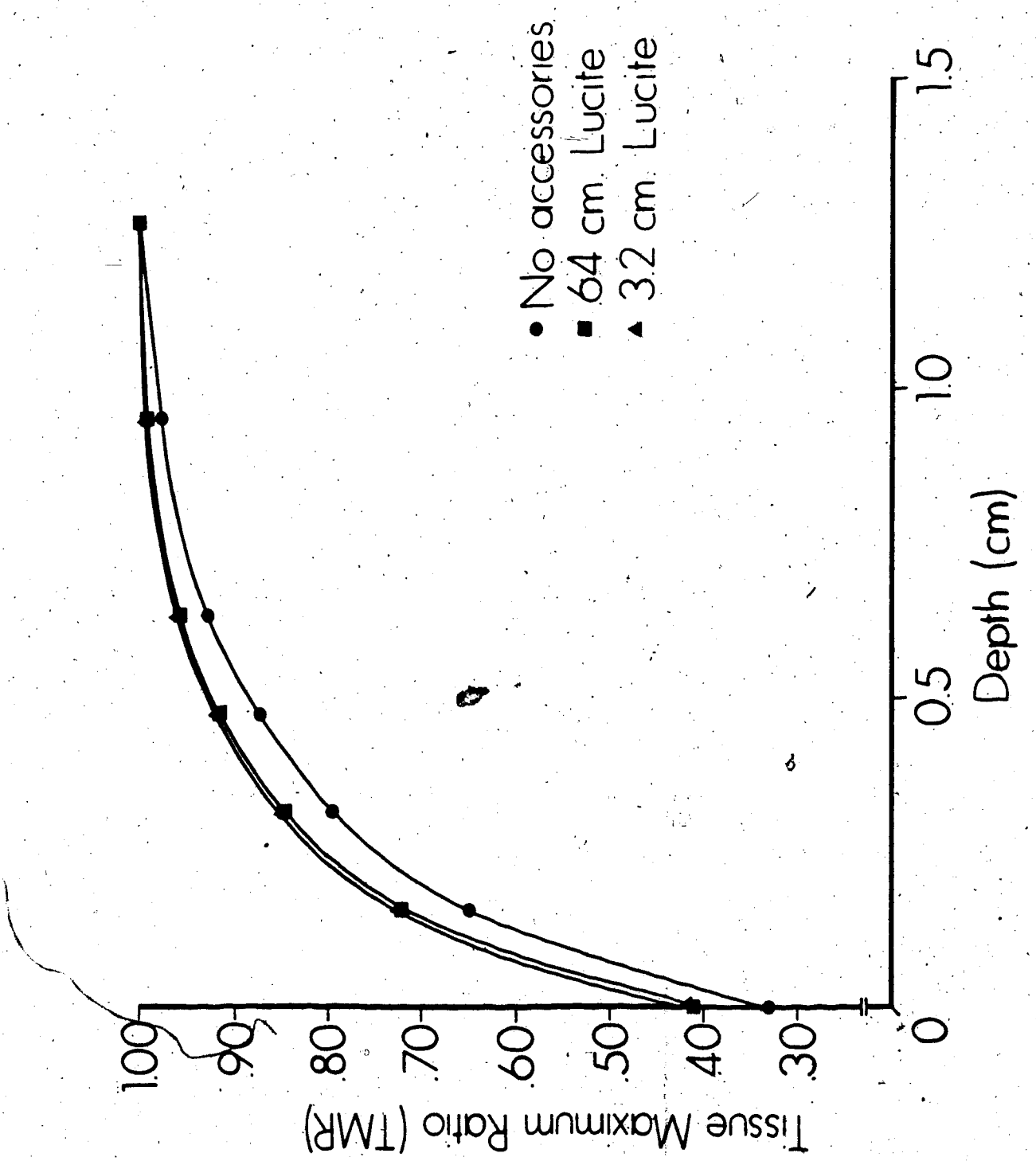

Figure 19. Accessory build-up curves at 100 cm SPD for a 6 MV beam.

is no difference between a 3.2 cm and a .64 cm thick Lucite accessory at an SPD of 100 cm. However, a small difference is observed in TMR between the same two thicknesses of Lucite when introduced at SPD = 75 cm. The depth at which d_{max} occurs is shifted from 1.6 cm to 1.3 cm with the introduction of the Lucite accessories at both SPD = 75 cm and 100 cm. A comparison between 6 MV and 15 MV was made by normalizing the depth to d_{max}. The comparison is illustrated in Figures 20 and 21. As observed for the open field build-up curves, the accessory build-up curves at 6 MV exceed those at 15 MV at the same relative depth. This applies for both source-to-probe distances of 75 cm and 100 cm.

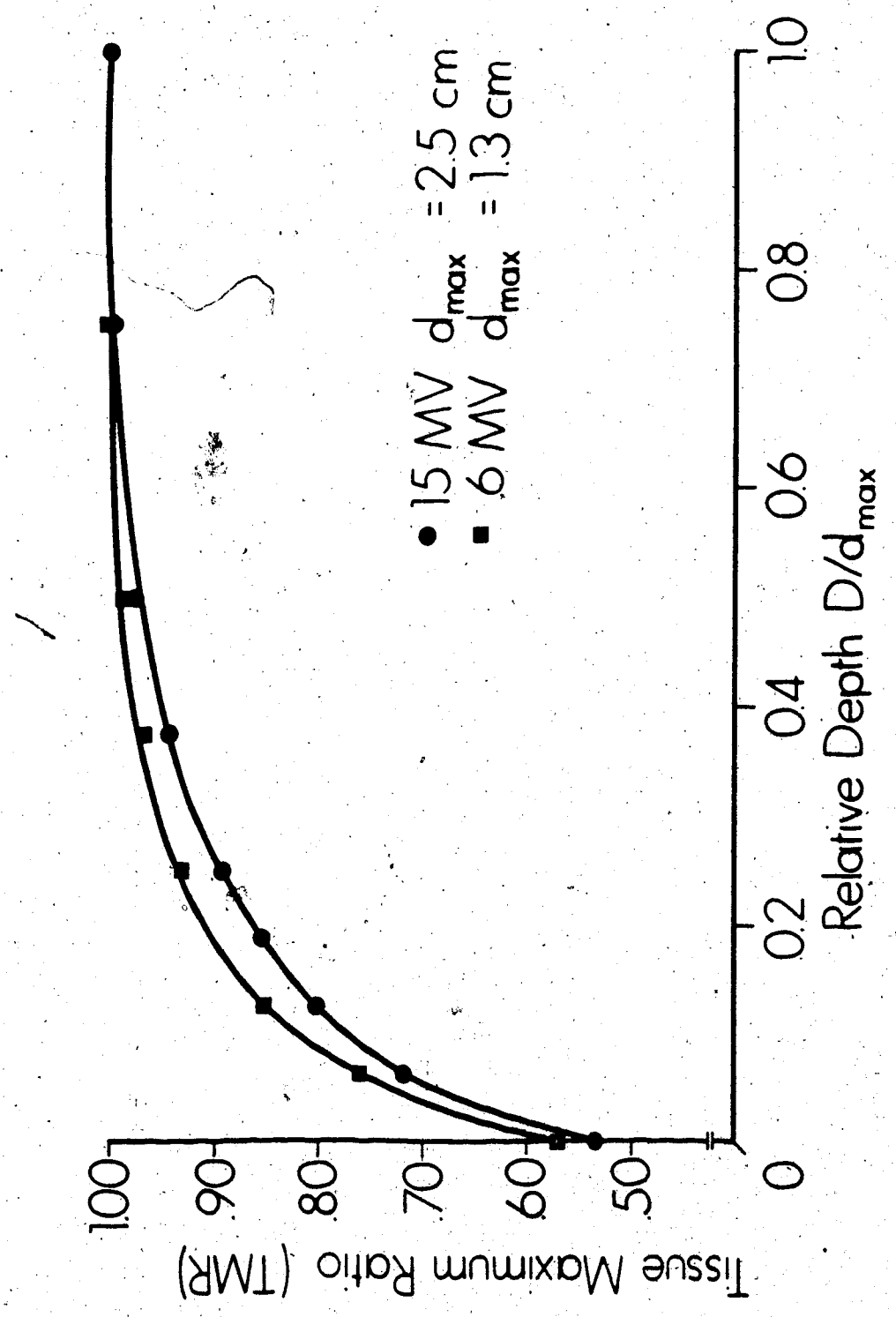

Figure 20. Comparison between 6 MV and 15 MV accessory build-up curves at 75 cm SPD.

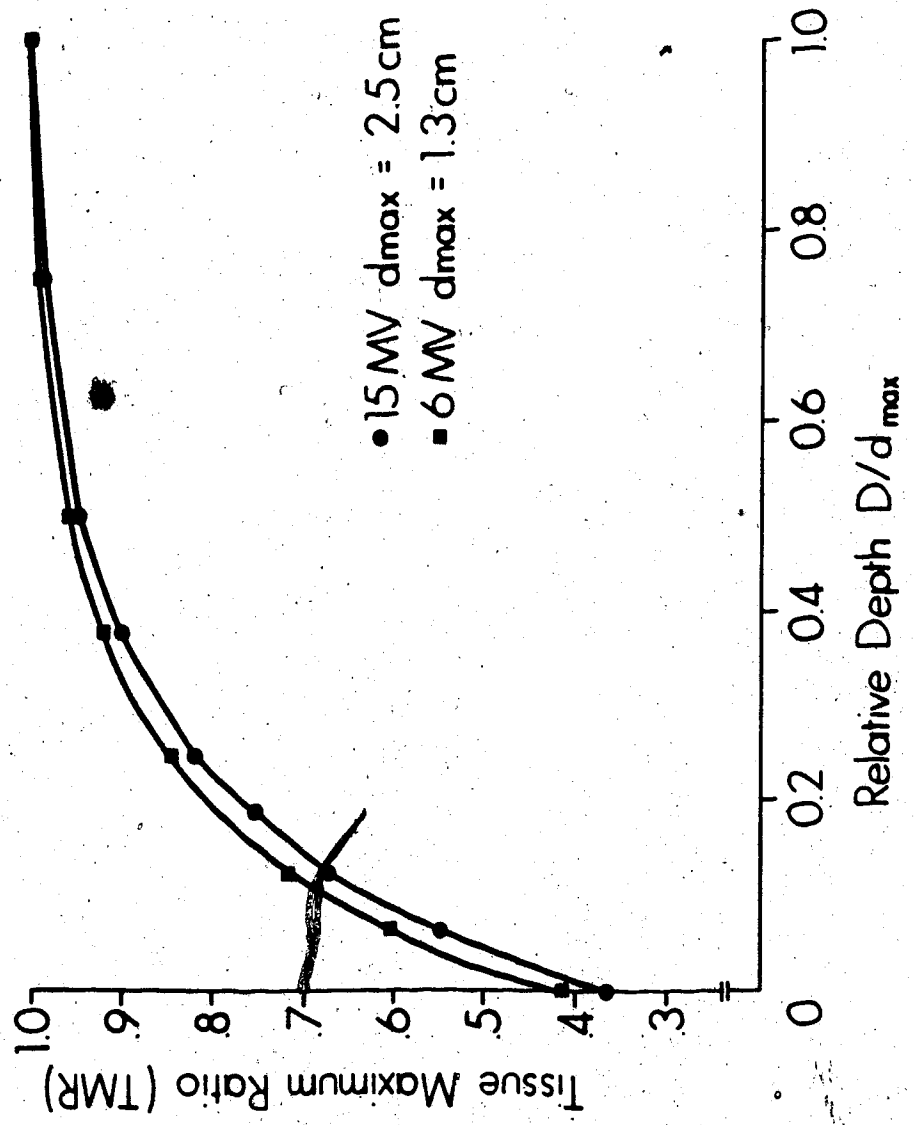

Figure 21. Comparison between 6 MV and 15 MV accessory build-up curves at 100 cm SPD.

2.3 Filtering the Electron Contamination

When at the surface, the chamber used has a sufficiently thin window to ensure that the build-up depth is approximately zero (5 μm polystyrene equivalent). The window thickness has an equivalent thickness of less than a centimeter of air. Only very low energy photons would have had a reasonable probability of interaction with such a window. In order to be detected these photons would have had to have been produced within a few centimeters of the chamber, otherwise they would have been rapidly attenuated in air. Primary photons with a low enough energy to have had a high probability of interaction with the window would have been completely attenuated when the beam emerged from the beam defining head. Therefore, the surface dose is not due to low energy forward directed photons. Some of the dose at the surface is attributable to backscatter, but most of the dose is due to contaminant electrons.

Filtering of electron contamination produced by accessories is rarely practiced for megavoltage energies above those of Co^{60}. The efficacy of electron filtering for materials of various atomic numbers at 6 MV and 15 MV was studied.

Placing a filter beneath an accessory produces a number of effects; the intensity of the primary beam is reduced, the number of interactions to produce electron contamination is increased and there is increased attenuation and scattering of electrons. The reduction of the primary beam can be taken into account by normalizing the readings taken at the surface to readings taken at d_{max} under the same conditions of filtration; in other words, by taking a tissue maximum ratio under conditions of filtration.

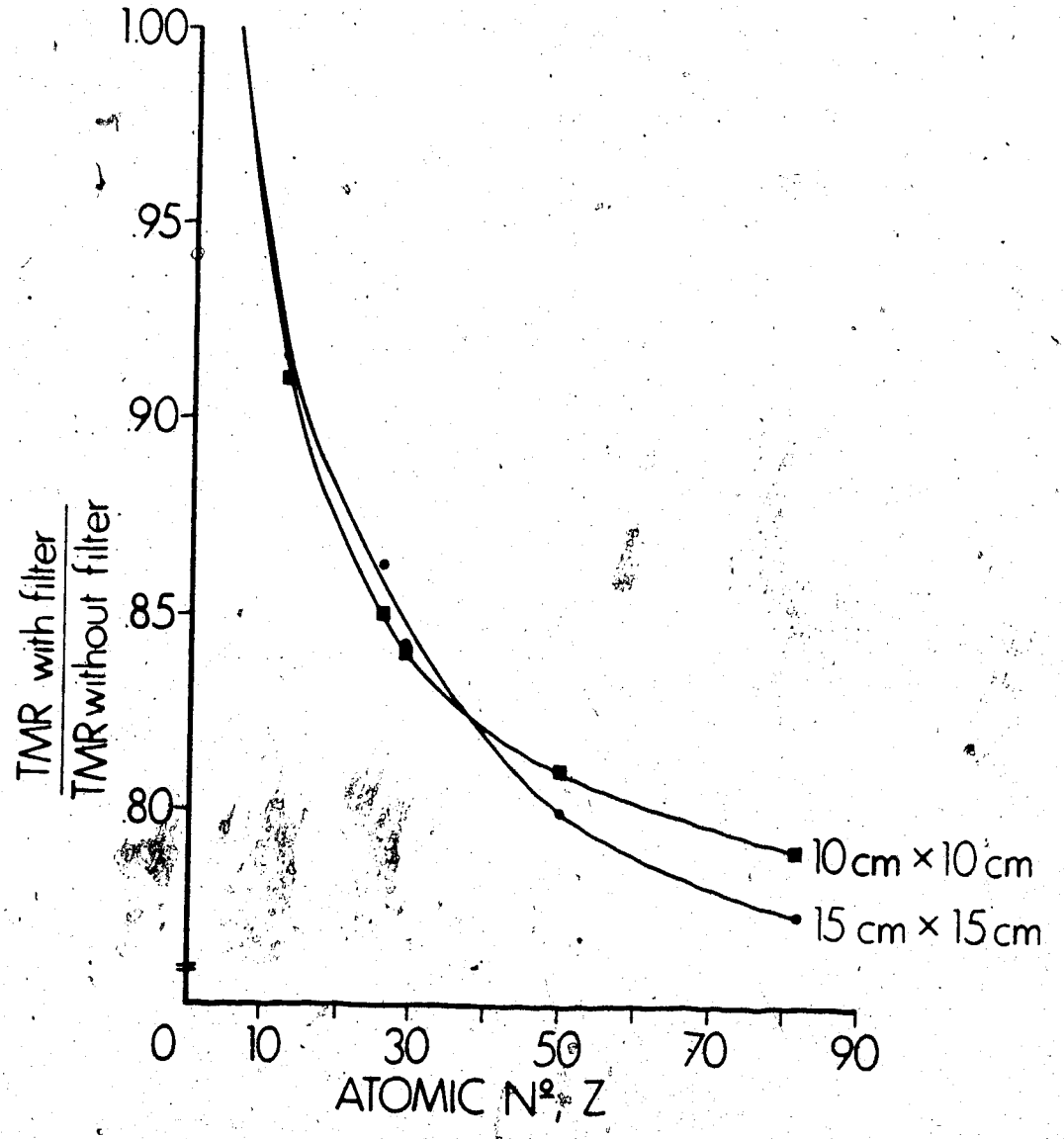

Figure 22. Reduction in the 15 MV surface dose when electron filters with materials of various atomic numbers are placed beneath the accessory tray. In all cases, an equilibrium thickness of filter was used.

It is unlikely that filtration changes the amount of electron contamination present in the beam because the amount of electron contamination did not continue to increase with thickness of accessory after 0.64 cm of Lucite at 15 MV (see Section 2.2 and Figure 16). This was verified by placing the filter material above the accessory tray (thickness = 0.64 cm of Lucite). The reading at the surface with the filter material above the accessory compared to d_{max} was no different within experimental error from that with the accessory tray in the field alone.

There was some reduction in the surface TMR when a filter with an atomic number higher than that of Lucite was placed beneath the accessory tray. The ratio of the TMR of the accessory tray alone to the TMR with a filter underneath the tray is shown in Figure 22 for 15 MV at field sizes of 10 cm x 10 cm and 15 cm x 15 cm with an SPD of 100 cm. High atomic number materials produce the most filtering although the effect is not very significant. Lead will reduce the surface dose by about 20%. An increased amount of electron scatter and absorption can be the only cause of the filtering effect.

Similar results were obtained at 6 MV for a field size of 15 cm x 15 cm at an SPD of 100 cm (see Figure 23). Again, lead proved to be the most effective filtering material at this energy. It reduced the surface dose by about 20% as well.

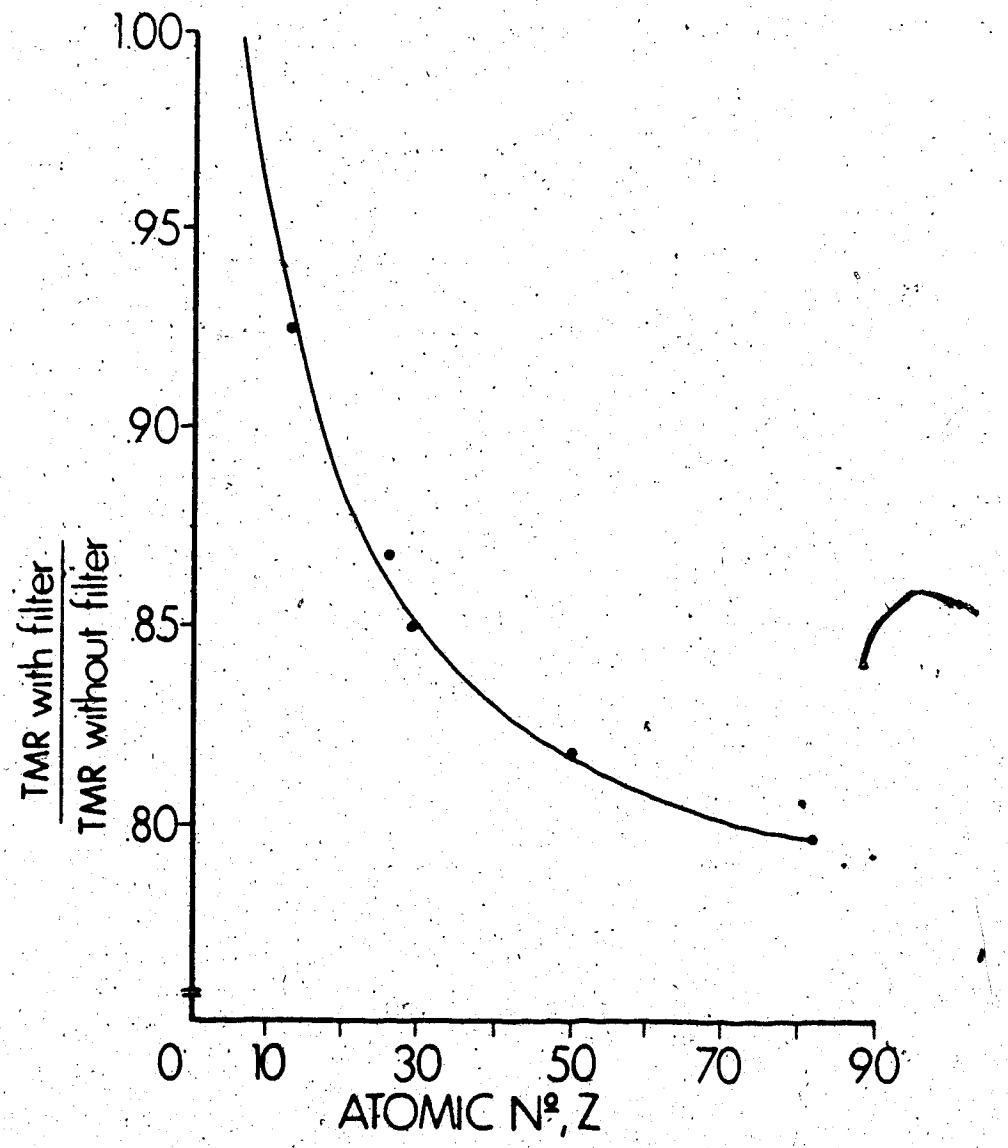

Figure 23. Reduction in the 6 MV surface dose when electron filters with materials of various atomic numbers are placed beneath the accessory tray for a field size of 15 cm x 15 cm.

2.4 Distance Distribution of the Surface Dose

2.4.1 SPD Dependence of the Surface Dose

The surface maximum ratio is defined to be the tissue maximum ratio measured with the chamber at the surface (i.e. d=0). Figure 24 illustrates that the surface maximum ratio in the open 15 MV beam increases rapidly as the source-to-probe distance decreases for both 20 cm x 20 cm and 30 cm x 30 cm field sizes.

The curves for field size collimated to 20 cm x 20 cm show the effect of a thin accessory. The Siemens Mevatron -20 is equipped with a removable 1 mm thick Lucite cross-hair tray which can be inserted at 40 cm from the source. When the source-to-probe distance is less than 75 cm, the surface dose with the cross-hairs in place is greater than when it is removed. However, the cross-hairs, when in place, reduce the surface dose in the clinical region of SPD greater than 75 cm. This is an exception to previous observations that accessories in the field increased the surface dose.

2.4.2 Determination of the Apparent Source of Contamination Electrons

As the source-to-probe distance increases, the volume of air between the target and probe increases. For Co^{60}, Nilsson and Brahme (46) have predicted an increase in absorbed dose as a function of source-to-probe distance due to Co^{60} photon interactions with air. In these experiments the reverse appears to be the case and a decrease in the dose as a function of increasing source-

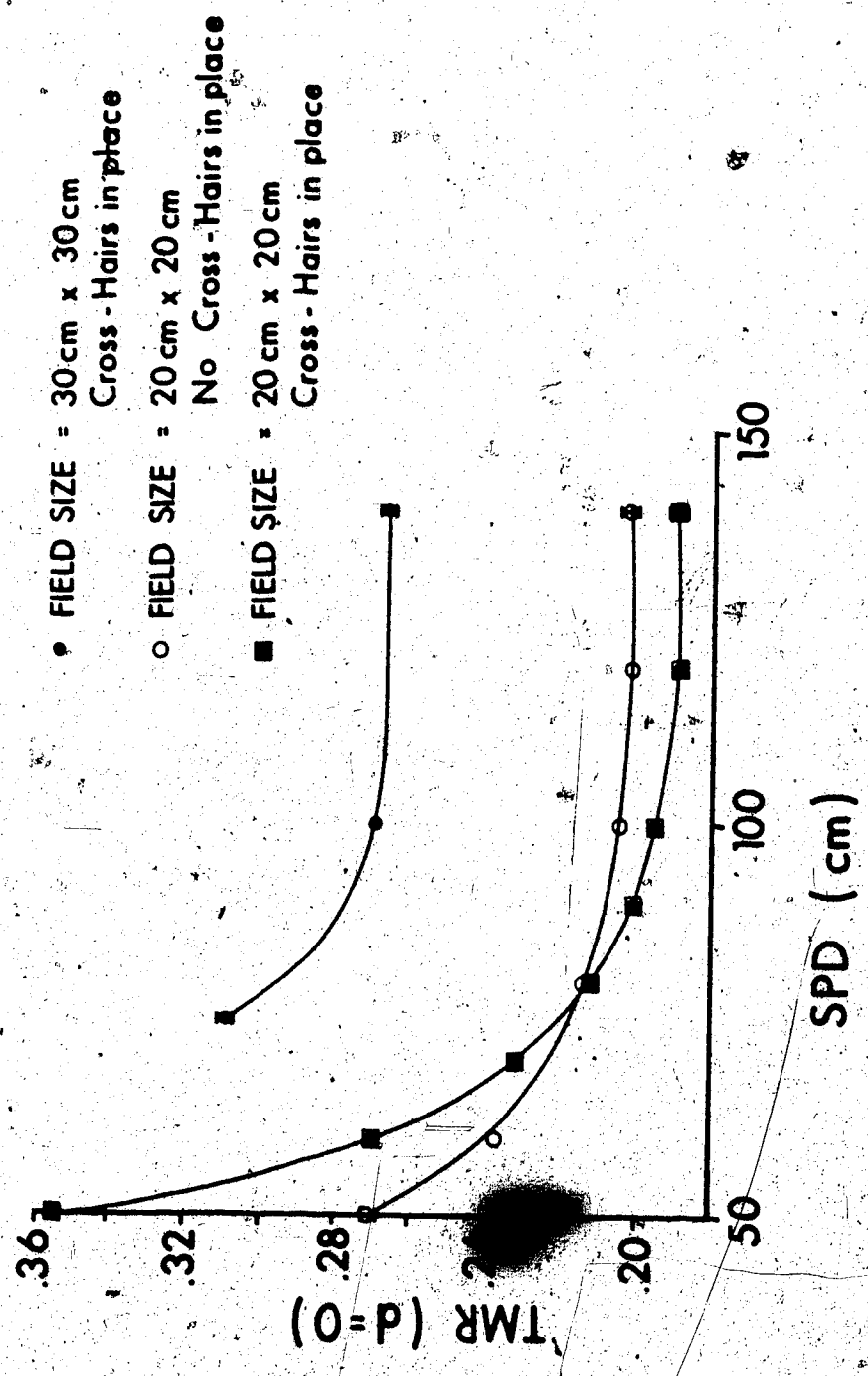

Figure 24. Distribution of the surface dose as a function of source-to-probe distance at 15 MV.

to-probe distance has been observed. This implies that at 15 MV, for a field size of 30 cm x 30 cm, the interaction of the primary photon beam with air is not the major source of electron contamination.

The surface maximum ratio is normalized to the dose measured at d_{max} within a polystyrene phantom. The maximum dose in a phantom is due almost entirely to primary photons for which the variation with distance falls off as $1/(SPD)^2$. However, the electron contamination does not necessarily arise at the source of primary photons. Instead of normalizing the surface dose at a given SPD to the dose at d_{max}, each surface dose at the same SPD is normalized to the dose measured at a convenient point inside a phantom using a standard field size and photon source-to-probe distance. The isocentric normalized dose, IND, is defined as:

$$IND = \frac{\text{Dose delivered to a point at an arbitrary d, SPD, field size}}{\text{Dose delivered at the isocenter}} \qquad (2.3.1)$$

The isocenter point was at d_{max} at SPD = 100 cm with a field size of 10 cm x 10 cm.

The apparent source of contamination electrons can be located assuming that it is a point source and there is no attenuation of electrons by air. Therefore, the isocenter normalized dose at the surface is directly proportional to the inverse square of the distance to the source of the

electron contamination, or:

$$IND(d=0) \propto \frac{1}{(SPD-d_o)^2} \qquad (2.3.2)$$

where d_o is the distance of the source of contamination electrons below the primary photon source.

Figure 25 is a graph of $\sqrt{1/IND(d=0)}$ versus SPD. The graph yields a straight line except for very large source-to-probe distances. Therefore, the source must be small and the inverse square approximation valid for source-to-probe distances less than 120 cm. The x-intercept of the graph yields a distance, d_o, of 12 cm below the primary source of photons. This corresponds approximately to the position of the bottom of the fixed head assembly which consists of the field flattening filter and the beam monitor ion chamber. The bottom surface of the field flattening filter is 3.1 cm in width, which at distances greater than 50 cm, subtends an angle no larger than 3.5^o which would approximate a point source.

The dependence of the surface isocentric normalized dose, IND(d=0), on SPD, was investigated for a 6 MV beam. The inverse root of the isocentric normalized dose, $1/\sqrt{IND}$, versus SPD is plotted in Figure 26. The intercept appears to be between 30 and 40 cm beneath the target, however, the line is not straight (in contrast to that obtained at 15 MV) indicating that a $1/r^2$ dependence from a localized source of contamination is not the entire explanation for the presence of the surface dose.

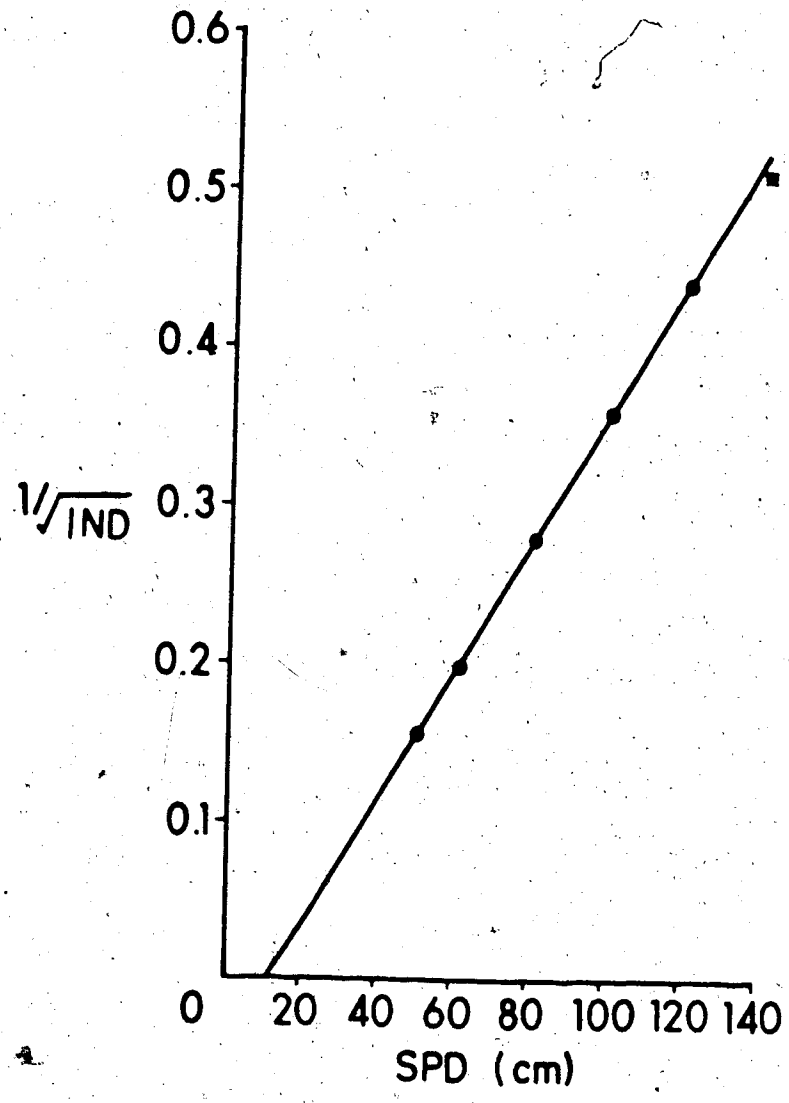

Figure 25. Graph illustrating the inverse square dependence of the surface dose on the distance to the source of contamination at 15 MV.

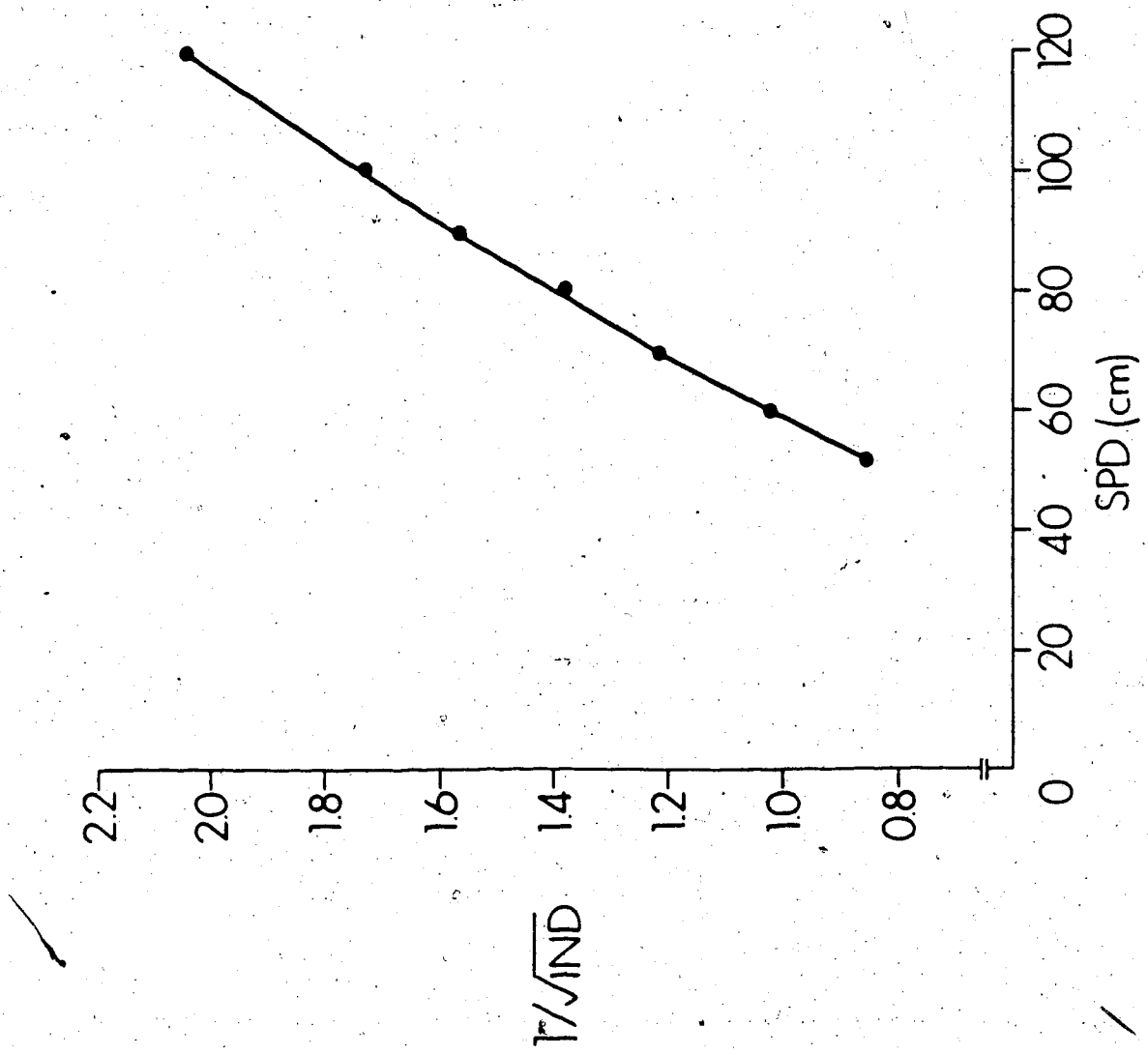

Figure 26. Graph illustrating the failure at 6 MV of the inverse square dependence to a localized source of contamination.

2.5 Lateral Distribution of the Surface Dose

The magnitude of surface dose as a function of lateral displacement from the central axis was measured for several source-to-probe distances. The central axis angle, C.A.A., was defined to be the angle between the central axis and a line joining the probe to the apparent source of electrons. This established parameters for the lateral direction in order to compare the distribution at various source-to-probe distances (see inset on Figure 27). In each case, the surface dose at any central axis angle and source-to-probe distance is normalized to the dose at d_{max} on the central axis (C.A.A.=0). The curves in Figure 27 follow a Gaussian distribution.

At all points across the field, a smaller SPD results in a larger electron contamination dose. This agrees with the surface dose dependence measured along the central axis. Both the lateral distribution and the dependence on the distance from the source of the electron contamination agree with the work of Almond (5).

The lateral surface dose distribution for 6 MV and 15 MV beams at SPD=100 cm is shown in Figure 28. The distribution for each beam has been normalized to the maximum surface dose. Since the distribution at 6 MV was mapped for only one source-to-probe distance the abscissa is left as the distance from the central axis. The ordinate is defined as the surface dose at some distance away from the central axis normalized to the dose at d_{max} measured at the central axis. There are two differences between the 6 and 15 MV lateral distributions. First, the maximum dose does not occur at the central axis but from 4 to 6 cm off the central axis. These "horns" in the surface dose are a very small but real effect. Secondly, there is a more rapid decrease in

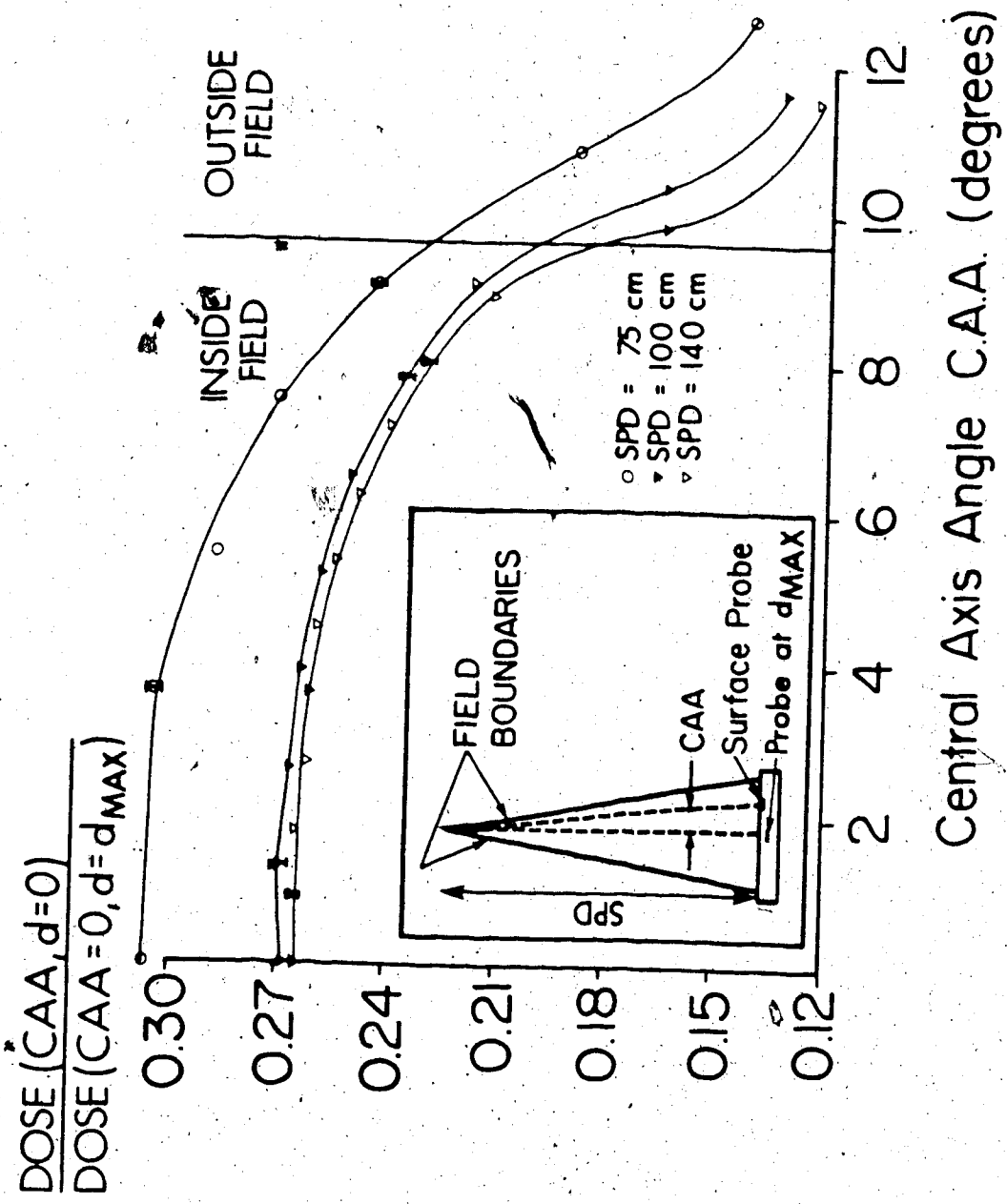

Figure 27. Gaussian distribution of the surface dose at 15 MV. The inset is a schematic diagram of the experimental arrangement.

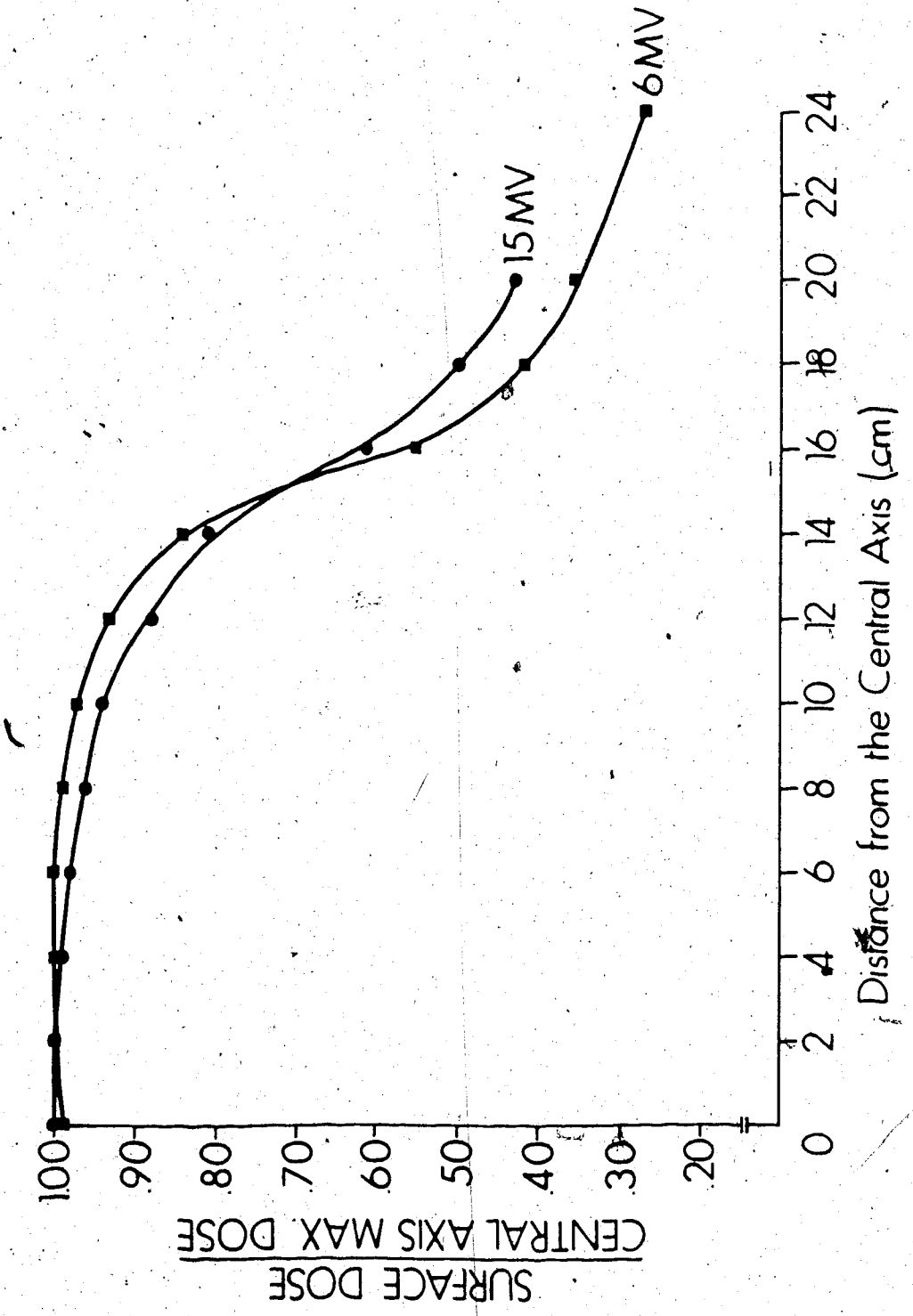

Figure 28. Comparison between 6 MV and 15 MV of the lateral distribution of the surface dose at 100 cm SPD. The lateral distribution is not Gaussian at 6 MV. The field size is 30 cm x 30 cm.

the surface dose of the 6 MV beam near the field edge compared to the 15 MV beam. The lateral distribution at 6 MV is not Gaussian.

2.6 Surface Dose Measured for Rectangular Fields

The surface isocentric normalized dose was measured for rectangular and square fields. Both collimator openings were varied by 5 cm increments at 100 cm SPD so that the dose at all such fields between 5 cm x 5 cm and 30 cm x 30 cm were determined. Table 2 illustrates the results.

The surface isocentric normalized dose as measured at SPD = 100 cm depends on which collimator defines the long or short axis. If Field A (upper collimator) is the long axis (lower left hand part of Table 2) the surface dose tends to be greater than if Field B (lower collimator) is the long axis for the same field dimension. For example, the surface isocentric normalized dose at A = 10 cm and B = 25 cm is .106 whereas the dose at B = 10 cm and A = 25 cm is .109.

In general, the larger the field area, the greater the surface dose. If a square and rectangular field have the same area the square field will have the greater surface isocentric normalized dose. For example, if A = 10 cm and B = 10 cm, the surface dose is .071 but if A = 5 cm and B = 20 cm, the surface dose is .065 (if A = 20 cm and B = 5 cm, the dose is .064).

The equivalent square field dose for a rectangular field was determined by plotting the dose as a function of square field width and finding the square field that has the same dose as the rectangular field. Table 2 also lists the results of the equivalent square determination. For large fields (greater than 10 cm x 15 cm) the equivalent square field area is approximately equal to the geometric field area. For example, if A = 20 cm and B = 10 cm, the equivalent square area is (13.8 ± 4)cm x (13.8 ± 4)cm = (190 ± 10)cm^2 and the

Table 2 Surface Normalized Dose For Rectangular Fields.

Field A (cm) \ Field B (cm)	5.0	10.0	15.0	20.0	25.0	30.0
5.0	0.037	0.049	0.057	0.062	0.067	0.070
10.0	0.049	0.071	0.087	0.098	0.106	0.112
15.0	0.057	0.088	0.109	0.125	0.138	0.147
20.0	0.064	0.100	0.126	0.146	0.161	0.173
25.0	0.069	0.109	0.139	0.163	0.181	0.195
30.0	0.072	0.116	0.150	0.176	0.196	0.211

Equivalent Square Fields For The Surface Dose

Field A (cm) \ Field B (cm)	5.0	10.0	15.0	20.0	25.0	30.0
5.0	5.0	6.6	7.7	8.5	9.1	9.5
10.0	6.6	10.0	11.9	13.5	14.7	15.5
15.0	7.7	12.0	15.0	17.3	19.1	20.4
20.0	8.7	13.8	17.5	20.0	22.5	24.2
25.0	9.3	15.0	19.3	22.7	25.0	27.3
30.0	9.8	16.0	20.9	24.7	27.5	30.0

geometric area is (20.0 ± .1) cm x (10.0 ± .1) cm = (200 ± 3) cm^2. However, for small fields the equivalent square field area is less than the geometric field area. The surface equivalent square field is very different from the equivalent square field at d_{max}.

2.7 Penetration Curves Outside the Field

2.7.1 Transmission Through the Collimators

The transmission of primary photons through the collimators was studied by placing a Capintec 0.6 cc cylindrical ion chamber (Model PR-06C) at d_{max}. A measurement was taken at the central axis with a field size of 20 cm x 20 cm. All subsequent readings were normalized to this measurement.

Transmission measurements were made with one or both collimator sets closed. Figures 29a) to d) illustrate the position of the upper and lower collimators and the relative dose received. The percentage transmission at the field boundary through one collimator is about 1% and about 0.1% through both collimators.

2.7.2 Determination of the Penetration Curves Outside the Field

By definition, except for transmission through the collimators, the primary photon dose outside the field boundary is zero. Only contamination electrons and scattered photons can contribute to this dose. This was studied experimentally.

Nilsson and Brahme have shown that the scattered photon spectrum at the field edge is almost identical to the photon spectrum at the central axis for a 20 cm x 20 cm field for nominal beam energies of 6 MV and 21 MV. It is unlikely that the electron contamination spectrum changes appreciably between the center and edge of the field.

In order to get as close as possible to the field

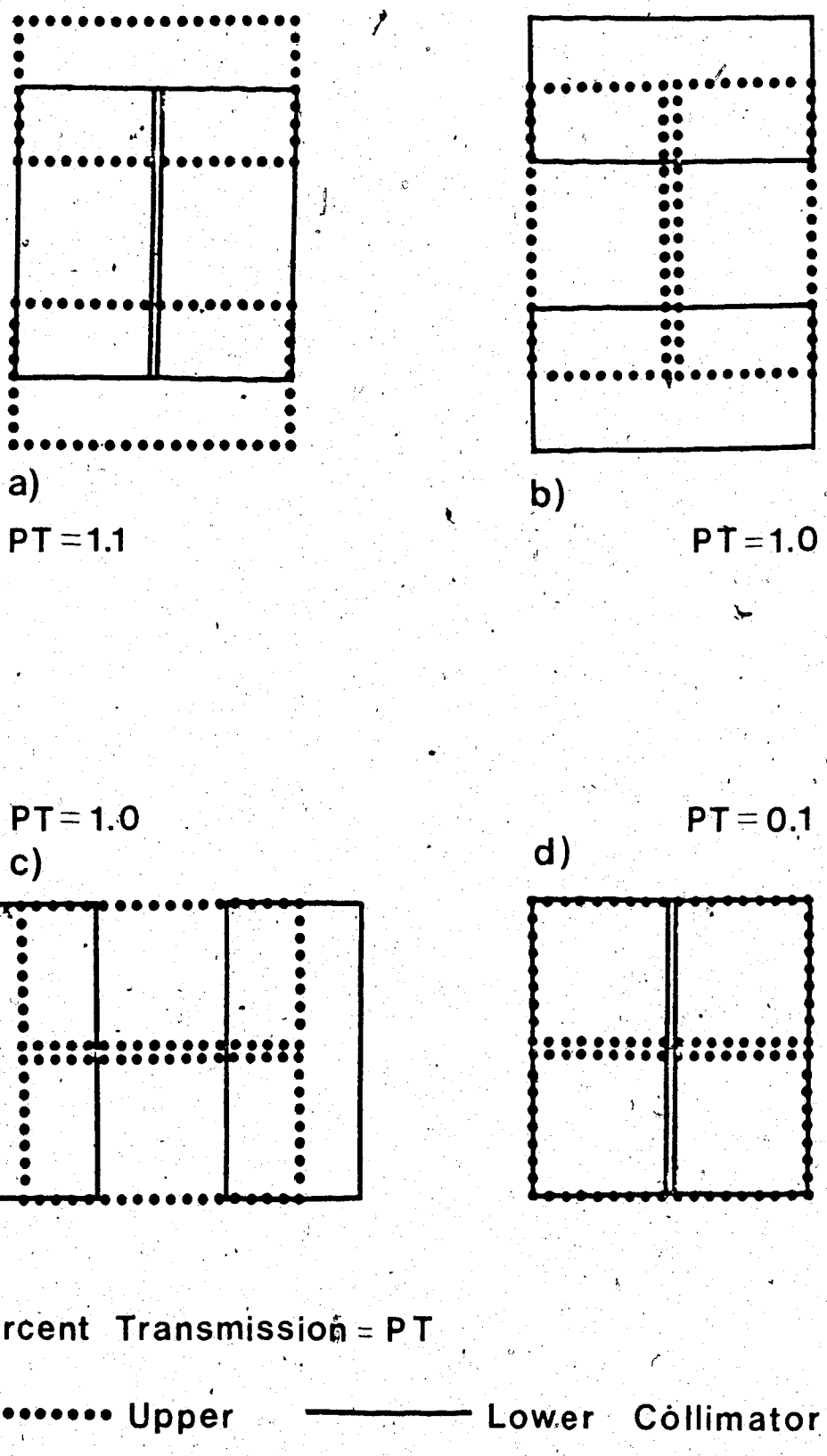

Figure 29. Transmission measurements on the Mevatron 20. a) Lower collimator closed, upper open; b) Upper collimator closed, lower open with collimator assembly rotated 90°; c) As in b) but collimator assembly not rotated; d) Both collimator sets closed.

boundary, the thin-window parallel-plate probe was placed near the edge of the phantom (see Figure 30). The phantom was tilted at an angle of 8.5^{o}* so that the position of the phantom surface would not move closer or further from the field boundary with the addition of build-up layers. This also reduced the number of particles incident at oblique angles upon the phantom at oblique angles.

Figure 31 illustrates the penetration curve 3 cm outside a 30 cm x 30 cm field. The penetration curve has a peak at a shallow depth (1-2 mm) then falls off rapidly at depths greater than 1 cm. The curve has a relatively slow fall-off at depths beyond about 2 cm. The general shape of the curve agrees with the work of Scrimger and Kolitsi (30) for 8 MV x-rays.

The penetration curve 3 cm outside the field was measured at 6 MV for the same field size (30 cm x 30 cm) and SPD (100 cm) as the comparable experiment carried out at 15 MV. The phantom was again tilted at 8.5^{o}. Figure 32 illustrates a rapid decrease in the penetration curve at shallow depths with a levelling out at greater depths. The maximum dose is at the surface at 6 MV rather than at a shallow depth beneath the surface. This suggests the dose at shallow depths is again due mainly to contamination electrons while the dose at deeper depths is due to scattered photons.

The relative dose in the plateau region ($d \geq d_{max}$) for both the 6 MV and 15 MV curves outside the field is approximately 0.3 of the maximum dose received.

* The angle of tilt = $\tan^{-1} \frac{\text{Field Width}}{2 \text{ SPD}}$

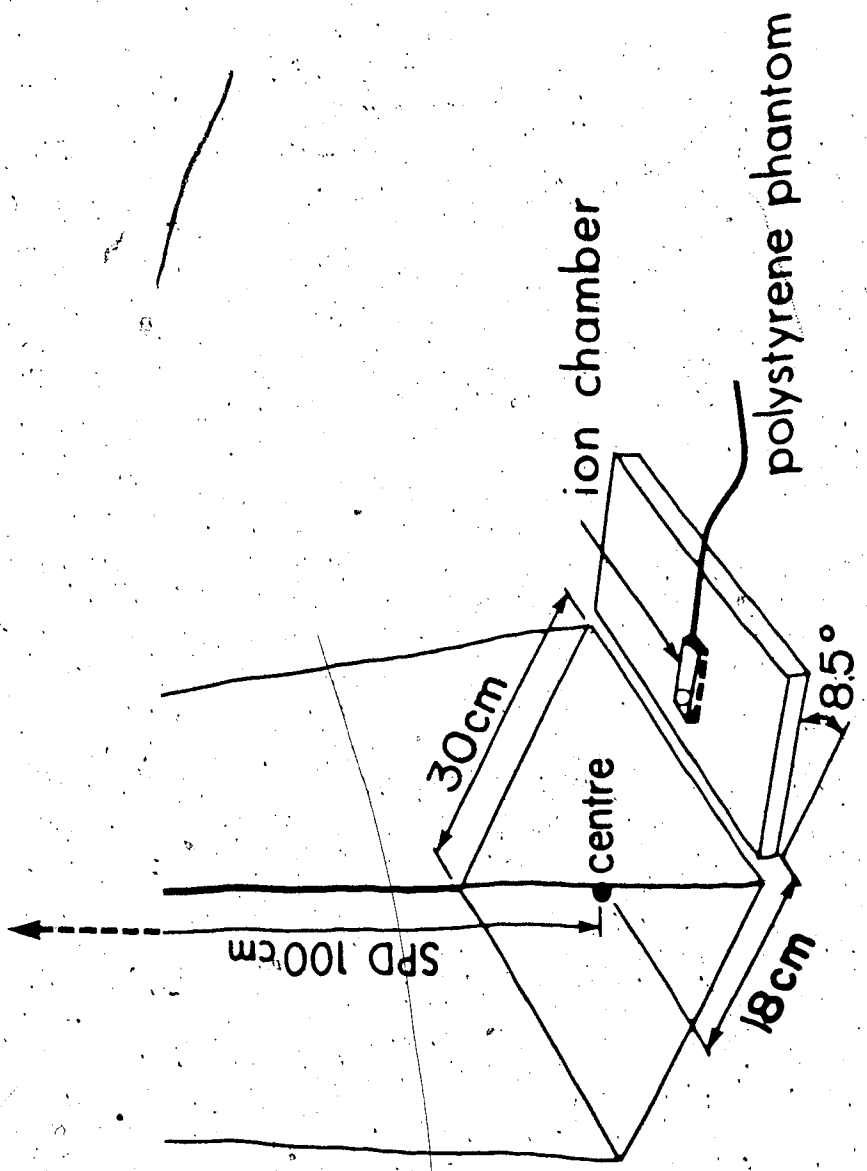

Figure 30. Diagram of the experimental arrangement to determine the penetration curve outside the field.

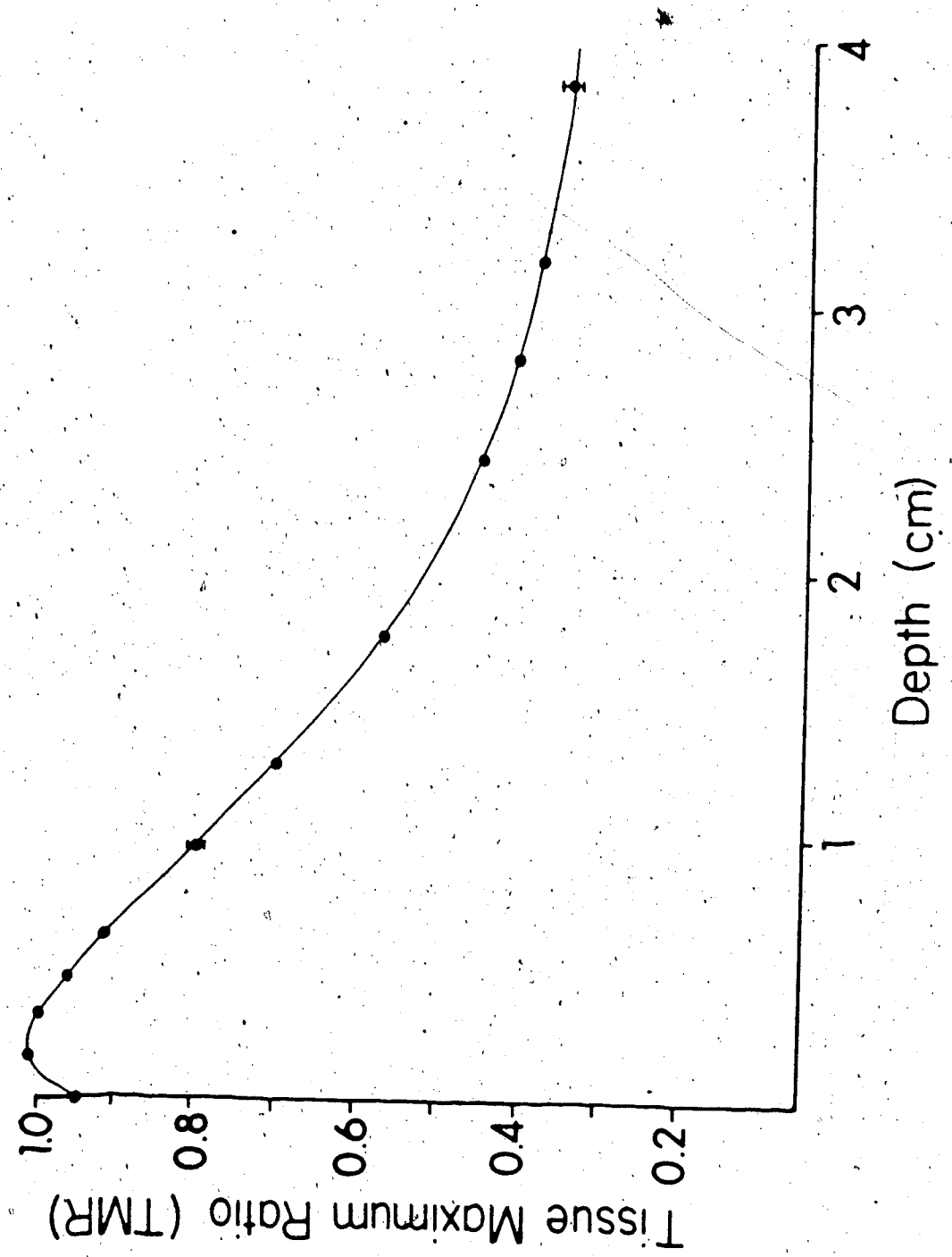

Figure 31. Penetration curve at 15 MV obtained 3 cm outside of a 30 cm x 30 cm-field (see Figure 30 for the experimental arrangement).

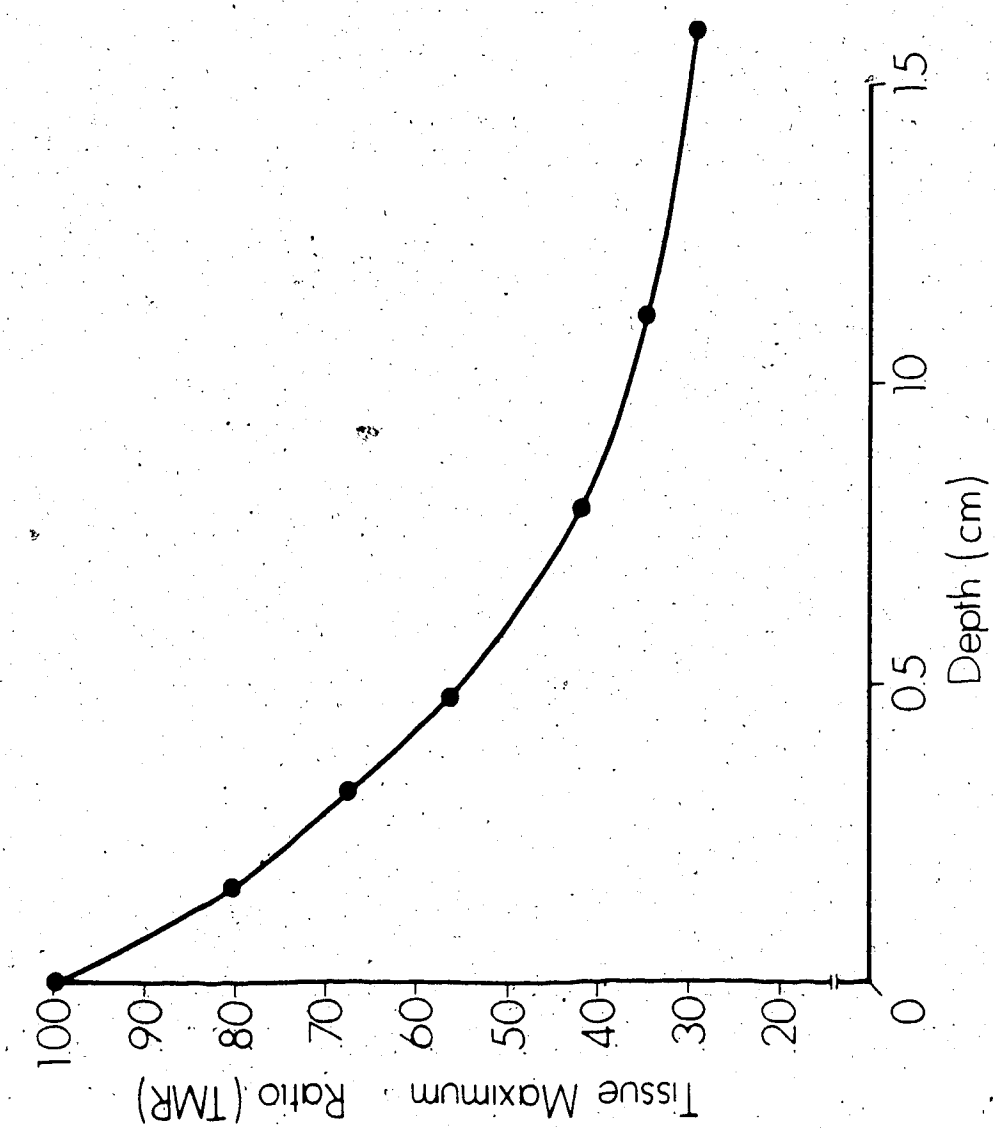

Figure 32. Penetration curve at 6 MV obtained 3 cm outside of a 30 cm x 30 cm field.

2.8 Increase in Dose with Increasing Field Width

2.8.1 Measurement of the Stem Effect

Exposure to ionizing radiation may cause a spurious signal attributable to the ion chamber cable such as a leakage current which is mistaken for ionization in the chamber volume. These phenomena are called the stem effects. A stem effect, if present, should increase with increasing field size. The manufacturer's claim that the stem effect for their thin window ion chamber is less than 1%.

The stem effect was measured by exposing the chamber at d_{max} in a phantom to a rectangular field as wide as the chamber volume and as long as the phantom. One measurement was taken with the cable completely in the field and another with the cable completely outside the field. The stem effect was found to be less than 0.5%.

2.8.2 Increase in Dose with Increasing Field Width

A number of authors (15-21,25,28,29,31-35) have commented on the dependence of the surface dose on the square root of field width both with and without accessories present in the beam. Many of these authors calculated TMR surface doses, in other words, normalized the surface dose at each field size to the dose at d_{max} for the same field size. However, since the dose at d_{max} increases with field size (as expressed by the output factor), such a plot would not unambiguously express the dependence of surface dose on field size.

A more general form of the isocentric normalized dose can be used to more clearly describe the dose dependence on field size. The ionization readings at some field size and a given source-to-probe distance are normalized to the maximum ionization readings (at d_{max}) obtained at a field size of 10 cm x 10 cm at the same source-to-probe distance. This quality will be called the normalized dose, ND. It is given by:

$$ND = \frac{\text{Dose delivered to a point at an arbitrary d, SPD, field size}}{\text{Dose delivered to } d_{max} \text{ at the same SPD at a field size of 10 cm x 10 cm}} \qquad (2.8.1)$$

The normalized dose is equal to the isocentric normalized dose at 100 cm SPD.

The tissue maximum ratio is directly proportional to the normalized dose. The constant of proportionality is the output factor. The relationship is given by:

$$ND\ (d,SPD,W) = \text{Output Factor}\ (SPD,W) \times TMR\ (d,SPD,W) \qquad (2.8.2)$$

where W represents the field size.

The normalization reading (the denominator of Equation 2.8.1) is not field size dependent so ND clearly illustrates dependence of the reading (the numerator of Equation 2.8.1) on field size.*

* Data acquisition is simpler using the concept of normalized dose. Only one set of measurements at d_{max} for a field size of 10 cm x 10 cm need be taken. A set of readings at d_{max} at all field sizes is not required. If an output factor curve has been determined, the TMR value may be obtained, if desired, using Equation 2.8.2.

The normalized dose, ND, for a variety of conditions at d=0 is plotted as a function of field width in Figure 33. Field width is defined as the square root of field area for square fields. Under these conditions, at 15 MV there is a linear increase in the surface dose with respect to field width. Note that either decreasing the SPD or placing the accessories in the field increases the slope of the curve. Since the surface dose for any given field size is proportional to the slope of the line, the slope is also a measure of the electron contamination, but with the advantage that it is not dependent on the field width.

A small phantom was placed completely within the field so that an increase in detected signal due to increasing field size could only be attributed to beam contamination. To obtain the dose as a function of depth for as many field widths as possible, the phantom lateral dimensions were kept as small as possible (i.e. 10 cm x 10 cm) which in turn dictated a minimum field size used in the determination of the contamination depth-dose curve of 15 cm x 15 cm. The maximum square field size attainable for the machine studied was 30 cm x 30 cm. These field sizes defined the range of the study.

The dose as a function of field width was measured for a number of depths with the limited polystyrene phantom of the type illustrated in Figure 34. Since there was build-up material on top of the ion chamber, it could not be assumed that all of the contamination

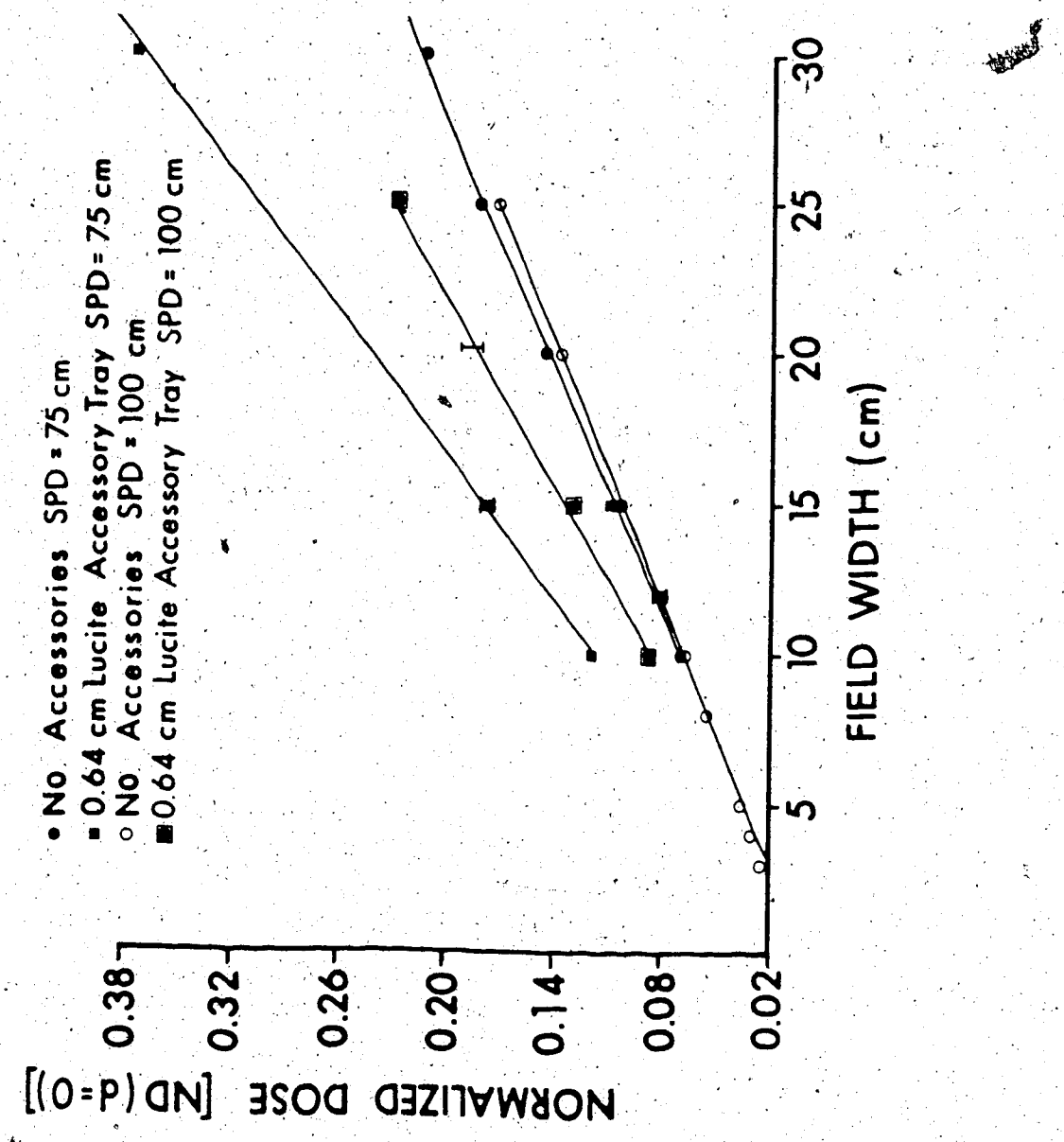

Figure 33. Linearity of the surface dose with respect to field width under a variety of conditions at 15 MV.

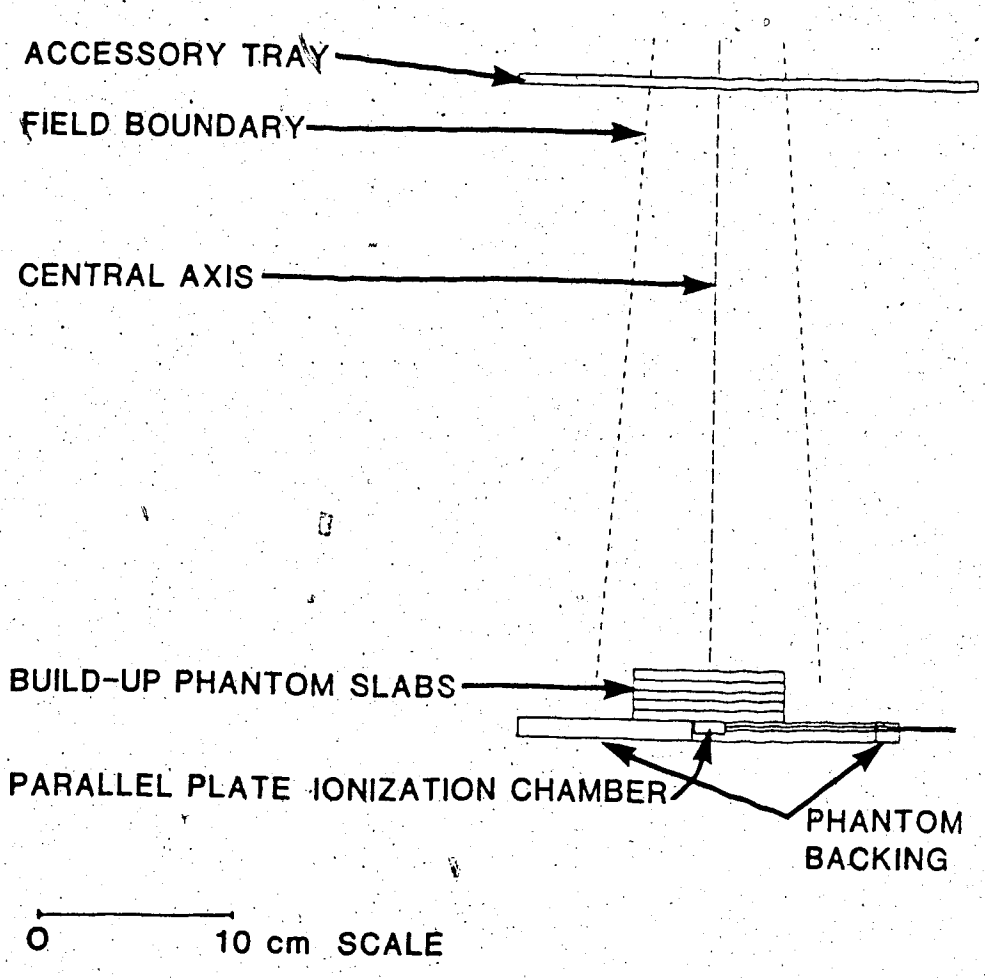

Figure 34. Diagram of the experimental arrangement to measure the increase in contamination with increasing field width. The phantom slab cross-section was 100 cm^2 and the slabs were always within the field boundary.

contributing to the dose was due to electrons.

Figure 35 illustrates that at 100 cm SPD for various depths in the phantom less than d_{max} there is a linear dependence of normalized dose on field width. Qualitatively, the slope at shallow depths is greater than the slope at deeper depths. As has been discussed for the dose at the surface, the slope of normalized dose versus field width is a measure of the magnitude of the contamination penetrating to the depth specified. Therefore, there is a greater magnitude of contamination at shallow depths than at deeper depths.

Figure 36 is a graph of normalized dose versus field width at 75 cm SPD for various depths into the limited phantom. The linear fit at 75 cm SPD is nearly as good as that obtained at 100 cm SPD.

Normalized dose measurements were made on the 15 MV accelerator at field sizes of 15 cm x 15 cm, 20 cm x 20 cm and 25 cm x 25 cm at 100 cm SPD when Lucite accessories of 0.64 cm and 3.18 cm were placed in the field at the accessory tray position. There is approximately a linear increase in dose as a function of field width with a 3.18 cm accessory in place (see Figure 37).

Figure 38 is a graph of normalized dose versus field width for various depths at 100 cm SPD for the 6 MV accelerator. Like the curves at 15 MV, the linear fit is good.

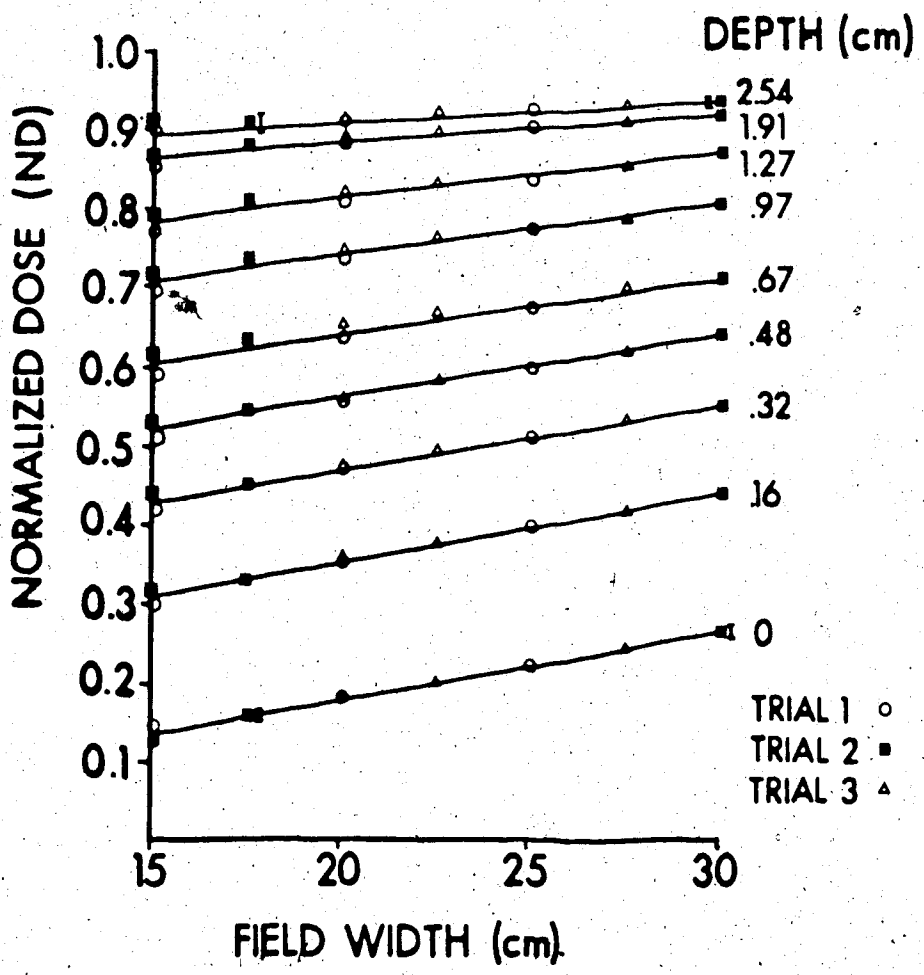

Figure 35. The increase in normalized dose with respect to field width for various depths beneath the surface of the phantom in an open field at 100 cm SPD for the 15 MV beam. The increase can only be attributed to contamination because the phantom was completely within the field boundary (see Figure 34).

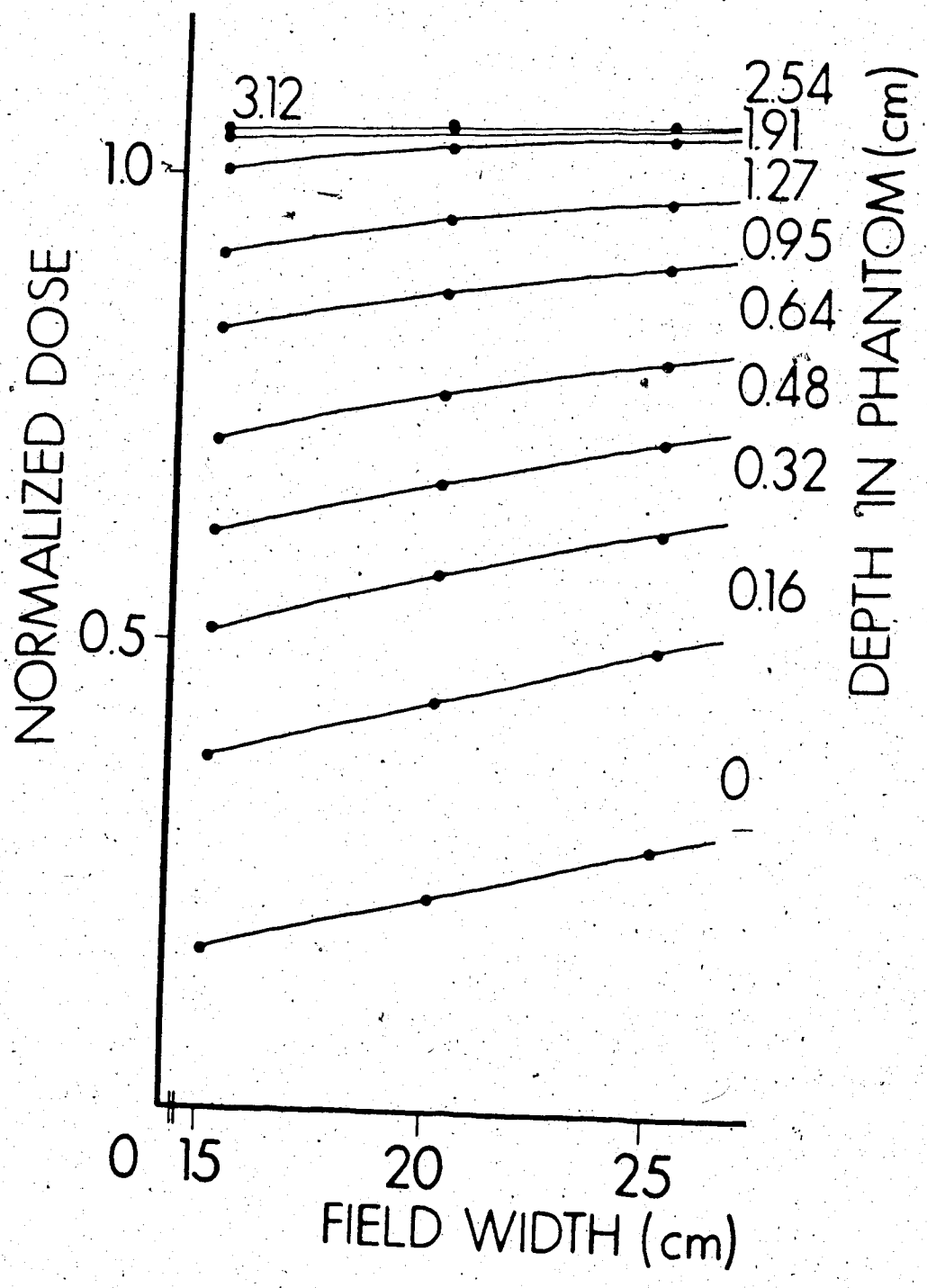

Figure 36. The increase in normalized dose with respect to field width for various depths beneath the phantom surface in an open field at 75 cm SPD at 15 MV.

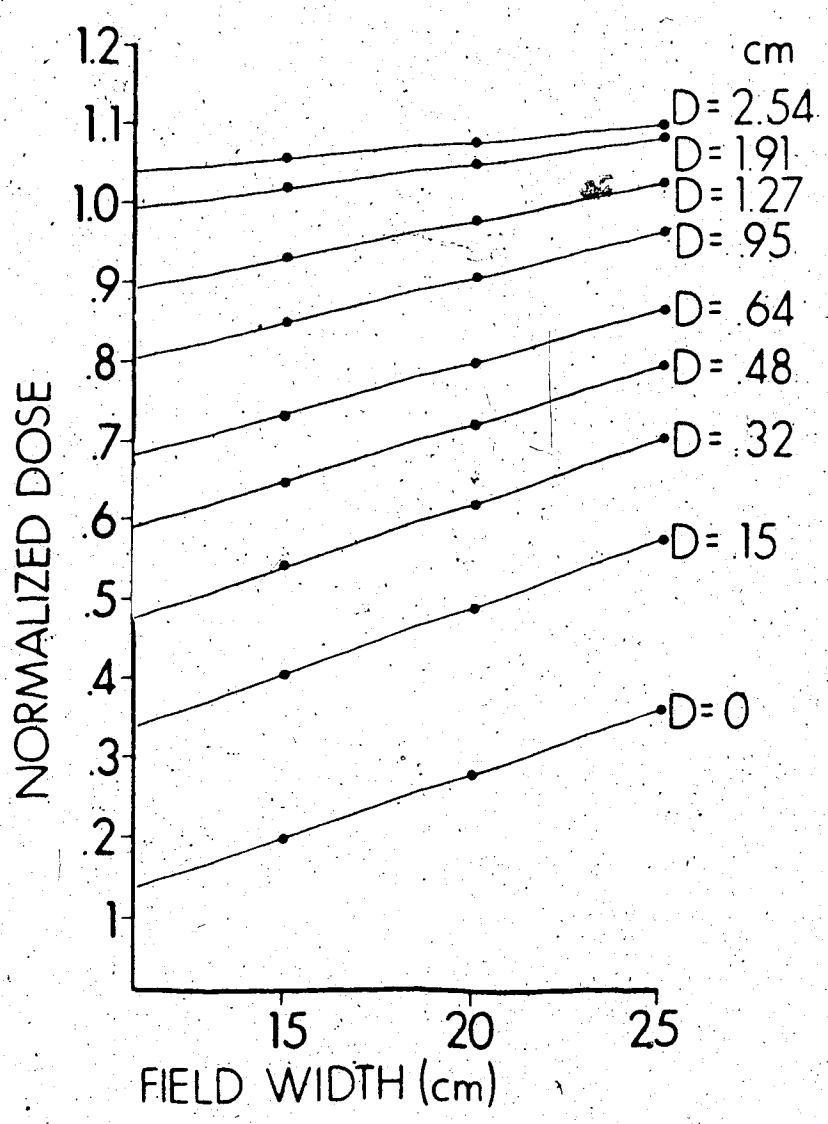

Figure 37. The increase in normalized dose at 15 MV with respect to field width for various depths beneath the phantom surface with the probe at 100 cm from the source with a 3.18 cm accessory in place.

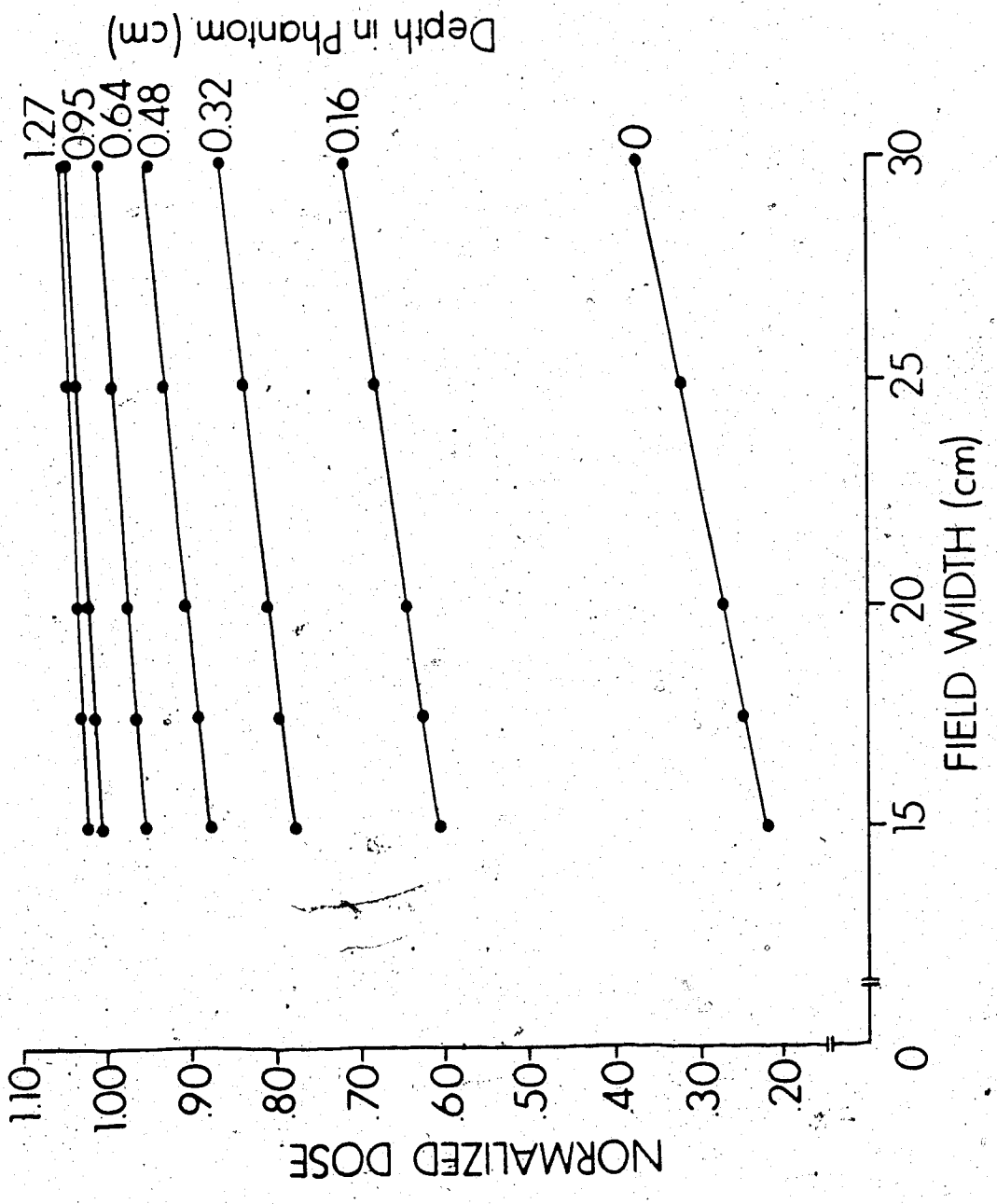

Figure 38. The increase in normalized dose with respect to field width for various depths beneath the phantom surface in an open field at 100 cm SPD at 6 MV.

2.9 Determination of the Amount of Photon Backscatter from the Phantom

The surface dose is the sum of backscatter from the phantom and contamination produced outside the phantom. By the definition of phantom generated radiation (Section 1.5), backscatter is part of this component of the beam. Backscatter photons are any photons scattered through 90^{o} or more so that they have a sense in the direction component normal to the phantom that is opposite to the sense of the primary photons. A determination of the amount of backscatter dose is essential in order to isolate the dose due to contamination at the surface.

The amount of backscatter due to photons generated in the phantom was measured. The thin window parallel-plate chamber was first placed on a thick slab of polystyrene (>20 cm thick) which had a cross-section larger than any field size used. The surface dose was measured for field sizes between 3.5 cm x 3.5 cm and 20 cm x 20 cm and source-to-probe distances between 80 cm and 120 cm. The normalized dose, N.D. (Equation 2.8.1) was obtained.

The full phantom was replaced with various thicknesses of backscatter. The thinnest layer was approximately 1.5 mg/cm^2 and the thickest layer was 480 mg/cm^2 of unit density material. There was virtually no difference between the readings at 1.5 mg/cm^2 and 480 mg/cm^2 indicating that there is little contribution from charged particles set in motion near the surface of the phantom which scatter backwards. The normalized dose difference was obtained between the normalized doses with full phantom and with 1.5 mg/cm^2. The normalized dose difference represents the normalized dose due to backscatter photons. The results are shown in Figures 39 and 40 as a function of field width for 6 and 15 MV at various source-to-probe distances.

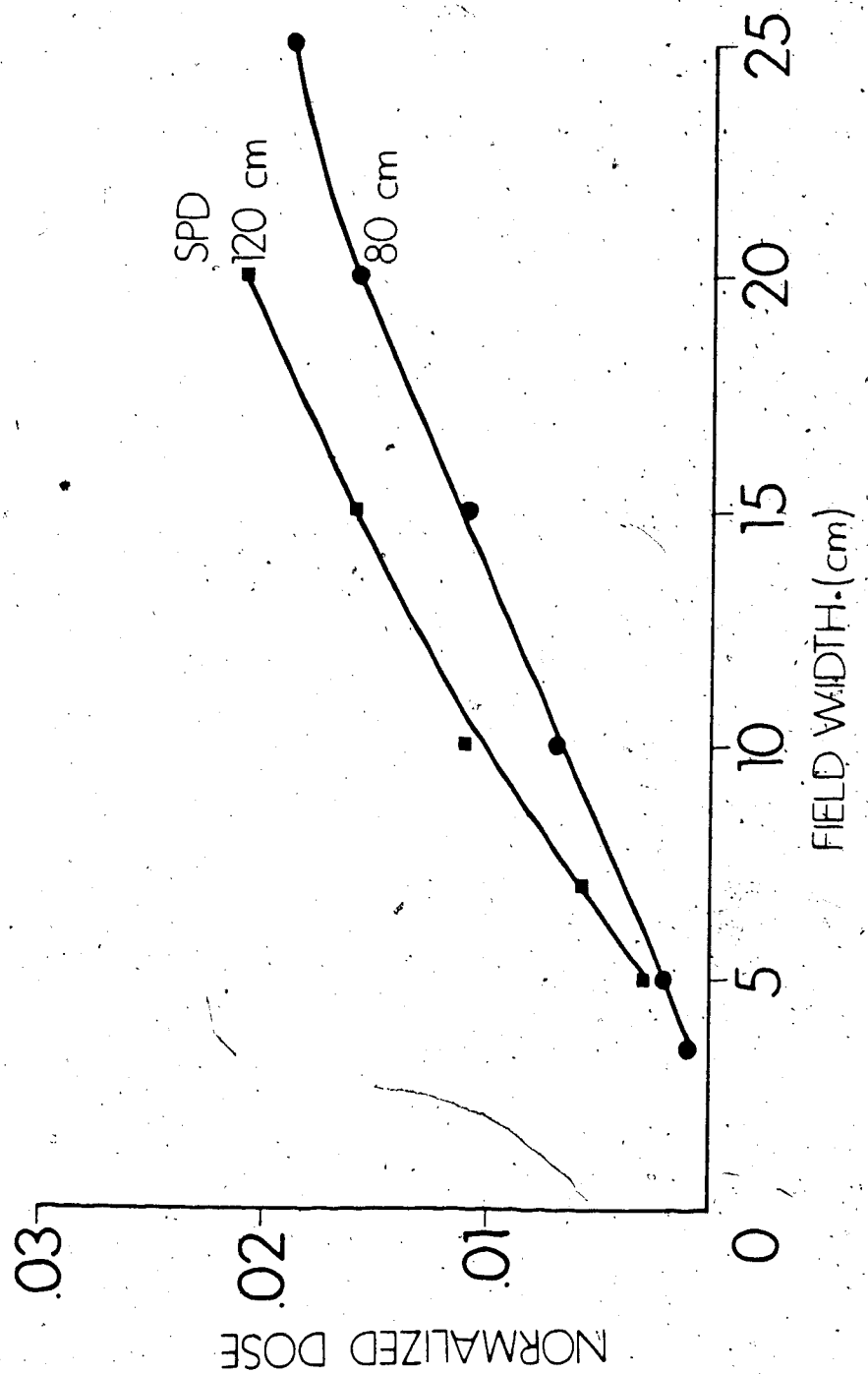

Figure 39. The normalized dose due to backscatter photons as a function of field width for source-to-probe distances of 80 cm and 120 cm at 6 MV.

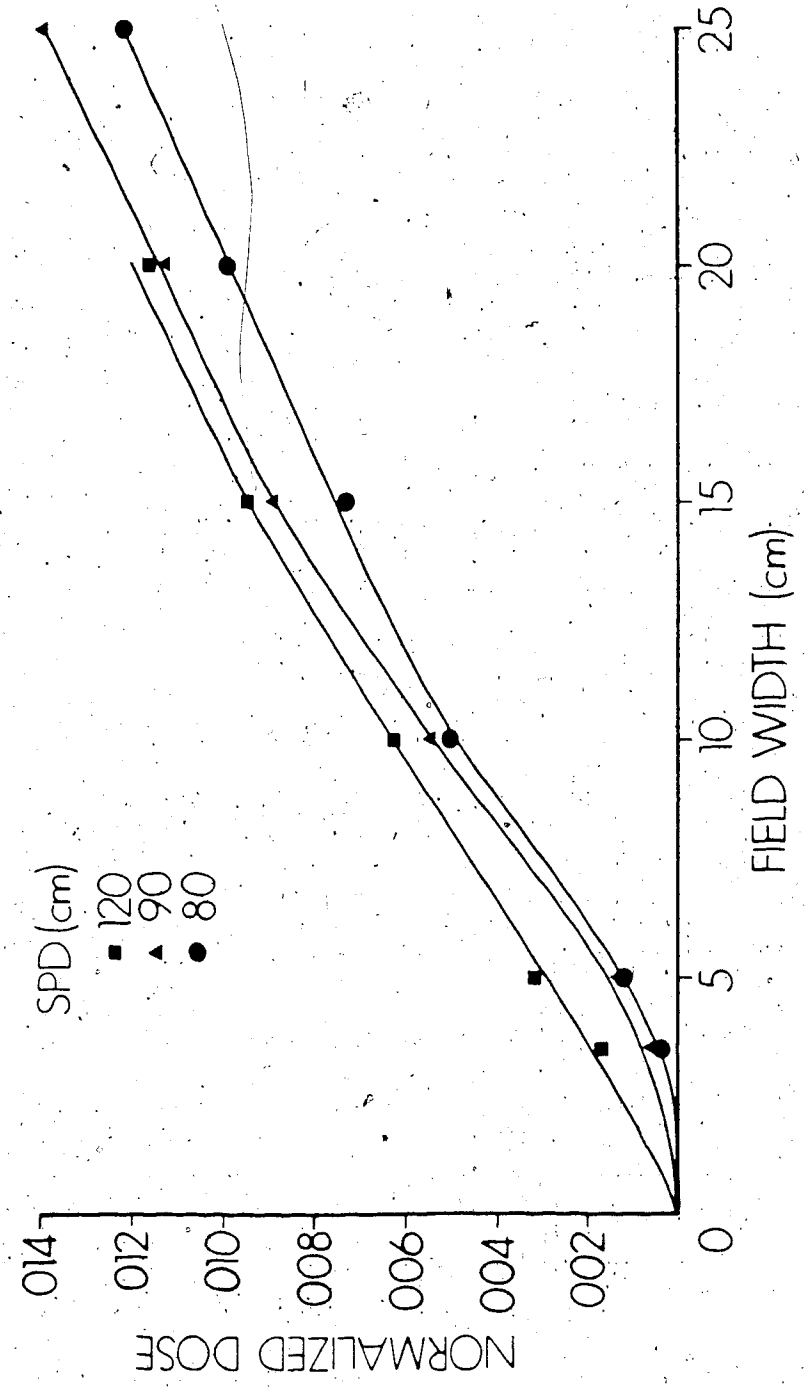

Figure 40. The normalized dose due to backscatter photons as a function of field width for source-to-probe distances of 80 cm, 90 cm and 120 cm at 15 MV.

Between field widths of 5 cm and 20 cm, the amount of backscatter increases with field width for all source-to-probe distances. The amount of photon backscatter at 6 MV is about 50% greater than at 15 MV for the same field width and source-to-probe distance. At all field sizes and source-to-probe distances for both accelerators, the amount of dose due to photon backscatter was much less than the amount of dose due to contamination electrons at the surface of the phantom.

2.10 Sweeping Electrons from the Field Using a Permanent Magnet

2.10.1 Determination of the Field Distribution of the Magnet

A survey of the literature (41, 42, 43, 44, 45) has shown that the central field magnetic strength must be somewhere between 1 and 3 kG in order to sweep a 10 cm x 10 cm field free of contamination electrons produced by photons in the energy range of 4 MV to 25 MV when the source-to-probe distance, SSD, is about 85 cm.

The magnetic field strength distribution of a discarded magnetron magnet was determined using a Rawson-Lush Rotating Coil Gaussmeter Type 820 Probe and a Type 501 Indicator manufactured by Rawson Electrical Instruments Co. of Cambridge, Massachusetts.

The uncertainty in the strengths at maximum field strength was ± 30 G. The magnet was a permanent type with the pole gap fixed at 7.5 cm. The maximum central field was found to be 1340 G. Figure 41 illustrates the measured magnetic field distribution. The central distribution was mapped every 2 cm until the magnetic field fell to 60 G.

2.10.2 Verifying Electrons are Swept by the Magnet

If the amount of bending is small, to a first approximation, the electrons will travel along the central axis in and near the magnet. The angle of deflection (in radians) for an electron travelling a distance, d, in a uniform magnetic field is given by (see Figure 42):

$$\phi_{deflect} = \frac{d}{r} = \frac{deBc}{m_o c^2} \frac{1}{\left[((T+m_o c^2)/m_o c^2)^2 - 1\right]^{\frac{1}{2}}} \qquad (2.10.1)$$

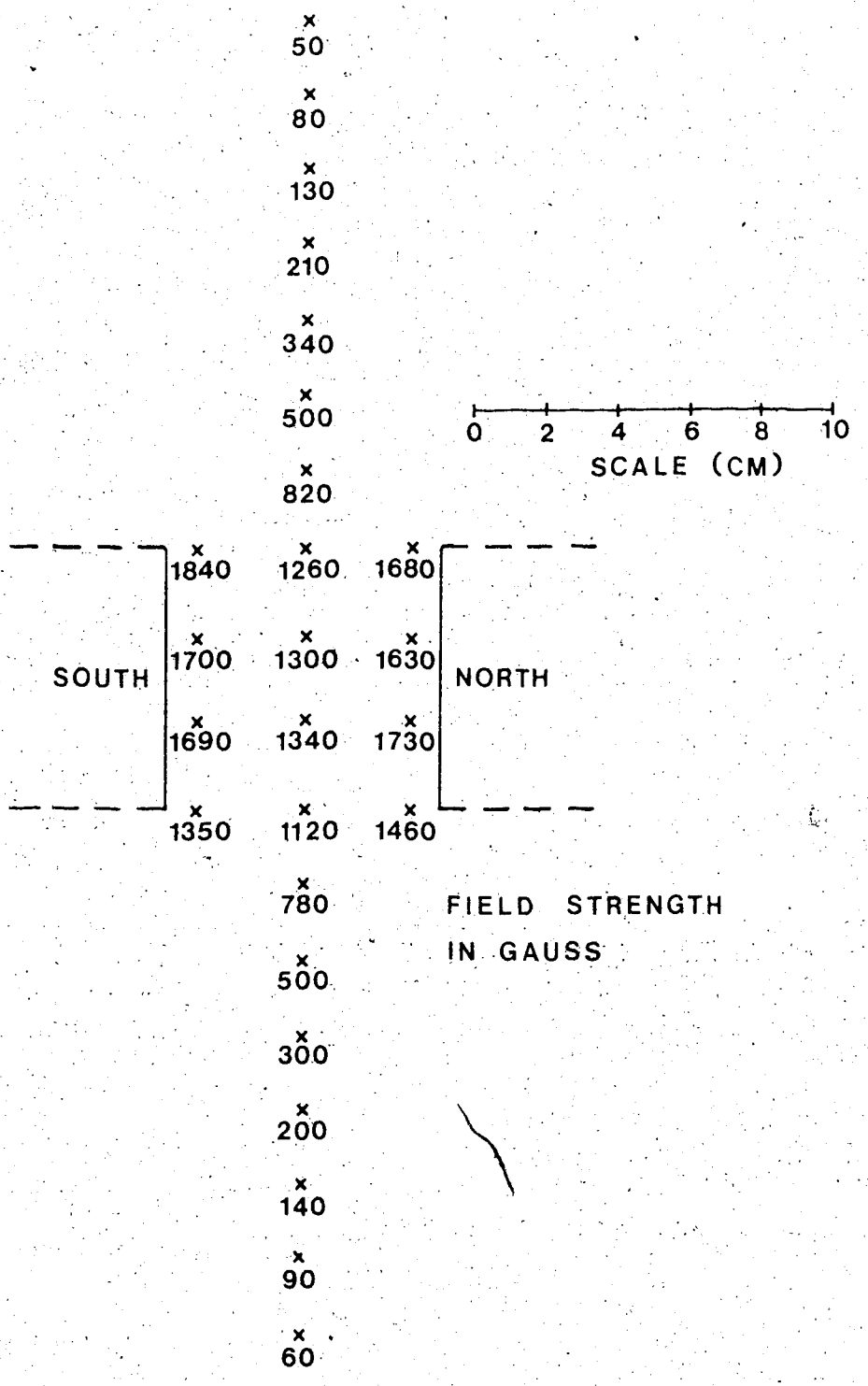

Figure 41. The measured magnetic field distribution along the direction of the photon beam.

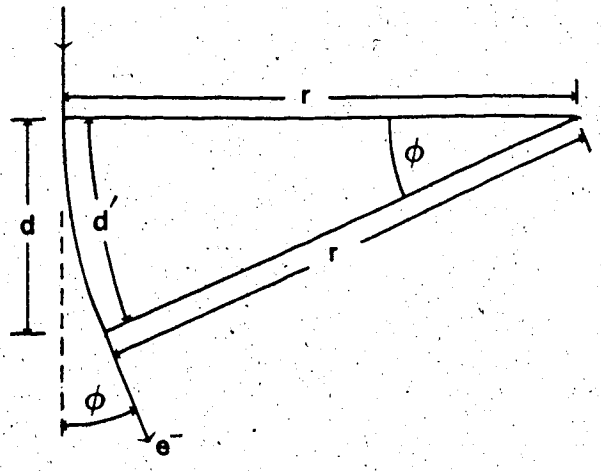

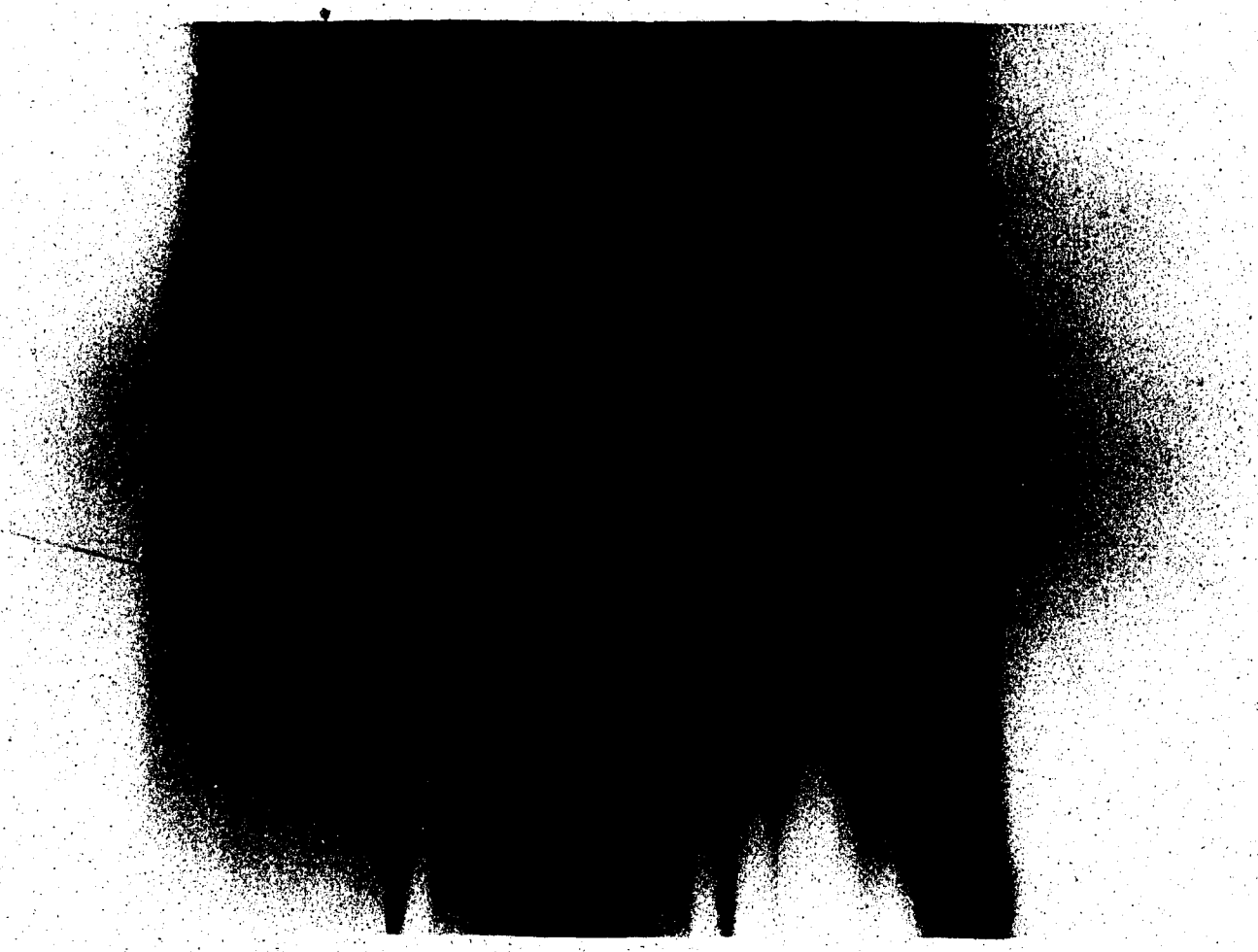

Figure 42. The angle of deflection of an electron in a uniform magnetic field (above) and the measured deflection of 18 MeV electrons (below).

The above equation uses the definition of a radius of curvature (Equation 1.4.1). The total amount of deflection can be found by summing the amount of angular deflection occurring along the central axis:

$$\left[\phi_{deflect}\right]_{total} = \frac{ec}{m_o c^2} \frac{1}{\left[(T+m_o c^2)/m_o c^2)^2 - 1\right]^{\frac{1}{2}}} \Sigma d_i B_i \qquad (2.10.2)$$

The field, B_i, was measured every 2 cm so d_i is a constant (d_i=const=2 cm). The Mevatron -20 can produce mono-energetic 18 MeV electrons. The electron contamination of the 15 MV beam will not have kinetic energies this high so that if the 18 MV beam can be deflected then the electron contamination can also be swept. The amount of deflection predicted by Equation 2.10.2 for 18 MeV electrons in the measured magnetic field distribution is approximately 17^o.

The magnet was mounted 65 cm from the source, so the largest field size (measured at SPD=100 cm) that can be swept is 10 cm x 10 cm. This defines a central axis angle of 2.9^o. Clearly, this simple theory predicts enough deflection will occur.

The analysis was verified semi-qualitatively by experiment. A sheet of film (Kodak XV-2) was placed parallel to a beam of electrons. An equal amount of exposure was delivered with an open electron applicator

with and without the magnet beneath the applicator. Figure 42 illustrates the results. The angle of deflection between the image of the beams is about 20^{o}.

The deflection of contamination electrons was directly verified by placing a half cylinder of film beneath the magnet. Figure 43 illustrates the setup. The contamination electrons produced a broad hazy patch on the film (see Figure 44). The width of the image increased as a function of angle swept. This is to be expected because the amount of bending and the amount of scatter increases with decreasing electron energy. The overexposed central patch is mainly due to photons. Transmission through the collimator can be discerned. There is no direct evidence of positron contamination which would be deflected in the opposite direction.

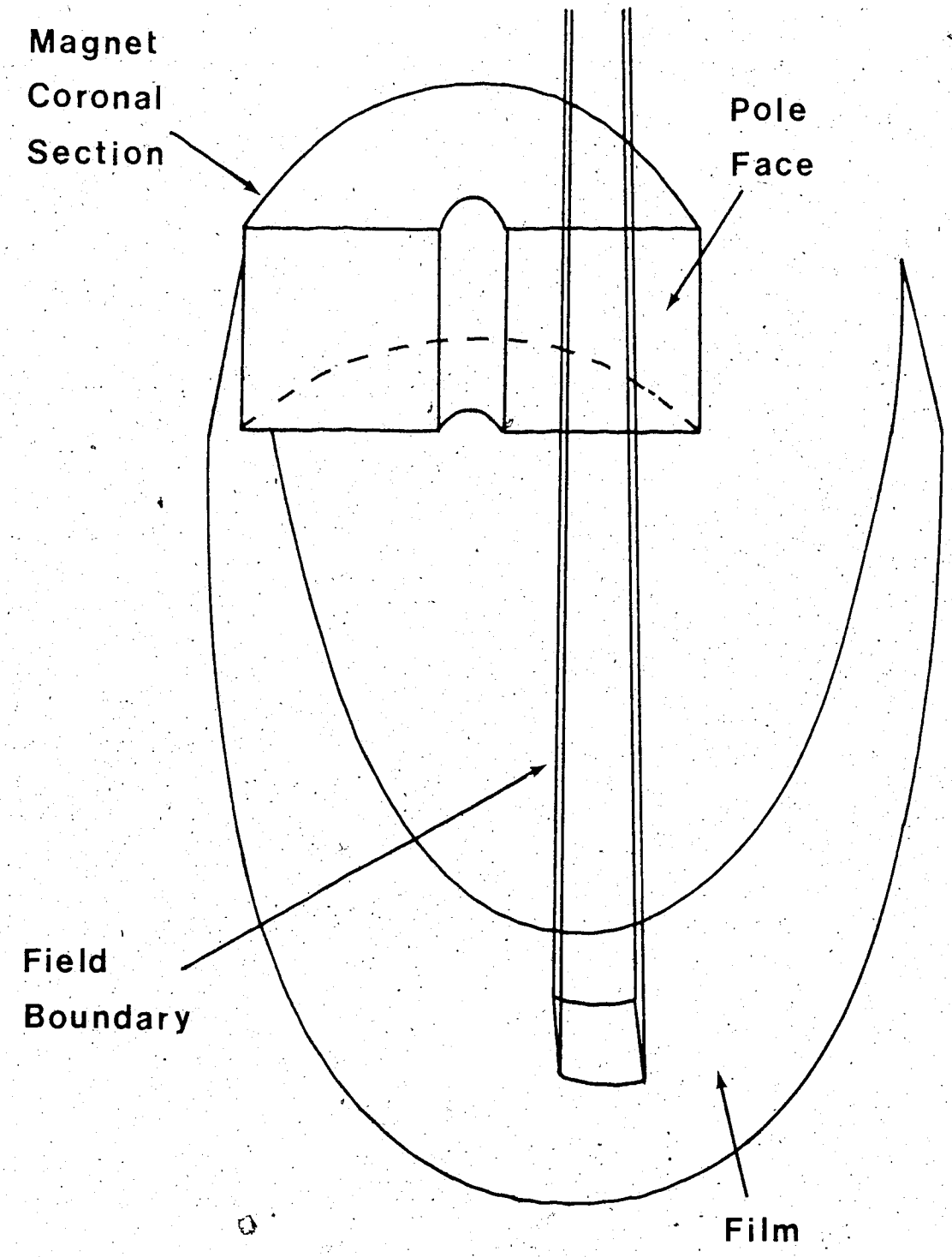

Figure 43. The set-up to verify that contamination electrons were being swept from the field of the 15 MV beam.

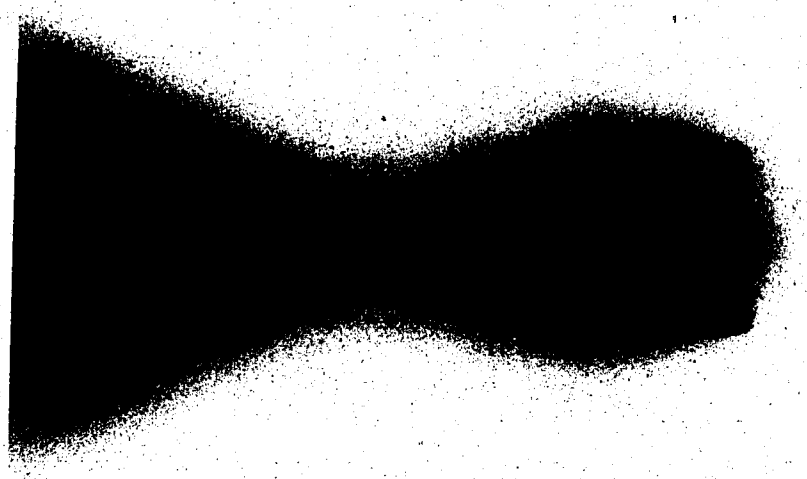

Figure 44. Image of the swept electron contamination.

2.10.3 The Surface Dose With and Without the Magnet in Place

The magnet was mounted on a holder so that it could be placed just beneath the accessory holder position. The holder had a square hole cut in it enabling a 10 cm x 10 cm beam to pass through without interacting with it. A photograph of the magnet attached to its holder is shown in Figure 45. Figure 46 shows the magnet mounted from the accessory holder position.

With the magnet in place the electron contamination produced between the target and magnet is swept from the beam. The surface dose under this condition is due to electron contamination produced between the magnet and phantom and photon backscatter produced from the phantom. Since air is the only material in the beam between the magnet and phantom, the electron contamination with the magnet in place is produced by interactions of the photon beam with air between the magnet and phantom.

The dose was measured at the surface of a full phantom (>20 cm thick and with a cross-sectional area greater than the width of the beam). The measurements were taken under various conditions of field size and SPD and presence of accessories. The small magnet pole separation meant that the target field could be no greater than 10 cm x 10 cm.

Figure 47 illustrates the dependence of the normalized dose at the surface, when the magnet is in place, on field width for various accessory configurations at an SPD of 100 cm. The maximum doses used to normalize these curves

Figure 45. The magnet attached to its holder.

Figure 46. The magnet mounted from the accessory holder position.

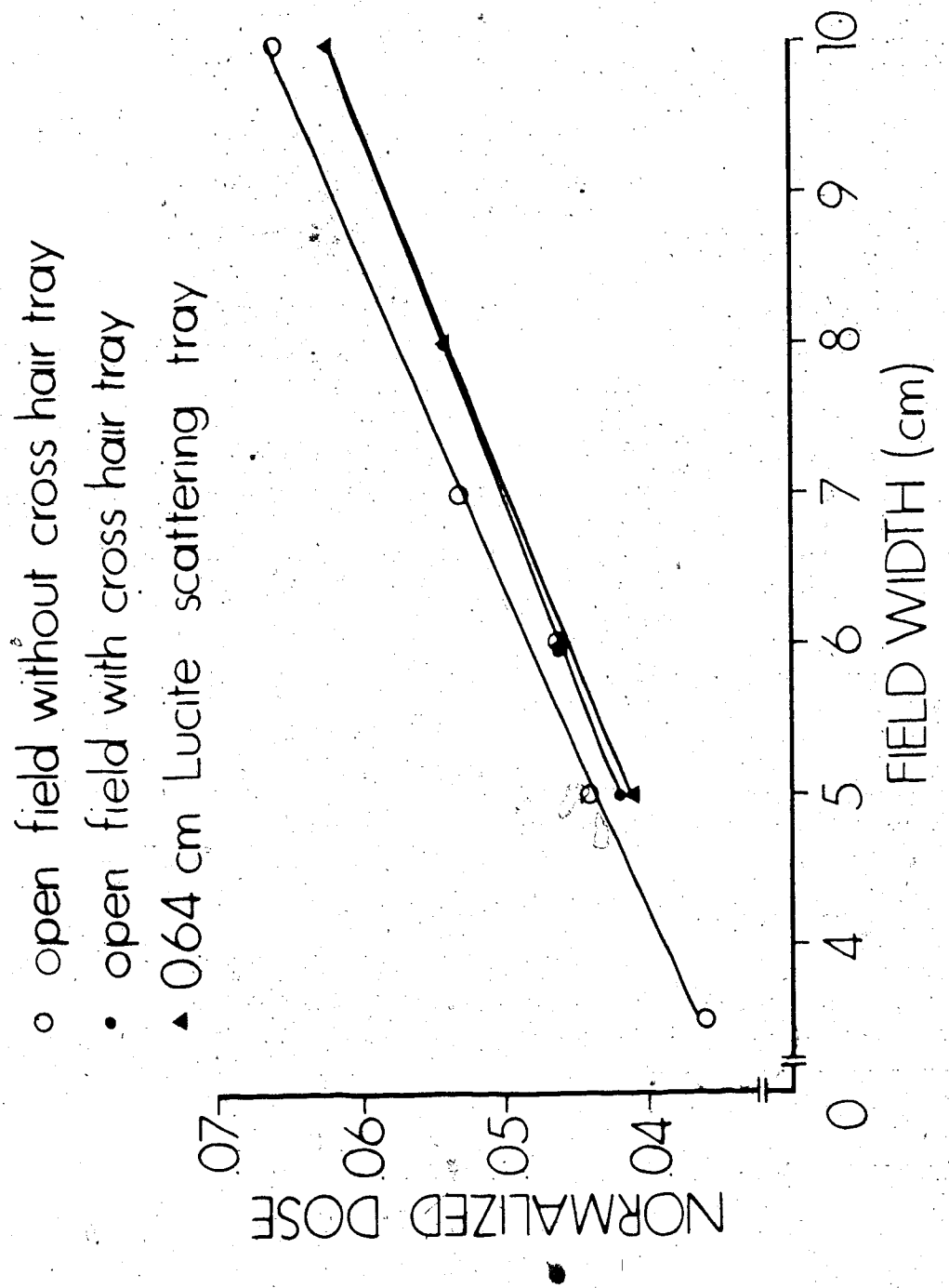

Figure 47. The surface normalized dose with the magnet in place for various conditions at 100 cm SPD for the 15 MV beam.

were measured at an SPD of 100 cm at a depth of d_{max} for a field size of 10 cm x 10 cm under the same accessory configuration. The normalized dose curves are the same within 0.005. This is to be expected because electron contamination produced by the accessories is swept from the field by the magnet. The normalization procedure takes into account the reduction in the primary dose available for the production of electron contamination in air and photon backscatter.

The dose due to photon backscatter can be subtracted from the surface dose with the magnet in place to leave the dose due to electron contamination produced in air* as the only component. Figures 48 and 49 illustrate the normalized dose due to contamination produced in air as a function of field width for various source-to-probe distances when an open field is used (with cross-hair tray in place) for a 15 MV and 6 MV photon beam, respectively. At each source-to-probe distance the normalized dose increased as a function of field width. This increase was larger for smaller field widths.

The measurements suggest that curves taken at various source-to-probe distances converge to a zero normalized dose at a zero field width. The behavior at field sizes less than the chamber diameter cannot easily be determined.

The difference between readings with and without the magnet in place can only be due to what is being swept by the magnet when it is in place; namely electron

* This refers to air between the magnet and phantom.

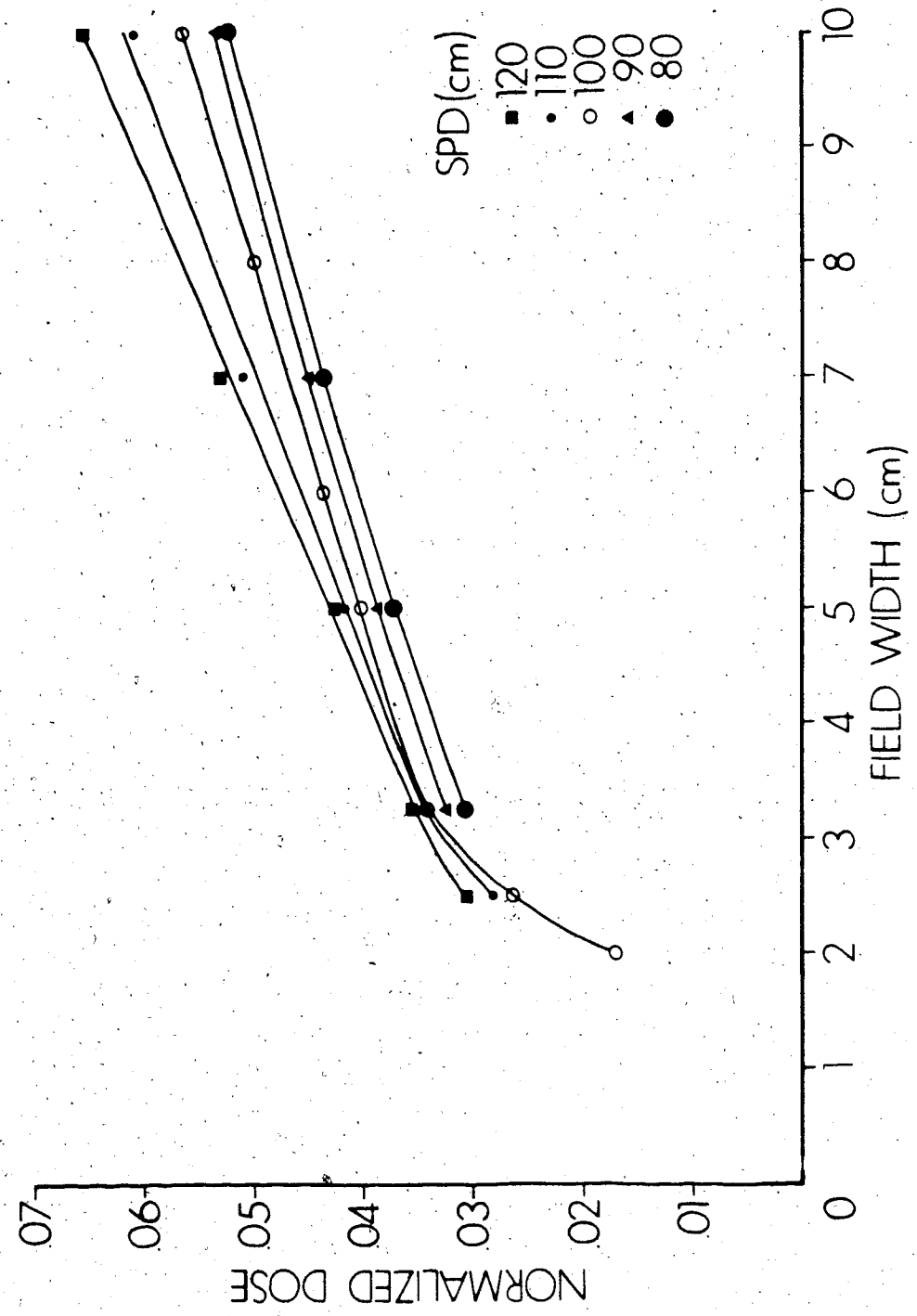

Figure 48. Normalized dose due to contamination produced in air as a function of field width for various source-to-probe distances for an open field at 15 MV.

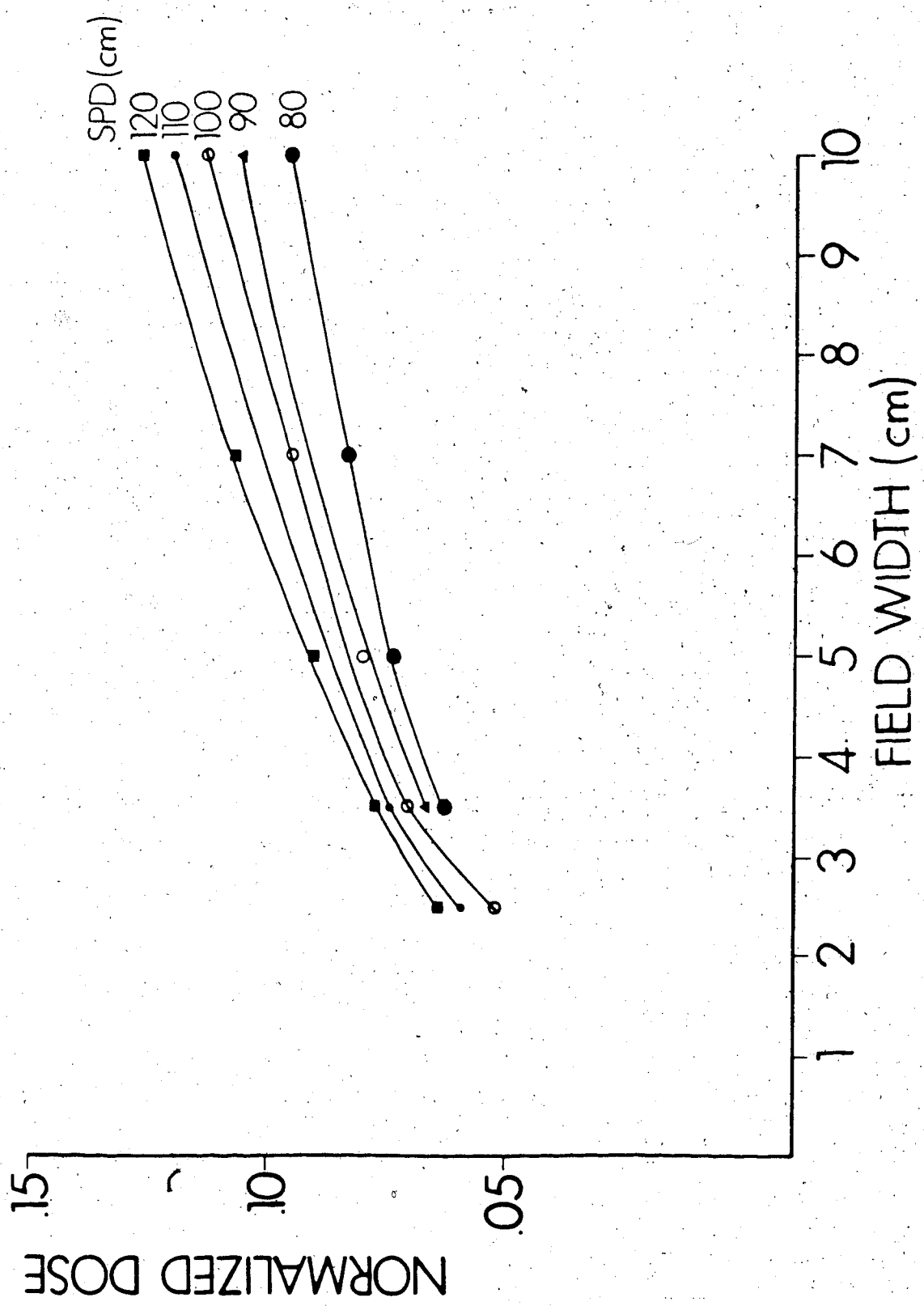

Figure 49. Normalized dose due to contamination produced in air as a function of field width for various source-to-probe distances for an open field at 6 MV.

contamination produced between the target and magnet.* Figures 50 and 51 are graphs of the normalized dose difference between magnet in and out for 15 MV and 6 MV photon beams, respectively. The normalized dose is very small at small field sizes, but increases rapidly as a function of field size. The normalized dose due to contamination produced between the magnet and target increases approximately in direct proportion to the beam cross-sectional area.

There is considerable difference between the electron contamination contributions due to air and due to interactions between the target and phantom at small field sizes. (less than 10 cm x 10 cm). The contributions due to air exceed those of contributions produced between target and magnet for both 6 MV and 15 MV photon beams at all source-to-probe distances. The increase in dose as a function of field width at very small field sizes (less than 5 cm x 5 cm) is greater for electron contamination produced in air than for electron contamination produced between the target and magnet. The most interesting difference between these curves is that the normalized dose for air-produced electron contamination is greater for large SPD whereas the target-to-magnet electron contamination is greater for smaller source-to-probe distances. The source-to-probe

* It did not matter if normalization measurements were done with the magnet in or out. The difference at d_{max} between readings taken with the magnet in place compared to readings with the magnet not in place was less than 0.5%. This indicates that few contamination electrons produced between the target and magnet penetrate to d_{max}.

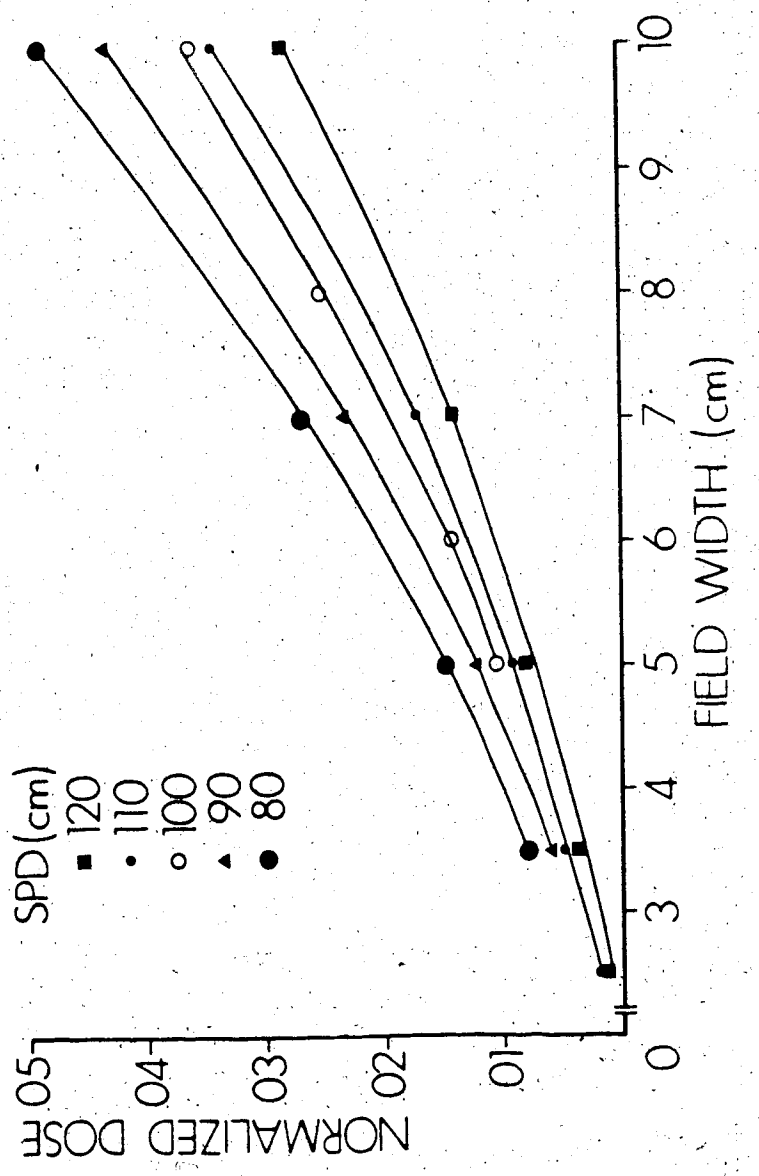

Figure 50. Normalized dose difference between magnet in place and out of place for a 15 MV beam as a function of field width for various source-to-probe distances for an open field.

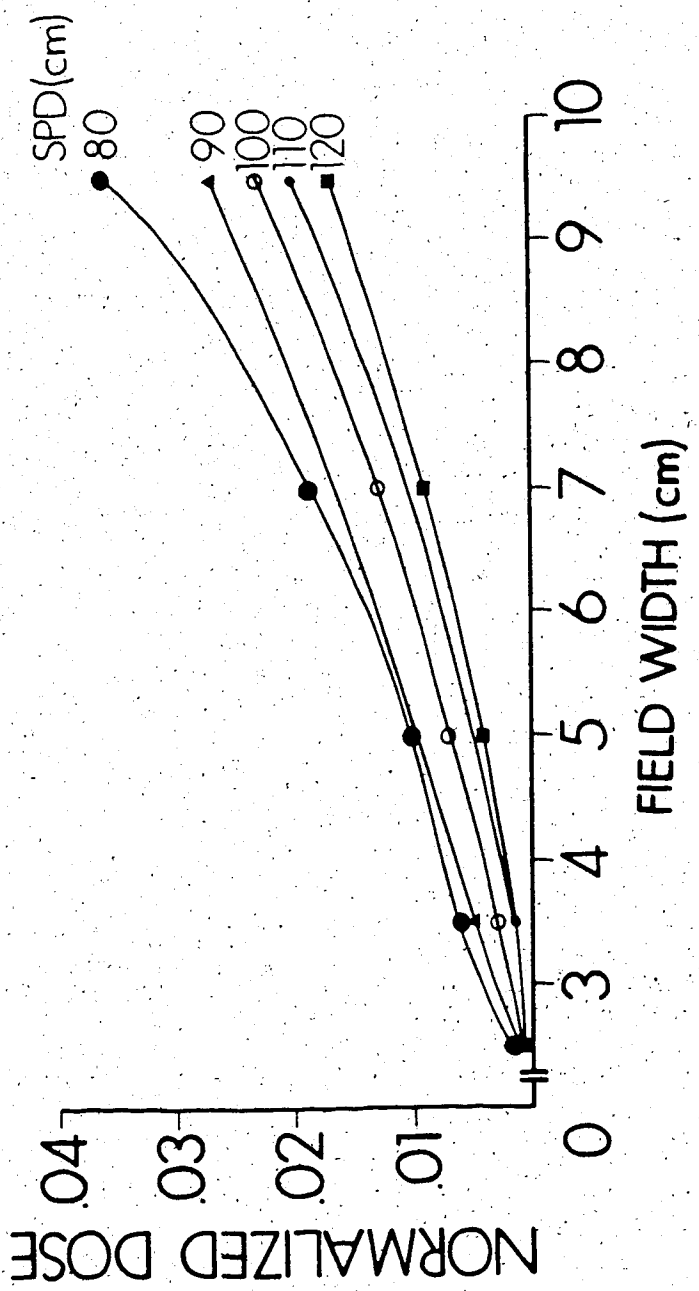

Figure 51. Normalized dose difference between magnet in place and out of place for a 6 MV beam as a function of field width for various source-to-probe distances for an open field.

dependence of the surface dose is better illustrated in Figures 52 to 55. Figures 52 and 53 are graphs of normalized dose versus SPD at 15 MV for air contamination and contamination between the target and magnet, respectively, for a family of field widths. Figures 54 and 55 are for contamination produced in air and between the target and magnet, respectively, under the same measurement conditions as 15 MV but done at 6 MV.

If an assumption is made that the location where the contamination is produced between the target and magnet is a point source, then the same procedure used in Section 2.4.3 to locate the apparent source of contamination electrons can be used again. The difference in the absolute readings taken with the magnet not in place and magnet in place is a measure of the contamination dose produced between the target and magnet. If the readings were taken at nearly the same time, then the difference in absolute readings need not be normalized. Figure 56 is a graph of the square root of the difference in absolute readings versus SPD at 15 MV for a number of field sizes. The apparent source of electron contamination is at 40 cm SPD. The electron contamination appears to be coming from the cross-hair tray. A similar result was obtained at 6 MV (see Figure 57).

The cross-hair tray was removed and the readings repeated at 15 MV. Figure 58 illustrates that the apparent source of contamination is shifted to between 30 cm and

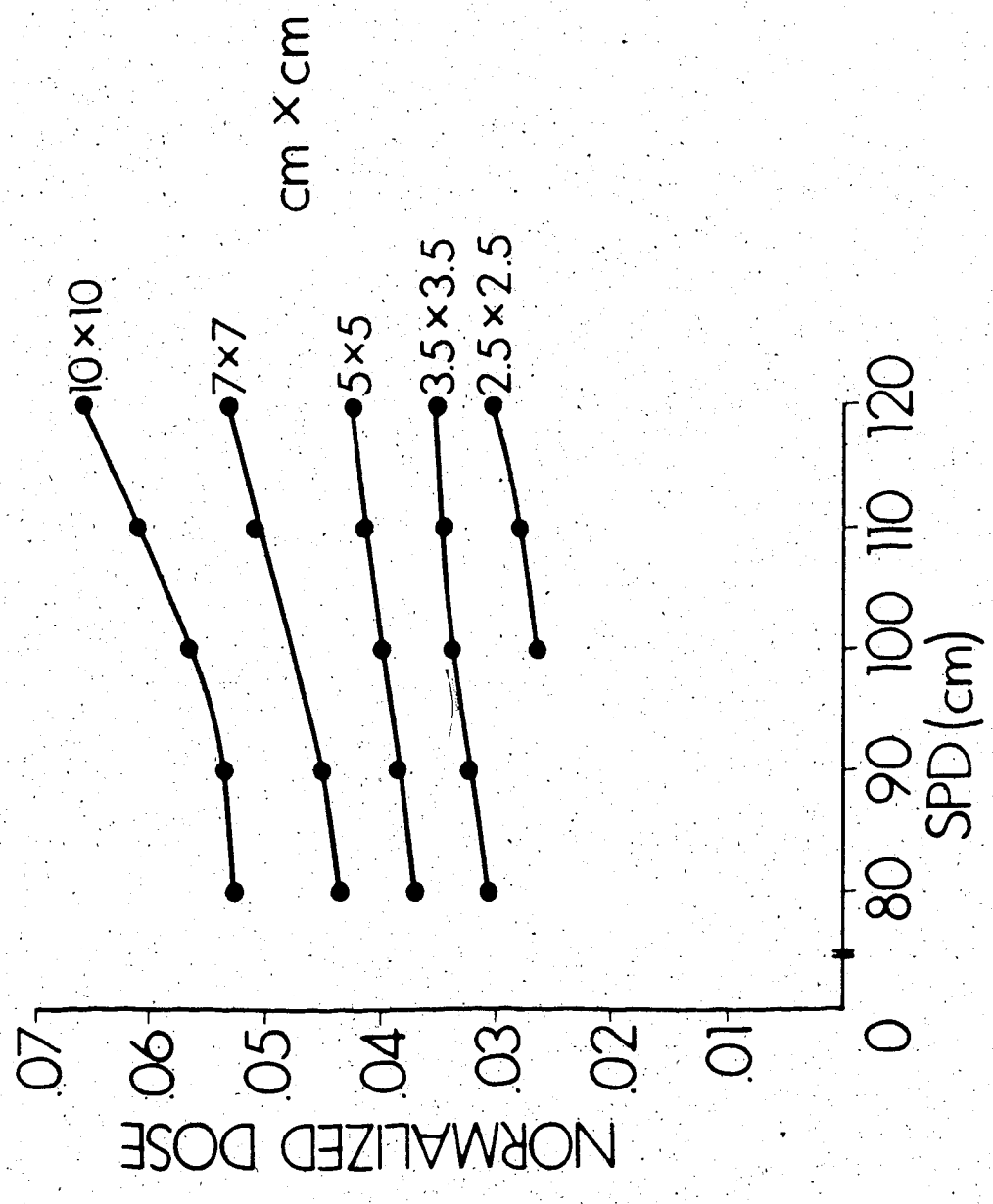

Figure 52. Normalized dose due to contamination produced in air as a function of source-to-probe distance for various field widths for an open field at 15 MV.

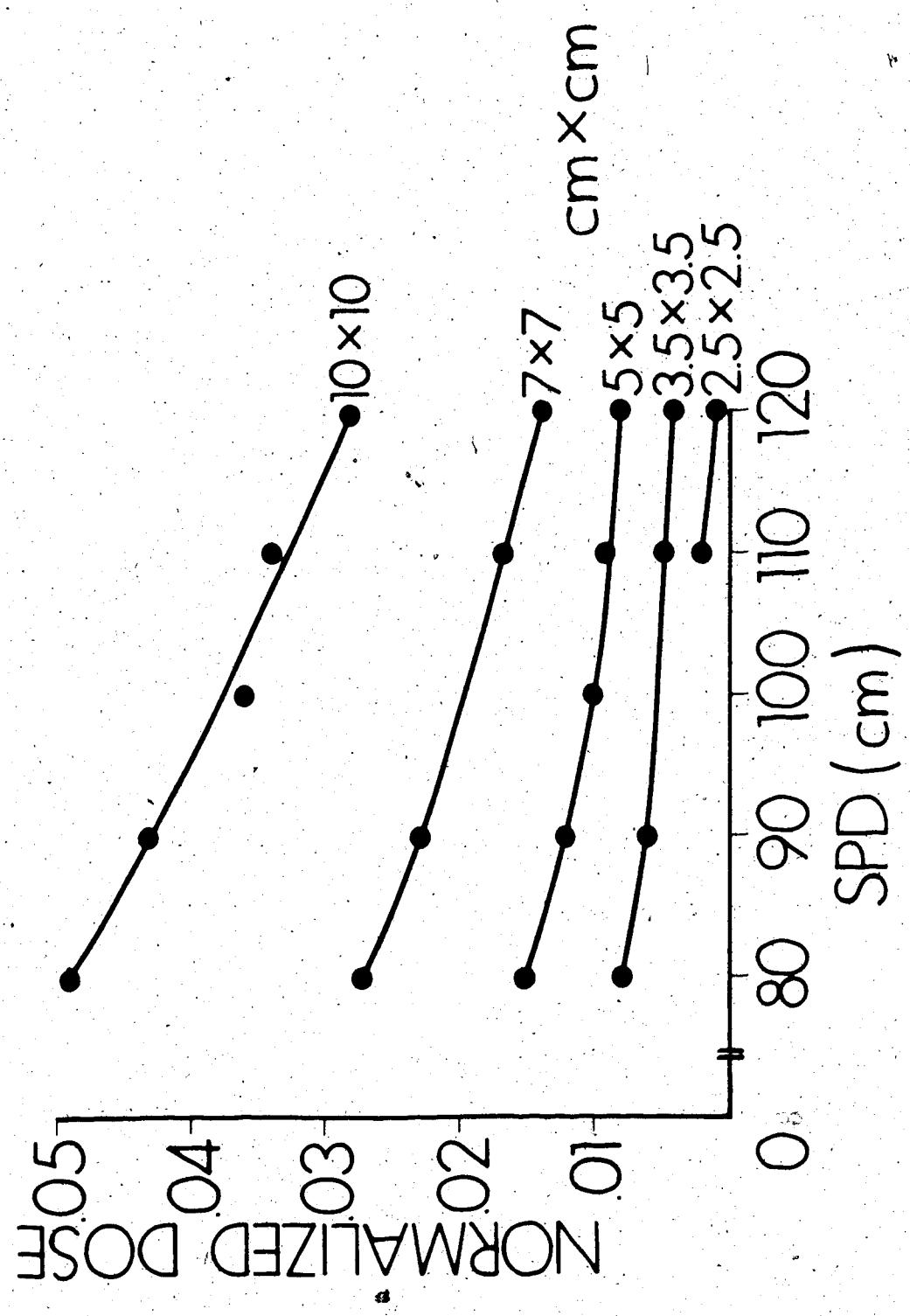

Figure 53. Normalized dose produced between the target and magnet in a 15 MV beam as a function of source-to-probe distances for various field widths for an open field.

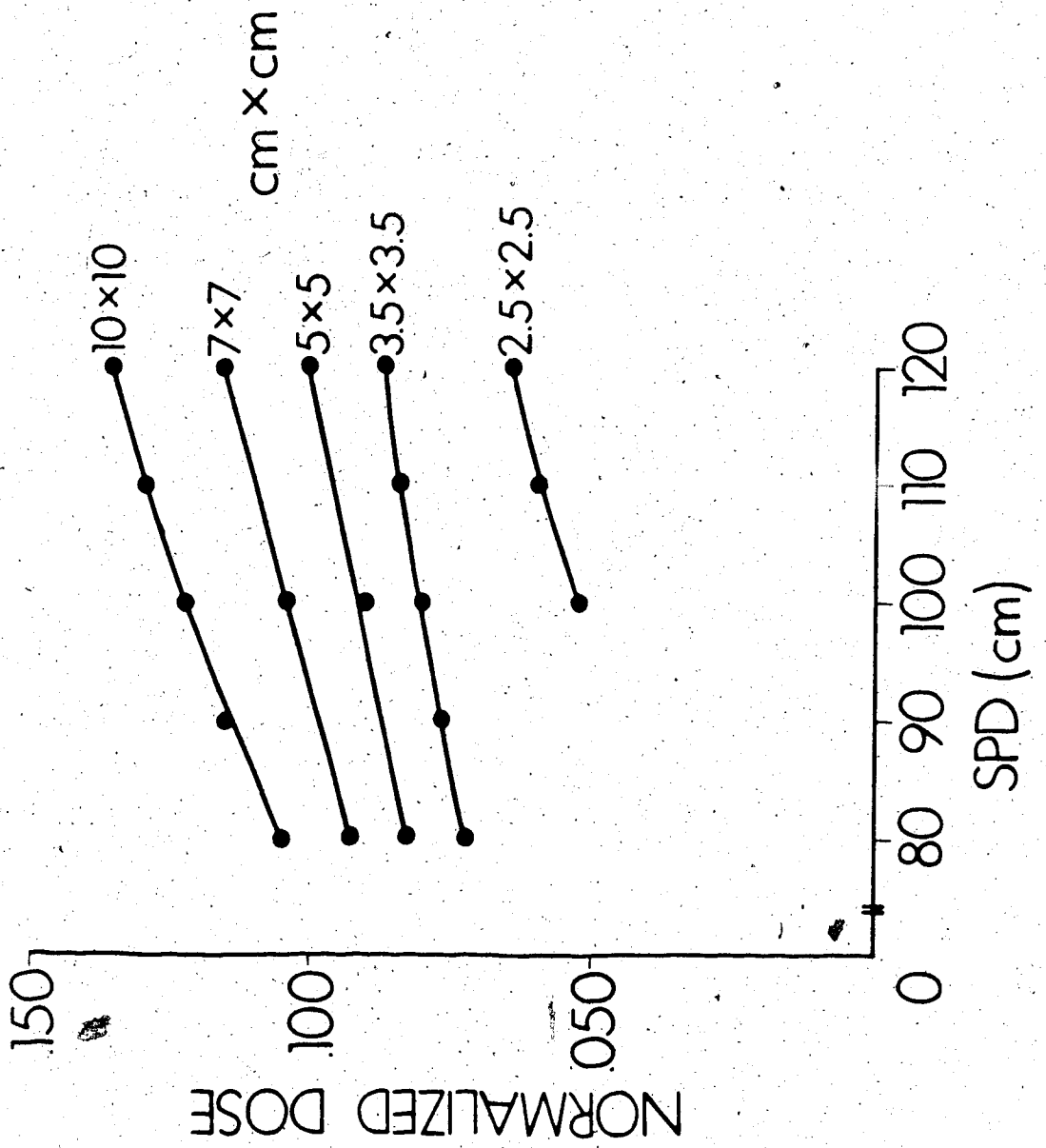

Figure 54. Normalized dose due to contamination produced in air as a function of source-to-probe distance for various field widths for an open field at 6 MV.

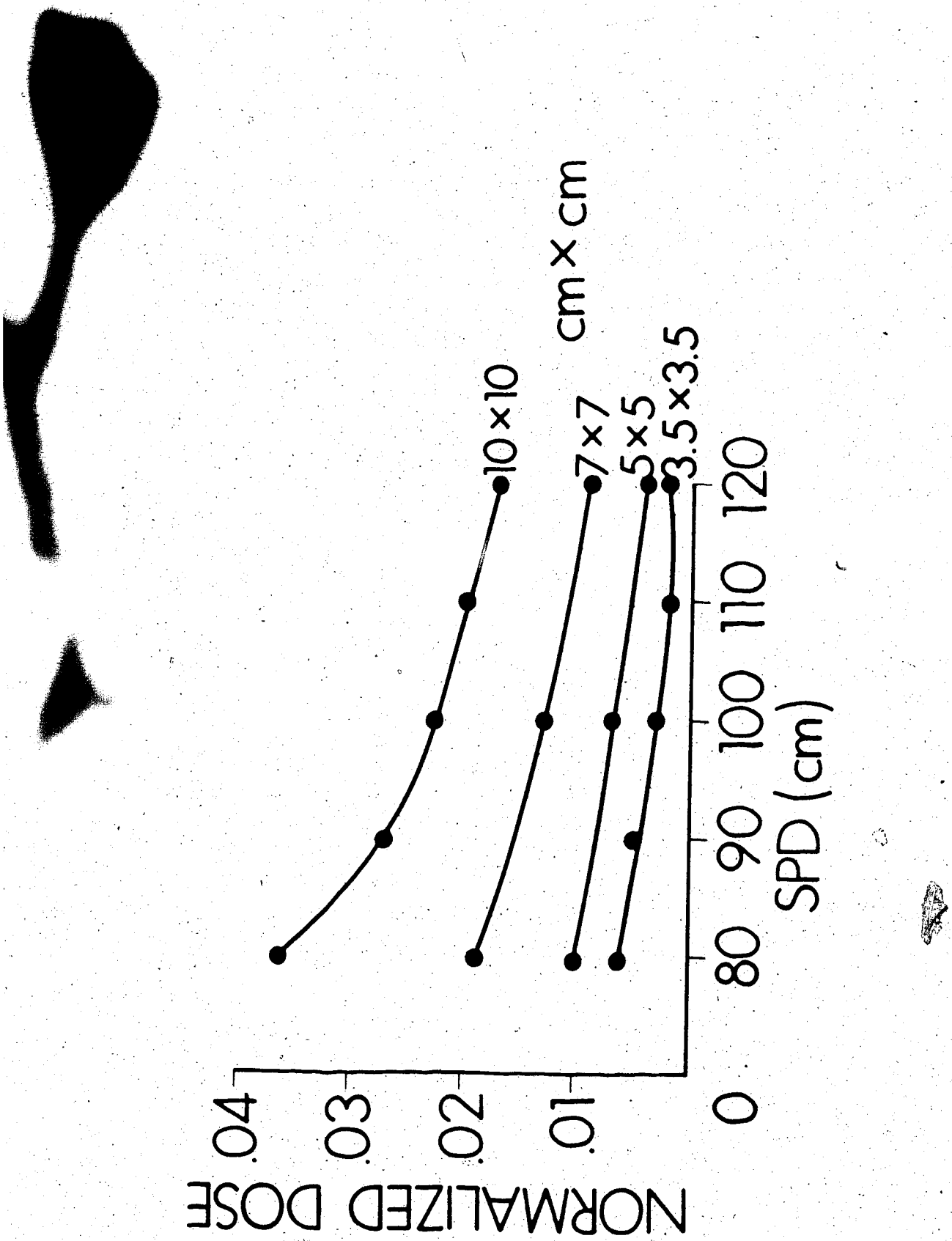

Figure 55. Normalized dose produced between the target and magnet in a 6 MV beam as a function of source-to-probe distances for various field widths for an open field.

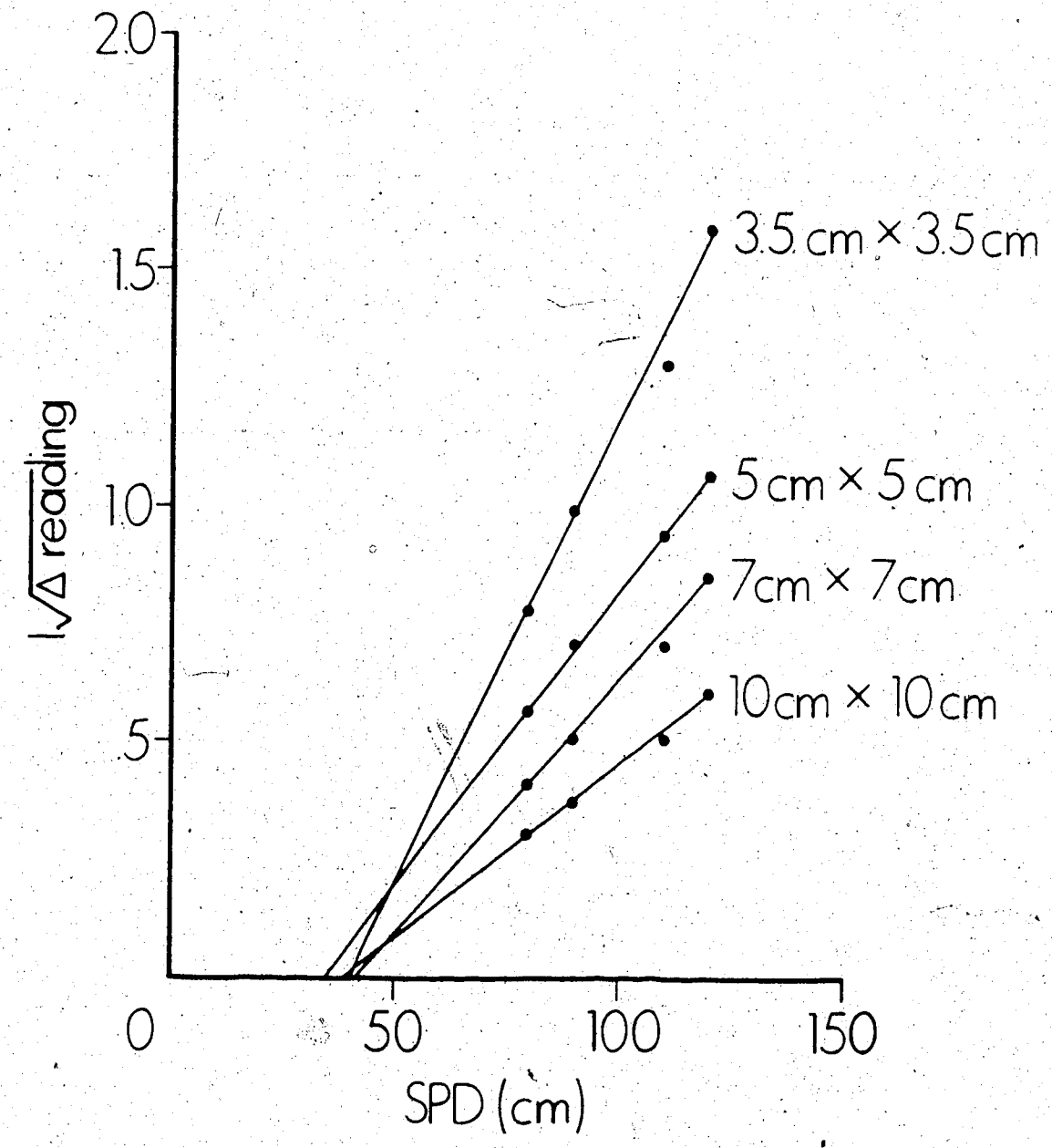

Figure 56. Dependence of the dose produced between the target and magnet on the inverse square of the distance from the apparent source at 15 MV when the cross-hair tray was in place.

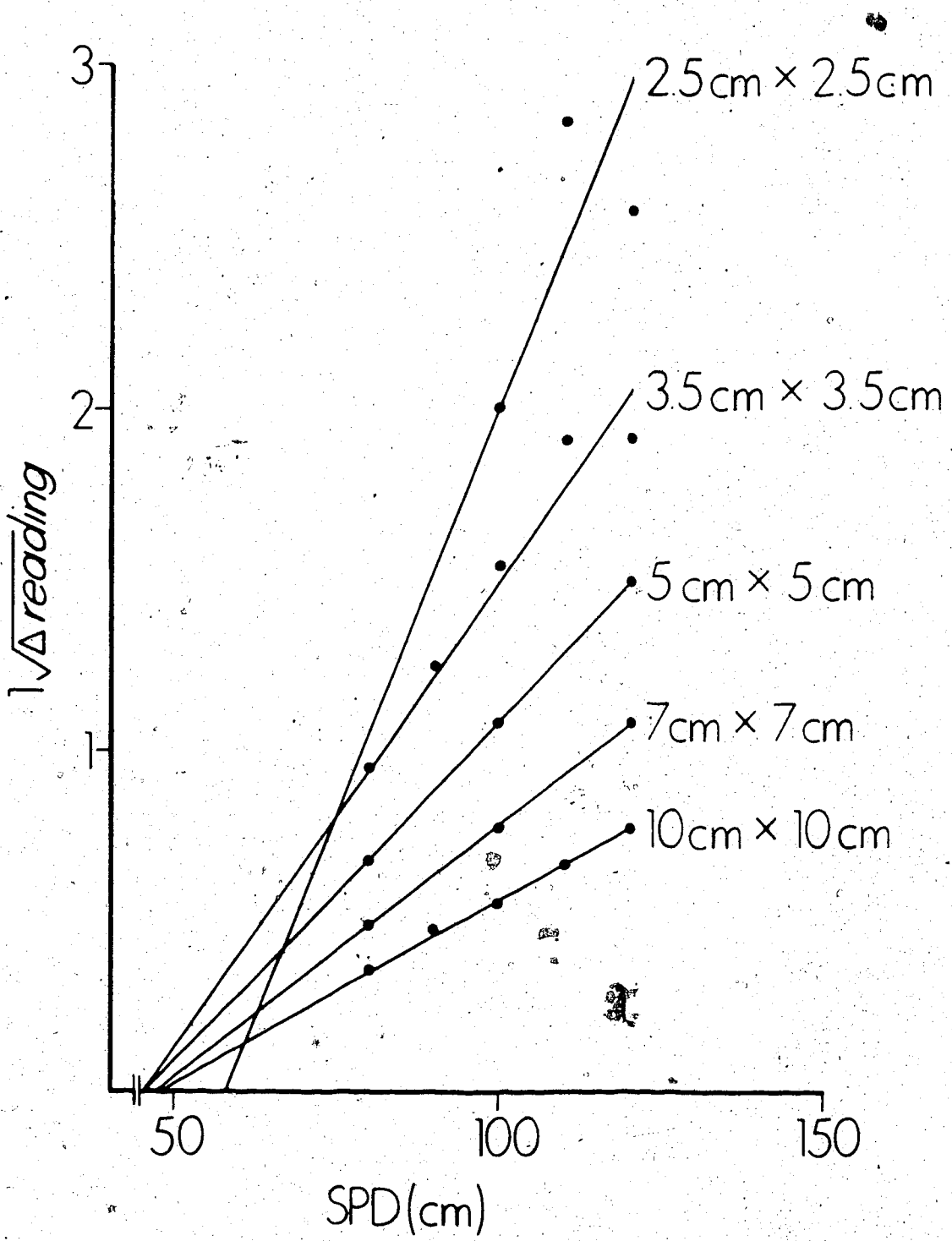

Figure 57. Dependence of the dose produced between the target and magnet on the inverse square of the distance from the apparent source at 6 MV when the cross hair tray was in place.

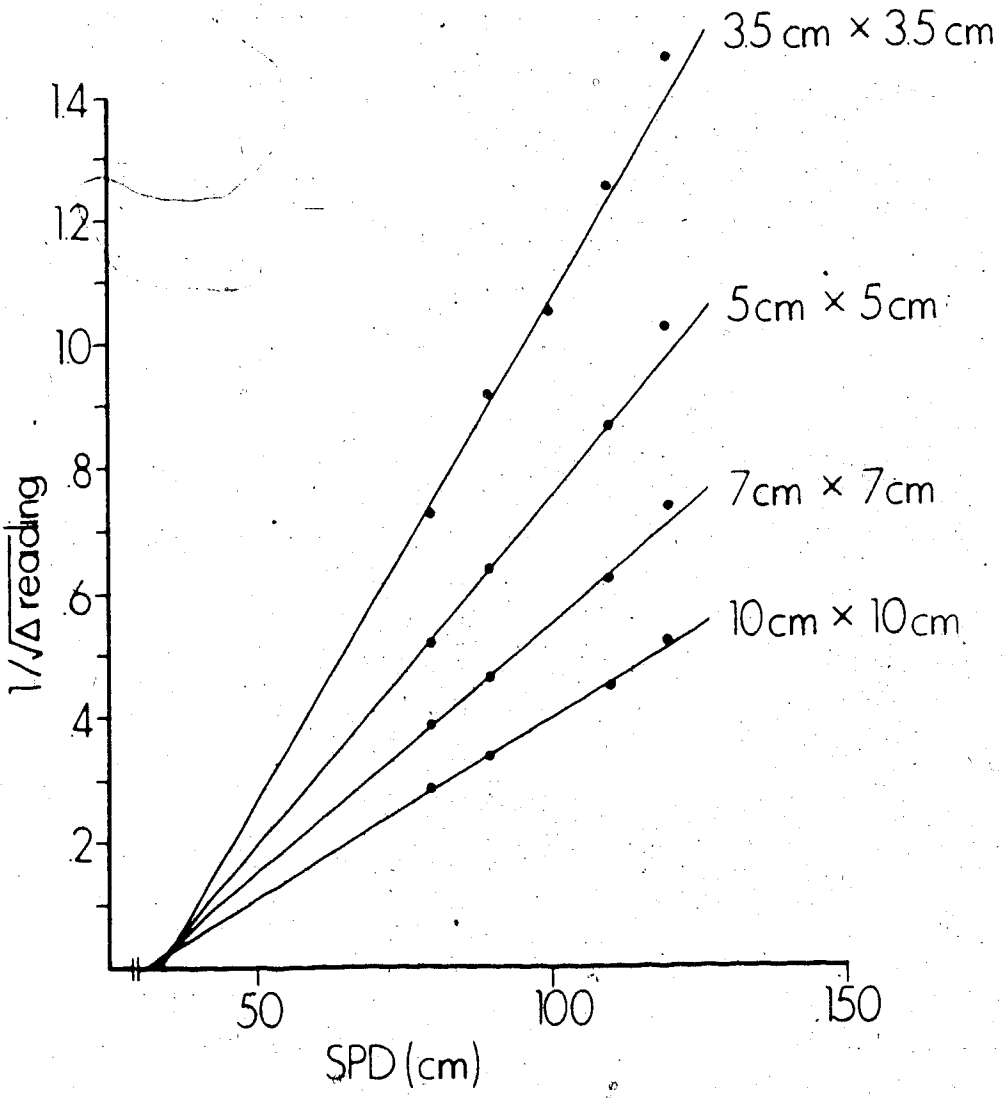

Figure 58. Dependence of the dose produced between the target and magnet on the inverse square of the distance from the apparent source at 15 MV when the cross-hair tray was not in place.

35 cm. The range of x-intercepts corresponds approximately to the position of the collimators.

2.10.4 Determination of the Penetration Curves of Electron Contamination Produced Between the Target and Magnet

Electrons produced by interactions between the target and magnet should penetrate some distance into a phantom. The penetration curve can be obtained by measuring the difference between readings taken without and with the magnet in place when the same thickness of overlying material is placed over the ion chamber.

Figure 59 illustrates the central axis penetration curve for electron contamination produced by the 15 MV beam between the target and magnet as measured by a probe at 100 cm SPD in a 10 cm x 10 cm field. This penetration curve has its maximum at about 0.15 cm in the phantom and a relative plateau in dose of about 1 cm. From 1 cm to 3.5 cm the dose drops rapidly as a function of depth. At 2.9 cm the dose deposited is only 20% of the dose deposited at 0.15 cm.

An almost identical penetration curve was produced when the probe was 3 cm outside a field with a size of 10 cm x 10 cm at 100 cm SPD for a 15 MV beam (see Figure 60). The phantom setup was similar to the inset in Figure 30 except the phantom was tilted at 5.7^{o}.

Figure 61 illustrates the penetration curve for electron contamination produced between the target and magnet for the 6 MV beam. The shape of the curve is similar to the result at 15 MV except that the maximum dose occurs at the surface at 6 MV and this beam reaches its 20% level at 1.3 cm instead of 2.9 cm. Figure 62 compares the penetration curves for electron

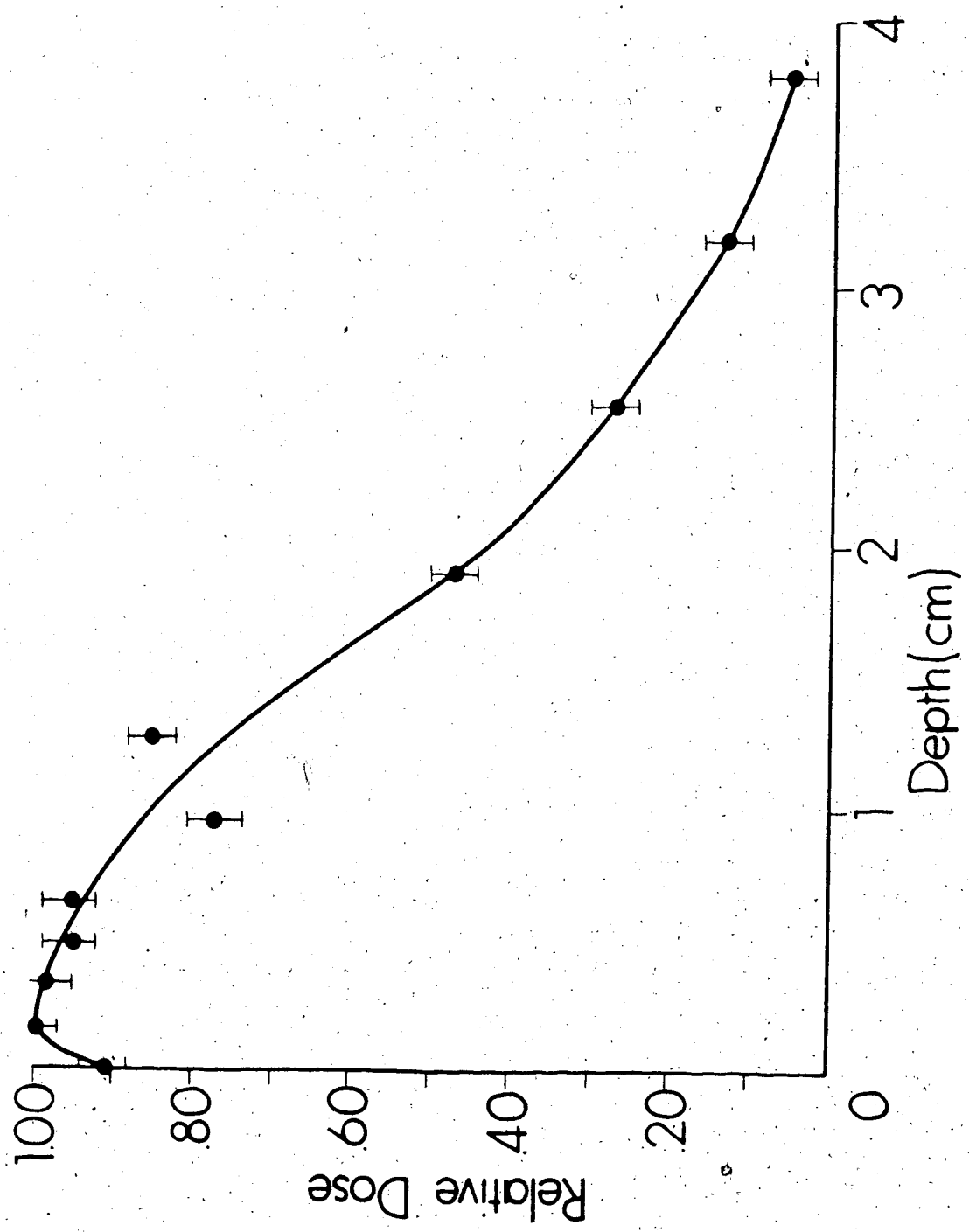

Figure 59. Central axis penetration curve for electron contamination produced between the target and magnet by the 15 MV beam at 100 cm SPD for a field size of 10 cm x 10 cm.

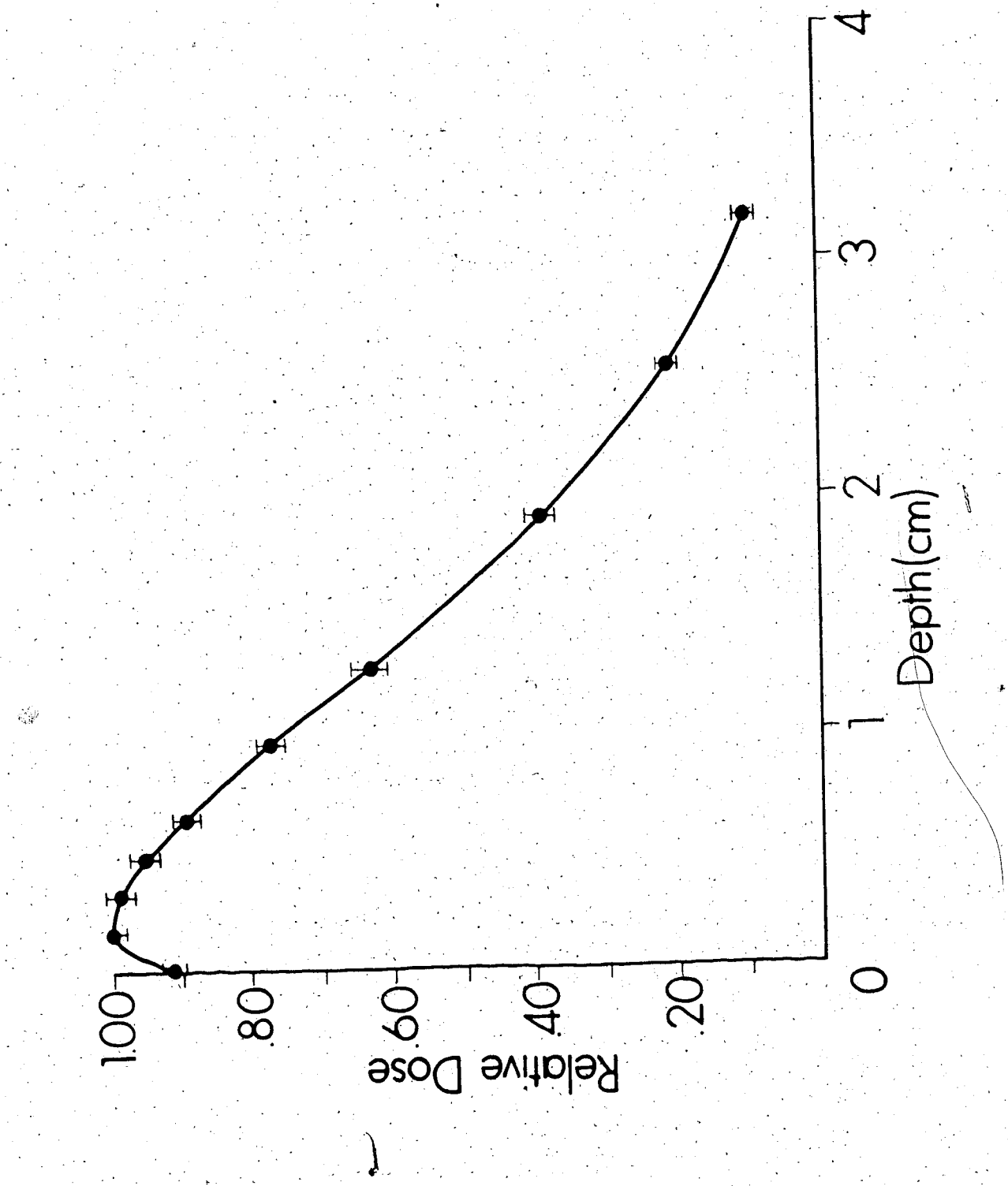

Figure 60. Penetration curve for electron contamination between the target and magnet measured 3 cm outside a 10 cm x 10 cm field at 100 cm SPD for a 15 MV beam.

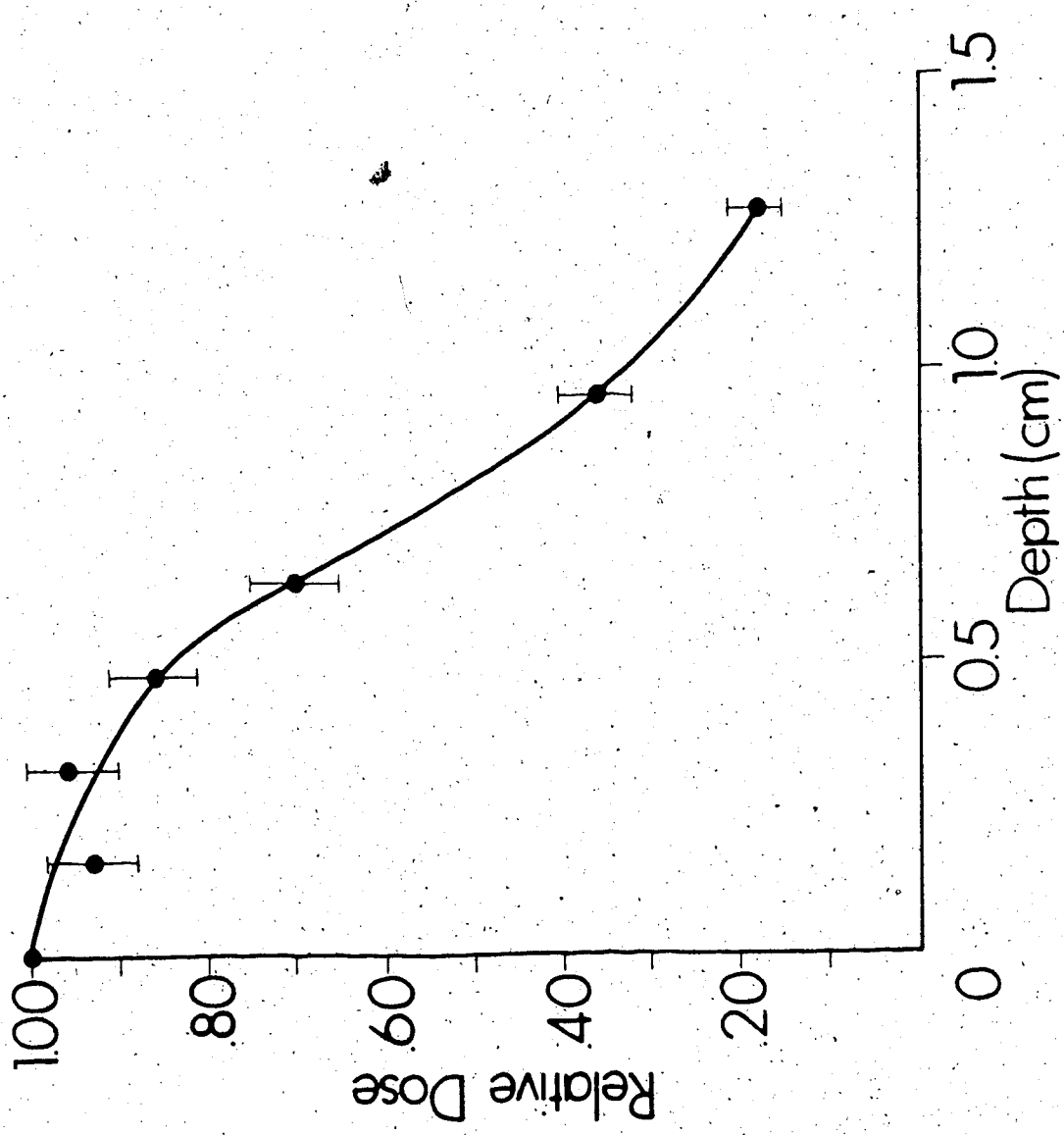

Figure 61. Central axis penetration curve for electron contamination produced between the target and magnet by the 6 MV beam at 100 cm SPD for a field size of 10 cm x 10 cm.

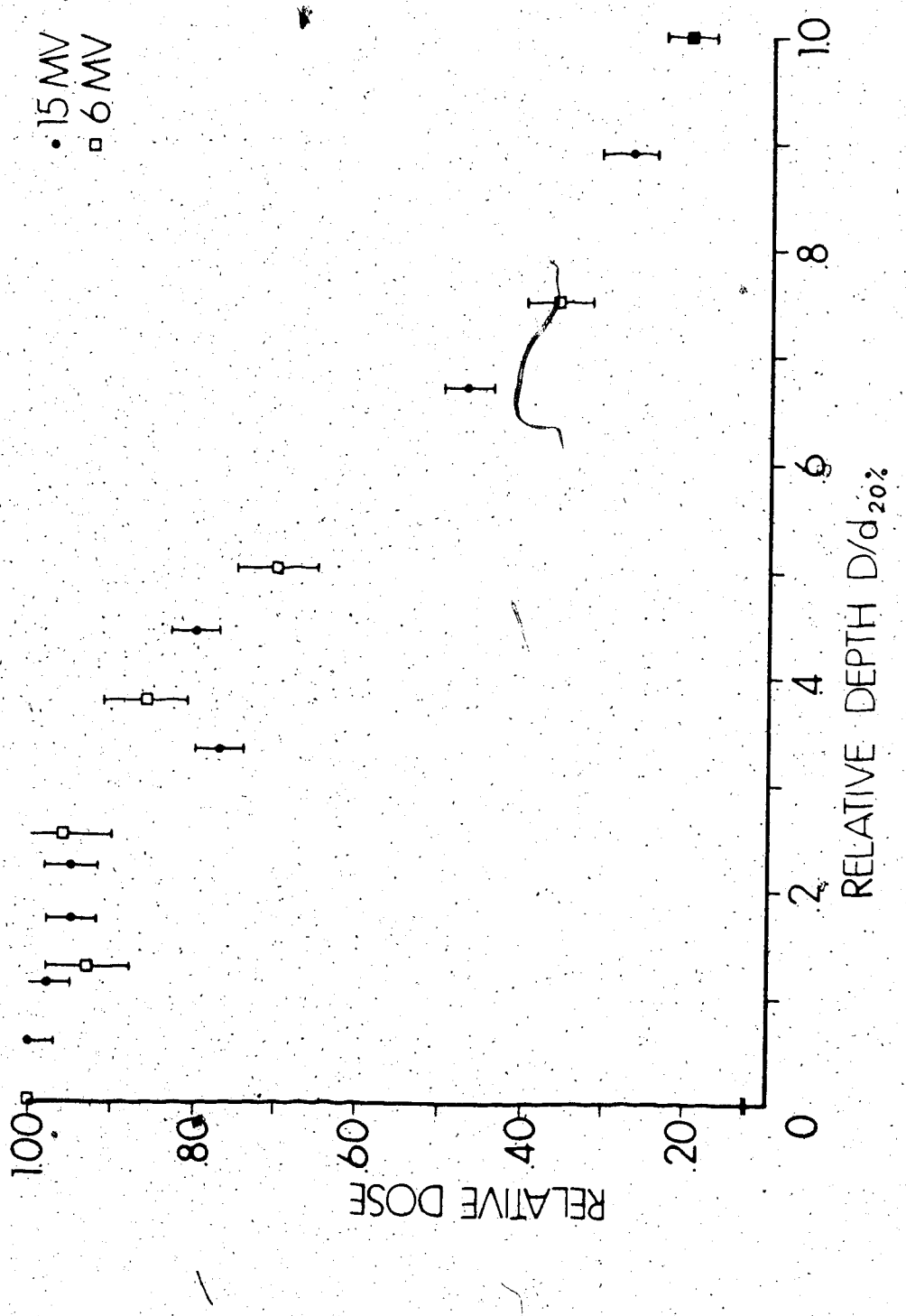

Figure 62. Comparison between the 15 MV and 6 MV contamination penetration curves produced between the target and magnet in a 10 cm x 10 cm beam at 100 cm SPD.

contamination produced between the target and magnet for 6 MV and 15 MV by normalizing the depth of penetration with respect to the depth required to reach the 20% level. The curves are almost identical.

2.11 A Method for Separating Contamination from Phantom Generated Penetration Curves

2.11.1 Determination of the Contamination Penetration Curves

The graphs of normalized dose versus field width allow one to separate the dose due to contamination from the dose due to photons interacting in the phantom. The total dose, T(d,SPD,W), is a sum of the phantom generated dose, P(d,SPD), and the contamination dose, C(d,SPD,W). The phantom generated dose is not a function of the field width, W, when measured with a limited phantom (see Figure 34). The phantom generated dose is due to primary photons interacting with the phantom and scattered photons generated by the primary interactions in the phantom. The phantom generated dose is due to the primary photon component of the beam, Mathematically.

$$T(d,SPD,W) = P(d,SPD) + C(d,SPD,W) \qquad (2.11.1)$$

where $T(d,SPD,W) = \frac{\text{Total Reading}}{\text{Standard Reading}}$

$$P(d,SPD) = \frac{\text{Reading Due To Primary Photons}}{\text{Standard Reading}}$$

$$C(d,SPD,W) = \frac{\text{Reading Due To Contamination}}{\text{Standard Reading}}$$

The standard reading used is the same as in Equation 2.8.1.

$$\frac{dT(d,SPD,W)}{dW} = \frac{dP(d,SPD)}{dW} + \frac{dC(d,SPD,W)}{dW} \qquad (2.11.2)$$

but $\frac{dP(d,SPD)}{dW} = 0$

Therefore,

$$\frac{dT(d,SPD,W)}{dW} = \frac{dC(d,SPD,W)}{dW} \qquad (2.11.3)$$

where $\frac{dT(d,W)}{dW}$ is the slope of the line of normalized dose versus field width at a depth, d, source-to-probe distance, SPD, and field width, W. The normalized dose due to contamination, C(d,SPD,W), is found by integrating Equation 2.8.3. This makes an assumption that the nature of the contamination does not change as a function of field width, but the magnitude of contamination does. Mathematically,

$$C(d,SPD,W) = \int_{W_1}^{W_2} \frac{dT(d,SPD,W)dW}{dW} \qquad (2.11.4)$$

If $\frac{dT(d,SPD,W)}{dW}$ is not a constant then,

$$C(d,SPD,W_1,W_2) \propto T(d,SPD,W_2) - T(d,SPD,W_1) \qquad (2.11.5)$$

If $\frac{dT(d,SPD,W)}{dW}$ is a constant then,

$$C(d,SPD) \propto \text{Slope of Line} \qquad (2.11.6)$$

where the last equation does not have any dependence on field width. An assumption is implicit that dose increase of small field size is the same as dose increases for larger sizes.

The slopes in Figures 35 to 38 were linear so Equation 2.11.6 can be used. Therefore, the amount of contamination is independent of field width. Table 3 lists the amount of contamination as a function of depth normalized to the maximum amount of contamination for the 15 MV beam. The penetration characteristics of the contamination are relatively independent of the thickness of accessory and source-to-probe distance. Therefore, to a good approximation, the relative amount of contamination only depends on the depth of measurement in the phantom. A plot of the contamination penetration curve at SPD = 100 cm is shown in Figure 63.

The open field penetration behaviour at 100 cm SPD was obtained for the 6 MV accelerator also by using the increase in normalized dose versus field width. The normalized contamination penetration curve is shown in Figure 64.

The contamination penetration curves are equivalent to the tissue maximum ratio of the contaminant component if they were the only component in the beam.

2.11.2. Determination of the Phantom Generated Build-Up Curves

The phantom generated build-up contribution is obtained by subtracting the contamination component from the total build-up curve. The total build-up curve is measured with a full phantom (that is, the

Table 3 Contamination Dose Normalized To The Maximum Contamination Dose At 15 MV

Depth (cm)	SPD = 100cm No Accessory	SPD = 100cm 0.64cm Lucite Accessory	SPD = 100cm 3.18cm Lucite Accessory	SPD = 75cm No Accessory
0.00	0.94	0.98	0.95	0.99
0.16	1.00	1.00	1.00	1.00
0.32	0.94	0.96	0.95	0.92
0.48	0.89	0.88	0.88	0.84
0.64	0.83	0.79	0.80	0.78
0.95	0.69	0.64	0.67	0.63
1.27	0.61	0.51	0.55	0.50
1.91	0.48	0.34	0.36	0.31
2.54	0.28	0.23	0.24	0.21
2.86	0.23	0.19	0.21	0.16
3.18	0.21	0.16	0.18	0.18
3.49	0.18	0.14	0.17	0.16
3.81	0.15	0.13	0.15	0.17
4.13	0.15	0.12	0.14	0.11

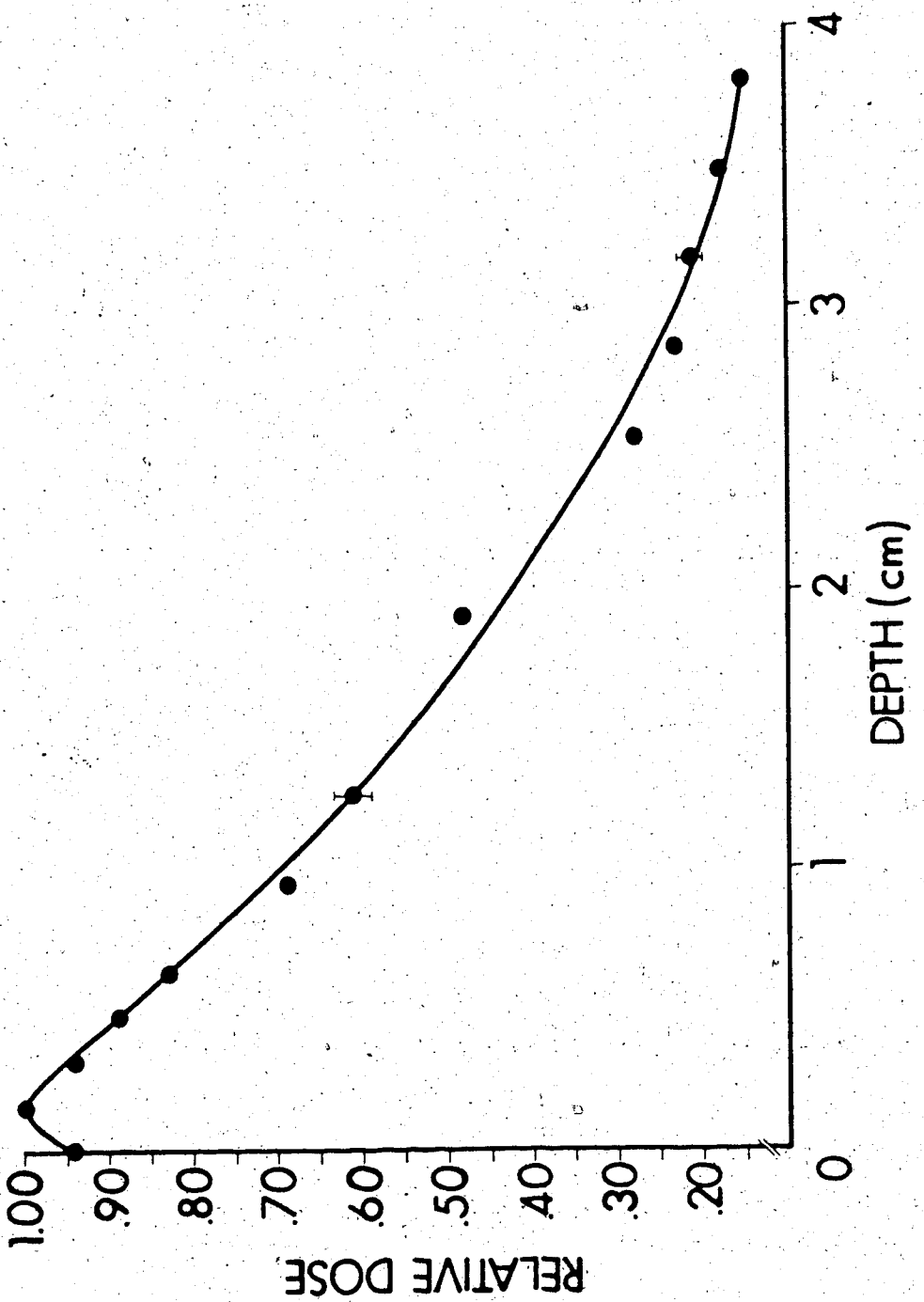

Figure 63. Contamination penetration curve determined by the increase in dose in a limited phantom as a function of field width at 100 cm SPD for a 15 MV beam.

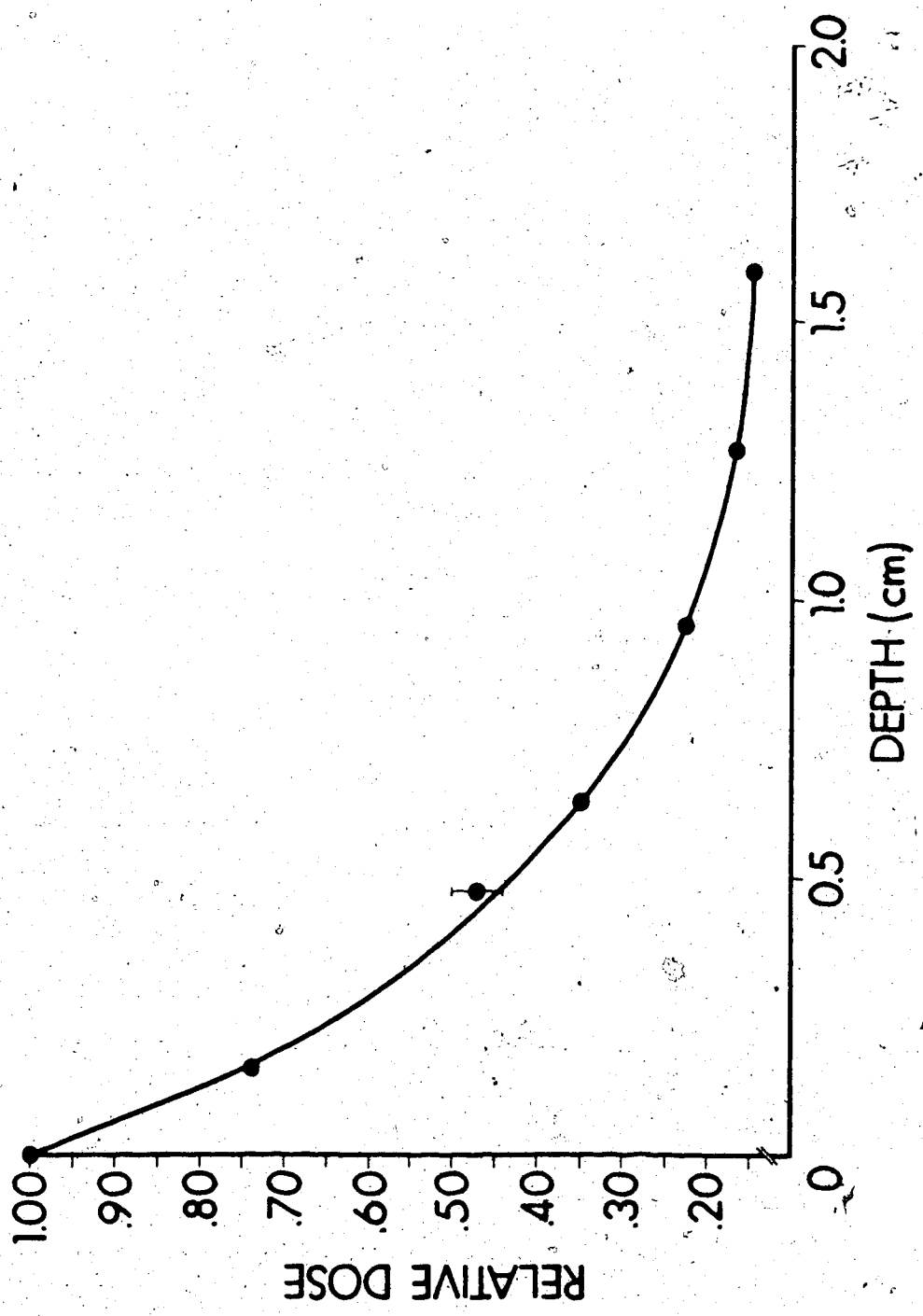

Figure 64. Contamination penetration curve determined by the increase in dose in a limited phantom as a function of field width at 100 cm SPD for a 6 MV beam.

cross-sectional area is greater than the field width). The magnitude of contamination under any condition is determined by equating the difference between the total build-up curve and the photon backscatter at the surface with the magnitude of the contamination dose at the surface. Mathematically,

$$C(d=0,SPD,W) = T(d=0,SPD,W) - PBS(d=0,SPD,W) \quad (2.11.7)$$

where PBS(d=0,SPD,W) is the amount of photon backscatter at the surface of the phantom. The amount of contamination at any depth is determined from a knowledge of the amount of contamination there is at the surface and the penetration characteristics. Mathematically,

$$C(d,SPD,W) = C(d=0,SPD,W) \frac{CTMR(d)}{CTMR(d=0)} \quad (2.11.8)$$

where CTMR(d) is the value of the normalized contamination penetration curve at a depth, d, in the phantom.

Having established the magnitude of contamination at any depth in the phantom, the contamination component is subtracted from the total build-up component to yield the phantom generated build-up curve.

A computer program called Seprimary.For* (for a listing and documentation of Seprimary.For see Appendix 5) calculates the phantom generated build-up curves. The input data lists the normalized contamination penetration data as a function of depth, the photon backscatter normalized dose at the surface as a function of field size as well as SPD and the total build-up normalized dose as a function of field size, SPD, depth and amount of accessories in the field.

The "pseudo-unit" of the output is normalized dose. This can be converted to the tissue maximum ratios of the phantom generated build-up curves by dividing the curves by the maximum normalized dose value of each curve.

An estimate of the limit errors in the calculated quantities is also computed. The errors in the measured quantities are entered with the input data.

Tables 4 to 15 list the phantom generated normalized dose and tissue maximum ratio curves as a function of depth along with their associated limit errors for a variety of conditions of field size, SPD and presence of accessories for the 15 MV and 6 MV accelerators. The phantom generated normalized dose at d_{max} increases as a function of

* The suffix, '.For', indicates an executable Fortran program. The suffix, '.Dat', indicates a data file storing constant values.

Table 4

15 MV SPD = 100cm
No Accessories
Field Size = 3.0cm X 3.0cm
Photon Backscatter N.D. = 0.001

Depth (cm)	ND	Error in ND	TMR	Error in TMR
0.00	0.001	0.000	0.00	0.00
0.16	0.168	0.008	0.21	0.01
0.32	0.290	0.008	0.36	0.01
0.48	0.388	0.008	0.48	0.01
0.64	0.456	0.008	0.56	0.01
0.95	0.577	0.007	0.71	0.01
1.27	0.663	0.007	0.82	0.01
1.91	0.759	0.006	0.93	0.01
2.54	0.802	0.005	0.99	0.01
2.86	0.811	0.005	1.00	0.01
3.18	0.813	0.005	1.00	0.01
3.50	0.813	0.005	1.00	0.01
3.81	0.812	0.005	1.00	0.01

15 MV SPD = 100cm
No Accessories
Field Size = 4.0cm X 4.0cm
Photon Backscatter N.D. = 0.001

Depth (cm)	ND	Error in ND	TMR	Error in TMR
0.00	0.001	0.000	0.00	0.00
0.16	0.173	0.009	0.20	0.01
0.32	0.303	0.009	0.34	0.01
0.48	0.402	0.008	0.46	0.01
0.64	0.486	0.008	0.55	0.01
0.95	0.614	0.008	0.70	0.01
1.27	0.706	0.007	0.80	0.01
1.91	0.818	0.006	0.93	0.01
2.54	0.862	0.006	0.98	0.01
2.86	0.872	0.005	0.99	0.01
3.18	0.881	0.005	1.00	0.01
3.50	0.882	0.005	1.00	0.01
3.81	0.880	0.005	1.00	0.01

Table 5

15 MV SPD = 100cm
No Accessories
Field Size = 5.0cm X 5.0cm
Photon Backscatter N.D. = 0.002

Depth (cm)	ND	Error in ND	TMR	Error in TMR
0.00	0.002	0.001	0.00	0.00
0.16	0.173	0.010	0.19	0.01
0.32	0.304	0.010	0.33	0.01
0.48	0.407	0.010	0.44	0.01
0.64	0.504	0.009	0.55	0.01
0.95	0.633	0.009	0.69	0.01
1.27	0.728	0.008	0.79	0.01
1.91	0.840	0.007	0.91	0.01
2.54	0.897	0.006	0.97	0.01
2.86	0.910	0.006	0.99	0.01
3.18	0.917	0.006	1.00	0.01
3.50	0.922	0.006	1.00	0.01
3.81	0.920	0.005	1.00	0.01

15 MV SPD = 100cm
No Accessories
Field Size = 8.0cm X 8.0cm
Photon Backscatter N.D. = 0.004

Depth (cm)	ND	Error in ND	TMR	Error in TMR
0.00	0.004	0.001	0.00	0.00
0.16	0.194	0.012	0.20	0.01
0.32	0.332	0.012	0.34	0.01
0.48	0.439	0.011	0.46	0.02
0.64	0.532	0.011	0.55	0.02
0.95	0.669	0.010	0.69	0.02
1.27	0.765	0.010	0.79	0.02
1.91	0.881	0.008	0.91	0.01
2.54	0.940	0.007	0.98	0.01
2.86	0.953	0.007	0.99	0.01
3.18	0.957	0.007	0.99	0.01
3.50	0.964	0.007	1.00	0.01
3.81	0.963	0.006	1.00	0.01

Table 6

15 MV SPD = 100cm
No Accessories
Field Size =10.0cm X10.0cm
Photon Backscatter N.D. = 0.006

Depth (cm)	ND	Error in ND	TMR	Error in TMR
0.00	0.006	0.001	0.01	0.00
0.16	0.191	0.013	0.19	0.01
0.32	0.333	0.013	0.34	0.02
0.48	0.443	0.012	0.45	0.02
0.64	0.540	0.012	0.55	0.02
0.95	0.677	0.011	0.69	0.02
1.27	0.774	0.010	0.79	0.02
1.91	0.897	0.009	0.91	0.02
2.54	0.955	0.008	0.97	0.01
2.86	0.970	0.007	0.99	0.01
3.18	0.977	0.007	0.99	0.01
3.50	0.983	0.007	1.00	0.01
3.81	0.983	0.007	1.00	0.01

15 MV SPD = 100cm
No Accessories
Field Size =12.0cm X12.0cm
Photon Backscatter N.D. = 0.007

Depth (cm)	ND	Error in ND	TMR	Error in TMR
0.00	0.007	0.001	0.01	0.00
0.16	0.205	0.015	0.21	0.02
0.32	0.349	0.014	0.35	0.02
0.48	0.462	0.014	0.47	0.02
0.64	0.556	0.013	0.56	0.02
0.95	0.699	0.012	0.70	0.02
1.27	0.796	0.012	0.80	0.02
1.91	0.914	0.010	0.92	0.02
2.54	0.973	0.009	0.98	0.02
2.86	0.987	0.008	0.99	0.02
3.18	0.993	0.008	1.00	0.02
3.50	0.992	0.008	1.00	0.02
3.81	0.993	0.008	1.00	0.02

Table 7

15 MV SPD = 100cm
No Accessories
Field Size =15.0cm X15.0cm
Photon Backscatter N.D. = 0.009

Depth (cm)	ND	Error in ND	TMR	Error in TMR
0.00	0.009	0.001	0.01	0.00
0.16	0.207	0.017	0.21	0.02
0.32	0.354	0.016	0.35	0.02
0.48	0.463	0.016	0.46	0.02
0.64	0.560	0.015	0.56	0.02
0.95	0.704	0.014	0.70	0.02
1.27	0.806	0.013	0.80	0.02
1.91	0.921	0.011	0.92	0.02
2.54	0.975	0.010	0.97	0.02
2.86	0.991	0.010	0.99	0.02
3.18	0.997	0.009	0.99	0.02
3.50	1.002	0.009	1.00	0.02
3.81	1.004	0.009	1.00	0.02

15 MV SPD = 100cm
No Accessories
Field Size =20.0cm X20.0cm
Photon Backscatter N.D. = 0.012

Depth (cm)	ND	Error in ND	TMR	Error in TMR
0.00	0.012	0.002	0.01	0.00
0.16	0.205	0.020	0.20	0.02
0.32	0.353	0.020	0.35	0.02
0.48	0.462	0.019	0.46	0.02
0.64	0.565	0.018	0.56	0.02
0.95	0.708	0.017	0.70	0.02
1.27	0.802	0.016	0.80	0.02
1.91	0.922	0.014	0.92	0.02
2.54	0.982	0.012	0.98	0.02
2.86	0.997	0.011	0.99	0.02
3.18	1.001	0.011	0.99	0.02
3.50	1.004	0.011	1.00	0.02
3.81	1.007	0.011	1.00	0.02

Table 8

15 MV SPD = 100cm
No Accessories
Field Size =25.0cm X25.0cm
Photon Backscatter N.D. = 0.015

Depth (cm)	ND	Error in ND	TMR	Error in TMR
0.00	0.015	0.002	0.01	0.00
0.16	0.208	0.024	0.21	0.03
0.32	0.357	0.023	0.36	0.03
0.48	0.471	0.022	0.47	0.03
0.64	0.565	0.022	0.56	0.03
0.95	0.710	0.020	0.71	0.03
1.27	0.802	0.019	0.80	0.03
1.91	0.919	0.016	0.92	0.03
2.54	0.977	0.014	0.97	0.03
2.86	0.994	0.014	0.99	0.03
3.18	0.999	0.013	0.99	0.03
3.50	1.001	0.013	1.00	0.03
3.81	1.004	0.013	1.00	0.03

Table 9

15 MV SPD = 75cm
No Accessories
Field Size =10.0cm X10.0cm
Photon Backscatter N.D. = 0.007

Depth (cm)	ND	Error in ND	TMR	Error in TMR
0.00	0.007	0.001	0.01	0.00
0.16	0.202	0.014	0.21	0.02
0.32	0.339	0.013	0.35	0.02
0.48	0.449	0.013	0.46	0.02
0.64	0.539	0.012	0.55	0.02
0.95	0.682	0.011	0.69	0.02
1.27	0.777	0.011	0.79	0.02
1.91	0.896	0.009	0.91	0.02
2.54	0.959	0.008	0.98	0.02
2.86	0.971	0.008	0.99	0.02
3.18	0.978	0.008	1.00	0.02
3.50	0.981	0.007	1.00	0.02
3.81	0.982	0.007	1.00	0.01

15 MV SPD = 75cm
0.64cm Lucite Accessory
Field Size =10.0cm X10.0cm
Photon Backscatter N.D. = 0.00[illegible]

Depth (cm)	ND	Error in ND	TMR	Error in TMR
0.00	0.007	0.001	0.01	0.00
0.16	0.202	0.019	0.21	0.02
0.32	0.342	0.018	0.35	0.02
0.48	0.449	0.018	0.47	0.02
0.64	0.538	0.017	0.56	0.02
0.95	0.679	0.016	0.70	0.02
1.27	0.765	0.015	0.79	0.02
1.91	0.880	0.013	0.91	0.02
2.54	0.942	0.011	0.97	0.02
2.86	0.955	0.011	0.99	0.02
3.18	0.961	0.011	0.99	0.02
3.50	0.963	0.010	1.00	0.02
3.81	0.966	0.010	1.00	0.02

Table 10

15 MV SPD = 75cm
No Accessories
Field Size =30.0cm X30.0cm
Photon Backscatter N.D. = 0.018

Depth (cm)	ND	Error in ND	TMR	Error in TMR
0.00	0.018	0.002	0.02	0.00
0.16	0.210	0.029	0.21	0.03
0.32	0.353	0.028	0.35	0.03
0.48	0.462	0.027	0.46	0.03
0.64	0.551	0.026	0.55	0.03
0.95	0.692	0.024	0.69	0.03
1.27	0.782	0.023	0.78	0.03
1.91	0.900	0.020	0.90	0.03
2.54	0.967	0.017	0.97	0.03
2.86	0.984	0.016	0.99	0.03
3.18	0.991	0.016	0.99	0.03
3.50	0.995	0.016	1.00	0.03
3.81	0.998	0.015	1.00	0.03

15 MV SPD = 75cm
0.64cm Lucite Accessory
Field Size =30.0cm X30.0cm
Photon Backscatter N.D. = 0.018

Depth (cm)	ND	Error in ND	TMR	Error in TMR
0.00	0.018	0.002	0.02	0.00
0.16	0.180	0.045	0.19	0.05
0.32	0.302	0.043	0.32	0.05
0.48	0.390	0.042	0.41	0.05
0.64	0.463	0.041	0.49	0.06
0.95	0.599	0.037	0.63	0.06
1.27	0.680	0.035	0.72	0.06
1.91	0.816	0.031	0.86	0.05
2.54	0.901	0.027	0.95	0.05
2.86	0.927	0.026	0.98	0.05
3.18	0.936	0.026	0.99	0.05
3.50	0.946	0.025	1.00	0.05
3.81	0.948	0.024	1.00	0.05

Table 11

15 MV SPD = 100cm
3.18cm Lucite Accessory
Field Size =30.0cm X30.0cm
Photon Backscatter N.D. = 0.013

Depth (cm)	ND	Error in ND	TMR	Error in TMR
0.00	0.013	0.002	0.01	0.00
0.16	0.171	0.028	0.17	0.03
0.32	0.319	0.027	0.31	0.03
0.48	0.433	0.026	0.42	0.03
0.64	0.537	0.025	0.52	0.03
0.95	0.686	0.023	0.67	0.03
1.27	0.782	0.022	0.76	0.03
1.91	0.914	0.019	0.89	0.03
2.54	0.987	0.017	0.96	0.03
2.86	1.004	0.016	0.98	0.03
3.18	1.014	0.016	0.99	0.03
3.50	1.019	0.015	1.00	0.03
3.81	1.024	0.015	1.00	0.03

15 MV SPD = 140cm
No Accessories
Field Size =30.0cm X30.0cm
Photon Backscatter N.D. = 0.017

Depth (cm)	ND	Error in ND	TMR	Error in TMR
0.00	0.017	0.002	0.02	0.00
0.16	0.194	0.035	0.20	0.04
0.32	0.339	0.034	0.34	0.04
0.48	0.445	0.033	0.45	0.04
0.64	0.540	0.032	0.55	0.04
0.95	0.678	0.029	0.69	0.04
1.27	0.749	0.028	0.76	0.04
1.91	0.876	0.024	0.89	0.04
2.54	0.949	0.021	0.96	0.04
2.86	0.965	0.020	0.98	0.04
3.18	0.969	0.020	0.98	0.04
3.50	0.976	0.019	0.99	0.04
3.81	0.986	0.019	1.00	0.04

Table 12

6 MV SPD = 100cm
No Accessories
Field Size = 5.0cm X 5.0cm
Photon Backscatter N.D. = 0.002

Depth (cm)	ND	Error in ND	TMR	Error in TMR
0.00	0.002	0.001	0.00	0.00
0.16	0.391	0.011	0.42	0.02
0.32	0.581	0.010	0.62	0.02
0.48	0.698	0.009	0.75	0.02
0.64	0.785	0.008	0.84	0.02
0.95	0.878	0.008	0.94	0.02
1.27	0.917	0.007	0.99	0.02
1.91	0.930	0.007	1.00	0.02

6 MV SPD = 100cm
No Accessories
Field Size =10.0cm X10.0cm
Photon Backscatter N.D. = 0.009

Depth (cm)	ND	Error in ND	TMR	Error in TMR
0.00	0.009	0.001	0.01	0.00
0.16	0.420	0.014	0.43	0.02
0.32	0.617	0.012	0.63	0.02
0.48	0.739	0.011	0.76	0.02
0.64	0.831	0.010	0.85	0.02
0.95	0.926	0.009	0.95	0.02
1.27	0.968	0.009	0.99	0.02
1.91	0.978	0.009	1.00	0.02

Table 13

6 MV SPD = 100cm
No Accessories
Field Size =20.0cm X20.0cm
Photon Backscatter N.D. = 0.018

Depth (cm)	ND	Error in ND	TMR	Error in TMR
0.00	0.018	0.002	0.02	0.00
0.16	0.437	0.019	0.43	0.02
0.32	0.640	0.017	0.64	0.02
0.48	0.766	0.016	0.76	0.02
0.64	0.859	0.014	0.85	0.02
0.95	0.954	0.013	0.95	0.02
1.27	0.994	0.012	0.99	0.02
1.91	1.005	0.012	1.00	0.02

6 MV SPD = 100cm
No Accessories
Field Size =30.0cm X30.0cm
Photon Backscatter N.D. = 0.026

Depth (cm)	ND	Error in ND	TMR	Error in TMR
0.00	0.026	0.003	0.03	0.00
0.16	0.445	0.024	0.44	0.03
0.32	0.647	0.022	0.64	0.03
0.48	0.772	0.020	0.77	0.03
0.64	0.865	0.018	0.86	0.03
0.95	0.957	0.016	0.95	0.03
1.27	0.996	0.015	0.99	0.03
1.91	1.005	0.015	1.00	0.03

Table 14

6 MV SPD = 75cm
No Accessories
Field Size =30.0cm X30.0cm
Photon Backscatter N.D. = 0.029

Depth (cm)	ND	Error in ND	TMR	Error in TMR
0.00	0.029	0.003	0.03	0.00
0.16	0.468	0.026	0.46	0.03
0.32	0.667	0.023	0.66	0.03
0.48	0.789	0.021	0.78	0.03
0.64	0.878	0.019	0.87	0.03
0.95	0.966	0.017	0.96	0.03
1.27	1.003	0.016	0.99	0.03
1.91	1.011	0.016	1.00	0.03

6 MV SPD = 75cm
0.64cm Lucite Accessory
Field Size =30.0cm X30.0cm
Photon Backscatter N.D. = 0.029

Depth (cm)	ND	Error in ND	TMR	Error in TMR
0.00	0.029	0.003	0.03	0.00
0.16	0.481	0.038	0.49	0.05
0.32	0.658	0.034	0.67	0.05
0.48	0.763	0.032	0.78	0.05
0.64	0.852	0.029	0.87	0.05
0.95	0.937	0.026	0.96	0.05
1.27	0.973	0.025	0.99	0.05
1.91	0.981	0.024	1.00	0.05

Table 15

6 MV SPD = 75cm
3.18cm Lucite Accessory
Field Size =30.0cm X30.0cm
Photon Backscatter N.D. = 0.029

Depth (cm)	ND	Error in ND	TMR	Error in TMR
0.00	0.029	0.003	0.03	0.00
0.16	0.497	0.040	0.49	0.05
0.32	0.678	0.036	0.67	0.05
0.48	0.784	0.033	0.78	0.05
0.64	0.877	0.030	0.87	0.05
0.95	0.963	0.027	0.96	0.05
1.27	0.999	0.026	0.99	0.05
1.91	1.006	0.025	1.00	0.05

6 MV SPD = 100cm
3.18cm Lucite Accessory
Field Size =10.0cm X10.0cm
Photon Backscatter N.D. = 0.009

Depth (cm)	ND	Error in ND	TMR	Error in TMR
0.00	0.009	0.001	0.01	0.00
0.16	0.420	0.014	0.43	0.02
0.32	0.621	0.013	0.64	0.02
0.48	0.742	0.012	0.76	0.02
0.64	0.832	0.011	0.85	0.02
0.95	0.925	0.010	0.95	0.02
1.27	0.965	0.009	0.99	0.02
1.91	0.976	0.009	1.00	0.02

field size. The ratio of the phantom generated normalized dose at d_{max} to the phantom generated normalized dose at a field size of 10 cm x 10 cm are the phantom generated output factors. Figures 65 and 66 illustrate the phantom generated output factors compared to the total output factors for 6 MV and 15 MV, respectively, as a function of field width. The phantom generated output factor increases as a function of field width due only to increased scatter to d_{max} as a function of field width. The increase in output as a function of field width due to contamination has been removed. There is only a few percent difference between the total and phantom generated output factors because there is little contamination present at d_{max}. However, the phantom generated output curve is greater than the total output curve at small field sizes and reaches a plateau at a field size greater than 20 cm x 20 cm.

Tables 4 to 8, 12 and 15 indicate that the phantom generated TMR curve is independent of field size. Tables 9 to 11, 14 and 15 illustrate that the phantom generated TMR curve is independent of SPD and the presence of accessories.

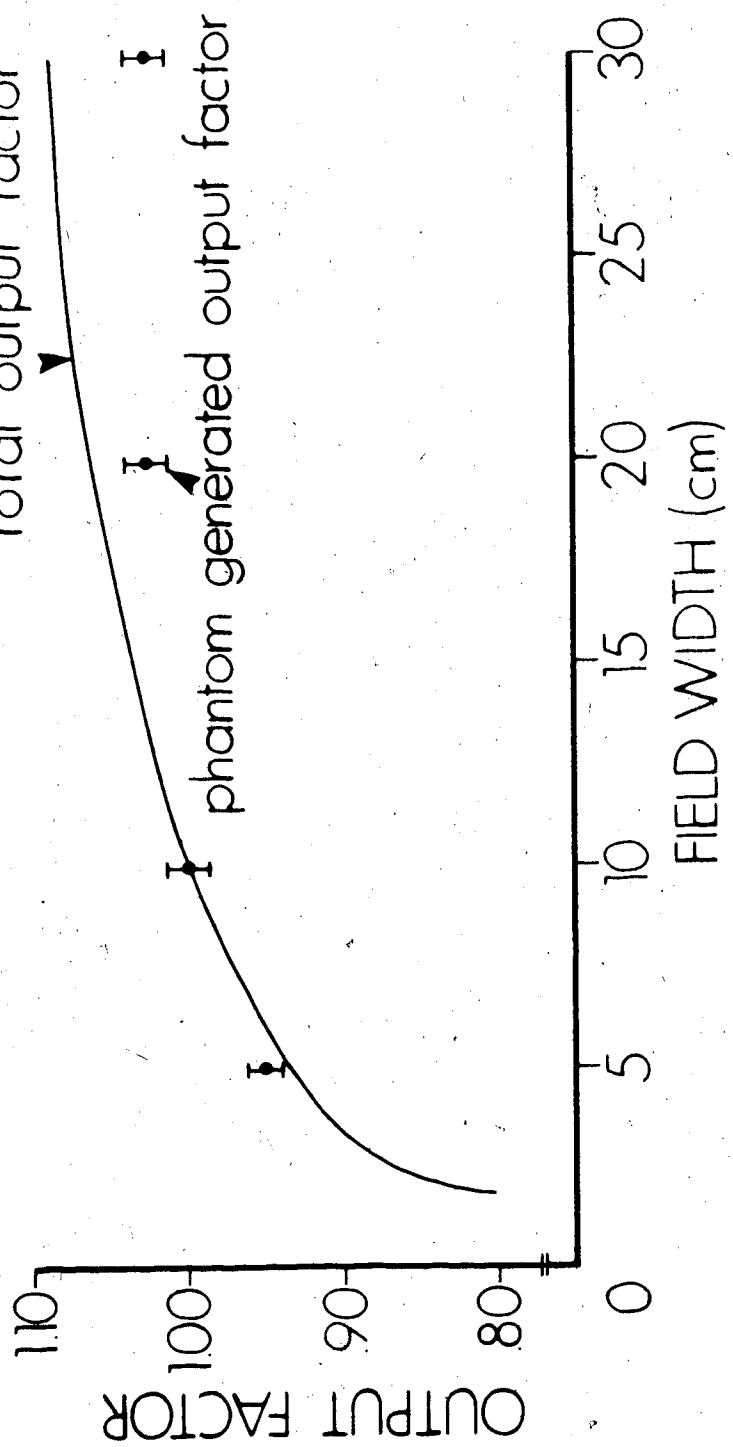

Figure 65. The phantom generated output factor curve compared to the total output factor curve at 6 MV.

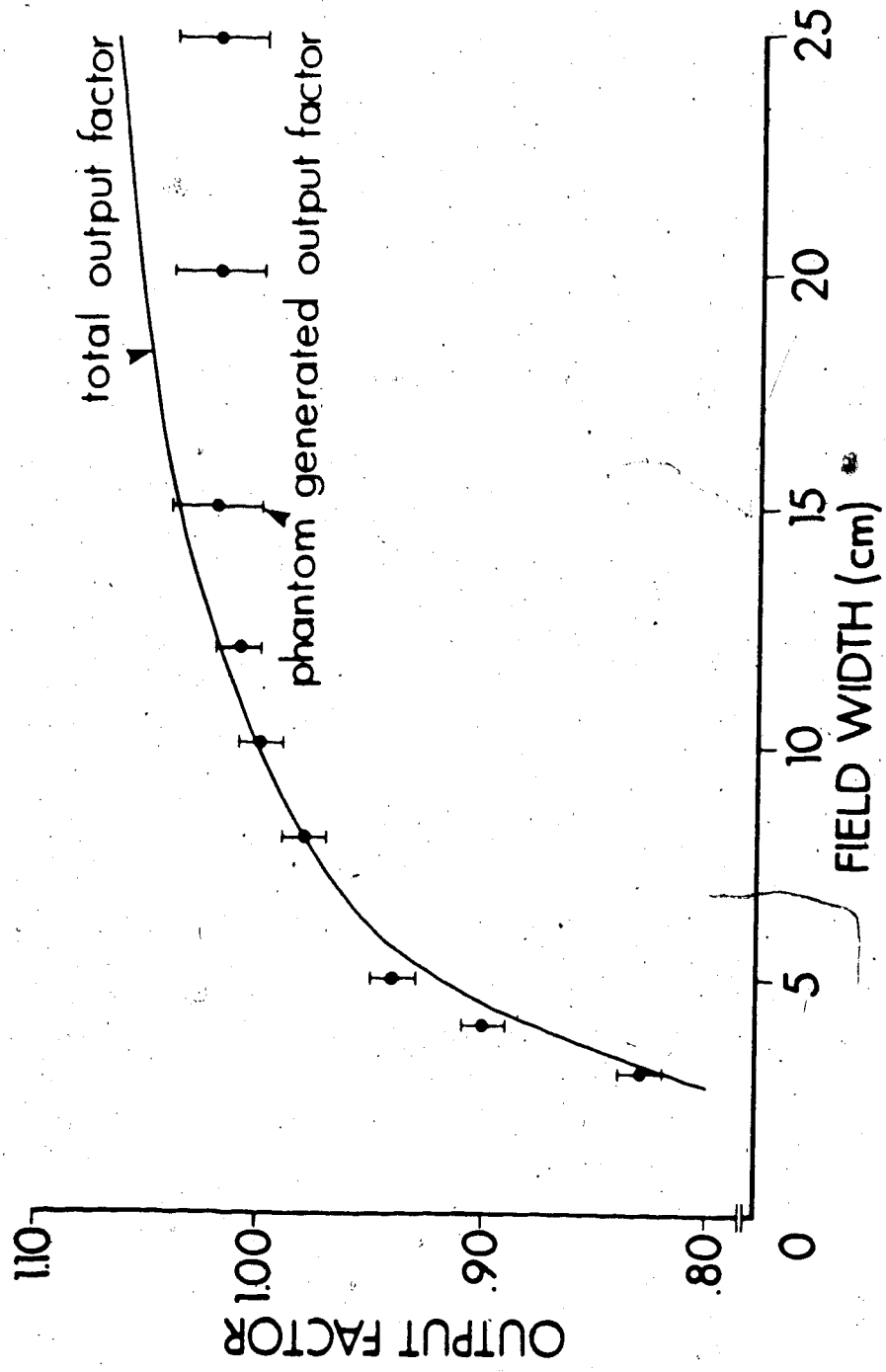

Figure 66. The phantom generated output factor curve compared to the total output factor curve at 15 MV.

2.12 Blocking the Primary Beam

A conical ingot of cerrobend or Lippowitz's metal (an alloy of lead, tin and bismuth which will attenuate half the dose in a thickness of 1.05 cm at 6 MV and 1.7 cm at 15 MV) 10 cm in length was produced such that the sides of the ingot were parallel to the beam direction when it was placed on the accessory tray. The ingot blocked the primary beam from a conical region of space underneath it. At 100 cm SPD the maximum diameter of the blocked region was 4.3 cm.

If the surface dose with the block in and out is constant, then the electron contamination and photon backscatter are not perturbed by the addition of the beam block. Table 16 lists the surface normalized dose at 100 cm SPD both with and without the beam block in place and the difference between these conditions under a variety of circumstances. There is a difference between the surface dose with the block in and out so the block does modify the surface dose.

A field size at 100 cm approximately 4 cm x 4 cm* is being blocked by the ingot. The surface normalized dose for a beam of 4 cm x 4 cm with an accessory tray in place is listed in Table 16. The surface dose for a 4 cm x 4 cm field size is almost the same as the difference between the dose with the beam block in and the beam block out. The remainder is the contribution to the surface dose due to photon backscatter between 4 cm x 4 cm to the field size listed. Therefore, the beam block stops an amount of electron contamination corresponding to the projected area of the block at SPD = 100 cm as well as blocking the primary beam.

The normalized dose as a function of depth in a phantom was

* The area of a 4.3 diameter circle is approximately the same as the area of a square with sides measuring 4 cm.

Table 16

Surface Normalized Dose At 100cm SPD
With And Without A Cerrobend Primary
Beam Block Present On The Accessory Tray

Energy	Field Size	Block Out	Block In	Difference
6 MV	10cm X 10cm	0.169	0.071	0.098 ± 0.007
6 MV	20cm X 20cm	0.300	0.204	0.096 ± 0.007
15 MV	20cm X 20cm	0.271	0.220	0.051 ± 0.004

Surface Normalized Dose At 100cm SPD
With The Accessory Tray In Place For
A 4cm X 4cm Field Size

Energy	Surface Normalized Dose
6 MV	0.092 ± 0.005
15 MV	0.048 ± 0.003

obtained with the block in and the block out. The difference between these readings is due to both a lack of the primary beam and a partial loss of contamination.

The loss of electron contamination is reflected by the loss of surface dose. If it is assumed that the scattered photon component of the contamination is attenuated by the beam block to the same extent as the electron component, then the contamination TMR curve obtained in Section 2.11.1 can be used to obtain the phantom generated N.D. and TMR for the portion of the beam blocked. This was obtained using the program Seprimary.For described in Section 2.11.2. The result is shown in Table 17. The phantom generated TMR values agree with the phantom generated TMR values obtained in Section 2.11.2.

Table 17 Difference Between The Primary Beam Blocked And Not Blocked With The Contamination Dose Removed

15 MV SPD = 100cm
0.064 Lucite Accessory Tray Left In When Block Removed
Field Size =20.0cm X20.0cm
Photon Backscatter N.D. = 0.003

Depth (cm)	ND	Error in ND	TMR	Error in TMR
0.00	0.003	0.003	0.00	0.00
0.16	0.200	0.017	0.21	0.02
0.32	0.336	0.016	0.36	0.02
0.48	0.447	0.016	0.47	0.02
0.64	0.543	0.015	0.58	0.02
0.95	0.675	0.014	0.72	0.02
1.27	0.765	0.013	0.81	0.02
1.91	0.874	0.011	0.93	0.02
2.54	0.923	0.009	0.98	0.02
2.86	0.935	0.009	0.99	0.02
3.18	0.939	0.009	1.00	0.02
3.50	0.941	0.008	1.00	0.02
3.81	0.939	0.008	1.00	0.02

2.13 Penetration Curve Outside a Magnetically Swept Field

The techniques described in Section 2.7 (Penetration Curves Outside the Field), Section 2.10 (Sweeping Electrons from the Field using a Permanent Magnet) and Section 2.11 (A Method for Separating Contamination from Phantom Generated Penetration Curves) can be used to determine the penetration curve of the scattered photon contamination component.

An ion chamber in a partial phantom as illustrated in Figure 30 was placed 3 cm outside an open 10 cm x 10 cm field. Readings as a function of the thickness of overlying phantom were obtained with the magnet in place. The probe was placed on the side of the field opposite to the direction of deflection of the electrons. The only contribution to the dose under these conditions is due to scattered photons and electrons produced in air between the magnet and the partial phantom. The readings as a function of overlying phantom normalized to the maximum reading obtained is shown in Figure 67. This curve is characteristic of photons. If it is assumed that the surface dose is entirely due to electrons produced in air (in other words, neglecting the backscatter surface dose produced by the scattered photons), then this contribution can be subtracted using the technique of Section 2.11. The result is also shown in Figure 67. The scattered photon build-up curve is characteristic of a megavoltage photon beam between 6 MV and 15 MV. The depth of the maximum dose is at approximately 2.5 cm compared to 1.6 cm for 6 MV and 3.5 cm for 15 MV.

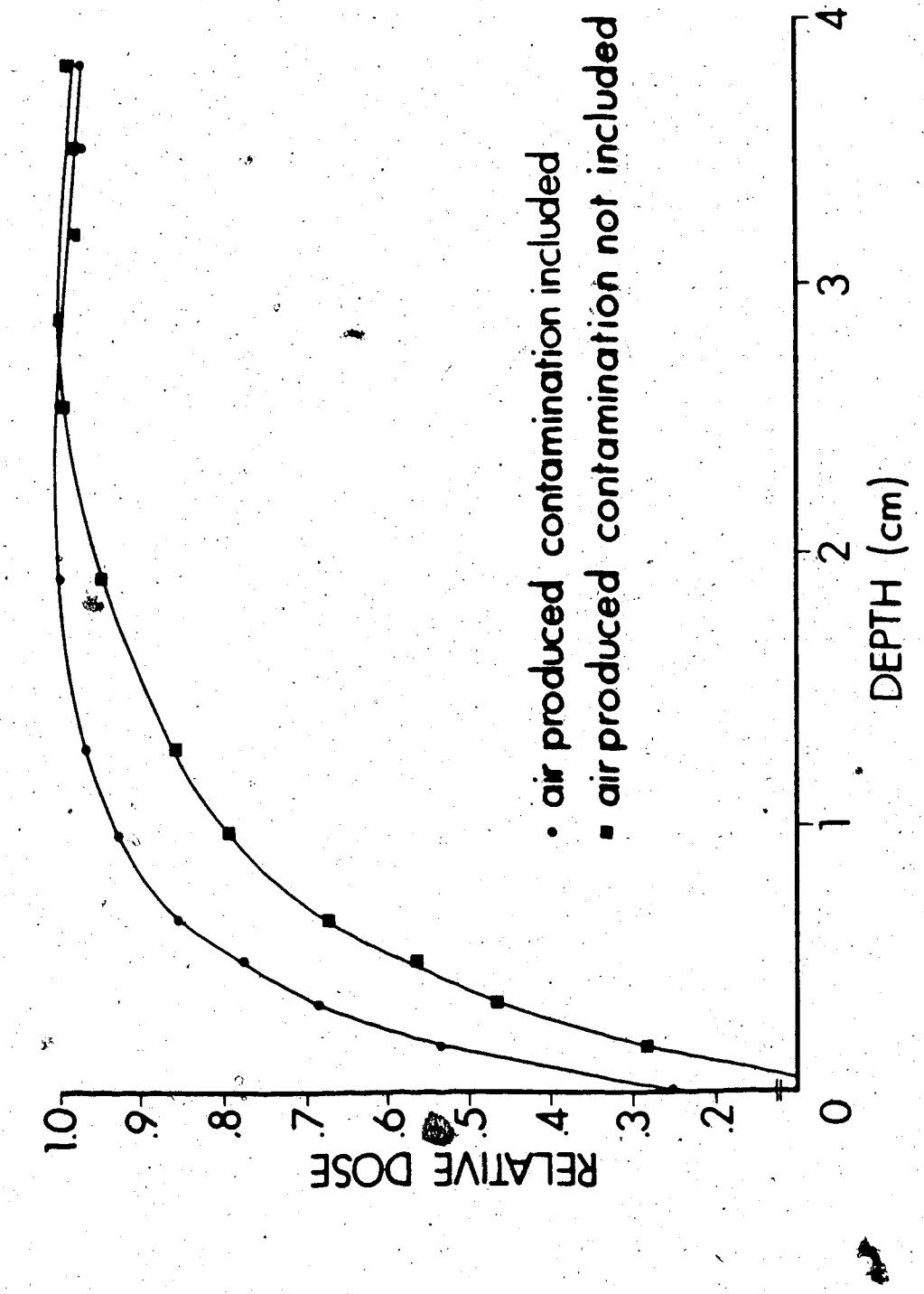

Figure 67. The scattered photon contamination build-up curve obtained 3 cm outside a magnetically swept 10 cm x 10 cm field at 100 cm SPD for the 15 MV beam.

3. DISCUSSION

It is truth very certain that,
when it is not in our power
to determine what is true
we ought to know,
what is probable.

René Descartes

3.1 Independent Modelling of the Phantom Generated Build-Up Curves

3.1.1 Introduction

The phantom generated build-up curves were determined using a computer model. This was done to verify the phantom generated build-up curves produced by the subtraction of the contamination contribution from the total build-up curves. The computer program called Buildup3.For was written in Fortran -77 to run on the VMS operating system of a VAX 11/760 computer. Buildup3 is listed in Appendix 6. Buildup3 models the generation of charged particles set in motion in water from megavoltage photon spectra and has the capability to harden the spectra. The charged particles are followed through the phantom using the Monte Carlo method and the dose absorbed by the phantom is determined.

3.1.2 Data Preparation Programs

Two additional programs prepared the look-up Tables for the program, Buildup3. The program, Quadint3.For, interpolates the total scattering and stopping power data. The program, Normdist.For, generates the value of the error function, erf(x).

The amount of energy lost per unit path length, stopping power, and the root mean square angular scattering power for representative energies are stored in a data file called Master.Dat. Quadint3.For interpolates using the quadratic method (47), the scattering and stopping power data from Master.Dat. The output of Quadint3.For is a listing of the stopping and scattering power data for 0.1 MeV increments

in energy from 0.2 MeV to 18.0 MeV. This listing is stored in a file called Quadint3.Dat. Buildup3 reads the value of Quadint3.Dat before execution.

Normdist.For generates the error function, erf(x):

$$\mathrm{erf}(x) = \frac{1}{2\pi}\int_{-x}^{x} e^{-(t^2)/2}dt \qquad (3.1.1)$$

Normdist.For is listed in Appendix 7. The value of erf(x) represents the probability of a value of t being within the limits of integration, $[-x,x]$, if t follows a Gaussian distribution with a mean equal to 0 and a standard deviation equal to 1.

The file named Gaus.Dat lists the inverse error function from 0.00 to 0.99 in increments of 0.01. It was generated by interpolation of the inverse error function from the above values of the error function. Gaus.Dat is used to determine a normally distributed random scattering angle from a uniformly distributed random number between 0 and 1. Figure 68 graphically illustrates the procedure used in a number of places in the program and will be discussed further in the following section.

3.1.3 Generation of Charged Particles Set In Motion by Photons

Buildup3 requires the photon number spectrum to be entered as a function of photon energy. The number spectrum was not measured but was interpolated from spectra published in a paper by C.W. Sandifer and M. Taherzadeh of

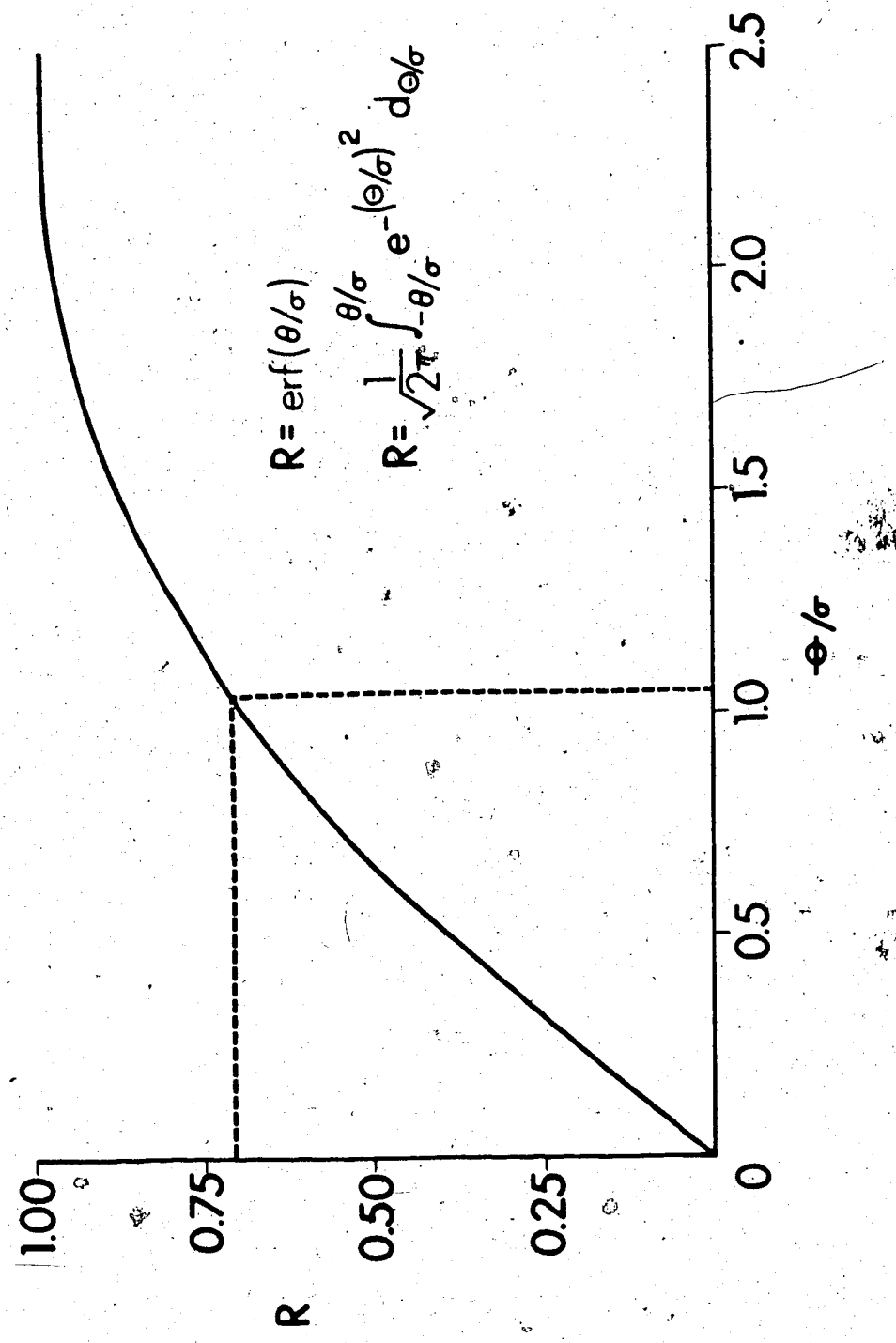

Figure 68. The probability of an angle, θ, occurring when the root mean scattering angle, σ, is equal to R. Conversely, if a random number, R, between 0 and 1 is chosen, a ratio, θ/σ, can be found. Knowing σ, then θ is determined. This figure illustrates that a random number of 0.71 results in a value of θ/σ of 1.06.

E.G. and G. Inc. (48). They measured thick-target bremsstrahlung spectra produced by electrons impinging on a 0.2 radiation-length gold-tungsten (Z of gold = 79, Z of tungsten = 74) target for electron energies in the range of 5.3 to 20.9 MeV. The electrons were accelerated by a 90^{o} bent beam linac. An aluminum block was placed behind the target to absorb low energy electrons emerging from the target.

The Siemens Mevatron -20 and Mevatron -6 are similar except for a number of features. The target is pure gold in both the Mevatron -20 and Mevatron -6. The Siemens accelerators have a 270^{o} bend instead of the research accererator's 90^{o} bend.

Sandifer and Taherzadeh measured spectra produced by electron energies very close to the nominal photon energies of the Siemens accelerators; 5.3 MV compared to the Siemens 6 MV and 14.8 MV compared to the Siemens 15 MV. The desired Siemens nominal energy was determined by normalizing the nearest measured differential energy spectra greater than and less than the desire[illegible]gy to unity and linearly interpolating between these spectra to obtain the spectrum at the desired energy. Table 18 summarizes the determination of the 6 MV differential spectrum. The number spectrum, which is the number of photons in discrete bins as a function of energy, is determined by multiplying the value of the differential spectrum of an energy bin by the energy

Table 18 Determination of the 6 MV Differential Spectrum from Measured Spectra

Maximum Bin Energy (MeV)	Experimental 5.3 MV dN/dhν (1/MeV)	Experimental 10.0 MV dN/dhν (1/MeV)	Derived 6.0 MV dN/dhν (1/MeV)
0.16	5.34×10^{-1}	2.53×10^{-1}	4.92×10^{-1}
0.25	1.00	1.00	1.00
0.36	7.00×10^{-1}	6.76×10^{-1}	6.96×10^{-1}
0.49	6.51×10^{-1}	6.05×10^{-1}	6.44×10^{-1}
0.64	5.49×10^{-1}	4.94×10^{-1}	5.41×10^{-1}
0.81	4.86×10^{-1}	4.39×10^{-1}	4.79×10^{-1}
1.00	4.11×10^{-1}	3.58×10^{-1}	4.03×10^{-1}
1.21	2.83×10^{-1}	2.74×10^{-1}	2.82×10^{-1}
1.44	2.37×10^{-1}	2.38×10^{-1}	2.37×10^{-1}
1.69	1.92×10^{-1}	2.18×10^{-1}	1.96×10^{-1}
1.96	1.62×10^{-1}	1.98×10^{-1}	1.67×10^{-1}
2.25	1.40×10^{-1}	1.80×10^{-1}	1.46×10^{-1}
2.56	1.09×10^{-1}	1.59×10^{-1}	1.16×10^{-1}
2.89	1.00×10^{-1}	1.37×10^{-1}	1.06×10^{-1}
3.24	8.34×10^{-2}	1.32×10^{-1}	9.06×10^{-2}
3.61	6.43×10^{-2}	1.14×10^{-1}	7.17×10^{-2}
4.00	5.63×10^{-2}	9.80×10^{-2}	6.25×10^{-2}
4.41	4.17×10^{-2}	1.01×10^{-1}	5.05×10^{-2}
4.81	2.51×10^{-2}	8.67×10^{-2}	3.43×10^{-2}
5.29	8.20×10^{-3}	7.61×10^{-2}	1.83×10^{-2}
5.76	2.67×10^{-3}	7.24×10^{-2}	1.31×10^{-2}

width of the bin:

$$N_i = \left(\frac{dn}{dh\nu}\right)_i (\Delta h\nu)_i \qquad (3.1.2)$$

where $(\Delta h\nu)_i$ is the width of the bin

$\left(\frac{dn}{dh\nu}\right)_i$ is the value of the differential energy spectrum at the bin energy

N_i is the number of photons in the energy bin

The number spectrum is smoothed graphically (see Figures 69 and 70) and is normalized so that the sum of the bins is unity:

$$F_i = \frac{\tilde{N}_i}{\Sigma_i N_i} \qquad (3.1.3)$$

where $\tilde{N}_i$ is the smoothed value of number spectrum at the bin energy

F_i is the smoothed normalized number spectrum at the bin energy

The mean energy of the photon number spectrum is determined by a linear weighting with respect to energy:

$$\overline{h\nu} = \Sigma_i F_i (h\nu)_i / \Sigma_i F_i = \Sigma_i F_i (h\nu)_i \qquad (3.1.4)$$

because $\Sigma_i F_i = 1$

where $\overline{h\nu}$ is the mean value of the photon number spectrum The mean value of the 6 MV photon beam is 1.5 MeV and the mean value of the 15 MV photon beam is 3.9 MeV.

The central energy of the photon bin, the value of the number spectrum, F_i, the total attenuation coefficient,

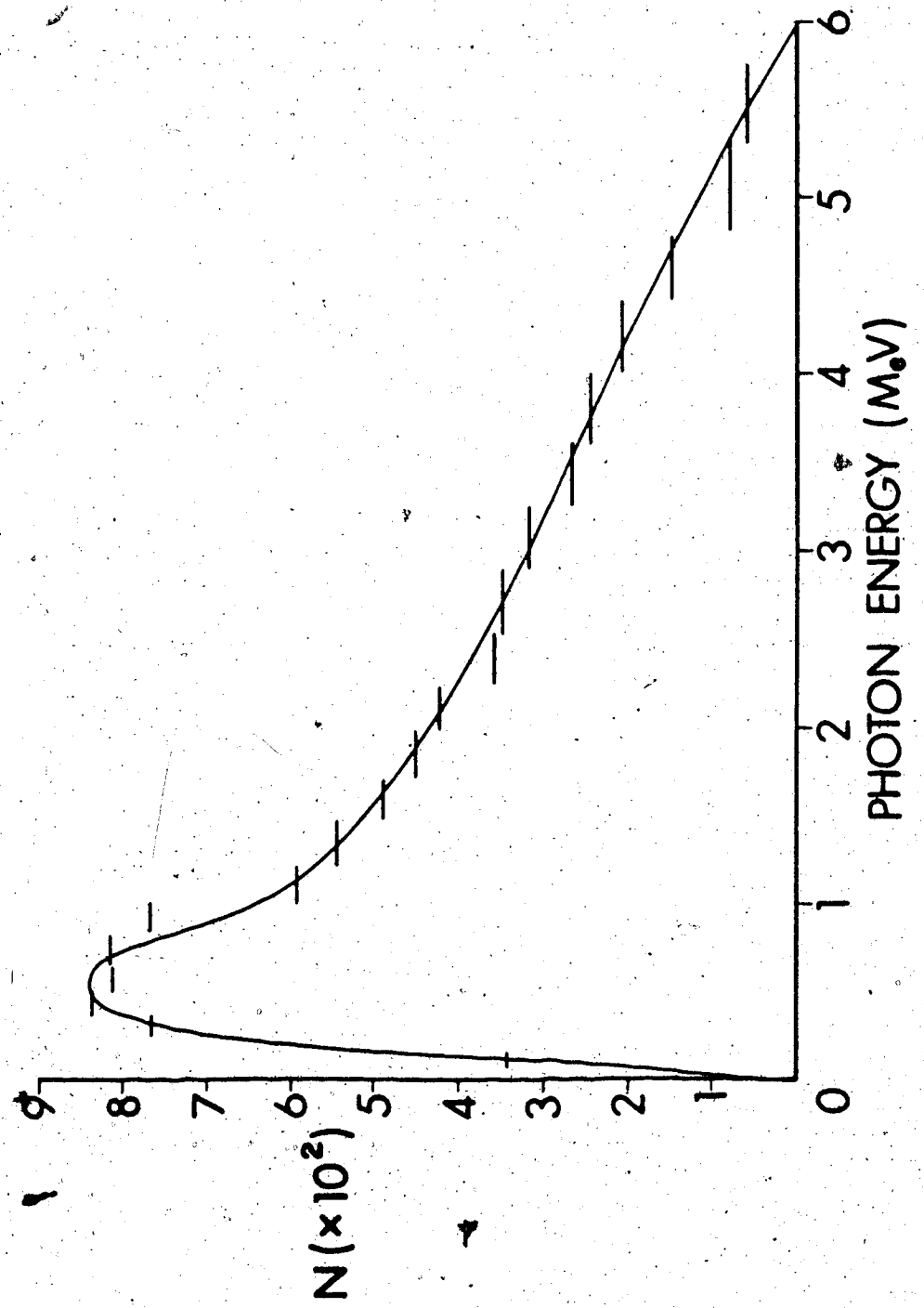

Figure 69. The smoothed and unsmoothed unnormalized primary photon number spectrum at 6 MV.

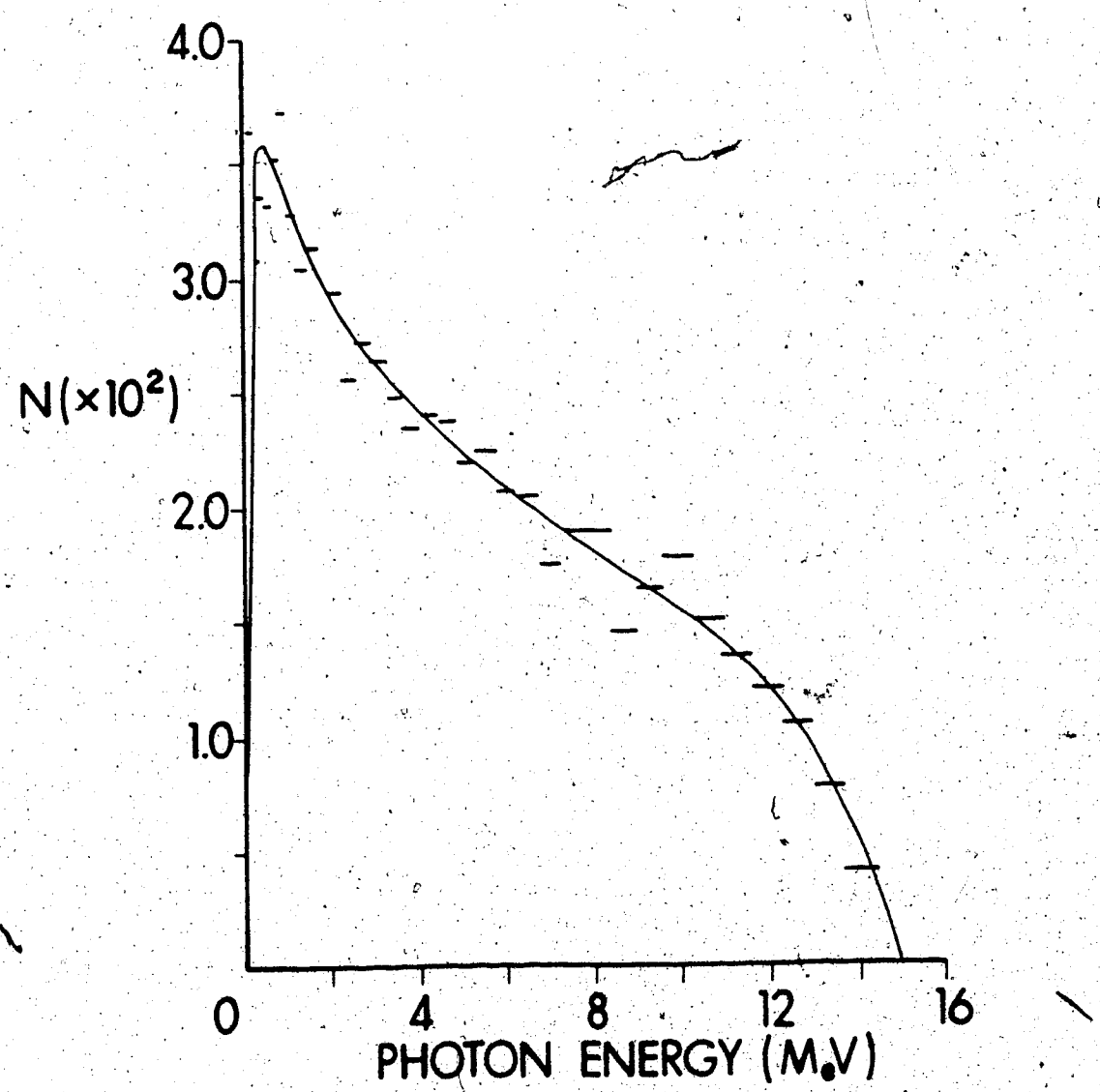

Figure 70. The smoothed and unsmoothed unnormalized primary photon number spectrum at 15 MV.

μ_{tot}/ρ for water, and the total Compton absorption coefficient, σ_{tot}/ρ for water, are listed in files named Photon6 for 6 MV and Photon15 for 15 MV.

The subroutine, Impulse, generates the charged particle set in motion spectrum due to photon interactions in a 1 mm slab of water. The photons are assumed to be initially directed normally into the slab.

The maximum photoelectric attenuation coefficient for the spectrum occurs at the lowest energy bin (0.13 Mev) and is the only 2% of the value of the Compton attenuation coefficient. The ratio between the photoelectric and Compton attenuation coefficients for the center of the second energy bin (0.21 MeV) is only 0.5% and the ratio for the third energy bin (0.31 MeV) is less than 0.1% (9). Therefore, the photoelectric effect need not be and was not taken into account.

A flow chart of the subroutine, Impulse, is shown in Figure 71. The loop at the left of the figure is repeated for both the Compton and, if required, the pair production interactions.

The number of photons from each photon energy bin in a 1 mm slab, N_i', (the variable used in the program for N_i' is nteract(i), that is, $N_i' \rightarrow$ nteract(i)*), is determined knowing the number fluence incident on the slab, F_i, and the total mass attenuation coefficient, $(\mu_t/\rho)_i$ ($(\mu_t/\rho)_i \rightarrow$ mu(i)*):

* The arrow indicates a transformation from a mathematical variable to a variable or array element defined in a program if the variables are different.

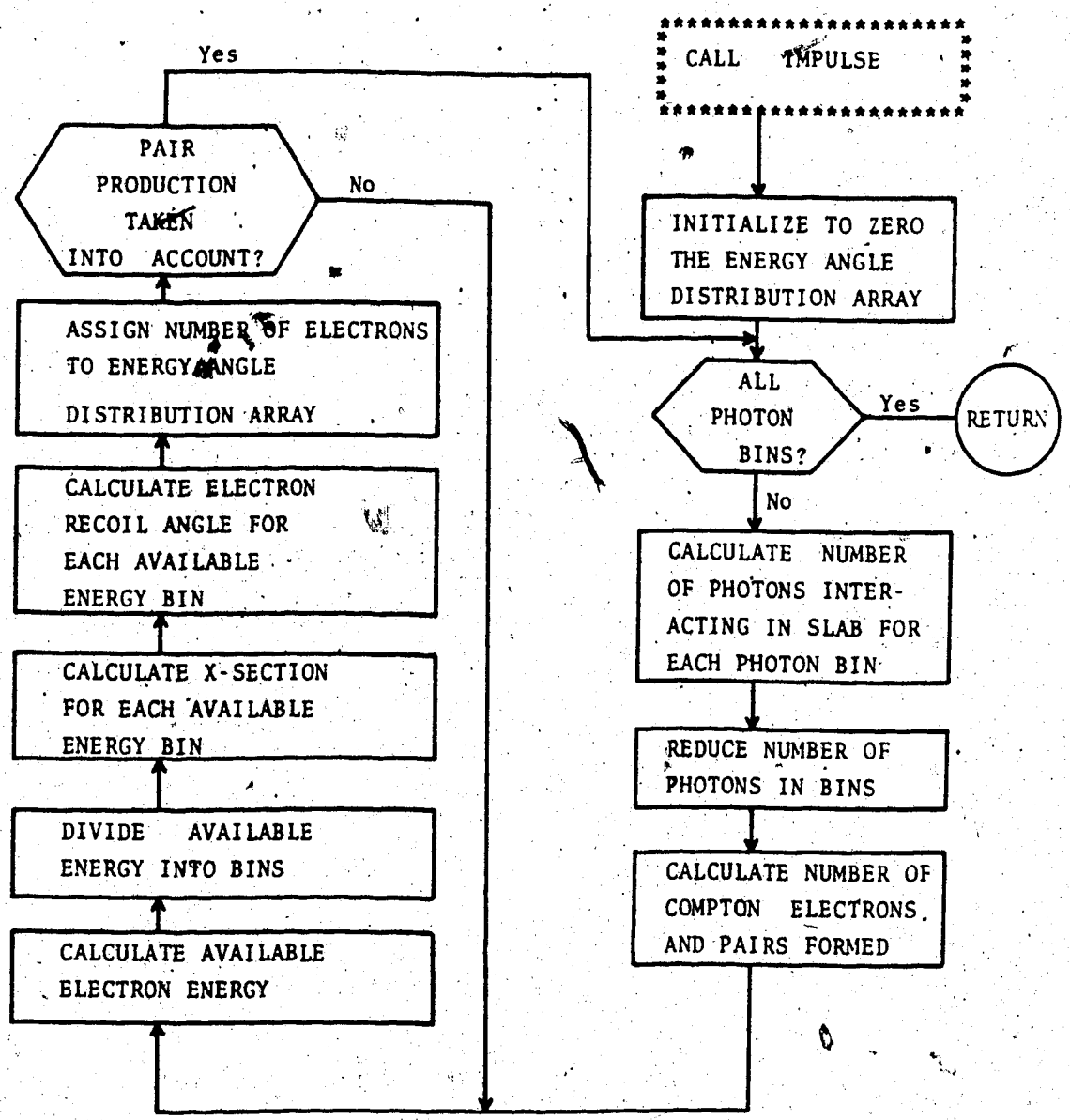

Figure 71. A flow chart for the subroutine, Impulse. The loop at the left is repeated for both Compton and pair production interactions.

$$N_i' = F_i\left(1 - e^{-(\mu_t/\rho)_i(0.1\ g/cm^2)}\right) \qquad (3.1.5)$$

If the Compton scattered photons do not interact again (corresponding to narrow beam geometry), then the only photon bin which needs to be modified is the bin from which the primary photon came:

$$(F_i)_{\substack{\text{after}\\ \text{slab}}} = (F_i)_{\substack{\text{before}\\ \text{slab}}} e^{-(\mu_{tot}/\rho)_i(0.1\ g/cm^2)} \qquad (3.1.6)$$

The number of the interacting photons at a given energy bin due to the Compton interaction , $NCOMP_i$, is given by:

$$NCOMP_i = \frac{(\sigma_{tot}/\rho)_i}{(\mu_{tot}/\rho)_i} N_i' \qquad (3.1.7)$$

The number due to pair production, NPP_i, is given by:

$$NPP_i = 2(N_i' - NCOMP_i) \qquad (3.1.8)$$

The above expression assumes that positrons can be treated like electrons. Additionally, the total attenuation coefficient takes into account pair production in the field of atomic electrons, "triplet production", however, the factor 2 does not take this completely into account. At the mean photon energy of the 15 MV beam (~4 MeV), the

triplet cross-section is about 3% of the pair production cross-section and the pair production cross-section is, in turn, only about 6% of the total attenuation cross-section (9). This results in slightly fewer charged particles with a slightly larger mean energy. The failure to take into account triplet production rigorously will not significantly affect the distribution of charged particles set in motion.

The kinetic energy available to a charged particle is always less than the photon energy, $h\nu$ ($h\nu \rightarrow$ xnrg(i)). The maximum energy of a Compton electron, T_{max}, ($T_{max} \rightarrow$ nrgmax), can be derived from the conservation of energy and momentum:

$$T_{max} = \frac{2\alpha_o}{2\alpha_o + 1} h\nu \qquad (3.1.9)$$

The electron may have any energy up to and including the energy, T_{max}. The difference between the photon energy and the kinetic energy of the recoil electron, T, is the energy of the scattered photon.

The available kinetic energy of the pair production interaction, T_A ($T_A \rightarrow$ nrgmax), must be shared between the electron and positron:

$$T_A = h\nu - 1.022 \text{ MeV} \qquad (3.1.10)$$

where 1.022 MeV represents the combined rest mass of the electron and positron.

The available kinetic energy is divided evenly into

20 bins. The kinetic energy dependent part of the differential cross-section with respect to kinetic energy is calculated at each of the 20 kinetic energy bins. The kinetic energy differential cross-section for the Compton effect $d\sigma/dT$ is given by the Klein-Nishina equation (see Equations 1.2.5 and 1.2.6).

The absolute differential cross-section is not calculated because it is not needed. The number of photons interacting by the Compton effect is known (see Eqn. 3.1.7). The relative number interacting at each available kinetic energy bin is determined by normalizing each cross-section factor, $C(h\nu,T_i)$, to the sum, $\Sigma_i C(h\nu,T_i)$, where the sum is carried out over all 20 available kinetic energy bins.

The differential cross-section for the pair production interaction , $d\pi/dT$, is given by Equations 1.2.7, 1.2.8 and 1.2.9. When considering the Compton interaction calculation, the kinetic energy dependent part of the differential cross-section, $P(h\nu,T)$, needs to be calculated. The sum, $\Sigma_i P(h\nu,T_i)$, is used to normalize the cross-section so that the appropriate number of electrons is set in motion at each energy, T_i.

The initial zenith direction of the Compton recoil electron, with respect to the primary photon direction, θ, is given by Equation 1.2.4. If Equations 1.2.3 and 1.2.4 are combined with Equation 3.1.9, the Compton

electron, with respect to the primary photon direction, θ, is given by Equation 1.2.4. If Equations 1.2.3 and 1.2.4 are combined with Equation 3.1.9, the Compton electron recoil angle, θ, can be determined:

$$\theta = \arctan\left(\frac{1}{1+\alpha_o}\,\frac{\sqrt{(T_{max}-T)(2\alpha_o+1)}}{\sqrt{T}}\right) \qquad (3.1.11)$$

An element of the energy-angle distribution array is incremented by an amount corresponding to the number of electrons set in motion at that kinetic energy and zenith angle:

$$S_{k\ell} = S_{k\ell} + NCOMP_p \frac{C(h\nu,T_i)}{\sum_i C(h\nu,T_i)} \qquad (3.1.12)$$

where $S_{k\ell}$ ($S_{k\ell}$ + SPECTR(k,ℓ)) is the energy-angle distribution array

k is the energy bin number

ℓ is the angle bin number

The available kinetic energy bins, represented by i for the calculation of the number of interactions at each available energy, is not the same as the energy-angle distribution kinetic energy bin, represented by k, in the above expression. There are 90 energy bins for the energy-angle distribution array spaced evenly between 0.0 and 18.0 MeV. Each energy bin of the energy-angle distribution is 0.2 MeV wide. Therefore, if the primary photon energy is low, many available kinetic energy bins may be mapped into one energy bin of the energy-angle distribution array.

There are 36 angle bins, represented by ℓ, in

Equation 3.1.12 to cover any zenith angle between 0 and 180^{o}. The 36 bins are distributed uniformly so that each bin is 5^{o} wide. It is assumed that the initial zenith angle for the bin equals the center of the bin. Therefore, the possible initial zenith angles are (2.5^{o}, 7.5^{o}, 12.5^{o}... 177.5^{o}). The maximum zenith angle for an electron produced by a Compton photon interaction is 90^{o}, however, there is a small possibility of a charged particle having an angle greater than 90^{o} when produced by the pair production effect.

The root mean square zenith angle, $\langle\phi^2\rangle^{\frac{1}{2}}$, between the trajectory of a charged particle and that of the primary photon is given by Equation 1.2.11. It is assumed that the distribution is Gaussian (5).

The zenith scattering angle is chosen by the direct or inversion method of random sampling. The cumulative probability, P(t), associated with a random variable, T, is:

$$P(t) = \text{Probability } (T<t) \qquad (3.1.13)$$

If P(t) is normalized, then $0<P(t)<1$. By generating a random number, R, such that $0<R<1$, and identifying R with P(t), a random sample, T, may be obtained from the distribution, P(t), by inversion (49). The cumulative probability for a particle having a zenith angle, ϕ ($\phi \rightarrow g$), when the root mean square angle is $\langle\phi^2\rangle^{\frac{1}{2}}$, is given by:

$$P(t) = \text{erf}(t) = \frac{1}{2\pi}\int e^{-t^{-2}/2}dt \qquad (3.1.14)$$

where $t = \phi/\langle\phi^2\rangle^{\frac{1}{2}}$

A numerical method was chosen to invert the above expression. P(t) was generated for values of t between 0 and 3.0. The value of t as a function of P(t) is listed in the file, Gaus.Dat. A random number, R, is chosen and is identified with P(t). A value, t, corresponding to P(t) is obtained from a look-up table (see Figure 68).

After the charged particles have been set in motion by photons from all the photon bins, the energy-angle distribution is passed back to the main program of Buildup3. The angular distribution is shown in Figure 72 for a 15 MV beam interacting in a slab 0.1 cm thick. The mean charged particle energy (in MeV) is indicated as the numbers in the bins. The characteristic bilobal forward peaked distribution is evident. The forward directed charged particles have a much higher energy than the charged particles set in motion at larger angles. There are very few electrons set in motion at angles greater than 60° from the initial photon direction.

3.1.4 The Monte Carlo Program

Monte Carlo methods are applied to the solution of physical problems when the microscopic behaviour is better understood than the macroscopic behaviour or the geometry of the problem does not lend itself to a closed analytic solution. The process to be studied must have some intrinsic random nature. In the case of charged particle interactions with matter, the slowing down and

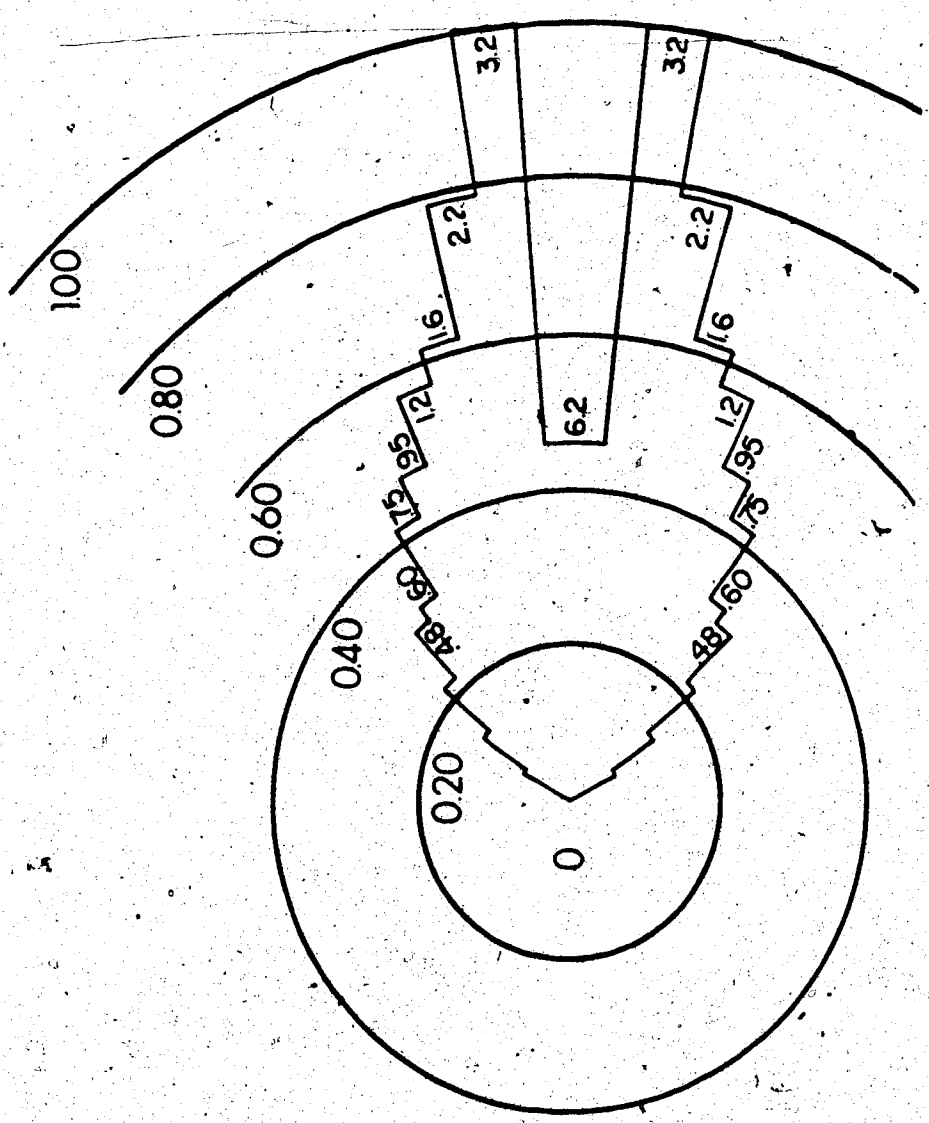

Figure 72. The angular distribution of charged particles interacting in a 0.1 cm slab at 15 MV. The mean charged particle energy (in MeV) is indicated by the numbers in the histogram. Each angle bin is 5^{o} wide.

the scattering direction is microscopically indeterminate.

The number of Coulomb interactions resulting in ionization and excitation of water molecules per centimeter of path length is as high as 10^5. It would be impractical to model every interaction. The total path length of an electron (the distance required to come to rest in the phantom) is approximated by a number of sub-path lengths or steps. Each step, therefore, is part of a random walk. At the end of each step the combined effects of many collisions are taken into account. The amount of energy lost and, therefore, the dose deposited in the phantom, the amount of scattering and the position of the electron is evaluated for each step. The electron is considered to have stopped when its kinetic energy falls below the cut-off energy which was chosen to be 0.2 MeV.* The remaining energy is deposited in the slab where this occurs.

This Monte Carlo algorithm employs two major approximations: the continuous slowing down approximation, C.S.D.A., and the Gaussian scattering approximation. In the C.S.D.A., fluctuations of energy loss are disregarded and the particle is taken to be a deterministic function of the path length travelled. In the Gaussian approximation, the net angular multiple scattering deflections are the result of the combined effect of many small individual deflections. This leads to a Gaussian distribution of the zenith scattering angle.

* The mean range at this energy is much less than the slab thickness of 0.1 cm.

The flow chart of the Monte Carlo algorithm is illustrated in Figure 73. The number of histories followed at a given energy and angle depends on the value of the energy-angle distribution as calculated by the subroutine, Impulse. The value of the energy-angle distribution, a floating-point array, is converted to an integer. This integer is decremented by one for each history followed.

The initial position and the cosine and sine of the zenith and azimuthal angles of the charged particles are determined. It is assumed that all the charged particles generated in a slab are set in motion half way through the slab. The initial sine and cosine of the zenith scattering angle are determined by the angle bin number that specifies the energy-angle distribution array. The initial azimuthal angle is randomly distributed through 2π radians.

A history can end only if one of two conditions are met; the energy of the particle falls below 0.2 MeV or the particle leaves the phantom. The first condition is top tested in the Monte Carlo step loop (see Figure 73). The test to see if the particle has left the phantom is bottom tested. Since the phantom is semi-infinite in extent, a particle can only leave the phantom from the top surface.

The energy lost in each step is a constant fraction of the energy at the beginning of the step. Such an

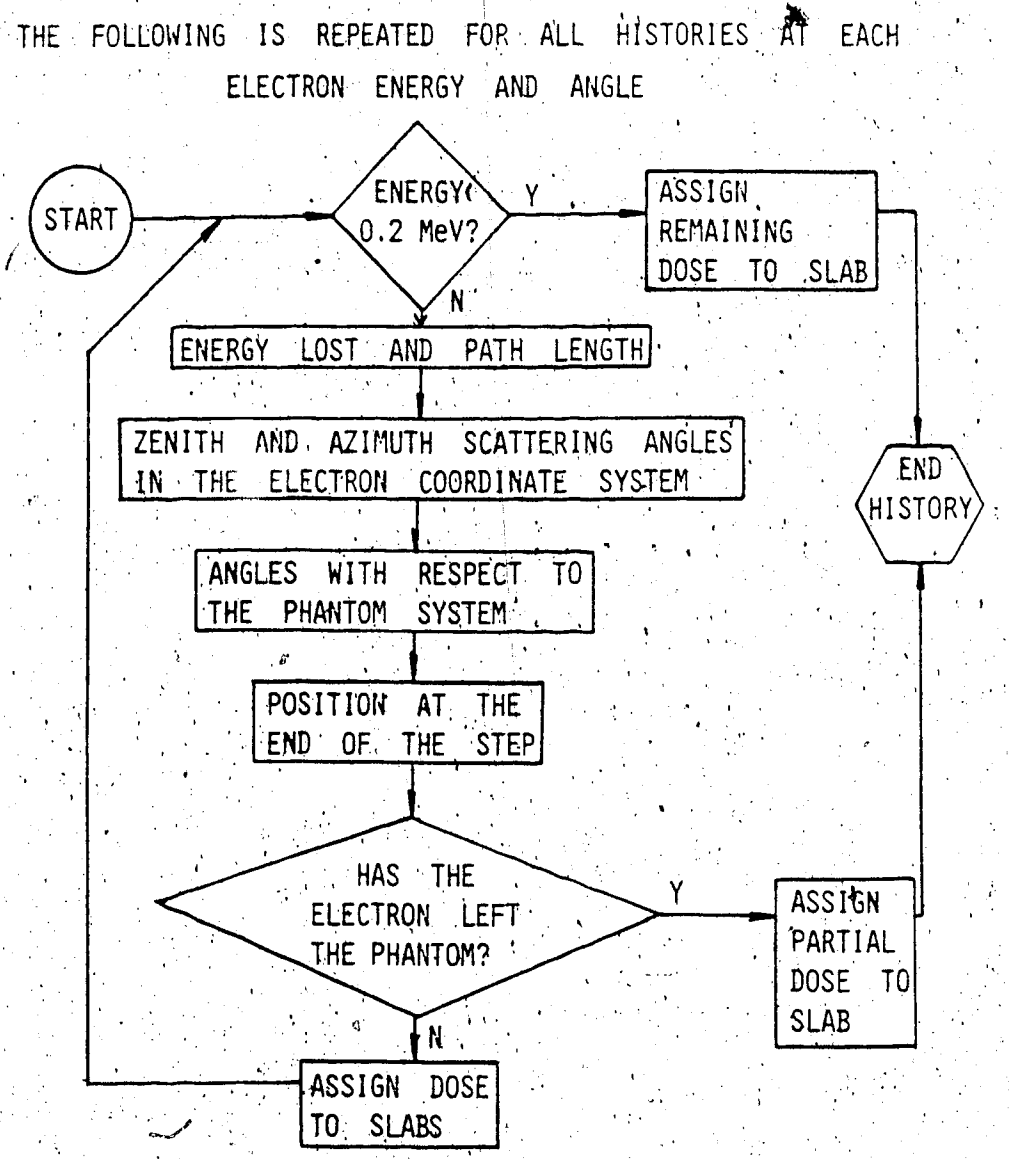

Figure 73. A flow chart for the Monte Carlo section of the main program of Buildup3.For.

energy loss criteria is called logarithmic spacing because the length of the step, ΔS, decreases logarithmically as a function of path length traversed through the phantom. Logarithmic spacing has the advantage that the average zenith angle changes little from step to step. The smaller the fraction of energy lost per step the greater the number of steps required to model the history. This will result in a more accurate depiction of the history, but it will require more time to execute. A fractional energy loss factor of 0.1 was chosen as a compromise between the contradictory demands of accuracy and speed:

$$(\Delta T)_j = 0.1\ T_j \qquad (3.1.15)$$

where $(\Delta T)_j$ is the particle kinetic energy lost in the j^{th} step ($(\Delta T)_j \rightarrow$ EP)

T_j is the particle kinetic energy at the beginning of the step ($T_j \rightarrow$ E)

The number of steps required to complete a history is:

$$\frac{\text{Number of Steps}}{\text{History}} = 15.3 + \frac{\ell n(T_o)}{0.105} \qquad (3.1.16)$$

where T_o ($T_o \rightarrow$ E0) is the initial energy of the particle (Note: the number of steps/history is an integer. The result of the previous expression must be rounded up to the nearest integer.) Therefore, a particle with an initial energy of 1.0 MeV will require 16 steps and a

particle with T_o = 10 MeV will require 38 steps to complete its history.

The path length traversed in a step is given by:

$$(\Delta S)_j = \frac{(\Delta T)_j}{\left[\frac{dT}{dS}\right]_{T_j - ((\Delta T)_j)/2}} \qquad (3.1.17)$$

where $(\Delta S)_j$ is the path length

$\left[\frac{dT}{dS}\right]_{T_j - ((\Delta T)_j)/2}$ is the stopping power for the particle energy half way through the step

The zenith scattering angle is the cumulative amount of scatter that occurs in a step so the angle is measured with respect to the direction of the particle at the beginning of the step.

The scattering angle is obtained by:

$$\phi = \langle \phi^2 \rangle^{\frac{1}{2}} t \qquad (3.1.18)$$

where t is determined from random sampling (see Figure 68, Sections 3.1.2 and 3.1.3 for more details).

The azimuthal angle of scattering in the step, with respect to the direction at the beginning of the step, is chosen at random to lie in any 2π direction.

The subroutine, Geom, transforms the zenith and azimuthal angle in the coordinate system travelling with the particle to the coordinate system "attached" to the phantom. The algorithm will be discussed in more detail later (see Section 3.1.5).

The distance travelled in the z, or depth direction, (the direction perpendicular to the phantom face with the sense directed into the phantom) in the step is given by:

$$z = (\Delta S)\cos(\Phi) \qquad (3.1.19)$$

where Φ ($\cos\Phi \rightarrow$ cal) is the zenith angle in the phantom coordinate system

The depth traversed in the step is added to the cumulative depth, z_s, (the phantom surface is $z_s = 0.0$).

A test is made to see if the particle has left the phantom. The particle has left the phantom if the cumulative depth is negative. If the particle has not left the phantom, the dose it deposited in slabs through which it traversed are assigned. If it did leave the phantom, the dose in the slabs before it left are deposited. The subroutine, Assign, assigns the absorbed dose to the phantom slabs (see Section 3.1.6 on Assign). If the particle did not leave the phantom, the control of the calculation is passed to the test to see if the energy is above the cut-off energy. If it did leave, control is passed to the statement controlling the number of histories at each initial energy and angle. If the particle does come to the end of its range its remaining energy is assigned to the slab it last entered.

After all the histories are followed, for all charged particles' energies and angles generated in all the slabs,

the dose is deposited as a function of depth and then normalized to the maximum dose received. The normalized dose as a function of depth is printed as the output of the calculation.

The Monte Carlo program was run, without the charged particle set in motion part of the program (in other words, withouth Subroutine Impulse) with a set of initially monoenergetic, monodirectional electrons. The energy of the electrons was varied between 2.0 MeV and 10.0 MeV. The penetration profile obtained was compared with results of a well-established analytic technique due to Spencer using the moments method (50). Spencer's method also employed continuous slowing down. This comparison is made in Figure 74.

3.1.5 Scattering Angle Transformation

The subroutine, Geom, transforms scattering angles from the coordinate system travelling with the particle to the coordinate system fixed to the phantom (see Figure 75). The direction with respect to the particle reference system in polar coordinates is specified by a zenith angle, ϕ, ($\phi \rightarrow g$), and an azimuthal angle, ψ, ($\psi \rightarrow r$).

Directions in the phantom reference system are also in polar coordinates. The zenith direction in the phantom system is α and the azimuthal angle is β. It is useful to specify the direction sine and cosines. The direction of the particle in the phantom system at the beginning of the step is specified by cos α (cos $\alpha \rightarrow$ oldcal) or sin α (sin $\alpha \rightarrow$ oldsal) and cos β (cos $\beta \rightarrow$ oldcbeta) or

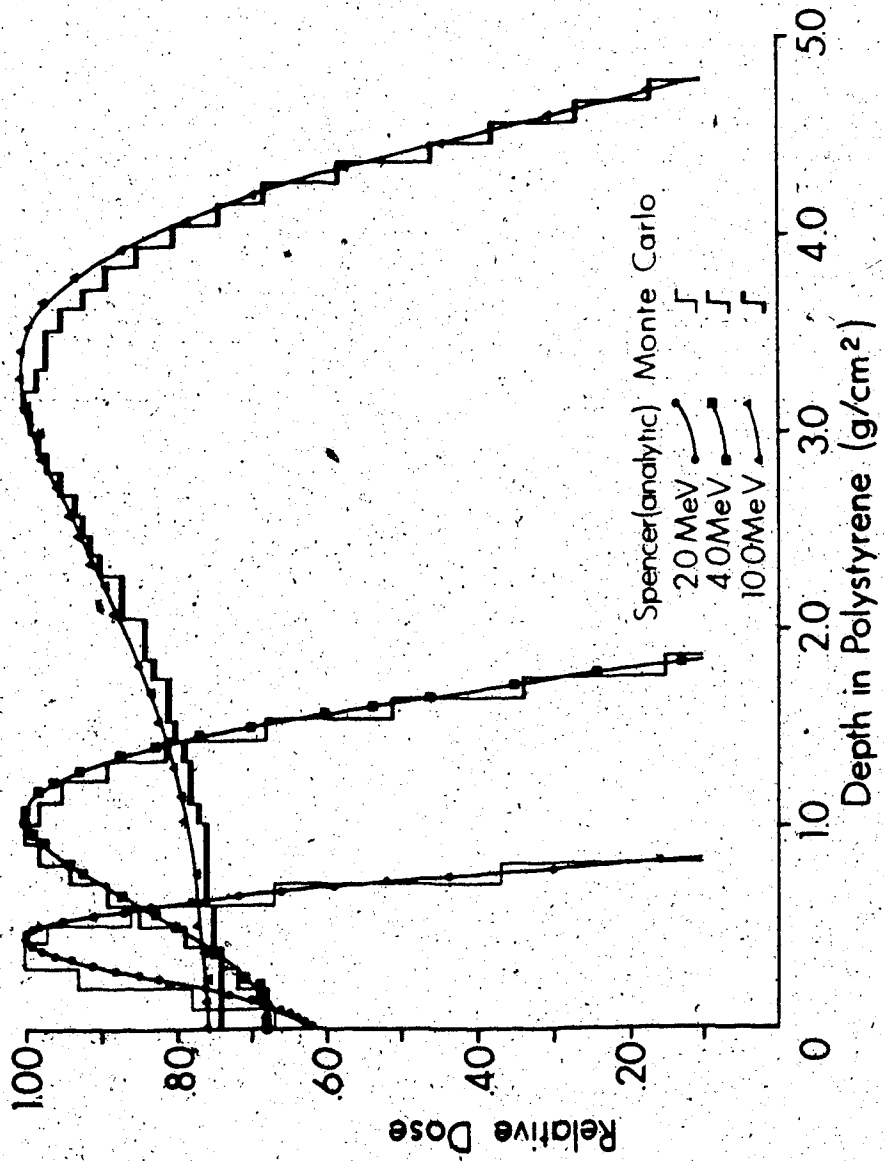

Figure 74. Comparison between the Monte Carlo program of Buildup3. For and Spencer's analytic formalism to predict the dose deposited by various monoenergetic electrons in water.

sin β (sin β → oldsbeta). The direction of the particle in the phantom system at the end of the step (after scattering has taken place) is given by cos α′ (cos α′ → cal) or sin α′ (sin α′ → sal) and cos β′ (cos β′ → cbeta) or sin β′ (sin β′ → sbeta). The relationship between the directions in the particle and the phantom system are shown in Figure 75.

To determine the position of the charged particle inside the phantom, a transformation must be made to the coordinate system fixed with respect to the phantom. The transformation is given by (51)*:

$$\cos(\alpha') = \sin(\phi)\cos(\psi)\sin(\alpha) + \cos(\phi)\cos(\alpha) \qquad (3.1.20)$$

$$\sin(\alpha') = \sqrt{1 - \cos^2(\alpha')} \qquad (3.1.21)$$

$$\sin(\beta'-\beta) = \frac{\sin(\phi)\sin(\psi)}{\sin(\alpha')} \qquad (3.1.22)$$

$$\cos(\beta'-\beta) = \frac{\cos(\phi) - \cos(\alpha)\cos(\alpha')}{\sin(\alpha)\sin(\alpha')} \qquad (3.1.23)$$

β′ can be found by taking the inverse sin or cos of the above expressions but it is more convenient to define sin(β′) and cos(β′) as:

$$\sin(\beta') = \sin(\beta'-\beta)\cos\beta + \cos(\beta'-\beta)\sin\beta \qquad (3.1.24)$$

$$\cos(\beta') = \cos(\beta'-\beta)\cos\beta - \sin(\beta'-\beta)\sin\beta \qquad (3.1.25)$$

Having obtained sinα′, cosα′, sinβ′ and cosβ′, these values are passed back to the main program.

* The error in the formulation of Equation 3.1.22 in Bruce and Johns (51) has been corrected.

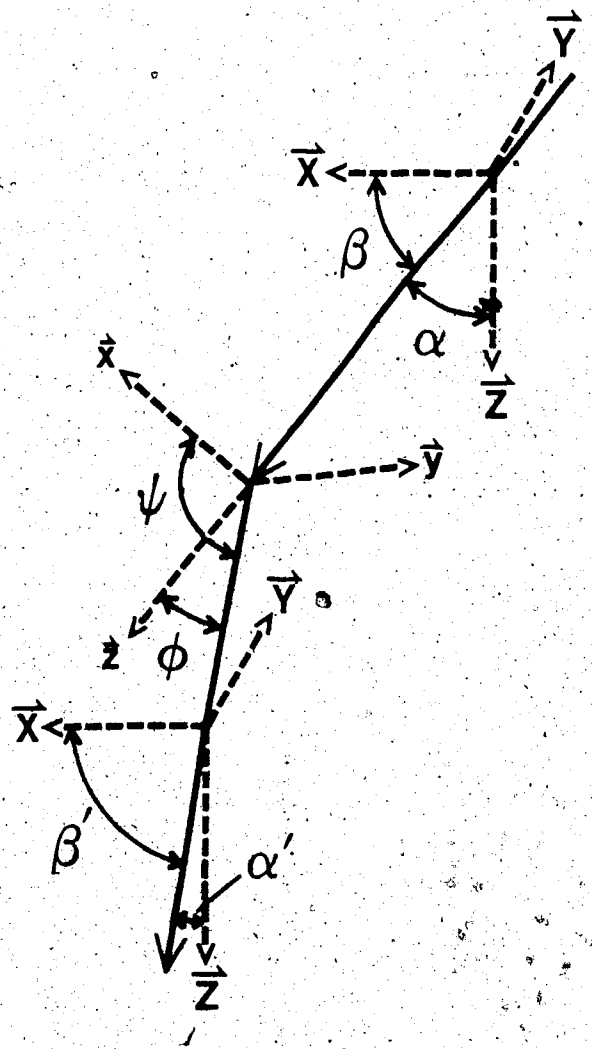

Figure 75. Relationship between scattering angles in the particle and phantom coordinate system.

3.1.6 Assigning Dose

When called, the subroutine, Assign, deposits the required dose in the slab or slabs traversed between the beginning and end of the step. Dose is assigned for each of the following three situations: The particle energy is greater than or equal to the step cut-off energy (0.2 MeV), the particle energy is less than the step cut-off energy at the end of the step or the particle has left the phantom during the step.

The simplest possible case and the most often occurring case is when the particle does not leave the slab it was in at the beginning of the step. The total dose received by the slab, up to and including the step, Dose'(k), (k → kay), should be given by:

$$\text{Dose}'(k) = \text{Dose}(k) + \frac{(\Delta T)_j}{\rho V_{slab}} \qquad (3.1.26)$$

where Dose(k) is the total dose received by the slab up to and not including the step. Since the phantom is semi-infinite, the mass of the slab, ρV_{slab}, is infinite! This difficulty is eliminated by redefining Dose'(k) as:

$$\text{Dose}'(k) = \text{Dose}(k) + (\Delta T)_j \qquad (3.1.27)$$

Now Dose'(k) is not equal to the absolute dose. However, since the slabs have the same thickness, Dose'(k) is directly proportional to the absolute dose. The final output of the program is the dose at each slab normalized

to the maximum dose received by any slab in the phantom, so absolute dose is not required.

If the particle traverses more than one slab during a step, the energy lost is assigned to the slabs in proportion to the fraction of the path length spent in each slab.*

If the particle traversed completely through one or more slabs, the dose deposited in those slabs will be:

$$\text{Dose}'(k) = \text{Dose}(k) + \frac{(\Delta T)_j}{z_j/0.1 \text{ cm}} \qquad (3.1.28)$$

where 0.1 cm is the slab thickness. The denominator in the last term represents the number (floating point) of slabs traversed.

If the particle traverses only part of two slabs the fraction of the total dose deposited, Dose Fraction, (Dose Fraction → Dosefrac), in one of the slabs due to a step is calculated. The remaining energy is deposited in the other slab.

Similar procedures are followed if the particle

* The situation for which this will occur is at the top of the phantom and the particle has a large initial kinetic energy. For example, the distance travelled by a 15 MeV electron in its first step $(\Delta S)_1$ is given by:

$$(\Delta S)_1 = \frac{1.5 \text{ MeV}}{2.306 \text{ MeV/cm}} = 0.65 \text{ cm}.$$

Therefore, the dose imparted to 7 slabs will have to be calculated. The mean square angle of scattering will be:

$$\langle \phi^2 \rangle^{\frac{1}{2}} = \sqrt{3.95 \times 10^{-2} \text{ rad}^2/\text{cm})(0.65 \text{ cm})} = .16 \text{ rad}$$

which is about 9^o.

leaves the phantom, except that dose is not assigned for that portion of the path outside the phantom.

3.1.7 Results

The program was run to model 6 MV and 15 MV accelerators under narrow beam (or small field) and broad (or large field) beam conditions. The program was designed to calculate the energy-angle spectrum of charged particles set in motion in thin phantom slabs. The Monte Carlo part of the program follows the charged particles through the rest of the phantom. This procedure is common to both the small field and large field approximations. Figures 76 and 77 illustrate the dose delivered to a phantom due to charged particles set in motion in a 0.1 cm slab of water at the surface of the phantom by a 6 MV and 15 MV photon beam, respectively. To a good approximation, the dose due to charged particles set in motion in a thin slab attenuates exponentially with distance from the slab. The charged particle energy absorption coefficient, $\mu_e^{\pm}$, can be found by finding the slope of the line of a graph of $\ln(1.0/D(x))$ versus depth where $D(x)$ is the relative dose at a depth, x (the maximum dose = 1.0). The charged particle energy absorption coefficient is 3.1 cm^{-1} for 6 MV and 1.15 cm^{-1} for 15 MV photon beams.

In the broad beam, or large field approximation, the scattered photons generated in the phantom are not

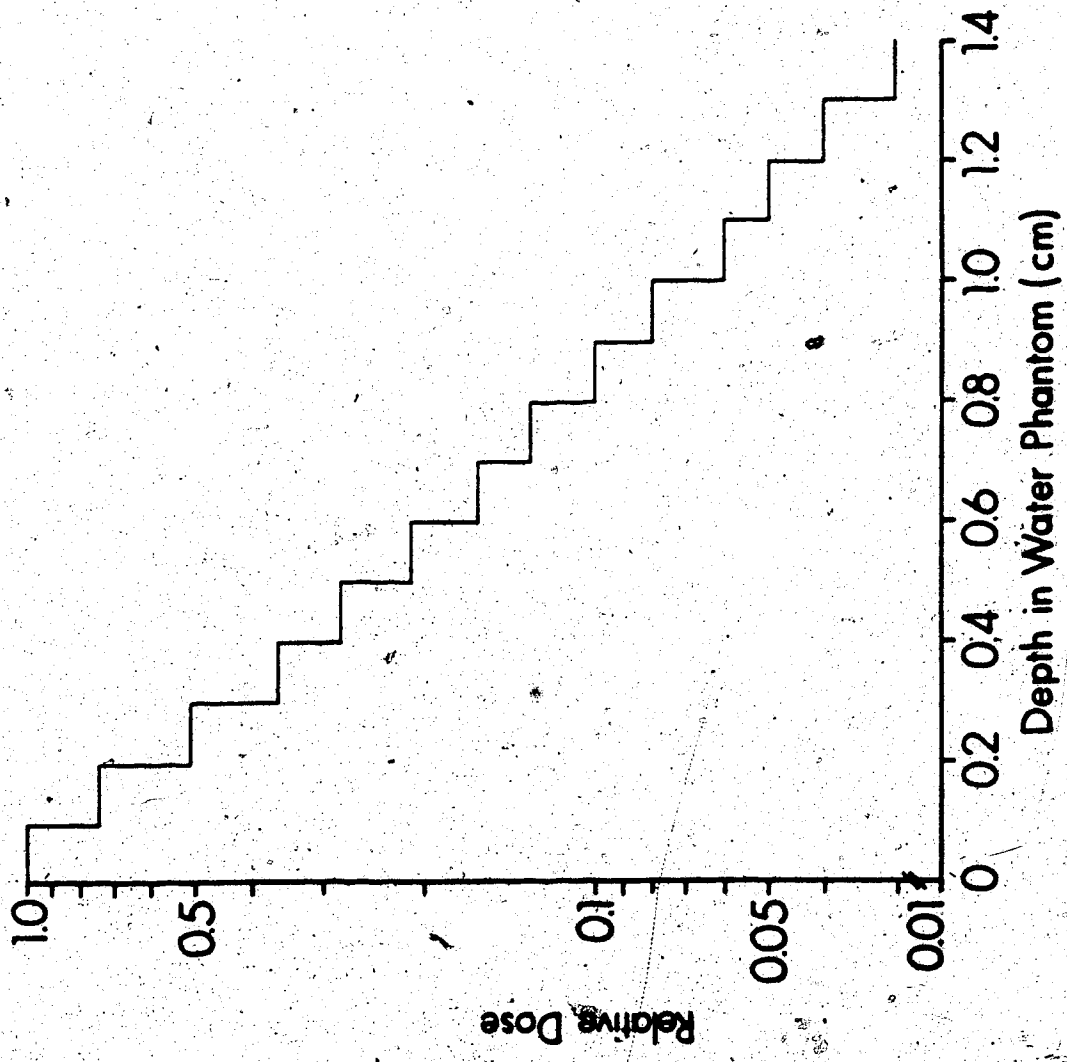

Figure 76. Distribution of dose in a semi-infinite water phantom due to electrons set in motion in the top 0.1 cm slab by a 6 MV photon beam.

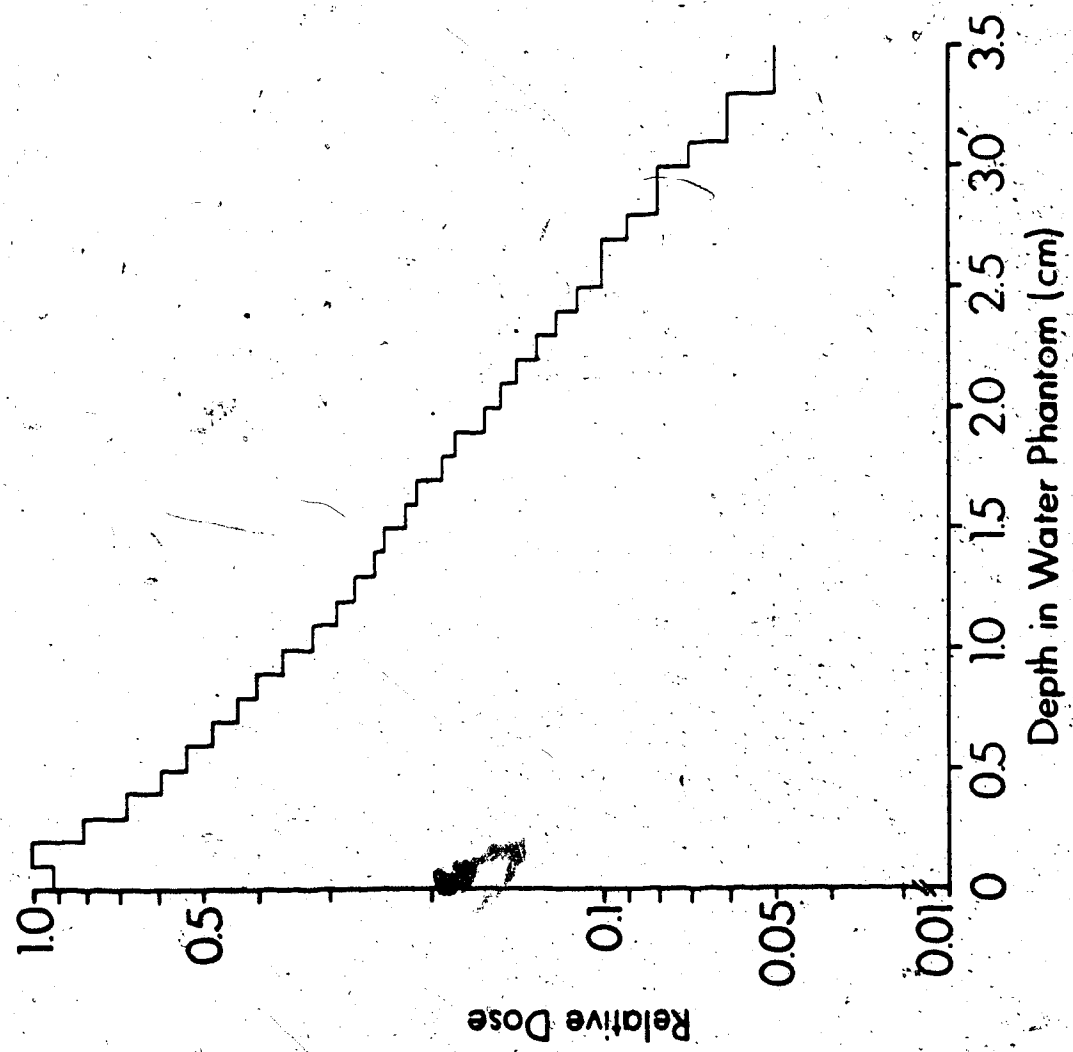

Figure 77. Distribution of dose in a semi-infinite water phantom due to electrons set in motion in the top 0.1 cm slab by a 15 MV photon beam.

lost from the beam. Scattered photons have a spectrum that has a similar shape, but an effective nominal energy lower than the primary beam (36). It was also seen in Section 2.13 that the depth of d_{max} of the scattered radiation is less than that of the primary radiation. The primary photon spectrum tends to harden as it penetrates into the phantom. Lower energy scattered photons tend to replenish the low energy photons lost from the spectrum due to hardening. Large field geometry is approximated by assuming that the primary photon spectrum is unaltered as the beam penetrates the phantom.

With the primary photon spectrum remaining the same as a function of depth in the phantom, the penetration characteristics of the charged particles set in motion remain the same. The number of charged particles set in motion at any depth decreases exponentially with depth. The appropriate attenuation coefficient is the mean energy absorption coefficient which is an energy fluence weighted average normalized to the total energy fluence of the beam. Mathematically, the mean energy absorption coefficient is given by:

$$\bar{\mu}_{en} = \frac{\sum_i F_i (h\nu)_i (\mu_{en})_i}{\sum_i F_i (h\nu)_i} \qquad (3.1.29)$$

Equation 3.1.29 has the same form as Equation 1.5.10. The mean attenuation coefficient for the 6 MV spectrum

is 0.029 cm^{-1} and 0.021 cm^{-1} for the 15 MV spectrum.

The dose deposited by the charged particles set in motion attenuates exponentially in the phantom and the primary photon beam attenuates exponentially. The assumption, therefore, that large field geometry can be modelled by keeping the primary spectrum constant with depth is identical to the build-up model presented in Section 1.5.

The method of computing the dose in the build-up region for broad beam geometry is to attenuate the dose due to charged particles set in motion in a thin slab at a depth, x, by a factor $e^{-\bar{\mu}_{en}x}$. This is done for 100 thin slabs (each 0.1 cm thick). The dose received at any point in the phantom is a sum of the dose reaching the point from the charged particles set in motion from all the slabs above the point.

This procedure is done by the program, Addose.For. The input for this program is the thin slab charged particle set in motion dose penetration profiles shown in Figures 76 and 77. The depth of maximum dose, d_{max}, as predicted by the large field model computed by Buildup3.For and Addose.For, is the same as the d_{max} point predicted by Equation 1.5.11. The output for Addose.For is normalized by dividing the dose by the dose at d_{max}. The result is the broad beam TMR curve in the build-up region. Appendix 8 contains the listing and

documentation for Addose.For.

Small field geometry assumes that all the scattered photons produced by the beam in the phantom do not interact again. This is modelled by hardening the beam. Every photon that interacts in the phantom is removed from the number spectrum. This is accomplished by the subroutine of Buildup3.For called Impulse (see Equation 3.1.16). Small field geometry requires more computer time to model than large field geometry because the charged particle set in motion energy-angle distribution has to be recalculated for each slab. More importantly, each charged particle set in motion in the slab has to be followed through the rest of the phantom. The relative dose was calculated to a depth of 10 cm so the small beam geometry requires approximately 100 times (10 cm/0.1 cm) as much time to model as the large beam geometry.

The build-up curves of the small and large field, together with the experimental results from Section 2.11 are shown in Figures 78 and 79 for 6 MV and 15 MV photon beams, respectively. As was found experimentally, there is little difference between small and large field geometries in the build-up region. There is good agreement between the computer modelled and experimental build-up curves.

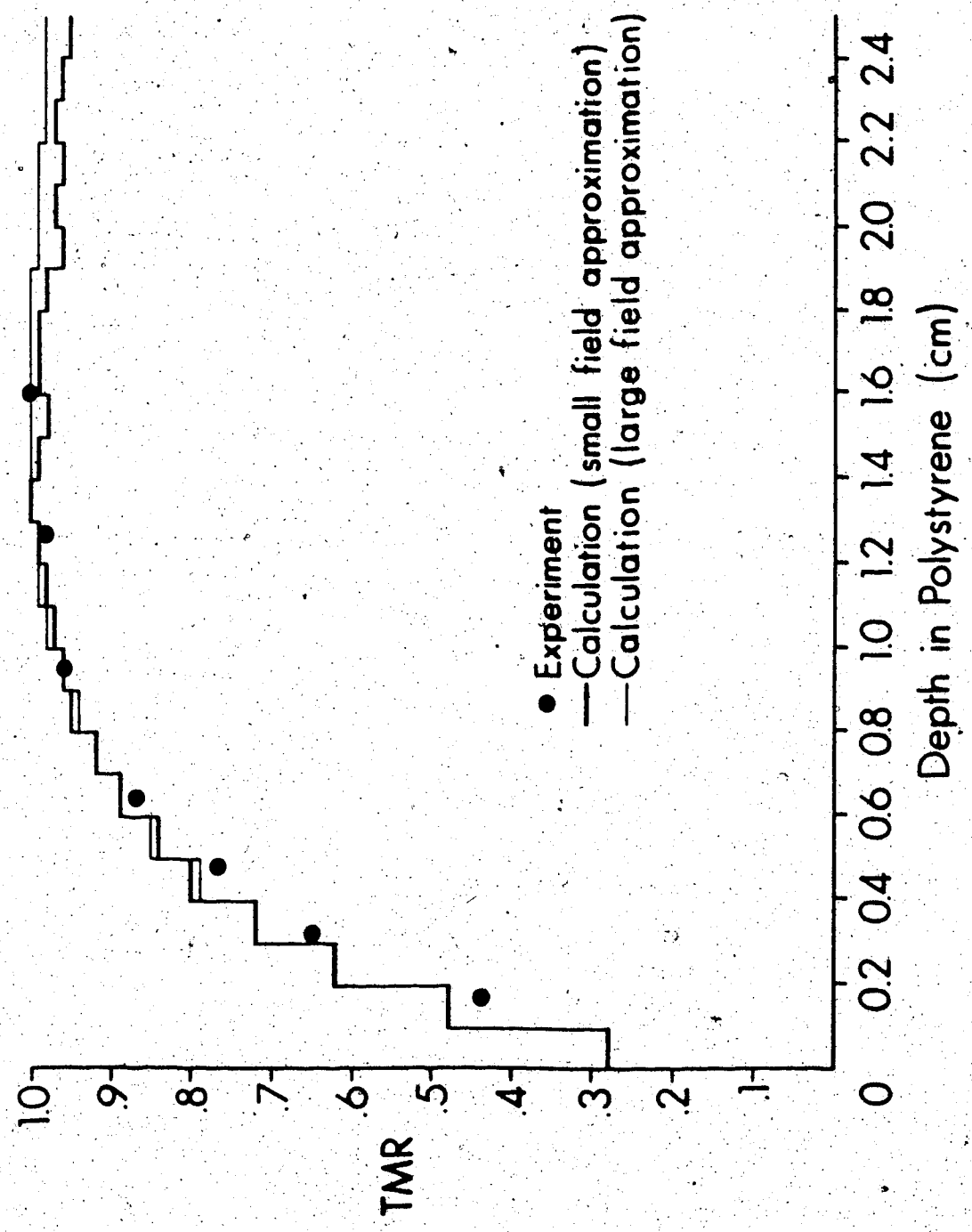

Figure 78. Comparison between experiment and computer modelling of the phantom generated TMR curve at 6 MV.

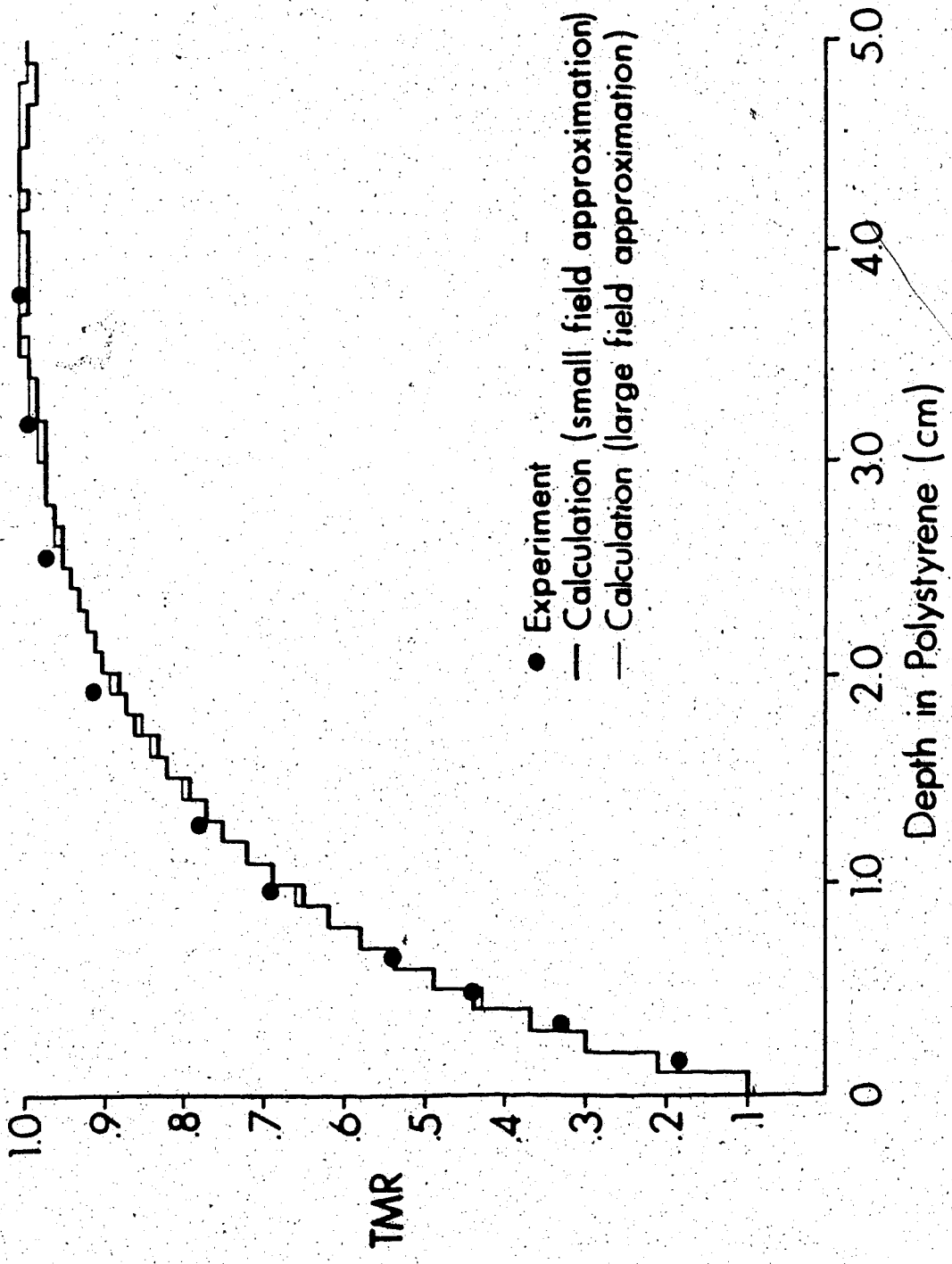

Figure 79. Comparison between experiment and computer modelling of the phantom generated TMR curve at 15 MV.

3.2 Nature and Source of Contamination

The definition of contamination stated in the introduction implies that radiation reaching the phantom, other than primary radiation*, is to be considered as contamination. Primary radiation is the photon component of the beam that is directed away from the source.

The utility of this definition of contamination is that it allows one to determine the dose deposited by primary photons in a phantom. This is called the phantom generated dose. The phantom generated dose is deposited by charged particles set in motion by primary photons and scattered photons produced in the phantom. Therefore, contamination dose is exogenous whereas the phantom generated dose is endogenous to the phantom. Scatter, measured by an increase in dose with increasing field size using a full phantom in the build-up region, cannot be confused with contamination generated outside the phantom. Changes in the phantom generated dose can only be due to changes in the phantom size, density or configuration. A modification of the phantom in these respects will not affect the nature of the contamination component (although it will affect the interaction of the contamination component in the phantom).

The TMR build-up curves in Section 2.1 demonstrate a field size dependence, especially at or near the phantom surface, greater than can be expected from lateral scattering of photons and electrons generated in the phantom.

Adding small additional thicknesses of accessories increased the TMR in the build-up region. As the thickness of accessory increases,

* The dose due to charged particles set in motion by neutrons is not considered.

the amount of contamination produced by the accessory increases. However, contamination produced at shallow depths within the accessory is shielded by deeper layers of the accessory. At an equivalent thickness less than 3.2 cm of Lucite, there is a balance between production and absorption of contamination.

The surface dose displays the characteristics of electron contamination. High atomic number "filters" can reduce the surface normalized dose due to an accessory when placed beneath the accessory. When placed above the accessory the high atomic number material did not alter the surface normalized dose. The number of interactions produced by the high Z material above and below the accessory are approximately the same. The mass stopping power is relatively independent of atomic number and, indeed, the mass stopping power of Lucite, for example, is slightly higher than lead (5). Therefore, the only possible difference between the configurations of high Z material above and below Lucite resulting in a reduced surface normalized dose is the difference between the amount of scattering of contamination electrons outside the beam. This is not surprising considering that the scattering power of lead is nearly an order of magnitude higher than water* (see Appendix 4). Therefore, nearly as many contamination electrons emerge from the bottom surface of the high Z "filter" as emerge from the bottom surface of the accessory, but fewer of the electrons are forward directed. Therefore, a high atomic number material placed in the beam should be called an electron scatterer rather than an electron filter.

The distance from the source distribution and lateral distribution

* The scattering power of water and Lucite are within 10% at energies less than 15 MeV (5).

of the surface dose for large open fields at 15 MV are typical of electron distributions. The distance distribution of the surface dose falls off as $1/r^2$ from a point 12 cm below the target which corresponds to the position of the field flattening filter. The field flattening filter has, at its thickest point, 5.4 cm of stainless steel in the beam. It is the only component present in an open field which has a sufficient thickness to produce a maximum fluence of contamination electrons*, so it is likely to contribute to the dose due to contaminant electrons.

The lateral surface distribution is Gaussian. This indicates that the surface dose is due to electrons and indicates that the electrons could have been produced from a small source. Therefore, the surface dose at 15 MV for large fields behaves in accordance with Equation 1.3.4.

The situation at 6 MV is quite different. The assumption that the surface dose decays as $1/r^2$ at large field sizes is not valid.** Additionally, the lateral distribution is not Gaussian. The surface dose inside the field is larger than can be expected from a normal distribution and the surface dose outside the field is smaller. Both of these are contraindications that localized source is responsible for most of the electron contamination for large fields at 6 MV.

The source of electron contamination at small fields is better understood due to magnetic separation of the electrons produced by

* A Lucite accessory with a thickness greater than 3.2 cm will not contribute to greater contamination. The equivalent thickness of steel is about 40 cm.

** A $1/r^2$ dose decay with distance from an apparent source of contamination is necessary although not a sufficient condition for identifying the source of contamination unequivocally.

two regions of the beam. The surface normalized dose was measured for various conditions of field size (the largest field size was 10 cm x 10 cm) and source to probe distance inside the field with the magnet in place and not in place at the accessory holder position. Air contributes most of the surface dose at 6 MV and 15 MV for these field sizes. At 15 MV, however, the increase in the dose, as a function of field width due to electron contamination produced between the target and magnet, suggests that at a field size of about 15 cm x 15 cm for a source to probe distance of 100 cm, this contribution will be greater than the contribution due to air.* At 15 MV, when the SPD=100 cm for a field size of 30 cm x 30 cm, (which was the condition of the measurement of the distance distribution in Section 2.4), the contribution due to air will be a minority component. Therefore, the results obtained at small field sizes does not contradict the results at large field sizes at 15 MV. At 6 MV the surface dose for large field sizes is mostly due to air contamination (with the possible exception of small source to probe distances). This is why the source of electron contamination could not be localized to a small region for the 6 MV large field beam in Sections 2.4 and 2.5.

Qualititively, the SPD dependence of the contamination components are easy to explain. The greater the thickness of air intervening between the magnet, the greater the dose due to contamination produced in air. Conversely, increasing the distance between the region of production of contamination between the target and magnet will result in a smaller normalized dose.

* Based on a linear extrapolation of the increase in dose between a field width of 7 cm and 10 cm.

Plotting graphs of the square root of the reading due to contamination produced between target and magnet will determine the position of the source of contamination if the source is confined to a small region. At small fields at both 6 MV and 15 MV with the cross-hair tray in place, the source appears to be the cross-hair tray. At 15 MV, with the cross-hair tray not in place, the source appears to be the collimators. This agrees with the observation that the surface dose appears to be produced by the field flattening filter at 15 MV for large field sizes. At small field sizes the contamination produced by the field flattening filter is largely blocked by the collimators.

A general conclusion can be hypothesized by these findings. Electron contamination measured at a point tends to be produced by mass close to that point. Contamination produced further away is stopped or scattered by mass lying close to the measuring point. Therefore, air is a significant contributor under most conditions. Accessories and the cross hair tray when present contribute. Collimators at small field sizes produce some contamination*. The field flattening filter can be the major source of electron contamination at large field sizes (therefore not blocked by the collimators) if the cross hair tray or accessories are not in the field.

All these possible sources of electron contamination result in a greater magnitude of electron contamination reaching the probe as a function of field size. A greater field size results in a greater interaction volume for air, accessory and cross hair tray sources. As the collimator jaws are opened a greater amount of contamination produced by the field flattening filter emerges through the collimator

* At small field sizes the perimeter of the collimator compared to the field area is much larger than the same ratio at large field sizes.

opening.

The key to the separation of the contamination from the phantom generated dose is to know the contribution of contamination to the dose at one point. Except for the photon backscatter* which can be independently measured, the surface dose is due to contamination electrons generated outside the phantom. Knowing the contamination contribution at the surface and the penetration characteristics of the contamination component, the phantom generated dose can be obtained by the subtraction of the dose due to contamination.

The same contamination penetration curve was used to determine the amount of contamination for each field width, SPD and accessory configuration. This assumes that different beam geometries or the presence of accessories in the field do not change the nature of the contamination. Justification for this assumption was provided at [illegible] MV by determining the contamination penetration curve at different [illegible]'s and accessory configurations. The contamination penetration characteristics were within 5% (see Table 3). The surface dose is usually less than 40% of the maximum dose so an uncertainty in the correct amount of contamination at the surface will be less than 2% of the maximum dose. At deeper depths the uncertainty will be even less.

The validity of the contamination curve at 15 MV was verified in a number of other ways. The shape of the contamination penetration curve is characteristic of mixed electron and photon contamination. The surface contamination is established as being due to electrons. These electrons must penetrate to some depth beneath the phantom.

* Some of the photon backscatter is due to scattered photon backscatter, but it need not be taken into account. The photon backscatter at most makes up about 20% of the electron contamination which usually makes up no more than 30% of the phantom generated dose, therefore, scattered photon backscatter will likely contribute less than 6% to photon backscatter. Photon backscatter is a small quantity so scattered photon backscatter is negligible.

The peak and rapid fall off at shallow depths are characteristic of electrons. The slow fall off at depths greater than 2 cm is characteristic of photons. Therefore, the contamination radiation appears to be a combination of an electron contribution primarily at shallow depths and photons contributing primarily at greater depths.

The derived contamination penetration curve, using the increase in dose in a limited phantom versus the increase in field width (greater than the phantom dimensions) at 15 MV, is similar in shape to the contamination curves measured outside the field. The difference in shape (see Figures 63 and 31) can be attributed to a difference between the relative amount of contamination electrons and photons present inside and outside the field boundary. Figure 27 demonstrated a Gaussian lateral distribution of the surface dose. Consequently, for a 30 cm x 30 cm field size there were about 45% fewer electrons present at 18 cm from the central axis as were present at the central axis. This largely accounts for the difference observed between Figures 31 and 63.

The most convincing evidence that the phantom generated build-up curves are correct is their agreement with computer modelling obtained independently (see Figure 79). The computer model also verifies that the phantom generated TMR curves are independent of field size.

The validity of subtracting the contamination component from the total build-up curve to yield the phantom generated build-up curve at 6 MV was tested as well. The contamination penetration had its maximum at the surface and decayed rapidly with depth at shallow depths (see Figure 64). The curve levelled off at deeper depths. This, as was found at 15 MV, is indicative of electrons contributing at shallow depths and scattered photons contributing at deeper depths. The contam-

ination curves derived inside the field (Figure 64) and measured outside the field (Figure 32) are in approximate agreement if the lateral surface dose distribution is taken into account. Approximately 60% fewer electrons are present 3 cm outside of a 30 cm x 30 cm, 6 MV field as compared to the central axis. This accounts for the difference in the shape of Figures 64 and 32. The computer model of the phantom generated dose as a function of depth agreed with the experimentally derived phantom generated dose build-up curve at 6 MV (see Figure 78).

The computer model established that the dose due to electrons set in motion in a thin phantom slab decays exponentially in the phantom as a function of depth from the slab. Therefore, Equations 1.5.8, 1.5.11 and 1.5.16 should be valid descriptions of the dose in the build-up region*.

Values of μ_{e^-} of 3.1 cm^{-1} and 1.15 cm^{-1} for the mean energy absorption coefficient of electrons set in motion by 6 MV and 15 MV photon beams, respectively, were found (see Section 3.1.7). The value of μ_γ was found from Equation 3.1.29 to be 0.029 cm^{-1} for 6 MV and 0.021 cm^{-1} for 15 MV photon beams.

The d_{max} predicted by Equation 1.5.11 is 1.5 cm for 6 MV and 3.6 cm for 15 MV, respectively. This compares with the experimentally determined d_{max} values (after the contamination component has been removed) of 1.6 cm for 6 MV and 3.5 cm for 15 MV.

Table 19 lists the TMR dose for 6 MV and 15 MV beams in the build-up region as predicted by Equation 1.5.16. This agrees well with the phantom generated build-up TMR dose. Therefore, the simple differential Equation 1.5.6 is physically acceptable and accurately predicts* the dose in the build-up region received by a homogeneous unit density phantom.

* The model fails to predict the surface dose due to backscattered photons.

Table 19 Tissue Maximum Ratios in the Build-Up Region as Predicted By Equation 1.5.16

Depth (cm)	6 MV TMR	15 MV TMR
0.00	0.000	0.000
0.16	0.408	0.181
0.32	0.654	0.331
0.48	0.802	0.455
0.64	0.890	0.557
0.95	0.971	0.708
1.27	0.996	0.814
1.91	0.995	0.932
2.54	-	0.982
3.18	-	0.998
3.81	-	1.000

region received by a homogeneous unit density phantom.

The contamination electrons are set in motion by matter between the target and magnet by the same processes that set electrons in motion in the phantom. The major difference between contamination electrons produced between the target and magnet that reach the phantom surface and electrons set in motion by primary photons interacting with the phantom near the surface is that the contamination electrons will be more forward directed. Those contamination electrons that were set in motion with a large zenith angle will have left the beam. Figure 72 illustrated that the forward directed electrons that are set in motion by a 15 MV beam have a higher average energy than those that are set in motion with large zenith angles. Therefore, contamination electrons have a higher average energy compared to electrons set in motion in the phantom. Having a higher average energy results in greater penetration of the contamination electrons compared to phantom generated electrons. Additionally, contamination electrons that are set in motion further away from the phantom are more likely to have been produced with a smaller zenith angle than contamination electrons produced closer to the phantom. Therefore, electrons produced further away from the phantom are likely to be more energetic* and, therefore, more penetrating than those produced close to the phantom.

Figure 80 compares the relative dose imparted to a phantom from electrons set in motion in the top 0.1 cm of a phantom compared to the electron contamination penetration curve from a 15 MV photon beam and

* The slowing down of electrons in air is insignificant. The stopping power of air for 3 MeV electrons is about 1.8 MeV cm^2/g (5). One hundred centimeters of air has a mass thickness of about 0.13 g/cm^2 so an electron will lose about 0.2 MeV or 7% of its energy in traversing this distance. The range of 3 MeV electrons in air is about 11 m.

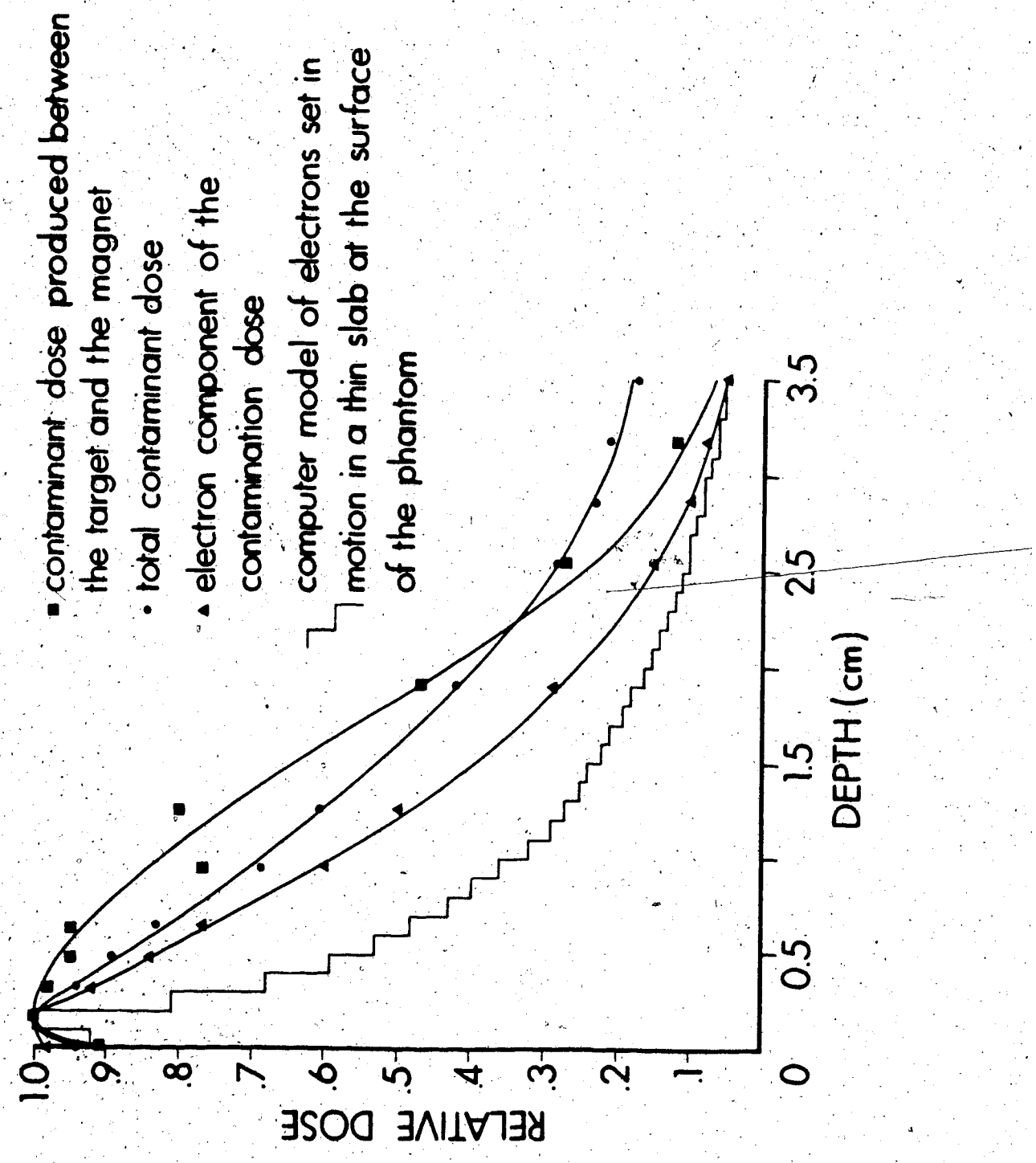

Figure 80. Comparison between various penetration curves at 15 MV.

the electron contamination produced between the target and magnet. The contamination penetration curve contains electrons as well as scattered photons so the comparison cannot be made fairly. In Section 2.13 the scattered photon build-up curve was obtained. The electron contamination component can be obtained by subtraction of the scattered photon contamination component. An assumption is made that there are no contamination electrons penetrating to a depth of 4.4 cm of polystyrene so the dose at this depth is entirely due to scattered photons. Figure 80 shows the result. The electron contamination component is more penetrating than the electrons set in motion in the phantom at shallow depths. This is because the electron contamination component contains fewer low energy electrons compared to the electrons set in motion in the photon which are stopped at shallow depths in the phantom. The electron contamination component produced between the target and magnet is more penetrating than the total electron contamination curve. The maximum range of the contamination electrons is approximately equal to the maximum range of the electrons set in motion by the phantom. This is because the maximum energy of contamination electrons produced at any position in the beam is the same as the maximum energy of electrons set in motion in the phantom. All the electron penetration curves in Figure 80 have their maximum at about 1.5 mm depth in the phantom.

Figure 81 is a comparison between the dose due to electrons set in motion in a thin slab at the top of the phantom and total dose due to contamination for the 6 MV beam. The contamination curve has not had the scattered photons removed. By comparing the total contamination and electron set in motion curves between 15 MV (Figure 80) and 6 MV (Figure

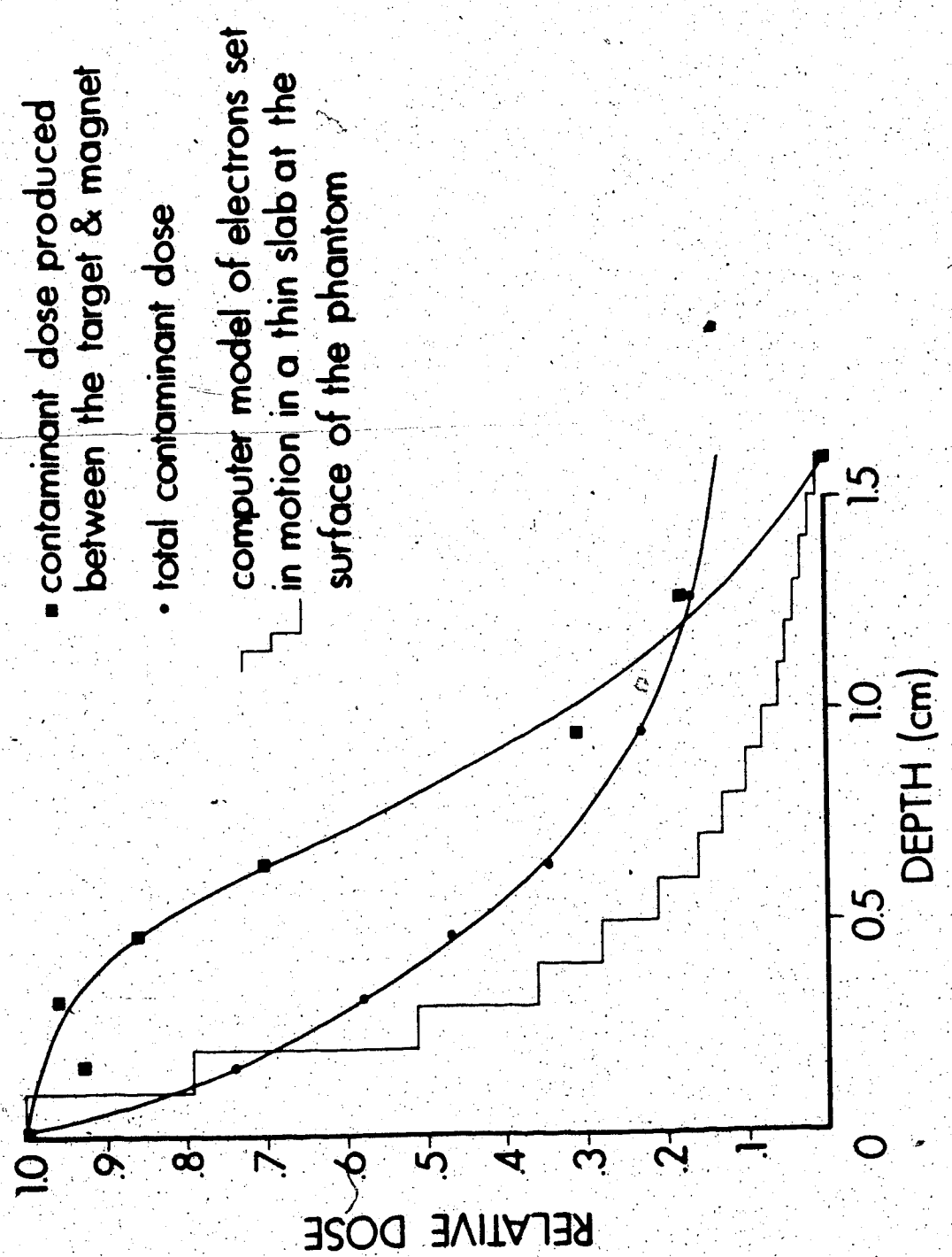

Figure 81. Comparison between various penetration curves at 6 MV.

81) it can be seen that the 6 MV curves would be very similar had the scattered photon component been removed. Therefore, the electron contamination component at 6 MV has similar penetration characteristics to electrons set in motion at the surface of a phantom implying that the contamination electrons are produced close to the phantom. This confirms the results of Section 2.10 which indicated that most of the contamination at 6 MV is produced in air between the magnet and phantom.

Figure 81 also illustrates the penetration curve of electrons produced between the target and magnet at 6 MV. The penetration of this fraction of the electron contamination is much greater at shallow depths than the electrons set in motion at the surface of the phantom, however, this component contributes very little to the total contamination at 6 MV. As at 15 MV, the maximum range of electrons set in motion at the surface of the phantom and contamination electrons produced between the target and magnet are almost identical.

Decreasing the source-to-probe distance increases the fraction of detected contamination produced between the target and magnet and decreases the amount of contamination produced by air between the magnet and phantom that arrives at the probe. Therefore, the relative proportion of electron contamination that is produced by these sources changes as a function of SPD. Since these sources each have different penetration characteristics measured at the same SPD, the penetration characteristics of the total electron contamination component could change as the SPD changes. However, as the source to probe distance decreases, more electrons produced between the target and magnet are going to be arriving at the probe produced with larger zenith angles. As the probe gets closer to a source of electron contamination more lower energy

electrons will arrive at the probe so the contamination component will be less penetrating at shallow depths. More lower energy electrons arriving from a source between the target and magnet will tend to compensate for fewer electrons produced in air. Therefore, the total penetration characteristics of contamination electrons likely does not change significantly as a function of source-to-probe distance.

At depths approaching d_{max}, most of the contamination dose is due to scattered photons. The Compton effect produces a scattered photon for every recoil electron produced. Therefore, the sources of electrons are also going to be the sources of scattered photons.

Nilsson and Brahme, using computer Monte Carlo modelling, found that the field flattening filter and the collimator are the main sources of scattered photons (36). This can be qualitatively explained. The mean interaction distance for the scattered photons is of the order of the inverse of their mean energy absorption coefficient, $1/\bar{\mu}_{en}$. Section 3.2 illustrated that one could define an effective energy absorption coefficient for the dose deposited by electrons set in motion. The mean interaction distance is of the order of the inverse of this coefficient which is $1/\bar{\mu}_{e^{\pm}}$. Scattered photons will emerge from a depth from a source of the order $1/\bar{\mu}_{en}$ while contamination electrons will emerge from a depth of the order $1/\bar{\mu}_{e^{\pm}}$. Both the collimators and the field flattening filter have thicknesses greater than $1/\bar{\mu}_{en}$ so many more scattered photons will emerge compared to contamination electrons. Sources of contamination with a thickness of the order of $1/\bar{\mu}_{e^{\pm}}$, like accessories and air, will produce approximately equal numbers of contamination electrons and scattered photons in the beam.

Contamination electrons produce a higher maximum dose illustrated

by the surface dose of Figures 63 and 64 than scattered photons illustrated by the dose plateau in the same figures. The ratio of the electron energy fluence produced by scattered photons deposited at any point is from Equation 1.5.8 and is approximately equal to:

$$\frac{\psi_{e^{\pm}}(x)}{(\psi_{\gamma})_o} \simeq \frac{\mu_{\gamma}}{\mu_{e^{\pm}} - \mu_{\gamma}} \left(e^{-(\mu_{\gamma}/\rho)x} - e^{-(\mu_{e^{\pm}}/\rho)x} \right)$$

At d_{max} the term $(e^{-(\mu_{\gamma}/\rho)d_{max}} - e^{-(\mu_{e^{\pm}}/\rho)d_{max}})$ is approximately equal to 1. Since μ_{γ} is much less than $\mu_{e^{\pm}}$:

$$\frac{\psi_{e^{\pm}}(d_{max})}{(\mu_{\gamma})_o} \simeq \frac{\mu_{\gamma}}{\mu_{e^{\pm}}} \qquad (3.2.1)$$

It has been shown previously that contamination electrons penetrate somewhat further than electrons set in motion in the phantom by scattered photons, however, they are both of the same order of magnitude. Therefore, the relative energy fluence of contamination electrons compared to scattered photons is approximately:

$$\frac{(\psi_{e^-})_{\text{contamination}}}{(\mu_{\gamma})_{\text{scattered photon}}} \simeq \frac{\text{Dose } (d=0)}{\text{Dose } (d_{max} \text{ scattered photon})} \frac{\mu_{\gamma}}{\mu_{e^{\pm}}} << 1 \qquad (3.2.2)$$

Therefore, despite the fact that the maximum dose due to contamination electrons is greater than the maximum dose due to scattered photons, the energy fluence arriving at the phantom surface of scattered photons is greater than the energy fluence due to contamination electrons.

The greater energy fluence of scattered photons compared to contamination electrons is due in part to thick sources like the collimators and the field flattening filter. Additionally, electrons

more readily multiple scatter* out of the beam compared to photons.

The shift in d_{max}, especially when accessories are present in the beam, can be attributed to electron contamination. Since the build-up curve for scattered photon contamination is similar to the primary photon build-up curve, scattered photons are unlikely to contribute significantly to the shift in d_{max}. The peak in the contamination penetration curve due to electrons occurs at very shallow depths so increasing the magnitude of electron contamination results in a d_{max} shift towards shallower depths. This also explains why the shift in d_{max} is accompanied by an increased surface dose. These findings agree with Biggs and Ling (41) who observed that a shift in d_{max} did not occur when electrons were swept from the beam.

* For example, a 3 MeV electron in air has a mass angular scattering power of 0.602 radians^2 · cm^2/g (5) which, after passage through 100 cm of air, corresponds to a mean scattering angle of 16.0°.

3.3 Clinical Uses of the Results

Low energy photon beams (isotope sources with an energy less than or equal to $m_o c^2$ or accelerator sources less than about 1 MV) produce a maximum dose at the surface of a patient. If these photon sources were used to treat tumors at a depth under the patient's skin surface, skin reactions could occur.

Skin reactions may be minor such as erythema (reddening of the skin) or more serious such as moist desquamation (peeling of the skin with blistering). The type of reaction, if it occurs, varies considerably as a function of dose from patient to patient (7). Skin reactions are similar to sunburns in morphology and histology, however, the onset of the ionizing radiation induced skin reaction occurs several days after exposure rather than a few hours.

Few skin reactions occur to patients undergoing megavoltage radiation therapy. The main reason is that the maximum dose is received at a depth well below the skin. The dose due to contamination electrons reduces this skin sparing effect.

Another effect produced by contamination electrons and scattered photons is an elevated dose outside the field boundary. A situation where this may be clinically important arises when the eyes lie just outside the field. The lens of the eye is susceptible to the formation of radiation induced cataracts. Cataracts are likely to form if the total dose received over 30 days is 1500 rads (52).

The amount of contamination increases with accessories in the field, greater field size and smaller SPD. Skin reactions or high dose outside the field may result even at megavoltage energies if two or more of these conditions are encountered.

Passing the beam through the poles of a magnet could be effective in reducing the electron contamination arriving at a patient. To ensure that few electrons are produced in air between the magnet and patient, the magnet would have to be placed as close to the patient as possible. In a clinical situation the contamination electrons should not strike the patient outside of the treatment area, therefore, the electrons should be swept through at least 90^{o}. A magnetic field of nearly 1 Tesla would be required. Electron contamination increases as a function of field size so the pole gap should be as wide as possible. The field gradient should be steep enough to ensure that the dose distribution, due to electrons set in motion in the patient is not affected. These requirements could only be met with an electromagnet. In addition, such a magnet would likely have to be liquid cooled.

When an accessory is in place, the surface dose inside the field can be reduced by about 20% if a lead (or other high atomic number material) sheet is placed underneath the accessory. The "filter" scatters electrons out of the field so a reduction of surface dose inside the field would be concomitant with an increase in the surface dose outside the field. The "filter" would then be clinically acceptable only if the increased dose outside the field would not cause complications and if the reduced dose inside the field significantly reduced the probability of the occurrence of skin reactions.

A useful, immediately applicable feature of the removal of the contamination component is that the TMR in the build-up region is independent of field size, SPD and presence of accessories and, therefore, is ameniable to data storage in computers. Instead of listing all of the values of the TMR curves in the build-up region for field widths, SPD's and presence of accessories applicable to treatment planning, only

[redacted]ves; one, the phantom generated TMR curve and the other, t[redacted]nation TMR curve and the surface dose as a function of these co[redacted]s need be listed. The surface dose dictates the magnitude of the[redacted]se received in the build-up region due to contamination.

The separation of the contamination component of dose and the [redacted]tom generated dose may prove to be important for treatment planning [redacted] the build-up region in the presence of inhomogeneities. The treat-[redacted]nt planning algorithms most often employed (developed by Dr. Jack [redacted]nningham) separate the contribution to the dose to a point into [redacted]mary and scattered photon contributions. In the build-up region, the phantom generated scattered contribution can be confused with the contamination contribution.

[redacted]he primary dose at a given depth is determined by extrapolating a [redacted]ve of TMR versus field width to the y-axis. The TMR value at the y-axis is called the zero-area TMR value at that depth. The difference between the TMR value at any other field width is assumed to be due to scatter generated within the phantom.

The usual measure of the amount of phantom generated scatter contributing to a point at energies of 6 MV or higher is the scatter maximum ratio or SMR. The scatter maximum ratio is the difference between the TMR at a given field width and depth and the zero-area TMR at the same depth.

Since the amount of contamination also increases with field width, some of the contamination is attributed to scatter in this scheme. This is merely an academic distinction in treatment planning of homogeneous phantoms. In treatment planning of inhomogeneous regions, the scatter contribution from a region is increased if the inhomogeneity has a high electron density and it is decreased if the electron density is low. This

reflects the direct proportionality of the Compton cross-section with electron density. If the inhomogeneity is in the build-up region, then the contamination dose erroneously attributed to phantom generated scatter will be similarily modified. In fact, the electron component of the contamination dose should be reduced if high electron density inhomogeneities are present in the build-up region and increased if low electron densities are present, which is opposite to the treatment planning for phantom generated scatter.

4. CONCLUSIONS

Conclusions are usually
consolidated guesses.

Anonymous

4.1 Conclusions

The Mevatron -6 and Mevatron -20 accelerators produce photon beams which were found to be contaminated by electrons and scattered photons. The dose measured at the surface of a phantom was due mainly to electron contamination. The magnitude of the surface tissue maximum ratio varied greatly under the conditions studied between 0.05 (in an open 5 cm x 5 cm 15 MV field at an SPD of 100 cm) to 0.60 (in a 30 cm x 30 cm field with a 3.2 cm Lucite accessory in place in a 6 MV beam). The other contribution to the surface dose due to photon backscatter was usually an order of magnitude lower.

The electron component of the surface dose was clearly evident. The magnitude of the displacement of the TMR curves with increasing field width was greatest at the surface. Under the same conditions of field width, SPD and accessory configuration, the 6 MV accelerator had a greater dose than the 15 MV accelerator at the same relative depth.

Adding additional thicknesses of accessories increased the surface TMR up to a thickness approximately equal to or greater than the electron range in the accessory ($\sim 1/\mu_{e^-}$) when increases in the accessory thickness did not cause further increases in the surface TMR.

Electron "filters" reduced the surface dose when an accessory was in place by as much as 20% if the atomic number of the "filter" was equal to lead. The "filter" acted by scattering electrons out of the field. A reduction of dose inside the field accompanies an increase in dose outside the field.

The surface dose increased rapidly when the source-to-probe distance decreased. At 15 MV the isocentric normalized dose dependence on SPD for a 30 cm x 30 cm field size was consistent with the field flattening filter being the source of contamination. At 6 MV the isocentric

normalized dose did not decrease according to the inverse square dependence so the source was not localized.

The lateral distribution of the surface dose for a field size of 30 cm x 30 cm at 15 MV was Gaussian. This further suggested that the surface contamination was due to electrons which emanate from a localized source. The surface dose in a 30 cm x 30 cm field at 6 MV was not normally distributed which was consistent with a source or sources of electron contamination that are not localized.

The measurements were always taken with square fields except in Section 2.6 where the surface dose of a 15 MV beam was measured for rectangular fields. The surface dose was somewhat greater if the upper collimator defined the long axis compared to the situation when the lower collimator defined the long axis. The surface equivalent square field was very different from the equivalent square field at d_{max}.

The surface dose has been shown to be a useful measure of the amount of electron contamination incident on the phantom. The amount of contamination at the surface of a phantom was more accurately assessed by determining the amount of dose due to photons backscattering from the phantom.

Contamination electrons produced between the target and accessory tray were swept from the field by passing the beam through the poles of a permanent magnet positioned at the accessory tray. The surface dose with the magnet in place and the photon backscatter dose taken into account, was due to electrons produced in air between the magnet and phantom. This source of electron contamination was the most important at 6 MV and for small field sizes at 15 MV. The air-produced electron contamination increased rapidly as a function of field size at small field sizes and increased as a function of SPD.

Electron contamination produced between the target and magnet, as indicated by surface dose with the photon backscatter removed, increased approximately in direct proportion to the cross-sectional area of the beam. This contribution to electron contamination decreased as a function of SPD.

The inverse square fall-off in the surface dose produced between the target and magnet along with the SPD dependence of the surface dose at large fields with no magnet in place suggested that electron contamination tended to be produced by mass close to the phantom and this material attenuated or scattered electrons produced further from the phantom.

The clinical aspects of an electromagnet to sweep contamination electrons from the field were discussed. The requirements for such a magnet were contradictory and would be difficult to achieve in practice.

The penetration of contamination into polystyrene, both inside and outside the field, had similar characteristics. The contamination inside the field was obtained by equating the increase in the dose as a function of field size in a limited phantom (where the field size is greater in extent than the phantom) at various depths in the phantom with the amount of contamination penetrating to that depth. The contamination as a function of depth in a phantom outside the field was measured by tilting the phantom so that the phantom would not change its relative distance from the field boundary as the phantom thickness increased. Both penetration characteristics illustrated that electrons deposit their energy at shallow depths in the phantom and scattered photons contributed at deeper depths. The difference between the shape of the curves was due to a difference in the relative proportion of electrons and scattered photons inside and outside the field.

The penetration curve of electrons produced between the target and magnet and a penetration curve of electrons set in motion in a thin slab at the surface of the phantom were also obtained. Electrons which were produced further away from the phantom were more penetrating at shallow depths and, therefore, more energetic than those produced close to or at the phantom surface. However, the maximum range of the electrons was independent of where they were produced.

The contamination penetration curves normalized to their own maxima were approximately independent of the configuration of the beam or the condition of measurement. Only the amount of contamination varied as a function of field width, SPD and presence of accessories. The phantom generated normalized dose at any depth was found by subtracting the amount of contamination penetrating to that depth. Since the shape of the contamination penetration curve was invariant, the amount subtracted at any depth was determined by the amount of electron contamination at the surface.

The output factor for the phantom generated normalized dose was larger at small field sizes and plateaued to a smaller value at larger field sizes compared to the total output factor. The phantom generated normalized dose curves were divided by the maximum normalized dose of each curve to obtain the phantom generated tissue maximum ratio curve. The phantom generated tissue maximum ratios were independent of field width, SPD and presence of accessories.

The phantom generated dose in the build-up region was computer modelled independently of experiment. The calculated results agreed with the experimental phantom generated tissue maximum ratios and were independent of field width.

The computer model showed that electrons set in motion in a thin layer produced a dose in the phantom which decreased exponentially. Therefore, an analytic model of the phantom generated dose in the build-up region could be adopted in which the primary photons and electrons set in motion fall exponentially, each with their own characteristic attenuation constant.

The separation of contamination from phantom generated contributions could reduce the data storage requirements of small computer treatment planning systems. Large computer planning systems could employ the results to produce a more accurate model of dose deposition when inhomogeneities are present in the build-up region.

The energy fluence of scattered photons is greater than the energy of electron contamination even though the maximum dose of contamination electrons is greater than the maximum dose of scattered photons. The shift in d_{max} is due to contamination electrons.

REFERENCES

(1) Fitzgerald, J.J., Mathematical Theory of Radiation Dosimetry, Gordon and Breach Science Publishers, Inc., New York, 1967.

(2) Johns, H.E., Laughlin, J.S., "Interaction of Radiation with Matter", Chapter 2 of Radiation Dosimetry, Gerald J. Hine, Gordon L. Brownell, Ed., Academic Press, New York, 1956.

(3) Nelms, Ann T., Graphs of the Compton Energy-Angle Relationship and the Klein-Nishina Formula from 10 keV to 500 MeV, N.B.S. Circular, 542, U.S. Department of Commerce, 1953.

(4) Rossi, Bruno, High Energy Particles, Prentice-Hall Inc., Englewood Cliffs, New Jersey, 1952.

(5) Almond, P.R., "Dosimetry Considerations of Electron Beams", In: Kramer, S., Suntharalingam, N., Zinninger, G.F., Ed., High-Energy Photons and Electrons, J. Wiley and Sons, New York, 1976: 129-168.

(6) Karzmark, C.J., Morton, R.J., A Primer on Theory and Operation of Linear Accelerators in Radiation Therapy, U.S. Department of Health and Human Services, 1981.

(7) Cunningham, J.R., Johns, H.E., The Physics of Radiology, Charles C. Thomas, Publisher, 1974.

(8) ICRU Report 24, Determination of Absorbed Dose in a Patient Irradiated by Beams of X- or Gamma Rays in Radiotherapy Procedures, International Commission on Radiation Units and Measurements, Washington, D.C., 1976.

(9) Hubbell, J.H., Photon Cross-Sections, Attenuation Coefficients, and Energy Absorption Coefficinets from 10 keV to 100 GeV, NSRDA - NBS 29, U.S. Department of Commerce, 1969.

(10) Cassen, B., Corrigan, K.E., Hayden, H.S., Attenuation and Transition Effects in the Absorption of Supervoltage Radiation, Radiology, 31, 319-324, (1938).

(11) Koch, H.W., Kerst, D.W., Morrison, P., "Experimental Depth Dose for 5, 10, 15 and 20 - Million - Volt X-Rays", Radiology, 40, 120-127, (1943).

(12) Laughlin, J.S., Beattie, J.W., Lindsey, J.E., Harvey, R.A., "Dose Distribution Measurements with the University of Illinois 25 MeV Medical Betatron", American Journal of Roentgenology, 65, 787-799, (1951).

REFERENCES (CONT'D)

(13) Johns, H.E., Darby, E.K., Haslam, R.N.H., Katz, L., Harrington, E.L., "Depth Dose Data and Isodose for Radiations from a 22 MeV Betatron", American Journal of Roentgenology, 62, 257-268, (1949).

(14) Johns, H.E., Epp, E.R., Cormack, D.V., Fedoruk, S.O., "Depth Dose Data and Diaphragm Design for the Saskatchewan 100 Curie Cobalt Unit", British Journal of Radiology, 25, 302-308, (1952).

(15) Richardson, J.E., Kerman, H.O., Brucer, M., "Skin Dose from a Cobalt 60 Teletherapy Unit", Radiology, 63, 25-36, (1951).

(16) Kemp, L.A.W., Burns, J.E., "Physical Measurements on the London Hospital Picker C 3000 Cobalt Unit", Acta Radiologica, 49, 471-484, (1958).

(17) Saylor, W.L., Quillin, R.M., "Methods for the Enhancement of Skin Sparing in Cobalt 60 Teletherapy", American Journal of Roentgenology, 111, 174-179, (1971).

(18) Velkley, D., Manson, D.J., Purdy, J.A., Oliver, G.D., "Build-Up Region of Megavoltage Photon Radiation Sources", Medical Physics, 2, 14-19, (1975).

(19) Gagnon, W.F., Grant, W.G., "Surface Dose from Megavoltage Therapy Machines", Radiology, 117, 705-708, (1975).

(20) Leung, P.M.K., Sontag, M.R., Maharaj, H., Chenery, S., "Dose Measurements in the Build-Up Region for Cobalt-60 Therapy Units", Medical Physics, 3, 169-172, (1976).

(21) Smith, C.W., Sutherland, W.H., "Electron Contamination of Telecobalt Beams", British Journal of Radiology, 49, 562-563, (1976).

(22) Khan, F.M., "Use of Electron Filters to Reduce Skin Dose in Cobalt Teleotherapy, American Journal of Roentgenology, 111, 180-181, (1971).

(23) Wilson, C.W., Perry, B.J., "Secondary Electron Emission Generated by X-Rays,": British Journal of Radiology, 24, 293, (1951).

(24) Hughes, H.A., "Measurements of Superficial Absorbed Dose with 2 MV X-Rays used at Glancing Angles", British Journal of Radiology, 32, 255-258, (1959).

(25) Gray, L., "Relative Surface Doses from Supervoltage Radiation", Radiology, 109, 437-442, (1973).

(26) Ibbott, G,S,, Hendee, W.R., "Beam-Shaping Platforms and the Skin Sparing Advantage of Co^{60} Radiation", American Journal of Roentgenology, 111, 193-196, (1970).

REFERENCES (CONT'D)

(27) Leung, P.M.K., Johns, H.E., "Use of Electron Filters to Improve the Build-Up Characteristics of Large Fields from Cobalt-60 Beams", Medical Physics, 4, 441-444, (1977).

(28) Rao, P.S., Pillai, K., Gregg, E.C., "Effect of Shadow Trays on Surface Dose and Build-Up for Megavoltage Radiation", American Journal of Roentgenology, 117, 168-174, (1973).

(29) Wu, A., "Effects of an Acrylic Resin Tray on Relative Surface Doses for 10 MV X-Ray Beams", International Journal of Radiation Oncology, Biology and Physics, 6, 1257-1260, (1980).

(30) Scrimger, J., Kolitsi, Z., "Scattered Radiation from Beam Modifiers Used with Megavoltage Therapy Units", Radiology, 130, 233-236, (1979).

(31) Baily, N.A., Beyer, N.S., "Surface and Entrance Dose for a 2 MV_p X-Ray Beam", Radiology, 69, 553-557, (1957).

(32) Chamberlain, E.C., Baily, N.A., "Entrance and Exit Absorbed Dose Characteristics for a 6 MeV X-Ray Generator", Radiology, 82, 267-271, (1964).

(33) Bagne, F., "Physical Aspects of Supervoltage X-Ray Therapy", Medical Physics, 1, 266-274, (1974).

(34) Dawson, D.J., "Percent Depth Doses for High Energy X-Rays", Physics in Medicine and Biology, 21, 226-235, (1976).

(35) Dawson, D.J., "Tissue-Maximum Ratios for High Energy X-Rays", Medical Physics, 4, 423-430, (1977).

(36) Nilsson, B., Brahme, A., "Absorbed Dose from Secondary Electrons in High Energy Photon Beams", Physics in Medicine and Biology, 24, 901-912, (1979).

(37) Marbach, J.R., Almond, P.R., "Scattered Photons as the Cause for the Observed d_{max} Shift with Field Size in High-Energy Photon Beams", Medical Physics, 4, 310-314, (1977).

(38) Tolbert, D.D., Lane, R.G., Paliwal, B.R., Frost, S.W., Chin, K.B., Dercks, J., "Characteristics of Clinac-18 Wedged Fields for 10 MV X-Rays", Medical Physics, 4, 419-422, (1977).

(39) Almond, P., Van Roosenbeck, E., "Variation in the Position of the Central Axis Maximum Build-Up Point with Field Size for High-Energy Photon Beams", British Journal of Radiology, 43, 911, (1970).

(40) Bagne, F., "A Method for Calculating Megavoltage X-Ray Dose and Dose Parameters", Medical Physics, 7, 664-671, (1980).

REFERENCES (CONT'D)

(41) Biggs, P.J., Ling, C.C., "Electrons as the Cause of the Observed d_{max} Shift with Field Size in High Energy Photon Beams", Medical Physics, 6, 291-295, (1979).

(42) Padikal, T.N., Deye, J.A., "Electron Contamination of a High-Energy X-Ray Beam", Physics in Medicine and Biology, 23, 1086-1092, (1978).

(43) Ling, C., Private Correspondence, (1981).

(44) Ling, C., Rustgi, S., Gromadzki, Z., "Production of Secondary Radiation by 10 MV Photons", Presented to the American Association of Physicists in Medicine Meeting, August 1981, Boston, Mass.

(45) Ling, C.C., Schell, M.C., Rustgi, S.N., "Magnetic Analysis of the Radiation Components of a 10 MV Photon Beam", Medical Physics, 9, 20-26, (1982).

(46) Nilsson, B., Brahme, A., "Contamination of High-Energy Photon Beams by Scattered Photons", Strahlentherapie, 157, 181-186, (1981).

(47) Tremblay, J.P., Bunt, R.B., "An Introduction to Computer Science, An Algorithmic Approach, McGraw-Hill Book Company, New York, 1979.

(48) Sandifer, C.W., Taherzadeh, M., "Measurement of Linac Thick-Target Bremsstrhalung Spectra using a large NaI Scintillation Spectrometer", Published by E.G. and G. Inc., Goleta, California.

(49) Raeside, D.E., "Monte Carlo Principles and Applications", Physics in Medicine and Biology, 21, 181-197, (1976).

(50) Spencer, L.V., "Energy Dissipation by Fast Electrons, National Bureau of Standards Monograph 1", United States Department of Commerce, (1959).

(51) Bruce, W.R., Johns, H.E., "The Use of the Monte Carlo Method", Section II in British Journal of Radiology, Supplement Number 9, (1960).

(52) Hall, E.J., Radiobiology for the Radiologist, Harper and Row, New York, 1978.

(53) Nahum, A.E., "Water/Air Mass Stopping Power Ratios for Megavoltage Photon and Electron Beams", Physics in Medicine and Biology, 23, 24-38, (1978).

(54) Cohen, M. Jones, D.E.A., Greene, D., "Central Axis Depth Dose Data for Use in Radiotherapy", British Journal of Radiology, Supplement No. 11, The British Institute of Radiology, London, (1972).

APPENDICES

All the mathematical sciences are founded on relations between physical laws and laws of numbers, so that the aim of exact sciences is to reduce the problem of nature to the determination of quantities by operations with numbers.

James Clerk Maxwell

5.1 Appendix 1 Numerical Values For Constants

$e = 1.602 \times 10^{-19}$ Couloumb

$h = 6.626 \times 10^{-34}$ Joule-second

$\hbar = 1.055 \times 10^{-34}$ Joule-second.

$m_o = 9.110 \times 10^{-31}$ kilogram

$c = 2.998 \times 10^{8}$ meter/second

$m_o c^2 = 0.5110$ MeV

$r_o = 2.818 \times 10^{-15}$ meter

$N_o = 6.022 \times 10^{22}$ molecules/mole

$I(\text{water}) \sim 70$ eV

$W(\text{water}) \sim 34$ eV/ion pair

The quantity $q(T,h\nu,Z)$ for water (see Equation 1.2.11) is listed below as a function of ν (see Equation 1.2.8)

ν	0.0	0.1	0.2	0.3	0.4	0.5	0.6	0.7	0.8	0.9
$q(T,h\nu,Z)$	5.0	3.5	1.9	1.3	1.1	.88	.77	.69	.62	.58

5.2 Appendix 2 Total and Compton Attenuation Coefficients for Water (9)

Energy (MeV)	Total Attenuation Coefficient (1/cm)	Compton Attenuation Coefficient (1/cm)
0.10	0.168	0.165
0.15	0.149	0.148
0.20	0.136	0.136
0.30	0.118	0.118
0.40	0.106	0.106
0.50	0.0967	0.0967
0.60	0.0895	0.0895
0.80	0.0786	0.0786
1.00	0.0707	0.0706
1.50	0.0575	0.0574
2.00	0.0494	0.0490
3.00	0.0397	0.0385
4.00	0.0340	0.0322
5.00	0.0303	0.0278
6.00	0.0277	0.0245
8.00	0.0243	0.0201
00	0.0220	0.0171
00	0.0194	0.0127
	0.0181	0.0102

5.3 Appendix 3 Total Stopping Power of Electrons in Water (5)

Energy (MeV)	Stopping Power (MeV/cm)	Energy (MeV)	Stopping Power (MeV/cm)
0.10	4.202	1.00	1.893
0.15	3.304	2.00	1.889
0.20	2.850	3.00	1.931
0.25	2.580	4.00	1.974
0.30	2.401	5.00	2.014
0.35	2.280	6.00	2.051
0.40	2.190	7.00	2.085
0.45	2.123	8.00	2.119
0.50	2.071	9.00	2.152
0.55	2.032	10.00	2.183
0.60	2.000	15.00	2.327
0.65	1.975	20.00	2.470
0.70	1.955		
0.75	1.939		
0.80	1.926		
0.85	1.915		
0.90	1.906		
0.95	1.899		

5.4 Appendix 4 Mean Square Mass Angular Scattering Power of Electrons in Water and Lead

Energy (MeV)	Water ($rad^2 g/cm^2$)	Lead ($rad^2 g/cm^2$)
0.10	1.31×10^{2}	9.15×10^{2}
0.15	6.59×10^{1}	4.68×10^{2}
0.20	4.10×10^{1}	2.95×10^{2}
0.30	2.14×10^{1}	1.56×10^{2}
0.40	1.37×10^{1}	1.00×10^{2}
0.50	9.71	7.17×10^{1}
0.60	7.36	5.45×10^{1}
0.80	4.75	3.55×10^{1}
1.00	3.39	2.55×10^{1}
1.50	1.82	1.38×10^{1}
2.00	1.16	8.83
3.00	6.00×10^{-1}	4.63
4.00	3.72×10^{-1}	2.89
5.00	2.55×10^{-1}	1.99
6.00	1.87×10^{-1}	1.46
8.00	1.13×10^{-1}	8.87×10^{-1}
10.00	7.61×10^{-2}	6.00×10^{-1}
15.00	3.67×10^{-2}	2.91×10^{-1}
20.00	2.17×10^{-2}	1.73×10^{-1}

* From "ICRU Report 21, Electrons with Initial Energies Between 1 and 50 MeV", International Commission on Radiation Units and Measurements, Washington, D.C., 1972

5.5 Appendix 5 Listing and Documentation For 'Seprimary.For'

```
      program seprimary

c     ***************************************************************
c     *                                                             *
c     * This program subtracts the contamination normalized dose from *
c     * the total normalized dose to yield the phantom generated norm- *
c     * alized dose. The amount of contamination arriving at the phan- *
c     * tom is the proportional to the difference between the total  *
c     * and photon backscatter normalized doses. The phantom generated *
c     * TMR curve is calculated after a search has found the maximum  *
c     * normalized dose. The error in the normalized dose and TMR    *
c     * values are calculated.                                      *
c     *                                                             *
c     ***************************************************************

      integer i,n
      real depth(20),ctmr(20),w,nd(20),bsnd
      real ernd,ebsnd,cmax,pnd(20),epnd(20)
      real recmax,max,remax,ptmr(20),eptmr(20)

c     ***************************************************************
c     *                                                             *
c     * depth(20) is the depth in the phantom.                      *
c     * ctmr(20) is the contamination tissue maximum ratio,TMR, as a *
c     *          function of depth.                                 *
c     * w is the field width.                                       *
c     * nd(20) is the total normalized dose as a function of depth. *
c     * bsnd is the backscatter normalized dose.                    *
c     * ernd is the error in the normalized dose.                   *
c     * ebsnd is error in the backscatter normalized dose.          *
c     * cmax is the value of maximum contamination normalized dose  *
c     * pnd(20) is the phantom generated normalized dose as a function *
c     *         of depth.                                           *
c     * epnd(20) is the error in the phantom generated normalized   *
c     *          dose as a function of distance.                    *
c     * recmax is the relative error in cmax.                       *
c     * max is the maximum phantom generated normalized dose.       *
c     * remax is the relative error in max.                         *
c     * ptmr(20) is the phantom generated normalized dose as a function *
c     *          of depth.                                          *
c     * eptmr(20) is the error in the phantom generated normalized  *
c     *           dose as a function of depth.                      *
c     *                                                             *
c     ***************************************************************

      open(unit=1,status='old',file='contam15.dat')
      open(unit=2,status='old',file='nd15no16.dat')
      open(unit=3,status='new',file='prim15.dat')

c     ***************************************************************
c     *                                                             *
c     * contam.dat stores contamination TMR values as a function of *
c     *            depth.                                           *
c     * nd15no16.dat stores the total normalized dose curve as a func- *
c     *              tion of depth and the value of the photon back- *
c     *              scatter normalized dose for a particular config- *
c     *              uration of field size and SPD at 15 MV.        *
c     * prim15.dat is the output file that lists the phantom generated *
c     *            normalized dose and TMR values along with their  *
c     *            associated errors.                               *
c     *                                                             *
```

```
c     ********************************************************************

        read (1,100) n
        do 5 i=1,n
5         read (1,500) depth(i),ctmr(i)
        read (1,600) ectmr
        read (2,700) w
        do 10 i=1,n
10        read (2,1000) nd(i)
        read (2,1100) ernd,bsnd,ebsnd

c     ********************************************************************
c     *                                                                  *
c     * The following statements calculates the maximum amount of con- *
c     * tamination and the amount of contamination occurring as a        *
c     * function of depth. The contamination is removed from the total *
c     * normalized dose. The relevant errors are calculated as well.     *
c     *                                                                  *
c     ********************************************************************

        cmax=(nd(1)-bsnd)/ctmr(1)
        recmax=(ernd+ebsnd)/(nd(i)-bsnd)+ectmr/ctmr(1)
        pnd(1)=bsnd
        epnd(1)=ebsnd
        do 20 i=2,n
          pnd(i)=nd(i)-cmax*ctmr(i)
20        epnd(i)=ernd+(recmax+ectmr/ctmr(i))*cmax*ctmr(i)

c     ********************************************************************
c     *                                                                  *
c     * The maximum phantom generated normalized dose is found and the *
c     * phantom generated TMR is calculated along with the associated    *
c     * errors. These quatities are then tabulated.                      *
c     *                                                                  *
c     ********************************************************************

        max=pnd(1)
        do 30 i=1,n
          if(pnd(i) .ge. max) then
            max=pnd(i)
            remax=epnd(i)/pnd(i)
          end if
30      continue
        do 40 i=1,n
          ptmr(i)=pnd(i)/max
40        eptmr(i)=(remax+epnd(i)/pnd(i))*ptmr(i)
        write (3,1200) 'Field Size =',w,'cm X',w,'cm'
        write (3,1300) 'Photon Backscatter N.D. =',bsnd
        write (3,*)' '
        write (3,1500) 'Depth','ND','Error in ND','TMR','Error in TMR'
        write (3,1600) '(cm)'
        do 50 i=1,n
50        write(3,1700) depth(i),pnd(i),epnd(i),ptmr(i),eptmr(i)

100     format(' ',i2)
500     format(' ',f4.2,2x,f4.2)
600     format(' ',f4.2)
700     format(' ',f4.1)
1000    format(' ',f5.3)
1100    format(' ',3(f5.3,2x))
1200    format(' ',a12,f4.1,a4,f4.1,a2)
```

```
1300    format(' ',a25,1x,f5.3)
1500    format(' ',a5,5x,a2,4x,a11,2x,a3,3x,a12)
1600    format(' ',a4)
1700    format(' ',f4.2,5x,f5.3,5x,f5.3,5x,f4.2,5x,f4.2)

        close(1)
        close(2)
        close(3)

        stop
        end
```

5.6 Appendix 6 Listing and Documentation For 'Buildup3.For'

```
      program buildup3

c     ************************************************************************
c     * Electron Monte-Carlo program to determine the electron dose          *
c     * in a semi-infinite water phantom for polyenergetic electrons using *
c     * the Rossi Gaussian lateral scattering approximation.                 *
c     ************************************************************************

c     ************************************************************************
c     ** Complete variable documentation appears in file Buildup3.doc *
c     ************************************************************************

      integer l,ii,nerg
      real r,zs,cal,sal,cbeta,sbeta
      real stop(179),tha(179),ep,cay
      real eo,e,dose(200),pl,gaus(100),g
      real z,max,ang,en(36),spectr(90,36)
      integer i,j,m,p,kay
      real xnrg(36),mu(36),sig(36),local,que(10)

      common /blk1/xnrg,en,mu,sig,local,spectr,que
      common /blk2/zs,z,ep,dose

c     ************************************************************************
c     * Gaus.dat stores a table of x's as a function of erf(x).             *
c     * Quadint3.dat stores values of interpolated scattering and stopping  *
c     *              power data in step sizes of 0.1 MeV.                   *
c     * Dose.dat stores normalized absorbed dose as a function of depth     *
c     *          in millimeters.                                            *
c     * Photon15.dat stores the normalized number of photons/bin,total      *
c     *               absorption and Compton absorption coefficients as a   *
c     *               function of bin energy. At the end of this file is    *
c     *               a coefficient array which is used in Stearn's         *
c     *               determination of a pair production electron trajectory.*
c     ************************************************************************

      open(unit=1,status='old',file='gaus.dat')
      open(unit=2,status='old',file='quadint3.dat')
      open(unit=4,status='new',file='dose.dat')
      open(unit=11,status='old',file='photon6.dat')

c     ************************************************************************
c     * The following statements read the look-up tables and initializes. *
c     ************************************************************************

      do 2 l=1,179
        read(2,420) tha(l),stop(l)
2     continue
      do 10 i=1,36
        read(11,340) xnrg(i),en(i),mu(i),sig(i)
10      en(i)=en(i)*1000.0
      read(11,350) (que(i),i=1,10)
      do 30 l=1,100
30      read(1,422) gaus(l)
      ii=285019
      cay=0.90

c     ************************************************************************
c     * Subroutine Impulse is called to determine the electron-set-in-motion *
c     * number speotrum,'spectr(t,theta)',where 't' is the electron energy   *
```

```
c     * and 'theta' is the original direction with respect to the photon      *
c     * direction. The program is repeated at all electron energies and       *
c     * angles for all histories as specified by 'spectr(t,theta)'. The       *
c     * following statements count histories and initializes the electron     *
c     * energy and angle.                                                     *
c     ************************************************************************

        do 120 kay=10,100
         call impulse
         dose(kay)=dose(kay)+local
         do 120 j=1,75
          eo=floatj(j)/5.0+.1
          do 120 p=1,18
           ang=floatj(p)*5.0-2.5
           do 120 l=1,jnint(spectr(j,p))
            e=eo
            zs=floatj(kay)/10.0-.05
            cal=cos(ang/57.296)
            sal=sin(ang/57.296)
            r=6.2832*ran(i1)
            cbeta=cos(r)
            sbeta=sin(r)

c       ************************************************************
c       * 'Tha(nerg)' and 'stop(nerg)' are arrays that contain the  *
c       * mass angular scattering and mass stopping powers respec-  *
c       * tively. 'E' is the kinetic energy of the electron and     *
c       * 'ep' is the amount deposited in the path length 'pl'.     *
c       * 'Gaus(rg+1) contains equally probable scattering angles   *
c       * for a Gaussian distribution with mean=0 and standard dev- *
c       * iation=1. When this distribution is multiplied by the     *
c       * mean scattering angle the result is 'g',the zenith scat-  *
c       * tering angle. The final value of 'r' in each scattering   *
c       * event represents the scattering azimuth angle. The Sub-   *
c       * routine Geom determines the angles in the coordinate      *
c       * system fixed with respect to the phantom.                 *
c       ************************************************************

33       do 110 while(e .gt. 0.2)
            ep=(1-cay)*e
            nerg=e*10.0-ep*5.0
            pl=ep/stop(nerg)
            e=e-ep
            g=sqrt(tha(nerg)*pl)*gaus(jifix(100.0*ran(i1))+1)
            r=6.2832*ran(i1)
            call geom(r,g,cal,sal,cbeta,sbeta)
            z=pl*cal
            zs=zs+z

c         ************************************************************
c         * The following statement checks for the edge of the phantom. *
c         ************************************************************

            if (zs .lt. 0.0 ) go to 115

c         ************************************************************
c         * The energy loss is assigned to the cumulative dose        *
c         * received by the phantom using the Subroutine Assign.      *
c         ************************************************************

            call assign
```

```
110         continue

c       ********************************************************************
c       * At this point the primary electron has an energy less than       *
c       * 0.2 MeV. The remainder of the energy is assigned to the dose     *
c       * at last depth interval.                                          *
c       ********************************************************************

115       call assign
120       continue

c       ********************************************************************
c       * The following statements normalize the dose to the maximum       *
c       * dose encountered and write the normalized dose.                  *
c       ********************************************************************

        max=0.0
        do 122 i=1,100
          if (dose(i) .gt. max) max=dose(i)
122     continue
        do 125 i=1,100
          write(4,250) i,dose(i)/max
125     continue

250     format(' ',i3,2x,f6.2)
340     format(' ',f5.2,2x,f5.3,2x,2(f5.2,2x))
350     format(' ',10(f4.2,2x))
420     format(' ',e10.4)
422     format(e10.4)

        close(1)
        close(2)
        close(3)
        close(4)
        close(11)

        stop
        end


          subroutine geom(r,g,cal,sal,cbeta,sbeta)

          real r,g,cal,sal,cbeta,sbeta
          real ss,cc,oldcal,oldsal,oldcbeta,oldsbeta

c         ********************************************************
c         * 'Sal' and 'cal' are the sine and cosine respectively of *
c         * the zenith angle in the phantom system. 'Sbeta' and    *
c         * cbeta are the sine and cosine respectively of the azi- *
c         * muth angle in the phantom system.                      *
c         ********************************************************

          oldsal=sal
          oldcal=cal
          oldcbeta=cbeta
          oldsbeta=sbeta
          cal=cal*cos(g)+sal*sin(g)*cos(r)
          if (abs(cal) .ge. 1.0) then
            cal=1.0*sign(1.0,cal)
            sal=0.0
```

```
            cbeta=cos(r)
            sbeta=sin(r)
            go to 400
          end if
          sal=sqrt(1.0-cal**2)
          if (oldsal .eq. 0.0) then
            cbeta=cos(r)
            sbeta=sin(r)
            go to 400
          end if
          ss=sin(g)*sin(r)/sal
          cc=(cos(g)-oldcal*cal)/oldsal/sal
          if (abs(ss) .ge. 1.0) ss=1.0*sign(1.0,ss)
          if (abs(cc) .ge. 1.0) cc=1.0*sign(1.0,cc)
          cbeta=cc*oldcbeta-ss*oldsbeta
          sbeta=ss*oldcbeta+cc*oldsbeta
          if (abs(cbeta) .ge. 1.0) cbeta=1.0*sign(1.0,cbeta)
          if (abs(sbeta) .ge. 1.0) sbeta=1.0*sign(1.0,sbeta)
400       continue

          return
          end



      subroutine impulse

      real en(36),spectr(90,36)
      real xnrg(36),mu(36),sig(36),local
      integer i,j
      real nteract(36),ncomp(36),npp(36)
      real nrgmax,sum,que(10),q
      real kinrg(20),nrgdif,a,b,c,dsigdt(20),arg
      real theta(20),v,vee,g1,g2,g(20),nbin,angle,prob
      integer binang,binum,vint

      common /blk1/xnrg,en,mu,sig,local,spectr,que

c     ***********************************************************************
c     * The following statements determine the number of photons that       *
c     * interact in the phantom slice and the number due to the Compton     *
c     * and pair production interactions in each photon energy bin.         *
c     ***********************************************************************

      do 5 i=1,90
        do 5 j=1,36
5         spectr(i,j)=0.0
      local=0.0
      do 40 i=1,36
        q=en(i)*exp(-mu(i)*.001)
        nteract(i)=en(i)-q
        en(i)=q
        ncomp(i)=sig(i)/mu(i)*nteract(i)
        npp(i)=2*(nteract(i)-ncomp(i))

c     ***********************************************************************
c     * The following statements generate the electrons-set-in-motion       *
c     * due to the Compton interaction.                                     *
c     ***********************************************************************

        nrgmax=(2*xnrg(i)/.511)*xnrg(i)/(2*xnrg(i)/.511+1)
```

```
            sum=0.0
            do 10 j=1,20
              kinrg(j)=(floatj(j)-.5)*nrgmax/20.0
              nrgdif=xnrg(i)-kinrg(j)
              a=(.511*kinrg(j)/(xnrg(i))**2)**2
              b=2*(nrgdif/xnrg(i))**2
              c=((kinrg(j)-.511)**2-.261)*nrgdif/(xnrg(i))**3
              dsigdt(j)=(a+b+c)/nrgdif**2
              sum=sum+dsigdt(j)
              arg=(nrgmax-kinrg(j))*(2*xnrg(i)/.511+1)/kinrg(j)
              theta(j)=57.296*atan(sqrt(arg)/(1+xnrg(i)/.511))
10          continue
            do 12 j=1,20
              dsigdt(j)=dsigdt(j)/sum
              nbin=dsigdt(j)*ncomp(i)
              binang=jifix(theta(j)*.2)+1
              if (kinrg(j) .lt. .2) then
                local=local+nbin*kinrg(j)
              else
                binum=jifix(kinrg(j)*5.0)
                spectr(binum,binang)=spectr(binum,binang)+nbin
              end if
12          continue

c           ***************************************************************
c           * The following statements generates the electrons-set-in-motion *
c           * due to the pair production interaction.                       *
c           ***************************************************************

            nrgmax=xnrg(i)-1.022
            sum=0.0
            if (npp(i) .gt. 0) then
              do 15 j=1,20
                kinrg(j)=(float(j)-.5)*nrgmax/20.0
                v=(kinrg(j)+.511)/xnrg(i)
                vee=1-v
                g1=v**2+vee**2+2.0*v*vee/3.0
                g2=alog(2.0*xnrg(i)*v*vee/.511)-.5
                g(j)=g1*g2
                sum=sum+g(j)
                vint=jifix(v*10.0)+1
                theta(j)=57.296*que(vint)*alog(xnrg(i)/.511)*.511/xnrg(i)
15            continue
              do 17 j=1,20
                g(j)=g(j)/sum
                nbin=g(j)*npp(i)
                binum=jifix(kinrg(j)*5.0)
                do 17 binang=1,36
                  angle=floatj(binang)*.08727-.04363
                  prob=.06963/theta(j)*exp(-(angle/theta(j))**2/2.0)
                  spectr(binum,binang)=spectr(binum,binang)+nbin*prob
17            continue
              end if
40          continue
            return
            end

            subroutine assign

            integer i,j,k,kp,dk
            real zs,z,dosefrac,ep,dose(200)
```

```
      common /blk2/zs,z,ep,dose

c     ************************************************************************
c     * The fractions of dose to be assigned to all elements traversed       *
c     * are calculated.                                                      *
c     ************************************************************************

      k=10.0*zs
      kp=10.0*(zs-z)
      if (k .lt. 0) then
        do 5 i=1,kp
5         dose(kp+1-i)=dose(kp+1-i)-ep/z/10.0
        dose(kp+1)=dose(kp+1)+ep*((z-zs)+floatj(kp)/10.0)/z
        go to 55
      end if
      dk=k-kp
      j=0
      if (jiabs(dk) .gt. 1) then
        j=jiabs(dk)-1
        do 10 i=1,j
10        dose(kp+1+sign(i,dk))=dose(kp+1+sign(i,dk))+abs(ep/10.0/z)
      end if
      if (dk) 40,45,50
40      dosefrac=(zs-floatj(k+1)/10.0)/z
        dose(k+1)=dose(k+1)+ep*dosefrac
        dose(kp+1)=dose(kp+1)+ep*(1-floatj(j)/10.0/z-dosefrac)
        go to 55

45      dose(k+1)=dose(k+1)+ep
        go to 55

50      dosefrac=(zs-floatj(k)/10.0)/z
        dose(k+1)=dose(k+1)+ep*dosefrac
        dose(kp+1)=dose(kp+1)+ep*(1-floatj(j)/10.0/z-dosefrac)

55    continue
      return
      end
```

Variable Documentation For Buildup3.For

Main Program

Integer
i,j,l,p, Dummy indices.
ii, Random number seed.
kay, Slab number (1 is the top slab) in which the photon beam interacts .
nerg, Energy parameter specifying locations in look-up tables.

Real
tha(179), A look-up array storing the scattering power of water in radian**2/(cm**2/g).
stop(179), A look-up array storing the stopping power of water in MeV/(cm**2/g).
xnrg(36), An array storing the photon bin energy.
en(36), The normalized number (in %) of photons in the bin.
mu(36), The total attenuation coefficient for water.
sig(36), The total Compton absorption coefficient for water.
que(10), Stearn's coefficients used in the determination of pair production electron trajectory.
gaus(100), Values of the inverse of erf(x).
cay, Represents the fractional amount of energy retained by the electron after each step.
dose(200), The accumulated dose received by the slab.
local, Dose deposited in the slab by electrons set in motion with an energy < 0.2 MeV.
eo, The initial energy of the electrons.
e, The energy of the electron.
ang, The zenith angle (degrees) at which the electrons are set in motion.
spectr(90,36), Generated by Subroutine Impulse, this array contains the number of electrons set in motion as a function of energy (90 bins) and zenith angles (36 bins).
zs, The depth of penetration into the phantom.
cal, The cosine of the zenith angle in the phantom coordinate system.
sal, The sine of the zenith angle in the phantom coordinate system.
r, The azimuth scattering angle (radian) in the electron frame.
cbeta, The cosine of the azimuth angle in the phantom coordinate system.
sbeta, The sine of the azimuth angle in the phantom coordinate system.
ep, The energy absorbed by the phantom in a step.
pl, The path length (g/cm**2) travelled by the electron during the step.
g, The zenith scattering angle (radian) in the electron frame.
z, The change in the penetration during the step.
max, The maximum dose received by the phantom.

Subroutine Geom (Variables listed only where different from the Main Program.)

Real
oldsal, The value of sal at the end of the previous step.

oldcal, The value of cal at the end of the previous step.
oldcbeta, The value of cbeta at the end of the previous step.
oldsbeta, The value of sbeta at the end of the previous step.
ss,cc, Parameters used to simplify geometric calculations.

Subroutine Impulse (Variables listed only where different from the Main Program.)

Integer
binang, Parameter specifying angle bin.
binum, Parameter specifying energy bin.
vint, Parameter used to specify Stearn's coefficient.

Real
q, The number of photons transmitted through the slab.
nteract(36), The total number of photons in the bin interacting in the slab.
ncomp(36), The number of electrons set in motion by photons in the bin that interact in the slab due to the Compton effect.
npp(36), The number of electrons or positrons set in motion by photons in the bin interacting in the slab due to pair production.
nrgmax, The energy that is available to transfer to charged particles.
sum, Sum of the cross-section parameters. Used for normalization.
kinrg(20), Electron kinetic energy.
nrgdif, Difference between photon and electron kinetic energy.
a,b,c, Terms used to calculate the parameter proportional to the Klein-Nishina differential cross-section with respect to electron energy.
dsigdt(20), A parameter proportional to the Klein-Nishina differential cross-section.
arg, The argument used to simplify the calculation of recoil electron zenith angle for the Compton effect.
theta(20), The charged particle recoil zenith angle.
nbin, Product of normalized cross-section and number of charged particles set in motion.
v, Ratio of total electron energy to photon energy.
vee, Ratio of difference between total electron energy and photon energy compared to photon energy.
g1,g2, Terms used to calculate the parameter proportional to the pair production differential cross-section with respect to charged particle energy.
g(20), A parameter proportional to the pair production differential cross-section.

Subroutine Assign (Variables listed only where different from the Main Program)

Integer
k, The slab number (counting from the top down; the first slab is labelled 0) the electron is in at the end of the step.
kp, The slab number the electron was in at the end of the previous step.
dk, The number of slab boundaries crossed.

Real
dosefrac, The fraction of dose deposited to slabs across boundaries.

5.7 Appendix 7 Listing and Documentation For 'Normdist.For'

```
      program normdist

c     ************************************************************************
c     *  This program calculates erf(x) using a modified approximation of the *
c     *  formalae listed in Dwight's Tables Of Integrals And Other            *
c     *  Mathematical Data page 136.                                          *
c     ************************************************************************

      integer*4 factor
      do 10 tea=0.0001,2.6,0.0001
        n = 1
        sum = 0.0
        test = 1.0
        do 9 while (test.ge.0.0001)
          term=(-1)**(n-1)*(tea**n-1)/n*factor(n-1)
          sum=sum+term
          test=term/sum
9         n=n+1
        sum=sum/1.25331
10      print 11,tea,sum
11      format (f8.5,10x,f8.5)
      stop
      end


      function factor (i)

c     ************************************************************************
c     * The subroutine Factor calculates the factorial of an integer.        *
c     ************************************************************************

      integer factor
      factor=1
      if (i.le.1) return
      do 13 j=2,i
13      factor=factor*j
      return
      end
```

5.8 Appendix B Listing and Documentation For 'Addose.For'

```
      program addose

c     ********************************************************************
c     * Addose.for calculates the dose as a function of depth in a       *
c     * phantom from electrons set in motion in 0.1cm slabs. The photon   *
c     * energy fluence is attenuated exponentially. The result is the    *
c     * broad beam TMR build-up values at 0.1cm intervals of depth.      *
c     ********************************************************************

      integer i,j,k
      real dose(100),max,adose(100)

      open(unit=1,status='old',file='dose.dat')
      open(unit=2,status='new',file='addose.dat')

      do 10 i=1,100
10      read(1,100) k,dose(k)

c     ********************************************************************
c     * The following statements attenuates the photon energy fluence    *
c     * at the depth at which the electrons are being set in motion.     *
c     * The attenuation coefficient is 0.029/cm which is the average     *
c     * energy absoption coefficent at 6 MV.                             *
c     ********************************************************************

      do 45 i=1,100
        do 40 j=1,i
          adose(i)=adose(i)+dose(j)*exp(-.0290*(float(i+j-1)*.1-.05))
40        continue
45      print*,'i=',i,'adose(i)=',adose(i)
      max=0.0
      do 50 k=1,100
50      if (adose(k) .gt. max) max=adose(k)
      do 60 k=1,100
60      write(2,100)k,adose(k)/max

100   format(' ',i3,2x,f6.2)

      close(1)
      close(2)
      stop
      end
```

[Reprinted from RADIOLOGY, Vol. 144, No. 2, Pages 403-409, July, 1982.]
Copyright 1982 by the Radiological Society of North America, Incorporated

Contamination of a 15-MV Photon Beam by Electrons and Scattered Photons[1]

Thomas R. Mackie, B.Sc.
John W. Scrimger, Ph.D.

The 15-MV photon beam of a linear accelerator (Siemens Mevatron 20) was studied for electron and scattered photon contamination. The surface dose, attributable almost entirely to contamination electrons, has a Gaussian lateral distribution, a linear dependence on field width for square fields, and an inverse square dependence on distance from the bottom of the fixed head assembly. This geometrical dependence is consistent with the proposal that the field flattening filter is the main source of electron contamination when accessories are absent. A tissue-maximum-ratio curve in the build-up region for the electron and photon contamination was produced utilizing the linearity of dose with respect to field width. The derived contamination curve inside was similar to the measured build-up curve outside the field. The primary photon component, obtained by subtracting the contaminant contribution, showed no dependence on field size, source-to-probe distance, or presence of accessories.

Index terms: Electrons • Linear accelerator • Radiations, measurement • Therapeutic Radiology, instrumentation

Radiology 144: 403–409, July 1982

AN understanding of the role of electron and secondary photon contamination in megavoltage therapy machines is required to characterize dosimetry in the build-up region. Clinically, high-energy x-ray build-up produces a skin-sparing effect and contamination tends to reduce this effect.

Electron contamination has been identified as the major source of dose at the surface of a phantom for ^{60}Co (1, 2) and a wide range of accelerator energies (1–7). Most of these studies have employed thin-window parallel-plate chambers to measure the surface dose. Padikal and Deye, and Biggs and Ling, have measured the electron contamination directly by sweeping the electrons magnetically from the beam (3, 4).

There has been widespread disagreement concerning the origin of the contamination electrons. The collimator jaws (1–3, 5), field flattening filter (1, 2), and intervening air between the source and detector (2, 8) have been cited as possible sources. It is generally agreed that the presence of assessories in the field of the beam will increase the magnitude of electron contamination (1, 5, 6, 8–10). Bagne as well as Nilsson and Brahme, have derived expressions for dose in the build-up region by assuming that the surface dose is due to the presence of contamination electrons (8, 11).

Although electrons provide most of the contamination at the surface, contamination should be defined to include secondary photons generated outside the phantom. Throughout this paper the contamination component of the beam is defined as electrons and scattered photons produced by interactions of the primary photon beam with material outside the phantom. The primary photon beams are photons emerging through the collimator which have been produced by bremsstrahlung interactions in the target and modified by the fixed head assembly (Fig. 1).

I. OPEN-FIELD BUILD-UP CURVES

Materials and Methods

Build-up curves were measured for a 15-MV photon beam from a Siemens Mevatron 20 linear accelerator. A schematic diagram of the beam defining head is shown in Figure 1. All measurements were made at constant source-to-probe distances (SPD) using 0.16-cm ($\frac{1}{16}$-in.) thick and 0.64-cm ($\frac{1}{4}$-in.) thick square polystyrene slabs as illustrated in Figure 2. The phantom slabs used in the determination of the open-field build-up curves each had a cross-sectional area of 625 cm^2.

The detector used was a Capintec 192A electrometer with a PS-033

[1] From the Physics Department, University of Alberta and Cross Cancer Institute, Edmonton, Alberta, Canada. Received July 24, 1981; accepted and revision requested Nov. 13; revision received Feb. 16, 1982.

Figure 1

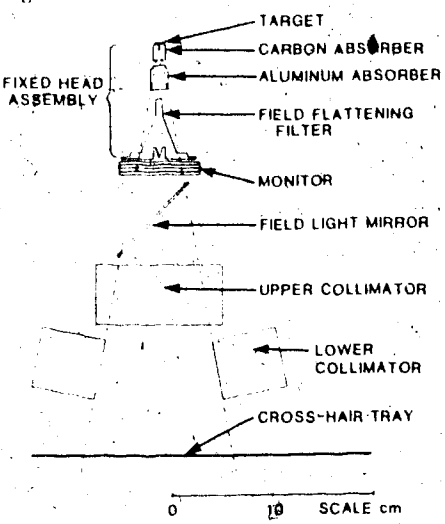

Diagram of the head assembly.

Figure 2

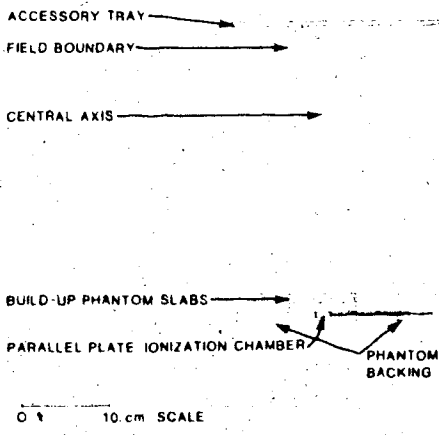

Diagram of the experimental arrangement. When determining the contamination depth dose, the phantom slab cross-sectional area was 100 cm^2 and the slabs were always within the field boundary. The phantom slab cross-sectional area for all other measurements was 625 cm^2.

thin-window parallel-plate ionization chamber with an effective volume of 0.5 ml. The entrance window was aluminized polyester film 0.5 mg/cm^2 thick. The tissue maximum ratio (TMR) is defined to be the dose at some depth, d, in the phantom normalized to the maximum dose occurring at a depth d_{max}, for the same field area A and energy E.

$$\text{TMR} = \frac{\text{Dose}\,(d,A,E)}{\text{Dose}\,(d_{max},A,E)} \qquad [1]$$

Throughout this paper the field size is referred to as the lateral field dimensions defined at 100 cm. Only square fields were used.

Results

The central axis build-up curves for various field sizes are illustrated in Figure 3. These build-up curves demonstrate a dependence on field size. The TMRs for all depths below d_{max} increase with increasing field size. The greatest relative difference between these curves occurs at or near the surface.

Discussion

The spread in the curves is greater than can be expected from lateral scattering of photons and electrons generated in the phantom. Indeed, in the absence of backscatter or contamination, the TMR at the surface for all field sizes should approach zero. The field size dependence and the finite surface dose can be attributed to contamination since backscatter is negligible at the energy investigated.

II. ACCESSORY BUILD-UP CURVES

Materials and Methods

Various thicknesses of Lucite (density 1.18 g/cm^3) alone or Lucite and lead (density 11.4 g/cm^3) slabs were placed in the beam to determine their effect on the build-up curves. The distal surface of the slabs was placed at the accessory tray holder position 56 cm from the source. In all cases a Lucite surface was distal to the source. The build-up curves were measured as in Part I.

Results

Figures 4 and 5 show the build-up at an SPD of 100 cm and 75 cm, respectively. The field size in both cases is 30 cm × 30 cm. When accessories are placed in the field at the tray holder position, a larger TMR for all depths less than d_{max} is observed. There is also a shift in the point of d_{max} to shallower depths. This is more pronounced at SPD = 75 cm (Fig. 5). There is virtually no difference in the build-up curves between a 3.2-cm (1¼-in.) Lucite accessory and a 0.30-cm lead slab on top of a 0.64-cm lucite accessory.

At smaller SPDs, there is a greater difference between the TMR with and without accessories. Therefore, as the distance to the source of contamination decreases, the dose increases. The TMR for SPD = 75 cm (Fig. 5) is greater than that for SPD = 100 cm (Fig. 4) at all depths and for all accessory conditions.

Figure 3

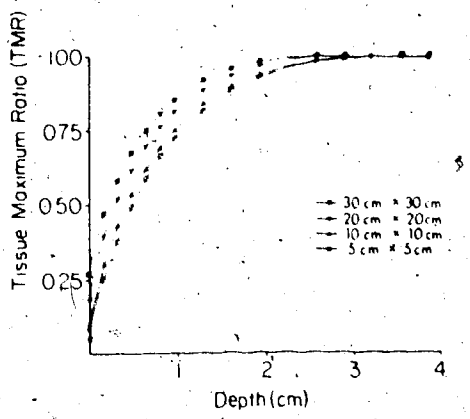

Open-field build-up curves at 100-cm source-probe distance for various field sizes.

Figure 4

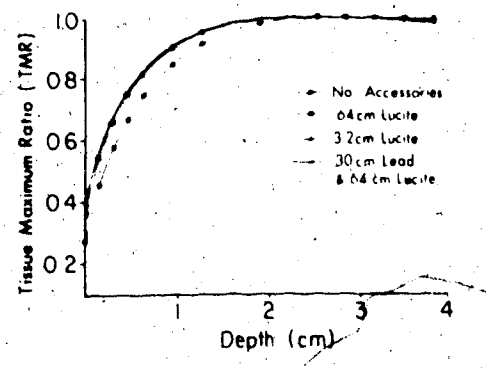

Effect of accessories on the build-up curves for a field size of 30 cm × 30 cm. Source-probe distance = 100 cm.

Figure 5

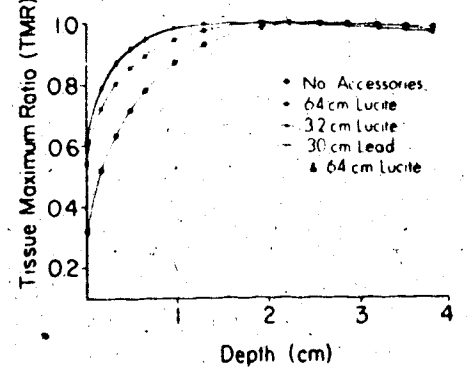

Effect of accessories on the build-up curves for a field size of 30 cm × 30 cm. Source-probe distance = 75 cm.

The difference between the TMR as a function of SPD is most pronounced at the surface.

Discussion

As the thickness of accessory increases, the amount of contamination it produces increases. However, contamination produced at shallow depths within the accessory is shielded by the deeper layers. At a thickness equivalent to 3.2 cm (1¼ in.) of Lucite, there is a balance between production and absorption of contamination.

These observations agree qualitatively with those of Velkley *et al.* (5) for 25 MV x-rays collimated to a 10-cm × 10-cm field and Gray (1) for 4 MV x-rays.

Figure 6

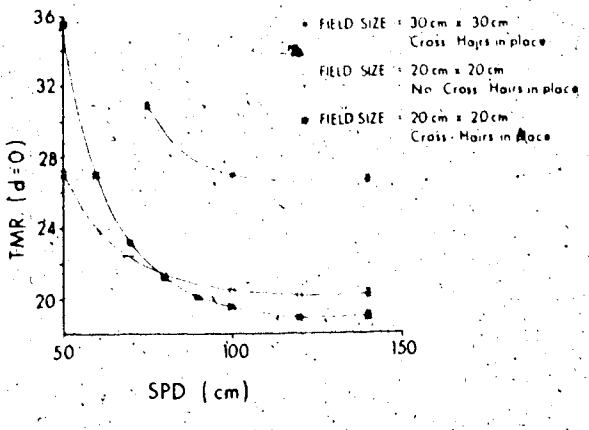

Distribution of the surface dose as a function of source-probe distance. *TMR* = tissue maximum ratio.

III. DISTANCE DISTRIBUTION OF SURFACE DOSE

Materials and Methods

The surface maximum ratio is defined as the TMR measured with the chamber at the surface (*i.e.* $d = 0$). When at the surface, the chamber used has a sufficiently thin window to ensure that the build-up depth is approximately zero (5 μm polystyrene equivalent). The window thickness has an equivalent mass stopping power of less than one centimeter of air. Only very low energy photons have a reasonable probability of interacting with such a window. In order to be detected, such photons have to be produced within a few centimeters of the chamber, otherwise they will be rapidly attenuated in air. Primary photons of low enough energy to interact with the window are completely attenuated when the beam emerges from the beam defining head. Therefore, most of the dose at the surface is attributable to contaminant electrons.

Results

Figure 6 illustrates that the surface maximum ratio in the open beam increases rapidly as the SPD decreases for both 20-cm × 20-cm and 30-cm × 30-cm fields.

The curves for a collimated field size of 20 cm × 20 cm show the effect of a thin accessory. The Siemens Mevatron 20 is equipped with a removable, 1-mm thick, Lucite cross-hair tray which can be inserted at 40 cm from the source. When the SPD is less than 75 cm, the surface dose with the cross-hairs in place is greater than when it is removed. However, the cross-hairs, when in place, reduce the surface dose in the clinical region of SPD greater than 75 cm.

Discussion

The reduction in dose when the cross-hairs are in place is a notable exception to previous observations that accessories in the field increased the surface dose. If it is assumed that all the electrons set in motion in the thin Lucite accessory by the incident photon beam emerge, they will be fewer than the number of incident electrons stopped. This is because the probability of production of electrons increases with increasing slab thickness whereas the survival of electrons already produced decreases with increasing thickness.

As the SPD increases, the volume of air between the target and probe increases. For ^{60}Co, Nilsson and Brahme (8) predicted an increase in dose as a function of SPD due to ^{60}Co photon interactions with air. In these experiments, the reverse appears to be the case and a decrease in dose as a function of increasing SPD has been observed. This implies that at 15 MV the interaction of the primary photon beam with air is not the major source of electron contamination.

The surface maximum ratio is normalized to the dose measured at d_{max} within a polystyrene phantom. The maximum dose in a phantom is due almost entirely to primary photons for which the variation with distance falls off as $1/(\text{SPD})^2$. However, the electron contamination does not necessarily arise at the source of primary photons. Instead of normalizing the surface dose at a given SPD to the dose at d_{max}, each surface dose at the same SPD is normalized to the dose measured at a convenient point inside a phantom using a standard field size and photon SPD. The normalized dose is defined as:

$$\text{ND} = \frac{\text{Dose to point at arbitrary } d, \text{ SPD, field size,}}{\text{Dose to standard point}} \qquad [2]$$

The standard point chosen was at the d_{max} point at SPD = 100 cm and field size = 10 cm × 10 cm.

The apparent source of contamination electrons can be located assuming that it is a point source and there is no attenuation of electrons by air. Therefore, the normalized dose at the surface is directly proportional to the inverse square of the distance to the source of the electron contamination, or:

$$\text{ND}(d = 0) \propto \frac{1}{(\text{SPD} - d_0)^2} \qquad [3]$$

where d_0 is the distance of the source of contamination electrons below the primary photon source.

Figure 7 is a graph of the inverse square root of the normalized surface dose *versus* SPD. The graph yields a straight line except for very large SPDs. Therefore, the source must be small and the inverse square approximation valid for SPDs less than 120 cm. The a-intercept of the graph yields a dis-

Figure 7

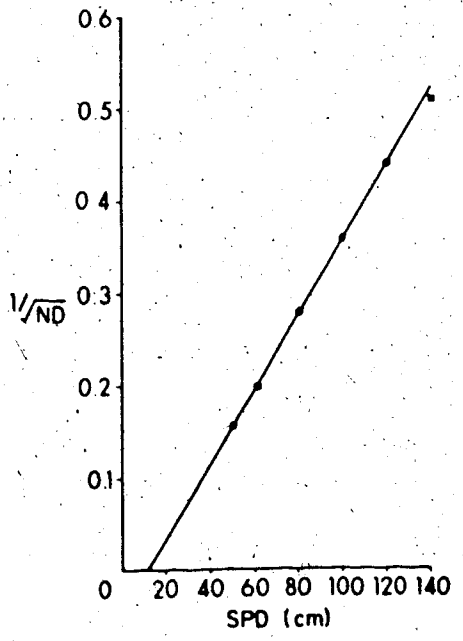

Graph illustrating the inverse square dependence of the surface dose (ND) on the distance to the source of contamination (SPD)

Figure 8

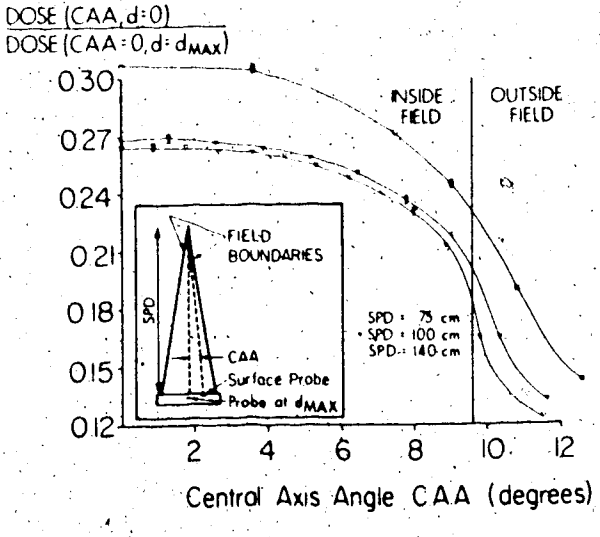

The Gaussian distribution of the surface dose. The inset is a schematic diagram of the experimental arrangement

tance d_0 of 12 cm below the primary source of photons. This corresponds approximately to the position of the bottom of the fixed head assembly which consists of the field flattening filter and the beam monitor. The bottom surface of the field flattening filter is 3.1 cm wide; at distances greater than 50 cm this subtends an angle no larger than 3.5°, which approximates a point source.

The field flattening filter has a maximum thickness of 5.4 cm of stainless steel, which represents the largest interaction cross-section of any component in the beam defining head. The beam monitor is the last major component completely in the beam before the phantom, so it is likely to contribute to the dose due to contaminant electrons.

IV. GAUSSIAN LATERAL DISTRIBUTION OF SURFACE DOSE

Materials and Methods

The magnitude of surface dose as a function of lateral displacement from the central axis was measured for several SPDs. The central axis angle (CAA) was defined as the angle between the central axis and a line joining the probe to the apparent source of electrons. This established parameters for the lateral direction in order to compare the distribution at various SPDs (Fig. 8, inset). In each case, the surface dose at any CAA and SPD is normalized to the dose at d_{max} on the central axis (CAA = 0).

Results

The curves in Figure 8 approximate a Gaussian distribution. At all points across the field, a smaller SPD results in a larger electron contamination dose.

Discussion

The surface dependence measured along the central axis is in agreement with the finding at all points across the field that a larger electron contamination dose is the result of a smaller SPD. Both the lateral distribution and the dependence on the distance from the source of the electron contamination agree with the work of Almond (12).

V. BUILD-UP CURVES OUTSIDE THE FIELD

Materials and Methods

The primary photon dose outside the field boundary is very small (approximately 1% of the central axis dose at d_{max}). Contamination electrons and scattered photons provide the largest contribution to the dose outside the field. This was studied experimentally. In order to get as close as possible to the field boundary, the probe was placed near the edge of the phantom (Fig. 9). The phantom was tilted at an angle[2] so that its surface would not move closer to or farther from the field boundary with the addition of build-up layers. This also reduced the number of particles incident at oblique angles upon the phantom.

Figure 9

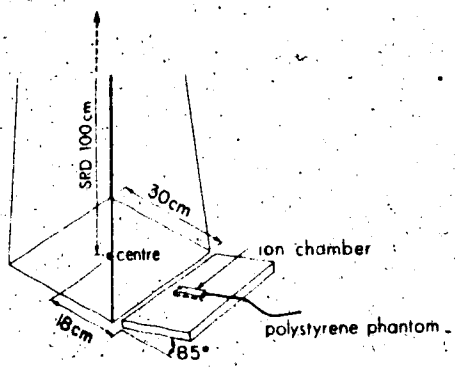

Diagram of the experimental arrangement to determine the build-up curve outside the field.

[2] Angle of tilt = $\tan^{-1}\left(\frac{\text{field width}}{2\,\text{SPD}}\right)$

Figure 10

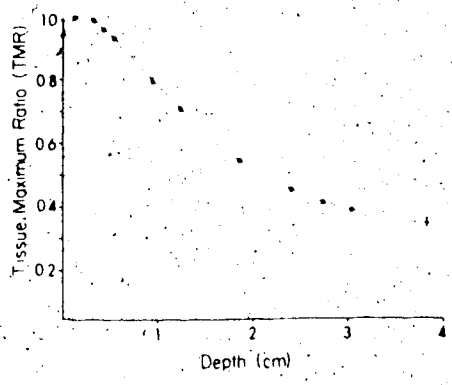

Build-up curve obtained 3 cm outside of a 30-cm × 30-cm field (see Fig. 9).

Figure 11

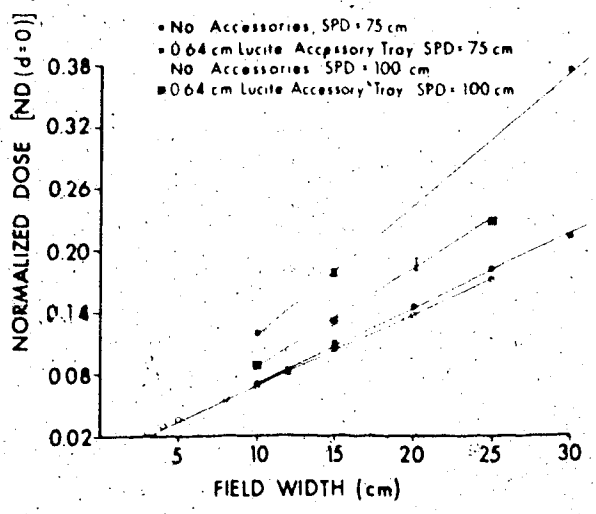

Linearity of the surface dose with respect to field width under a variety of conditions.

Results

Figure 10 illustrates the depth dose curve 3 cm outside a 30-cm × 30-cm field. The TMR has a peak at a shallow depth (1–2 mm), then falls off rapidly at depths beyond about 2 cm.

Discussion

The general shape of the curve agrees with the work of one of the authors (10) for 8-MV x-rays. This curve represents the contamination depth-dose due to electrons and scattered photons beyond the field edge. The peak at shallow depth followed by a rapid fall-off in dose is typical of the depth-dose curve for electrons. The relatively slow fall-off at depths beyond 2 cm is due in large part to scattered photons.

VI. LINEARITY OF DOSE *vs.* FIELD WIDTH

Materials and Methods

The dose as a function of field width was measured for a number of depths with the limited polystyrene phantom of the type illustrated in Figure 2. Since there was unit density material on top of the ion chamber, it could not be assumed that all of the contamination contributing to the dose was due to electrons.

The phantom was placed completely within the field so an increase in detected signal due to increasing field size could only be attributed to beam contamination. To obtain the dose as a function of depth for as many field widths as possible, the phantom lateral dimensions were kept as small as possible (*i.e.*, 10 cm × 10 cm), which in turn dictated a minimum field size used in the determination of the contamination depth-dose curve of 15 cm × 15 cm. The maximum square field size attainable for the machine studied was 30 cm × 30 cm. These field sizes defined the range of the study.

Results

The normalized dose (as defined by Equation 2) for $d = 0$ is plotted as a function of field width in Figure 11. Under a wide range of conditions there is a linear increase in the surface dose with respect to field width. Note that either decreasing the SPD or placing accessories in the field increases the slope. Since the surface dose for any given field size is proportional to the slope of the line, the slope is also a measure of the electron contamination, but with the advantage that it is not dependent on the field width.

Figure 12 illustrates that for various depths less than d_{max} there is a linear dependence of dose on field width. Qualitatively, the slope is greater at shallow depths than at deeper depths. As has already been seen for the dose at the surface, the slope of normalized dose *versus* field width is a measure of the magnitude of contamination penetrating to the depth specified. Therefore, there is a greater magnitude of contamination at shallow depths.

Figure 12

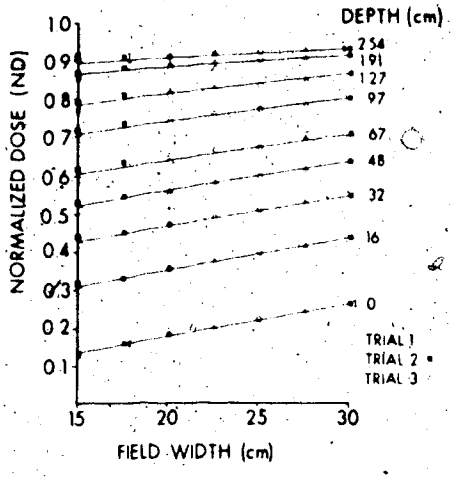

The increase in the normalized dose with respect to field width for various depths within the phantom. The increase can only be attributed to contamination because the phantom (lateral dimensions = 10 cm × 10 cm) was completely contained within the field boundary.

Discussion

A number of authors (3, 5, 6, 8) have commented on the dependence of the surface dose on the square root of field area both with and without accessories. Velkley *et al.* (5) normalized the surface dose at each field size to the dose at d_{max} for the same field size. However, since the dose at d_{max} increases with field size, such a plot would not unambiguously express the dependence of surface dose on field size. The concept of normalized dose, however, eliminates the ambiguity because the dose is nor-

malized to a quantity that does not change as a function of field size.

The magnitude of contamination has been shown to be proportional to the slope of normalized dose plotted against field width. To obtain a depth-dose profile for the contaminant contribution, the surface slope is set equal to the surface dose. This establishes a conversion between the slope at some depth and the dose due to contamination at the same depth. An assumption is made, as was previously discussed, that the dose measured by a thin-window ion chamber without any build-up is due to contamination electrons.

The primary photon contribution is obtained by subtracting the contamination component from the total build-up curve. Figure 13 shows the separate contribution from the contamination and primary photon components of the total build-up curve for a 20-cm × 20-cm field. The contaminant contribution curve dominates the exposure dose at depths less than about 1 mm. At depths near d_{max}, the contamination contribution is less than 5% of the primary photon component.

If the contaminant contribution is renormalized to its own maximum, the depth-dose profile becomes more evident. Figure 14 shows the renormalized contaminant contribution curve. The peak in this depth dose curve occurs at about 1–2 mm. There is a rapid fall-off at depths slightly greater than the d_{max}. At depths greater than a couple of centimeters, the curve exhibits a slow fall-off with depth. This curve is similar qualitatively to the build-up curve measured outside the field (Fig. 10).

Since the contamination contribution was obtained by attributing the increase in dose to an increase in field size, the primary photon component should be independent of field size. TABLE I confirms this. Thus, the magnitude of contamination depends on the field size but the spectral characteristics of the contamination do not.

The derived primary photon TMRs in TABLE I are independent of field size. TMR was not, however, designed to be independent of field size for conditions other than an open field and SPD = 100 cm. The primary photon contribution is independent of SPD and the presence of accessories. The primary photon build-up curves for various conditions of SPD and accessory states are shown in TABLE II. The conditions of SPD were tested for 75 cm, 100 cm, and 140 cm, whereas the electron contamination curve was derived for SPD = 100 cm. The independence of the primary photon build-up curve for these wide-ranging conditions illustrates that contamination accounts for the difference in depth-dose curves encountered. By definition, the primary photon contribution to the total build-up dose is due to that portion of the beam that does not interact before reaching the phantom. Changes in the primary photon build-up could only be due to changes in the phantom size, density, or configuration.

Figure 13

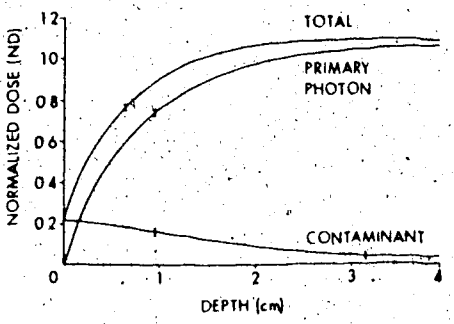

The contributions of the contaminant and primary photon components to the total build-up curve for a field size of 20 cm × 20 cm.

Figure 14

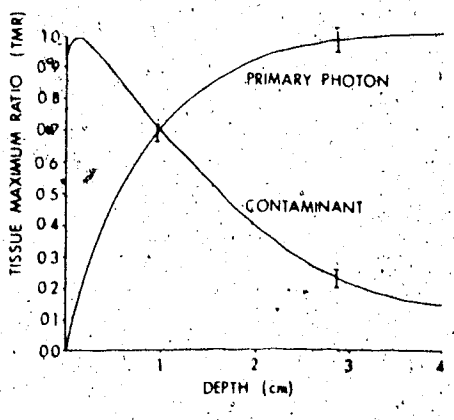

The contaminant and primary photon components in Figure 13 renormalized to their separate maxima.

TABLE I: Primary Photon Tissue Maximum Ratios for Various Field Sizes (No Accessories, Source–Probe Distance = 100 cm)

No. of Slabs	Depth (cm)	Tissue Maximum Ratio for Field Sizes: 5 cm × 5 cm	10 cm × 10 cm	15 cm × 15 cm	20 cm × 20 cm	25 cm × 25 cm
0	0.00	0.00	0.00	0.00	0.00	0.00
1	0.16	0.19	0.19	0.18	0.19	0.18
2	0.32	0.33	0.33	0.33	0.33	0.33
3	0.48	0.44	0.44	0.44	0.44	0.44
4	0.64	0.54	0.54	0.54	0.54	0.54
6	0.95	0.68	0.68	0.69	0.69	0.69
8	1.27	0.79	0.78	0.79	0.79	0.79
12	1.91	0.91	0.91	0.91	0.91	0.91
16	2.54	0.97	0.97	0.97	0.97	0.97
20	3.18	1.00	0.99	0.99	0.99	0.99
24	3.81	1.00	1.00	1.00	1.00	1.00

TABLE II: Primary Photon Tissue Maximum Ratios under Various Conditions (Field Size = 30 cm × 30 cm)

No. of Slabs	Depth (cm)	Tissue Maximum Ratios: SPD = 75 cm No Access.	SPD = 100 cm No Access.	SPD = 140 cm No Access.	SPD = 100 cm 0.64-cm LTA*	SPD = 100 cm 3.2-cm LTA*
0	0.00	0.00	0.00	0.00	0.00	0.00
1	0.16	0.19	0.19	0.18	0.19	0.18
2	0.32	0.34	0.33	0.32	0.33	0.33
3	0.48	0.45	0.44	0.43	0.45	0.45
4	0.64	0.54	0.54	0.53	0.56	0.55
6	0.95	0.68	0.68	0.67	0.70	0.69
8	1.27	0.78	0.78	0.77	0.80	0.79
12	1.91	0.90	0.90	0.90	0.91	0.91
16	2.54	0.97	0.96	0.96	0.97	0.98
20	3.18	0.99	0.99	0.99	1.00	1.00
24	3.81	1.00	1.00	1.00	1.00	1.00

* LTA = Lucite tray accessory

CONCLUSIONS

The contamination depth-dose curve (Fig. 14) and the build-up curve outside the field boundary (Fig. 10) have similar shapes. The surface dose has been established as being due to contaminant electrons. The contaminant electrons evident at the surface must penetrate to some depth beneath the phantom. The peaks and rapid fall-off at shallow depths illustrated in Figures 10 and 14 are characteristic of electrons. The slow fall-off at depths greater than 2 cm is probably due to scattered photon contamination. Thus, the contamination radiation appears to be a combination of an electron contribution primarily at shallow depths and photons contributing primarily at greater depths.

Figures 10 and 14 differ in shape due to a difference between the relative amount of contamination electrons and photons present inside and outside the field boundary. Figure 8 demonstrated a Gaussian lateral distribution of the surface dose. Consequently for a 30-cm × 30-cm field there were about 45% fewer electrons present at 18 cm from the central axis than were present at the central axis.

Although the contaminant electrons are produced by the fixed components in the beam defining head, the size of the collimator opening dictates the relative amount of electron contamination emerging from the beam defining head. Low energy electrons are scattered by air through wide angles. The product of mass angular scattering power, density, and the electron path length for low energy electrons in air is of the same order of magnitude as the central axis angle.[3] Therefore, the angle of an electron when emerging through the collimators is not critical in determining whether it will arrive at the detector. The greater the collimator opening, the greater the flux of contamination electrons arriving at the detector. It has been shown empirically that the magnitude of electron contamination reaching the detector at the central axis is directly proportional to field width for square fields.

The contamination attributable to photons was derived from the increase in the dose as a function of field width. Therefore, the amount of material with which the primary photons could have interacted to produce scattered photons must be dependent on field size. The surface area of the collimator faces and the amount of air in the field both increase with field size. The contamination dose due to photons and the surface area of the collimator faces are both approximately proportional to field width, so it is likely the contamination photons are photons scattered by interaction of the primary photon beam with the collimators.

The shift in d_{max}, especially when accessories are present in the beam, can be attributed to a greater magnitude of electron contamination. Since the depth-dose profile for the scattered photons is likely to be similar to the primary photon profile, they are unlikely to contribute significantly to the shift in d_{max}. The peak in the contamination curve due to electrons occurs at very shallow depths, so increasing the magnitude of electron contamination results in a d_{max} shift towards shallower depths. This also explains why the shift is accompanied by an increased surface dose. These findings agree with Biggs and Ling (4) who observed that a shift in d_{max} did not occur when electrons were swept from the beam.

Acknowledgment: This research was sponsored in part by the Alberta Heritage Foundation for Medical Research, the Provincial Cancer Hospitals Board (Alberta), the Alberta Division of the Canadian Cancer Society, and the Physics Department, University of Alberta.

Physics Department
Cross Cancer Institute
University of Alberta
Edmonton, Alberta
Canada T6G 1Z2

[3] For example Rossi (13) states that a 3-MeV electron in air has a mass angular scattering power of 0.602 radians^2-cm^2/g which, after passage through 100 cm of air, corresponds to a mean scattering angle of 16.0°.

References

1. Gray L. Relative surface doses from supervoltage radiation. Radiology 1973; 109: 437–442.
2. Jackson W. Surface effects of high-energy X rays at oblique incidence. Br J Radiol 1971; 44: 109–115.
3. Padikal TN, Deye JA. Electron contamination of a high-energy X-ray beam. Phys Med Biol 1978; 23: 1086–1092.
4. Biggs PJ, Ling CC. Electrons as the cause of the observed d_{max} shift with field size in high energy photon beams. Med Phys 1979; 6: 291–295.
5. Velkley DE, Manson DJ, Purdy JA, Oliver GD Jr. Build-up region of megavoltage photon radiation sources. Med Phys 1975; 2: 14–19.
6. Wu A. Effects of an acrylic resin tray on relative surface doses for 10 MV x-ray beams. Int J Radiat Oncol Biol Phys 1980; 6: 1257–1260.
7. Dawson DJ. Percentage depth doses for high energy x-rays. Phys Med Biol 1976; 21: 226–235.
8. Nilsson B, Brahme A. Absorbed dose from secondary electrons in high energy photon beams. Phys Med Biol 1979; 24: 901–912.
9. Gagnon WF, Grant W III. Surface dose from megavoltage therapy machines. Radiology 1975; 117: 705–708.
10. Scrimger J, Kolitsi Z. Scattered radiation from beam modifiers used with megavoltage therapy units. Radiology 1979; 130: 233–236.
11. Bagne F. A method for calculating megavoltage x-ray dose and dose parameters. Med Phys 1980; 7: 664–671.
12. Almond PR. Dosimetry considerations of electron beams. In: Kramer S, Suntharalingam N, Zinninger GF, eds. High-energy photons and electrons. New York: J Wiley and Sons, 1976: 129–168.
13. Rossi B. Radiation dosimetry: electrons with initial energies between 1 and 50 MeV. ICRU Report 24, 1972: p 13.

Preface

Volume 1 entitled, "Contamination of Megavoltage X-Ray Beams By Electrons And Scattered Photons", was originally written as a thesis for the partial fulfilment of a Master of Science degree. At the defense of the thesis in September of 1982, it was felt by the examining committee that Volume 1 should be used towards a Doctor of Philosophy degree.

Section 3, in Volume 1, addressed the problem of the transport of charged particles in the build-up region of a unit-density phantom. The committee felt that this Section provided a good foundation for a more complete study of the transport of charged particles generated by photon beams in an inhomogeneous medium. A decision was made to undertake this investigation to complete the thesis. Volume 2 contains the results of this study as well as a method to calculate the primary and scattered dose in heterogeneous media.

It was decided to break the thesis into two Volumes because Volume 1 is a self-contained study of photon beam contamination. The contents of Volume 2 are not referenced in Volume 1. For this reason, the Discussion, Conclusions and Appendices concerning contamination are left in Volume 1. However, in a number of instances, the reader of Volume 2 is referred to Volume 1, therefore, the pagination in Volume 2 is a continuation of Volume 1.

TABLE OF CONTENTS FOR VOLUME 2

Chapter — Page

5. INTRODUCTION TO RADIOTHERAPY DOSE COMPUTATION ... 257

5.1 Statement of Purpose 258
5.2 Electronic Equilibrium 262
5.3 Contour Corrections 273
5.4 Corrections For Tissue Heterogeneity 281

6. MODELLING DOSE USING THE EGS MONTE CARLO CODE ... 295

7. A CONVOLUTION METHOD OF CALCULATING DOSE 308

7.1 Introduction 309
7.2 Primary Dose Spread Arrays 311

7.2.1 Definition of a Primary Dose Spread Array 311
7.2.2 The Generation of Dose Spread Arrays Using the MOCA Monte Carlo Code 311
7.2.3 Results 321

7.3 Scatter Dose Spread Arrays 332
7.4 Convolution Dose Calculation in a Homogeneous Phantom 337
7.5 Extension to Heterogeneous Media 360
7.6 The Spatial Invariance of the Dose Spread Arrays 380
7.7 Comparison with Other Methods and Potential Improvements 384
7.8 Dose in a Non-Water-Like Heterogeneous Phantom 394

8. DISCUSSION AND CONCLUSIONS CONCERNING THE CONVOLUTION METHOD 397

8.1 Discussion 398
8.2 Conclusions 403

REFERENCES 406

APPENDICES 411

10. Listing of the MOCA Monte Carlo Code ... 412
11. Listing of the program Volve.for 429
12. Comparison of Heterogeneous Dose Spread Arrays Calculated by the Convolution Method and by the Monte Carlo Method 441

VITA 460

LIST OF TABLES FOR VOLUME 2

Table Page

20. Parameters for determining the effective attenuation coefficient for 15 MV x-rays 339

LIST OF FIGURES FOR VOLUME 2

Figure		Page
82.	The state of longitudinal equilibrium in a heterogeneous phantom	263
83.	Lateral electronic equilibrium in a homogeneous phantom	266
84.	Lateral electronic equilibrium in a heterogeneous phantom	268
85.	The experimental set-up to measure the inhomogeneity correction factor	270
86.	The correction factor, for the experimental set-up illustrated in Figure 85	271
87.	Geometry to take into account contour corrections	274
88.	The definition of the zero-area TAR and the scatter-air-ratio	278
89.	The geometrical parameters required for the Batho or power-law method	283
90.	An illustration of O'Connor's theorem	284
91.	In the equivalent TAR method, the 3-dimensional electron density information is "coalesced" into one cross-sectional slice	288
92.	The measurement of the perturbation of dose by a polystyrene annulus placed in a water tank	292
93.	The dose at point P gets a dose contribution from an annulus by "revolving" a pencil dose distribution about point P	298
94.	The measured TMR is compared to the EGS calculation of the TMR	299
95.	A comparison between pencil beam isodose curves in homogeneous and heterogeneous phantoms	302
96.	A comparison of measured inhomogeneity correction factors and ones calculated using the EGS Monte Carlo code	304
97.	A comparison between the calculated profiles of KERMA and dose for a heterogeneous and a homogeneous phantom	305

LIST OF FIGURES FOR VOLUME 2 (CONT'D)

Figure — Page

98. A comparison between dose and KERMA correction factors for the 15 MV spectrum and its spectral components 307

99. Primary photons interact in the interaction voxel and the charged particles set in motion are followed through the phantom 312

100. Flow chart for photon transport part of MOCA 314

101. Flow chart for the part of MOCA dealing with the type of photon interaction 315

102. Flow chart for the charged particle transport part of MOCA 316

103. The Compton differential cross-section as function of kinetic energy 318

104. The choice of the kinetic energy for a Compton recoil electron 319

105. The choice of the kinetic energy for a pair production charged particle set in motion 320

106. A comparison of components of the percent dose predicted by MOCA and EGS for Cobalt-60 photons 322

107. A comparison of components of the percent dose predicted by MOCA and EGS for 5 MeV photons 323

108. Primary dose spread arrays for 15 MV photons for gravimetric densities of 1.0, 0.8, and 0.6 when the voxel dimension is 1cm 324

109. Primary dose spread arrays for 15 MV photons for gravimetric densities of 0.4 and 0.2 when the voxel dimension is 1cm 325

110. Primary dose spread arrays for 6 MV and Co-60 photons 328

111. Primary dose spread array for 15 MV photons for a gravimetric density of 0.2 when the voxel dimension is 5cm 330

112. Truncated first scatter (TFS) dose spread array for 15 MV photons 334

Figure Page

113. Residual first and multiple scatter (RFMS) dose spread array for 15 MV photons 335

114. Illustration of the dose contribution from the interaction point of view 338

115. The variation of the effective attenuation coefficient as a function of depth 341

116. The variation of the measured effective attenuation coefficients as a function of nominal beam energy .. 342

117. Illustration of the dose contribution from the the dose deposition point of view 346

118. Measured and calculated TMR's for a 15 MV beam as a function of depth along the central axis 349

119. Measured and calculated percent depth-dose data for a 6 MV beam as a function of depth along the central axis 350

120. Measured and calculated dose profiles at dmax for a 15 MV beam 351

121. Dose profiles at dmax in homogeneous phantoms with various densities 352

122. The relative primary fluence profile for 15 MV beam wedges and the fluence profile used to obtain the calculated isodose curve in Figure 123 .. 354

123. The calculated isodose curve for the fluence profile shown in Figure 122 and the measured isodose curve for a 60 degree wedge for a 15 MV beam 355

124. The measured dose profile at a depth of 5 cm when a shield is placed in the 15 MV beam 357

125. The bar shield represented by three fields 359

126. Components of the percent depth dose in a homogeneous water phantom predicted by MOCA for a 6 MV beam 361

127. Components of the percent depth dose in a heterogeneous phantom predicted by MOCA for a 6 MV beam 362

Figure Page

128. Determination of the average density between the interaction and dose deposition voxels 364

129. Ray tracing is performed by sampling the density between the interaction and dose deposition voxels 366

130. Schematic representation of the slab phantoms tested to verify the approximations used in determining the dose in heterogeneous phantoms 370

131. The experimental and measured TMR correction factor for a 15 MV 5cm x 5cm beam 373

132. The experimental and measured TMR correction factor for a 15 MV 10cm x 10cm beam 374

133. The calculated homogeneous and heterogeneous TMR profile for a 15 MV 376

134. A comparison of separating the task of determining the wedge dose distribution and calculating an inhomogeneity correction factor and performing the calculation in one step 378

135. The dose spread array should be tilted to simulate the dose deposition from a divergent primary pencil beam interacting at i,j,k 382

136. A comparison of the convolution method with existing dose calculating methods 386

137. A flow chart of the host computer calculations required if an array processor is used to perform part of the convolution calculations 390

138. A flow chart of the array processor calculations ... 391

139. The part of an average density array calculated for one beam, that intersects with the average density array of another beam, may be reused by the second beam 392

140. The flow chart of the determination of the dose spread array and primary attenuation coefficient based on the transmission spectrum of a linear accelerator 401

VOLUME 2

A CONVOLUTION METHOD OF CALCULATING RADIATION DOSE FOR MEGAVOLTAGE X-RAY BEAMS

5. Introduction To Radiotherapy Dose Computation

We need 3-D CT for CA RT.

(3-Dimensional Computer Tomography for Cancer Radiotherapy)

L.E. Reinstein (62)

5.1 Statement of Purpose

The goal of radiotherapy planning is to obtain a high therapeutic ratio, defined as:

$$\text{Therapeutic Ratio} = \frac{\text{Tumor Control}}{\text{Normal Tissue Complication}} \tag{5.1.1}$$

This can be achieved by giving a sufficiently high and uniform radiation dose to the target volume and a lower dose to the surrounding normal tissue. This implies localizing the tissues to be irradiated accurately and optimizing the dose distribution.

X-ray images have traditionally been the main technique for the localization of tumor tissue. They are obtained by passing an x-ray beam through a patient and detecting the transmitted x-rays in a 2-dimensional plane perpendicular to the beam. The x-ray image represents the transmission through all the tissues where the x-rays are passing. As a result, the tissue volume through which the diagnostic x-ray beam is passing is "compressed onto a 2-dimensional view.

A radiotherapy "simulator" is a specialized radiographic device which produces radiological images and also has the same degrees of freedom of movement as radiotherapy units. It is primarily used to localize the tumor site with respect to the radiotherapy beam. Even when the tumor volume is accurately localized from several such views, the 3-dimensional information is rarely used directly in treatment planning. Instead a "contour" of a

2-dimensional cross-sectional slice through the region of interest is usually obtained. This is usually done using a mechanical or optical distance indicator attached to the simulator gantry which can rotate about the patient. Section 5.3 investigates existing methods of correcting dose distributions for patient-specific surface contours.

Internal outines of heterogeneous regions can be included by noting the maximum extent of the region in lateral and anterior transverse views. The cross-sectional view of the heterogeneity is then interpolated by using a standard anatomy atlas. The density of such internal structures is noted when they are greatly different from that of water (e.g. lung or bone). The correction for tissue heterogeneity correctly takes into account only the primary fluence, estimates are made of the effects on the scattered radiation dose. Because of the uncertainties in their location, there was often no correction at all for internal heterogeneous tissue contours. Therefore, until the recent advances in imaging, there has been little incentive to improve the accuracy of the calculations of dose deposited in heterogeneous tissue.

Imaging techniques such as computed tomography (CT scanning) (55,56), nuclear medicine tomographic imaging and nuclear magnetic resonance (NMR) imaging have improved the localization of tumor volumes. This alone is expected to improved the success of radiotherapy. This information can also be used to simplify three aspects of treatment planning.

1) The patient-specific anatomy can replace estimates based on cross-sectional anatomy atlases.

2) It can eliminate the need for measuring and modifying the external contour.

3) It can eliminate the need to assume the density of internal tissues. X-ray CT provides "pixel-by-pixel" (a pixel is a "picture element") information on tissue density. The problem of extracting the density information from CT scans has been studied by a great number of authors (57-61)

Tomography also provides information in 3-dimensions. Therefore there has been an incentive to use this 3-dimensional information more fully in treatment planning (62). In the discussion of dose calculation methods (Section 5.4), this aspect will be emphasized.

Another important advance in radiotherapy, which can improve the therapeutic ratio, is the increased availability of reliable high energy linear accelerators. A greater amount of dose from these sources is deposited at greater depths in the patient. Therefore, deep-seated tumors will receive a greater dose. At the same time, the build-up region extends to a greater depth reducing the dose near the patient surface. At higher energies, the range of charged particles set in motion can be several centimeters. The problem of charged particle transport will be introduced in Section 5.2 and investigated using the Monte Carlo method in Section 6. A dose computation procedure to take this into account will be proposed in Section 7. The effect of

charged particle transport is greater for 15 MV x-rays than for 6 MV x-rays, and therefore, this investigation has concentrated on 15 MV x-rays.

5.2 Electronic Equilibrium

The energy transport in an x-ray beam is a two-stage process. Photons must first interact to set in motion fast charged particles. The charged particles then interact continuously with matter and deposit their energy as dose. This process was investigated in Volume 1 to explain the increase in central axis dose in the build-up region. It was assumed that the charged particle transport was predominantly in the forward direction. The justification of the assumption was as follows: If the distance from the point of measurement to the field boundary is larger than the lateral range of charged particles set-in-motion, then for every charged particle leaving the region of the central axis there would be a charged particle arriving from lateral regions. When this condition is true, lateral electronic equilibrium exists (63). In Volume 1, the forward transport of charged particle fluence from the point of production was approximated by an exponential term. The constant in the exponential, $\mu_{e^{\pm}}$, describing forward transport, was many times larger then the coefficient, μ_{γ}, describing the primary photon attenuation.

Equation 1.5.8 can be used to estimate the state of longitudinal electronic equilibrium in a heterogeneous region (illustrated in Figure 82). It will be assumed that all regions of the phantom are composed of material with the same atomic number. Therefore, there is only a difference in gravimetric density. The amount of primary energy

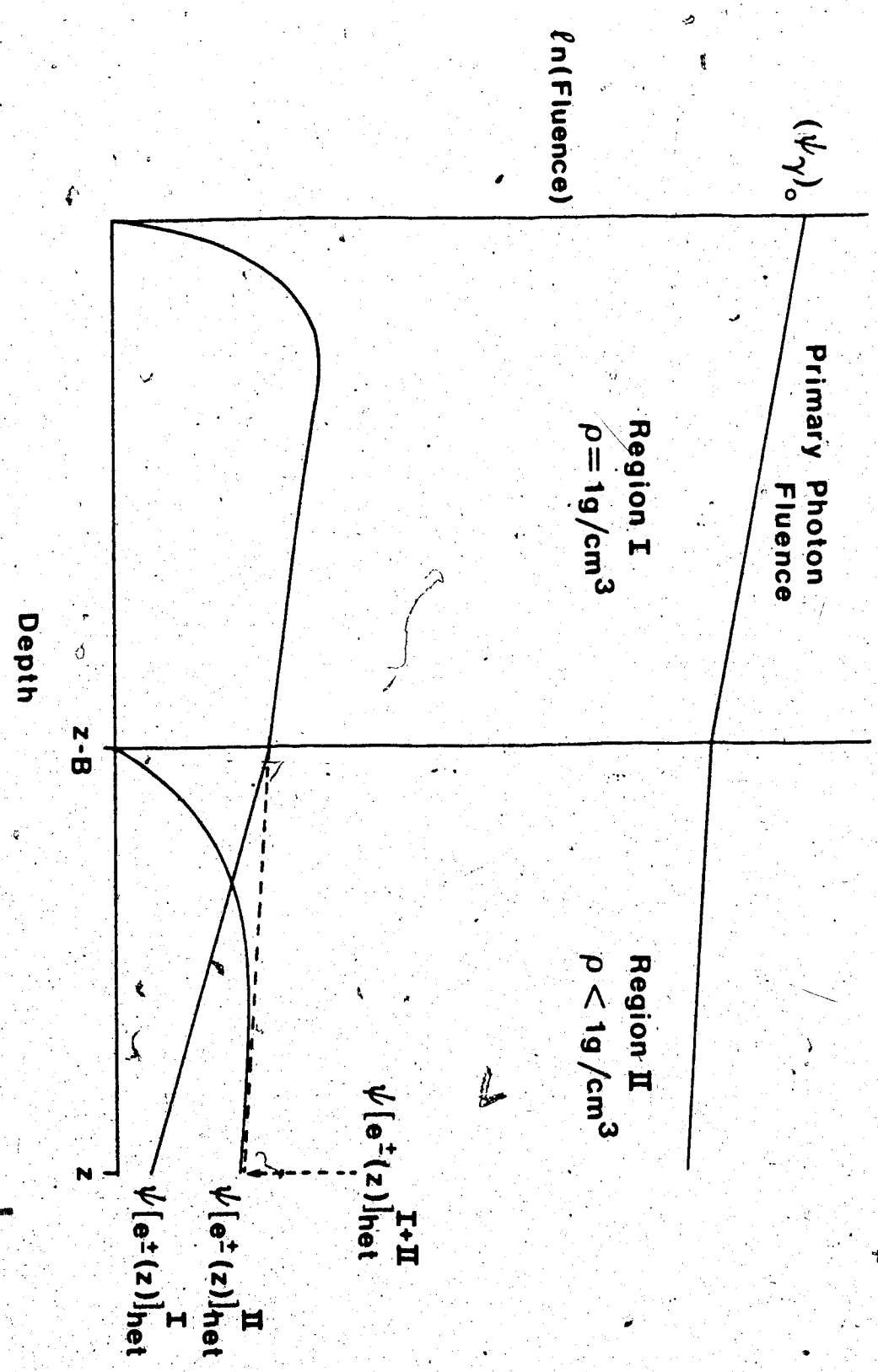

Figure 82. The state of longitudinal equilibrium in a heterogeneous phantom.

fluence at a depth, z, inside the heterogeneous phantom, is the sum of two contributions, one from a unit density region (Region I) of thickness z-B, $\Psi[e^{\pm}(z)]^{I}_{het}$, and one from a region (Region II) of lower gravimetric density (compared to water), ρ, and thickness B, $\Psi[e^{\pm}(z)]^{II}_{het}$:

$$\Psi[e^{\pm}(z)]^{I}_{het} = \frac{\mu_\gamma(\Psi_\gamma)_o}{\mu_{e^\pm} - \mu_\gamma}\left[e^{-\mu_\gamma(z-B)} - e^{-\mu_{e^\pm}(z-B)}\right] e^{-\mu_{e^\pm}(\rho B)} \tag{5.2.1}$$

$$\Psi[e^{\pm}(z)]^{II}_{het} = \frac{\mu_\gamma(\Psi_\gamma)_o}{\mu_{e^\pm} - \mu_\gamma}\left[e^{-\mu_\gamma \rho B} - e^{-\mu_{e^\pm}\rho B}\right] e^{-\mu_\gamma(z-B)} \tag{5.2.2}$$

$$\Psi[e^{\pm}(z)]^{I+II}_{het} = \frac{\mu_\gamma(\Psi_\gamma)_o}{\mu_{e^\pm} - \mu_\gamma}\left[e^{-\mu_\gamma[z+(\rho-1)B]} - e^{-\mu_{e^\pm}[z+(\rho-1)B]}\right] \tag{5.2.3}$$

The term, $e^{-\mu_{e^\pm}(\rho B)}$, in Equation 5.2.1 describes the attenuation in the low-density region of the charged particle fluence generated in the unit density region. The attenuation of the primary photon beam by the unit density region is accounted for by the term, $e^{-\mu_\gamma(z-B)}$ in Equation 5.2.2. If Region II is well beyond d_{max} i.e. z-B is large, then:

$$\Psi[e^{\pm}(z)]_{het}^{I+II} \cong \frac{\mu_\gamma(\Psi_\gamma)_o}{\mu_{e^\pm} - \mu_\gamma} e^{-\mu_\gamma z} e^{-\mu_\gamma(1-\rho)B} \qquad (5.2.4)$$

The correction factor CF is equal to the ratio of the charged particle fluence in a heterogeneous phantom to the charged paticle fluence in a homogeneous phantom:

$$CF(z) = \frac{\Psi[e^{\pm}(z)]_{het}^{I+II}}{\Psi[e^{\pm}(z)]_{hom}} = e^{\mu_\gamma(1-\rho)B} \qquad (5.2.5)$$

Equation 5.2.5 has no dependence on $\mu_{e^\pm}$. This means that if longitudinal equilibrium has been established, then longitudinal electronic equilibrium will not be perturbed in the low-density material. Equation 5.2.5 predicts that the inhomogeneity correction of the primary dose should always be greater than unity.

Perturbations in lateral equilibrium are not so easily described quantitatively. Analytic solutions of equations describing the transport of charged particles have yet to be achieved for generalized boundary conditions. Only Monte Carlo calculations provide a method to accurately quantify the role of lateral equilibrium. However, a qualitative description of the establishment of lateral equilibrium in a homogeneous phantom and its loss in a heterogeneous phantom is instructive.

Figure 83a) illustrates a homogeneous phantom irradiated by a non-divergent photon beam with a field size

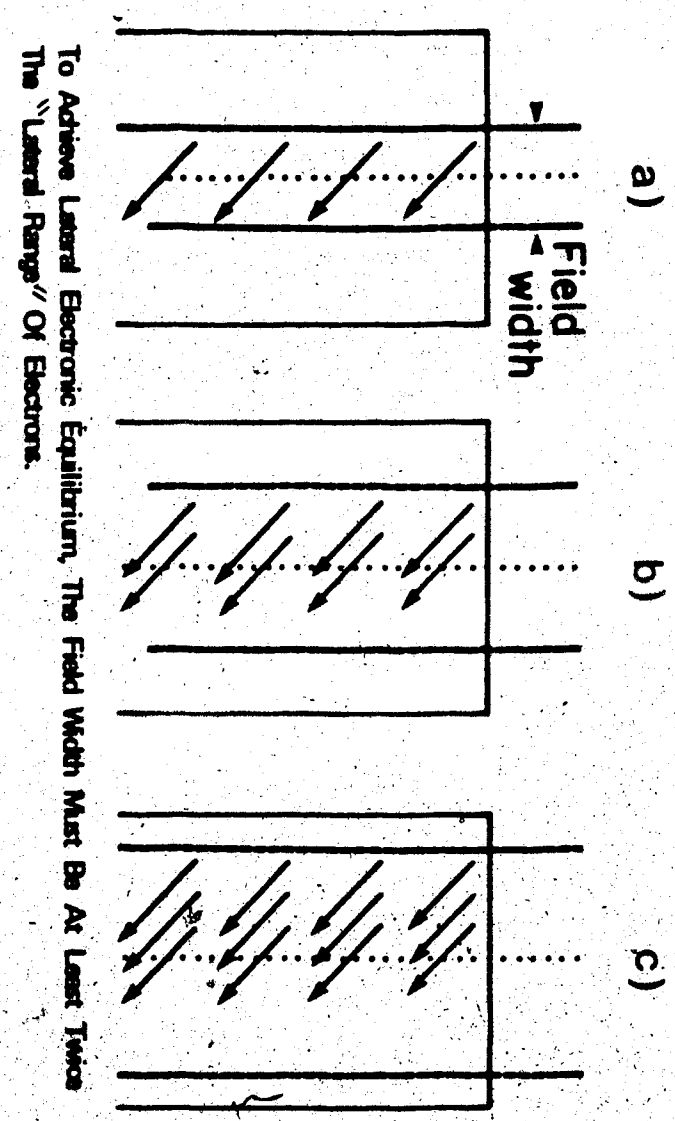

Figure 83. Lateral equilibrium does not exist at the central axis when the field size is less than twice the lateral range of electrons. Lateral equilibrium never exists near the field boundary.

smaller than the lateral charged particle range. The charged particles are assumed to be set in motion at a fixed angle with respect to the incident photon beam. For the sake of demonstration, it is assumed here that they do not deviate from their initial direction. The charged particles originating near the beam boundary deposit energy at the central axis and travel beyond (the dashed lines) to the end of their range. If the field size is increased (Figure 83b)) charged particles originating near the new boundary have enough range to reach the central axis increasing the dose deposited there. Lateral electronic equilibrium is established when a further increase in field size will not result in a further increase in dose because charged particles set in motion near the field boundary (Figure 83c)) do not have sufficient range to reach the central axis.

Figure 84a) illustrates the loss of lateral electronic equilibrium inside a heterogeneous region with a density of one half of the density in Figure 83. Since the range of particles in the low-density region will be double that in the unit density region, a field size sufficient to establish equilibrium in a unit density medium must be doubled in order to obtain equilibrium in the low-density region.

Even though this analysis of electronic equilibrium is heuristic it would be expected that the establishment and loss of lateral electronic equilibrium in heterogeneous phantoms may be a more important effect than that of

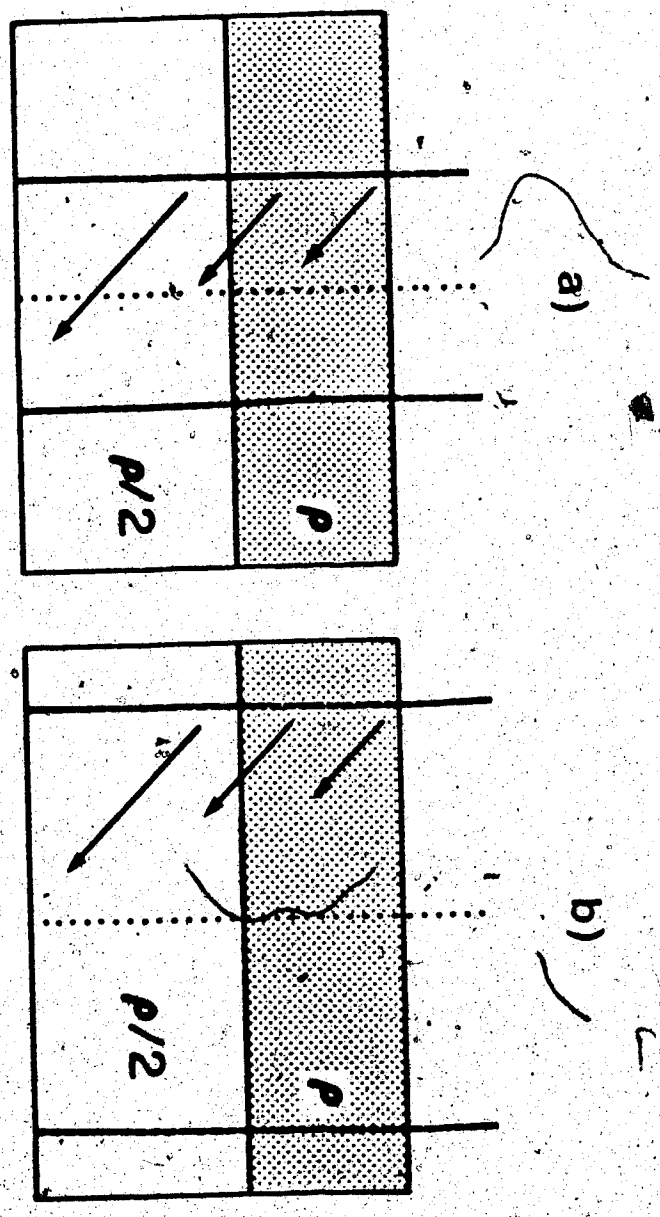

Figure 84. a) A field size large enough to establish lateral equilibrium at the central axis may not be large enough in a low-density region. b) If the heterogeneous region has a density of one-half, the field size must be doubled to re-establish lateral equilibrium.

longitudinal equilibrium.

A series of experiments was used to verify this hypothesis. Figure 85 illustrates the experimental set-up. An ion chamber (Capintec PR-06C) without a build-up cap was placed at the central axis a constant 100 cm from the source. The thickness of the cork region was also kept constant at 7.9 cm ± 0.2 cm. The total thickness of overlaying material was 15.6 cm ± 0.4 cm. The position of the cork was varied with respect to the ion chamber. The quantity, A, is the distance from the first interface to the probe. The correction factor, CF, was defined to be:

$$CF(z,A,W) = \frac{\text{Heterogeneous Phantom TMR}(z,A,W)}{\text{Homogeneous Phantom TMR}(z,W)} \qquad (5.2.6)$$

Figure 86 illustrates the correction factor as a function of A for various field sizes. At small field sizes inside cork, the correction factor is less than unity. This means that the dose in the low-density heterogeneous phantom is less than the dose in the homogeneous phantom even though the photon fluence in the low-density heterogeneous phantom is greater than in the homogeneous phantom. A small increase in the field size at field sizes less than 10 cm x 10 cm (for example from 5 cm x 5 cm to 6 cm x 6 cm) results in a relatively large increase in the correction factor. At a field size of 10 cm x 10 cm there is little further increase in the correction factor with field size. Both these effects are expected if lateral equilibrium did not exist for the smaller fields.

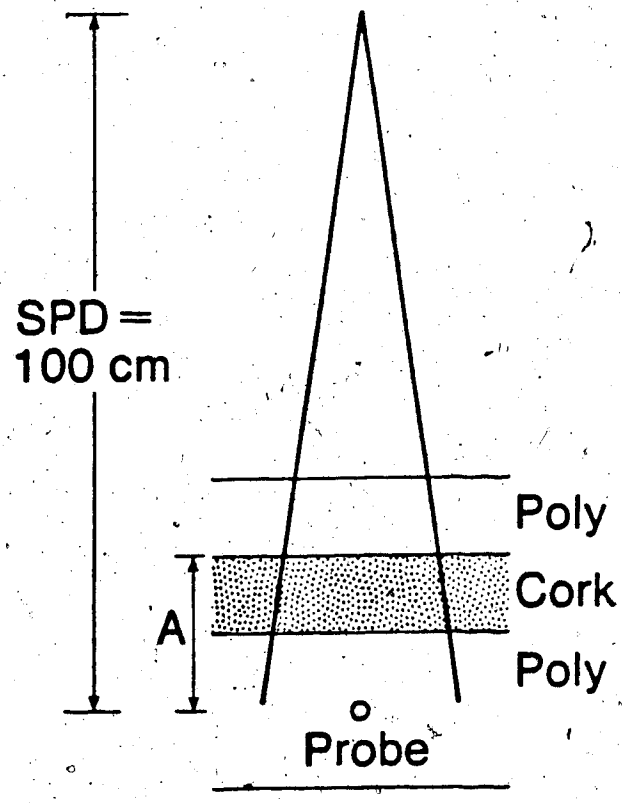

Figure 85. The experimental set-up to measure the inhomogeneity correction factor. The source-to-probe distance, the thickness of cork, and the depth of the probe from the surface was fixed. The position of the cork with respect to the probe is varied.

$$\text{Correction Factor} = \frac{\text{Heterogeneous Tissue Maximum Ratio}}{\text{Homogeneous Tissue Maximum Ratio}}$$

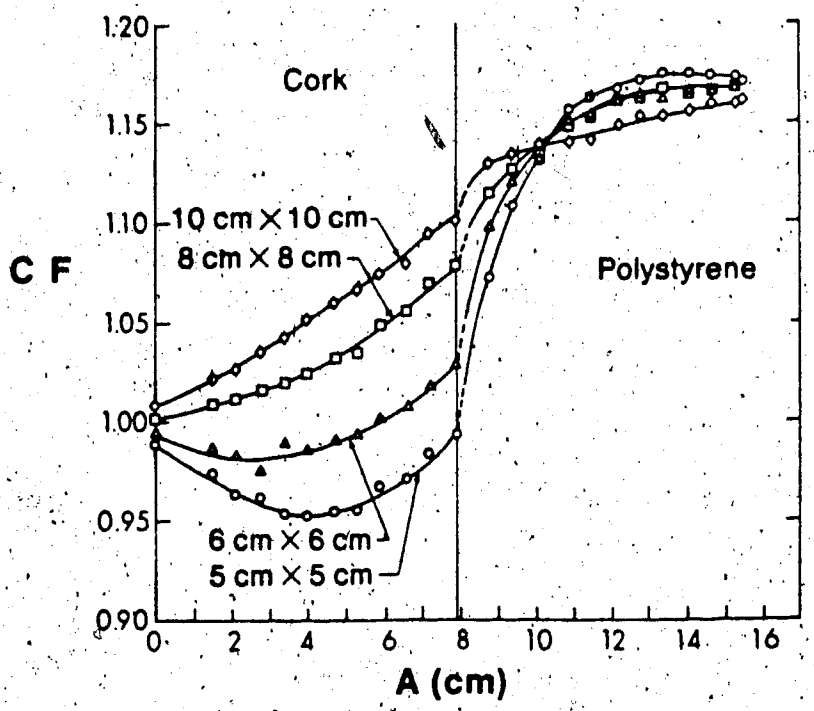

Figure 86. The correction factor, for the experimental set-up illustrated in Figure 85, for various field sizes.

Similar measurements have been performed by Young and Kornelsen for 10 MV x-rays (64). They also report a loss in lateral equilibrium in lung-equivalent materials when the field size is small.

5.3 Contour Corrections

Measurements of absorbed dose from a megavoltage x-ray beam are usually obtained in a water tank or phantom. The central axis of the beam is perpendicular to the water surface and the dimension of the tank is larger than any beam width to be measured. Figure 87a) illustrates the geometrical arrangement for the measurement of dose at point P. The surface of a patient is rarely flat, and thus the central axis, where the beam enters, is generally not perpendicular to the surface. The measured dose must be corrected to take patient surface contours into account. Figure 87b) shows the arrangement for the calculation of dose at point P which nows lies under a curved contour. A "ray" from the radiation source through P represents a pencil beam.

The "effective attenuation coefficient method" takes the surplus or deficit of tissue into account by the subtraction or addition of dose (63). The true depth, z', of a pencil beam through tissue with a contour is determined. The difference between the depth in the all-water situation from a reference surface, z, and the true distance, z', is multiplied by an empirically determined coefficient, k_{eff}, that depends on the photon energy to obtain the contour corrected dose:

$$DOSE(z') = DOSE(z)\, e^{k_{eff}(z-z')} \cong DOSE(z)[1 + k_{eff}(z-z')] \qquad (5.3.1)$$

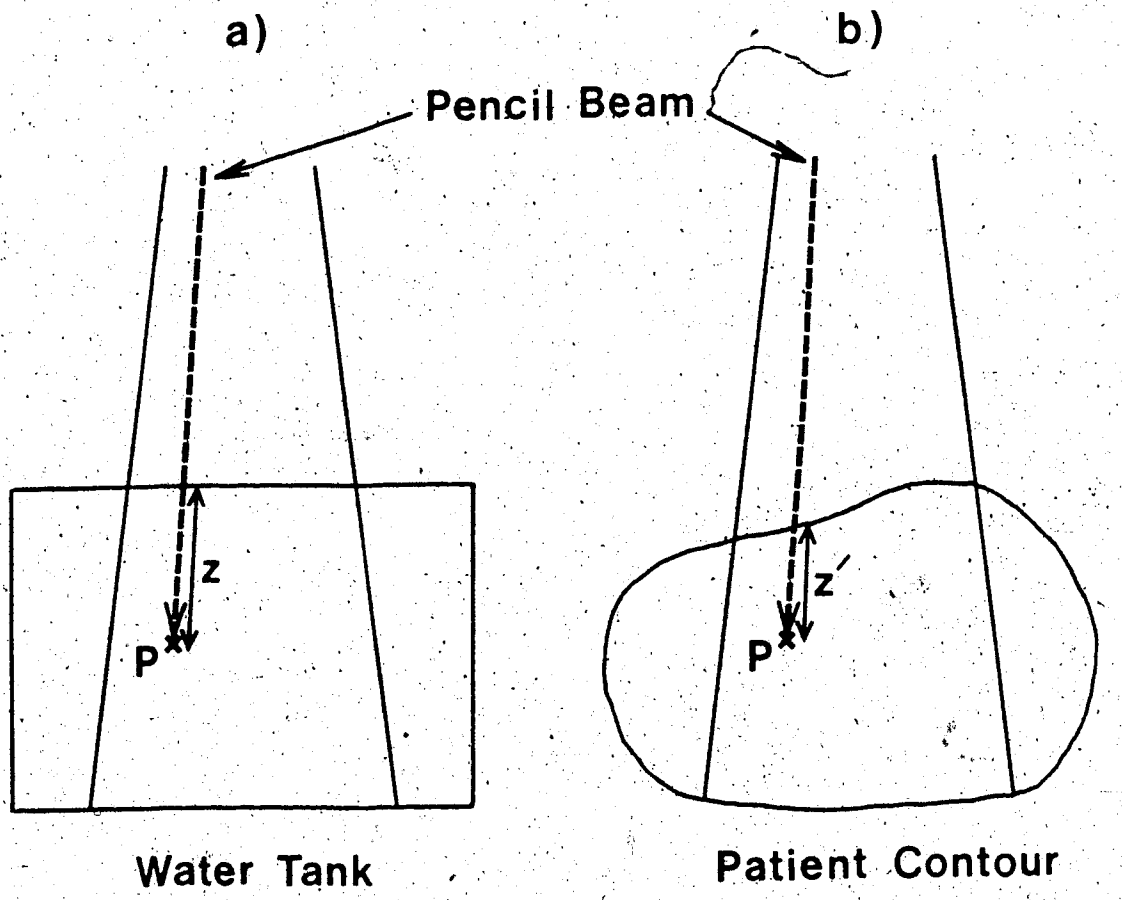

Figure 87. a) Measurement of the dose in a water tank. b) The dose must be modified to take into account the patient surface contour.

The coefficient, k_{eff}, for Co-60 beams is smaller than the linear attenuation coefficient so the effective attenuation coefficient method must take an unspecified amount of forward directed scatter as well as primary attenuation into account. The dose must be corrected at all depths for each pencil beam.

The "isodose shift method" (63), shifts the depth of all isodose lines by an amount directly proportional to the difference between the true and reference distance, $z'-z$. If the true thickness of tissue is less than the all-water thickness, the isodose lines are shifted towards the surface and in the opposite situation, the lines are shifted away from the surface. The method is computationally simpler than the effective attenuation coefficient method because the shift does not have to be applied at each depth. The constant of proportionality depends mainly on the beam quality and like the effective attenuation coefficient in the previous method it must be determined empirically. The isodose shift method is inaccurate very near the surface of the phantom.

The main disadvantage of the effective attenuation coefficient method and the isodose shift method is the determination of their empirically derived coefficients. In general, the coefficients depend not only on the energy of the beam but also to some extent on the beam size, depth of the calculation point, and the source-to-surface distance (SSD).

Two other methods, the "ratio of TAR" and "effective

SSD" methods, also employ the true length through tissue, z', but explicitly take into account the beam size, and therefore, account indirectly for some scattered radiation. The ratio of TAR method is based on measured tissue-air-ratio (TAR) data.* The tissue-air-ratio under a contour is found by interpolating in a look-up table, compiled as a function of depth and field size, using the true depth. Since TAR's are usually measured along the central axis, the method is, strictly-speaking, limited to correcting the dose there. However, in practice, this limitation is ignored and off-axis corrections are estimated using the central axis data.

The effective SSD method corrects the tabulated percent depth-dose data in a manner similar to the ratio of TAR correction method. The percentage depth-dose must also be corrected to "remove" the inverse square attenuation. The corrected percentage depth-dose P(z',W,SSD') is:

$$P(z',W,SSD') = P(z',W,SSD)\left(\frac{SSD + z}{SSD + z'}\right)^2 \qquad (5.3.2)$$

* TAR measurements are obtained in a similar manner as tissue-maximum-ratio (TMR) data (see Figure 11), except the normalization value is obtain with the probe in air surrounded by a build-up cap of sufficient thickness to establish electronic equilibrium. Like TMR measurements the measurements for TAR's are obtained at a fixed distance from the source.

This correction can be made to off-axis positions as well as positions on the central axis.

Since TAR's and percentage depth-dose data contain scatter as well as primary dose, these corrections may correct somewhat for perturbation in the scatter dose. The major drawback of these methods is a failure to consider explicitly the influence of the scatter contribution to the contour correction.

The "differential scatter-air-ratio (dSAR)" method takes the contour configuration into account (65). The differential scatter-air-ratios are produced from scatter-air-ratio (SAR) data which are in turn derived from tissue-air-ratio (TAR) data:

$$SAR(z,r) = TAR(z,r) - TAR(z,0) \qquad (5.3.3)$$

Where, r, is the field radius. TAR(z,0) is called the "zero-area" tissue-air-ratio. It cannot be measured directly but is extrapolated from TAR data as the field radius is decreased (see Figure 88). The zero-area TAR corresponds to the primary dose if the charged particle energy is locally deposited (i.e. if electronic equilibrium exists). The SAR values are then a measure of the dose contribution of scattered radiation in a beam.

The dSAR values at a specific depth, z, are equal to the difference in SAR values per unit change in the field size:

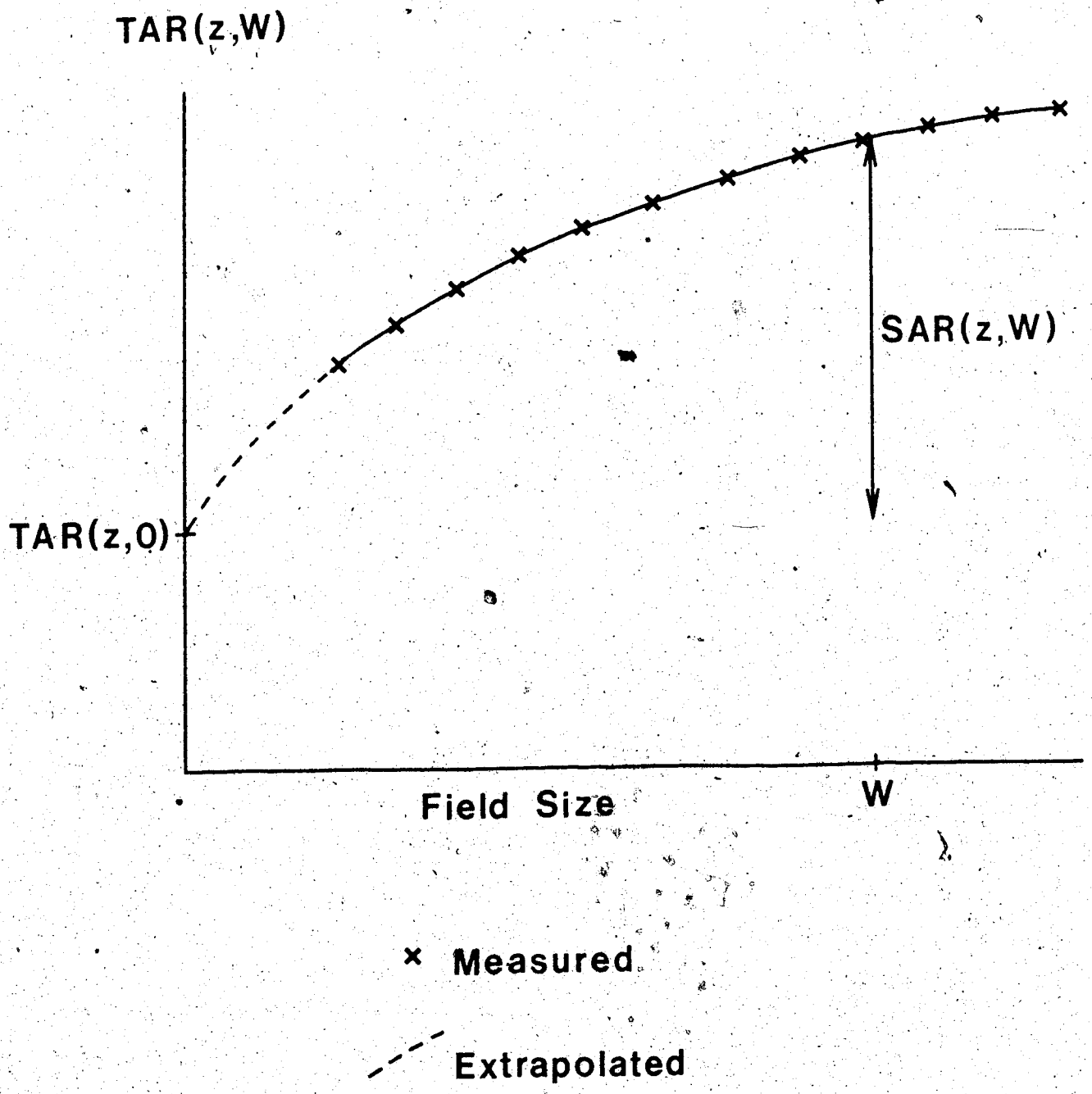

Figure 88. The definition of the zero-area TAR, TAR (z,0) and the scatter-air-ratio SAR (z,W). TAR (z,0) is found by extrapolated TAR measurements to a field size of zero.

$$\frac{d^2S(z,r)}{drd\theta} = \frac{1}{2\pi} \frac{[SAR(z,r+\delta r) - SAR(z,r-\delta r)]}{\delta r \delta\theta} \qquad (5.3.4)$$

Equation 5.3.4 represents the scatter contribution for a pencil beam at radius, r, and angle, θ. The total scatter dose is found by summing the contributions as a function of radius and angular position:

$$D_{Scatter}(z,R) = D_A \sum_{ji}^{2\pi R} \sum f(r_i,\theta_j) \frac{d^2S(z_i,r_i)}{drd\theta} \delta r_i \delta\theta_j \qquad (5.3.5)$$

D_A is the dose in air at a distance from the source that corresponds to the depth, z. $f(r_i,\theta_j)$ is the relative primary fluence at the radius, r_i, and angular position, θ_j, incident on such pencil beams.

One of the main difficulties with the dSAR method is the extrapolation of TAR's to get the zero-area TAR values. The extrapolation takes place where the TAR values are changing rapidly in a non-linear fashion making the procedure technically difficult. There is a more fundamental problem. The TAR concept is defined only if electronic equilibrium exists, but this is impossible for a pencil beam of zero-area. Electronic equilibrium only exists in a lateral direction if the field size is larger than the lateral range of charged particles set in motion. The TAR's are extrapolated to field sizes where equilibrium does not exist. The dSAR method was first introduced for use with Co-60 beams such that the pencil beam is

sufficiently wide to establish equilibrium. The assumption of electronic equilibrium starts to break down for higher x-ray energies.

A second problem is that central axis data is applied to off-axis points. This may not be serious in practice, but the approximation has not been validated by modelling or experiment.

A final problem, is that the dSAR method does not take into account the contour where the beam exits the patient. Therefore, backscatter is not dealt with properly.

5.4 Correction For Tissue Heterogeneity

Contour corrections are simply a special case of corrections to account for heterogeneous tissue densities. The density outside the patient can be considered to be approximately zero. The only fundamental difference between contour corrections and other low-density heterogeneity corrections is that the dose in air outside the patient is irrelevant to the treatment and need not be calculated. For this reason, the effective attenuation coefficient, isodose shift, TAR ratio, and effective SSD methods have been applied to tissue inhomogeneity corrections. The true distance in the tissue, z', (discussed in Section 5.3) is now interpreted as the "radiological" or water-equivalent distance in the heterogeneous region. The major fault of these methods, when applied to heterogeneity corrections, is a failure to take into account the relative position of the heterogeneous region with respect to the calculation point.

The Batho or power-law method takes the depth of the heterogeneity, with respect to the depth of the point of measurement, into account. The original Batho method assumed that the heterogeneous region was a slab at right angles to the beam with an extent larger than the field boundary (66). Electronic equilibrium was assumed not to be perturbed and that only the dose beyond the heterogeneous region was required. The method was extended to include the dose inside, as well as distal to, the heterogeneous region by Sontag and Cunningham (67). Their formulation for the

correction factor, CF was:

$$CF(z_1,z_2,W) = \frac{TAR(z_2,W)^{\rho_2-\rho_1}}{TAR(z_1,W)^{1-\rho_1}} \qquad (5.4.1)$$

z_1 and z_2 are shown in Figure 89 and ρ_1 and ρ_2 are the relative electron densities (compared to water) of regions 1 and 2, respectively.

The Batho method has been subsequently modified by Cassell, Hobday and Parker (61) and Lulu and Bjärngaard (68) to take into account multiple slab geometries and estimate the correction factor when the lateral extent of the heterogeneity is less than the beam width. Limited success has been achieved by modifying the Batho method to take into account electronic disequilibrium (69).

The equivalent TAR method developed by Sontag and Cunningham (70) was inspired by O'Connors theorem. O'Connor (71) proposed that the dose at corresponding points in two media with different density, but the same atomic number, will be the same everywhere provided all distance measurements are scaled with the density (see Figure 90). The basis for the theorem is the linear dependence of the attenuation coefficient on density.

The premise on which Sontag and Cunningham based their method, was that an equivalent TAR could be found in tabulated TAR tables with the depth and field size suitably scaled:

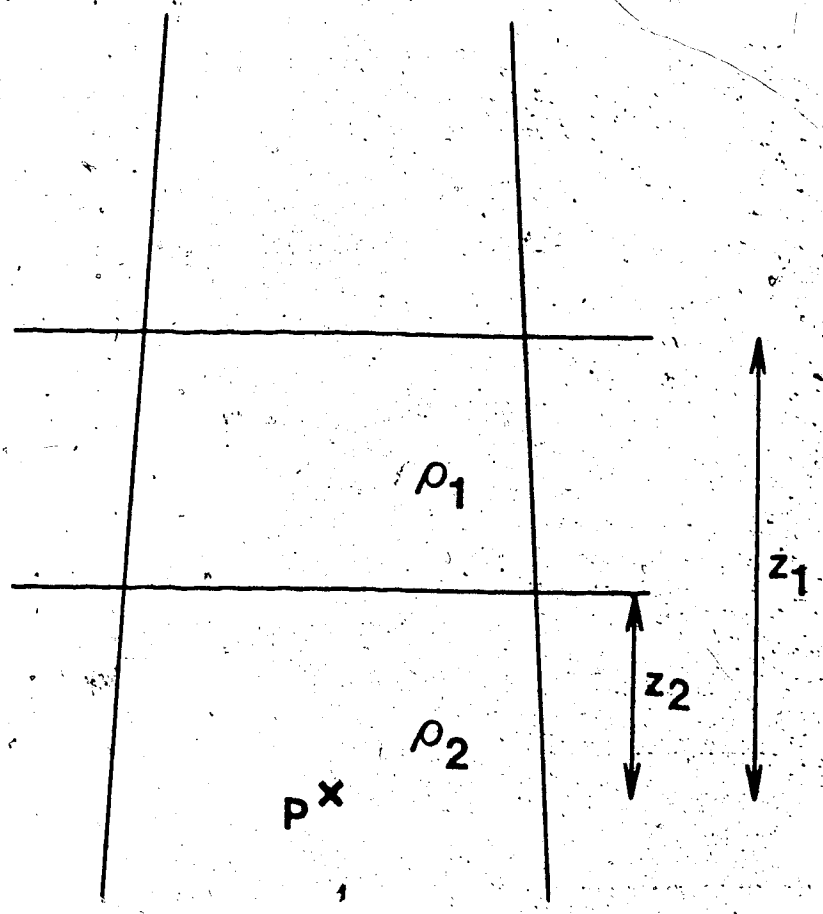

Figure 89. The geometrical parameters required for the Batho or power law method.

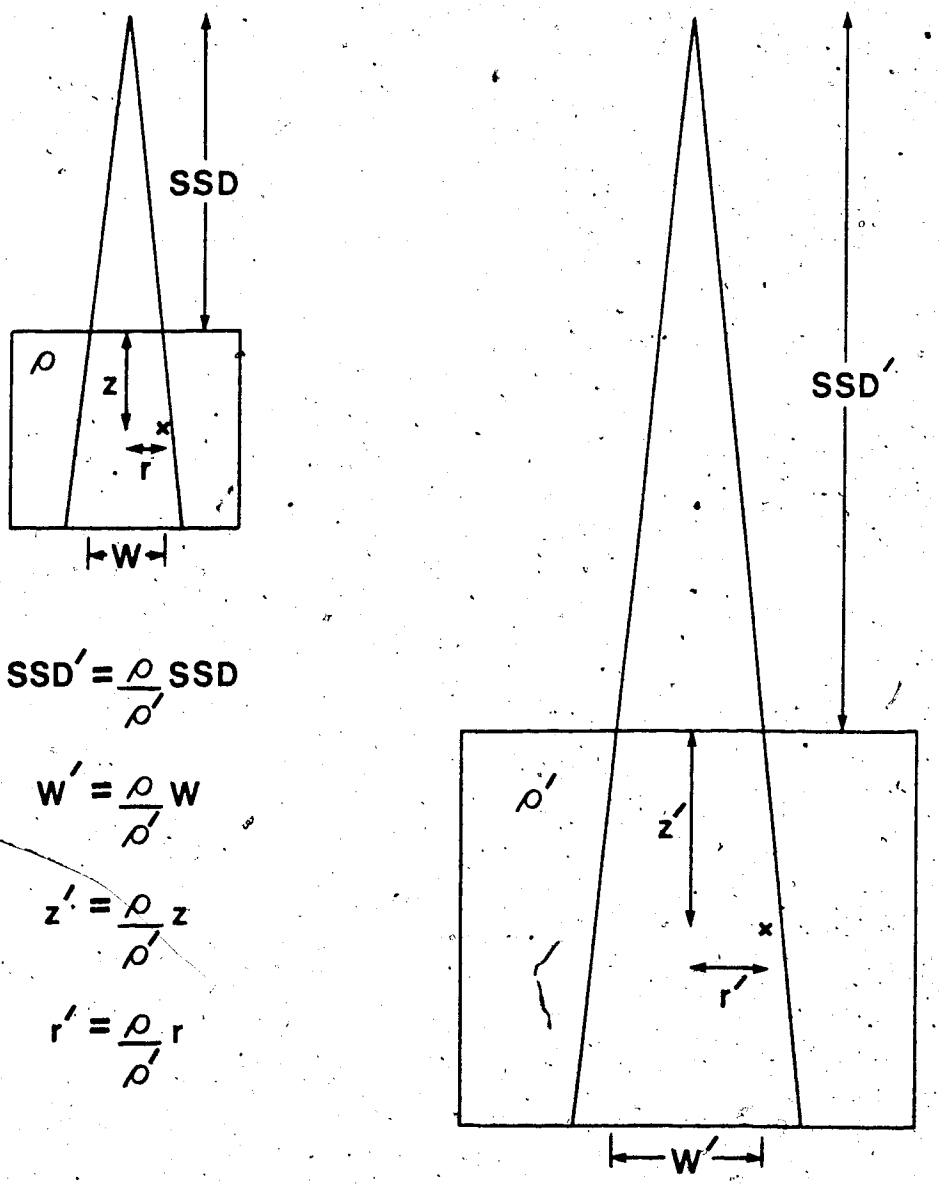

$$SSD' = \frac{\rho}{\rho'} SSD$$

$$W' = \frac{\rho}{\rho'} W$$

$$z' = \frac{\rho}{\rho'} z$$

$$r' = \frac{\rho}{\rho'} r$$

$$Dose(z',r',W',SSD') = Dose(z,r,W,SSD)$$

Figure 90. An illustration of O'Connor's theorem. All the distance measurements in this figure are inversely proportional to density.

$$CF(z',\hat{W}) = \frac{TAR(z',\hat{W})}{TAR(z,W)} \qquad (5.4.2)$$

The tissue-air-ratio was divided into primary (zero-area TAR) and scatter components:

$$TAR(z',\hat{W}) = TAR(z',0) + SAR(z',\hat{r}) \qquad (5.4.3)$$

$$\hat{r} = r \cdot \hat{\varepsilon} \qquad (5.4.4)$$

The term, r, is a circular field radius that produces the same dose at all depths along the central axis in a homogeneous phantom in a rectangular field. The term, $\hat{\varepsilon}$, is an effective relative electron density, weighted with respect to the scatter dose contributions from tissue elements surrounding the calculation point. The weighting procedure should be carried out over 3-dimensions:

$$\hat{\varepsilon} = \frac{\sum\sum\sum_{ijk} \varepsilon_{ijk} \cdot W_{ijk}}{\sum\sum\sum_{ijk} W_{ijk}} \qquad (5.4.5)$$

The weighting factors, W_{ijk}, is the contribution to the scatter dose from points surrounding the calculation point. The weighting factors are large in regions proximal to the calculation point and for points close to the calculation point.

Weighting in 3-dimensions, to arrive at an effective

electron density for each point, was felt to be too time consuming for computers available at the time. Since CT information is produced and stored in cross-sectional slices, the 3-dimensional dose was estimated using this plane-by-plane format. The electron density information, for all the slices neighboring the slice in which the dose calculation was being performed, was "coalesced" into a 2-dimensional effective relative electron density array (see Figure 91):

$$\hat{\varepsilon}_{ik} = \frac{\sum_j \varepsilon_{ijk} \cdot W_k}{\sum_j W_k} \qquad (5.4.6)$$

This 2-dimensional array is produced before the dose is calculated. It represents the scatter dose weighted electron density as if all the scatter dose was coming from one neighboring slice located at an effective location. A weighted relative electron density is determined for each calculation point in the slice:

$$\hat{\varepsilon} = \frac{\left(\sum_{ik}\sum_j \left[\sum \varepsilon_{ijk} \cdot W_j\right] W_{ik}\right) \Big/ \sum_j W_j}{\sum_{ik}\sum W_{ik}(Y_{eff})} \qquad (5.4.7)$$

The above procedure is repeated for each point in the calculation plane. It has been assumed that the weighting factor can be separated into space components:

$$W_{ijk} = W_j \cdot W_{ik}(Y_{eff})$$

(5.4.8)

The term W_j is given by:

$$W_j = SAR(z=10cm, r_2) - SAR(z=10cm, r_1)$$

(5.4.9)

The radius terms r_1 and r_2 are related to the equivalent circular field and the distance between neighboring slices in a non-linear fashion. The effective distance to the coalesced scatter slice, Y_{eff} is given by (see Figure 91):

$$Y_{eff} = \frac{\sum_j Y_j \cdot W_j}{\sum_j W_j}$$

(5.4.10)

The calculation is speeded up by the spatial separation of the weighting factor because the summation for each calculation point is carried out over two dimensions instead of three. However the assumption that the non-calculation planes can be replaced by one effective plane placed at an effective distance away was never validated by Monte Carlo modelling or experiment. The procedure could not be proved by a comparison of Equation 5.4.5 with 5.4.7 because the 3-dimensional weighting factors were never obtained. A simplification of the equivalent TAR method has been proposed by Tatcher and Palti (72). Equation 5.4.3 is maintained except, z', is the radiological length through the heterogeneous region and, $\hat{W}$, is replaced by:

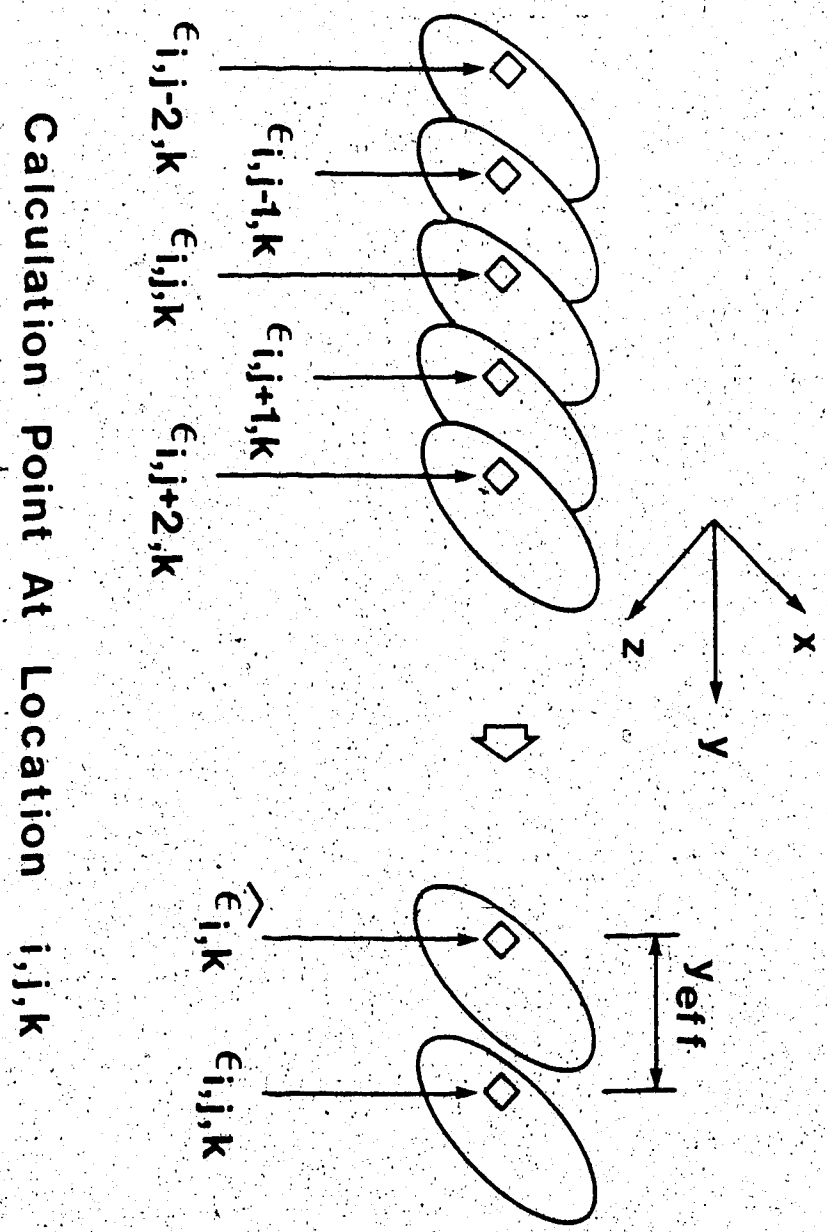

Figure 91. In the equivalent TAR method, the 3-dimensional electron density information is "coalesced" into one cross-sectional slice.

$$\hat{W} = W\tilde{\rho} \tag{5.4.11}$$

$$\tilde{\rho} = \frac{V_w + \Sigma\Sigma\Sigma_{ijk} V_{ijk}\, \rho_{ijk}\, f_{ijk}}{V_w + \Sigma\Sigma\Sigma_{ijk} V_{ijk}\, f_{ijk}} \tag{5.4.12}$$

Where $\tilde{\rho}$ and ρ_{ijk} refers to the relative density compared to water. V_w and V_{ijk} are the volumes of the water-equivalent and heterogeneous parts of the phantom, respectively. f_{ijk} is equal to 3 for cork and equal to ∞ (ie. $\tilde{\rho} = 1$) for teflon. It is later claimed that f_{ijk} is not sensitive to variations in density! It is also claimed that f_{ijk} is nearly independent of geometrical position although it is only applied when calculating the dose in heterogeneous phantoms!

The delta-volume method was originally suggested by Cunningham and Beudoin (73) and refined by Larson and Prasad (74) and Wong and Henkelman (75). The method, as formulated by Wong and Henkelman, divides the dose into primary, first scatter augmented by some second scatter, and residual multiple scatter dose. Mathematically, the expression is given by:

$$\text{DOSE} = \text{PRIMARY} + \sum_{ijk}\sum\sum \rho_{ijk}\, \Delta S^{*}_{1;ijk}\, f_{o;ijk}\, f_{1;ijk} + S_m \qquad (5.4.13)$$

$$S_m = \frac{SAR_m(\tilde{\rho}\cdot d, \tilde{\rho}\cdot r)}{SAR_m(d,r)} \left[S_m(\text{med}) + \sum_{ijk}\sum\sum \left(\frac{\tilde{\rho}-\rho_{ijk}}{\tilde{\rho}}\, \Delta H_{ijk}\right)\right] \qquad (5.4.14)$$

where ρ_{ijk} is the density of the volume element (voxel) which is the origin of the first or augmented second scatter dose at point i,j,k. $\Delta S^{*}_{1;ijk}$ is the contribution of first and augmented second scatter dose (second scatter dose contained within an angle of 45^{o} centered about the first scatter ray) to the calculation point i,j,k determined for a homogeneous water phantom. $f_{o;ijk}$ is the change in the primary attenuation along the primary ray to the point i,j,k. $f_{1;ijk}$ is the change in the first scatter attenuation along the path between the point i,j,k and the calculation point. The term $S_m(\text{med})$ approximates the residual multiple scatter dose in a heterogeneous medium. ΔH_{ijk} is the perturbation in the multiple scatter dose from a small void at the point i,j,k. It is determined by the difference between the experimentally measured dose perturbation (see Figure 92) and the calculated value using $\Delta S^{*}_{1;kjk}$. $\tilde{\rho}$ is the overall mean density of the heterogeneous phantom. $SAR_m(d,r)$ is the residual multiple scatter-air-ratio for a homogeneous water phantom and is

obtained using SAR values and the augmented first scatter values. The determination of ΔH_{ijk} is worthy of note. It is obtained by displacing water by low-density polystyrene foam constructed in conical rings about the central axis (76). The small perturbation in dose due to the displacement of the ring is measured. The radius of the ring, the depth of the measurement point and the position of the ring with respect to the measurement point is varied. The experimental set-up is shown in Figure 92. The number of measurements involved requires automation of the procedure. The first and augmented second scatter dose are calculated and their contribution is subtracted from the total scatter perturbation measurements to arrive at the multiple scatter dose perturbation values.

The Δ-Volume method was the first "true" 3-dimensional dose calculation algorithm. It exactly corrects the first scatter dose due to the presence of heterogeneities (assuming electronic equilibrium of the scatter photons) and estimates the multiple scatter dose correction.

The delta-volume method has not been optimized for speed of calculation. As many operations are carried out to determine the dose corrections for first and augmented second scatter dose as for the residual multiple scatter dose, even though the contribution of the latter is much smaller. Calculation time should be appropriated on the basis of the importance of the contribution of the calculation to the overall result. However, the speed limitations may not be critical. The method is being

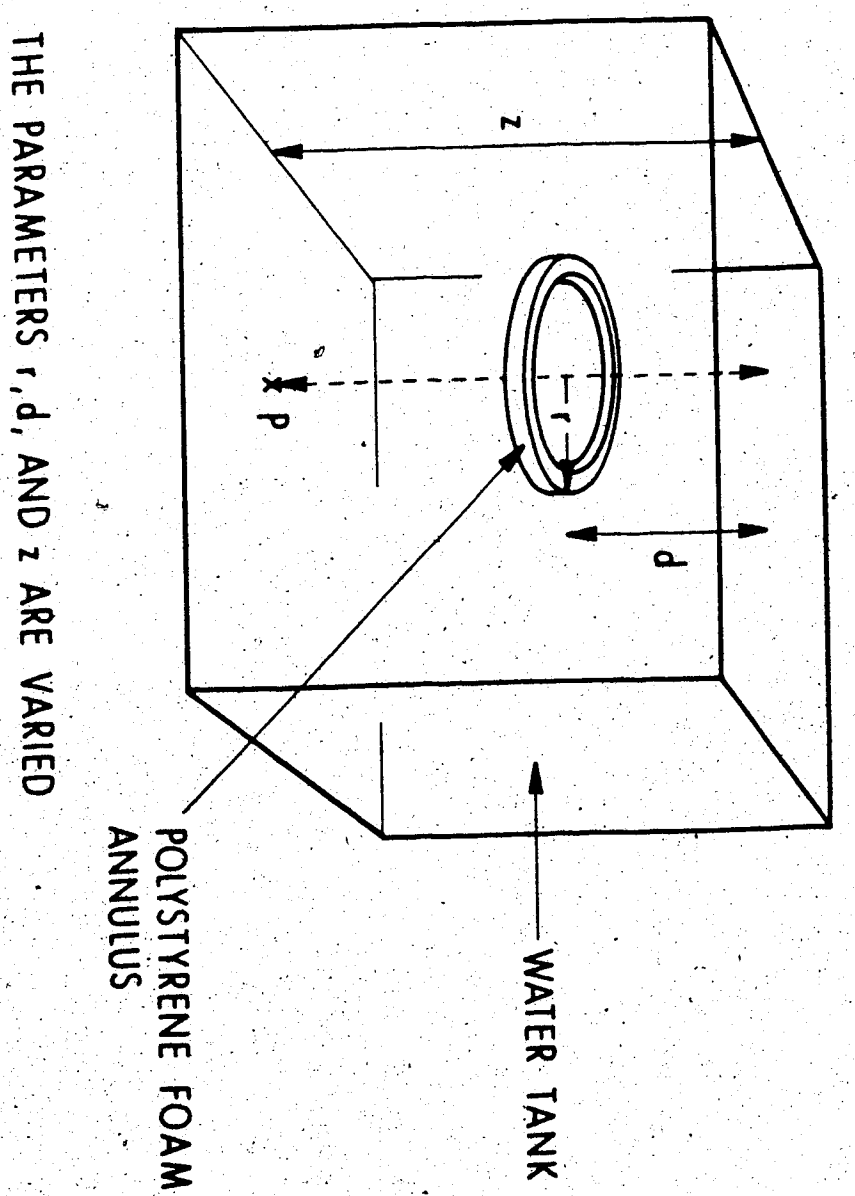

Figure 92. Polystyrene foam conical annuli were placed in a water tank. The perturbation in dose compared to the all-water saturation was measured.

implemented using a dedicated microcomputer. A group promoting the Δ-volume method (Mallinckrodt) is using Very Large Scale Integration (VLSI) microelectronic technology to develope a "chip" that will do the "ray-tracing" portion of the Δ-volume calculation rapidly (77).

A major criticism of all the above methods is that the inherent assumptions are not identified explicitly and they have not been validated directly by measurements or simulation (eg. the Monte Carlo method). Consequently, their scope of applicability is ill-defined, and the clinical situations in which they are limited are difficult to identify a priori.

The major fault of the equivalent TAR and delta-volume methods is an inability to handle situations of electronic disequilibrium. Most of the dose arriving at a point is due to primary dose which will be most perturbed by changes in the state of electronic equilibrium. A related problem with these methods is that they are based on the separation of primary and scatter dose using the zero-area TAR and SAR's obtained empirically. The concept becomes more and more untenable at higher photon energies as electronic equilibrium becomes more important and the extrapolation of TAR's to such fields is incompatible with the equilibrium requirement.

The need for considering non-local energy deposition has been documented by several authors (78-81). Some photon dose parametrization models have accounted for electronic "build-up" longitudinally along the central axis, but none

have rigorously treated the lateral spread of charged particles set-in-motion (40,82) (see Section 3 in Volume 1). Young and Kornelsen (64) have taken into account the dose reduction caused by a lack of charged particle lateral equilibrium using a semi-empirical "loss factor".

6. Modelling Dose Using The EGS Monte Carlo Code

The state-of-the-art of the Monte Carlo method in 1952:

"The electrons or photons were followed through successive intervals and their fate in passing through a given interval was decided by spinning a wheel of chance; the fate being read from one of a family of curves drawn on a cylinder"..."the [cylinder] motor was observed to stop at random ..."

R.R. Wilson (83)

It has been shown that lateral electronic equilibrium does not exist near field boundaries and along the central axis in low-density heterogeneities for small fields (see Figure 86). The EGS (Electron Gamma Shower) Monte Carlo code was used to investigate regions of lateral disequilibrium directly by simulating the transport of photons and charged particles set in motion.

EGS was originally developed at Stanford University for the study of the cascade of charged particles and photons produced by high energy (up to 1 GeV) cosmic rays or photons (83). Rogers, at the National Research Council of Canada, has corrected and modified the code to make it applicable to the energies encountered in medical physics and health physics problems (84-86).

EGS takes into account most of the radiation physics required for megavoltage energies. The interactions treated for photons are pair production, Compton, and the photoelectric effect, and for charged particles, multiple scattering (Moliere's theory as formulated by Bethe), "knock-on" collisions (Moller scattering for electrons and Bhabha scattering for positrons), continuous slowing down, bremsstrahlung and positron annhilation. The only present flaw is an inaccuracy (up to a factor of two) in calculating correct bremsstrahlung spectra (86). The charged particle "cut-off" energy, below which the residual energy can be deposited "on the spot", can be varied continuously upward from 10 keV.

The program was implemented to produce the dose

distribution in homogeneous and heterogeneous phantoms from primary pencil photon beams. The modelled beam was a 0.50 cm in radius, monoenergetic parallel beam. The phantom was composed of 20 cm of either "water" or a combination of "water" and "cork" (water-like in chemical composition but with a gravimetric density of 0.25) slabs totalling 20 cm in overall thickness.

The pencil beam dose distribution was also used to compose the central axis dose due to a broad photon beam. Figure 93 illustrates the procedure schematically for a pencil beam directed into the page. The small circle of area, A_{pencil}, represents the pencil beam. The dashed lines represent an annulus in which dose has been deposited from the pencil beam. DOSE CONTRIBUTION (P) is the dose contribution at point P from an annulus of area $A_{annulus}$ (shown by solid lines):

$$\text{DOSE CONTRIBUTION (P)} = \frac{A_{ANNULUS}}{A_{PENCIL}} [\text{DOSE}]_{ANNULUS} \qquad (6.1)$$

The ratio of the area of the annulus to the area of the pencil beam gives the relative amount of energy being released in the annulus compared to the pencil beam.

A widely used "rule of thumb" states that the mean energy of x-rays produced in an accelerator is approximately one-third of its nominal energy. Therefore, the mean energy of a 15 MV x-ray beam should be approximately 5 MeV. Figure 94 illustrates that the calculated tissue-maximum-ratio as a function of depth is within 5 % of the measured values for a

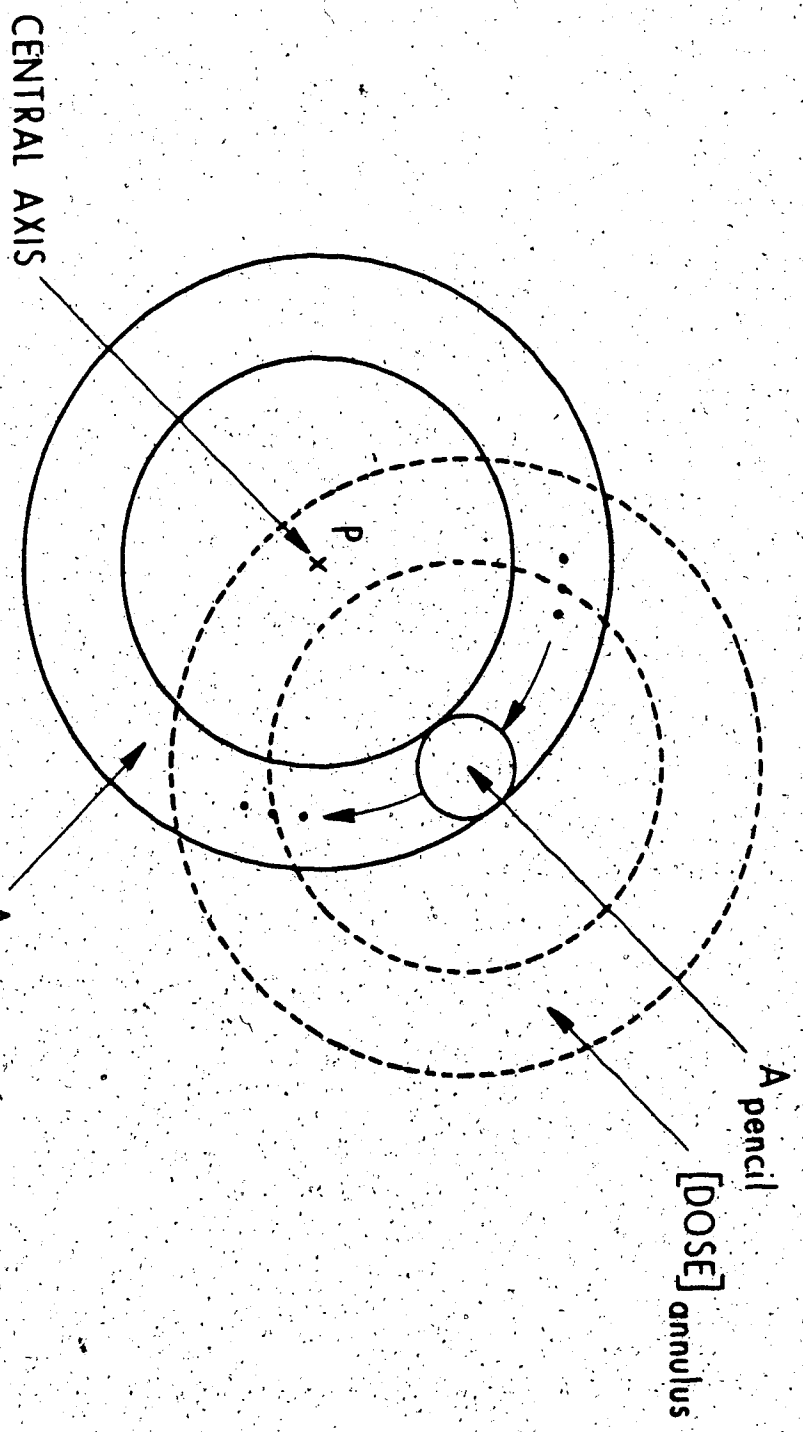

Figure 93. The dose at point P gets a dose contribution from an annulus by "revolving" a pencil dose distribution about point P. The value of the pencil dose distribution is $[DOSE]_{annulus}$

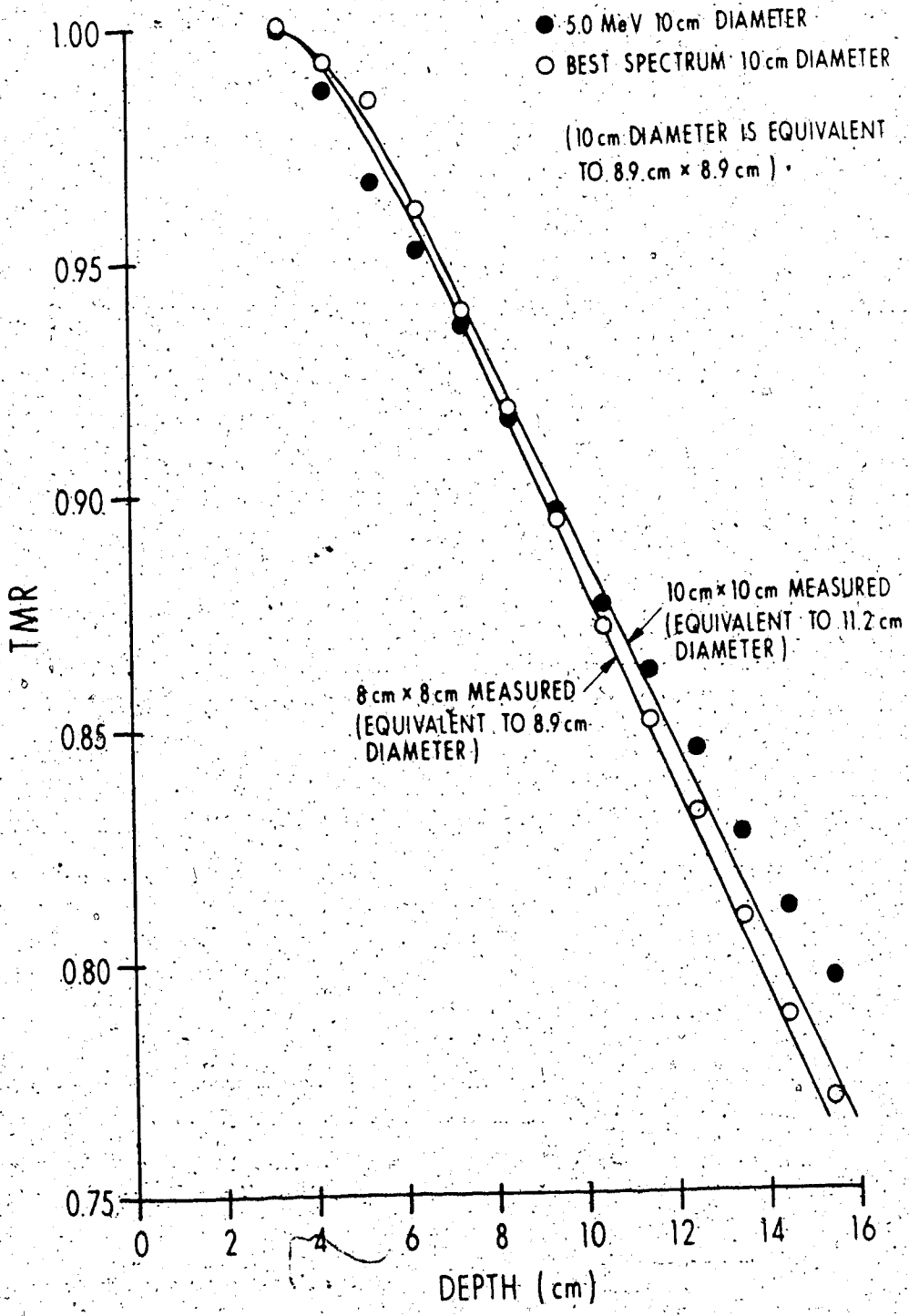

Figure 94. The measured TMR is compared to the EGS calculation of the TMR.

field size equivalent to a 10.0 cm diameter field.* The present version of the program accepts only a monoenergetic initial photon energy, so that each energy component in the spectrum requires a separate run of the program. The 15 MV spectrum used to model the dose in the build-up region (see Figure 70) had 36 energy components. Therefore, this would require 36 runs of the program to produce the dose results for the x-ray spectrum. It was felt that if the dose, as a function of depth (see Figure 94), could be modelled with good precision with only one energy component (5 MeV), then a spectrum containing six components would improve the agreement. The energy range between 0 and 15 MeV was, therefore, divided into six components and the mean energy of each component determined. The 36-component 15 MV spectrum (Figure 70) was used as a starting point. The mean energy of the six components were chosen with the mean energy of the bins of the 36-component spectrum, $(h\nu_o)_{nm}$, using:

$$(h\nu_o)_n = \frac{\sum_m (h\nu_o)_{nm} \cdot F_{nm}}{\sum_m F_{nm}} \qquad (6.2)$$

Where F_{nm} is the fluence of photons in each component of the 36-component spectrum. The photon energies that resulted

* The EGS program assumed cylindrical geometry so the equivalent circular field was used to model rectangular fields (54).

were 0.18 MeV, 0.67 MeV, 2.57 MeV, 6.61 MeV, 11.12 MeV and 13.78 MeV. A determination of the weighting of the spectral components, to give the best agreement with measured data, was made using the least-squares method. Figure 94 illustrates that the photon fluence, weighted in the proportions 0:11:11:11:5:0, improved the agreement of the calculated and measured dose to within 0.5 %.

The effect of a low-density water-like slab heterogeneity on pencil and broad beam geometries was investigated. The cut-off kinetic energy for the charged particle was chosen to be 189 keV (total energy of 700 keV). Figure 95 illustrates a comparison between pencil isodose curves in a homogeneous (on the right) and a heterogeneous phantom (on the left). The 50 % isodose line is not present inside the heterogeneous portion of the pencil beam. The 5 % and lesser isodose lines "bulge" outwards. This indicates that charged particles are "streaming" outward from the pencil beam into the surrounding low-density region. At first sight, the 0.1 % isodose line does not seem to be a very important contribution to the dose. However, $A_{annulus}$ increases with distance from the central axis. Therefore, Equation 6.1 suggests that a shift in isodose lines to greater radius will produce a greater contribution when summed for a broad beam.

The TMR inhomogeneity correction factor for a broad beam was determined by summing pencil beam contributions for a heterogeneous and homogeneous phantoms. The thickness and density of the heterogeneity was fixed at 8 cm and

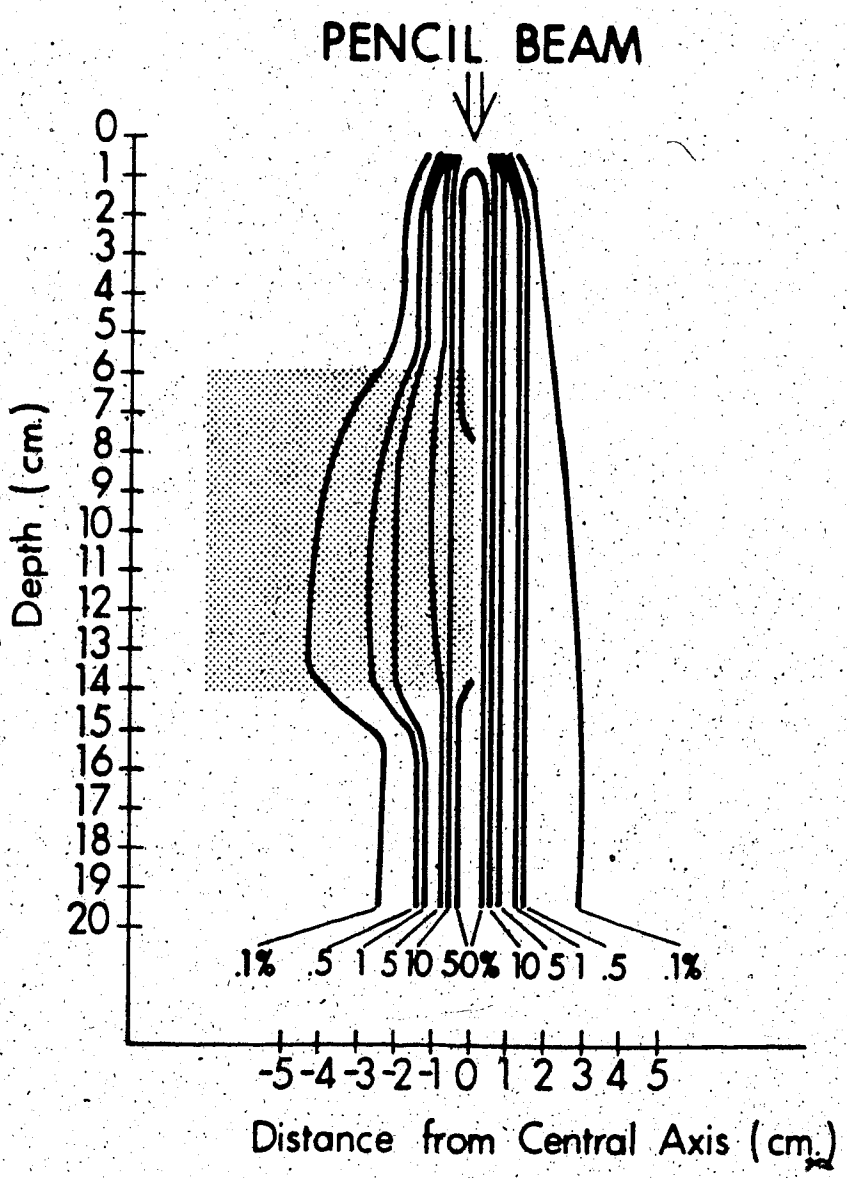

Figure 95. A comparison between pencil beam isodose curves in a homogeneous (right) and heterogeneous phantoms (left). The shaded region has a density of 0.25 g/cm^3.

0.25g/cm^3, respectively. The total thickness of overlying material was 15.5 cm (actually, the average dose between 15 and 16 cm was determined). Figure 96 illustrates the calculated correction factor. Also shown is the measured correction factor from Figure 86 obtained with cork as the low-density heterogeneity (with a density of 0.30 ± 0.02 g/cm^3). There is a 2 % discrepancy between the calculated and measured data. Most of the discrepancy is probably due to the difference between the actual cork density (0.30g/cm^3) used in the measurements and the density used in the Monte Carlo simulation (0.25g/cm^3). When determining the correction factor from measurement there was an underlying assumption that the mean stopping power of charged particles in a disequilibrium situation was equal to the mean stopping power in an equilibrium situation. This is equivalent to assuming that Equation 1.5.15 can be simplified to a simple ratio of ionization measurements. In contrast, the Monte Carlo correction factor implicitly takes into account the particle's changing stopping power as it loses energy. It is unlikely that this effect would produce a discrepancy of 2 % (53).

Lateral disequilibrium was investigated directly by setting the charged particle cut-off equal to the incident photon energy. This forced all of the charged particle energy to be deposited "on the spot". In this way, the KERMA, rather than the dose, is determined. Figure 97 illustrates a comparison between the profiles of KERMA and dose for a homogeneous and a heterogeneous phantom for a 5.0

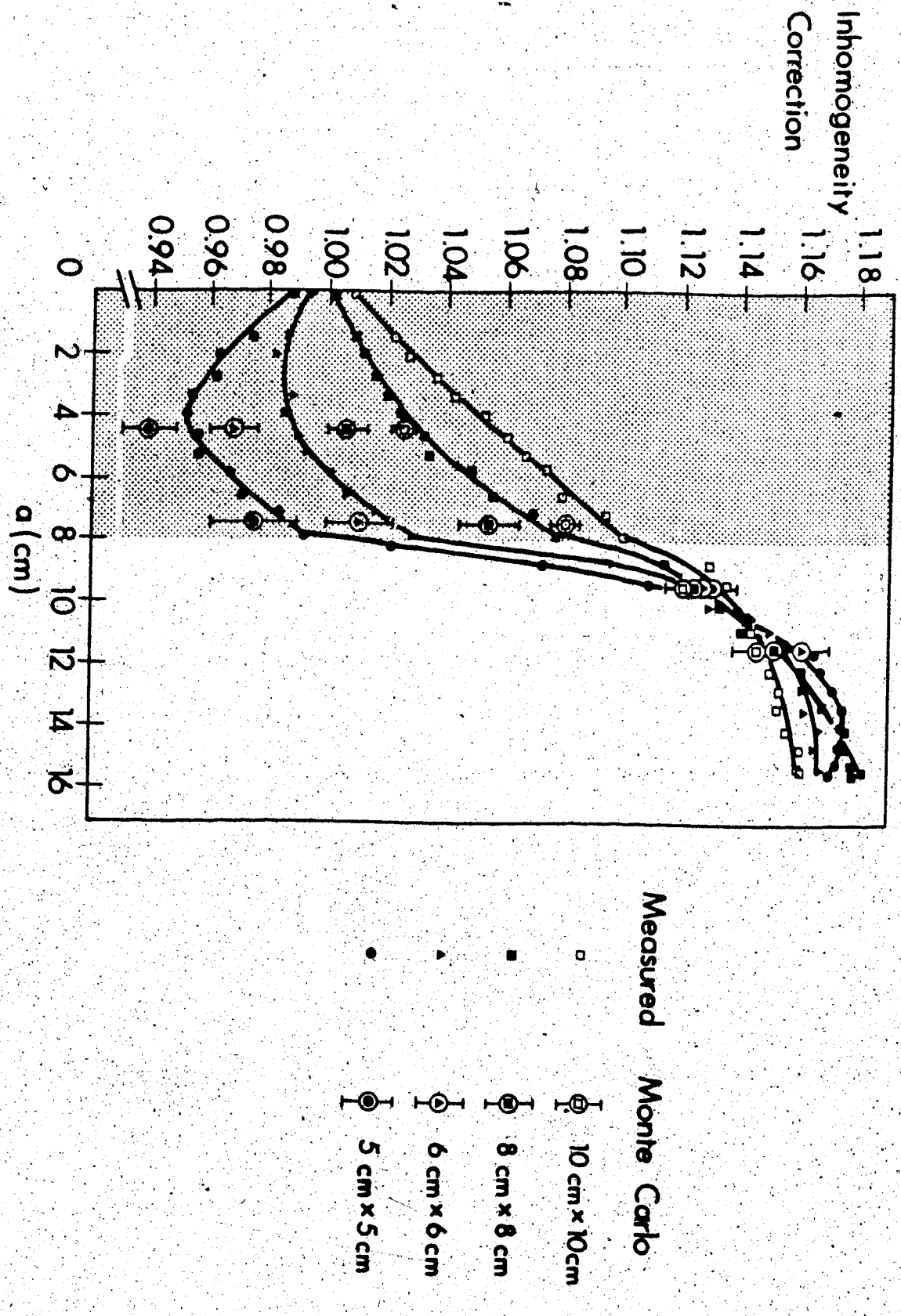

Figure 96. A comparison of measured inhomogeneity correction factors and ones calculated using the EGS Monte Carlo code.

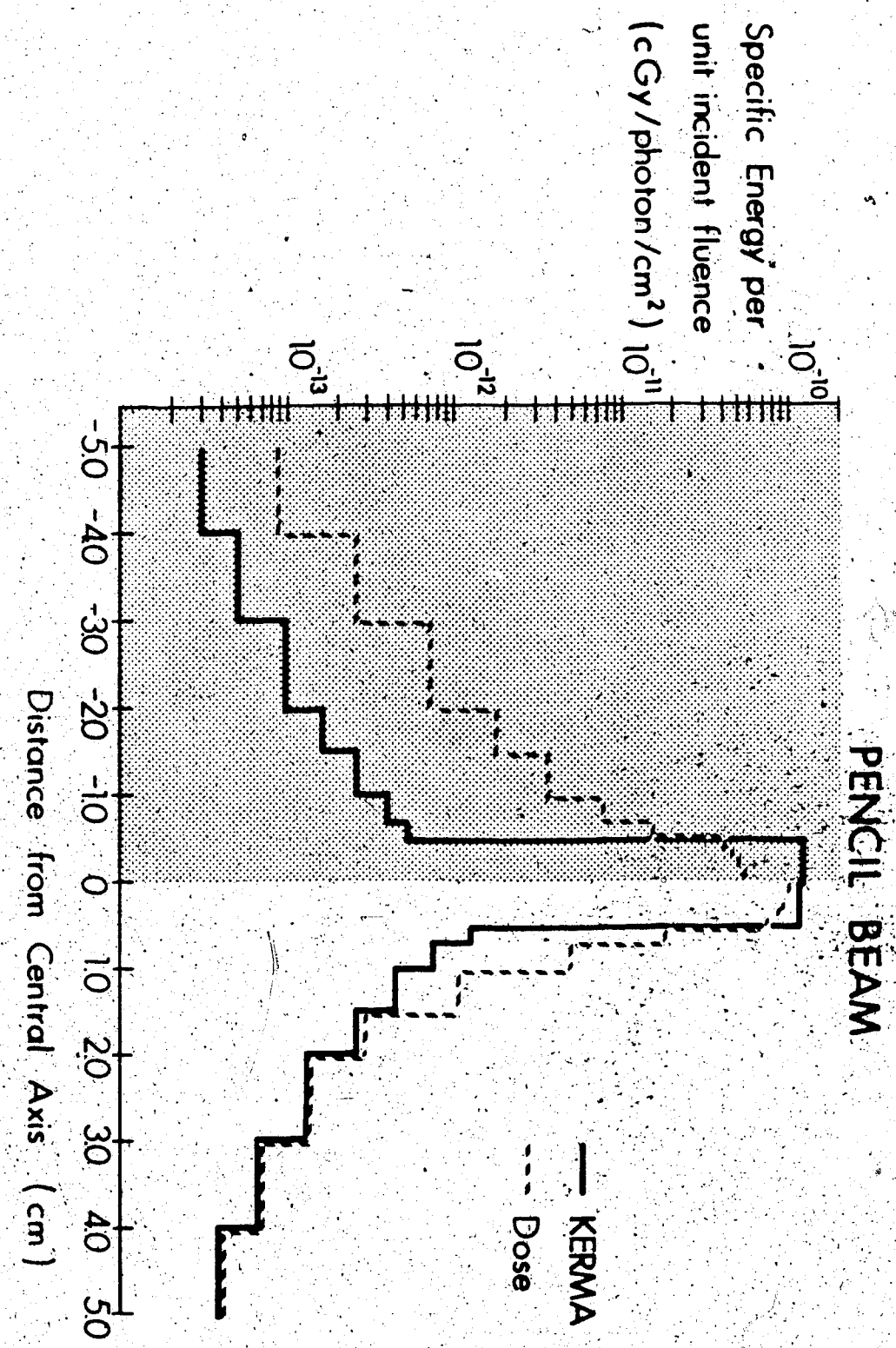

Figure 97. A comparison between the calculated profiles of KERMA and dose for a heterogeneous (left) and a homogeneous phantom (right).

MeV pencil beam. The profiles were taken at a depth of 10.5 cm. In the homogeneous case, the parameter, A, was 4.5 cm. It can be seen that in a homogeneous phantom, KERMA equals dose at a lateral distance of 1.5 to 2.0 cm from the central axis of the pencil beam. However, dose does not equal KERMA in a heterogeneous phantom even at a distance of 5.0 cm from the central axis of the pencil beam.

Broad beam KERMA distributions were produced from the pencil beam KERMA distributions. Figure 98 illustrates a comparison between the dose and KERMA correction factors for the 15 MV spectrum and its spectral components. The dose correction factor at first increases as a function of field radius and then decreases. The KERMA correction factor only decreases. At an energy of 0.67 MeV the dose and KERMA correction factors are in close agreement at field radii greater than 1 cm. At higher energies, the discrepancy between dose and KERMA correction facors becomes greater. Therefore, at lower energies KERMA is a good approximation to dose, but at higher energies, the KERMA equality with dose breaks down.

The measured correction factor is also shown in Figure 98. For higher energy beams the dose increases as a function of field size, whereas the KERMA always decreases as a function of field size. The increasing trend of the masured correction factor as a function of depth agrees best with the calculated correction factor using non-local energy deposition (the dose curves, rather than the KERMA curves).

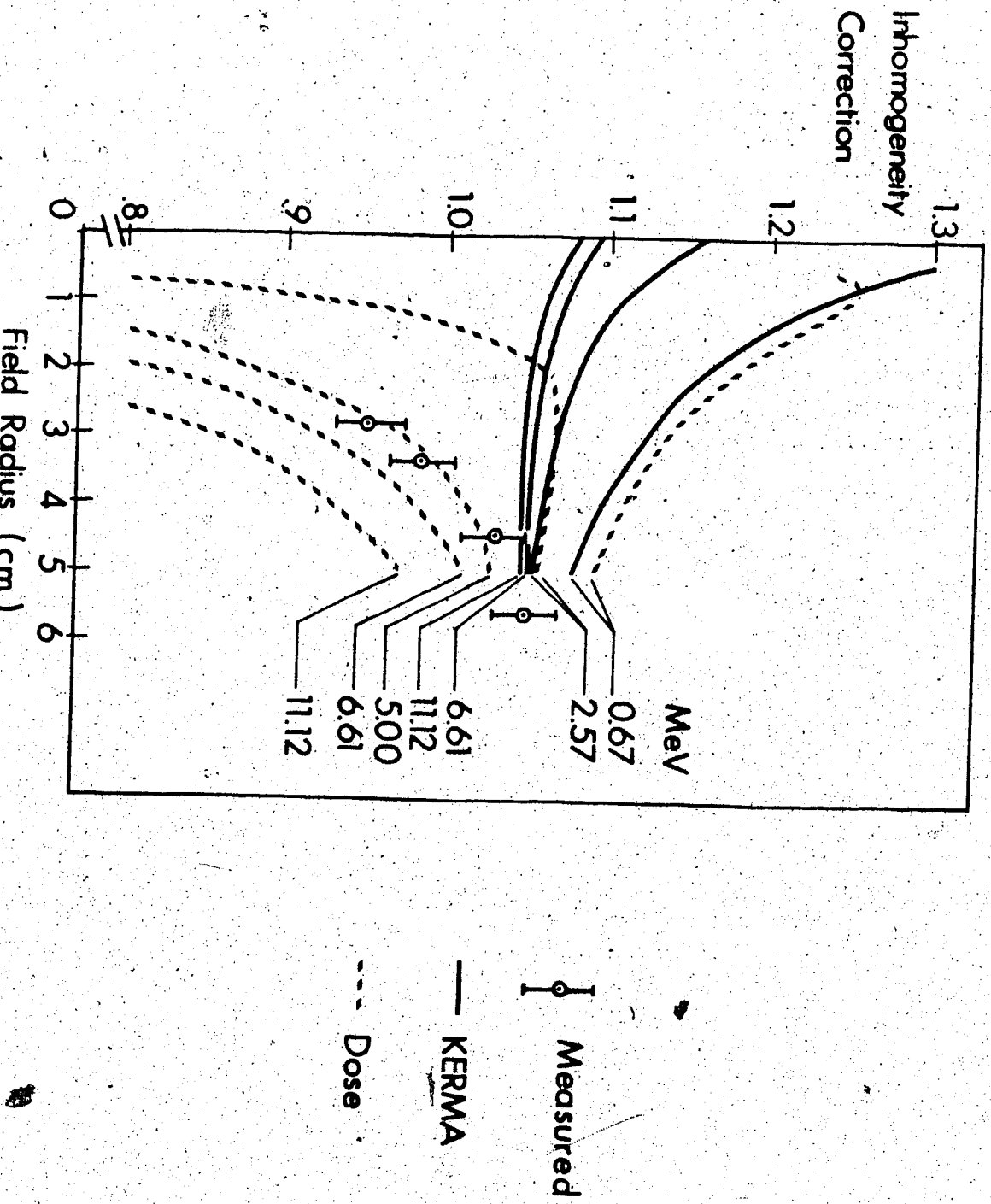

Figure 98. A comparison between dose and KERMA correction factors for the 15 MV spectrum and its spectral components.

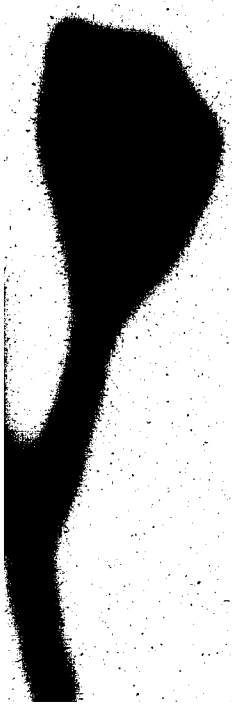

Convolution Method Of Calculating Dose

Knowledge finds differences, but
understanding seeks similarities.

7.1. Introduction

Section 3 in Volume 1 indicated that simulating the longitudinal transport of charged particles set-in-motion enabled the dose in the build-up region to be predicted. Section 6 in this Volume illustrated that the lateral transport of charged particles must be included to predict lateral disequilibrium phenomena. Therefore, a dose deposition model for megavoltage x-ray beams is required which explicitly takes into account charged particle transport.

In this section, a method of analysis which is physically sound and internally consistent will be discussed, which allows calculation of 3-dimensional dose distributions in homogeneous or heterogeneous phantoms irradiated with fields of high energy photons when electronic equilibrium is not present. The method is versatile enough to allow for rectangular fields, irregularly-shaped fields and the placement of beam blocks or compensators in the field. The use of measured data as a data base is abandoned and replaced with data generated from first principles by Monte Carlo techniques.

The Monte Carlo method is used to map the spatial distribution of charged particle energy away from a primary photon interaction site. This distribution, called a "primary dose spread array", is convolved spatially with the kinetic energy released (KER) at all the primary interaction sites to yield the primary dose distribution. In a

heterogeneous phantom, the dose spread arrays need to be modified.

Any current method separating primary from scatter dose can be improved with the methodology proposed here. Since convolution is a well-understood mathematical technique, there are conceptual and practical advantages for implementing a convolution framework for the spread of energy due to scattered photons* as well as charged particles set-in-motion.

The proposed method was based on concepts which will not become obsolete as improved computational power becomes available. The fundamental reason for this is the sound physical basis of the Monte Carlo and convolution procedures. Another reason is an inherent flexibility to compromise between speed and accuracy. Therefore, as computers become faster, greater accuracy can be achieved without modifying the algorithm substantially. As well, the present availability of "array processors" is compatible with the array structure of convolution mathematics.

* Dean (86) has used this approach to find where the scatter dose was being absorbed from Cobalt-60 primary photons interacting in one location of a water phantom.

7.2 Primary Dose Spread Arrays

7.2.1 Definition Of A Primary Dose Spread Array

A primary dose spread array* is the 3-dimensional spatial distribution of energy deposited by electrons and positrons which spread from the site of the primary photon interactions. It is generated by tracking the motion of charged particles away from primary interaction sites occurring within a cubic volume element (voxel). These charged particles are followed using the Monte Carlo method in a homogeneous phantom consisting of voxels with the same size, atomic number, and density. The amount of energy deposited at, and in the neighborhood of, the interaction voxel is scored. Figure 99 illustrates the procedure schematically.

7.2.2 The Generation Of Dose Spread Arrays Using The MOCA Monte Carlo Code

The dose spread arrays were generated by a "home-made" Monte Carlo code called MOCA developed from the program Buildup3.for, the Monte Carlo code used to calculate the

* The "dose spread array" is analogous to the "point spread array" used in image processing.

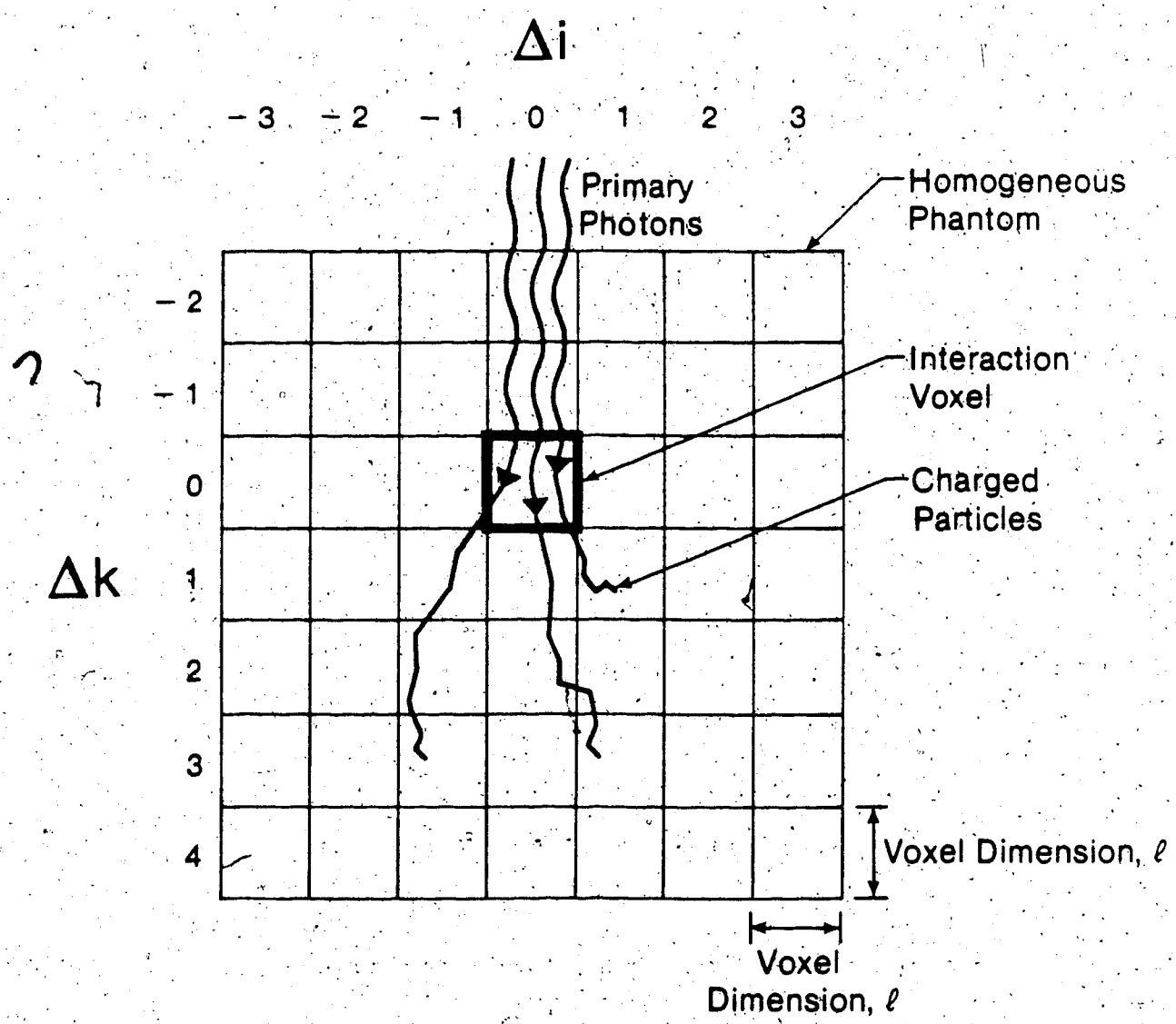

Figure 99. Primary photons interact in the interaction voxel and the charged particles set in motion are followed through the phantom to see where they deposit their kinetic energy.

build-up dose in Section 3 of Volume 1. MOCA takes into account the photoelectric effect, Compton effect and pair production. MOCA produces 0.511 MeV photons when the positron annhilates. Like Buildup3.for, MOCA employs the approximations of continuous slowing down (without generation of secondary "knock-on" electrons) and Gaussian lateral scattering for charged particles. Bremsstrahlung was not included in MOCA. Figures 100 to 102 are flow charts of the program MOCA.

A photon history begins, in MOCA, by initializing its energy, position and direction. The distance the photon travels before it interacts is first determined. The photon (or the scattered photon created by a Compton interaction) is followed until its energy falls below the photon energy cut-off, or it interacts by the photoelectric or pair production effects, or it leaves the phantom. The type of photon interaction is chosen by finding "partial fractions" based on the Compton and pair production attenuation coefficients. Charged particles generated by photon interactions are placed in a "queue" for further processing after the end of the photon history.

MOCA employs a novel technique to determine the kinetic energy acquired by a charged particle following a Compton or a pair production interaction. The Compton interaction cross-section per unit kinetic energy of the recoil electron, $d\sigma/dT$, has a complex dependence on kinetic energy, T. The method provides a way of numerically inverting the differential cross-section with respect to

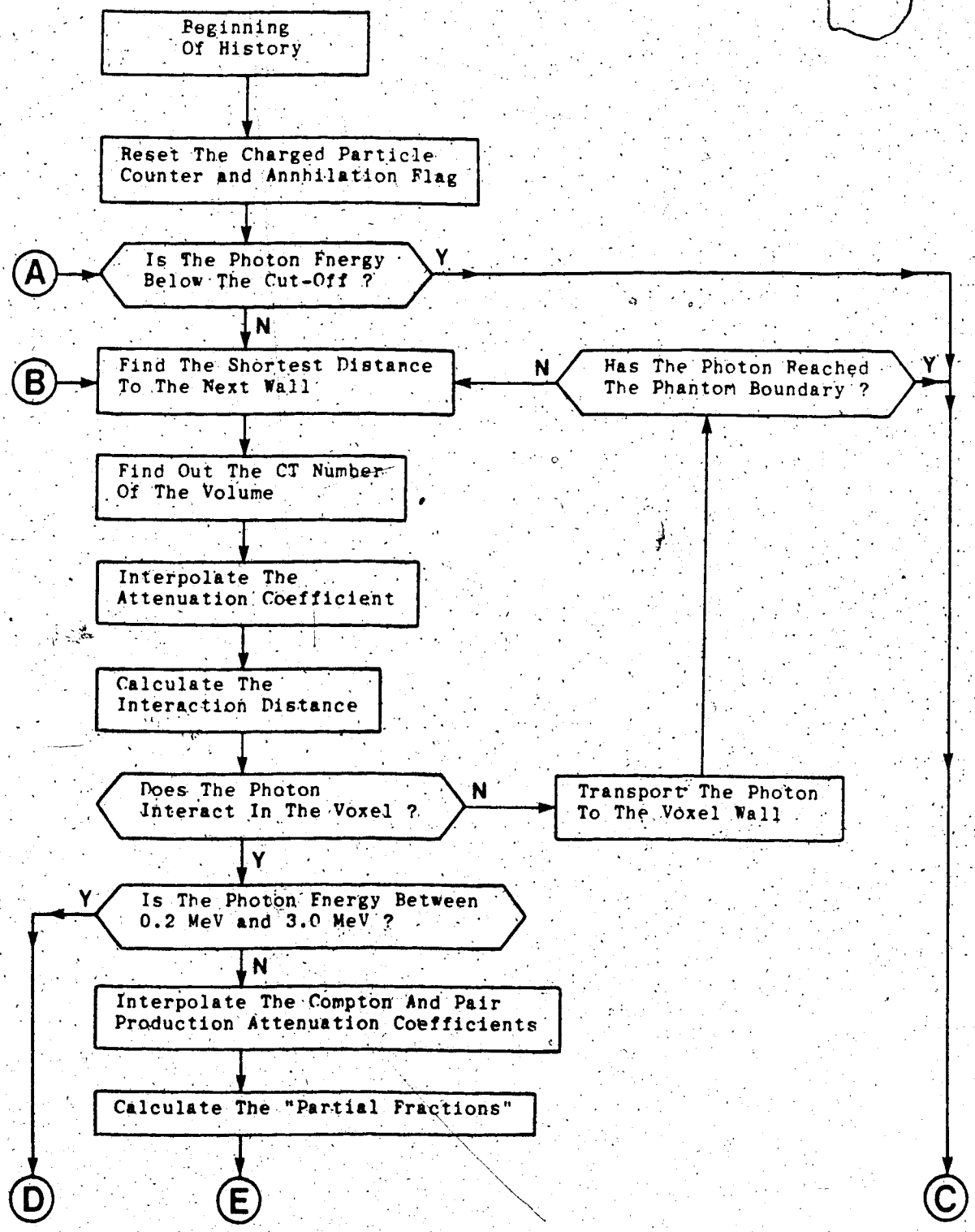

Figure 100. Flow chart for photon transport part of MOCA. A) and B) are from Figure 101. B) can also come from Figure 102. C), D) and E) enter Figure 101.

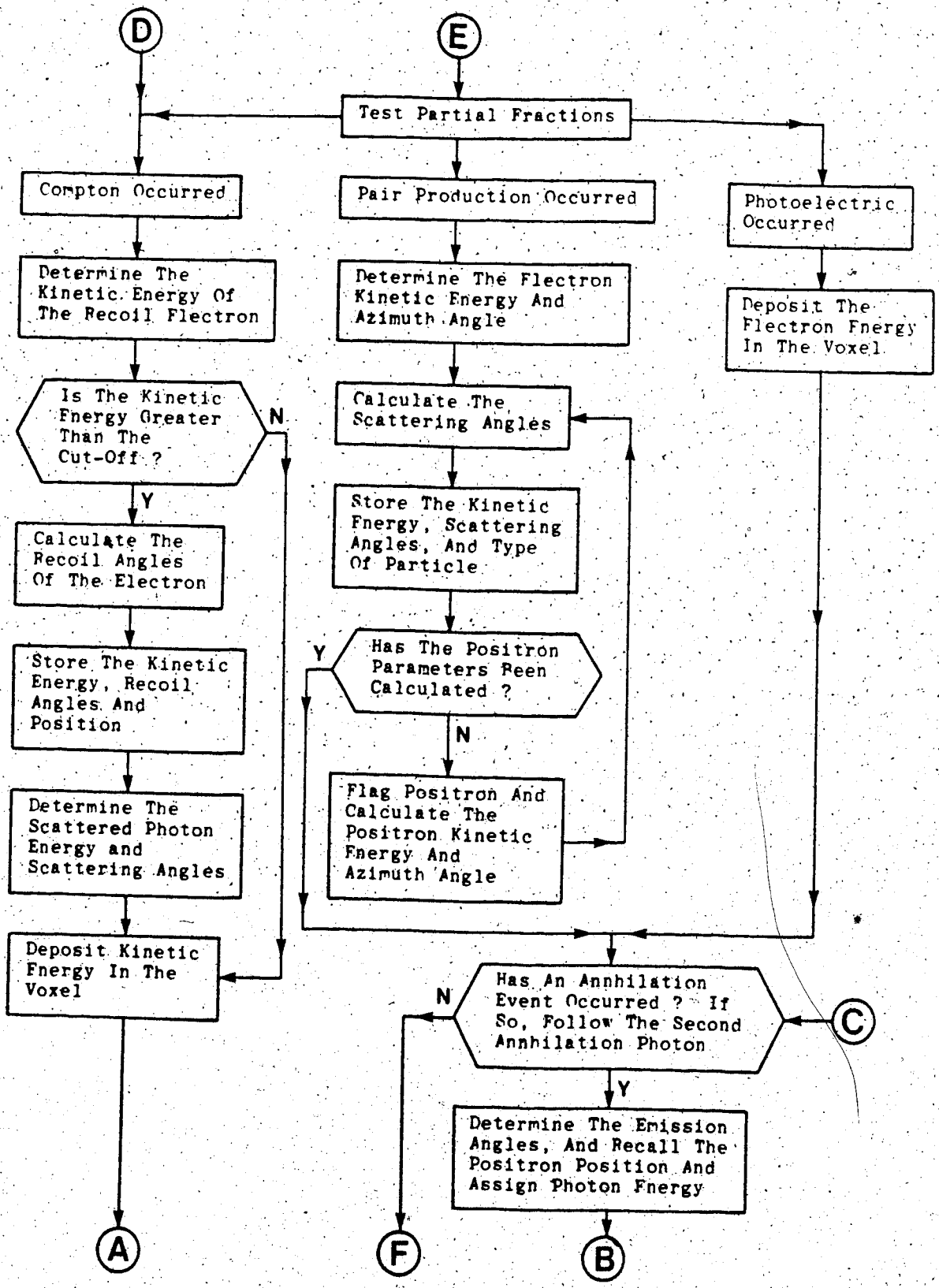

Figure 101. Flow chart for the part of MOCA dealing with the type of photon interaction. C), D) and E) are from Figure 100. A) and B) enter Figure 100. F) enters Figure 102.

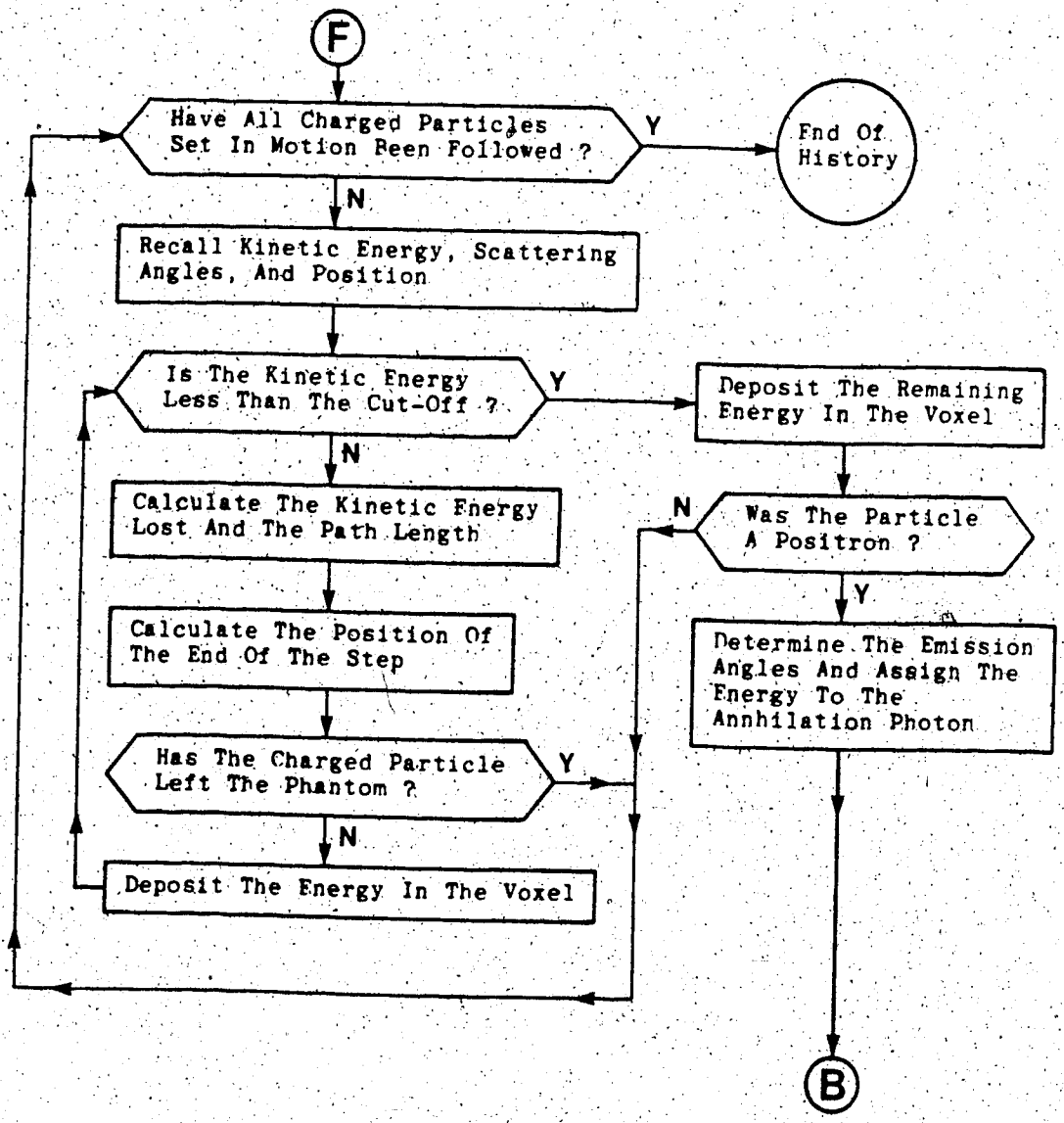

Figure 102. Flow chart for the charged particle transport part of MOCA. F) is from Figure 101. B) enters Figure 100.

kinetic energy.

Figure 103 illustrates the Compton differential cross-section as a function of kinetic energy up to the maximum kinetic energy, Tmax. The total area under the curve is equal to the total Compton cross-section, σ. The curve in Figure 103 is subdivided into N intervals such that the area of each interval has an equal area σ/N. Each interval represents an equiprobable occurrence of interaction. The corresponding kinetic energy of each interval, $T_i(h\nu)$, is found. Since each $T_i(h\nu)$ is equally likely to be the recoil energy of the electron, there can be a one-to-one correspondence with a random number. This is accomplished by normalizing the interval kinetic energy, $T_i(h\nu)$, to the maximum kinetic energy.

Figure 104 illustrates the values of $T(h\nu)/Tmax$ as a function of random number, R, for various values of incident photon energy, $h\nu$(MeV). It can be seen that at higher incident photon energies there is a greater probability of the generation of high energy recoil electrons.

The pair production interaction is treated in the same manner as the Compton interaction except that the maximum kinetic energy, T_A, is now given by Equation 3.1.10. Figure 105 illustrates the values of $T(h\nu)/T_A$ as a function of random number for 3.0 MeV and 10.0 MeV photons. The most probable kinetic energy of a charged particle is around half the maximum energy.

The charged particles generated by a photon are taken from the "queue" at the end of the photon history. Their

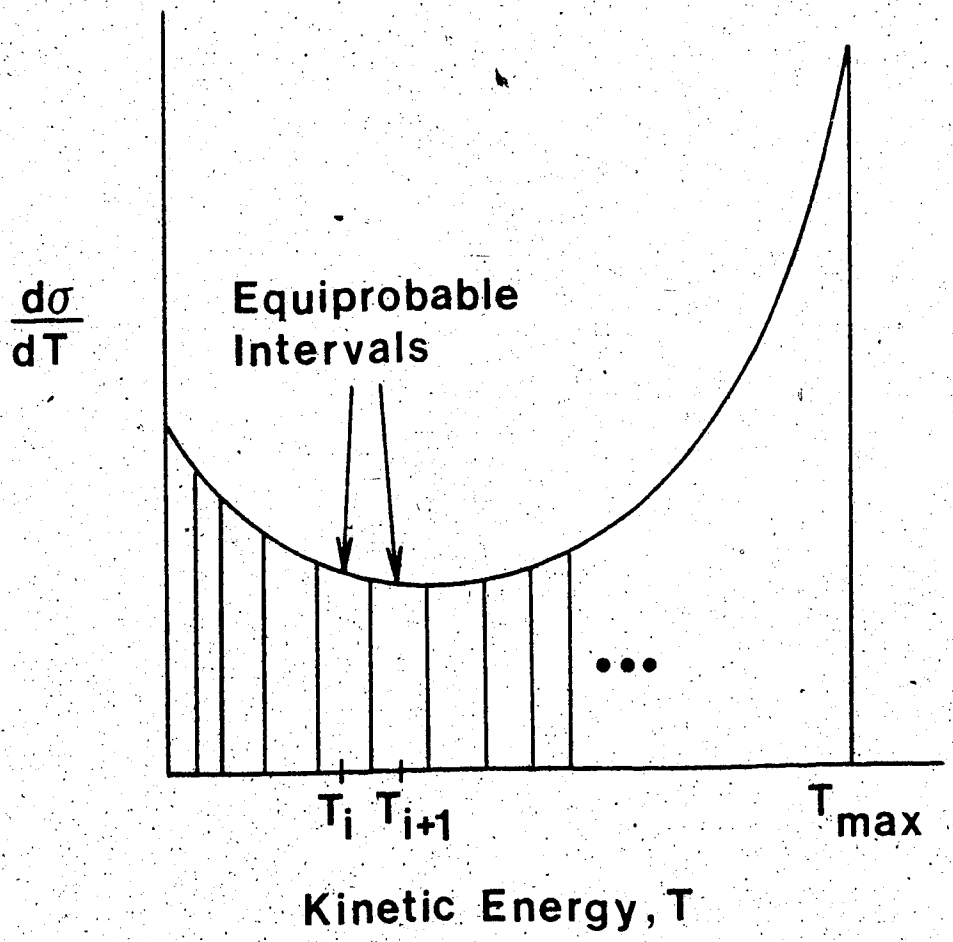

Figure 103. The Compton differential cross-section as a function of kinetic energy. The area under the curve, equal to the total interaction cross-section, is divided up into equiprobable areas.

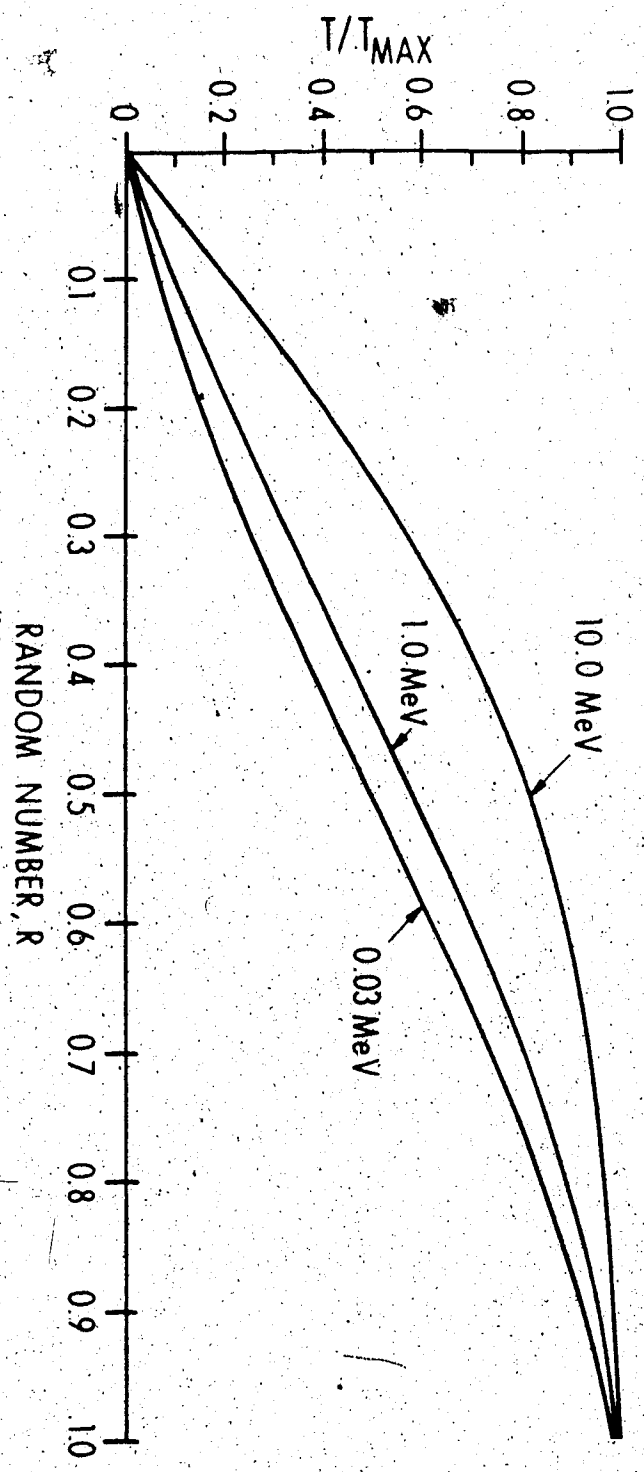

Figure 104. $T(h\nu)/T_{max}$ as a function of random number, R, for various incident photon energies. The Compton recoil electron kinetic energies can be chosen with equally weighted random numbers chosen between 0 and 1.

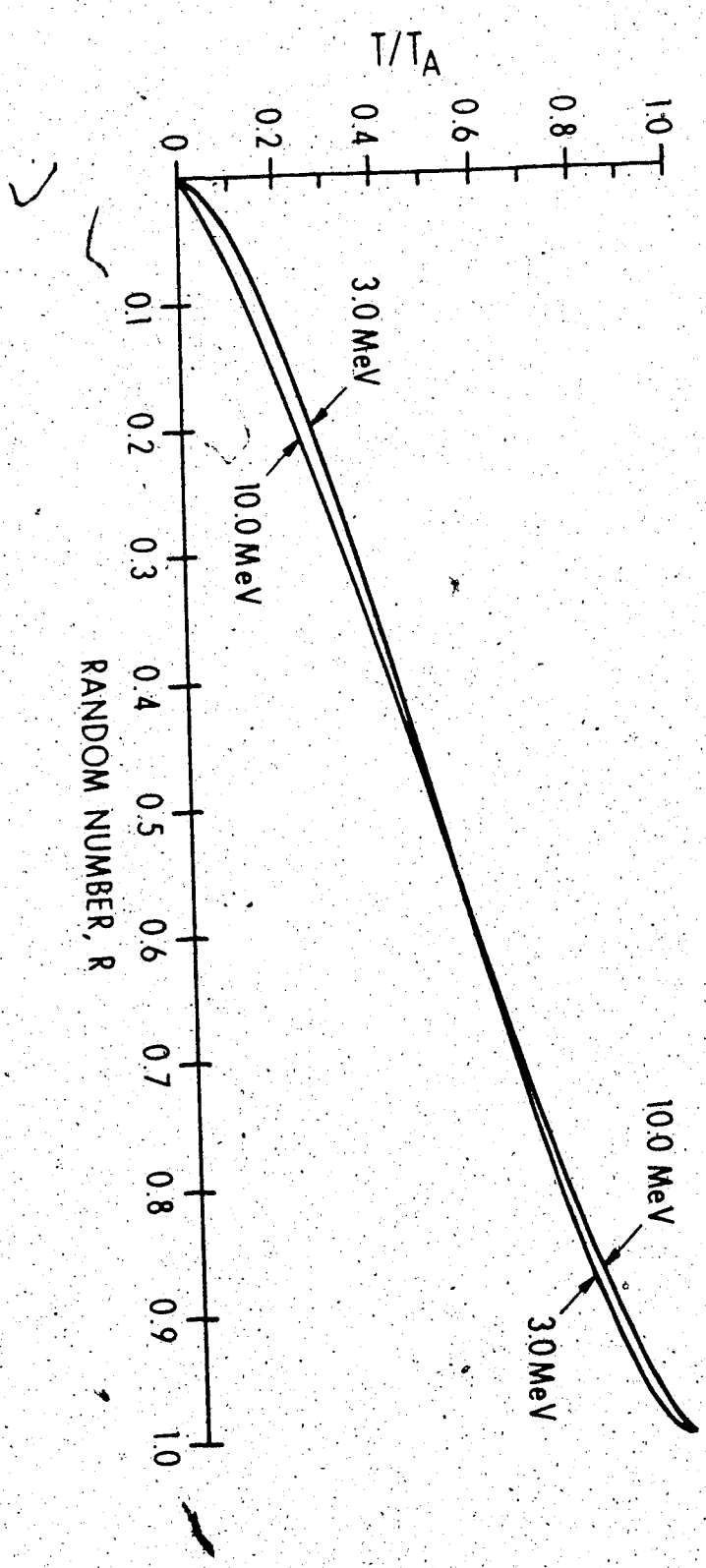

Figure 105. $T(h\nu)/T_A$ as a function of random number, R, for various incident photon energies. The kinetic energy of pair production charged particles can be chosen with equally weighted random numbers chosen between 0 and 1.

kinetic energy, position and direction in which they were set in motion is recalled. The charged particle transport is almost identical to Buildup3.for. The exception is that annhilation photons are produced when a positron reaches the end of its range ("annhilation in flight" is ignored). The annhilation photons are treated as a scattered photon.

Appendix 10 contains a listing of the program MOCA. MOCA was used instead of EGS because MOCA was much simpler than EGS and, therefore, there was much more control over the programming of the geometry to describe the dose spread arrays. Despite its simplicity, MOCA produces almost the same results as EGS. Figures 106 and 107 are a comparison between MOCA and EGS Monte Carlo calculations of the depth-dose from 1.25 MeV and 5 MeV photon beams, respectively. The field size was 10 cm x 10 cm for the MOCA calculation and a field radius of 5.6 cm (the equivalent circular radius for a 10 cm x 10 cm field) for the EGS calculation. Also included in Figure 106 is the measured depth-dose for a Cobalt-60 beam. There is good agreement between the Monte Carlo programs at both energies and with measured data.

7.2.3 Results

Figures 108 and 109 show voxel elements of primary dose spread arrays for a pencil beam of 15 MV x-rays interacting in a homogeneous phantom with cubic voxel dimensions of

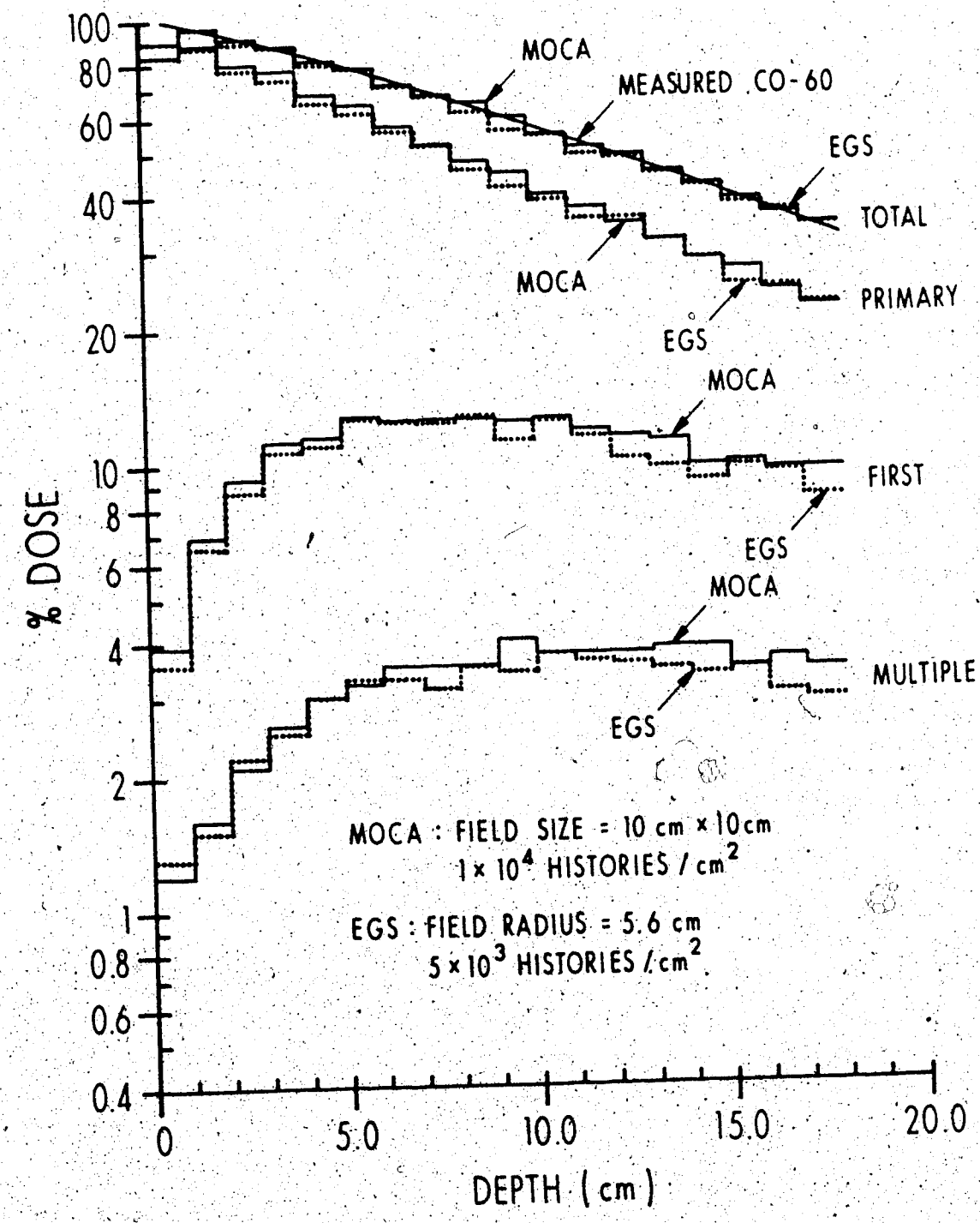

Figure 106. A comparison of components of the percent dose predicted by MOCA and EGS for Cobalt-60 photons (1.25 MeV). The measured total dose is also shown for comparison.

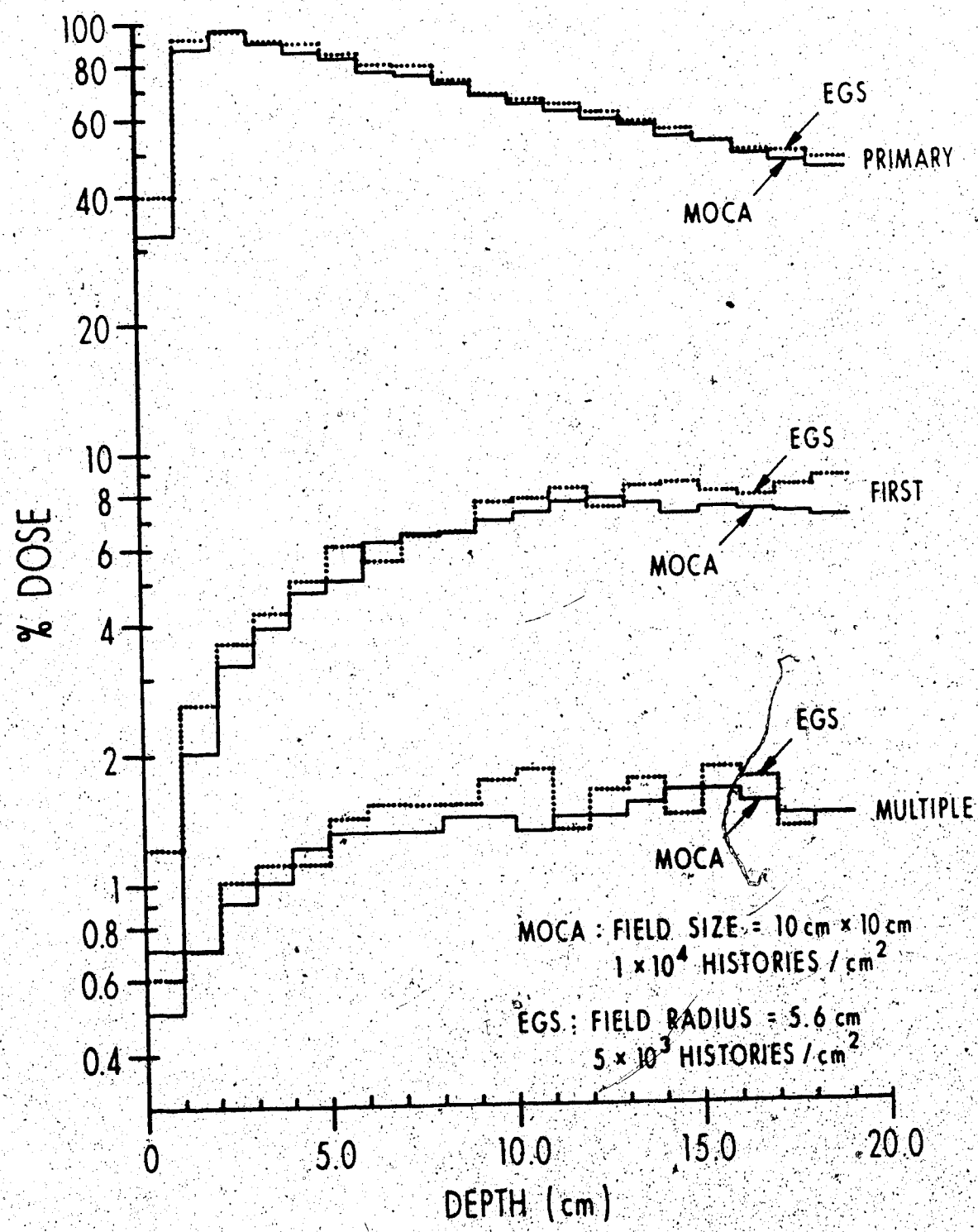

Figure 107. A comparison of components of the percent dose predicted by MOCA and EGS for 5 MeV photons.

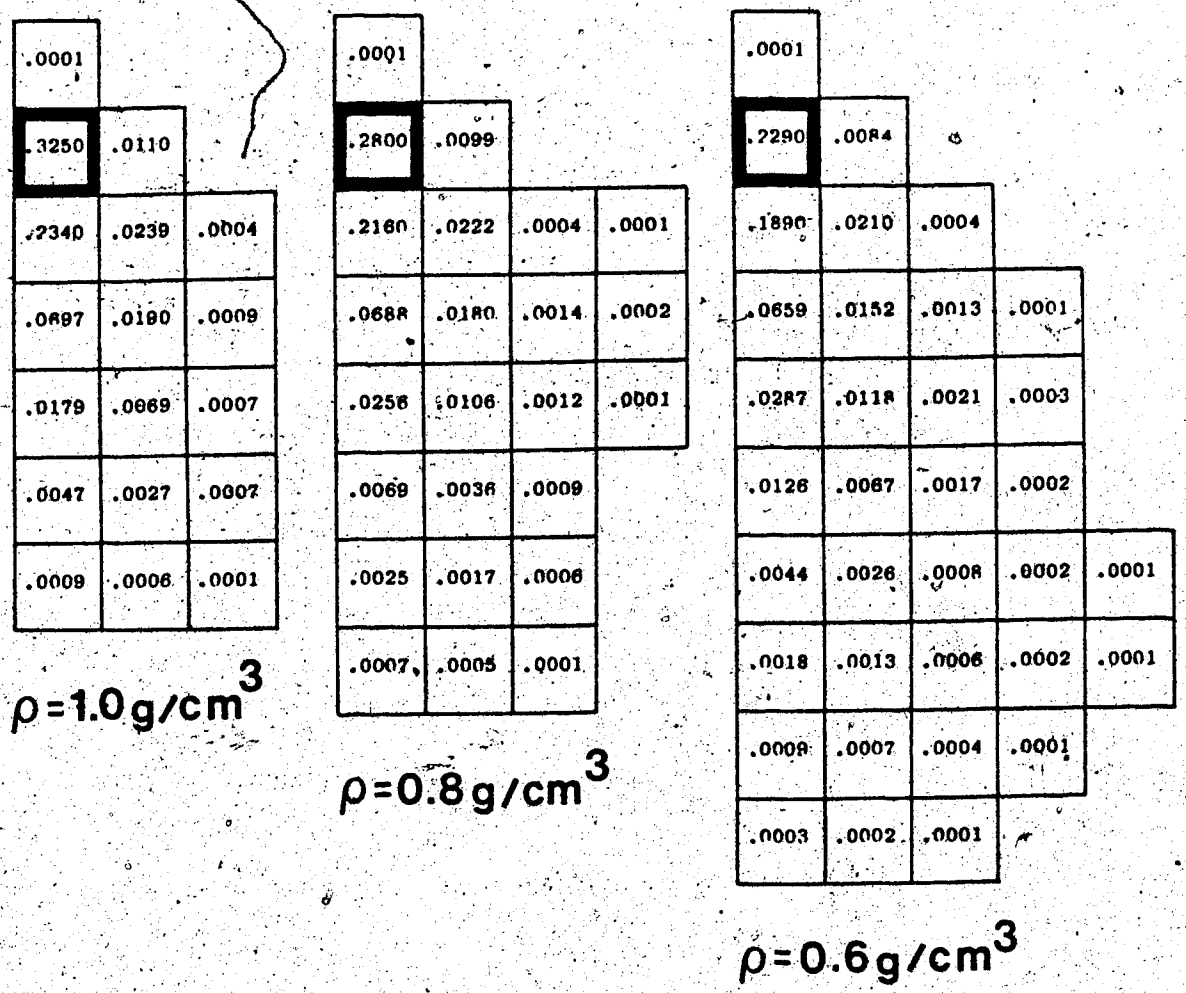

Figure 108. Primary dose spread arrays for 15 MV photons interacting in an interaction voxel (shown with bold boundaries). The voxels are cubic with dimensions of 1.0 cm on each side.

.0001				
.1730	.0065	.0001		
.1440	.0177	.0007		
.0631	.0146	.0010	.0001	
.0275	.0094	.0014	.0003	.0001
.0142	.0070	.0018	.0005	.0002
.0077	.0048	.0017	.0006	.0002
.0041	.0029	.0013	.0004	.0001
.0019	.0015	.0007	.0003	.0001
.0009	.0007	.0004	.0002	.0001
.0005	.0005	.0003	.0002	.0001
.0003	.0003	.0002	.0002	.0001
.0002	.0002	.0001	.0001	
.0001	.0001	.0001		

ρ=0.4g/cm^3

.0001						
.1120	.0051	.0001				
.0908	.0101	.0006	.0001			
.0439	.0104	.0013	.0003			
.0249	.0087	.0018	.0004	.0001		
.0143	.0063	.0015	.0004	.0001		
.0080	.0043	.0012	.0004	.0002	.0001	
.0048	.0031	.0011	.0004	.0002	.0001	
.0031	.0023	.0010	.0005	.0002	.0001	
.0020	.0016	.0009	.0005	.0002	.0001	.0001
.0014	.0012	.0007	.0005	.0002	.0001	.0001
.0010	.0009	.0006	.0004	.0002	.0002	.0001
.0007	.0007	.0005	.0003	.0002	.0001	.0001
.0005	.0005	.0004	.0002	.0002	.0001	.0001
.0003	.0003	.0003	.0002	.0001	.0001	
.0002	.0002	.0002	.0002	.0001	.0001	
.0001	.0001	.0001	.0001	.0001		
.0001	.0001	.0001	.0001	.0001		
.0001	.0001					

ρ=0.2g/cm^3

Figure 109. Primary dose spread arrays for 15 MV photons (see Figure 108).

1.0 cm. The incident photon fluence spectrum obtained using EGS in Section 6 was also used by MOCA. The density of the arrays is from $0.2 g/cm^3$ to $1.0 g/cm^3$ in steps of $0.2 g/cm^3$. The media are assumed to be water-like in chemical composition. The voxels shown in these figures are in the same plane as both the interaction voxel and the primary pencil beam. The beams have the same cross-sectional area as the voxels and are made to interact only in the interaction voxel (bold borders). At least 10^6 charged particles/cm^2 were set in motion by primary photons to generate these arrays. To speed up the convolution process for rectangular fields, the dose spread arrays are produced in a 3-dimensional Cartesian geometry. The dose spread arrays are quadrilaterally symmetric about the primary photon direction, which is designated as the Δk axis. Therefore, an element of a dose spread array can be given by:

$$\begin{aligned} A_p(\rho,\ell,\Delta i,\Delta j,\Delta k) &= A_p(\rho,\ell,-\Delta i,\Delta j,\Delta k) \\ &= A_p(\rho,\ell,\Delta i,-\Delta j,\Delta k) \\ &= A_p(\rho,\ell,-\Delta i,-\Delta j,\Delta k) \end{aligned} \qquad (7.2.1)$$

The dose spread arrays are also symmetric with respect to interchange of the Δi and Δj axis, therefore:

$$A_p(\rho,\ell,\Delta i,\Delta j,\Delta k) = A_p(\rho,\ell,\Delta j,\Delta i,\Delta k) \qquad (7.2.2)$$

Figures 108 and 109 clearly illustrate that the

assumption of local energy deposition at 15 MV is untenable. The value of the dose spread array at the interaction voxel (location 0,0,0) in a 1.0g/cm^3 phantom with a voxel size of 1 cm is 0.325 which indicates 32.5 % of the energy released at the interaction site is deposited there. The value at the same location for a 0.2g/cm^3 phantom with a voxel size of 1 cm is only 0.112. The maximum longitudinal range of charged particles set in motion in a 1.0g/cm^3 phantom is about 4 to 6 cm and in a 0.2g/cm^3 phantom the maximum longitudinal range is about 20 cm! In the lateral direction charged particles can contribute dose about 1 to 3 cm and 5 to 7 cm from the interaction site for 1.0g/cm^3 and 0.2g/cm^3 phantoms, respectively. Figure 110 illustrates the primary dose spread arrays for 6 MV x-rays and a Co-60 (1.25 MeV) photon beam. The spectrum used to determine the 6 MV build-up curves (see Figure 69) was used. The density of the phantoms was 0.5g/cm^3 and the voxel dimension was 1.0 cm. As the energy decreases, more of the primary energy is deposited in the interaction voxel and the longitudinal and lateral range of the charged particles is reduced. At 1.25 MeV in a phantom of density 0.5g/cm^3, the primary energy is deposited within 1.0 cm from the primary interaction site. Therefore, the assumption of local primary energy deposition is more reasonable for Co-60 beams.

The primary dose spread array values indicate the primary energy deposited in each voxel normalized to the collision fraction of the total energy released in the

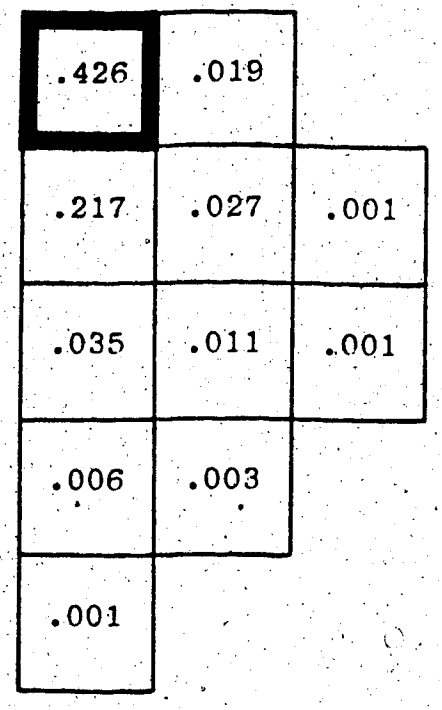

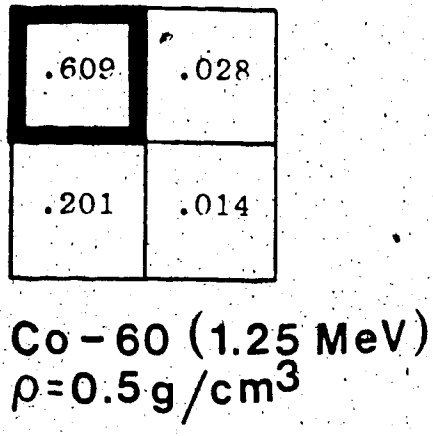

Figure 110. Primary dose spread arrays for 6 MV and Co-60 photons. The voxel dimension is 1.0 cm.

interaction voxel:

$$A_p(\rho,\ell,\Delta i,\Delta j,\Delta k) = \frac{T(\rho,\ell,\Delta i,\Delta j,\Delta k)}{KER(\rho,\ell,0,0,0)} \qquad (7.2.3)$$

Where $Ap(\rho,\ell,\Delta i,\Delta j,\Delta k)$ is the primary dose spread array at a distance $\Delta i,\Delta j,\Delta k$ from the interaction voxel. $T(\rho,\ell,\Delta i,\Delta j,\Delta k)$ is the energy deposited at that site. $KER(\rho,\ell,0,0,0)$ is the total energy of charged particles set in motion at the interaction site that is lost to electron collisions (not bremsstrahlung) in the phantom (87).

Since the phantom is homogeneous, the interaction and dose deposition voxels have the same density. Therefore, the array value is also equal to the dose deposited due to electron collisions in the neighboring voxels per unit kinetic energy released per unit mass, Kc (collision KERMA) (87), at the interaction voxel. If the dose spread arrays are spatially invariant (Section 7.6 will discuss the implications of spatial invariance), Equation 7.2.3 can be expressed as:

$$A_p(\rho,\ell,\Delta i,\Delta j,\Delta k) = \frac{DOSE(\rho,\ell,i+\Delta i,j+\Delta j,k+\Delta k)}{K_c(\rho,\ell,i,j,k)} \qquad (7.2.4)$$

The primary dose spread arrays can be produced for different voxel dimensions and for a variety of water-like phantoms with different densities. Figure 111 illustrates the dose spread arrays with a voxel and beam dimension of 5.0 cm and a density of $0.2 g/cm^3$. The values of the dose

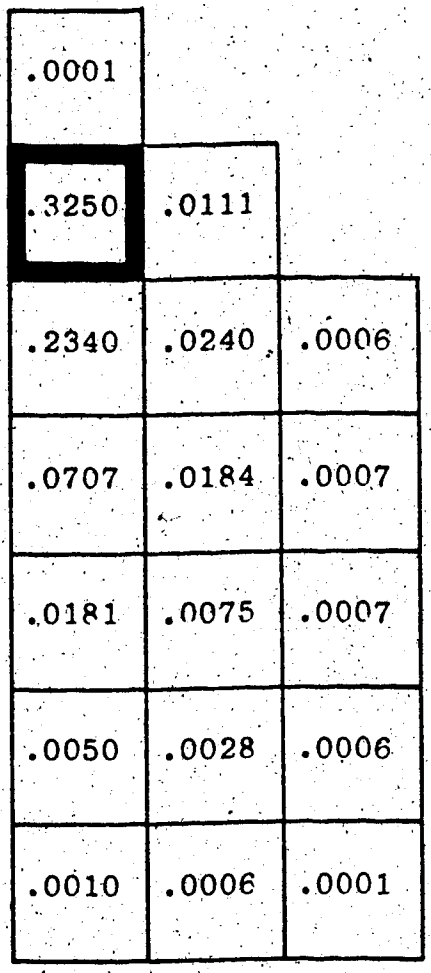

Figure 111. Primary dose spread array for 15 MV photons. The value of $\rho \cdot \ell$ is the same as Figure 108 (left).

spread array elements of Figure 111 are nearly equal to those of Figure 108 (left dose spread array). Therefore, the product of the phantom density, $\rho(g/cm^3)$, and voxel dimension, $\ell(cm)$, is a fundamental measure of the voxel "size" in units of g/cm^2. This is just an extension of O'Connors theorem (71). O'Connors theorem can now be said to be independent of the state of electronic equilibrium. This is expected because, for a material of fixed atomic number, both the stopping power and the angular scattering power are directly proportional to the density (88). This has also been shown experimentally by Young and Kornelson (64,80).

The primary dose spread arrays are stored for various values of voxel size expressed in units of radiological depth, $\rho \cdot \ell$ (from $\rho \cdot \ell = 0.2 g/cm^2$ to $1.0 g/cm^2$ in step sizes of $0.2 g/cm^2$). This allows flexibility in the choice of voxel dimensions for dose computations and hence the spacing of calculation points. For example, a choice of a voxel size of $0.2 g/cm^2$ can be used either for a medium with $\rho = 1.0 g/cm^3$ to establish calculation points spaced at a distance of 0.2 cm or in a medium with $\rho = 0.2 g/cm^3$ for calculation points spaced 1 cm apart. When the desired spatial resolution and density yields a value of $\rho \cdot \ell$ which has not been stored, the dose spread array values need to be interpolated from the stored arrays.

7.3. Scatter Dose Spread Arrays

The Monte Carlo program used to determine the primary dose spread arrays is also used to follow scattered photons and charged particles produced by the scattered photons. The first scattered dose is scored separately from higher order multiple scatter. The dose due to first scatter photons, which is deposited "relatively" close to the primary interaction site, is placed in a truncated first scatter (TFS) dose spread array. The first scatter dose deposited "relatively" far from the primary interaction site is included with multiple scatter in a residual first and multiple scatter (RFMS) dose spread array. Positron annhilation photons are treated as if they were multiple scattered photons. Since, at megavoltage energies, first scattered photons are mainly forward directed, the location of the interaction voxel within the dose spread array has been optimized so that more voxels of the TFS dose spread array are scored "down-stream" of the primary interaction site than "up-stream".

The bulk of first scatter photons have been separated from the multiple scatter photons because of their different spatial distribution and magnitude of contribution to the total dose . Figures 106 and 107 have illustrated the relative contributions of primary, first scatter, and multiple scatter dose for 1.25 MeV and 5.0 MeV photons using EGS and MOCA Monte Carlo programs. The contribution of first scatter photons is almost an order of magnitude lower

than that of primary photons. The contribution of multiple scatter at this field size is less than one half that of first scatter at depths to 20 cm. Separating most of the first scatter from multiple scatter also allows a choice of optimal sizes for each type of dose spread array. Having a high spatial resolution when little dose is being deposited is not an effective use of computation time (89). The size of the TFS dose spread array and the voxel dimension of both the scatter dose spread arrays and the primary dose spread array is selected to compromise speed and accuracy. The more elements in the TFS dose spread array, the slower the convolution calculation. The TFS dose spread array voxel dimension can be made smaller than the RFMS dose spread array, reflecting its proximity and greater importance in contributing to the total dose. The TFS dose spread array is produced and stored for the same $\rho \cdot \ell$ values as the primary dose spread array whereas the RFMS dose spread array is stored for values of $\rho \cdot \ell$ from $1.0 g/cm^2$ to $5.0 g/cm^2$ in steps of $1.0 g/cm^2$. The TFS dose spread array may be truncated without compromising too much accuracy because most first scatter dose is deposited close to the primary interaction site (77). In order to take into account the scatter dose arriving at a field boundary from primary interactions at the opposite boundary, the total lateral size of the RFMS dose spread array must be at least twice that of the largest field in which the dose is to be calculated.

Figures 112 and 113 illustrate examples of the TFS and

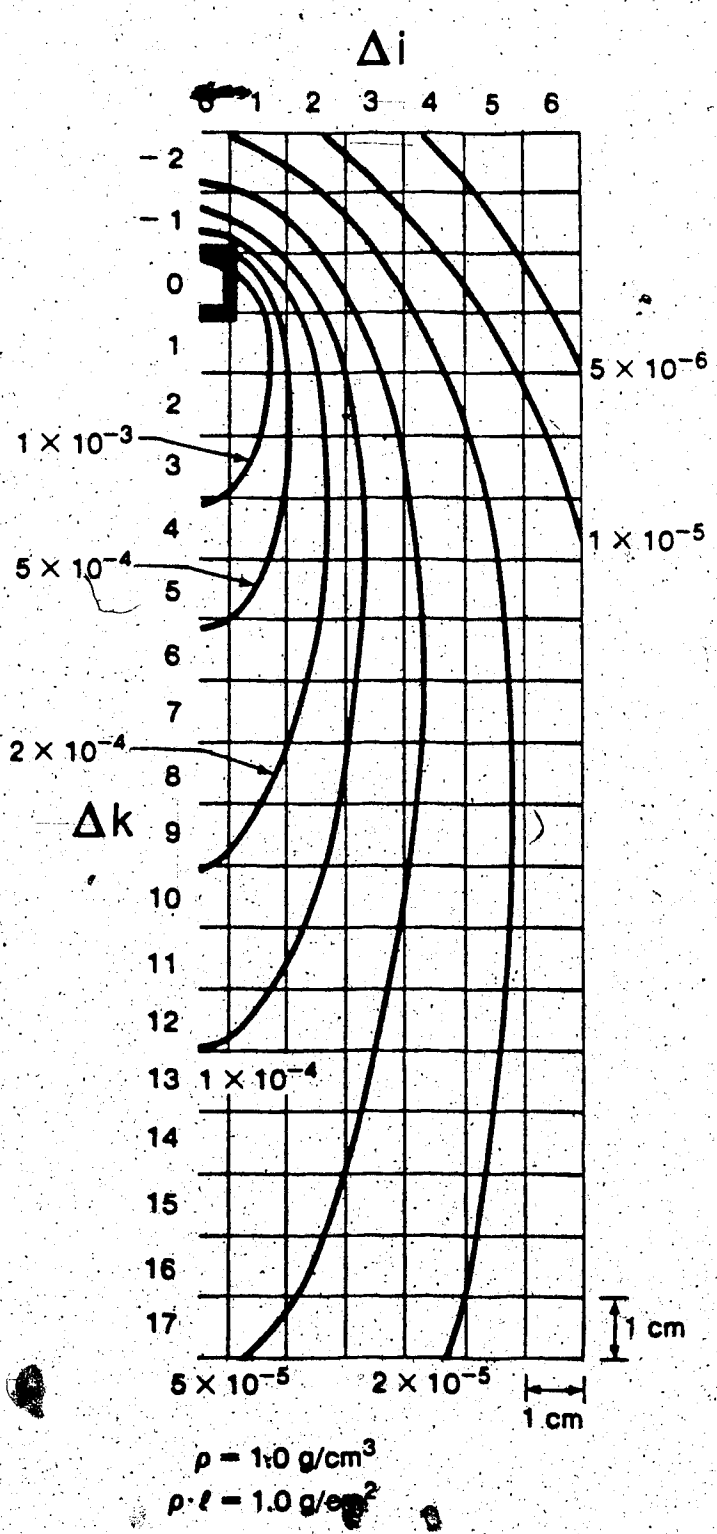

Figure 112. Truncated first scatter (TFS) dose spread array for 15 MV photons.

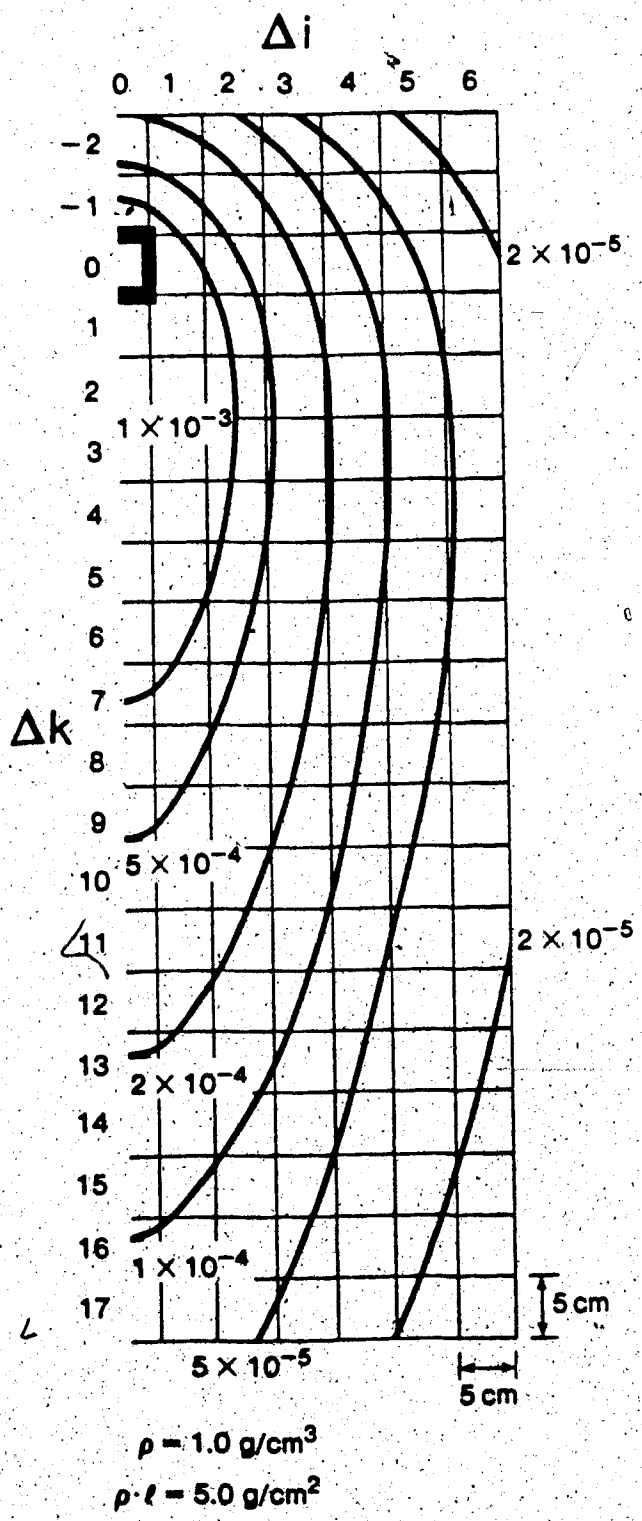

Figure 113. Residual first and multiple scatter (RFMS) dose spread array for 15 MV photons.

RFMS dose spread arrays, respectively. The TFS dose spread array has a $\rho \cdot \ell$ value of 1.0g/cm^2 and the RFMS dose spread array $\rho \cdot \ell$ value is 5.0g/cm^2. They are displayed as isodose curves. The energy deposited by scattered photons has been normalized to the same value as the primary dose spread array, namely to the collision fraction of the total charged particle energy released by primary photons. Therefore, the dimensionless numbers associated with the isodose lines represent the scatter dose per unit primary collision KERMA. The TFS dose spread array illustrated has a total width of 13 cm and a total height of 15 cm. Any first scatter photon energy not deposited within its boundary is included with the RFMS dose spread array.

7.4 Convolution Dose Calculation In A Homogeneous Phantom

The dose spread arrays can be viewed as the response throughout all the voxels in the phantom to a primary photon "impulse" occurring in one voxel. The dose spread arrays can, therefore, be used as the kernel in a convolution calculation to produce a 3-dimensional dose distribution. The dose contribution, DOSE CONTRIBUTION $(i+\Delta i, j+\Delta j, k+\Delta k)$ to a dose deposition voxel $i+\Delta i, j+\Delta j, k+\Delta k$ due to primary interactions at a voxel i,j,k in a homogeneous water phantom is illustrated in Figure 114 and given by (see Equation 7.2.4): *

$$\text{DOSE CONTRIBUTION } (i+\Delta i, j+\Delta j, k+\Delta k) = A(\rho \cdot \ell = \ell, \Delta i, \Delta j, \Delta k)\, K_c(\rho \cdot \ell = \ell, i, j, k) \qquad (7.4.1)$$

Equation 7.4.1 can be used to generate the absolute dose. However, usually only the relative dose distribution is required. If changes in the beam spectrum (or "hardening") is negliglible, $Kc(\rho \cdot \ell = \ell, i, j, k)$ may be replaced by the relative primary photon fluence:

$$\Phi'(i,j,k) = \frac{\Phi(i,j,k)}{\Phi(0,0,0)} \qquad (7.4.2)$$

* The density, ρ, in the equations of Section 7.4 and in the computer program, Volve.for, is taken to be the gravimetric density.

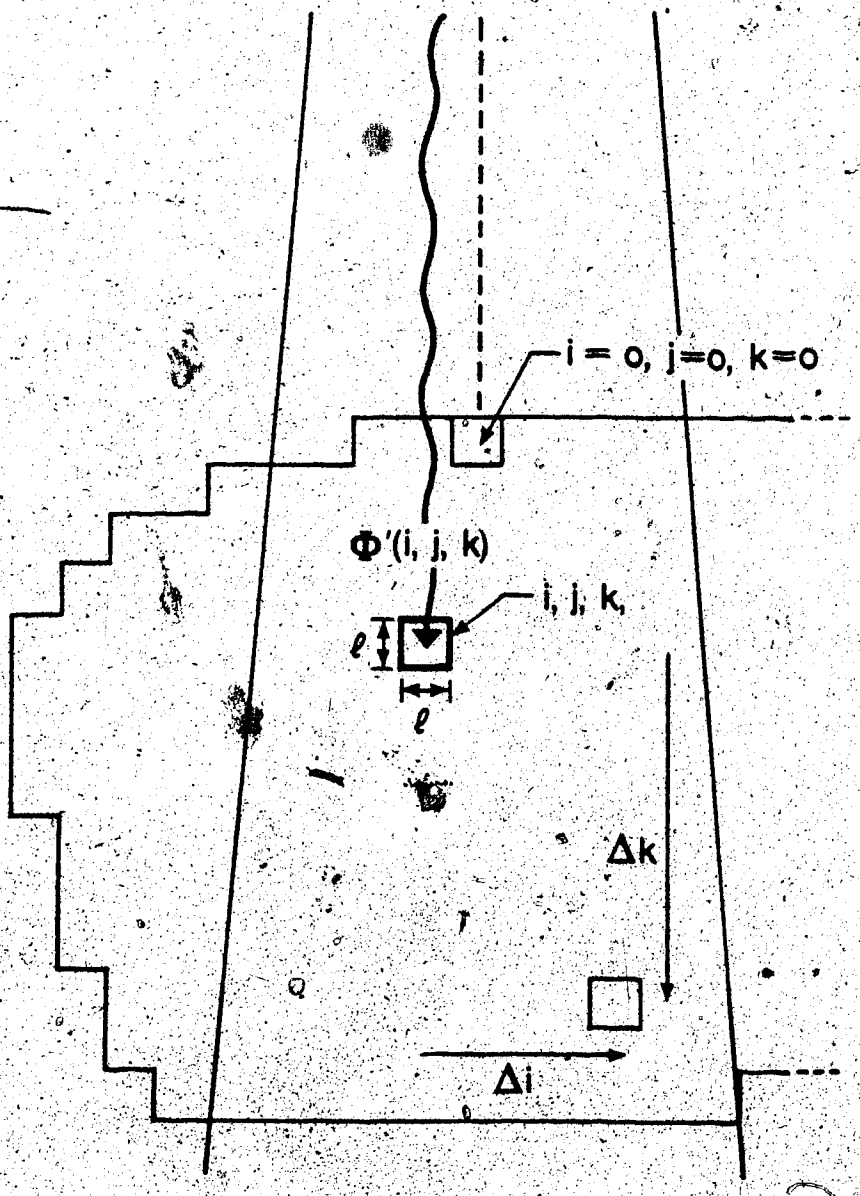

Figure 114. Illustration of the dose contribution at i+Δi, j+Δj, k+Δk due to primary photon interactions at i,j,k from the interaction point of view.

Table 20 Parameters For Determining $\tilde{\mu}$ For 15 MV X-Rays

Energy, $(h\nu_0)_n$ (MeV)	0.67	2.57	6.61	11.12
Fluence Weight, F_n	11	11	11	5
μ_n (cm^{-1})	0.0857	0.0439	0.0267	0.0173
$(\mu_{en}/\rho)_n$ (cm^2/g)	0.0326	0.0241	0.0176	0.0152

The relative fluence, $\Phi'(i,j,k)$, is the primary photon fluence at the interaction voxel normalized to the incident primary fluence at the central axis. For a parallel beam, $\Phi'(i,j,k)$ need only take into account the primary photon attenuation:

$$\Phi'(i,j,k) = \Phi'(i,j,0)e^{-\tilde{\mu}k} \qquad (7.4.3)$$

Where $\tilde{\mu}$ is the KERMA-weighted average attenuation coefficient and is calculated using:

$$\tilde{\mu} = \frac{-1}{k}\ell n\left[\frac{\sum_n F_n e^{-\mu_n k}(\mu_{en}/\rho)_n (h\nu_o)_n}{\sum_n F_n (\mu_{en}/\rho)_n (h\nu_o)_n}\right] \qquad (7.4.4)$$

The summation is over all the spectral components (9), where F_n is the relative weight of the spectral fluence component. The energy of the primary beam is $(h\nu_o)_n$. μ_n is the attenuation coefficient of the spectral component. Table 20 summarizes the parameters for the spectral components. Due to hardening, $\tilde{\mu}$ varies slightly as a function of depth. A constant 0.031 cm^{-1} was used. If the dose at very large depths is required, then the effective attenuation coefficient should be made a variable as a function of depth (i.e. $\tilde{\mu}(z)$). Figure 115 illustrates the value of $\tilde{\mu}$ as a function of depth. The value of $\tilde{\mu}$ agrees well with the 15 MV effective attenuation coefficients found from zero-area TMR data and transmission data (see Figure 116) (90-94). If

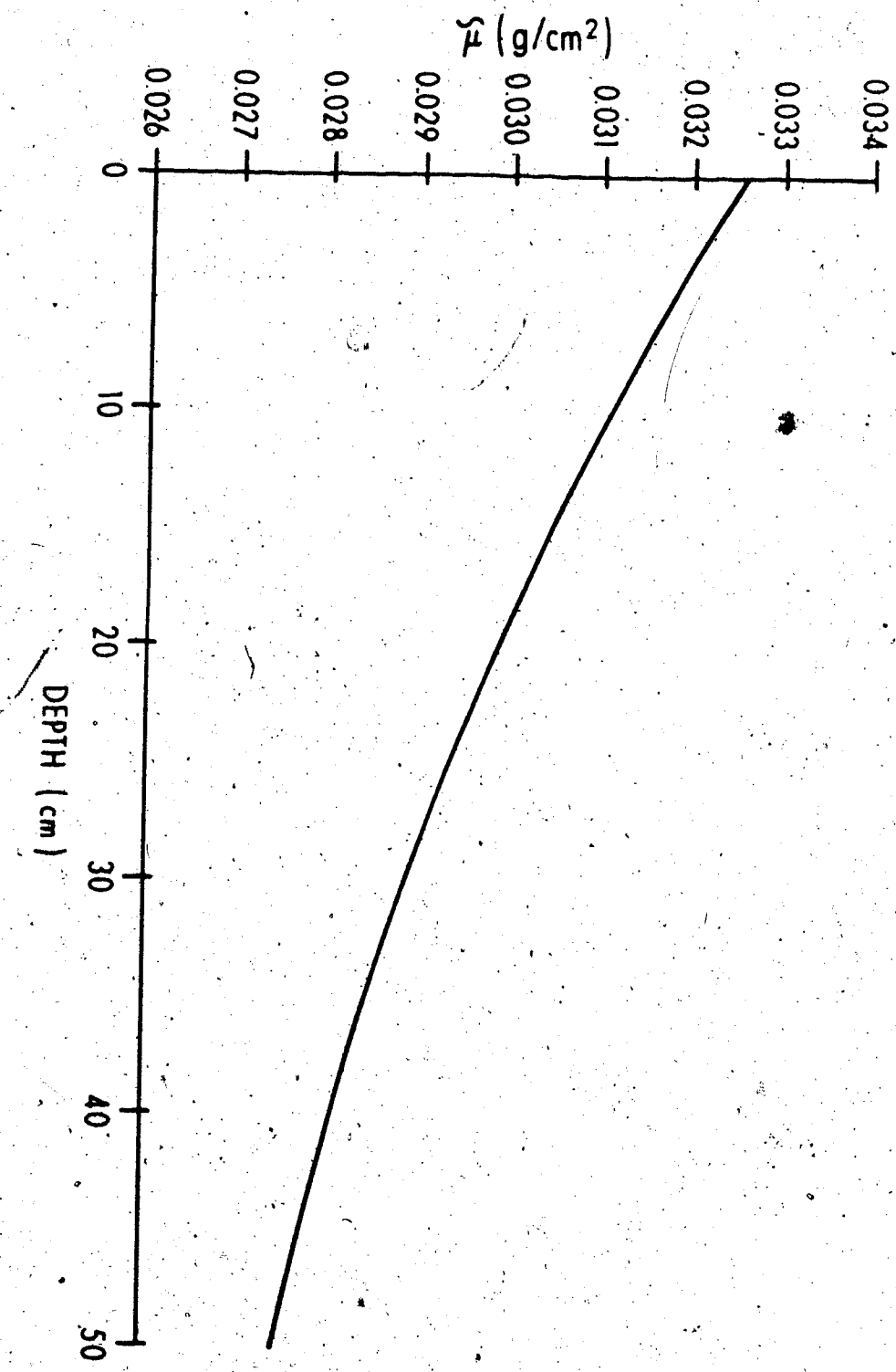

Figure 115. The variation of the effective attenuation coefficient as a function of depth. The parameters used to produce this graph are found in Table 20.

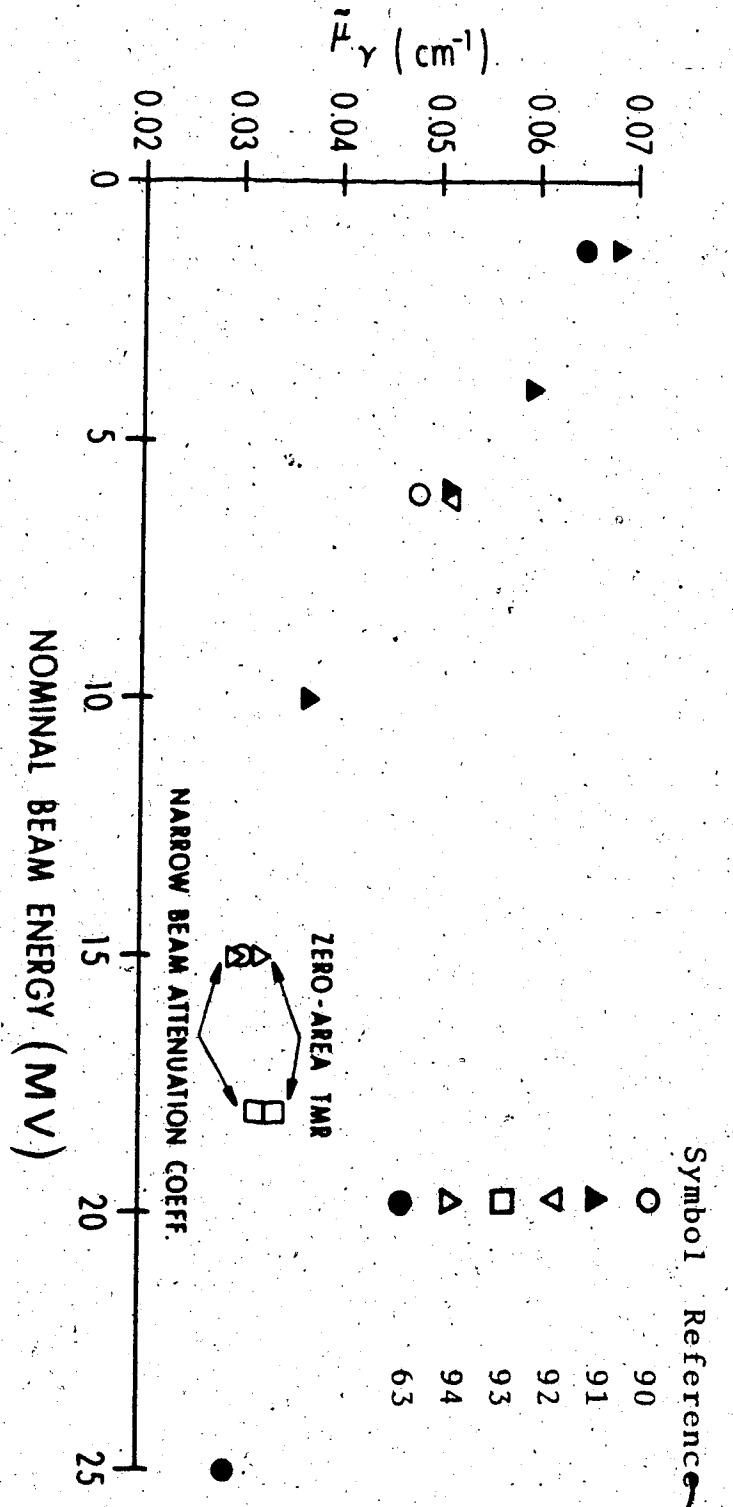

Figure 116. The variation of the measured effective attenuation coefficients as a function of nominal beam energy. This graph was produced from zero-area TMR and narrow beam attenuation experiments cited in the literature.

the beam is diverging, an inverse square reduction of the primary fluence must also be included:

$$\Phi'(i,j,k) = \Phi'(i,j,0)e^{-\tilde{\mu}(D-SSD)}\left(\frac{SSD+d_{max}}{D}\right)^2 \tag{7.4.5}$$

Where, D, is the distance from the source to the interaction site along the primary ray. $\Phi'(i,j,k)$ can also account for the external contour of the patient (in which case the factor, SSD, in the argument of the exponential in Equation 7.4.5 would not be a constant) and for beam modifying devices such as shielding that alters the relative primary fluence, but does not alter the dose spread arrays. Including the dose spread array, Equation 7.4.1 now becomes:

$$\text{DOSE CONTRIBUTION}(i+\Delta i, j+\Delta j, k+\Delta k) \propto \Phi'(i,j,k)A(\rho\cdot\ell=\ell,\Delta i,\Delta j,\Delta k) \tag{7.4.6}$$

The convolution of the dose spread arrays with the relative fluence can proceed in two different ways, called the "interaction point of view" and the "dose deposition point of view". In general the calculation may be done by either method, but there are circumstances where one approach is more efficient.

In the interaction point of view, the macroscopic beam is composed of a set of contiguous pencil beams each of which is followed through the phantom to see where the primary interactions occur. The dose spread array contributions throughout the phantom are summed for all such pencil beams. The dose distribution in the interaction

point of view is:

$$DOSE'(i+\Delta i,j+\Delta j,k+\Delta k) = \sum_i \sum_j \sum_k [\Sigma \Phi'(i,j,k)\, A(\rho \cdot \ell = \ell, \Delta i, \Delta j, \Delta k)] \qquad (7.4.7)$$

Where the i,j,k summation is over all interaction voxels, i.e. those voxels inside the phantom and the field boundary. Depending on the region of interest, the dose outside the beam boundary can also be computed.

Figure 114 illustrates the calculation of dose using the interaction point of view. The relative fluence is calculated for each point along a pencil beam (inside square brackets in Equation 7.4.7) by following the primary pencil beams through the phantom. When a beam blocking device such as a compensator is introduced in the beam, some of the primary pencil beams are affected. The interaction point of view can determine the effect of the changed primary pencil beams on the dose throughout the phantom without recalculating the entire beam. Appendix 11 lists a convolution program, Volve.for, which calculates the dose using the interaction point of view.

The interaction point of view gives the dose throughout a region of interest. Often only the dose at a few voxels is desired. In this case, the dose in [illegible] select voxels is calculated using the dose deposition point of view.

In a homogeneous, unbounded phantom there is a geometrical reciprocity between the primary interaction and dose deposition voxels.* Even though the dose spread arrays were produced to describe the transport and absorption of

dose throughout a phantom due to primary interactions at a voxel, they also describe the transport to and absorption at a dose deposition voxel due to an equal magnitude of primary interactions throughout the phantom. This is essentially the same principle as the source-target reciprocity used in health physics to calculate the organ dose due to internal isotopes (95).

Figure 117 illustrates the use of the dose spread arrays from the dose deposition point of view. The dose spread arrays now represent the dose deposited in the dose deposition voxel normalized to the collision KERMA produced in the interaction voxels. The dose deposition point of view calculation sums the dose contribution at the dose deposition voxel due to primary interactions throughout the phantom. The dose at a point I,J,K is given by:

$$DOSE(I,J,K) \propto \sum_{\Delta i}\sum_{\Delta j}\sum_{\Delta k} \Phi'(I-\Delta i, J-\Delta j, K-\Delta k) A(\rho \cdot \ell = \ell, \Delta i, \Delta j; \Delta k) \qquad (7.4.8)$$

If the dose at only a few voxels is required, the dose deposition point of view is far more efficient. For example, the dose deposition point of view should be used when determining the dose along the central axis or along transverse profiles. The dose deposition point of view is mathematically equivalent to taking the convolution using

* This reciprocity only rigorously applies to the RFMS dose spread array when the phantom is infinite.

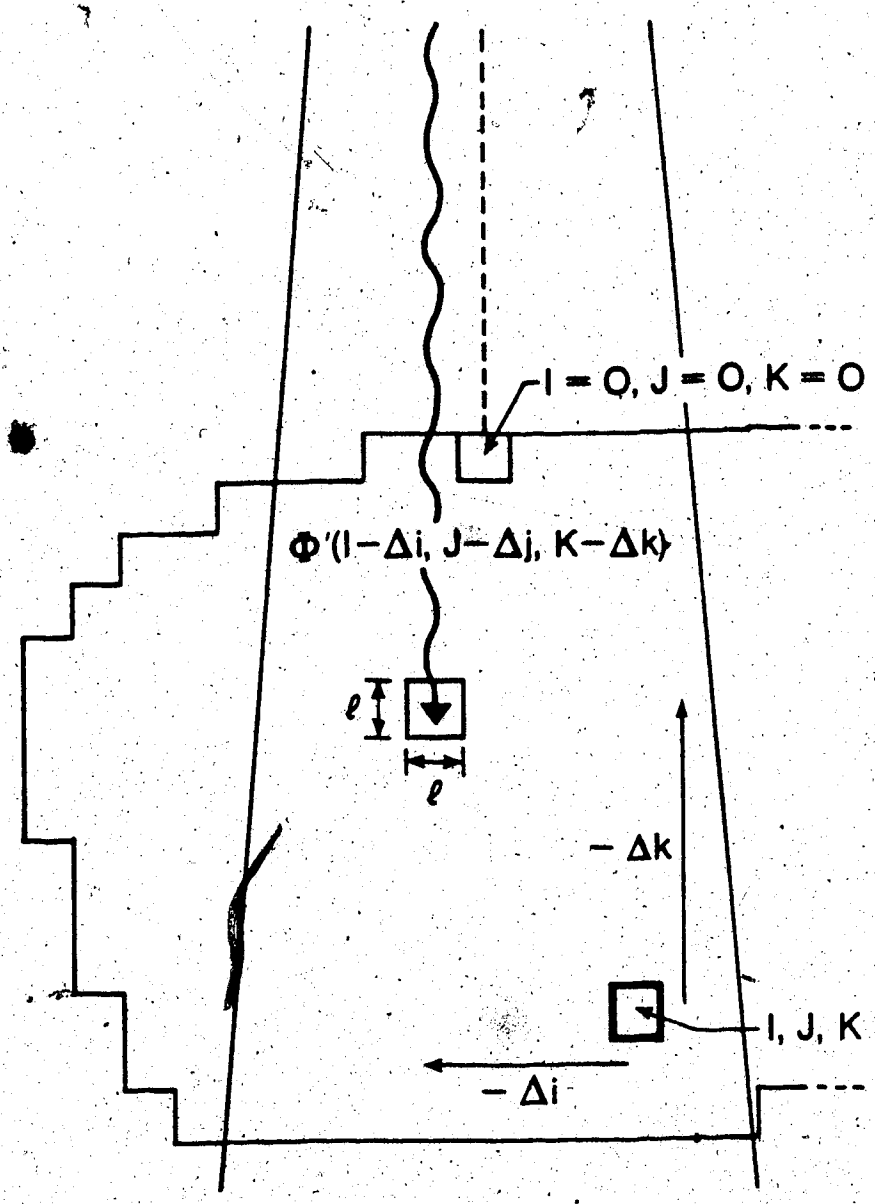

Figure 117. Illustration of the contribution of dose from primary photon interactions at I-Δi, J-Δj, K-Δk arriving at I,J,K using the dose deposition point of view.

the serial product (96). A disadvantage to calculating a large dose distribution using the dose distribution point of view is that a large array for the relative fluence must be pre-calculated and stored before Equation 7.4.8 can be used.

Equations 7.4.6, 7.4.7 and 7.4.8 do not specify which type of dose spread array is being convolved. The same general equations apply to all the dose spread arrays, except the number of terms in the summation and the value of the relative fluence will depend on the voxel dimension of the dose spread array.

The convolution method does not take into account the dose due to contamination. The measured contamination dose was added to the calculated dose. In Volume 1 it was found empirically that the magnitude of the contamination dose depends on five parameters; the 2-dimensional position from the central axis, the radiological depth in the phantom, and the width, a, and length, b, of the field. The amount of contamination is given by:

$$C(x,y,z,a,b) = G(\tilde{\rho}\cdot z)\, c\sqrt{a\cdot b}\; e^{-2x^2/a^2}\; e^{-2y^2/b^2} \qquad (7.4.9)$$

The amount of contamination as a function of radiological depth was found from Figure 63 inside the field and from Figure 31 outside the field. The mean density, along the primary ray, from the surface of the phantom to the calculation point is $\tilde{\rho}$. These graphs have been included in the form of a look-up table, $G(\tilde{\rho}\cdot z)$. The dependence of contamination on field width was found to be linear. The

constant of proportionality, c, was 1.0 %/cm for a 15 MV photon beam. The effective field size is assumed to be the square root of the product of the field dimensions. Equation 7.4.9 assumes a Gaussian dependence of the contamination on the distance from the the central axis.

Figure 118 illustrates the measured and calculated tissue-maximum-ratio (TMR) for a 15 MV beam as a function of depth in a homogeneous water phantom along the beam central axis for field sizes of 6 cm x 6 cm and 20 cm x 20 cm. The calculated TMR curve was obtained by assuming the beam was parallel, and had no inverse-square reduction of the fluence with depth, as required for comparison with measured TMR values. The agreement between the measured and calculated dose is better than 1 % beyond a depth of d_{max} and within 10 % in the build-up region. Figure 119 illustrates the percent depth-dose curves for a 6 MV x-ray beam for various field sizes. The agreement is within 1 % beyond d_{max} for 10 cm x 10 cm and 20 cm x 20 cm fields and within 3 % for a 4 cm x 4 cm field.

Figure 120 illustrates dose profiles at d_{max} for field sizes of 10 cm x 10 cm and 30 cm x 30 cm for a 15 MV beam. The fluence profile at the phantom surface was assumed to be uniform inside the beam boundary and zero outside the beam boundary. This assumption appears to be adequate for the 10 cm x 10 cm field, but does not account for the "horns" in the larger field profile. The fall-off in dose near the beam boundaries due to lateral electronic disequilibrium, not geometrical penumbra, is accounted for. Figure 121

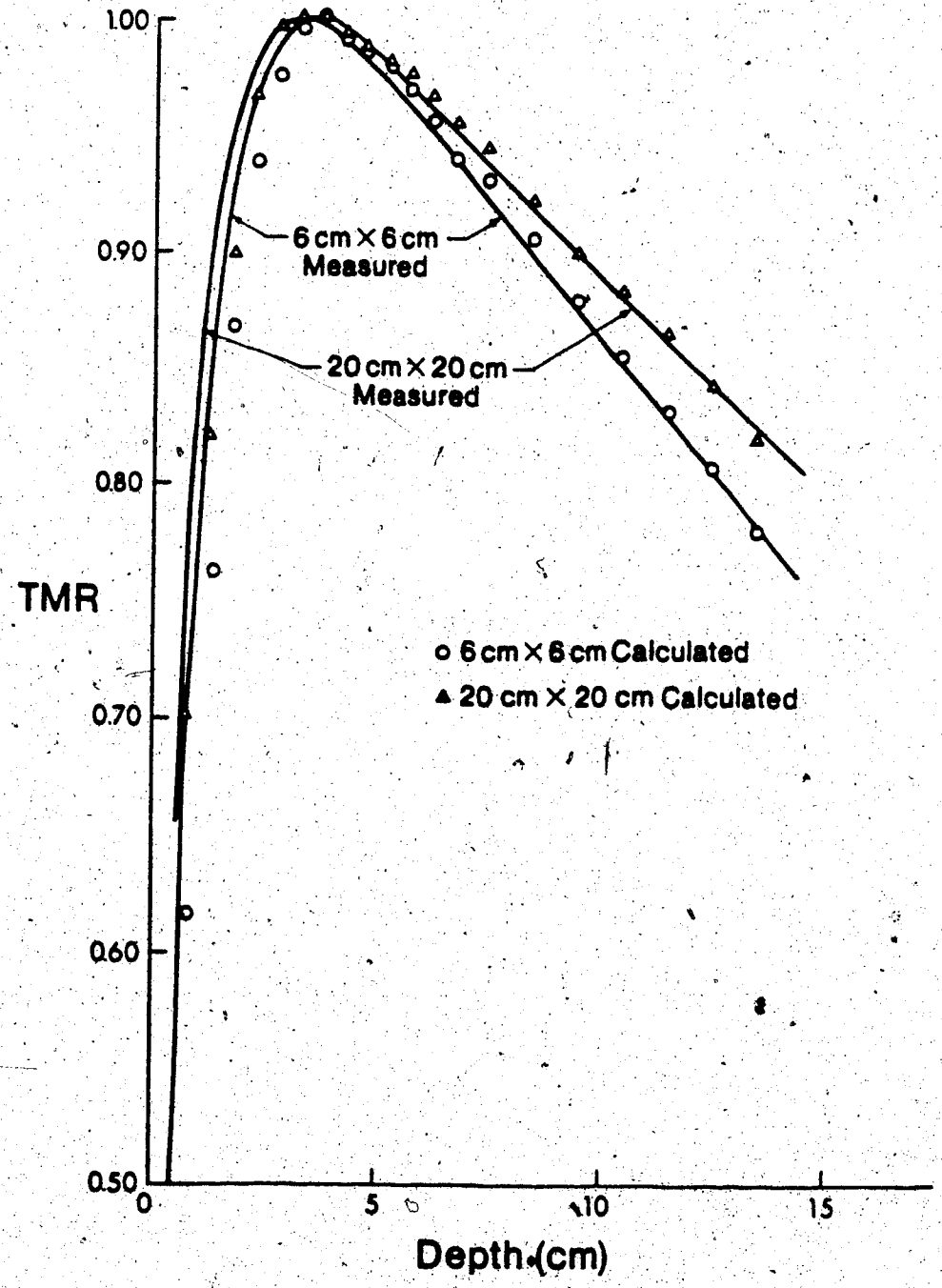

Figure 118. Measured and calculated TMR's for a 15 MV beam as a function of depth along the central axis in a homogeneous water phantom.

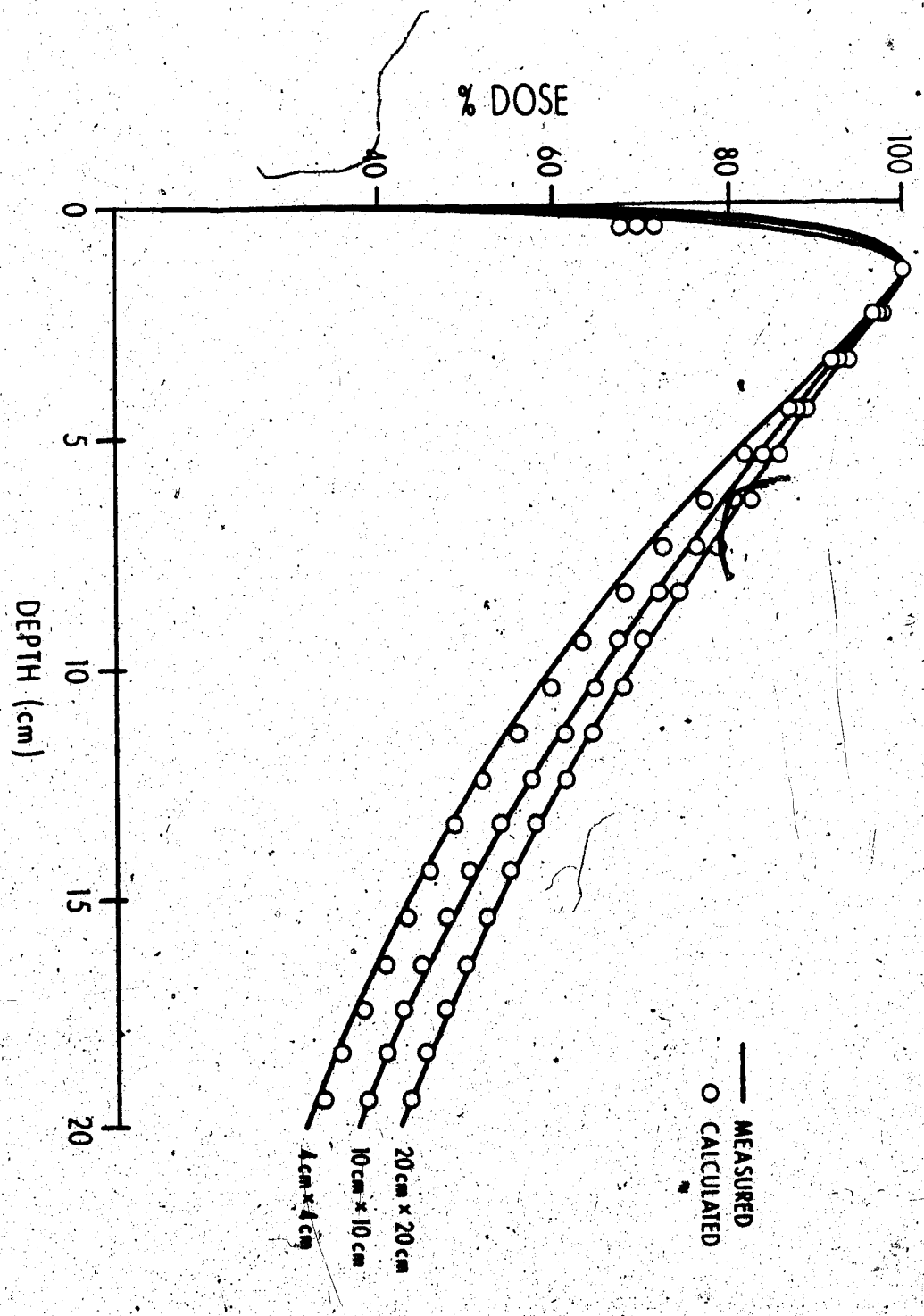

Figure 119. Measured and calculated percent depth-dose data for a 6 MV beam as a function of depth along the central axis in a homogeneous water phantom.

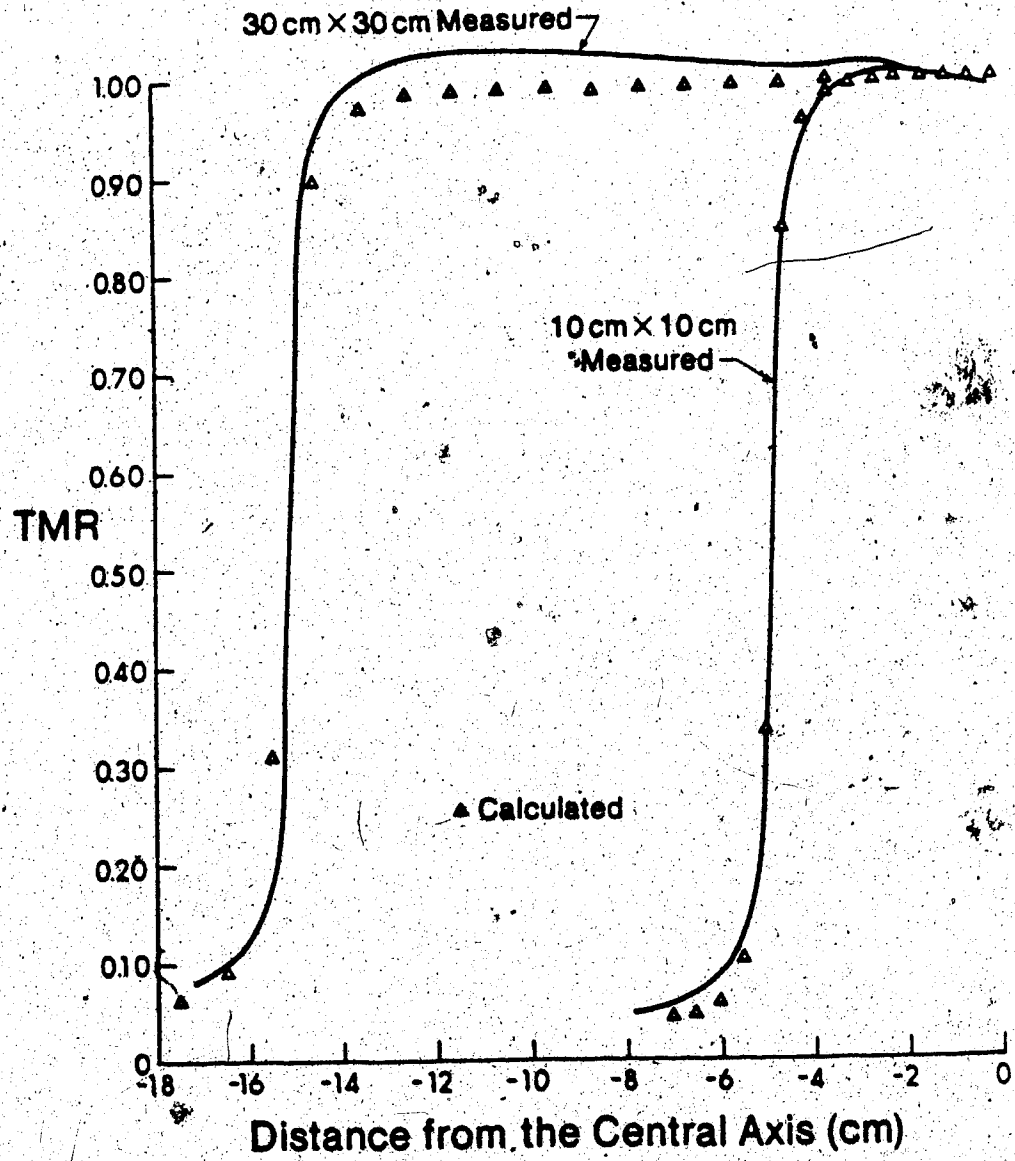

Figure 120. Measured and calculated dose profiles at d_{max} for a 15 MV beam.

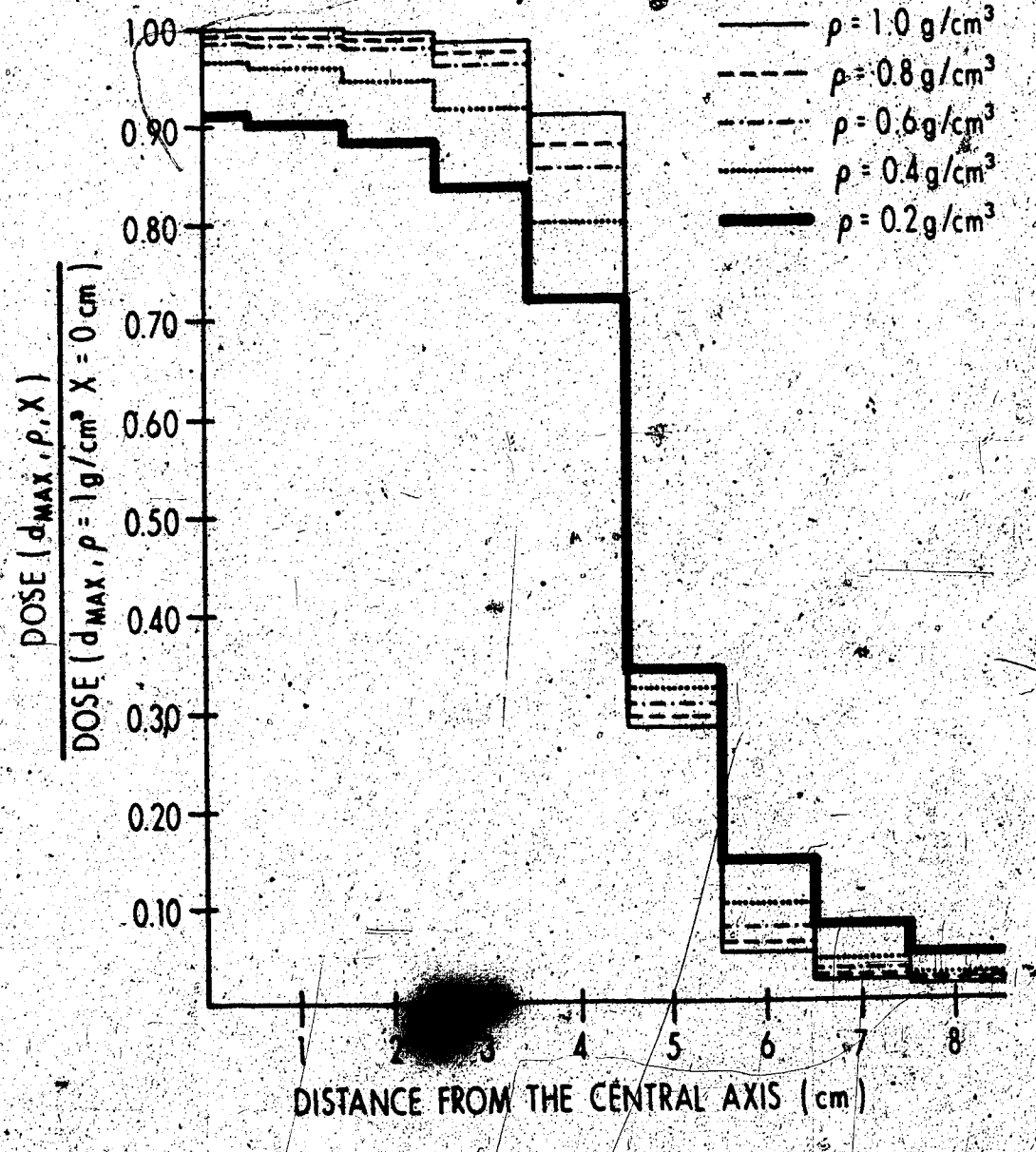

Figure 121. Dose profiles at d_{max} in homogeneous phantoms with various densities. The dose is normalized to the central axis dose in a unit density phantom.

illustrates the dose profiles in homogeneous phantoms with various densities. The dose is normalized to the dose in a unit density phantom at the central axis. The smaller the density, the smaller the dose inside the field. This is especially pronounced near the field boundary. The dose outside the field is greater for smaller densities. This effect has been observed by Kornelsen and Young for 10 MV x-rays (80). It is due to the enhanced range of charged particles in low-density materials. The reduced dose inside the field is mainly due to the charged particles migrating inward from outside the field and the increased dose outside the field is due to an increased number of charged particles "streaming" there from inside the field.

The method can be used to determine the dose in a wedged field. It was assumed that the wedge could be described mathematically as a linear (or "ramp") increase in the primary fluence from one side of the beam to the other. The primary fluence profile is shown in Figure 122 along with the fluence calculated for the 45^{o} and 60^{o} wedges (defined by the angle the isodose lines makes with a line parallel to the phantom surface at some specified depth) supplied by the accelerator manufacturer. The wedge material is steel with an effective attenuation coefficient of 0.284 cm^{-1} (97). The closest fluence profile curve to the linear profile curve is for a 60^{o} wedge. Figure 123 illustrates the calculated isodose curves for a 15 MV beam with a fluence profile as shown in Figure 122 and the measured isodose curve for a 60^{o} wedge. A diverging beam

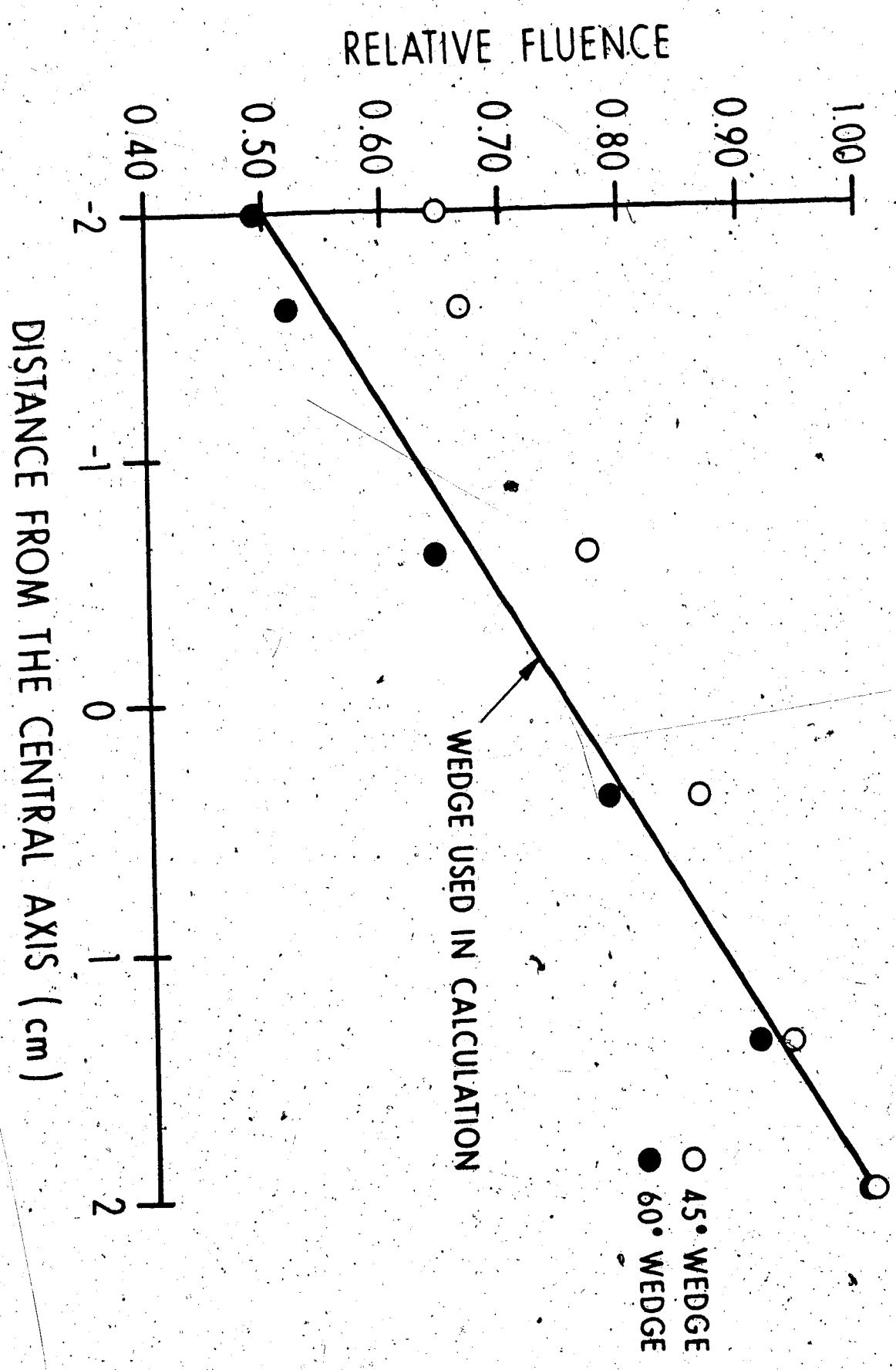

Figure 122. The relative primary fluence profile for 15 MV beam wedges and the fluence profile used to obtain the calculated isodose curve in Figure 123.

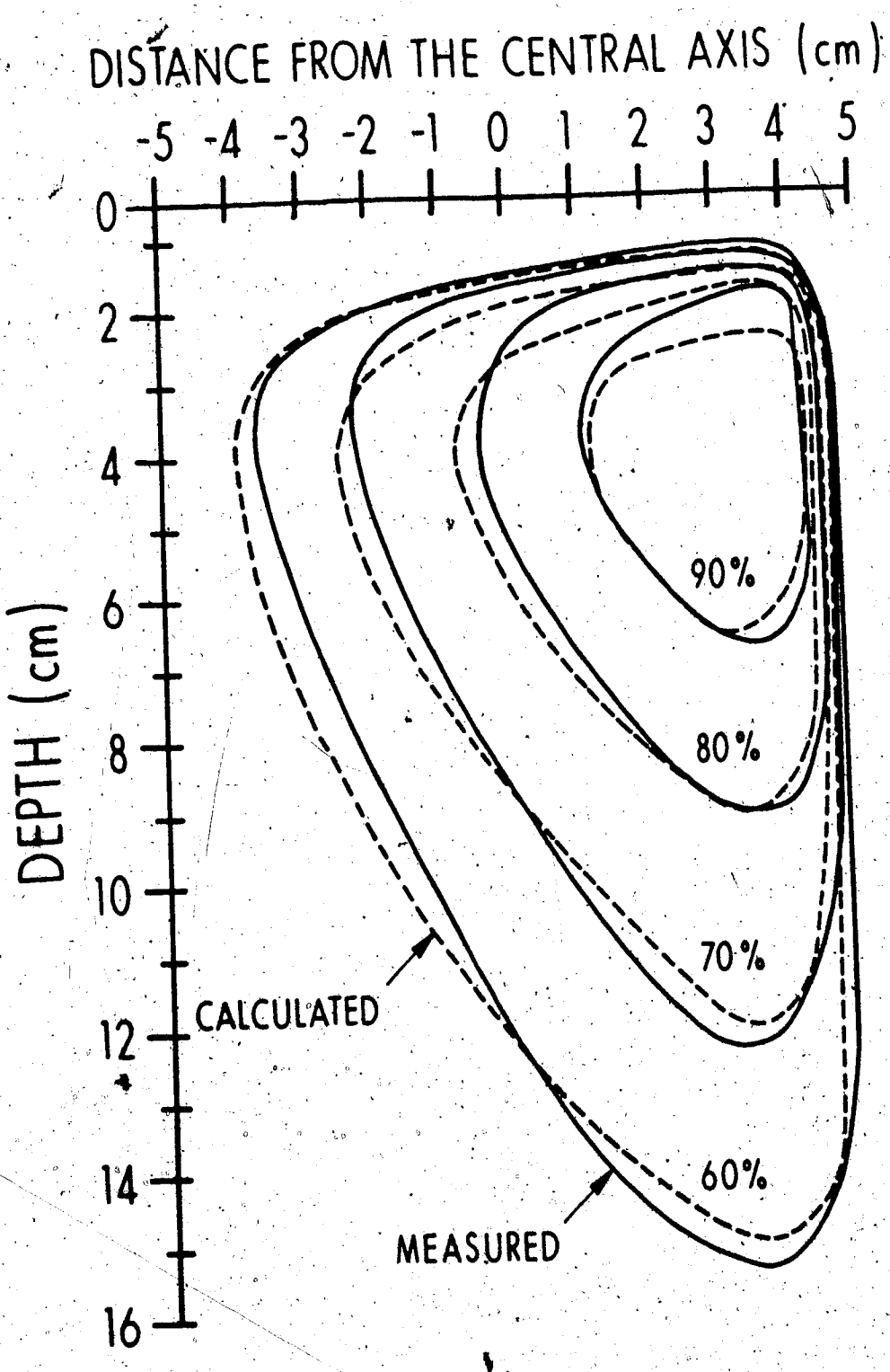

Figure 123. The calculated isodose curve for the fluence profile shown in Figure 122 and the measured isodose curve for a 60° wedge for a 15 MV beam.

was used with a field size of 10 cm x 10 cm defined at the surface of the phantom which was 100 cm from the source. The calculation predicts the characteristic reversal of the slope of the isodose lines in the build-up region. The agreement of the position of the isodose lines is good and might improve by a more closely matched fluence distribution.

The method can also take into account irregularly-shaped fields. Figure 124 illustrates the effect on the dose profile at a depth of 5 cm when a shield is placed in the 15 MV beam. The shield consisted of a bar of cerrobend (lead-tin-bismuth compound) extending completely across the field in a transverse direction to the profile. The width of the bar was 1.5 cm and it had a thickness of 8.5 cm. The primary fluence transmission through the cerrobend was calculated to be 3.1 %. Figure 124 also illustrates a calculation of the profile assuming the primary dose is deposited locally. The measured profile agrees best with the calculation using non-local primary energy deposition. This illustrates that charged particles are streaming into the region under the shield. Also illustrated in Figure 124 is a calculation of the dose using a Clarkson scatter summation technique (98). This involves finding the scatter by summing contributions from the unshielded portion of the field and then adding this to the primary dose under the shield, which is equal to the transmission factor (in this case 0.031) multiplied by the zero-area TMR. This method predicts about one-half of the

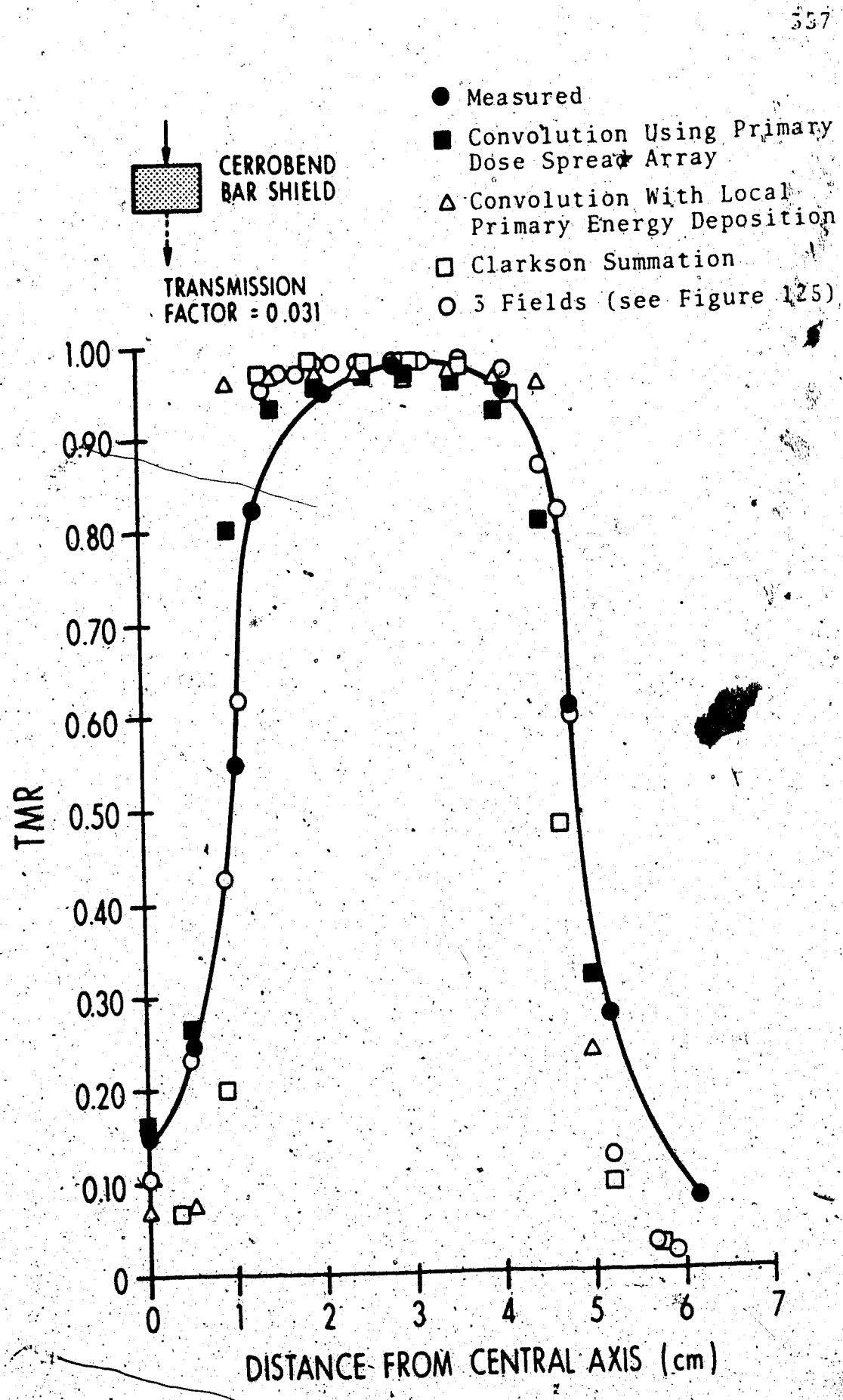

Figure 124. The measured dose profile at a depth of 5 cm when a shield is placed in the 15 MV beam. The relative position of the shield is indicated. Also shown are various calculated dose profiles for this situation.

dose under the shield compared to measured data or the convolution method. This is because this method assumes a total absence of primary dose under the shield being transported from the unshielded portion of the field. This method, which has an underlaying assumption that the primary energy is deposited locally, agrees well with the convolution method in which local primary energy deposition has been assumed here temporarily for comparison (this is achieved by replacing the calculated primary dose spread arrays with an array in which the interaction voxel has a value of 1.0 and all other voxels have values of zero).

The finding in Figure 121 that some of the "penumbra" is due to electronic disequilibrium suggests a simple calculation method for this shield based on measured dose distributions. Figure 125 illustrates that the bar shield can be represented by three fields. The middle field represents the radiation transmission through the shield. The fields have to be tilted so that neighboring field boundaries remain parallel. The relative weight of the shielded field compared to the unshielded field is equal to the transmission factor. Figure 124 also illustrates the calculated dose using this calculation method. It provides better agreement with the measured dose. The shield is acting like a collimator; it is shielding the fluence , but it does not prevent charged particles generated in the unshielded region from being transported to the shielded region.

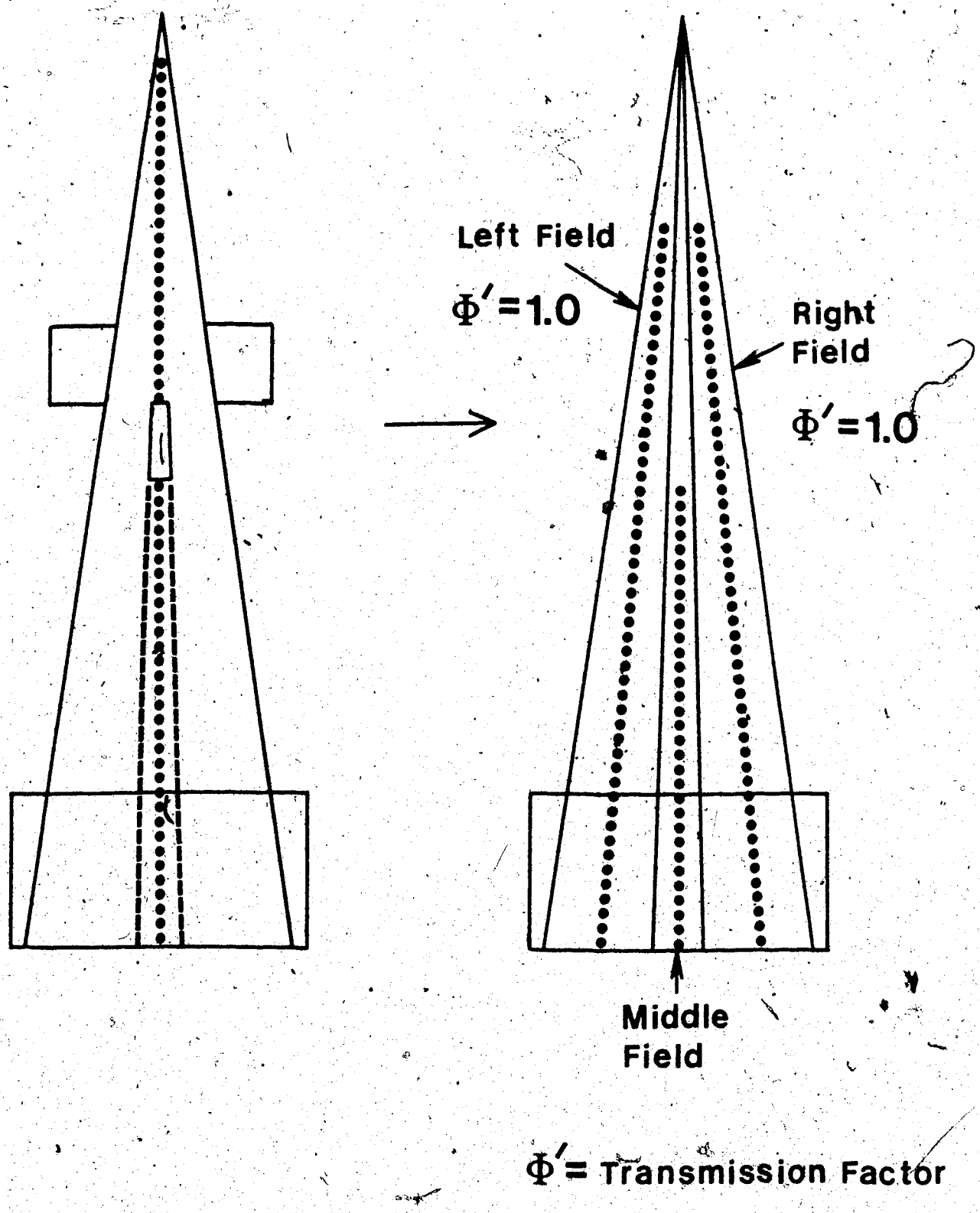

Figure 125. The bar shield represented by three fields. The central axes of the fields are shown with dotted lines. The results of the calculation with this representation is shown in Figure 124.

7.5 Extension to Heterogeneous Media

Charged particle transport through a heterogeneous medium is much more complex. To be rigorous, the primary dose spread arrays would have to be generated for each heterogenous situation that could be encountered. The number of possible combinations is enormous so that an acceptable approximation is necessary to take advantage of data stored in the dose spread arrays generated for homogeneous phantoms of different densities.

Figures 95 and 97 clearly illustrated that in a low-density medium, charged particles migrate a greater distance from the primary interaction site. This must be taken into account when describing the transport of charged particles from a unit density medium such as muscle into a low-density region such as lung. Figures 126 and 127 illustrate a MOCA Monte Carlo generation of the primary, first scatter and multiple scatter dose components for 6 MV x-rays in homogeneous and heterogeneous medium, respectively. The natural logarithm of the percentage of dose normalized to the maximum dose is plotted as a function of depth. The primary component decays approximately exponentially with depth beyond d_{max} in both the unit-density and low-density regions, however, the decay constant is smaller in the low-density medium. The multiple scatter dose has an extended build-up in the unit-density medium. It does not decay exponentially in the low-density medium. Instead, the multiple scatter component first

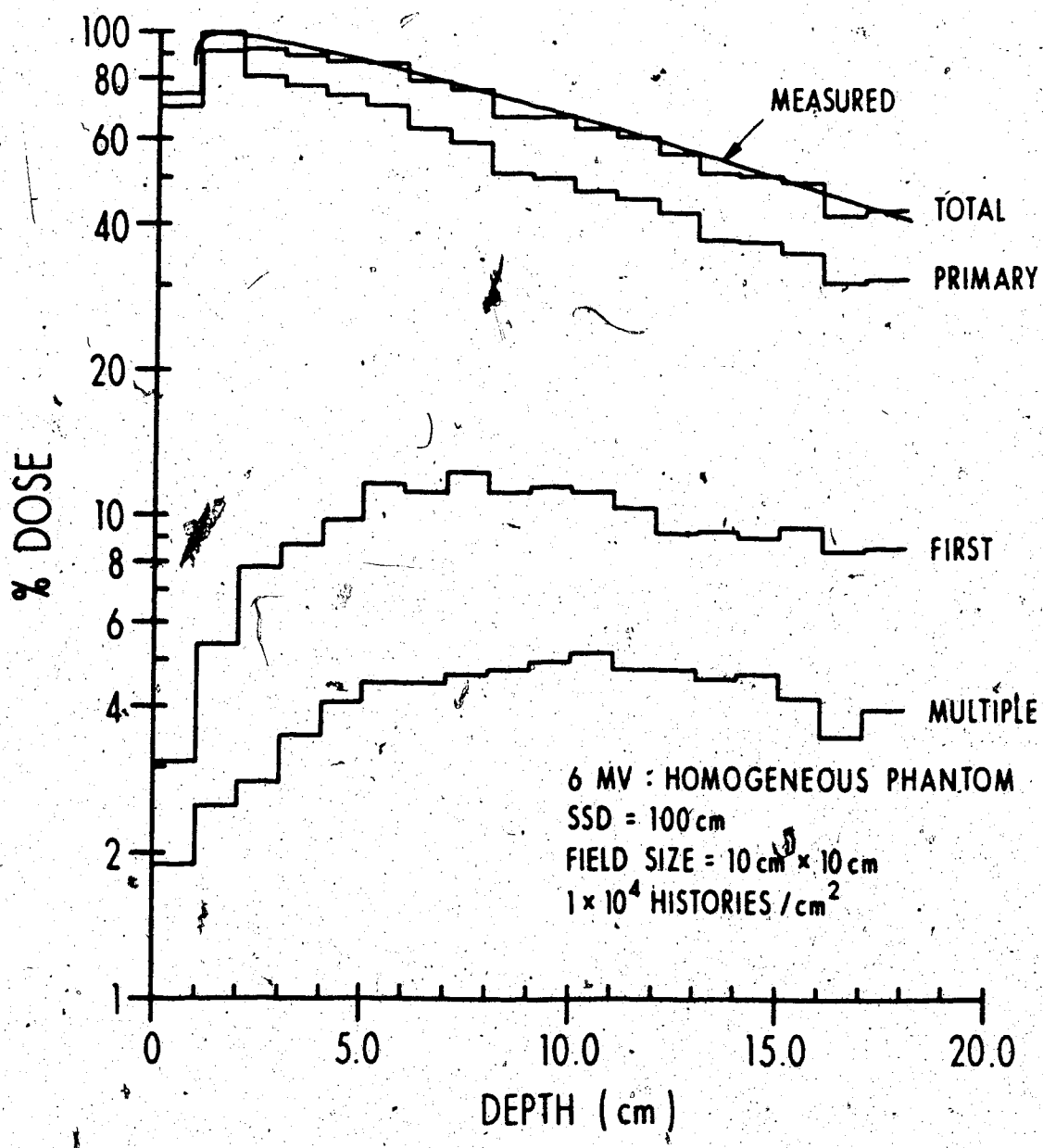

Figure 126. Components of the percent depth dose in a homogeneous water phantom predicted by MOCA for a 6 MV beam. The measured total dose is also shown for comparison.

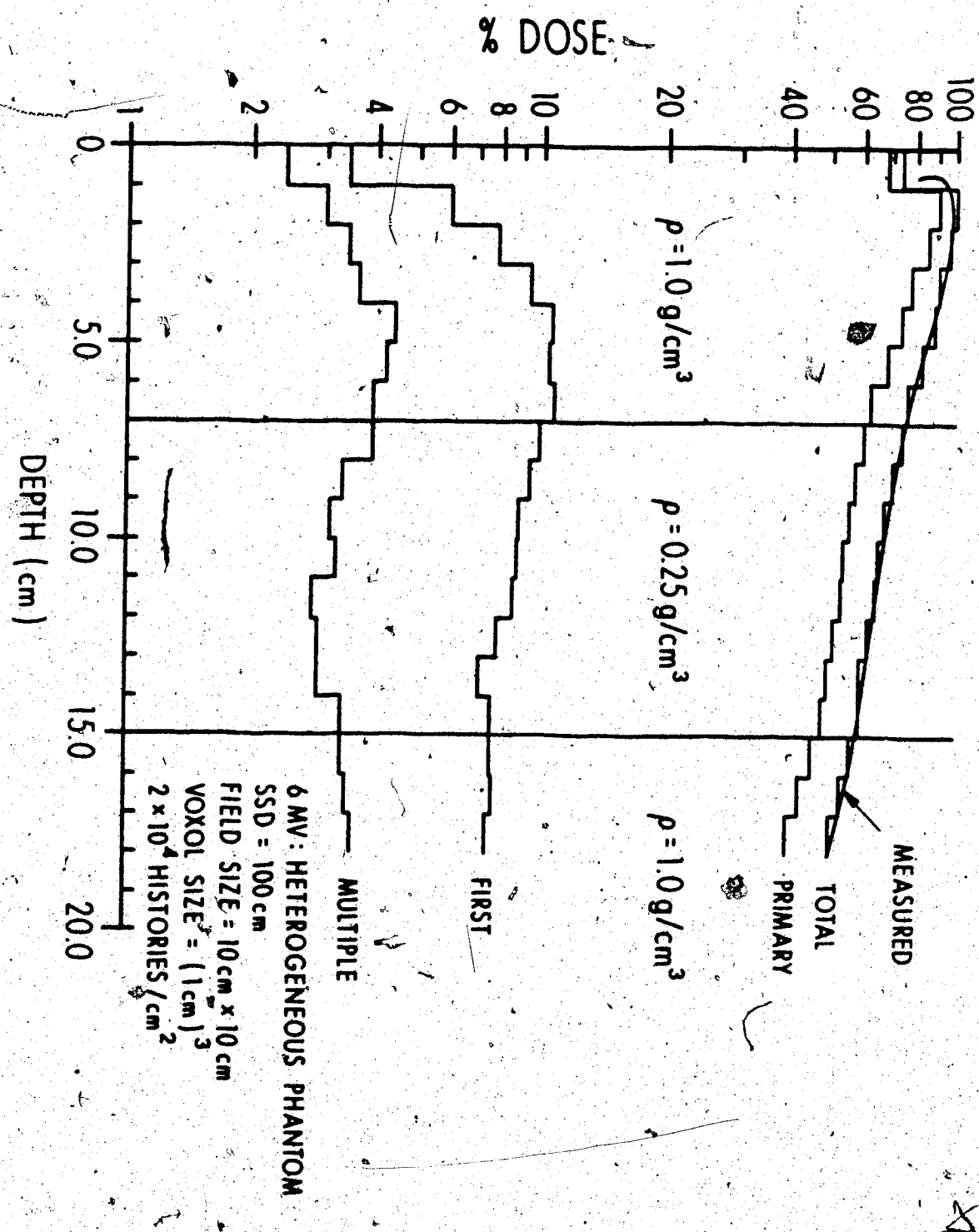

Figure 127. Components of the percent depth dose in a heterogeneous phantom (with water chemical composition) predicted by MOCA for a 6 MV beam. The measured total dose is shown for comparison.

decreases with depth after the first interface (until 10-14 cm beneath the surface) and then increases before the second interface. The first scatter dose has features of both the primary and multiple scatter components. It has a build-up in the unit density material similar to the multiple scatter dose but has an approximate exponential reduction in dose in the low-density material.

The extended build-up in the scatter dose seen in Figures 126 and 127 is reflected by the large longitudinal extent of their dose spread arrays. However, the behavior of the first scatter dose with depth in the heterogeneous medium resembles the primary dose component.

The extension of O'Connors theorem for charged particles set-in-motion suggests that range scaling may be used to approximate charged particle dose spread arrays in heterogeneous phantoms. The dose spread arrays stored for various values of $\rho \cdot \ell$ were, therefore, used. The spatial resolution of the dose calculation, ℓ, is chosen and fixed at the start of the calculation. As shown in Figure 128, the average density, $\tilde{\rho}$, between the interaction and dose deposition sites is found. The array value for the location, $\Delta i, \Delta j, \Delta k$ in a homogeneous phantom with the same $\tilde{\rho} \cdot \ell$ value is found by interpolating between dose spread arrays at fixed $\rho \cdot \ell$ values. Linear interpolation is sufficient because the array values vary relatively slowly as a function of $\rho \cdot \ell$.

There are many algorithms for finding the equivalent homogeneous density "environment" between the interaction and

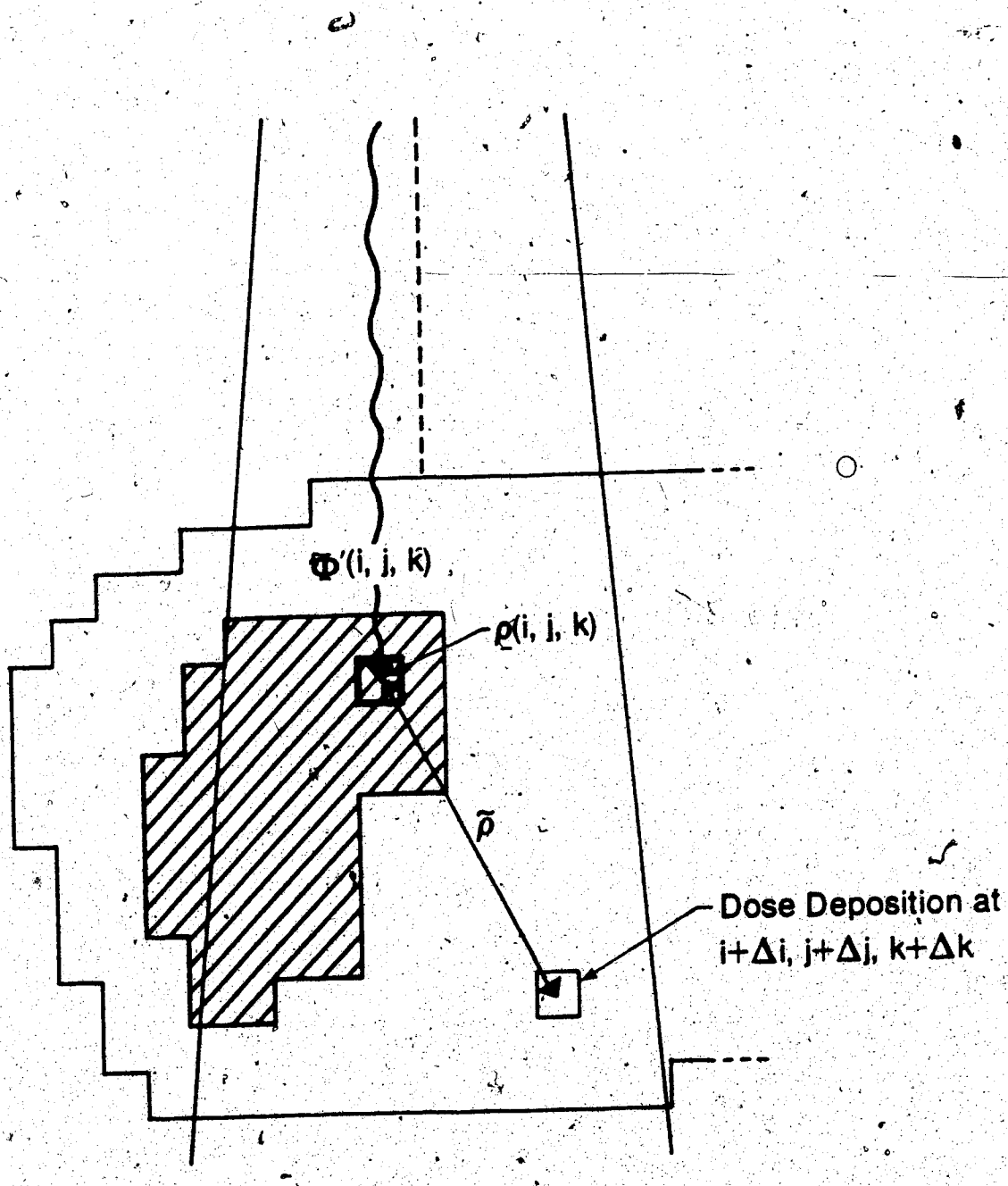

Figure 128. Determination of the average density between the interaction and dose deposition voxels.

dose deposition sites. The simplest, conceptually, is "ray-tracing". Samples of density are taken at evenly spaced intervals between these voxels. Figure 129 illustrates the procedure schematically. Suppose that the number of intervals is N. The number of samples is N+1 (including the beginning and end of the path). The length of each interval in the Cartesian directions is $\delta i, \delta j, \delta k$ where:

$$\delta i = \Delta i/N \tag{7.5.1}$$

$$\delta j = \Delta j/N \tag{7.5.2}$$

$$\delta k = \Delta k/N \tag{7.5.3}$$

The average density is given by:

$$\tilde{\rho} = [f_0\rho(i,j,k) + \sum_{n=1}^{N-1} \rho(i+n\delta i, j+j\delta j, k+n\delta k) + f_N\rho(i+\Delta i, j+\Delta j, k+\Delta k)]/N \tag{7.5.4}$$

The weights of the first and last voxel are f_0 and f_N, respectively. These weighting factors are usually set equal to 0.5 because the mean position of charged particles set-in-motion is in the middle of the interaction voxel.

Interpolating to get a dose spread array valid for an average density between the interaction and dose deposition sites, $\tilde{\rho}$, implies that it has been normalized to the total amount of energy released in an interaction voxel of the

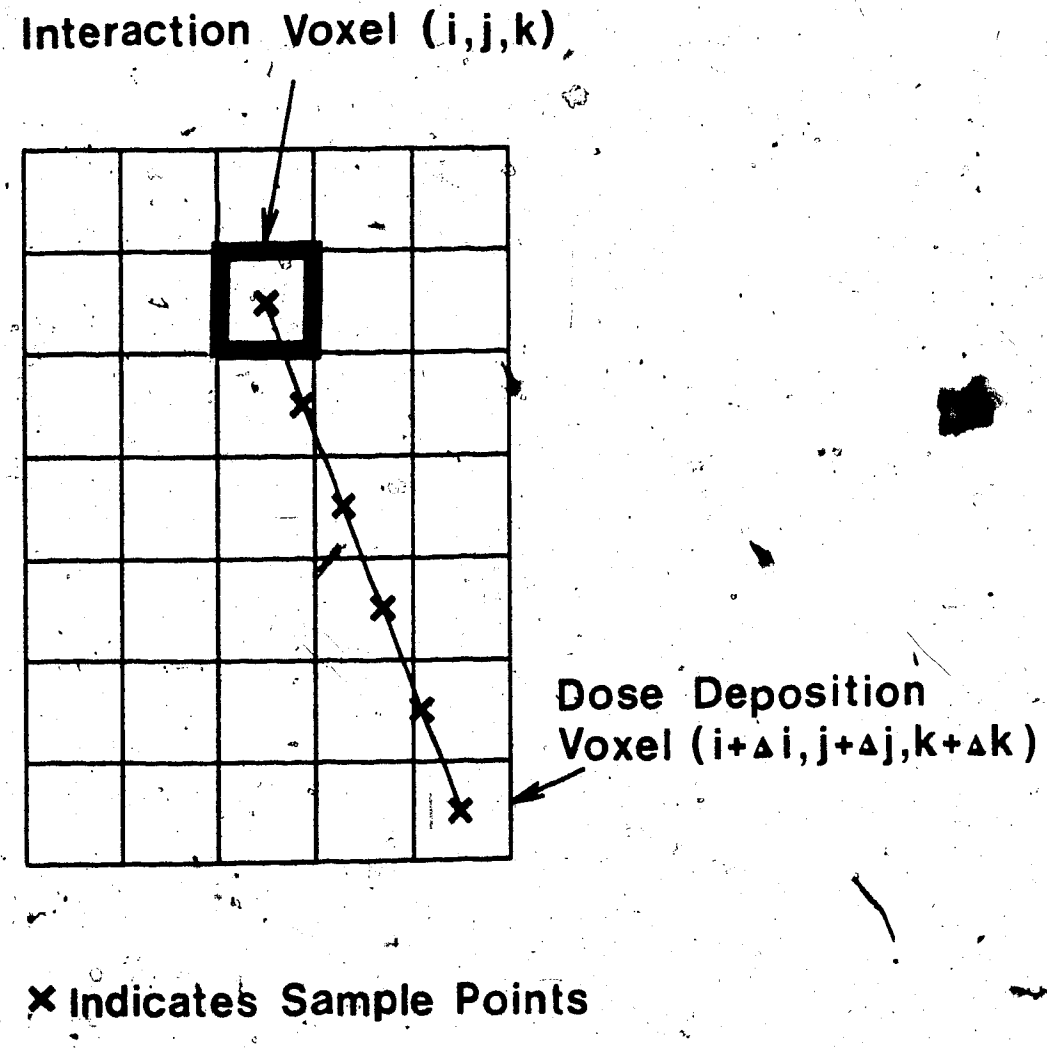

Figure 129. Ray tracing is performed by sampling the density between the interaction and dose deposition voxels.

same density. However, the density of the interaction voxel, $\rho(i,j,k)$, in a heterogeneous phantom, is generally not the same as the average density between the interaction and dose deposition voxel. The primary dose contribution to a dose deposition voxel, due to primary interactions at an interaction voxel of density $\rho(i,j,k)$ when the average density between these voxels is $\tilde{\rho}$, is given by:

$$\text{DOSE CONTRIBUTION}(i+\Delta i, j+\Delta j, k+\Delta k) \propto \Phi'(i,j,k) \frac{\rho(i,j,k)}{\tilde{\rho}} Ap(\tilde{\rho}\cdot\ell, \Delta i, \Delta j, \Delta k) \tag{7.5.5}$$

The factor $\rho(i,j,k)/\tilde{\rho}$ takes into account the different amount of kinetic energy released in the heterogeneous interaction voxel compared to the amount set in motion in the interpolated homogeneous voxel of density, $\tilde{\rho}$. Otherwise, the convolution is carried out in the same manner as in a homogeneous phantom. Therefore, this procedure avoids the need to first compute the dose in water and then calculate an "inhomogeneity correction" separately.

If the phantom is homogeneous, the factor $\rho(i,j,k)/\tilde{\rho}$ in Equation 7.5.5 becomes 1.0 and the equation simplifies to Equation 7.4.6. In any case, Equation 7.5.5 can be simplified to two terms. $\rho(i,j,k)$ depends only on the interaction voxel and $\tilde{\rho}$ depends on the average path density. Therefore, Equation 7.5.5 becomes:

$$\text{DOSE CONTRIBUTION}(i+\Delta i, j+\Delta j, k+\Delta k) \propto \Phi''(i,j,k) Ap'(\tilde{\rho}\cdot\ell, \Delta i, \Delta j, \Delta k) \tag{7.5.6}$$

Where:

$$\Phi''(i,j,k) = \Phi'(i,j,k)\rho(i,j,k) \tag{7.5.7}$$

$$Ap'(\tilde{\rho}\cdot\ell,\Delta i,\Delta j,\Delta k) = \frac{Ap(\tilde{\rho}\cdot\ell,\Delta i,\Delta j,\Delta k)}{\tilde{\rho}} \tag{7.5.8}$$

The TFS dose spread array may be range-scaled using the same algorithm. In fact, range scaling the TFS dose spread array gives the exact correction. This is because a first scatter photon interacting at the dose deposition voxel could not have interacted anywhere other than along the path between the primary interaction and dose deposition voxels. Since the primary dose spread array and the TFS dose spread array are stored for the same values of $\rho\cdot\ell$, the primary and TFS dose spread arrays may be combined where they coincide spatially. The TFS dose spread array need only be dealt with separately if it extends beyond the border of the primary dose spread array.

Equations 7.5.5 and 7.5.6 have two implicit assumptions;

1) charged particles only travel on the straight-line path or "ray" between the interaction and dose deposition sites.

2) each portion of the path between the interaction and dose deposition sites has an equal influence in the transportation process.

Both of the above assumptions are, strictly-speaking, untrue. Charged particles interact and scatter almost

continuously so they can travel on any path between the interaction and dose deposition sites with only the constraint that the overall distance travelled is less than the maximum possible pathlength or "range". Charged particle scattering between two points is a highly complex process which cannot be described exactly by an average density. However, the most probable of any path is the direct one between the interaction and dose deposition sites. Therefore, the assumptions should be viewed instead as a first-order approximation to the solution of charged particle transport.

The validity of the approximations were tested by computing primary dose spread arrays directly using the Monte Carlo method for a variety of water-like heterogeneous phantoms to simulate transport across tissue-lung, lung-tissue and air gaps. Figure 130 illustrates, schematically, the phantom and the position of the interaction voxel (the voxel with bold borders) in the phantoms that were tested. Dose spread arrays generated in the heterogeneous phantom from the Monte Carlo method were compared to the calculated dose spread arrays for a heterogeneous phantom using:

$$A^{het}_{p+1st}(\Delta i,\Delta j,\Delta k) = \frac{\rho(i,j,k)}{\tilde{\rho}} A_{p+1st}(\tilde{\rho}\cdot\ell,\Delta i,\Delta j,\Delta k) \qquad (7.5.9)$$

Where $A^{het}_{p+1st}(\tilde{\rho}\cdot\ell,\Delta i,\Delta j,\Delta k)$ is the primary and TFS dose spread arrays combined. Tables A to I in Appendix 12 compare the results of the two calculations. The dose

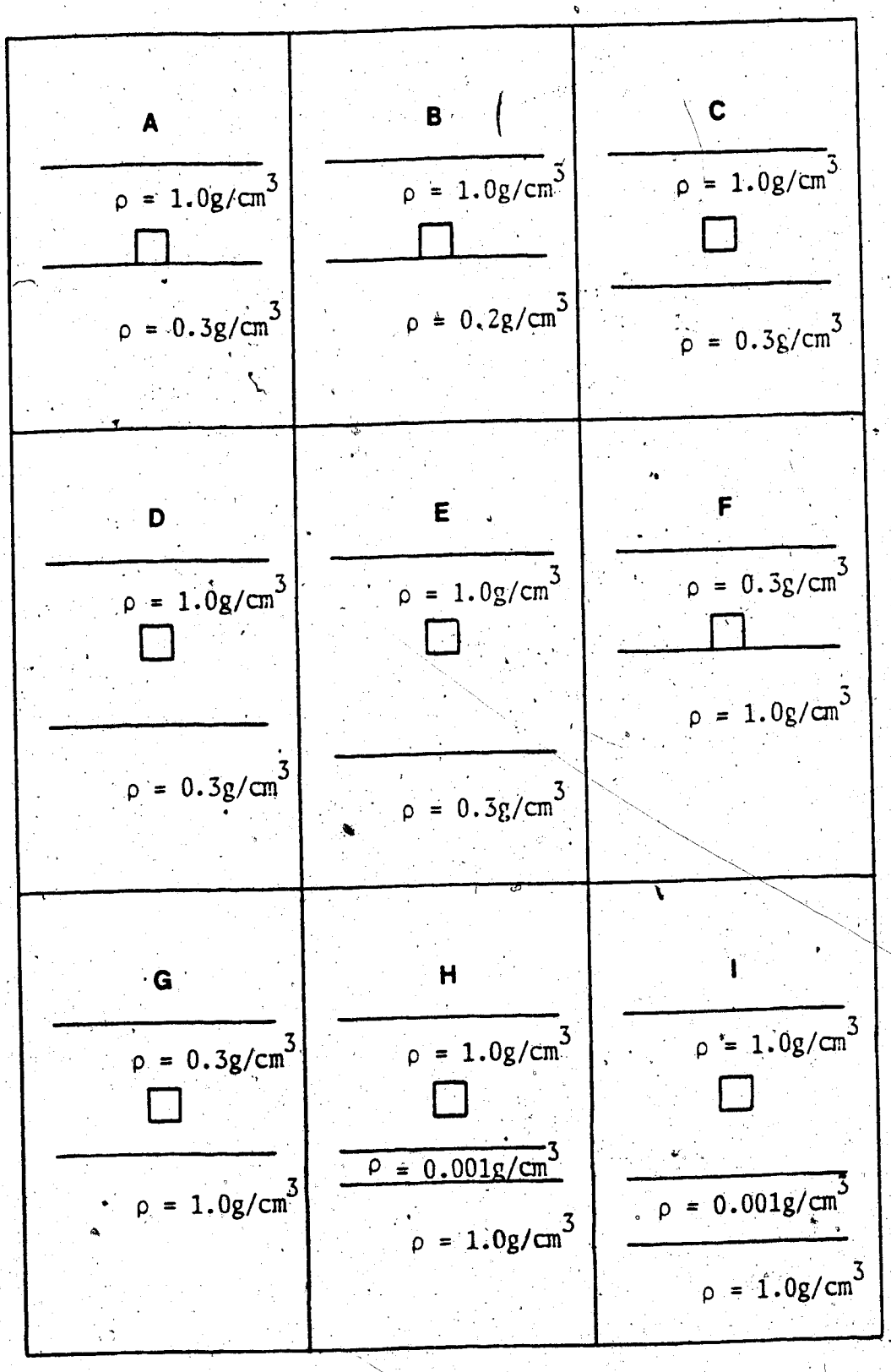

Figure 130. Schematic representation of the slab phantoms tested to verify the approximations used in determining the dose in heterogeneous phantoms. The interaction voxel is shown as a square. The results are found in Appendix 12.

spread arrays are in close agreement with respect to the range and absolute value. The maximum deviation between the two values occurs near the heterogeneity interface. A check was also made to see if the method chosen to find the dose spread arrays in Equation 7.5.9 conserved energy. Equation 7.5.9 gives the amount of dose/unit KERMA being deposited at the dose deposition site, therefore, the sum of energy/unit KERMA is given by:

$$\text{ENERGY SUM} = \sum_{\Delta i \Delta j \Delta k} \sum \sum A^{het}_{p+1st}(\Delta i, \Delta j, \Delta k)\rho(i+\Delta i, j+\Delta j, k+\Delta k) \tag{7.5.10}$$

The value obtained from Equation 7.5.10 was compared to the result from the Monte Carlo calculations using the following:

$$\%\ \text{DEVIATION OF ENERGY SUM} = \frac{\text{MONTE CARLO SUM} - \text{CONVOLUTION SUM}}{\text{MONTE CARLO SUM}} \tag{7.5.11}$$

The comparison is shown at the bottom of Tables A to I in Appendix 12. Energy was usually conserved to better than 5 %, except for Situation G, in which the percent deviation was 8 %. The results can be improved by modifying the ray-tracing algorithm. Instead of giving f_o a weight of 0.5 for all rays, some rays are given an f_o weight greater than 0.5. Tables A' to I' in Appendix 12 illustrate the heterogeneous calculation with f_o equal to 0.9 when Δk is positive and Δi and Δj are both 0 and f_o equal to 0.6 when Δk is positive and Δi or Δj (but not both) is ± 1. All other f_o values are still 0.5. Energy is now conserved to better

than 2 % for all values except those in Situation G for which energy was conserved to 5.5 %. The results would probably also improve if the value of f_N was not constant. This has not been tested.

Multiple scatter photons may have interacted anywhere within the phantom, not just between the primary interaction and dose deposition voxels. Therefore, the average "global" density of the phantom is used in Equation 7.5.5 and 7.5.8 instead of the mean density along the path between the interaction and dose deposition voxels. This approximation is further justified because multiple scattering is a minority contributor to the total dose. This approximation avoids calculating the mean density between the interaction and dose deposition voxels of the RFMS dose spread array resulting in a saving of computation time.

Figures 131 and 132 illustrate the TMR correction factor for a 15 MV beam along the central axis for a heterogeneous phantom consisting of horizontal slabs of low-density and unit density material for field sizes of 5 cm x 5 cm and 10 cm x 10 cm. The experimental measurements were the same as those obtained in Section 6. The correction factor is less than 1.0 in cork at 5 cm x 5 cm which indicates that the dose to cork is less than the dose in the homogeneous phantom even though the primary photon fluence is greater. This was shown (in Section 6) to be due to a loss of lateral electronic equilibrium because the distance from the central axis to

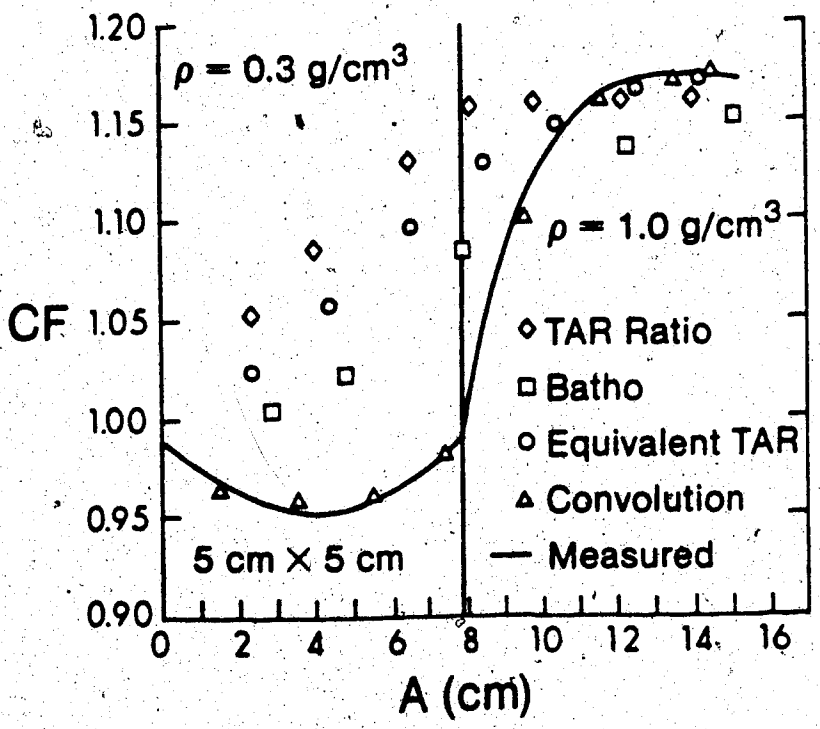

Figure 131. The experimental and measured TMR correction factor for a 15 MV beam. The experimental set-up is shown in Figure 85. The field size is 5 cm x 5 cm.

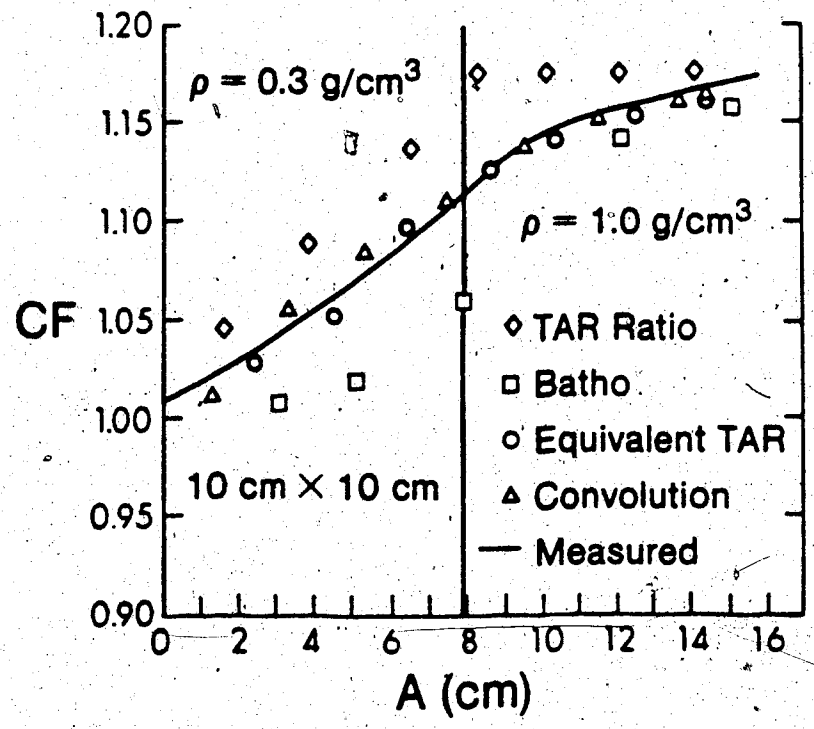

Figure 132. The experimental and measured TMR correction factor for a 15 MV beam. The experimental set-up is shown in Figure 85. The field size is 10 cm x 10 cm.

the field boundary is smaller than the lateral range of charged particles. The dose results of some existing methods are shown for comparison in Figures 131 and 132. The existing methods assume electronic equilibrium and poorly predict the dose in this situation. The convolution calculation predicts not only the correct trend but also predicts the measured correction factor to within 2 %. Lateral equilibrium is established at a field size of 10 cm x 10 cm, and for this situation, the convolution calculation and the equivalent TAR methods both predict the dose adequately.

The choice of weighting of the interaction voxel, f_o, in the ray-tracing algorithm altered the dose in this heterogeneous situation by only a few percent. Therefore, at least for the slab geometries tested, ray-tracing seems to be adequate for determining the average density "environment" between the interaction and dose deposition voxels.

Many dose calculation algorithms, such as the Batho and TAR ratio methods, only correct the dose at the central axis for tissue heterogeneities. Figure 133 illustrates the dose profile at a depth of 9.5 cm inside a $0.30 g/cm^3$ region of a heterogeneous phantom (see inset). The field size is 20 cm x 20 cm. At the central axis, the dose in this heterogeneous phantom is about 5 % greater than the dose in a homogeneous phantom at the same depth. However, the dose in the heterogeneous phantom decreases faster than the dose in a homogeneous phantom at greater distances from the

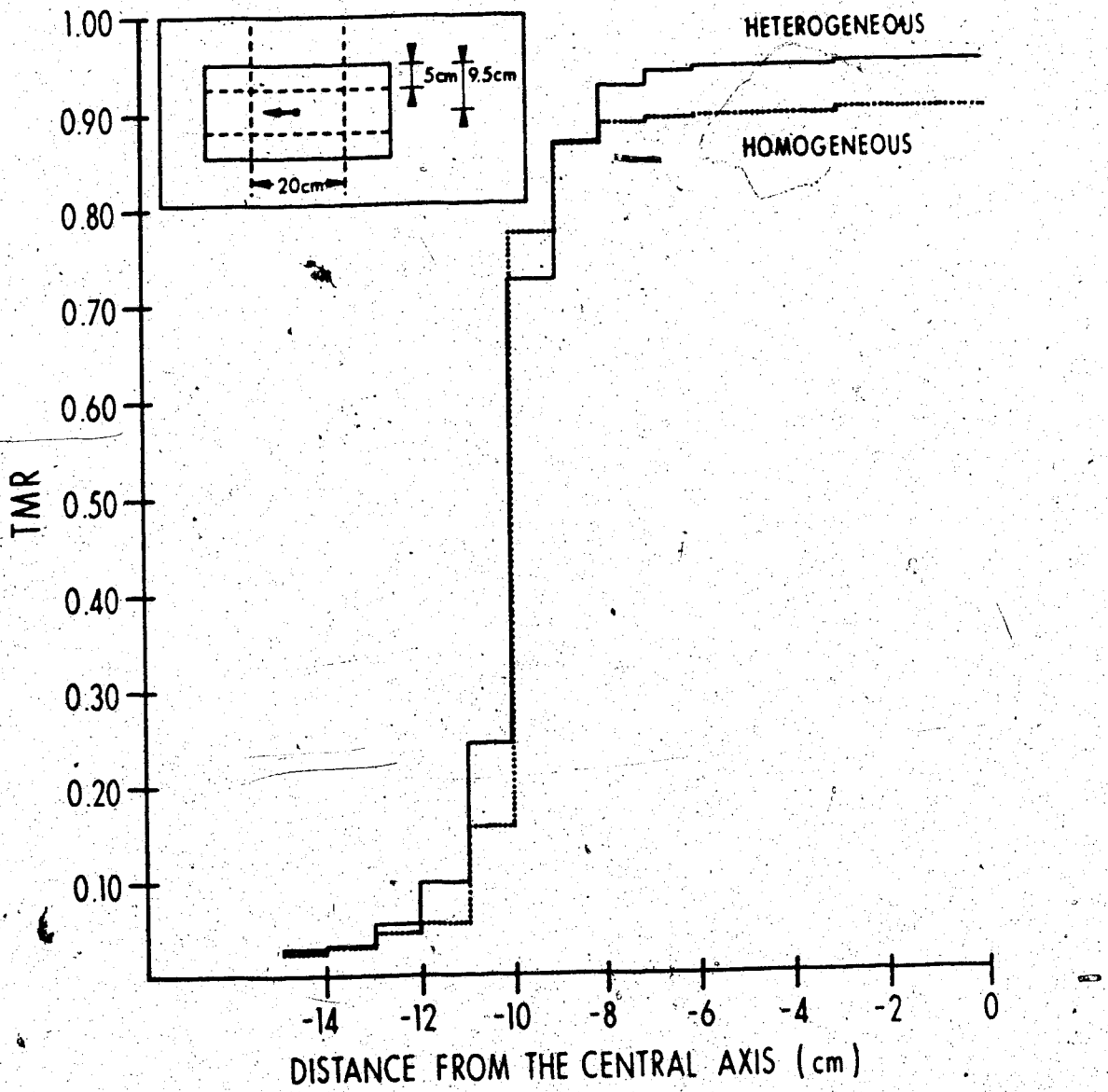

Figure 133. The calculated homogeneous and heterogeneous TMR profile at 9.5 cm depth (A = 4.5 cm) in a 20 cm x 20 cm field.

central axis. Just inside the field boundary, the dose in the heterogeneous phantom is less than the dose in a homogeneous phantom. Outside the field boundary, the dose in the heterogeneous phantom is once again greater than in the homogeneous phantom. The behavior near the field boundary, in the low-density material, can be attributed to charged particles streaming from inside the field (reducing the dose there) to outside the field (increasing the dose there). Therefore, an inhomogeneity correction factor obtained at the central axis cannot be applied throughout the field. Kornelsen and Young (80) have measured similar changes in 10 MV dose profiles in phantoms containing low-density regions.

Traditionally, the effects of a wedged field incident on a heterogeneous phantom on a dose distribution has been performed in two steps. The dose distribution is first calculated for a wedged field incident on a homogeneous phantom. The correction factor is then obtained for a heterogeneous phantom irradiated by an open field. The inhomogeneity correction factors are then multiplied by the dose distribution for the wedged field to obtain the dose distribution. This approach is non-rigorous and has never been tested for its validity. The convolution method is capable of determining the wedged field dose distribution for a heterogeneous phantom in one step.

Figure 134 illustrates that there is good agreement between separating the tasks of determining the wedge dose distribution and the heterogeneous correction and

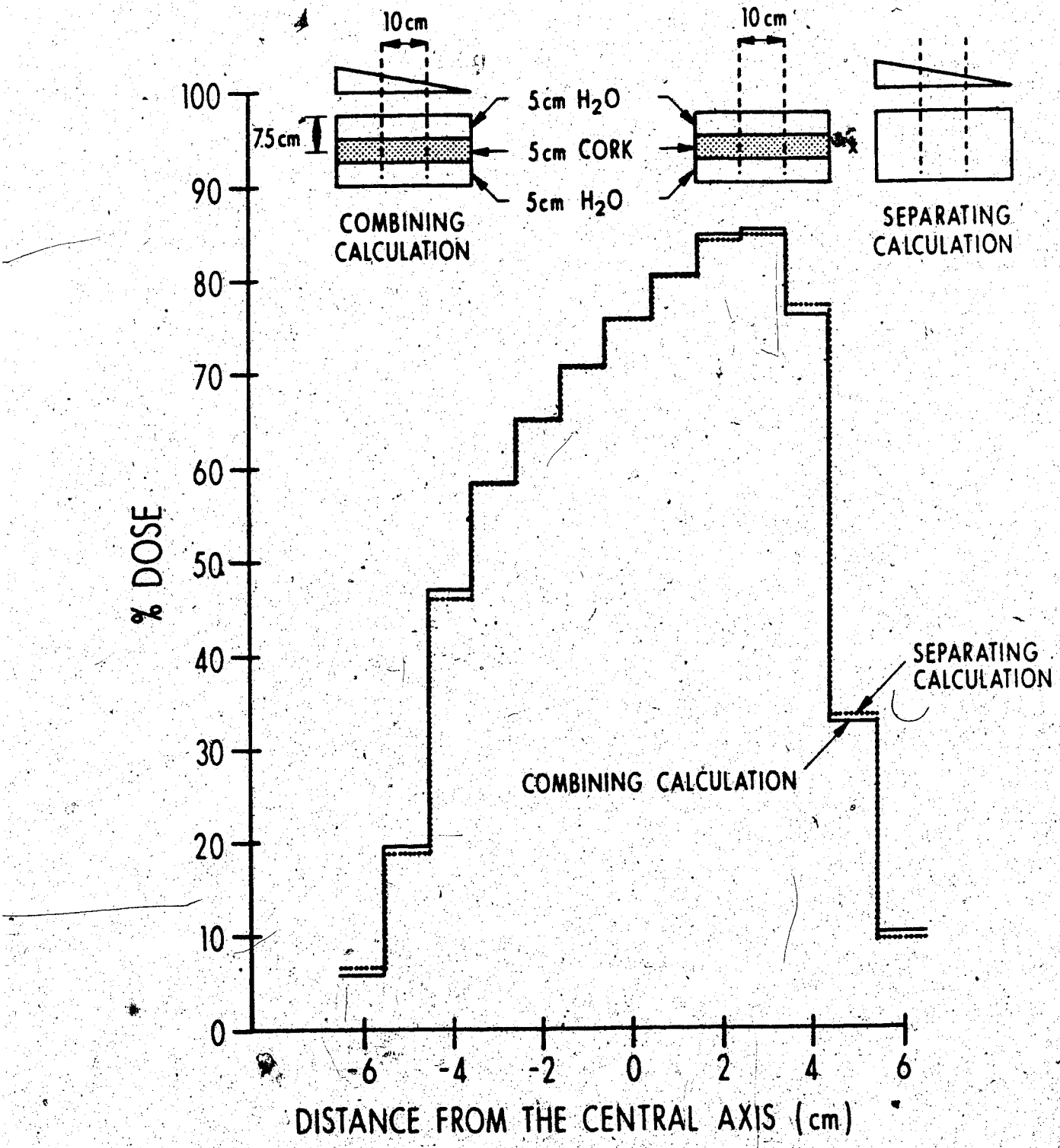

Figure 134. A comparison of separating the task of determining the wedge dose distribution and calculating an inhomogeneity correction factor and performing the calculation in one step. The result in either case is the percent dose profile. The field size is 10 cm x 10 cm. The heterogeneous phantom and wedge are shown schematically.

calculating the wedge and heterogeneous distribution directly in one step.

7.6 The Spatial Invariance Of The Dose Spread Arrays

The dose spread arrays are produced using a very large phantom. The primary dose spread array is finite in extent so the phantom need only have been larger than the maximum range of charged particles set-in-motion. The TFS dose spread array is completely independent of the size of the phantom used in the simulation. The size of the phantom will affect the RFMS dose spread array only. The use of this dose spread array near the edge of the phantom will introduce error. However, since this dose spread array contributes a small fraction to the total dose, this error due to the extent of the phantom, will be insignificant.

The dose spread arrays are not completely spatially invariant in homogeneous phantoms for two other reasons. Beam hardening is due to the preferential removal of low energy photons from the beam. It is possible that the beam will have a "hardened" spectrum near the central axis, due to a greater pathlength of the primary beam through the field flattening filter, as compared to near the beam boundary. In addition, as the beam penetrates the phantom, it contains a greater fraction of higher energy photons. Beam hardening effects were not included in the results described. If it is necessary to include hardening effects for some beams, the convolution can proceed using different dose spread arrays for different locations in the phantom.

Divergent beams have three geometrical characteristics which distinguish them from parallel beams. There is an

inverse square reduction of the primary photons and a linear increase in each field dimension as a function of depth. Another characteristic may have to be taken into account for this method. The dose spread arrays are not invariant for diverging beams. Figure 135 illustrates that a dose spread array should be "tilted" at an angle from the central axis equal to that of the primary beam. For example, the angle of tilt is about 8.5 degrees at a distance of 100 cm from the source at the edge of a 30 cm x 30 cm field. To be rigorous, the subscripts of the dose spread array at $i+\Delta i, j+\Delta j, k+\Delta k$ should be transformed to $i+\Delta i', j+\Delta j', k+\Delta k'$, where:

$$\Delta k' = \frac{(SSD+k)\Delta k + r\Delta r}{D} \qquad (7.6.1)$$

$$\Delta i' = \frac{\Delta i D - i\Delta k'}{SSD+k} \qquad (7.6.2)$$

$$\Delta j' = \frac{\Delta j D - j\Delta k'}{SSD+k} \qquad (7.6.3)$$

Where $r = \sqrt{i^2+j^2}$ and $\Delta r = \sqrt{\Delta i^2 + \Delta j^2}$. If $\Delta i'$, $\Delta j'$, or $\Delta k'$ are not integers, interpolation is necessary. This has not proven to be an important effect when calculating TMR's in the simple phantoms investigated so far. The transformation changes the value of the TMR at the central axis by less than 1 % up to a thickness of 20 cm in a 20 cm X 20 cm field at a distance of 100 cm from the source. However, beam

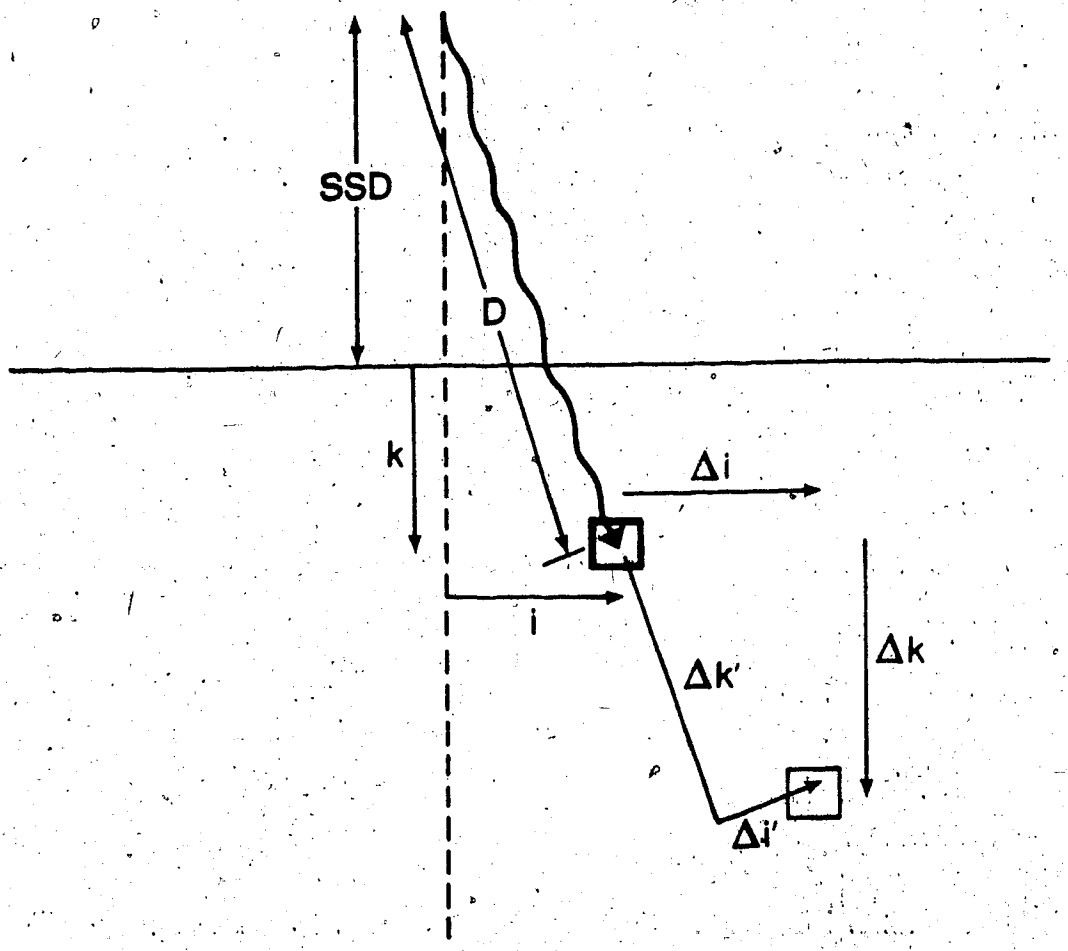

Figure 135. The dose spread array should be tilted to simulate the dose deposition from a divergent primary pencil beam interacting at i,j,k.

divergence will be an important effect when calculating percentage depth-dose for large fields or may be important when calculating dose in phantoms with complex heterogeneities.

7.7 Comparison With Other Methods and Potential Improvements

The convolution method presented has features similar to the equivalent TAR and Δ-Volume methods. Before the similarities are discussed, the characteristics of the method, which are unique, will be summarized.

1) The method explicitly takes into account the transport of charged particles which allows the calculation of dose in the build-up region and in lateral disequilibrium situations such as near beam boundaries or near low-density heterogeneities.

2) The use of experimental measurements as the data base is abandoned. Rather "synthetic measurements" are generated using the Monte Carlo method and validated by comparing the results of calculations with a limited set of experimental measurements.

3) Primary fluence is completely separated from dose deposition.

4) The primary dose, local first scatter dose and multiple scatter dose can be calculated separately. This allows optimization of the calculation resolution for each component to find the best compromise between speed and accuracy.

5) O'Connors theorem is explicitly used because the dose spread arrays are stored for a range of values of phantom

density times voxel dimension.

6) The same algorithm is used to calculate all the dose components.

Figure 136 illustrates a comparison between various dose calculation methods. The Monte Carlo method is the only method with the capabilities of the convolution method. However, it is yet far too slow for routine treatment planning. As computational power becomes less expensive and more available, this may change. Nevertheless, computational hardware improvements will also increase the speed of convolution calculations so that the convolution method will always remain faster than the Monte Carlo method. The convolution method retains the essential features of the Monte Carlo method for this application without the slow calculation time.

A procedure common to all other pencil beam and pixel-by-pixel calculation methods is" ray-tracing". The equivalent TAR method ray-traces to find the density weighted with respect to the amount of scatter originating at a location. The Δ-Volume method ray traces to find the contribution of first (and some second) scatter dose between the calculation point and all other points in the phantom where the primary beam interacts. The dose calculation for the first scatter dose contribution in a homogeneous phantom can be shown to be equivalent to a convolution calculation. This may be shown formally using a continuous 3-dimensional integral representation of first scatter fluence. The first

Algorithms For Making Dose Corrections In Heterogeneous Phantoms

Algorithm	Pathlength	Field Size	Position Of Structure	Shape Of Structure	Electronic Equilibrium
Linear Attenuation Coefficient	Yes	No	No	No	No
Ratio Of TAR's	Yes	Yes	No	No	No
Effective SSD	Yes	Yes	No	No	No
Isodose Shift	Yes	Yes	No	No	No
Batho (Power Law)	Yes	Yes	Yes	No	No
Equivalent TAR	Yes	Yes	Yes	Yes	No
Delta-Volume	Yes	Yes	Yes	Yes	No
Monte Carlo	Yes	Yes	Yes	Yes	Yes
Convolution	Yes	Yes	Yes	Yes	Yes

Figure 136. A comparison of the convolution method with existing dose calculating methods.

scatter photon fluence at a point $\vec{r}$ in a homogeneous phantom, due to primary interactions at a point $\vec{r}'$, is given by:

$$\Phi_{1st}(\vec{r}) = \int_{3D} \Phi p(\vec{r}') \frac{d\sigma}{d\Omega}(\vec{r}-\vec{r}') \frac{\rho(\vec{r}')}{|\vec{r}-\vec{r}'|^2} e^{-\tilde{\mu}|\vec{r}-\vec{r}'|} dV' \qquad (7.7.1)$$

Where $\Phi p(\vec{r}')$ is the primary fluence at point $\vec{r}'$ and $\rho(\vec{r}')$ is the density of the primary interaction site. $d\sigma(\vec{r}-\vec{r}')/d\Omega$ is the Compton scattering cross-section in units of cm^2/g. $e^{-\tilde{\mu}|\vec{r}-\vec{r}'|}$ is the attenuation of the first scatter dose between the interaction and dose deposition sites where the vector $\vec{r}-\vec{r}'$ is directed along the path between the interaction and dose deposition sites. Boyer (99) has shown formally that Equation 7.7.1 is a convolution integral. In a formalism used in continuous convolution theory (96) Equation 7.7.1 becomes:

$$\Phi_{1st}(\vec{r}) = \int_{3D} h(\vec{r}')g(\vec{r}-\vec{r}')dV' \qquad (7.7.2)$$

Where:

$$h(\vec{r}') = \Phi p(\vec{r}')\rho(\vec{r}') \qquad (7.7.3)$$

$$g(\vec{r}-\vec{r}') = \frac{d\sigma}{d\Omega}(\vec{r}-\vec{r}') \frac{e^{-\mu|\vec{r}-\vec{r}'|}}{|\vec{r}-\vec{r}'|^2} \qquad (7.7.4)$$

Equation 7.7.2 is just the 3-dimensional continuous analog

of Equation 7.4.8.

In general, the speed of pixel-based calculation methods is much slower than simpler methods. The time depends on the number and type of operations specified by the algorithm and the hardware used to run the program. Currently, the Δ-Volume method requires a significantly longer time than the convolution method when it is running on the same computer (VAX 11/780), presumably under the same operating conditions. The Δ-Volume requires 4.7 hours for a 16 x 16 x 16 dose matrix and 300 hours for a 32 x 32 x 32 matrix (77). The convolution method, by comparison, presently requires 50 min and 8.2 hours, respectively, for the same 3-dimensional distributions. The calculation times for both of these methods can be improved. The slowest part of the pixel-by-pixel methods is ray-tracing. Ray-tracing in the Δ-Volume method is being incorporated into a custom-integrated circuit which is expected to increase its speed by an order of magnitude (77). The convolution method should be particularly well-suited to array processing which should also decrease the calculation by an order of magnitude. The array processor calculation in the interaction point of view will be examined in some detail. The array processor would calculate the following equation for a given $\Delta i, \Delta j, \Delta k$ and relative fluence $\Phi''(i,j,k)$ (from Equation 7.5.7):

$$\Phi''(i,j,k)A'p(\tilde{\rho}\cdot\ell,\Delta i,\Delta j,\Delta k) \qquad (7.7.5)$$

The host computer would calculate $\Phi''(i,j,k)$ and also keep track of where the primary fluence was interacting in the phantom (i.e. the 3-dimensional intersection of the beam and the patient). A flow chart of the host computer calculations is shown in Figure 137. A flow chart of the array processor calculation is shown in Figure 138. The array processor would first calculate the mean density between the interaction site and all the dose deposition sites. The algorithm then specifies a loop for the calculation of Equation 7.7.5. The average density calculation could have been brought within the loop and not stored as an array. However, some of the average density array may be reused for a beam from a different direction also interacting at the same location (i,j,k). Figure 139 illustrates the idea schematically. The Δ-Volume method should also be able to benefit by storing an average density matrix for use with multiple beams. In turn, the convolution method could employ a custom-integrated circuit to calculate the average density array. Both the Δ-Volume and the convolution methods could benefit from an improved ray-tracing algorithm. The algorithm presently employed by both methods is summarized by Equations 7.5.1 to 7.5.4. A more efficient method would be to calculate the density along radial vectors. In the case of the convolution method, in the interaction point of view, the center of the radial vectors would be the interaction site. In this way, the average density, at one point on the radial vector, would use the summation of densities calculated at a point

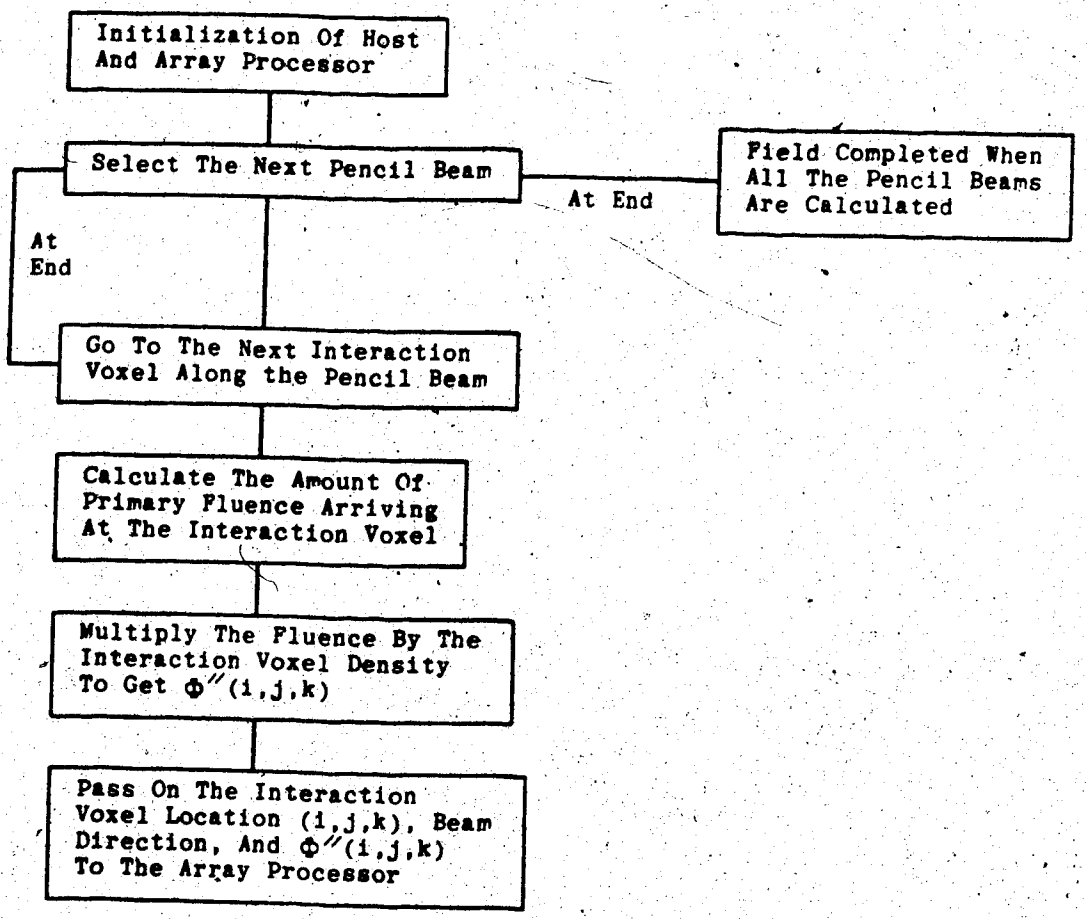

Figure 137. A flow chart of the host computer calculations required if an array processor is used to perform part of the convolution calculations (see Figure 138).

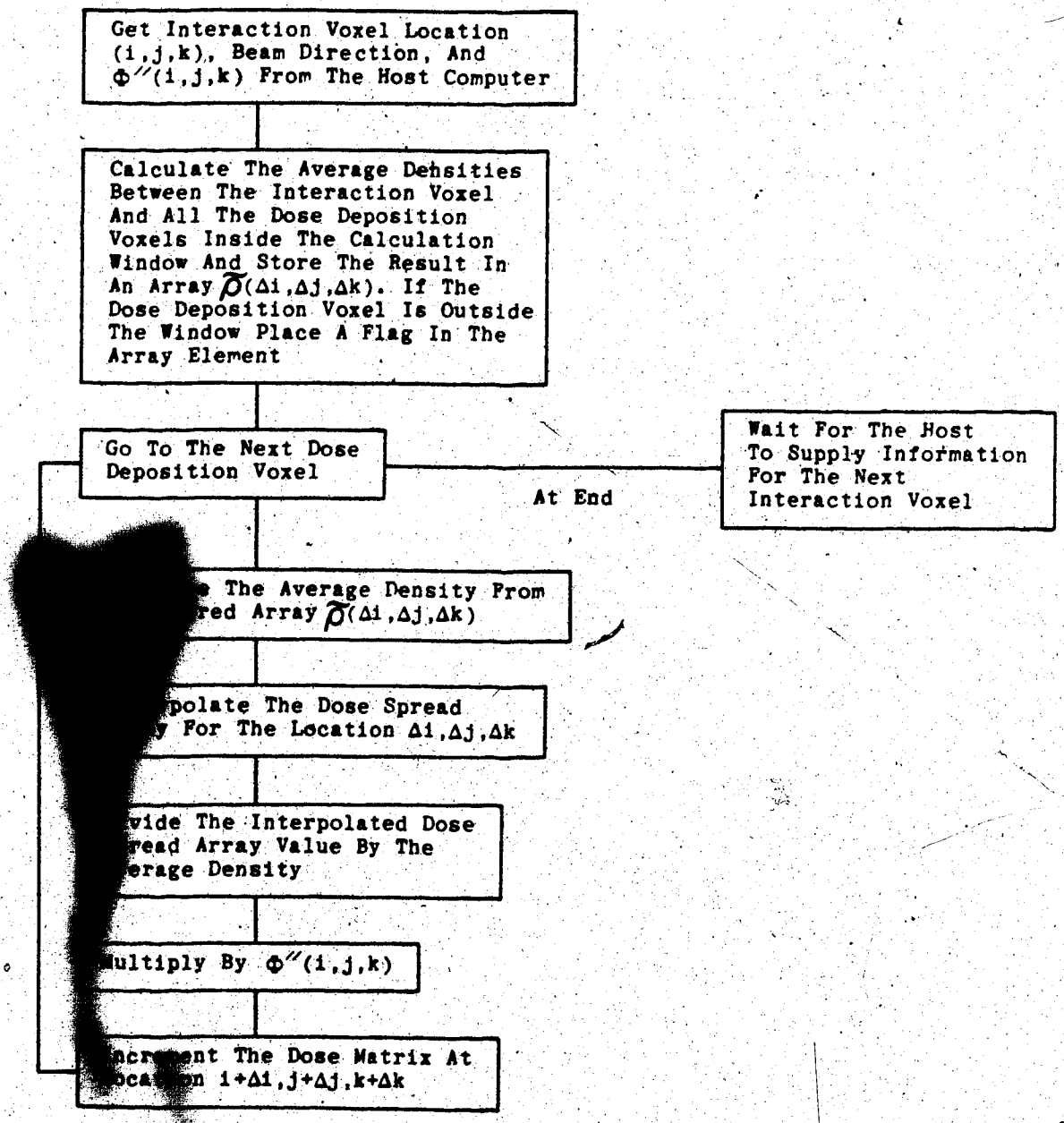

Figure 138. A flow chart of the array processor calculations (see Figure 137).

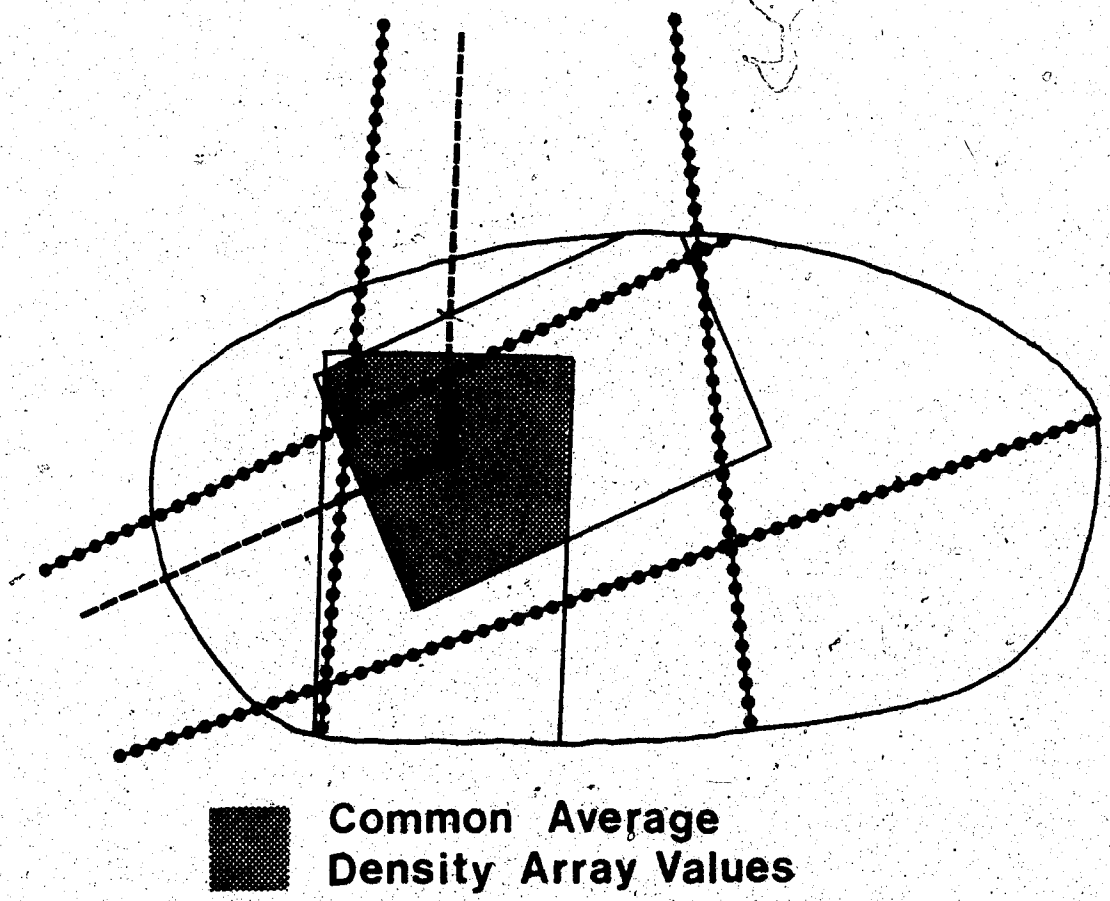

Figure 139. The part of an average density array calculated for one beam, that intersects with the average density array of another beam, may be reused by the second beam.

with a smaller radius. If the dose spread arrays were cubes with 'n' voxels per side, the number of calculations to assemble an average density matrix would be proportional to n^3, with this improved algorithm, compared to the presently used algorithm which is approximately proportional to n^4.

The proponents of the Δ-Volume method (77) have recently adopted a variable grid spacing capability to speed up the calculation. It is philosophically similar to the convolution method in that it calculates the contribution of scatter in a coarser grid resolution from contributions a long distance from the dose point.

7.8 Dose In A Non-Water-Like Heterogeneous Phantom

The present method has been used to calculate the dose in water-like heterogeneities such as lung which have a similar atomic composition. The method could be extended to other media of different atomic composition such as bone.

It is instructive to first examine the situation in a phantom near the junction of two materials with different atomic numbers. Equations 5.2.1 to 5.2.3 can be extended to determine the dose near a heterogeneity due to an atomic number change. Suppose the atomic number in a region of thickness, a, of a phantom is Z_1, and on the other side of the interface is Z_2. The direction of the photon beam is from region 1 to region 2. The dose in region 1 will be given by:

$$DOSE_1(z<a) \propto \left[\frac{\mu_{en}}{\rho}\right]_{Z_1}\left[\frac{S}{\rho}\right]_{Z_2}\left(e^{-(\mu_\gamma/\rho)\rho_1 z} - e^{-(\mu_e^{\pm}/\rho)\rho_1 z}\right) \tag{7.8.1}$$

The dose on the other side of the interface will be given by:

$$DOSE_2(z>a) \propto \left[\frac{\mu_{en}}{\rho}\right]_{Z_1}\left[\frac{S}{\rho}\right]_{Z_2}\left(e^{-\mu_\gamma/\rho)\rho_1 a} - e^{(\mu_e^{\pm}/\rho)\rho_1 a}\right) x$$

$$x\, e^{(\mu_e^{\pm}/\rho)\rho_2(z-a)} + \left[\frac{\mu_{en}}{\rho}\right]_{Z_2}\left[\frac{S}{\rho}\right]_{Z_2}\left(e^{-(\mu_\gamma/\rho)\rho_2(z-a)}\right.$$

$$\left. - e^{-(\mu_e^{\pm}/\rho)\rho_2(z-a)}\right) e^{-(\mu_\gamma/\rho)\rho_1 a} \tag{7.8.2}$$

The first term takes into account the production of charged particles in region 1 that arrive at a depth, z, and the second term takes into account the amount of dose arriving at the same depth, z, from the second region.

The charged particle fluence at the interface will be almost entirely generated in region 1 (except for a small amount of charged particles directed in the backwards direction which has not been included in the above equation). There will be a discontinuity of dose at the interface. The ratio of dose at the interface in region 2 compared to region 1 is equal to:

$$\frac{[\bar{S}/\rho]_{Z_2}}{[\bar{S}/\rho]_{Z_1}} \qquad (7.8.3)$$

This discontinuity has been observed by several authors (63,78,100).

The convolution method may be used to determine the dose in medium with different atomic numbers. The primary dose spread arrays may have to be recalculated for these types of tissue because charged particle scattering is strongly dependent on atomic number (88). The scatter dose spread arrays would not likely be affected because the Compton scattering cross-section per electron is approximately independent of atomic number (9). The density, ρ, would now have to be interpreted as the electron density relative to water (67). As in the simple model described by Equation 7.8.1 and 7.8.2, two additional factors would have to be included when the primary dose is

being calculated:

$$\text{DOSE CONTRIBUTION}(i+\Delta i, j+\Delta j, k+\Delta k) \propto \phi'(i,j,k) \frac{\rho(i,j,k)}{\tilde{\rho}} \times$$

$$\times \frac{[\frac{\mu_{en}}{\rho}]_{Z(i,j,k)}}{[\frac{\mu_{en}}{\rho}]_{\tilde{Z}}} \cdot \frac{[\frac{\bar{S}}{\rho}]_{Z(i+\Delta i, j+\Delta j, k+\Delta k)}}{[\frac{\bar{S}}{\rho}]_{\tilde{Z}}} A_p(\tilde{Z}, \tilde{\rho}\cdot\ell, \Delta i, \Delta j, \Delta k) \qquad (7.8.4)$$

$\tilde{Z}$ is the average effective atomic number between the interaction and dose deposition sites. The first ratio takes into account the relative difference in the amount of energy released in the real interaction voxel of effective atomic number, $Z(i,j,k)$, compared to the amount released in a homogeneous phantom of effective atomic number $\tilde{Z}$. The second ratio takes into account the amount of energy deposited in the real dose deposition voxel of effective atomic number $Z(i+\Delta i, j+\Delta j, k+\Delta k)$ compared to the amount deposited in the homogeneous phantom of effective atomic number $\tilde{Z}$.

8. Discussion and Conclusions Concerning The Convolution Method

The only justification for our concepts and system of concepts is that they serve to represent the complex of our experiences; beyond this they have no legitimacy.

Albert Einstein

(The Meaning Of Relativity, 1921)

8.1 Discussion

The dose spread arrays are "synthetic" macroscopic data determined from the microscopic transport of individual particles using the Monte Carlo method. This information cannot be obtained from measurement because a real primary photon beam cannot be "forced" to interact at only one region of the material. This requirement is necessary in order to describe the transport of secondary particles set in motion by primary photon interactions. All the dose spread arrays were generated with the inclusion of charged particle transport. The primary dose spread array is proportional to the energy deposited by charged particles set in motion by primary photons.. The scatter dose spread arrays are proportional to the energy deposited by charged particles set in motion by scattered photons. An analytic solution to photon-charged particle transport would be difficult (if not impossible) to obtain (101). For this reason, the Monte Carlo method was used to generate all the dose spread arrays.

The convolution procedure separates the photon - charged particle transport up into physically meaningful components. Primary photon interactions are separated from charged particle and secondary photon transport and energy deposition (101). This division of primary fluence from dose deposition is a more appropriate model of radiation transport than the modification of measured dose distributions in which these two effects are combined. This

does not undermine the importance of obtaining good measurements, since this provides the selection criteria for the photon spectrum used to compute the dose spread arrays.

The spectrum was determined by first finding a tentative "pre-spectrum" which is a measured spectrum obtained from a research accelerator (48). The agreement between the calculated dose and measured dose is a necessary condition for the acceptability of the spectrum, but it is not a sufficient condition. The spectrum may not be unique. Therefore, a better procedure would be to determine the actual spectrum directly by measurement. Transmission measurements, obtained with "good geometry", have been used to obtain spectra (102,103). A problem with spectra determined in this way is that small errors in measurements leads to large errors in the spectral determination. Therefore, the spectrum should be checked by getting the agreement between the measured and calculated dose using this spectrum. If it did not agree then the spectrum should be adjusted to obtain better agreement (although the modification must be kept within the experimental uncertainty).

Transmission measurements are relatively easy to obtain. Using a pre-spectrum based on these measurements, the convolution method could be adopted as the dose calculation method for any accelerator type or energy. What is first required is the dose spread arrays calculated as a function of $\rho \cdot \ell$ and Z for various monoenergetic energies from 0 to 50 MeV (no accelerator with a nominal energy above

50 MV is available). A spectrum would be obtained for energy components for which dose spread arrays have been calculated. The dose spread arrays for the spectrum are obtained using the pre-stored dose spread arrays. The primary attenuation coefficient would then be determined using Equation 7.4.4. The dose distribution would then be calculated for a wide range of field sizes. The calculated dose beyond d_{max} would be compared to the measured dose. If the agreement was not satisfactory, then the spectrum would be modified. The above procedure should be repeated for the new spectrum. Figure 140 is the flow chart of the proposed implementation procedure.

Basing photon dose calculations on the firm mathematical foundation of convolution may allow additional future improvements. In homogeneous phantoms, the dose spread arrays are spatially invariant so that the relative fluence array and dose spread arrays may be Fourier transformed into the spatial frequency domain. The convolution may then proceed much more quickly by multiplying the transformed arrays (99). The dose can then be obtained by taking the inverse Fourier transform of the result. For homogeneous water-like media, this procedure is described mathematically as:

$$DOSE(x,y,z) \propto F^{-1}[F\{\Phi'(i,j,k)\}*F\{A(\rho\cdot\ell=\ell,\Delta i,\Delta j,\Delta k\}] \quad (8.1)$$

Where F and F^{-1} describe symbolically the 3-dimensional Fourier and inverse Fourier transform, respectively (96).

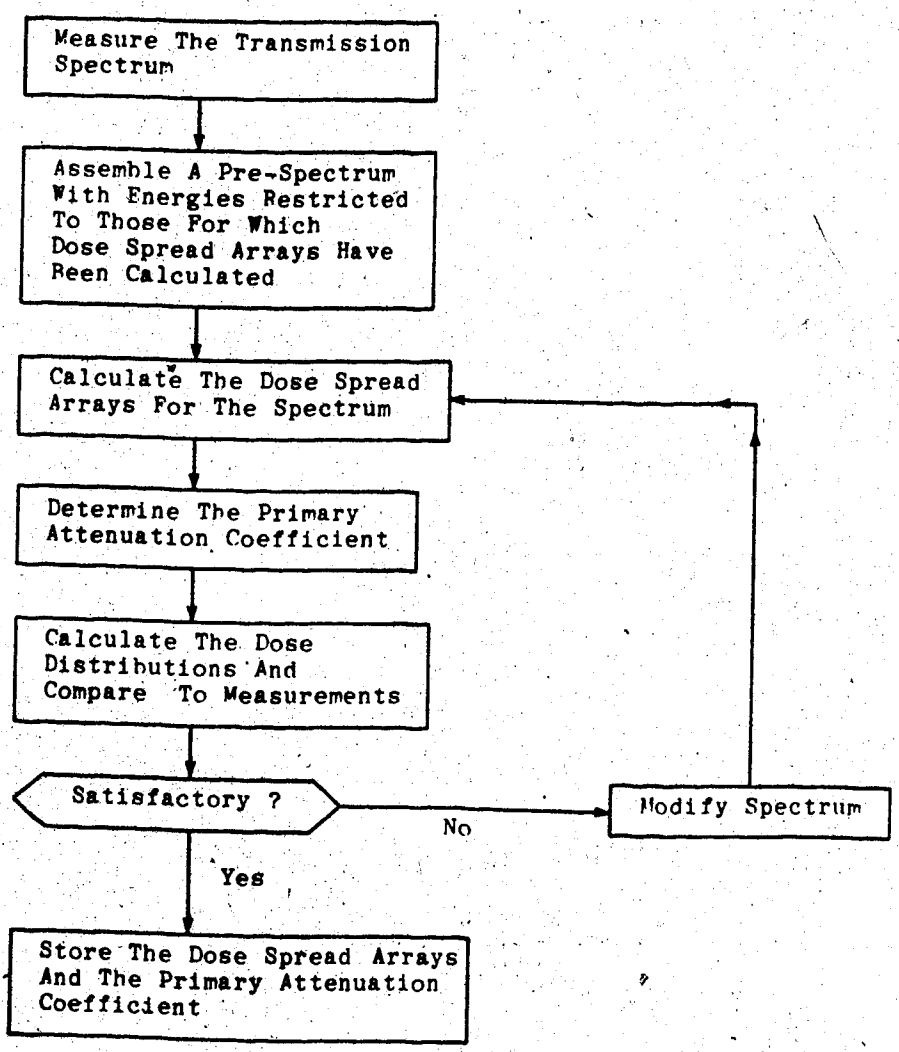

Figure 140. The flow chart of the determination of the correct dose spread array and primary attenuation coefficient based on the transmission spectrum of a linear accelerator.

This procedure is used routinely in image processing applications, and is especially appropriate if an array processor is available.

Deconvolution techniques may be useful in optimizing the delivery of radiation therapy. If one knows the attributes of an optimal dose distribution (eg. uniform dose to the target volume and minimal dose to surrounding tissue), and the beam directions and intensities, the dose spread array can be deconvolved from the ideal dose distribution to obtain the best primary fluence distribution. This information could be used to design modifying devices, such as beam compensators, to approach the ideal relative fluence distribution in homogeneous or heterogeneous media.

8.2. Conclusions

The EGS Monte Carlo modelling in Section 6 confirmed the interpretation in Section 5 that lateral disequilibrium is the reason for reduced dose at the central axis in a low-density medium for small field sizes. This situation is one aspect of a more general phenomenon. Lateral disequilbrium never exists near the field boundary penumbra. It was shown that the penumbra region for high energy linear accelerator beams is due in part to the lateral transport of charged particles. When the field size is small and the phantom has a low-density, the penumbra extends to the central axis. In order to describe the disequilibrium effects, the transport of charged particles have to be included into dose calculations.

A dose calculation method based on convolution was introduced in Section 7 which explicitly took into account charged particle transport. The method was general enough to include the transport of scattered photons. The method relied on the production of "dose spread arrays" to describe the transport of secondary particles from a primary photon interaction voxel to neighboring dose deposition voxels. The values of the elements of the dose spread arrays represent the dose deposited in dose deposition voxels per unit collision KERMA at a primary interaction voxel. The dose spread arrays were obtained from Monte Carlo simulations. The primary dose spread array accounts for the primary dose, the truncated first scatter (TFS) dose spread

array accounts for the first scatter dose deposition close to the primary interaction site, and the residual first and multiple scatter (RFMS) dose spread array accounts for the rest of the first scatter dose and all the multiple scatter dose. The primary dose spread arrays generated in homogeneous water-like phantoms of density, ρ , with voxel dimensions, ℓ , are equivalent to those generated using a phantom density, ρ', with dimensions, ℓ', provided; $\rho \cdot \ell = \rho' \cdot \ell'$. The scaling also applies to the scatter dose spread arrays. This indicates that O'Connors theorem applies to the primary dose even when there is electronic disequilibrium, as well as scatter dose, in a homogeneous phantom.

The dose distribution in 3-dimensions is obtained in a homogeneous phantom by convolving the dose spread array kernel, applicable to the density of the phantom and desired voxel resolution, with the relative fluence. There is a reciprocity between the interaction and dose deposition voxels. The dose spread arrays describe both the transport of dose from an interaction voxel and the arrival of dose at a dose deposition voxel. This allows the convolution to proceed in two ways called the interaction and dose deposition points of view. The method accurately predicts the dose in homogeneous phantoms in situations of electronic disequilibrium including the build-up region and near beam boundaries. The method was shown to provide a unified treatment of dose calculations in that it could account for the changes in dose due to fluence modifying devices such as

beam [redacted]d wedges.

T[redacted]e spread arrays, generated for homogeneous [redacted]tom[redacted]t various values of $\rho \cdot \ell$, are used to describe the t[redacted]spo[redacted] of dose in heterogeneous phantoms. The average de[redacted] $\tilde{\rho}$, between the interaction and dose deposition vo[redacted]s determined. The primary and TFS dose spread arr[redacted] are interpolated to obtain one appropriate for this aver[redacted] density. The convolution of these arrays in a heter[redacted]eneous phantom contains a factor to account for the diffe[redacted]ce in the amount of interactions between the heterogeneous interaction voxel and the homogeneous interac[redacted]on voxel with a density equal to the average path densit[redacted]he RFMS dose spread array in heterogeneous phanto[redacted]s is scaled using the average phantom density instead of the average path density. The method provided a good prediction of the dose in and near heterogeneous regions.

Although the method is presently only applicable to dose absorption in materials which are water-like in atomic composition, it could be extended to include non-water-like materials. The convolution framework of the method lends itself to Fourier and deconvolution techniques that could improve the calculation speed and optimization of dose.

REFERENCES

(55) Lichter, A.S., Fraas, B.A., van de Geijn, J., Fredrickson, H.A., Glatstein, E., "An Overview of Clinical Requirements and Clinical Utility of Computed Tomography Based Radiotherapy Treatment Planning", in Computed Tomography in Radiation Therapy, Ed., Ling, C.C., Rogers, C.C., Morton, R.J., Raven Press, New York, (1983).

(56) Meyer, J.E., "Computed Tomography in Radiation Therapy Treatment Planning: The Diagnostician", in Computed Tomography in Radiation Therapy, Ed., Ling, C.C., Rogers, C.C., Morton, R.J., Raven Press, New York, (1983).

(57) Geise, R.A., McCullough, E.C., "The Use of CT Scanners in Megavoltage Photon Beam Therapy Planning", Radiology, 124, 133-141, (1977).

(58) Sontag, M.R., Battista, J.J., Bronskill, M.J., Cunningham, J.R., "Implications of Computed Tomography for Inhomogeneity Corrections in Photon Beam Dose Calculations", Radiology, 124, 143-149, (1977).

(59) Battista, J.J., Rider, W.D., Van Dyk, J., "Computed Tomography for Radiotherapy Planning", International Journal of Radiation Oncology, Biology and Physics, 6, 99-107, (1980).

(60) Brooks, R.A., Mitchell, L.G., O'Connor, C.M., Di Chiro, G., "On the Relationship Between Computer Tomography Numbers and Specific Gravity", Physics in Medicine and Biology, Vol. 26, No. 1, 141-147, (1981).

(61) Cassell, K.J., Hobday, P.A., Parker, R.P., "The Implementation of a Generalized Batho Inhomogeneity Correction for Radiotherapy Planning with Direct Use of CT Numbers", Physics in Medicine and Biology, Vol. 26, No. 4, 825-833, (1981).

(62) Reinstein, L.E., McShan, D.L., Land, R.E., Glicksman, A.S., "Three-Dimensional Reconstruction of CT Images for Treatment Planning in Carcinoma of the Lung", in Computed Tomography in Radiation Therapy, Ed., Ling, C.C., Rogers, C.C., Morton, R.J., Raven Press, New York, (1983).

(63) Johns, H.E., Cunningham, J.R., The Physics of Radiology, Fourth Edition, Charles C. Thomas, Springfield, IL., (1983).

REFERENCES (CONT'D)

(64) Young, M.E.J., Kornelsen, R.O., "Dose Corrections for Low-Density Tissue Inhomogeneities and Air Channels for 10-MV X-rays", Medical Physics, Vol. 10, No. 4, 450-455, (1983).

(65) Cunningham, J.R., "Tissue Inhomogeneity Corrections in Photon Beam Treatment Planning", in Progress in Medical Physics, Ed., Orton, C.E., Plenum, New York, (1982).

(66) Batho, H.F., "Lung Corrections in Cobalt-60 Beam Therapy", Journal of the Canadian Association of Radiologists, 15, 79-83, (1964).

(67) Sontag, M.R., Cunningham, J.R., "Corrections to Absorbed Dose Calculations for Tissue Inhomogeneities", Medical Physics, Vol. 4, No. 5, 431-436, (1977).

(68) Lulu, B.A., Bjarngard, B.E., "A Derivation of Batho's Correction Factor for Heterogeneities", Medical Physics, Vol. 9, No. 6, 907-909, (1982).

(69) Lulu, B.A., Bjarngard, B.E., "An Improved Correction Factor for Heterogeneities", Medical Physics, Vol. 9, No. 4, 626 (Abstract), (1982).

(70) Sontag, M.R., Cunningham, J.R., "The Equivalent Tissue-Air-Ratio Method for Making Absorbed Dose Calculations in a Heterogeneous Medium, Radiology, 129, 787-794, (1978).

(71) O'Connor, J.E., "The Variation of Scattered X-rays with Density in an Irradiated Body", Physics in Medicine and Biology, 1, 352-369, (1957).

(72) Tatcher, M., Palti, S., "A Simple Equivalent Tissue-Air-Ratio Method for Calculating Absorbed Dose in a Heterogeneous Medium", Radiology, Vol. 146, No. 2, 527-529, (1983).

(73) Cunningham, J.R., Beaudoin, L., "Calculations for Tissue Inhomogeneities with Experimental Verification", in Proceedings of the XIII International Congress on Radiology, Madrid.

(74) Larson, K.B., Prasad, S.C., "Absorbed Dose Computations for Inhomogeneous Media in Radiation - Treatment Planning Using Differential Scatter-Air-Ratios", in Proceeding of the Second Annual Symposium on Computer Applications in Medical Care, Washington, D.C.

REFERENCES (CONT'D)

(75) Wong, J.W., Henkelman, R.M., "A New Approach to CT Pixel-Based Photon Dose Calculations in Heterogeneous Media", Medical Physics, Vol. 10, No. 2, 199-208, (1983).

(76) Wong, J.W., Henkelman, R.M., Andrew, J.W., Van Dyk, J., Johns, H.E., "Effect of Small Inhomogeneities on Dose in a Cobalt-60 Beam", Medical Physics, Vol. 8, No. 6, 783-791, (1981).

(77) Rosenberger, F., Krippner, K., Stein, D. Jr., Wong, J., "Implementation of the Delta-Volume Dose Calculation Algorithm; in Proceedings of the Eighth International Conference on the use of Computers in Radiation Therapy, Toronto, (1984).

(78) Dutreix, J., Bernard, M., "Dosimetry at Interfaces for High Energy X and Gamma Rays", British Journal of Radiology, 39, 205-210, (1966).

(79) Leung, P.M.K., Seaman, B., Robinson, P., "Low-Density Inhomogeneity Corrections for 22 MV X-ray Therapy", Radiology, 94, 449-451, (1970).

(80) Kornelsen, R.O., Young, M.E.J., "Changes in the Dose-Profile of a 10 MV X-ray Beam Within and Beyond Low-Density Material", Medical Physics, Vol. 9, No. 1, 114-116, (1982).

(81) McGinley, P.H., Sanders, M., "Lung Correction Factors for 45-MV X-ray Therapy", Medical Physics, Vol. 9, No. 5, 738-740, (1982).

(82) Mackie, T.R., Scrimger, J.W., "Modelling the Build-up Region of Megavoltage Photon Beams", Medical Physics, Vol. 9, No. 4, 620 (Abstract),(1982).

(83) Ford, R.L., Nelson, W.R., The EGS Code System: Computer Programs for the Monte Carlo Simulation of Electromagnetic Cascade Showers, Version 3, Stanford Linear Accelerator Report No. 210, Stanford, CA., (1978).

(84) Rogers, D.W.O., "More Realistic Monte Carlo Calculations of Photon Detector Response Functions", Nuclear Instruments and Methods, 199, 531-548, (1982).

(85) Mach, H., Rogers, D.W.O., "A Measurement of Absorbed Dose to Water Per Unit Incident 7-MeV Photon Fluence", Submitted Dec. 1983 to Physics in Medicine and Biology.

(86) Dean, R.D., "A Scattering Kernel for Use in True Three-Dimensional Dose Calculations", Medical Physics, Vol. 7, No. 4, 429 (Abstract), (1980).

REFERENCES (CONT'D)

(87) Attix, F.H., "The Partition of Kerma to Account for Bremsstrahlung", Health Physics, 36, 347-354, (1979).

(88) I.C.R.U. Report 21, Radiation Dosimetry: Electrons with Initial Energies Between 1 and 50 MeV, International Commission on Radiation Units and Measurements, Washington, D.C. (1972).

(89) Bloch, P., Wallace, R., "Computer Generated Scatter Dose Distributions for 6-MV Radiotherapy Photon Beams", Medical Physics, Vol. 6, No. 2, 149-152, (1979).

(90) Barnett, R., "Zero-Area TMR Data Compiled for Cross Cancer Institute, Edmonton, Canada", (Private Communication).

(91) Schell, M.C., Deye, J.A., "Empirical Equation for Tissue-Maximum-Ratios and Scatter-Maximum-Ratios for Indirectly Ionizing Radiotherapy Beams", Medical Physics, Vol. 6, No. 1, 65-67, (1979).

(92) Coffey, C.W. II, Beach, J.L., Thompson, D.J., Mendiondo, M., "X-ray Beam Characteristics of the Varian Clinac 6-100 Linear Accelerator", Medical Physics, Vol. 7, No. 6, 716-722, (1980).

(93) Patterson, M.S., Shragge, P.C., "Characteristics of an 18 MV Photon Beam from a Therac-20 Medical Linear Accelerator", Medical Physics, Vol. 8, No. 3, 312-318, (1981).

(94) Paul, J.M., Koch, F., Khan, F.R., Devi, B.S., "Characteristics of a Mevatron 77 15-MV Photon Beam", Medical Physics, Vol. 10, No. 2, 237-242, (1983).

(95) Cristy, M., "Applying the Reciprocity Dose Principle to Heterogeneous Phantoms: Practical Experience from Monte Carlo Studies", Physics in Medicine and Biology, Vol. 28, No. 11, 1289-1303, (1983).

(96) Bracewell, R., "The Fourier Transform and Its Applications", McGraw-Hill, New York, (1965).

(97) Barnett, R., Tom Baker Cancer Clinic, Calgary, Canada, (Private Communication).

REFERENCES (CONT'D)

(98) Clarkson, J.R., "A Note on Depth Dose in Fields of Irregular Shape", British Journal of Radiology, 14, 265, (1941).

(99) Boyer, A.L., Cancer Therapy and Research Center, San Antonio, TX, (Private Communication).

(100) Webb, S., "The Absorbed Dose in the Vicinity of an Interface Between Two Media Irradiated by a Co-60 Source", British Journal of Radiology, 52, 962-967, (1979).

(101) Roesch, W.C., Radiation Dosimetry, Ed., Attix, F.H., Roesch, W.C., Academic Press, New York, (1968).

(102) Twidell, J.W., "The Determination of X-ray Spectra Using Attenuation Measurements on a Computer Program", Physics in Medicine and Biology, 15, 529-539, (1970).

(103) Huang, P-H., Kase, K., Bjarngard, B.E., "Simulation Studies of 4-MV X-ray Spectral Reconstruction by Numerical Analysis of Transmission Data", Medical Physics, Vol. 9, No. 5, (1982).

Appendices

(Appendices 1 to 9 are in Volume 1)

"Agnes, ... do we know an Inhomogeneity?"

Appendix 10. Listing of the MOCA Monte Carlo Code

```
      Program MOCA

c MOnte-CArlo program to generate dose spread arrays.
c The variables are domumented as they occur in the program.

      integer l,ii,nerg,enn(36),intest
      real r,xs,cal,sal,cbeta,sbeta,total
      real stop(179),tha(179),ep,cay
      real eo,e,doset(25,25,25),pl,gaus(100),g
      real z,max,ang,en(36),dose(5,25,25,25)
      integer i,j,m,p,kay,quad(4),chargpart,inquad(4)
      real xnrg(100),mu(100,10),sig(100,10)
      real pi(100,10),que(10),shiftx,shifty

      integer k,nrgint,phantom(25,25,25),multi
      integer charge,ir,vint,annhilflag
      integer order,kinorder(25)
      real nrgx,xs,ys,diml,dimlz
      real lx,ly,lz,short,attentot,dist,attensig
      real attenpi,fractioni,fraction2
      real nrg(35),fac,nrgmax,frac1,frac2
      real tnrg1,tnrg2,compton(35,50),tnrg,arg
      real kinrg(25),kincal(25),kinsal(25)
      real kinsbeta(25),kincbeta(25),kinx(25)
      real kiny(25),kinz(25),kintype(25),rr
      real pairprod(35,50),v,ro,r1,r2,test(4),arr(25)
      real photox,photoy,photoz
      real oldcal,oldsal,oldcbeta,oldsbeta
      real s,th,arg2
      integer n,numspect
      real sum,sqsum,mean(25),stdev(25),sterr(25),maxmean
      real maxsterr,sumpart(4,25)
      real nearx,neary,nearz,near,maxpl,nearo
      integer nearinti,neari,nearintj,nearj,nearintk,neark
      integer history,mark,boundary(7)
      integer oldi,oldj,oldk,smalli,smallj,smallk
      common xs,ys,zs,i,j,k,cbeta,sbeta,cal,sal,diml,dimlz,short

c Gaus.dat stores a table of x's as a function of erf(x). See
c page 163 and 164 in Volume 1 and Appendix 7.

c Dose6.dat is a listing of the dose spread arrays.

c Compton.dat is a look-up table giving the elecron kinetic energies
c of equiprobable interactions. See Section 7.2.

c Pairprod.dat is a look-up table giving the electron or positron
c kinetic energies of equiprobable interactions. See Section 7.2.

c Pho15new.dat contains the 15 MV photon spectrum. See Sections 6.
c and 7.2.

c Atten.dat contains the attenuation data, scattering and stopping
c powers as a function of energy (from references 9 and 88).

c Debug.dat can contain information for debugging.

      open(unit=1,status='old',file='gaus.dat')
      open(unit=4,status='new',file='dose6.dat')
      open(unit=6,status='old',file='compton.dat')
```

```
      open(unit=8,status='old',file='pairprod.dat')
      open(unit=11,status='old',file='pho15new.dat')
      open(unit=12,status='old',file='atten.dat')
      open(unit=13,status='new',file='debug.dat')

c The following statements read the look-up tables and initializes.

      multi=1000              !# of incident photons
      intest=3                !interaction voxel depth indicator
      shiftx=50.0             !x-position to interaction voxel
      shifty=50.0             !y-position to interaction voxel
      diml=5.0                !voxel dimension in x and y direction
      dimlz=5.0               !voxel dimension in the z-direction

c Assign CT-number to the phantom voxels. There is a linear relation
c between density and CT-number (-1000=vacuum, 0=unit density).
c A heterogeneous phantom can be entered.

      do 6 k=1,25
        do 6 j=1,25
          do 6 i=1,25
6           phantom(i,j,k)=-800

c     do 7 k=4,25
c       do 7 j=1,25
c         do 7 i=1,25
c     7           phantom(i,j,k)=0

c     do 8 k=12,25
c       do 8 j=1,25
c         do 8 i=1,25
c     8           phantom(i,j,k)=0

      read(11,345) numspect                    !number of spectral bins
      do 10 i=1,numspect
        read(11,340) xnrg(i),en(i)             !spectrum weighting
10      enn(i)=en(i)/100.0*float(multi)        !# histories/bin
      read(11,350) (que(i),i=1,10)             !factor used in pair production
      do 12 l=1,100
12      read(1,422) gaus(l)                    !inverse error function

c 'Nrg' is the energy, 'mu' is the total attenuation coefficient, 'sig' is
c the Compton attenuation coefficient, 'pi' is the pair production
c attenuation coefficient, 'tha' is the scattering power and 'stop' is
c the stopping power.

      do 14 i=1,24
14      read(12,570) nrg(i),mu(i,1),sig(i,1),pi(i,1),tha(i),stop(i)

      do 17 i=17,24
        do 16 k=1,5
16        read (8,550) (pairprod(i,(k-1)*10+m),m=1,10)
17    continue
      do 19 i=1,24
        do 18 k=1,5
18        read (6,550) (compton(i,(k-1)*10+m),m=1,10)
19    continue

      i1=95835                 !random number seed
      cay=0.90                 !fraction of energy remaining after step
      annhilflag=0             !flags the production of annhilation photons
```

```
      charge=0                  !number of charged particles to process

      do 200 l=1,numspect       !do for all spectral bins
        do 180 m=1,enn(l)       !do for all photons in the bin

c Initialize the photon's energy, coordinate position and angle
c before transporting.

          xs=ran(i1)*diml+shiftx      !x-position
          ys=ran(i1)*diml+shifty      !y-position

          zs=10.0                     !z-position
          nrgx=xnrg(l)                !photon energy of the current bin
          history=history+1           !photon history counter
          cal=1.0                     !cos(alpha); alpha=zenith angle
          sal=0.0                     !sin(alpha)
          r=6.2832*ran(i1)
          cbeta=cos(r)                !cos(beta); beta=azimuth angle
          sbeta=sin(r)                !sin(beta)
          order=1                     !order of scattering; 1=primary
                                      !and 2=first scattered photon

c Scattered photons enter at line 20.
c Test to see if the photon's energy is below the photon
c cut-off energy.

20        if (nrgx .lt. 0.03) go to 50      !photon cut-off is 30 keV
          if (order .gt. 4) order=4         !order=4 is multiple scattering

c Photons which didn't interact in the last element
c enter at line 21. Annhilation photons enter here too.

21        continue

c Terminate the primary photon history if it doesn't interact
c in the interaction voxel.

      if (order .eq. 1 .and. zs .lt. 10.0 ) go to 180
      if (order .eq. 1 .and. zs .gt. 15.0 ) go to 180

c Find out the shortest distance to the next wall along
c the photon's path.

      call where

c Find out the C.T. number of the element and the type of
c tissue.

          p=1                   !signifies water

c Interpolate to find out the appropriate attenuation
c coefficient.

          nrgint=1
          do 25 while ( nrgx .gt. nrg(nrgint))
25          nrgint=nrgint+1
          if (nrgint .eq. 1) then
            attentot=mu(1,p)
          else
            fac=(nrgx-nrg(nrgint-1))/(nrg(nrgint)-nrg(nrgint-1))
            attentot=mu(nrgint-1,p)+(mu(nrgint,p)-mu(nrgint-1,p))*fac
```

```
            end if

c Find the interaction distance.

            r=ran(i1)
            if (r .le. 0.0) then
              dist=0.0
            else
              ro=float(phantom(i,j,k)*1000)/1000.0
              dist=-alog(r)/attentot/ro
            end if

c Determine if and if so, where, the photon interacts
c in the element. Rejection sampling is used. Short is the
c distance to the voxel wall in the direction of the photon.
c It was determined in Subroutine Where.

            if (short .gt. dist) then

              xs=xs+dist*sal*cbeta        !increment the
              ys=ys+dist*sal*sbeta        !position
              zs=zs+dist*cal              !variables

              i=jifix(xs/diml)+1          !determine the
              j=jifix(ys/diml)+1          !voxel
              k=jifix(zs/dimlz)+1         !location

c Discard the primary photon and choose another primary photon
c if it doesn't interact in the interaction voxel.

              if (order .eq. 1 .and. k .ne. intest) go to 180

c If the photon leaves the phantom, discard it and go on to follow its
c charged particles set in motion.

              if (xs .le. 0.0001 .or. xs .ge. 20.0*diml) go to 50
              if (ys .le. 0.0001 .or. ys .ge. 20.0*diml) go to 50
              if (zs .le. 0.0001 .and. cal .lt. 0.0) go to 50
              if (zs .ge. 20.0*dimlz) go to 50

c Interpolate to get the appropriate Compton and pair
c production attenuation coefficients. The type of
c interaction is determined. 'Fraction1' is the
c fraction of Compton interactions in the total and
c 'fraction2' is the fraction of Compton plus pair
c productions in the total. If the energy is between
c 0.2 and 3.0 MeV a Compton interaction must have occured.

              if (nrgx .gt. 0.2 .and. nrgx .lt. 3.0) go to 30

              attensig=sig(nrgint-1,p)+(sig(nrgint,p)-sig(nrgint-1,p))
     1                 *fac
              attenpi=pi(nrgint-1,p)+(pi(nrgint,p)-pi(nrgint-1,p))*fac
              fraction1=attensig/attentot
              fraction2=fraction1+attenpi/attentot

c Determine which interaction occured.

              rr=ran(i1)
              if (rr .lt. fraction1) then
```

```
c A Compton interaction has occured. The energy
c of the electron is determined.

30              continue

                nrgmax=(2.0*nrgx/.511)*nrgx/(2.0*nrgx/.511+1.0)  !Compton edge

                nrgint=1
                do 31 while (nrgx .gt. nrg(nrgint))
31                nrgint=nrgint+1

                frac1=(nrgx-nrg(nrgint-1))/
              1       (nrg(nrgint)-nrg(nrgint-1))
                r=ran(i1)
                ir=jifix(r*50.0)+1
                frac2=50.0*r-floatj(ir-1)

                if (ir .eq. 1) then

                  tnrg=(compton(nrgint-1,1)
              1         +(compton(nrgint,1)-compton(nrgint-1,1))*frac1)
              2         *frac2*nrgmax
                else

                  tnrg1=compton(nrgint-1,ir-1)
              1         +(compton(nrgint-1,ir)-compton(nrgint-1,ir-1))
              2         *frac2
                  tnrg2=compton(nrgint,ir-1)
              1         +(compton(nrgint,ir)-compton(nrgint,ir-1))
              2         *frac2
                  tnrg=(tnrg1+(tnrg2-tnrg1)*frac1)*nrgmax

                end if

c Test to see if the electron is greater than
c the charged particle cut off energy. If so,
c then calculate and store the scattering
c angles and store the kinetic energy and position.

                r=6.2832*ran(i1)              !azimuth angle in particle coords

                if (tnrg .gt. 0.1*ro) then

                  charge=charge+1

                  kinrg(charge)=tnrg

                  arg=(nrgmax-tnrg)*(2.0*nrgx/.511+1.0)/tnrg
                  g=atan(sqrt(arg)/(1.0+nrgx/.511))              !zenith angle

c Remember the incident photon's angles in the phantom system.

                  oldcal=cal
                  oldsal=sal
                  oldcbeta=cbeta
                  oldsbeta=sbeta

c Transform from the particle to the phantom coordinate system.

                  call geom(r,g,cal,sal,cbeta,sbeta)
```

```
c The energy, trigonometric information on the
c angle in the phantom coordinate system, the
c position of the electron and the type of particle
c is stored.

                  kinorder(charge)=order
                  kincal(charge)=cal
                  kinsal(charge)=sal
                  kincbeta(charge)=cbeta
                  kinsbeta(charge)=sbeta
                  kinx(charge)=xs
                  kiny(charge)=ys
                  kinz(charge)=zs

c Recall initial photon's angles.

                  cal=oldcal
                  sal=oldsal
                  cbeta=oldcbeta
                  sbeta=oldsbeta

c If the electron is less than the charged particle
c cut off energy, deposit the energy as dose.

                else
                  ro=float(phantom(i,j,k)+1000)/1000.0
                  dose(order,i,j,k)=dose(order,i,j,k)+tnrg/ro
                end if

c The scattered photon is now dealt with.

                order=order+1       !the order of scattering is incresed

c The energy and scattering angles of the scattered
c photon are determined.

                r=r-3.1416          !scattered photon has opposite azimuth angle

                arg2=1-tnrg*0.511/nrgx/(nrgx-tnrg)
                if (arg2 .le. -1.0) then
                  g=-3.1416
                else
                  g=acos(arg2)
                end if

                nrgx=nrgx-tnrg          !determine scattered photon energy

c Transform from the particle to the phantom coordinate system.

                call geom(r,g,cal,sal,cbeta,sbeta)

                go to 20        !scattered photon is followed

              else if (rr .lt. fraction2) then

c The pair production interaction has occured. First the
c energy and scattering angles of the electron are determined.

                  charge=charge+1
                  kintype(charge)=1    !signifies an electron
```

```
                nrgmax=nrgx-1.022    !available kinetic energy

                nrgint=1
                do 41 while (nrgx .gt. nrg(nrgint))
41                nrgint=nrgint+1
                frac1=(nrgx-nrg(nrgint-1))/
     1                (nrg(nrgint)-nrg(nrgint-1))
                r=ran(i1)
                ir=jifix(r*50.0)+1
                frac2=50.0*r-float(ir-1)
                if (ir .eq. 1) then
                tnrg=(pairprod(nrgint-1,1)
     1               +(pairprod(nrgint,1)-pairprod(nrgint-1,1))
     2               *frac1)*frac2*nrgmax
                else
                tnrg1=pairprod(nrgint-1,ir-1)
     1               +(pairprod(nrgint-1,ir)
     2               -pairprod(nrgint-1,ir-1))*frac2
                tnrg2=pairprod(nrgint,ir-1)
     1               +(pairprod(nrgint,ir)
     2               -pairprod(nrgint,ir-1))*frac2
                tnrg=(tnrg1+(tnrg2-tnrg1)*frac1)*nrgmax
                end if
                kinrg(charge)=tnrg

                r=6.2832*ran(i1)

c This part of the program is done for both the electron
c and positron.  'V' is the ratio of total charged particle
c energy to the energy of the photon.

43              v=(tnrg+0.511)/nrgx
                vint=jifix(v*10.0)+1
                g=que(vint)*alog(nrgx/.511)*.511/nrgx

c Remember the photon's angles in the phantom system

                oldcal=cal
                oldsal=sal
                oldcbeta=cbeta
                oldsbeta=sbeta

c Transform from the particle to the phantom coordinate system.

                call geom(r,g,cal,sal,cbeta,sbeta)

c Store the order of scattering, initial charged particle phantom
c angles and position.

                kinorder(charge)=order
                kincal(charge)=cal
                kinsal(charge)=sal
                kincbeta(charge)=cbeta
                kinsbeta(charge)=sbeta
                kinx(charge)=xs
                kiny(charge)=ys
                kinz(charge)=zs

c Recall the photon's angles.

                cal=oldcal
```

```
                    sal=oldsal
                    cbeta=oldcbeta
                    sbeta=oldsbeta

c The energy and scattering angles of the positron
c is determined after those of the electron.

                    if (kintype(charge) .eq. 1) then

                      charge=charge+1
                      kintype(charge)=-1          !signifies a positron
                      tnrg=nrgmax-tnrg
                      kinrg(charge)=tnrg

                      r=r-3.1416          !azimuth angle opposite of electron

                      go to 43            !sent to repeat calculation for positron

                    end if

                  else

c A photoelectric interaction has occurred. All of
c the photon energy is deposited as dose.

                    ro=float(phantom(i,j,k)+1000)/1000.0
                    dose(order,i,j,k)=dose(order,i,j,k)+nrgx/ro

                end if

              else

c An interaction has not occured in the element.
c The photon is transported to the far element
c wall.

                xs=xs+short*sal*cbeta
                ys=ys+short*sal*sbeta
                zs=zs+short*cal

c A test to see if the photon has left the phantom.

                if (xs .le. 0.0001 .or. xs .ge. 20.0*diml) go to 50
                if (ys .le. 0.0001 .or. ys .ge. 20.0*diml) go to 50
                if (zs .le. 0.0001 .and. cal .lt. 0.0) go to 50
                if (zs .ge. 20.0*dimlz) go to 50

                go to 21

              end if

c The photon part of the history is completed at line 50.

50        continue

c The second annhilation photon is set in motion.

          if (annhilflag .eq. 1) then

            annhilflag=0
```

```
            cal=cos(6.2832*r1-3.1416)      !this photon is
            sal=sqrt(1.0-cal*cal)          !in the opposite
            cbeta=cos(6.2832*r2-3.1416)    !direction of the first
            sbeta=sin(6.2832*r2-3.1416)    !annhilation photon.

            xs=photox
            ys=photoy
            zs=photoz

            nrgx=0.511    !photon energy assumed to be 0.511 MeV

            order=4       !treated as a multiple scatter photon

            go to 21

          end if

c The charged particles are transported. First the stored parameters
c are recalled.

          do 120 while (charge .ge. 1)

            e=kinrg(charge)                !kinetic energy

            cal=kincal(charge)             !particle's phantom angles
            sal=kinsal(charge)
            cbeta=kincbeta(charge)
            sbeta=kinsbeta(charge)

            xs=kinx(charge)                !particle's position
            ys=kiny(charge)
            zs=kinz(charge)

            order=kinorder(charge)         !order of scattering

            nrgint=24

            if (order .eq. 1)then
             chargpart=chargpart+1         !number of charged particles
            end if

c The location and distance to the element wall in the particles direction
c is determined.

            call where

            ro=floatj(phantom(i,j,k)+1000)/1000.0

c Do only while the particle's energy is above the cut-off. The cut-off
c depends on the density of the phantom element.

33          do 110 while (e .gt. 0.1*ro)

              call where

c The following statements find the distance to the voxel wall
c in the coordinate directions. The integer voxel locators are also found.

              nearx=abs(xs-floatj(i)*dim1)
              nearinti=i+1
              if (nearx .gt. 0.5*dim1) then
```

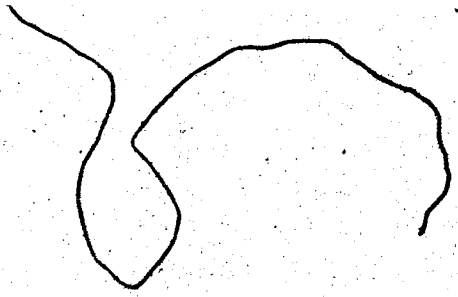

```
            nearx=diml-nearx
            nearinti=i-1
          end if

          neary=abs(ys-floatj(j)*diml)
          nearintj=j+1
          if (neary .gt. 0.5*diml) then
            neary=diml-neary
            nearintj=j-1
          end if

          nearz=abs(zs-floatj(k)*dimlz)
          nearintk=k+1
          if (nearz .gt. 0.5*dimlz) then
            nearz=dimlz-nearz
            nearintk=k-1
          end if

c The nearest voxel is found. The shortest distance to a voxel wall
c in the coordinate directions, 'near', is found.

          near=diml

          if (nearx .lt. near) then
            near=nearx
            neari=nearinti
            nearj=j
            neark=k
          end if

          if (neary .lt. near) then
            near=neary
            neari=i
            nearj=nearintj
            neark=k
          end if

          if (nearz .lt. near) then
            near=nearz
            neari=i
            nearj=j
            neark=nearintk
          end if

c The stopping power, 's' is found using log-linear interpolation.

          do 55 while (e .lt. nrg(nrgint))
55          nrgint=nrgint-1
          fraci=(e-nrg(nrgint))/(nrg(nrgint+1)-nrg(nrgint))
          s=stop(nrgint)+(stop(nrgint+1)-stop(nrgint))*fraci
          s=exp(s)

          ro=floatj(phantom(i,j,k)+1000)/1000.0

          maxpl=e/s/ro                    !maximum path length

          if (maxpl .lt. near) go to 112   !electron can not leave the voxel

c The scattering power, 'th' is found.

          th=tha(nrgint)+(tha(nrgint+1)-tha(nrgint))*fraci
```

```
            th=exp(th)

c 'Ep' is the amount of energy lost in the step.  'Pl' is the pathlength
c of the step.

            ep=(1-cay)*e
            pl=ep/s/ro

c If 'pl' is greater than short, then the pathlength must be shortened
c to 'short' so that the particle does not leave the voxel.  If so, the
c new energy lost, 'ep', must be calculated.

            if (pl .gt. short .and. short .gt. 0.0) pl=short
            ep=pl*s*ro

            x=pl*sal*cbeta       !distance travelled during the step
            y=pl*sal*sbeta
            z=pl*cal

            xs=xs+x              !position of the particle at the end of step
            ys=ys+y
            zs=zs+z

            oldi=i       !the voxel location before the step is stored
            oldj=j
            oldk=k

            i=jifix(xs/diml)+1   !voxel location after the step
            j=jifix(ys/diml)+1
            k=jifix(zs/dimlz)+1

            e=e-ep                                          !energy after step

            g=sqrt(th*pl*ro)*gaus(jifix(100.0*ran(ii))+1)   !zenith angle

            r=6.2832*ran(ii)                                !azimuth angle

c Transform from the particle to the phantom coordinate system.

            call geom(r,g,cal,sal,cbeta,sbeta)

c The following statement checks for the edge of the phantom.

            if (xs .le. 0.0001 .or. xs .ge. 20.0*diml) go to 115
            if (ys .le. 0.0001 .or. ys .ge. 20.0*diml) go to 115
            if (zs .le. 0.0001 .and. cal .lt. 0.0) go to 115
            if (zs .ge. 20.0*dimlz) go to 115

c By finding the smallest of the old or new voxel location the correct
c voxel to assign the dose is guaranteed, even if the particle is on
c a voxel wall.

            smalli=jmin0(oldi,i)
            smallj=jmin0(oldj,j)
            smallk=jmin0(oldk,k)

c Assign the energy lost during the step as dose.

            ro=float(phantom(smalli,smallj,smallk)+1000)/1000.0
            dose(order,smalli,smallj,smallk)=
     1              dose(order,smalli,smallj,smallk)+ep/ro
```

```
110         continue              !charged particle transport step ends here

c The following checks to see if the nearest voxel is outside the phantom.
c If it is half of the remaining energy will be deposited as dose.

            if (neari .le. 0 .or. neari .ge. 21) then
              e=e/2.0
              go to 112
            end if

            if (nearj .le. 0 .or. nearj .ge. 21) then
              e=e/2.0
              go to 112
            end if

            if (neark .le. 0 .or. neark .ge. 21) then
              e=e/2.0
              go to 112
            end if

c 'Nearo' is the density of the nearest voxel. The remaining energy is
c assigned to the last and nearest voxel such that they both get equal
c energies.

            nearo=floatj(phantom(neari,nearj,neark)+1000)/1000.0
            dose(order,i,j,k)=dose(order,i,j,k)+e/(ro+nearo)
            dose(order,neari,nearj,neark)=
           1     dose(order,neari,nearj,neark)+e/(ro+nearo)
            go to 113

c Statement 112 and its following statement are only done if it is found
c that the particle can not leave the phantom or if the neighboring voxel
c is outside the voxel.

112         ro=floatj(phantom(i,j,k)+1000)/1000.0
            dose(order,i,j,k)=dose(order,i,j,k)+e/ro

113       continue

c The following statements are done if the charged particle was a positron.

          if (kintype(charge) .eq. -1) then

            kintype(charge)=0
            charge=charge-1
            annhilflag=1                !sets flag for the second photon

            r1=ran(i1)
            cal=cos(6.2832*r1)
            sal=sqrt(1.0-cal*cal)
            r2=ran(i1)
            cbeta=cos(6.2832*r2)
            sbeta=sin(6.2832*r2)

            nrgx=0.511

            photox=xs                   !the last position of the
            photoy=ys                   !positron must
            photoz=zs                   !be stored
```

```
            order=4                          !include annhilation photons as
                                             !multiple scatter

            go to 21

            end if

115         continue

            charge=charge-1

120         continue                 !end of loop for the charged particle histories

180       continue                   !end of loop for the photon histories

200     continue                     !end of loop for the spectral bins

c The following statements normalize the dose to the maximum
c dose encountered and writes the normalized dose.

        total=0.0
        do 205 k=1,20
          do 205 j=1,20
            do 205 i=1,20
205           total=total+dose(1,i,j,k)          !total primary KERMA

c Print the beam parameters.

        write(4,*) 'Spectrum Multiplier=',multi
        write(4,*) '# Photon Histories=',history
        write(4,*) 'Shiftx=',shiftx
        write(4,*) 'Shifty=',shifty
        write(4,*) 'Primary Interaction Depth Integer=',intest
        write(4,*) 'X-Y Element Size=',dim1
        write(4,*) 'Depth Dimension=',dim1z
        write(4,*) 'Total Primary Dose=',total
        write(4,*) 'Number Of Primary Charged Particles',chargpart

        do 210 k=1,25
          do 210 j=1,25
            do 210 i=1,25
              do 210 q=1,5
                doset(i,j,k)=doset(i,j,k)+dose(q,i,j,k)   !total dose
                                                          !distribution

210     continue

c Two-dimensional primary dose distribution in the plane of the
c primary pencil beam. The dose is normalized to the total primary KERMA.

        write(4,*) 'Coronal Primary Dose Slice'
        do 215 k=1,20
          do 212 i=1,20
212         arr(i)=dose(1,i,11,k)/total
215       write (4,650) (arr(i),i=5,17)

c Three-dimensional total dose distribution normalized to the primary KERMA.

        do 229 k=1,20
          write(4,*)' '
          write(4,580) k
```

```
          do 225 j=1,20
            do 224 i=1,20
224           arr(i)=doset(i,j,k)/total
225         write(4,650) (arr(i),i=5,17)

c Three-dimensional distributions of the primary KERMA
c normalized dose components.

          do 229 q=1,4
            write(4,*) ' '
            if (q .eq. 1)then
              write(4,*) 'Primary Dose'
            else if (q .eq. 2) then
              write(4,*) 'First Scatter Dose'
            else if (q .eq. 3) then
              write(4,*) 'Second Scatter Dose'
            else if (q .eq. 4) then
              write(4,*) 'Multiple Scatter Dose'
            end if
            do 228 j=1,20
              do 227 i=1,20
227             arr(i)=dose(q,i,j,k)/total
228       write(4,650) (arr(i),i=5,17)
229       continue

c Three-dimensional distribution of the primary KERMA
c normalized total scatter dose.

          write(4,*) 'Total Scatter Dose'
          do 245 k=1,20
            write (4,*)' '
            write(4,580) k
            do 245 j=1,20
              do 244 i=1,20
244             arr(i)=(doset(i,j,k)-dose(1,i,j,k))/total
245           write(4,650) (arr(i),i=5,17)

c Three-dimensional distribution of the primary KERMA
c normalized primary plus first scatter dose.

          write(4,*) 'Primary + First'
          do 247 k=1,20
            write (4,*)' '
            write(4,580) k
            do 247 j=1,20
              do 246 i=1,20
246             arr(i)=(dose(1,i,j,k)+dose(2,i,j,k))/total
247           write(4,650) (arr(i),i=5,17)

250       format(' ',i3,2x,f6.2)
340       format(' ',f5.2,2x,f5.2)
345       format(' ',i2)
350       format(' ',10(f4.2,2x))
420       format(' ',e10.4)
422       format(e10.4)
550       format(' ',10(1x,f6.4))
570       format(' ',f5.2,1x,3(f6.4,1x),2(f6.3,1x))
580       format('*******************************k=',i2,'*****************')
650       format(' ',20(1x,e8.3))
655       format(' ',1x,a1,3x,a4,4x,a14,2x,a7,4x,a5,3x,a6,2x,a8)
750       format(' ',i2,2x,f5.3,8x,f4.3,6x,4(4x,f5.3))
```

```
      close(1)
      close(4)
      close(6)
      close(8)
      close(11)
      close(12)

      stop
      end


          subroutine geom(r,g,cal,sal,cbeta,sbeta)

c This subroutine performs the rotational transformations between
c the coordinate system 'attached' to the particle and the system
c 'attached' to the phantom.

          real r,g,cal,sal,cbeta,sbeta
          real ss,cc,oldcal,oldsal,oldcbeta,oldsbeta

c 'C' and 'r' are the sine and cosine respectively in the particle system.
c 'Sal' and 'cal' are the sine and cosine respectively of the zenith
c angle in the phantom system.  'Sbeta' and cbeta are the sine and
c cosine respectively of the azimuth angle in the phantom system.

          if (g .eq. 0.0) go to 400

          oldsal=sal
          oldcal=cal
          oldcbeta=cbeta
          oldsbeta=sbeta

          cal=cal*cos(g)-sal*sin(g)*cos(r)

          if (abs(cal) .ge. 1.0) then
            cal=1.0*sign(1.0,cal)
            sal=0.0
            cbeta=cos(r)
            sbeta=sin(r)
            go to 400
          end if

          sal=sqrt(1.0-cal*cal)

          if (oldsal .eq. 0.0) then
            cbeta=cos(r)
            sbeta=sin(r)
            go to 400
          end if

          ss=sin(g)*sin(r)/sal
          cc=(sin(g)*cos(r)*oldcal+cos(g)*oldsal)/sal

          if (abs(ss) .ge. 1.0) then
           ss=1.0*sign(1.0,ss)
          end if

          if (abs(cc) .ge. 1.0) then
           cc=1.0*sign(1.0,cc)
          end if
```

```
            cbeta=cc*oldcbeta-ss*oldsbeta
            sbeta=ss*oldcbeta+cc*oldsbeta

            if (abs(cbeta) .ge. 1.0) cbeta=1.0*sign(1.0,cbeta)
            if (abs(sbeta) .ge. 1.0) sbeta=1.0*sign(1.0,sbeta)

400         continue

            return
            end


        subroutine where

c This subroutine finds the position and distance to the voxel boundary
c in the particle direction.

            real xs,ys,zs,short,diml,dimlz
            real cbeta,sbeta,cal
            real lx,ly,lz
            integer i,j,k,ib,jb,kb
            common xs,ys,zs,i,j,k,cbeta,sbeta,cal,sal,diml,dimlz,short

c Determine which element the photon is in.

            i=jifix(xs/diml)+1
            j=jifix(ys/diml)+1
            k=jifix(zs/dimlz)+1

c Determine the position of the voxel's walls in the
c direction in which the pazrticle is headed.

            if (sal .eq. 0.0 .or. cbeta .eq. 0.0) then
              lx=999.9*diml
              go to 10
            end if

            if (cbeta .lt. 0.0) then
              if (xs .eq. (floatj(i-1))*diml) then
                lx=(floatj(i-2)*diml-xs)/sal/cbeta
              else
                lx=(floatj(i-1)*diml-xs)/sal/cbeta
              end if
            else
              lx=(floatj(i)*diml-xs)/sal/cbeta
            end if

10          if (sal .eq. 0.0 .or. sbeta .eq. 0.0) then
              ly=999.9*diml
              go to 20
            end if

            if (sbeta .lt. 0.0) then
              if (ys .eq. (floatj(j-1))*diml) then
                ly=(floatj(j-2)*diml-ys)/sal/sbeta
              else
                ly=(floatj(j-1)*diml-ys)/sal/sbeta
              end if
            else
              ly=(floatj(j)*diml-ys)/sal/sbeta
```

```
            end if

20          if (cal .eq. 0.0) then
              lz=999.9*dimlz
              go to 30
            end if

            if (cal .lt. 0.0) then
              if (zs .eq. (floatj(k-1))*dimlz) then
                lz=(floatj(k-2)*dimlz-zs)/cal
              else
                lz=(floatj(k-1)*dimlz-zs)/cal
              end if
            else
              lz=(floatj(k)*dimlz-zs)/cal
            end if

c Determine the distance to the wall that the particle
c in the direction of the particle.

30          short=lz
            if (ly .lt. short) short=ly
            if (lx .lt. short) short=lx

          return
          end
```

Appendix 11. Listing of the program Volve.for

```
      Program Volve

c This program convolves the fluence with dose spread arrays to
c yield a dose distribution. It is carried out in "the interaction
c point of view". The primary and truncated first scatter (TFS)
c dose spread arrays are combined. This fine resolution dose spread
c array is is convolved first. Then a lower resolution, residual
c first and multiple scatter dose spread array is convolved. The
c homogeneous and heterogeneous dose distribution is calculated
c separately and a correction factor is determined at the end. The
c dose due to contamination is included. The dose distribution
c can be smoothed. The variables are documented where they occur.
c Lines which have been "commented out" are optional.

      integer albnd,aubnd,blbnd,bubnd,depth,lbndi,ubndi
      integer albnd2,aubnd2,blbnd2,bubnd2,depth2
      integer lbndi2,ubndi2
      integer lbndj,ubndj,lbndk,ubndk
      integer lbndj2,ubndj2,lbndk2,ubndk2
      integer width1,height1,length1
      integer i,j,k,ii,jj,kk,deli,delj,delk
      integer clipwid,cliphei,cliplen,roe,roe2,kprime

      real mu,ro(-25:25,-25:25,50),ro2(-5:5,-5:5,10)
      real invsqr,ssd,dref
      real spray1(5,-6:6,-6:6,-2:12)
      real rfmspray(5,-6:6,-6:6,-2:12)
      real fluxinc,fluxfact
      real avdens,avdens2,avspray
      real dosehet(-25:25,-25:25,50),dosehet2(-5:5,-5:5,0:10)
      real dosehom(-25:25,-25:25,50),dosehom2(-5:5,-5:5,0:10)
      real kerma(50),kerma2(10)
      real oldkerma,cf(-25:25,-25:25,50),kermhet,kermhom
      real arrcf(20),arrhom(20),arrhet(20)
      real f0,f1,f2,c1,c2,row
      real hom(-25:25,-25:25,50),het(-25:25,-25:25,50)
      real contam(0:50,2),avcontam(2),resolv

      common deli,delj,delk,i,j,k,ro,avdens

c Spray.dat contains the primary plus truncated first scatter (TFS)
c dose spread arrays.

c Cf.dat contains the output homogeneous and  heterogeneous dose
c distributions and the correction factor distribution.

c Rfmspray.dat contains the residual first and multiple scatter (RFMS)
c dose spread arrays.

      open(unit=1,status='old',file='spray.dat')
      open(unit=3,status='new',file='cf.dat')
      open(unit=4,status='old',file='rfmspray.dat')

c User requested statements. A slab geometry is modelled by a cubic
c water-like phantom. The beam is parallel.

      ssd=100.0        !source to surface distance
      dref=3.5         !dmax
      resolv=1.0       !specifies voxel size for contamination calculation
```

```
      albnd=-4          !beam half-width in negative x-direction
      aubnd=4           !beam half-width in positve x-direction
      blbnd=-4          !beam half-width in negative y-direction
      bubnd=4           !beam half-width in positive y-direction
      depth=20          !phantom depth

c The calculation windows may be 1,2 or 3-dimensional.

c 3-Dimensional

c       lbndi=albnd     !calculation window in negative x-direction
c       ubndi=aubnd     !calculation window in positive x-direction
c       lbndj=blbnd     !calculation window in negative y-direction
c       ubndj=bubnd     !calculation window in positive y-direction
c       lbndk=1         !lower calculation window in z-direction
c       ubndk=depth     !upper calculation window in z-direction

c 2-Dimensional (in the plane of the central axis)

      lbndi=albnd-1     !calculation window in negative x-direction
      ubndi=aubnd+1     !calculation window in positive x-direction
      lbndj=0           !calculation window in negative y-direction
      ubndj=0           !calculation window in positive y-direction
      lbndk=1           !lower calculation window in z-direction
      ubndk=depth       !upper calculation window in z-direction

c 1-Dimensional (off axis at a specified depth)

c       lbndi=albnd-1   !calculation window in negative x-direction
c       ubndi=aubnd+1   !calculation window in positive x-direction
c       lbndj=0         !calculation window in negative y-direction
c       ubndj=0         !calculation window in positive y-direction
c       lbndk=16        !lower calculation window in z-direction
c       ubndk=16        !upper calculation window in z-direction

c 1-Dimensional (along the central axis)

c       lbndi=0         !calculation window in negative x-direction
c       ubndi=0         !calculation window in positive x-direction
c       lbndj=0         !calculation window in negative y-direction
c       ubndj=0         !calculation window in positive y-direction
c       lbndk=1         !lower calculation window in z-direction
c       ubndk=depth     !upper calculation window in z-direction

c       clipwid=2       !a parameter for delimiting width of dose spread array
c       cliphei=0       !delimits height (delk=negative)
c       cliplen=0       !delimits length (delk=positive)

c Read statements. Read height, length, width, and values of the
c dose spread arrays, and the density array.

      read(1,3000) height1,length1,width1
       do 100 n=1,5
        read(1,*)
        read(4,*)
        do 100 k=-height1,length1
         read(1,*)
         read(1,*)
         read(4,*)
         read(4,*)
         do 100 j=-width1,width1
```

```
            read(1,3010) (spray1(n,i,j,k),i=-width1,width1)
            read(4,3010) (rfmspray(n,i,j,k),i=-width1,width1)
100       continue

          read (4,*)
          read (4,*)
          do 125 n=1,5
           read (4,*)
           read (4,*)
           do 125 k=-1,3
            read (4,*)
            do 125 j=-1,1
             read (4,3010) (rfmspray(n,i,j,k),i=-1,1)
125       continue

c The relative fluence in a homogeneous
c phantom as a function of depth is calculated.

          kerma(1)=1.00
          mu=0.031
          atten=exp(-mu)
          do 150 k=2,depth+1
           kerma(k)=kerma(k-1)*atten
150       continue

c "Contam(depth,region)" is the measured depth dependence of contamination.
c The depth is measured in centimeters. Region=1 is inside the field.
c Region=2 is outside the field. See Volume 1 and Equation 7.4.9 in
c Volume 2.

          contam(0,1)=1.00
          contam(1,1)=0.89
          contam(2,1)=0.50
          contam(3,1)=0.28
          contam(4,1)=0.18
          contam(5,1)=0.12
          contam(6,1)=0.10

          contam(0,2)=1.00
          contam(1,2)=0.94
          contam(2,2)=0.64
          contam(3,2)=0.44
          contam(4,2)=0.37
          contam(5,2)=0.33
          contam(6,2)=0.30

c Beyond dmax the contamination decreases exponentially.

          atten=exp(-0.050)
          do 175 n=1,2
           do 175 k=7,50
            contam(k,n)=contam(k-1,n)*atten
175       continue

c The following statements describe a slab phantom. The central slab can be
c made up of two regions.

          do 200 k=1,15
           do 200 j=-25,25
            do 200 i=-25,25
             ro(i,j,k)=1.0
```

```
200     continue

        do 220 k=16,23
         do 220 j=-25,25
          do 220 i=-25,3
           ro(i,j,k)=0.3
220     continue

        do 230 k=16,23
         do 230 j=-25,25
          do 230 i=4,25
           ro(i,j,k)=0.3
230     continue

        do 240 k=24,50
         do 240 j=-25,25
          do 240 i=-25,25
           ro(i,j,k)=1.0
240     continue

c Convolve for all pencil beams at all depths by summing over all primary
c interaction voxels. "Fluxfact" is the ratio of heterogeneous to homo-
c geneous fluence at a point in a pencil beam.

        do 600 i=albnd-1,aubnd+1          !increment in the x-direction
         ii=jnint(floatj(i)/5.0)          !for RFMS in the x-direction

         do 600 j=blbnd-1,bubnd+1         !increment in the y-direction
          jj=jnint(floatj(j)/5.0)         !for RFMS in the y-direction

c The pencil beams just outside the field can be given a smaller fluence.
c This can account for a geometrical penumbra. 'Fluxinc is the incident
c relative fluence.

c         if (i .eq. albnd-1 .or. i .eq. aubnd+1 .or.
c      1      j .eq. blbnd-1 .or. j .eq. bubnd+1 ) then
c          fluxinc=0.20
c         else
c          fluxinc=1.00
c         end if

c The following can describes a bar shield.

c         if (i .eq. -1 .or. i .eq. 0 .or. i .eq. 1) then
c          fluxinc=0.031
c         end if

          fluxfact=1.00                   !fluxfact is the fluence compared to a
                                          !homogeneous phantom

          do 600 k=1,depth                !increment depth (z-direction)
           kk=(k-1)/5+1                   !for RFMS in the z-direction

c An inverse square factor can reduce the primary fluence.

c          invsqr=(ssd+dref)**2/
c     1           ((ssd+floatj(k)-.5)**2+
c     2           (floatj(j))**2+(floatj(i))**2)

           invsqr=1.0
```

```
c "Kermhom" and "kermhet" are factors dependent only on the point
c of interaction of the primary fluence.

            kermhom=kerma(k)*invsqr*fluxinc
            kermhet=kermhom*ro(i,j,k)*fluxfact

c Sum over all contributions of the fine resolution dose spread array
c by summing over all dose deposition voxels.

           do 500 deli=-width1+clipwid,width1-clipwid
            do 500 delj=-width1+clipwid,width1-clipwid
             do 500 delk=-height1+cliphei,length1-cliplen

c If the contribution is outside the dose calculation window
c don't bother summing.

              if (i+deli .lt. lbndi) go to 500
              if (i+deli .gt. ubndi) go to 500
              if (j+delj .lt. lbndj) go to 500
              if (j+delj .gt. ubndj) go to 500
              if (k+delk .lt. lbndk) go to 500
              if (k+delk .gt. ubndk) go to 500

c Subroutine "averdens" returns "avdens", the average density
c between the primary interaction and dose deposition voxels.
c "Roe" is an integer identifying a dose spread array obtained for
c a specific density (roe=1 for a physical density of 0.2 g/cm**3,
c roe=2 for 0.4 g/cm**3 ... roe=5 for 1.0 g/cm**3)

              call averdens

c "Avspray" is the dose/KERMA value linearly interpolated between dose
c spread arrays at fixed densities.

              avspray=spray1(roe,deli,delj,delk)+
     1                (spray1(roe+1,deli,delj,delk)-
     2                spray1(roe,deli,delj,delk))*
     3                (5.0*avdens-floatj(roe))

c Second order interpolation can be used if desired.

c             if (avdens .eq. 1.0) then
c              avspray=spray1(5,deli,delj,delk)
c             else
c              if (avdens .ge. 0.6) then
c               f0=spray1(roe-1,deli,delj,delk)
c               f1=spray1(roe,deli,delj,delk)
c               f2=spray1(roe+1,deli,delj,delk)
c               row=(avdens*5.0-floatj(roe))/5.0+0.2
c              else
c               f0=spray1(roe,deli,delj,delk)
c               f1=spray1(roe+1,deli,delj,delk)
c               f2=spray1(roe+2,deli,delj,delk)
c               row=(avdens*5.0-floatj(roe))/5.0
c              end if

c              c1=(row/0.2)*(-3.0*f0+4.0*f1-f2)/2.0
c              c2=(row/0.2)**2*(f0-2.0*f1+f2)/2.0

c              avspray=f0+c1+c2
```

```
c              end if

c "Dosehet" is the heterogeneous dose.

               dosehet(i+deli, j+delj, k+delk)=
     1               dosehet(i+deli, j+delj, k+delk)+
     2               kermhet/avdens*avspray

c "Dosehom" is the homogeneous dose.

               dosehom(i+deli, j+delj, k+delk)=
     1               dosehom(i+deli, j+delj, k+delk)+
     2               kermhom*spray1(5, deli, delj, delk)

500            continue

          fluxfact=fluxfact*exp(mu*(1.0-ro(i, j, k))) !cumulative relative fluence

          avdens2=avdens2+ro(i, j, k)                  !density sum for RFMS

         ro2(ii, jj, kk)=ro2(ii, jj, kk)+ro(i, j, k)   !for RFMS average voxel density

600      continue

c At this point the primary plus truncated first scatter dose spread arrays
c have been convolved. The residual first and multiple scatter (RFMS) dose
c spread array is now convolved.

         albnd2=jnint(float(albnd-1)/5.0)          !field boundaries
         aubnd2=jnint(float(aubnd+1)/5.0)
         blbnd2=jnint(float(blbnd-1)/5.0)
         bubnd2=jnint(float(bubnd+1)/5.0)
         depth2=(depth-1)/5.0+1

         lbndi2=jnint(float(lbndi)/5.0)-1          !dose calculation window
         ubndi2=jnint(float(ubndi)/5.0)+1
         lbndj2=jnint(float(lbndj)/5.0)-1
         ubndj2=jnint(float(ubndj)/5.0)+1
         lbndk2=0
         ubndk2=(ubndk-1)/5+2

c Calculation of fluence in a homogeneous phantom taking into account
c the coarser resolution.

         kerma2(1)=1.00
         do 700 k=2, depth2+1
          atten=exp(-mu*5.0)
          kerma2(k)=kerma2(k-1)*atten
700      continue

c Calculate the average density in the irradiated portion of the phantom.

         avdens2=avdens2/
         1     ((aubnd-albnd+3)*(bubnd-blbnd+3)*depth)

         roe=jifix(avdens2*5.0)

         roe2=(5.0*avdens2-float(roe))

         do 1200 i=albnd2, aubnd2          !increment in x-direction
```

```
      do 1200 j=blbnd2,bubnd2          !increment in y-direction

       fluxinc=1.00

c Calculate the fluence near the field boundary if the geometrical
c penumbra is being taken into account.

c       if (i .eq. aubnd2) then
c        fluxinc=(float(jiabs(aubnd)+3)
c     1          /5.0-float(jiabs(i)))*fluxinc
c       else if (i .eq. albnd2) then
c        fluxinc=(float(jiabs(albnd)+3)
c     1          /5.0-float(jiabs(i)))*fluxinc
c       end if
c
c       if (j .eq. bubnd2) then
c        fluxinc=(float(jiabs(bubnd)+3)
c     1          /5.0-float(jiabs(j)))*fluxinc
c       else if (j .eq. blbnd2) then
c        fluxinc=(float(jiabs(blbnd)+3)
c     1          /5.0-float(jiabs(j)))*fluxinc
c       end if

c The following is used with the bar shield.

c       if (i .eq. 0) then
c        fluxinc=0.40
c       end if


c The following is used with a wedge.

c       fluxinc=fluxinc*0.5*float(i-albnd2)/
c     1       float(aubnd2-albnd2)+0.5*fluxinc

      do 1200 k=1,depth2     !increment depth (z-direction) along
                              pencil beam

c Used with the inclusion of inverse square attenuation.

c       invsqr=(ssd+dref)**2/
c     1         ((ssd+5.0*float(k)-2.5)**2+
c     2         (5.0*float(j))**2+(5.0*float(i))**2)

       invsqr=1.00

       ro2(i,j,k)=ro2(i,j,k)/125.0          !finish average voxel density

       kermhom=kerma2(k)*invsqr*fluxinc     !homogeneous fluence

       kermhet=kermhom*ro2(i,j,k)       !heterogeneous fluence*voxel density

c Sum over all contributions of the RFMS dose spread array by summing
c over all dose deposition voxels.

       do 1100 deli=-width1,width1
        do 1100 delj=-width1,width1
         do 1100 delk=-height1,length1

          if (i+deli .lt. lbnd2) go to 1100        !inside dose window?
          if (i+deli .gt. ubnd2) go to 1100
```

```
                if (j+delj .lt. lbndj2) go to 1100
                if (j+delj .gt. ubndj2) go to 1100
                if (k+delk .lt. lbndk2) go to 1100
                if (k+delk .gt. ubndk2) go to 1100

c Interpolate the heterogeneous dose spread array.

                avspray=rfmspray(roe,deli,delj,delk)+
           1             (rfmspray(roe+1,deli,delj,delk)-
           2              rfmspray(roe,deli,delj,delk))*roe2

                dosehet2(i+deli,j+delj,k+delk)=          !increment hetero dose
           1      dosehet2(i+deli,j+delj,k+delk)+
           2      kermhet/avdens2*avspray

                dosehom2(i+deli,j+delj,k+delk)=          !increment homo dose
           1      dosehom2(i+deli,j+delj,k+delk)+
           2      kermhom*rfmspray(5,deli,delj,delk)

1100         continue

1200    continue

c Print the primary plus TPS dose before smoothing.

        write(3,*)'Homogeneous Dose Before Smoothing (No Multiple)'
        do 1202 k=lbndk,ubndk
         write(3,*)'******** k=',k,'********'
         do 1201 j=lbndj,ubndj
          do 1201 i=lbndi,ubndi
           arrhom(i)=dosehom(i,j,k)
1201      continue
          write(3,3100)(arrhom(i),i=lbndi,ubndi)
1202    continue

        write(3,*)'Heterogeneous Dose Before Smoothing (No Multiple)'
        do 1204 k=lbndk,ubndk
         write(3,*)'******** k=',k,'********'
         do 1203 j=lbndj,ubndj
          do 1203 i=lbndi,ubndi
           arrhet(i)=dosehet(i,j,k)
1203      continue
          write(3,3100)(arrhet(i),i=lbndi,ubndi)
1204    continue

c "9-point" smoothing.

c       j=0
c       delj=0
c       do 1210 k=lbndk+1,ubndk-1
c         do 1210 i=lbndi+1,ubndi-1
c           do 1210 deli=i-1,i+1
c             do 1210 delk=k-1,k+1
c               het(i,j,k)=het(i,j,k)+dosehet(deli,delj,delk)
c               hom(i,j,k)=hom(i,j,k)+dosehom(deli,delj,delk)
1210    continue

c       do 1220 k=lbndk+1,ubndk-1
c         do 1220 i=lbndi+1,ubndi-1
c           dosehet(i,j,k)=het(i,j,k)/9.0
c           dosehom(i,j,k)=hom(i,j,k)/9.0
```

```
c            het(i,j,k)=0.0
c            hom(i,j,k)=0.0
1220     continue

c Print the primary plus TFS dose after smoothing.

c        write(3,*)'Homogeneous Dose After Smoothing (No Multiple)'
c        do 1250 k=lbndk,ubndk
c         write(3,*)'******** k=',k,'********'
c         do 1250 j=lbndj,ubndj
c          do 1225 i=lbndi,ubndi
c           arrhom(i)=dosehom(i,j,k)
1225       continue
c          write(3,3100)(arrhom(i),i=lbndi,ubndi)
1250     continue

c        write(3,*)'Heterogeneous Dose After Smoothing (No Multiple)'
c        do 1300 k=lbndk,ubndk
c         write(3,*)'******** k=',k,'********'
c         do 1300 j=lbndj,ubndj
c          do 1275 i=lbndi,ubndi
c           arrhet(i)=dosehet(i,j,k)
1275       continue
c          write(3,3100)(arrhet(i),i=lbndi,ubndi)
1300     continue

c Print the phantom and voxel densities used for the RFMS convolution.

c        write(3,*)'Average Phantom Density',avdens2

c        write(3,*)'Average Voxel Density'
c        do 1310 k=lbndk2+1,ubndk2-1
c         write(3,*)'******** k=',k,'********'
c         do 1310 j=lbndj2+1,ubndj2-1
c          do 1305 i=lbndi2+1,ubndi2-1
c           arrhom(i)=ro2(i,j,k)
1305       continue
c          write(3,3100)(arrhom(i),i=lbndi2+1,ubndi2-1)
1310     continue

c Print the RFMS dose distribution.

c        write(3,*)'Homogeneous Multiple Dose'
c        do 1350 k=lbndk2,ubndk2
c         write(3,*)'******** k=',k,'********'
c         do 1350 j=lbndj2,ubndj2
c          do 1325 i=lbndi2,ubndi2
c           arrhom(i)=dosehom2(i,j,k)
1325       continue
c          write(3,3100)(arrhom(i),i=lbndi2,ubndi2)
1350     continue

c        write(3,*)'Heterogeneous Multiple Dose'
c        do 1400 k=lbndk2,ubndk2
c         write(3,*)'******** k=',k,'********'
c         do 1400 j=lbndj2,ubndj2
c          do 1375 i=lbndi2,ubndi2
c           arrhet(i)=dosehet2(i,j,k)
1375       continue
c          write(3,3100)(arrhet(i),i=lbndi2,ubndi2)
1400     continue
```

```
c Add the RFMS dose distribution on to the primary plus RFS dose
c distribution. Calculate the radiological depth for inclusion
c of the contamination dose.

        j=0
        delj=0
        do 1500 k=lbndk,ubndk
          do 1500 i=lbndi,ubndi
           do 1500 deli=i-2,i+2
             do 1500 delk=k-2,k+2
              het(i,j,k)=het(i,j,k)
     1          +dosehet2(jnint(float(deli)/5.0)
     2          ,jnint(float(delj)/5.0)
     3          ,(delk-1)/5+1)

              hom(i,j,k)=hom(i,j,k)
     1          +dosehom2(jnint(float(deli)/5.0)
     2          ,jnint(float(delj)/5.0)
     3          ,(delk-1)/5+1)

1500    continue

        do 1575 i=lbndi,ubndi
          avdens=0.0
          do 1575 k=lbndk,ubndk

            dosehet(i,j,k)=het(i,j,k)/25.0+dosehet(i,j,k)
            dosehom(i,j,k)=hom(i,j,k)/25.0+dosehom(i,j,k)

            avdens=avdens+ro(i,j,k)                          !radiological depth

            do 1550 n=1,2

              avcontam(n)=contam(jifix(avdens),n)+           !calculate the
     1                    (contam(jifix(avdens)+1,n)-        !contamintion
     2                     contam(jifix(avdens),n))*         !at the radiological
     3                     (avdens-float(jifix(avdens)))     !depth

1550    continde

c Calculate the contamination dose. The contamination dose has a Gaussian
c dependence on position in the field from the central axis, a linear increase
c with field size and a depth dependence found from a look-up table.

            if (i .ge. albnd .or. i .le. aubnd) then

              dosehet(i,j,k)=dosehet(i,j,k)+
     1            avcontam(1)*sqrt(float((aubnd-albnd)*
     2            (bubnd-blbnd)))*0.01*resolv

              dosehom(i,j,k)=dosehom(i,j,k)+
     1            contam(k,1)*sqrt(float((aubnd-albnd)*
     2            (bubnd-blbnd)))*0.01

            else

              dosehet(i,j,k)=dosehet(i,j,k)+
     1            avcontam(2)*sqrt(float((aubnd-albnd)*
     2            (bubnd-blbnd)))*0.01*resolv*
     3            exp(-2.0*float((i*i)/(float((aubnd-albnd))**2)*
```

```
     4        exp(-2.0*float(j*j)/(float(bubnd-blbnd))**2)

          dosehom(i,j,k)=dosehom(i,j,k)+
     1        contam(k,2)*sqrt(float((aubnd-albnd)*
     2        (bubnd-blbnd)))*0.01*
     3        exp(-2.0*float(i*i)/(float(aubnd-albnd))**2)*
     4        exp(-2.0*float(j*j)/(float(bubnd-blbnd))**2)

          end if

1575    continue

c Calculate and print the correction factor.

        write(3,*)'Correction Factor'
        do 1800 k=lbndk,ubndk
         write(3,*)'******** k=',k,'********'
         do 1800 j=lbndj,ubndj
          do 1700 i=lbndi,ubndi
           cf(i,j,k)=dosehet(i,j,k)/dosehom(i,j,k)
           arrcf(i)=cf(i,j,k)
           arrhom(i)=dosehom(i,j,k)
           arrhet(i)=dosehet(i,j,k)
1700       continue
          write(3,3100)(arrcf(i),i=lbndi,ubndi)
1800    continue

        write(3,*)'Total Smoothed Homogeneous Dose'
        do 2000 k=lbndk,ubndk
         write(3,*)'******** k=',k,'********'
         do 2000 j=lbndj,ubndj
          do 1900 i=lbndi,ubndi
           arrhom(i)=dosehom(i,j,k)
1900       continue
          write(3,3100)(arrhom(i),i=lbndi,ubndi)
2000    continue

        write(3,*)'Total Smoothed Heterogeneous Dose'
        do 2200 k=lbndk,ubndk
         write(3,*)'******** k=',k,'********'
         do 2200 j=lbndj,ubndj
          do 2100 i=lbndi,ubndi
           arrhet(i)=dosehet(i,j,k)
2100       continue
          write(3,3100)(arrhet(i),i=lbndi,ubndi)
2200    continue

3000    format(' ',30(i2,1x))
3010    format(' ',25(f8.6,1x))
3020    format(25(f4.2,1x))
3060    format(f5.1)
3070    format(' ',f6.3)
3100    format(' ',25(f5.3,1x))

        stop
        end


        subroutine averdens

c An integral differential analyzer algorithm to find the average
```

```
c density along a path between the primary interaction and dose
c deposition voxels. The algorithm samples the density along
c regular increments along the path.

      integer i,j,k,deli,delj,delk,longest

      real ro(-25:25,-25:25,50),avdens,xinc,yinc,zinc
      real scale,denom

      common deli,delj,delk,i,j,k,ro,avdens

      if (deli .eq. 0 .and. delj .eq. 0 .and. delk .eq. 0) then
       avdens=ro(i,j,k)
       go to 200
      end if

c The longest dimension between the interaction and dose deposition
c sites is found.

      longest=jmax0(abs(deli),abs(delj),abs(delk))

c The increments in each direction between the sample points.

      xinc=floatj(deli)/floatj(longest)
      yinc=floatj(delj)/floatj(longest)
      zinc=floatj(delk)/floatj(longest)

c The weight of the interaction voxel in the average density can
c be varied for different dose deposition voxel locations.

      if (deli .eq. 0 .and. delj .eq. 0) then
       f=0.5
      else if(jnint(sqrt(floatj(deli*deli+delj*delj))) .eq. 1)then
       f=0.5
      else if(jnint(sqrt(floatj(deli*deli+delj*delj))) .eq. 2)then
       f=0.5
      else
       f=0.5
      end if

      avdens=0.0

      do 100 n=0,longest
        scale=0.5+f
        if (n .eq. 0) then
         avdens=avdens+ro(i+n*xinc,j+n*yinc,k+jnint(n*zinc))*f
        else if (n .eq. longest) then
         avdens=avdens+ro(i+n*xinc,j+n*yinc,k+jnint(n*zinc))*0.5
        else
         avdens=avdens+ro(i+n*xinc,j+n*yinc,k+jnint(n*zinc))
        end if

100   continue

      avdens=avdens/(floatj(longest-1)+scale)  !divide by the # of sample pts

200   continue

      return
      end
```

Appendix 12. Comparison of Heterogeneous Dose Spread Arrays Calculated by the Convolution Method and by the Monte Carlo Method

Table A

Δk \ Δi	-3	-2	-1	0	1	2	3	
0	-	-	.012	.329	.012	-	-	
	-	-	.012	.328	.011	-	-	$\rho = 1.0 g/cm^3$
1	-	.001	.034	.306	.034	.001	-	$\rho = 0.3 g/cm^3$
	-	.002	.035	.281	.035	.002	-	
2	-	.003	.032	.137	.032	.003	-	
	.001	.004	.033	.124	.033	.004	.001	
3	.001	.004	.024	.067	.024	.004	.001	
	.001	.005	.023	.061	.023	.004	.001	
4	.001	.005	.019	.038	.019	.005	.001	
	.002	.005	.017	.032	.016	.005	.002	
5	.002	.005	.013	.021	.013	.005	.002	
	.002	.005	.012	.018	.012	.005	.002	
6	.001	.004	.008	.012	.008	.004	.001	
	.002	.004	.008	.011	.008	.004	.002	

Upper Number Is Calculated From Homogeneous Dose Spread Arrays.
Lower Number Is From Monte Carlo Simulation Of The Heterogeneous Phantom.

Energy Conserved To -2.8%

Table B

Δk \ Δi	-3	-2	-1	0	1	2	3	
0	-	-	.012	.329	.012	-	-	
	-	-	.012	.327	.012	-	-	$\rho = 1.0 g/cm^3$
1	-	.002	.036	.320	.036	.002	-	$\rho = 0.2 g/cm^3$
	-	.003	.037	.290	.037	.003	-	
2	.001	.003	.038	.159	.038	.003	.001	
	.001	.005	.036	.135	.036	.005	.001	
3	.001	.005	.028	.081	.028	.005	.001	
	.002	.006	.028	.072	.028	.006	.002	
4	.002	.006	.023	.048	.023	.006	.002	
	.002	.006	.020	.041	.020	.006	.002	
5	.002	.005	.016	.029	.016	.005	.002	
	.002	.005	.014	.024	.014	.005	.002	
6	.002	.005	.011	.018	.011	.005	.002	
	.002	.005	.010	.015	.010	.005	.002	

Upper Number Is Calculated From Homogeneous Dose Spread Arrays.
Lower Number Is From Monte Carlo Simulation Of The Heterogeneous Phantom.

Energy Conserved To -1.3%

Table C

Δk \ Δi	-3	-2	-1	0	1	2	3	
0	-	-	.012	.329	.012	-	-	
	-	-	.012	.329	.011	-	-	
1	-	.001	.025	.239	.025	.001	-	
	-	.001	.025	.239	.025	.001	-	
								$\rho = 1.0 g/cm^3$
2	-	.002	.023	.086	.023	.002	-	$\rho = 0.3 g/cm^3$
	.001	.003	.021	.074	.021	.003	.001	
3	-	.003	.018	.044	.018	.003	-	
	.001	.004	.016	.032	.016	.004	.001	
4	.001	.003	.013	.023	.013	.003	.001	
	.001	.004	.010	.016	.010	.004	.001	
5	.001	.003	.007	.012	.007	.003	.001	
	.001	.003	.006	.008	.006	.003	.001	
6	.001	.002	.005	.007	.005	.002	.001	
	.001	.002	.004	.004	.004	.002	.001	

Upper Number Is Calculated From Homogeneous Dose Spread Arrays.
Lower Number Is From Monte Carlo Simulation Of The Heterogeneous Phantom.

Energy Conserved To -2.1%

Table D

Δk	Δi: -3	-2	-1	0	1	2	3	
0	-	-	.012	.329	.012	-	-	
	-	-	.012	.329	.011	-	-	
1	-	.001	.025	.239	.025	.001	-	
	-	.001	.025	.238	.025	.001	-	
2	-	.001	.020	.073	.020	.001	-	
	.001	.001	.020	.073	.020	.001	-	
3	-	.001	.011	.027	.011	.001	-	$\rho = 1.0 g/cm^3$
	-	.002	.010	.022	.010	.002	-	$\rho = 0.3 g/cm^3$
4	-	.002	.007	.013	.007	.002	-	
	-	.002	.005	.009	.005	.002	-	
5	-	.001	.004	.007	.004	.001	-	
	.001	.001	.003	.004	.003	.001	-	
6	.001	.001	.003	.004	.003	.001	-	
	.001	.001	.002	.002	.002	.001	.001	

Upper Number Is Calculated From Homogeneous Dose Spread Arrays.
Lower Number Is From Monte Carlo Simulation Of The Heterogeneous Phantom.

Energy Conserved To -0.9%

Table E

Δk	Δi	-3	-2	-1	0	1	2	3	
0		-	-	.012	.329	.012	-	-	
		-	-	.012	.330	.012	-	-	
1		-	.001	.025	.239	.025	.001	-	
		-	.001	.025	.239	.025	.001	-	
2		-	.001	.020	.073	.020	.001	-	
		-	.001	.020	.073	.020	.001	-	
3		-	.001	.008	.020	.008	.001	-	$\rho = 1.0 g/cm^3$
		-	.001	.008	.020	.008	.001	-	
4		-	.001	.004	.007	.004	.001	-	$\rho = 0.3 g/cm^3$
		-	.001	.003	.006	.004	.001	-	
5		-	.001	.003	.004	.003	.001	-	
		-	.001	.002	.003	.002	.001	-	
6		-	.001	.002	.002	.002	.001	-	
		-	.001	.001	.002	.001	.001	-	

Upper Number Is Calculated From Homogeneous Dose Spread Arrays.
Lower Number Is From Monte Carlo Simulation Of The Heterogeneous Phantom.

Energy Conserved To -0.2%

Table F

Δk \ Δi	-3	-2	-1	0	1	2	3	
0	-	-	.006	.143	.006	-	-	
	-	-	.006	.145	.006	-	-	$\rho = 0.3 g/cm^3$
1	-	-	.010	.092	.010	-	-	$\rho = 1.0 g/cm^3$
	-	-	.009	.100	.009	-	-	
2	-	.001	.007	.026	.007	.001	-	
	-	-	.007	.029	.007	-	-	
3	-	-	.003	.008	.003	-	-	
	-	-	.003	.009	.003	-	-	
4	-	-	.001	.002	.001	-	-	
	-	-	.001	.002	.001	-	-	
5	-	-	-	.001	-	-	-	
	-	-	-	.001	-	-	-	
6	-	-	-	-	-	-	-	
	-	-	-	-	-	-	-	

Upper Number Is Calculated From Homogeneous Dose Spread Arrays.
Lower Number Is From Monte Carlo Simulation Of The Heterogeneous Phantom.

Energy Conserved To +4.3%

Table G

Δk \ Δi	-3	-2	-1	0	1	2	3	
0	-	-	.006	.143	.006	-	-	
	-	-	.006	.144	.006	-	-	
1	-	.001	.014	.119	.014	.001	-	
	-	.001	.014	.118	.014	.001	-	
								$\rho = 0.3 g/cm^3$
2	-	.001	.010	.041	.010	.001	-	$\rho = 1.0 g/cm^3$
	-	-	.010	.050	.010	.001	-	
3	-	.001	.006	.013	.006	.001	-	
	-	-	.006	.019	.006	.001	-	
4	-	.001	.002	.004	.002	.001	-	
	-	-	.002	.005	.002	-	-	
5	-	-	.001	.001	.001	-	-	
	-	-	.001	.002	.001	-	-	
6	-	-	-	-	-	-	-	
	-	-	-	-	-	-	-	

Upper Number Is Calculated From Homogeneous Dose Spread Arrays.
Lower Number Is From Monte Carlo Simulation Of The Heterogeneous Phantom.

Energy Conserved To +7.9%

Table H

Δk	Δi	-3	-2	-1	0	1	2	3	
0		-	-	.012	.329	.012	-	-	
		-	-	.012	.329	.011	-	-	
1		-	.001	.025	.239	.025	.001	-	
		-	.001	.025	.239	.025	.001	-	$\rho = 1.0 g/cm^3$
2		-	.002	.024	.093	.024	.002	-	
		-	.006	.023	.074	.023	.007	-	$\rho = 0.001 g/cm^3$
3		-	.003	.018	.043	.018	.003	-	$\rho = 1.0 g/cm^3$
		.001	.004	.017	.034	.016	.004	.001	
4		-	.002	.007	.012	.007	.002	-	
		-	.002	.007	.012	.007	.002	-	
5		-	.001	.003	.004	.003	.001	-	
		-	.001	.003	.004	.003	.001	-	
6		-	-	.001	.001	.001		-	
		-	-	.001	.001	.00		-	

Upper Number Is Calculated From Homogeneous Dose Spread Arrays.
Lower Number Is From Monte Carlo Simulation Of The Heterogeneous Phantom.

Energy Conserved To -1.3%

Table I

Δk	Δi = -3	-2	-1	0	1	2	3	
0	-	-	.012	.329	.012	-	-	
	-	-	.012	.329	.011	-	-	
1	-	.001	.025	.239	.025	.001	-	
	-	.001	.025	.238	.025	.001	-	
2	-	.002	.024	.093	.024	.002	-	
	.001	.002	.020	.072	.020	.002	-	$\rho = 1.0 g/cm^3$
3	.001	.004	.022	.057	.022	.004	.001	
	.003	.005	.016	.033	.016	.005	.004	$\rho = 0.001 g/cm^3$
4	.001	.004	.014	.027	.014	.004	.001	
	.001	.004	.012	.019	.012	.004	.001	
5	-	.002	.005	.008	.005	.002	-	$\rho = 1.0 g/cm^3$
	.001	.002	.005	.008	.005	.002	.001	
6	-	.001	.002	.003	.002	.001	-	
	-	.001	.002	.003	.002	.001	-	

Upper Number Is Calculated From Homogeneous Dose Spread Arrays.
Lower Number Is From Monte Carlo Simulation Of The Heterogeneous Phantom.

Energy Conserved To -1.5%

Table A

Δk \ Δi	-3	-2	-1	0	1	2	3	
0	-	-	.012	.329	.012	-	-	
	-	-	.012	.328	.011	-	-	$\rho = 1.0 g/cm^3$
1	-	.001	.033	.283	.033	.001	-	$\rho = 0.3 g/cm^3$
	-	.002	.035	.281	.035	.002	-	
2	-	.003	.031	.118	.031	.003	-	
	.001	.004	.033	.124	.033	.004	.001	
3	.001	.004	.023	.059	.023	.004	.001	
	.001	.005	.023	.061	.023	.004	.001	
4	.001	.005	.018	.032	.018	.005	.001	
	.002	.005	.017	.032	.016	.005	.002	
5	.002	.005	.013	.018	.013	.005	.002	
	.002	.005	.012	.018	.012	.005	.002	
6	.001	.004	.008	.011	.008	.004	.001	
	.002	.004	.008	.011	.008	.004	.002	

Upper Number Is Calculated From Homogeneous Dose Spread Arrays.
Lower Number Is From Monte Carlo Simulation Of The Heterogeneous Phantom.

Energy Conserved To 0.6%

Table B

Δk \ Δi	-3	-2	-1	0	1	2	3	
0	-	-	.012	.329	.012	-	-	
	-	-	.012	.327	.012	-	-	$\rho = 1.0 g/cm^3$
1	-	.002	.035	.290	.035	.002	-	$\rho = 0.2 g/cm^3$
	-	.003	.037	.290	.037	.003	-	
2	.001	.003	.035	.131	.035	.003	.001	
	.001	.005	.036	.135	.036	.005	.001	
3	.001	.005	.027	.068	.027	.005	.001	
	.002	.006	.028	.072	.028	.006	.002	
4	.002	.006	.022	.040	.022	.006	.002	
	.002	.006	.020	.041	.020	.006	.002	
5	.002	.005	.015	.024	.015	.005	.002	
	.002	.005	.014	.024	.014	.005	.002	
6	.002	.005	.011	.015	.011	.005	.002	
	.002	.005	.011	.015	.010	.005	.002	

Upper Number Is Calculated From Homogeneous Dose Spread Arrays.
Lower Number Is From Monte Carlo Simulation Of The Heterogeneous Phantom.

Energy Conserved to 0.3%

Table C

Δk \ Δi	-3	-2	-1	0	1	2	3	
0	-	-	.012	.329	.012	-	-	
	-	-	.012	.329	.011	-	-	
1	-	.001	.025	.239	.025	.001	-	
	-	.001	.025	.239	.025	.001	-	
								$\rho = 1.0 g/cm^3$
2	-	.002	.023	.084	.023	.002	-	$\rho = 0.3 g/cm^3$
	.001	.003	.021	.074	.021	.003	.001	
3	-	.003	.018	.041	.018	.003	-	
	.001	.004	.016	.032	.016	.004	.001	
4	.001	.003	.012	.021	.012	.003	.001	
	.001	.004	.010	.016	.010	.004	.001	
5	.001	.003	.007	.010	.007	.003	.001	
	.001	.003	.006	.008	.006	.003	.001	
6	.001	.002	.005	.006	.005	.002	.001	
	.001	.002	.004	.004	.004	.002	.001	

Upper Number Is Calculated From Homogeneous Dose Spread Arrays.
Lower Number Is From Monte Carlo Simulation Of The Heterogeneous Phantom.

Energy Conserved To -1.6%

Table D

Δk \ Δi	-3	-2	-1	0	1	2	3	
0	-	-	.012	.329	.012	-	-	
	-	-	.012	.329	.011	-	-	
1	-	.001	.025	.239	.025	.001	-	
	-	.001	.025	.238	.025	.001	-	
2	-	.001	.020	.073	.020	.001	-	
	.001	.001	.020	.073	.020	.001	-	$\rho = 1.0 g/cm^3$
3	-	.001	.011	.026	.011	.001	-	$\rho = 0.3 g/cm^3$
	-	.002	.010	.022	.010	.002	-	
4	-	.002	.007	.012	.007	.002	-	
	-	.002	.005	.009	.005	.002	-	
5	-	.001	.004	.006	.004	.001	-	
	.001	.001	.003	.004	.003	.001	-	
6	.001	.001	.003	.003	.003	.001	-	
	.001	.001	.002	.002	.002	.001	.001	

Upper Number Is Calculated From Homogeneous Dose Spread Arrays.
Lower Number Is From Monte Carlo Simulation Of The Heterogeneous Phantom.

Energy Conserved To -0.7%

Table E

Δk \ Δi	-3	-2	-1	0	1	2	3	
0	-	-	.012	.329	.012	-	-	
	-	-	.012	.330	.012	-	-	
1	-	.001	.025	.239	.025	.001	-	
	-	.001	.025	.239	.025	.001	-	
2	-	.001	.020	.073	.020	.001	-	
	-	.001	.020	.073	.020	.001	-	
3	-	.001	.008	.020	.008	.001	-	
	-	.001	.008	.020	.008	.001	-	$\rho = 1.0 g/cm^3$
4	-	.001	.004	.007	.004	.001	-	$\rho = 0.3 g/cm^3$
	-	.001	.003	.006	.004	.001	-	
5	-	.001	.003	.004	.003	.001	-	
	-	.001	.002	.003	.002	.001	-	
6	-	.001	.002	.002	.002	.001	-	
	-	.001	.001	.002	.001	.001	-	

Upper Number Is Calculated From Homogeneous Dose Spread Arrays.
Lower Number Is From Monte Carlo Simulation Of The Heterogeneous Phantom.

Energy Conserved To -0.2%

Table F

Δk \ Δi	-3	-2	-1	0	1	2	3	
0	-	-	.006	.143	.006	-	-	
	-	-	.006	.145	.006	-	-	$\rho = 0.3 g/cm^3$
1	-	-	.011	.098	.011	-	-	$\rho = 1.0 g/cm^3$
	-	-	.009	.100	.009	-	-	
2	-	.001	.007	.028	.007	.001	-	
	-	-	.007	.029	.007	-	-	
3	-	-	.004	.097	.004	-	-	
	-	-	.003	.091	.003	-	-	
4	-	-	.001	.003	.001	-	-	
	-	-	.001	.002	.001	-	-	
5	-	-	-	.001	-	-	-	
	-	-	-	.001	-	-	-	
6	-	-	-	-	-	-	-	
	-	-	-	-	-	-	-	

Upper Number Is Calculated From Homogeneous Dose Spread Arrays.
Lower Number Is From Monte Carlo Simulation Of The Heterogeneous Phantom.

Energy Conserved To -1.3%

Table G

Δk \ Δi	-3	-2	-1	0	1	2	3
0	-	-	.006	.143	.006	-	-
	-	-	.006	.144	.006	-	-
1	-	.001	.014	.119	.014	.001	-
	-	.001	.014	.118	.014	.001	-
							$\rho = 0.3 g/cm^3$
							$\rho = 1.0 g/cm^3$
2	-	.001	.010	.043	.010	.001	-
	-	-	.010	.050	.010	.001	-
3	-	.001	.006	.014	.006	.001	-
	-	-	.006	.019	.006	.001	-
4	-	.001	.002	.004	.002	.001	-
	-	-	.002	.005	.002	-	-
5	-	-	.001	.001	.001	-	-
	-	-	.001	.002	.001	-	-
6	-	-	-	-	-	-	-
	-	-	-	-	-	-	-

Upper Number Is Calculated From Homogeneous Dose Spread Arrays.
Lower Number Is From Monte Carlo Simulation Of The Heterogeneous Phantom.

Energy Conserved To +5.5%

Table H

Δk \ Δi	-3	-2	-1	0	1	2	3	
0	-	-	.012	.329	.012	-	-	
	-	-	.012	.329	.011	-	-	
1	-	.001	.025	.239	.025	.001	-	
	-	.001	.025	.239	.025	.001	-	$\rho = 1.0 g/cm^3$
2	-	.002	.024	.089	.024	.002	-	
	-	.006	.023	.074	.023	.007	-	$\rho = 0.001 g/cm^3$
3	-	.003	.017	.040	.017	.003	-	$\rho = 1.0 g/cm^3$
	.001	.004	.017	.034	.016	.004	.001	
4	-	.002	.006	.011	.006	.002	-	
	-	.002	.007	.012	.007	.002	-	
5	-	.001	.003	.004	.003	.001	-	
	-	.001	.003	.004	.003	.001	-	
6	-	-	.001	.001	.001	-	-	
	-	-	.001	.001	.001	-	-	

Upper Number Is Calculated From Homogeneous Dose Spread Arrays.
Lower Number Is From Monte Carlo Simulation Of The Heterogeneous Phantom.

Energy Conserved To -0.6%

Table I

Δk \ Δi	-3	-2	-1	0	1	2	3	
0	-	-	.012	.329	.012	-	-	
	-	-	.012	.329	.011	-	-	
1	-	.001	.025	.239	.025	.001	-	
	-	.001	.025	.238	.025	.001	-	
2	-	.002	.024	.093	.024	.002	-	
	.001	.002	.020	.072	.020	.002	-	
3	.001	.004	.022	.052	.022	.004	.001	$\rho = 1.0 g/cm^3$
	.003	.005	.016	.033	.016	.005	.004	
4	.001	.004	.014	.024	.014	.004	.001	$\rho = 0.001 g/cm^3$
	.001	.004	.012	.019	.012	.004	.001	
5	-	.002	.005	.007	.005	.002	-	$\rho = 1.0 g/cm^3$
	.001	.002	.005	.008	.005	.002	.001	
6	-	.001	.002	.002	.002	.001	-	
	-	.001	.002	.003	.002	.001	-	

Upper Number Is Calculated From Homogeneous Dose Spread Arrays.
Lower Number Is From Monte Carlo Simulation Of The Heterogeneous Phantom.

Energy Conserved To -0.8%

VITA

NAME: Thomas Rockwell Mackie

PLACE OF BIRTH: Eston, Saskatchewan, Canada

YEAR OF BIRTH: 1954

POST-SECONDARY EDUCATION AND DEGREES:

University of Saskatchewan
Saskatoon, Saskatchewan
1974-1978, 1979
B.Sc.(Honors) in Physics 1980

HONOURS AND AWARDS:

Alberta Heritage Foundation for Medical Research Studentship
1981-1984

First Prize, Young Investigators' Symposium
New York, 1983

RELATED WORK EXPERIENCE:

Assistant to Radiation Consultant
University of Saskatchewan
1977

Laboratory Assistant
University of Saskatchewan
1977-1980

Radiation Physicist
Keith Consulting Engineers
1978-1979

Radiation Consultant
1979-1980

Laboratory Assistant
University of Alberta
1980-1984

Summer Research Assistant
Cross Cancer Institute
1981

PUBLICATIONS:

The following was a critique solicited by the Cluff Lake Board of Inquiry chaired by Justice Bayda and delivered to the Inquiry in Regina, Saskatchewan, July 1977:

1. Review of "Appendix C, Radiological Health and Safety", Caplan, H., Mackie, T.R.

The following were published under the auspices of the Atomic Energy Control Board of Canada under the aegis of the Federal-Provincial Task Force on Radioactivity:

1. Mackie, T.R., "Reducing Airborne Radiation in Dwellings using Make-Up Air Ventilation", March 1979.

2. Crilly, R., Mackie, T.R., Haubrich, E.J.J., "A Study of Air Exchange Rates in Dwellings using SF_6 as a Tracer Gas", May 1980.

3. Crilly, R., Mackie, T.R., "Air Make-Up Units for Reducing Radiological Levels", May 1980.

The following article is reprinted in Appendix 9:

1. Mackie, T.R., Scrimger, J.W., "Contamination of a 15 MV Photon Beam by Electrons and Scattered Photons", Radiology, 144, 403-409, July 1982.

The following articles appeared in the proceedings of "The Eighth International Conference on the Use of Computers in Radiation Therapy", July 1984:

1. Mackie, T.R., Scrimger, J.W., "Computing Radiation Dose for High Energy X-rays using a Convolution Method".

2. Battista, J.J., Mackie, T.R., El-Khatib, E., Scrimger, J.W., "Lung Dose Corrections for 6 MV and 15 MV X-rays: Anomolies".

3. Mackie, T.R., Battista, J.J., "A Macroscopic Monte Carlo Method for Electron Beam Dose Calculations: A Proposal".

The following articles have been submitted to the journal, "Medical Physics":

1. Mackie, T.R., Scrimger, J.W., Battista, J.J., "A Convolution Method of Calculating Dose for 15 MV X-rays".

2. Mackie, T.R., El-Khatib, E., Battista, J.J., Scrimger, J.W., Van Dyk, J., Cunningham, J.R., "Lung Dose Corrections for 6 MV and 15 MV X-rays".